UNCLASSIFIED

AD NUMBER: AD0847113
LIMITATION CHANGES
TO:
Approved for public release; distribution is unlimited.
FROM:
Distribution authorized to US Government Agencies and their Contractors; Export Control; 1 Dec 1968. Other requests shall be referred to Air Force Flight Test Center, Edwards AFB, CA, 93523.
AUTHORITY
AFRPL ltr dtd 27 Oct 1971

THIS PAGE IS UNCLASSIFIED

AFRPL-TR-68-166-Vol II

Copy No. 19

AD847113

HOT GAS SECONDARY INJECTION THRUST VECTOR CONTROL DEMONSTRATION PROGRAM

PROGRAM FINAL REPORT

VOLUME II

Carver G. Kennedy, Manager,
Large Motor Programs

Roy T. Minert, Project Engineer

D. Morley Cox, Valve Engineer

DECEMBER 1968

DDC
RECEIVED
FEB 4 1969
D

HEADQUARTERS
AIR FORCE FLIGHT TEST CENTER
AIR FORCE SYSTEMS COMMAND
Edwards Air Force Base, California

382

AFRPL-TR-68-166-Vol II

HOT GAS SECONDARY INJECTION THRUST VECTOR CONTROL DEMONSTRATION PROGRAM

PROGRAM FINAL REPORT

VOLUME II

Carver G. Kennedy, Manager,
Large Motor Programs

Roy T. Minert, Project Engineer

D. Morley Cox, Value Engineer

DECEMBER 1968

STATEMENT #2 UNCLASSIFIED

This document is subject to special export controls and each transmittal to foreign governments or foreign nationals may be made only with prior approval of "AFRPL (RPPR-STINFO) EDWARDS, CALIF. 93523

Prepared by

THIOKOL CHEMICAL CORPORATION
WASATCH DIVISION
Brigham City, Utah

Publications No. 0169-20226

ACCESSION for
WHITE SECTION
DISTRIBUTION/AVAILABILITY CODES
AVAIL. and/or SPECIAL
2

SPECIAL NOTICES

This document is subject to special export controls and each transmittal to foreign governments or foreign nationals may be made only with prior approval of AFRPL (RPPR-STINFO), Edwards, California.

FOREWORD

The Hot Gas Secondary Injection Thrust Vector Control Program, Project No. 623A, was conducted under Contract AF 04(611)-11408 by Thiokol Chemical Corporation, Wasatch Division, Brigham City, Utah. The Air Force Project Officer was Capt. Dan Stump, RPMC. The program was started in February 1966 and completed in September 1968. The report, which was submitted in January 1969, contains no classified information extracted from other classified documents. The secondary report number is 1268-20226.

This technical report has been reviewed and is approved.

UNCLASSIFIED ABSTRACT

This program was established by the Air Force and Thiokol Chemical Corporation to design, develop, and demonstrate a hot gas secondary injection thrust vector control system (HGSITVC) for large solid propellant rocket motors. The program was initiated in February 1966. Phase I of the program was the design, analysis, and optimization of a 156 in. diameter motor HGSITVC system. The data from this baseline design was used to design four test pintle valves for demonstration on 65 in. diameter test motors. Phase II consisted of designing a four valve, 120 in. diameter motor HGSITVC system using the basic designs and design data developed under Phase I. The 120 in. diameter test motor demonstrated four full scale 156 in. diameter motor pintle valves. The 156 in. diameter motor uses 16 pintle valves of the design tested.

TABLE OF CONTENTS

		Page
I	INTRODUCTION AND SUMMARY	1
	A. Introduction	1
	B. Summary	2
II	DESIGN, FABRICATION, AND POST-TEST EVALUATION	9
	A. Design	9
	B. Fabrication	12
	C. Post-Test Evaluation	15
	1. Hardware Examination	15
	2. Port Performance	17
	3. Photographic Coverage	20
	4. Instrumentation Data	33
	5. Fabrication Data	35
	6. Summary	43
III	FAILURE ANALYSIS	101
	A. Aerodynamic Analysis	104
	1. Literature Survey	104
	2. Theoretical Flow Conditions in Valve Closed Cavity	118
	3. Cold Flow Test Study in Valve Closed Cavity	125
	4. Orifice Motor Test Data Correlation	128
	5. Erosion Effect on Cavity Flow	130
	6. Valve Open Flow	133
	B. Thermodynamic Analysis	134
	1. Orifice Port	134
	2. Valve Legs	137
	C. Stress Analysis	139
	1. Method of Analysis	139
	2. Literature Survey	144
	3. Discussion	151
	4. Throat Subassembly Movement	165

TABLE OF CONTENTS (Cont)

		Page
IV	CONCLUSIONS AND RECOMMENDATIONS	311
	A. Conclusions	314
	B. Recommendations	316
	1. Orifice Redesign	316
	2. Current Material Technology	319
	3. Alternative Designs	320
	4. Preliminary Analysis	326
	5. Final Selection	329

LIST OF ILLUSTRATIONS

Figure		Page
1	TU-520.04 Current Orifice Design	5
2	Improved Orifice Design	7
3	Orifice Port 3 Load Conditions	44
4	Pretest Machined Orifice Port 3 Inlet	45
5	Pintle Valve Assembly 3 Orifice Port	46
6	Nozzle-Orifice-Valve Assembly 1 and 2	47
7	Orifice Ports 1 and 4 in Nozzle Exit Cone	48
8	Four Orifice Ports in Nozzle Exit Cone	49
9	Nozzle-Orifice-Valve Aft Closure Assembly	50
10	Post-Test Orifice Valve 1	51
11	Valve 1 After Test	52
12	Valve and Orifice 1 After Test	53
13	External View of Nozzle Submerged Section and Valve 1	54
14	Nozzle-Orifice Ports Erosion at Exit Cone	55
15	Orifice Ports 1 and 2 Erosion	56
16	Post-Test Nozzle Exit Cone, Port Orifice 1	57
17	Post-Test Pintle Orifice, Port 1	58
18	Port 1 Nozzle Burnthrough	59

LIST OF ILLUSTRATIONS (Cont)

Figure		Page
19	Nozzle-Case Closure Burnthrough	60
20	Nozzle Burnthrough, Ports 2, 3, and 4	61
21	Submerged Nozzle Cross Section at Port 1	62
22	Port 1 Cross Section	63
23	Submerged Nozzle Cross Section 45 Deg Away From Port 1	64
24	Port 1 Graphite - Inlet Face	65
25	Port 1 Carbon Cloth Insulation Sleeve - Inlet Face	66
26	Port 1 Tungsten Throat and Retention Nut - Exit Cone Face	67
27	Port Inlet Graphite Ring Segments	68
28	Port Exit Cone PTB Ring Segments	69
29	Port Exit Cone PTB Ring and Layer Segments	70
30	Post-Test Port Components	71
31	Port 2 Tungsten Throat	72
32	Port 3 Tungsten Throat	73
33	Orifice Port 1 Erosion (0 to 180 Deg Plane)	75
34	Orifice Port 1 Erosion (90 to 270 Deg Plane)	77
35	Orifice Port 2 Erosion	79
36	Orifice Port 3 Erosion	81
37	Orifice Port 4 Erosion	83

LIST OF ILLUSTRATIONS (Cont)

Figure		Page
38	Camera 8 Speed vs Film Length and Firing Time	85
39	Motion Picture Analysis, Cameras 6 thru 8	86
40	Motion Picture Analysis, Cameras 1 thru 4	87
41	Valve-Orifice Interface Location and Chamber Pressure vs Time	88
42	Valve-Orifice Interface Location vs Time, at 0 to 16 Sec	89
43	TU-521.02 Motor Orifice-Valve Interface and Chamber Pressure vs Time	90
44	Orifice 3 Components	91
45	Orifice 3 Throat Subassembly - Forward View	92
46	Orifice 3 Throat Subassembly - Aft View	93
47	Orifice Tungsten Photomicrographs - Specimen Location	94
48	Orifice Tungsten Photomicrographs - Specimen 1	95
49	Orifice Tungsten Photomicrographs - Specimen 2	96
50	Orifice Tungsten Photomicrographs - Specimen 3	97
51	Orifice Tungsten Photomicrographs - Specimen 4	98
52	Orifice Tungsten Photomicrographs - Specimen 5	99
53	Orifice Tungsten Photomicrographs - Specimen 6	100
54	Orifice 3 Common Element Grid	168

LIST OF ILLUSTRATIONS (Cont)

Figure		Page
55	Plane of Gas Flow Conditions for Thermal Analysis	169
56	Nozzle Wall Mach Number	170
57	Nozzle Wall Pressure Ratio and Heat Transfer Coefficient	171
58	Flow in the Cavity	172
59	Stagnation Point Pressure and Mach Number Gradients	173
60	Mach Number vs Axial Location, Closed Cavity	174
61	Port h/cp vs Axial Location, at 0 Sec, Port Open and Closed	175
62	Pintle Valve h/cp vs Axial Location, Port Closed	176
63	Cold Flow Test Model and Pressure Probe Locations	177
64	Orifice Smear Photo, Perpendicular to Centerline	178
65	Orifice Smear Photo, Perpendicular to Centerline	179
66	Orifice Smear Photo, Perpendicular to Centerline	180
67	Orifice Smear Photo, Perpendicular to Centerline	181
68	Orifice Smear Photo, Perpendicular to Centerline	182
69	Orifice Smear Photo, Perpendicular to Centerline	183
70	Orifice Smear Photo, Perpendicular to Centerline	184
71	Orifice Smear Photo, Perpendicular to Centerline	185
72	Orifice Smear Photo, Perpendicular to Centerline	186

LIST OF ILLUSTRATIONS (Cont)

Figure		Page
73	Orifice Smear Photo, Perpendicular to Centerline	187
74	Orifice Smear Photo, Perpendicular to Centerline	188
75	Orifice Smear Photo, Perpendicular to Centerline	189
76	Orifice Smear Photo, Perpendicular to Wall	190
77	Orifice Smear Photo, Perpendicular to Wall	191
78	Orifice Smear Photo, Perpendicular to Wall	192
79	Orifice Smear Photo, Perpendicular to Wall	193
80	Orifice Smear Photo, Perpendicular to Wall	194
81	Orifice Smear Photo, Perpendicular to Wall	195
82	Orifice Smear Photo, Perpendicular to Wall	196
83	Cold Flow Pressure Data, Bottom of Cavity	197
84	Cold Flow Pressure Ratio Data, Bottom of Cavity	198
85	Orifice Smear Pattern, Perpendicular to Centerline, for PTB Missing	199
86	Orifice Smear Pattern, Perpendicular to Centerline, for PTB Missing	200
87	Orifice Smear Pattern, Perpendicular to Centerline, for PTB Missing	201
88	Orifice Smear Pattern, Perpendicular to Centerline, for PTB Missing	202

LIST OF ILLUSTRATIONS (Cont)

Figure		Page
89	Orifice Smear Pattern, Perpendicular to Centerline, for PTB Missing	203
90	Orifice Smear Pattern, Perpendicular to Centerline, for PTB Missing	204
91	Summary of Cavity Flow Patterns	205
92	TU-453 Orifice Erosion Data, Port 3	206
93	Orifice Wall h/cp vs Axial Locadon at 16 Sec - Final	207
94	Orifice Wall h/cp vs Axial Location at 16 Sec - Preliminary	208
95	Orifice Wall h/cp vs Axial Location at 25 Sec - Final	209
96	Orifice Wall h/cp vs Axial Location at 25 Sec - Preliminary	210
97	Orifice Wall Pressure Ratio and Mach Number - Port Open	211
98	Downstream Nozzle Wall h/cp vs Axial Location - Port Open and Closed	212
99	Injection Flow Conditions in the Nozzle	213
100	Upstream Nozzle Wall h/cp vs Axial Location - Port Open	214
101	Inlet h/cp vs Axial Location - Port Open	215

LIST OF ILLUSTRATIONS (Cont)

Figure		Page
102	Preliminary Thermal Gradients - Element Material Identification	216
103	Preliminary Upstream and Downstream Thermal Gradients at 5 Sec	217
104	Preliminary Upstream and Downstream Thermal Gradients at 16.0 Sec	219
105	Preliminary Upstream and Downstream Thermal Gradients at 16.1 Sec	221
106	Preliminary Upstream and Downstream Thermal Gradients at 25.0 Sec	223
107	Preliminary Upstream and Downstream Thermal Gradients at 25.1 Sec	225
108	Final Thermal Gradients - Element Material Identification	227
109	Final Downstream Thermal Gradients at 5 Sec	228
110	Final Downstream Thermal Gradients at 16.0 Sec	229
111	Final Downstream Thermal Gradients at 16.1 Sec	230
112	Final Downstream Thermal Gradients at 25.0 Sec	231
113	Final Thermal Gradients, Downstream at 25.1 Sec	232
114	h/cp on Seat Between Legs	233
115	h/cp Around Support Leg	234
116	Final Thermal Gradients, Element Material Identification - Legs	235
117	Leg Thermal Gradients at 5.0 Sec	236

LIST OF ILLUSTRATIONS (Cont)

Figure		Page
118	Leg Thermal Gradient at 16.0 Sec	237
119	Leg Thermal Gradient at 16.1 Sec	238
120	Leg Thermal Gradient at 25.0 Sec	239
121	Leg Thermal Gradient at 25.1 Sec	240
122	TU-520 HGSITVC Nozzle Section Analyzed	241
123	Orifice Port Boundary Conditions at 5 Sec, Valve Closed	242
124	Orifice Port Boundary Conditions at 25.0 Sec, Valve Open	243
125	Orifice Port Boundary Conditions at 25.1 Sec, Valve Closed	244
126	Graphite 90 CTE, E, Poisson's Ratio vs Temperature	245
127	Graphite 90 Ultimate Compressive Strength vs Temperature	246
128	Graphite 90 Ultimate Tensile Strength vs Temperature	247
129	Graphite 90 Ultimate Shear Strength vs Temperature	248
130	Tungsten CTE, E, Poisson's Ratio vs Temperature	249
131	Two Percent Thoria-98% Tungsten, Stress-Strain Curves at Temperature	250
132	Two Percent Thoria-98% Tungsten, at 25 Sec Modulus vs Temperature	251
133	Two Percent Thoria-98% Tungsten, at 25 Sec Modulus vs Stress	252

LIST OF ILLUSTRATIONS (Cont)

Figure		Page
134	Tungsten, Ultimate and Yield Strength vs Temperature	253
135	Tungsten, Ultimate Shear Strength	254
136	Pyrolytic Graphite, CTE, E, Poisson's Ratio vs Temperature, Tension Loaded	255
137	Pyrolytic Graphite, CTE, E, Poisson's Ratio vs Temperature, Compression Loaded	256
138	Pyrolytic Graphite, Ultimate Tensile, Compressive, Shear Strength vs Temperature (NG)	257
139	Pyrolytic Graphite, Ultimate Tensile, Compressive, Shear Strength vs Temperature (AG)	258
140	PTB CTE, Poisson's Ratio, E vs Temperature..........	259
141	PTB Ultimate Tensile, Compressive and Shear Strength vs Temperature.........................	260
142	PTB Revised, Ultimate Tensile, Compressive and Shear Strength vs Temperature	261
143	Carbon Cloth Phenolic, CTE, Poisson's Ratio, E vs Temperature - Compressive	262
144	Carbon Cloth Phenolic, CTE, Poisson's Ratio, E vs Temperature - Tensile	263
145	Carbon Cloth Phenolic, Ultimate Strength vs Temperature	264
146	Glass Cloth Phenolic, CTE, Modulus, Poisson's Ratio vs Temperature	265
147	Glass Cloth Phenolic, Ultimate Tensile, Compressive, Shear Strength vs Temperature	266

LIST OF ILLUSTRATIONS (Cont)

Figure		Page
148	4130 Steel, CTE, Modulus, Poisson's Ratio vs Temperature	267
149	4130 Steel, Ultimate Strength vs Temperature	268
150	Neoprene Rubber, CTE, Poisson's Ratio, Modulus vs Temperature	269
151	Epon 913 and 934, Typical Tensile-Shear Strength vs Temperature	270
152	Boundary Condition A, Radial Stress at 5.0 Sec, Valve Closed	271
153	Boundary Condition A, Axial Stress at 5.0 Sec, Valve Closed	272
154	Boundary Condition A, Hoop Stress at 5.0 Sec, Valve Closed	273
155	Boundary Condition A, Shear Stress at 5.0 Sec, Valve Closed	274
156	Boundary Condition A, Radial Displacements at 5.0 Sec, Valve Closed	275
157	Boundary Condition A, Axial Displacements at 5.0 Sec, Valve Closed	276
158	Boundary Condition A, Radial Stress at 25.0 Sec, Valve Open	277
159	Boundary Condition A, Axial Stress at 25.0 Sec, Valve Open	278
160	Boundary Condition A, Hoop Stress at 25.0 Sec, Valve Open	279

LIST OF ILLUSTRATIONS (Cont)

Figure		Page
161	Boundary Condition A, Shear Stress at 25.0 Sec, Valve Open	280
162	Boundary Condition A, Radial Displacements at 25.0 Sec, Valve Open	281
163	Boundary Condition A, Axial Boundary Displacements at 25.0 Sec, Valve Open	282
164	Boundary Condition A, Radial Stress at 25.1 Sec, Valve Closed	283
165	Boundary Condition A, Axial Stress at 25.1 Sec, Valve Closed	284
166	Boundary Condition A, Hoop Stress at 25.1 Sec, Valve Closed	285
167	Boundary Condition A, Shear Stress at 25.1 Sec, Valve Closed	286
168	Boundary Condition A, Radial Displacements at 25.1 Sec, Valve Closed	287
169	Boundary Condition A, Axial Boundary Displacements at 25.1 Sec, Valve Closed	288
170	Boundary Condition B, Radial Stress at 5.0 Sec, Valve Closed	289
171	Boundary Condition B, Axial Stress at 5.0 Sec, Valve Closed	290
172	Boundary Condition B, Hoop Stress at 5.0 Sec, Valve Closed	291
173	Boundary Condition B, Shear Stress at 5.0 Sec, Valve Closed	292

LIST OF ILLUSTRATIONS (Cont)

Figure		Page
174	Boundary Condition B, Radial Displacements at 5.0 Sec, Valve Closed	293
175	Boundary Condition B, Axial Displacements at 5.0 Sec, Valve Closed	294
176	Boundary Condition B, Radial Stress at 25.1 Sec, Valve Closed	295
177	Boundary Condition B, Axial Stress at 25.1 Sec, Valve Closed	296
178	Boundary Condition B, Hoop Stress at 25.1 Sec, Valve Closed	297
179	Boundary Condition B, Shear Stress at 25.1 Sec, Valve Closed	298
180	Boundary Condition B, Radial Displacements at 25.1 Sec, Valve Closed	299
181	Boundary Condition B, Axial Displacements at 25.1 Sec, Valve Closed	300
182	TU-520 HGSITVC, Overstressed Areas, Boundary Condition A at 5.0 Sec	301
183	TU-520 HGSITVC, Overstressed Areas, Boundary Condition A at 25.0 Sec	302
184	TU-520 HGSITVC, Overstressed Areas, Boundary Condition A at 25.1 Sec	303
185	TU-520 HGSITVC, Overstressed Areas, Boundary Condition B at 5.0 Sec	304
186	TU-520 HGSITVC, Overstressed Areas, Boundary Condition B at 25.1 Sec	305

LIST OF ILLUSTRATIONS (Cont)

Figure		Page
187	TU-520 HGSITVC Orifice Displacements, Boundary Condition A at 5.0 Sec	306
188	TU-520 HGSITVC Orifice Displacements, Boundary Condition A at 25.0 Sec	307
189	TU-520 HGSITVC Orifice Displacements, Boundary Condition A at 25.1 Sec	308
190	TU-520 HGSITVC Orifice Displacements, Boundary Condition B at 5.0 Sec	309
191	TU-520 HGSITVC Orifice Displacements, Boundary Condition B at 25.1 Sec	310
192	Alternative Orifice Design 1	339
193	Alternative Orifice Design 2	340
194	Alternative Orifice Design 3	341
195	Alternative Orifice Design 4	342
196	Alternative Orifice Design 5	343
197	Alternative Orifice Design 6	344
198	Alternative Orifice Design 7	345
199	Alternative Orifice Design 8	346
200	Alternative Orifice Design 9	347
201	Alternate Orifice Design 2, Material Callouts	348
202	Alternate Orifice Design 2, Thermal Gradients at 5.0 Sec	349

LIST OF ILLUSTRATIONS (Cont)

Figure		Page
203	Alternate Orifice Design 2, Thermal Gradients at 16.0 Sec	350
204	Alternate Orifice Design 2, Thermal Gradients at 16.1 Sec	351
205	Alternate Orifice Design 2, Thermal Gradients at 25.0 Sec	352
206	Alternate Orifice Design 2, Thermal Gradients at 25.1 Sec	353
207	Present and Modified Orifice Design, Temperature Profile, Section A-A at 25.1 Sec	354
208	Present and Modified Orifice Design, Hoop Stress Profile, Section A-A at 25.1 Sec	355
209	Present Design, Overstressed Material, Section A-A at 25.1 Sec	356
210	Modified Design, Overstressed Material, Section A-A at 25.1 Sec	357
211	Present and Modified Orifice Design, Temperature Profile, Section B-B at 25.1 Sec	358
212	Present and Modified Orifice Design, Hoop Stress Profile, Section B-B at 25.1 Sec	359
213	Present Design, Overstressed Material, Section B-B at 25.1 Sec	360
214	Modified Design, Overstressed Material, Section B-B at 25.1 Sec	361

LIST OF TABLES

Table		Page
I	Material Design Summary	3
II	Material Suppliers and Fabricators	13
III	Orifice Port Performance Summary	19
IV	Camera 6 Bright Objects	21
V	Camera 7 Bright Objects	22
VI	Camera 8 Bright Objects	25
VII	Camera 1 Bright Objects	28
VIII	Camera 2 Bright Objects	29
IX	Camera 3 Bright Objects	30
X	Camera 4 Bright Objects	31
XI	Orifice Assembly Material Review	37
XII	Nozzle Material Review	38
XIII	Orifice Material Tests	40
XIV	Orifice Material Tests of Graphite 90 Inlet	41
XV	Hot Gas Valve 120 In. Real Gas Flow Conditions - Nozzle Exit Cone	119
XVI	Cold Flow Pressure Data, Bottom of Cavity	127
XVII	Orifice 3 Performance at 21 to 23 Sec, Open Duty Cycle	132
XVIII	Orifice Equivalent Steel Load at Boundary Condition	143

LIST OF TABLES (Cont)

Table		Page
XIX	Downstream Orifice Throat - 2 Percent Thoria Tungsten	154
XX	Downstream Orifice Inlet - Graphite 90	155
XXI	Downstream Orifice Retention Nut - 20 Percent Copper - Tungsten	156
XXII	Downstream Orifice Forward Exit Cone - Pyrolytic Graphite	157
XXIII	Downstream Orifice Aft Exit Cone - PTB	158
XXIV	Other Orifice and Support Materials	159
XXV	Orifice Problems and Solutions	317
XXVI	Original Orifice and Alternate Design 2 Temperature Comparisons at 5, 16, and 25 Sec	327
XXVII	Material Properties of Candidate Orifice Erosion Liners	331
XXVIII	Orifice Inlet Materials - Comparison by Predicted Erosion	333
XXIX	Orifice Exit Materials - Comparison by Predicted Erosion	335

SECTION I

INTRODUCTION AND SUMMARY

A. INTRODUCTION

An orifice evaluation analysis and redesign effort was undertaken to show why three of the Hot Gas SITVC orifice ports failed during the test of the 120 in. TU-520.04 motor in August 1967 and how the orifices can be improved for reliable 120 sec performance.

The design, design criteria, and fabrication cycle are briefly discussed to orient the reader, but the bulk of these topics are covered in the Large Motor HGTVC Final Report.

A post-test evaluation includes interpretation of the test data (movies, photographs, instrumentation, erosion, and hardware) and the fabrication and material processing planning sheets to determine the modes and times of failure during the first 45 sec when orifice 3 was lost.

The analysis of the orifice port includes aerodynamic, thermodynamic, and structural analyses to verify the predicted orifice, failure times and modes and the extent of overstressed material. The aerodynamic analysis provides predicted pressure, heat transfer coefficients, and erosion vs time from closed port cold flow test data and theoretical analysis.

A thermodynamic analysis was made to predict the temperature gradients through the orifice and nozzle in the area of redesign. The heat transfer coefficients generated in the aerodynamic analysis were used as input to an axisymmetric heat transfer computer program. The structural analysis applies the predicted temperature, pressure, and pintle loads to the orifice-nozzle design to determine thermal mechanical stresses and overstressed material areas.

Design recommendations are made after evaluating the hardware, instrumentation and analyses to improve the orifice design concept for 120 sec survivability. Major problem areas are defined with their causes and solutions outlined for redesign guidelines.

A preliminary redesign effort was conducted to incorporate the design recommendations, current material technology (raw materials and new processing and fabrication) and the requirements of a 156 in. submerged Hot Gas TVC System. Nine alternate orifice designs are defined and a modified design is selected for preliminary evaluation. After preliminary aero, thermo and structural analyses, a preliminary redesign was recommended. The final orifice redesign includes the recommendations and solutions to major orifice problem areas.

The current and improved designs are shown in Figures 1 and 2. Design changes include the replacement of all overstressed materials with improved materials as indicated in Table I. Design changes also include a threaded connection of the throat subassembly to the insulation sleeve, moving the pintle support leg holes out to a larger diameter, and increasing the thickness of the aft exit cone liner.

B. SUMMARY

The three hot gas SITVC orifice ports failed because of the following problem areas.

1. The differential heating, pressure loads and erosion around the orifice nozzle exit cone. This condition was caused by the nozzle exit cone gas reattachment downstream inside the orifice cavity during the closed position and the nozzle exit cone gas shock from upstream of the orifice cavity during the open gas injection duty cycles.
2. The unpredictable orifice throat subassembly outward movements toward the valve pintle face during open

TABLE I

MATERIAL DESIGN SUMMARY

Port Orifice Item	Current Design: Material	Current Design: Fabrication Process	Improved Design: Material	Improved Design: Fabrication Process
1. Inlet	Graphite 90	Extrude, Machine Parallel to Centerline	Graphite Cloth Phenolic	Tape Wrap Parallel to Centerline, Cure, Regraphitize, Machine
2. Throat	2% Thoria 98% Tungsten	Forge, Machine Parallel to Centerline	2% Thoria 98% Tungsten	Forge, Machine Parallel to Centerline
3. Nut	20% Copper 80% Tungsten	Press and Sinter, Machine Perpendicular to Centerline	2% Thoria 98% Tungsten	Forge, Machine Parallel to Centerline
4. Forward Exit	Pyrolytic Graphite Edge Grain	Vapor Deposition, Machine Perpendicular to Centerline	Graphite Cloth Phenolic	Tape Wrap Parallel to Centerline, Cure, Regraphitize, Machine
5. Aft Exit	PTB Graphite Fiber Phenolic	Mold, Bake, Graphitize, Resin Impregnate, Cure, Machine Perpendicular to Centerline	Graphite Cloth Phenolic	Tape Wrap Parallel to Centerline, Cure, Regraphitize, Machine
6. Insulation Sleeve	Carbon Cloth Phenolic	Tape Wrap Parallel to Centerline, Cure, Machine	Carbon Cloth Phenolic	Tape Wrap Parallel to Surface, Cure, Machine

events and after 16.0 sec of motor firing time when the adhesive bond breaks down.

3 Insufficient throat subassembly outer diameter support due to valve leg cutouts in the carbon cloth insulation sleeve and graphite inlet ring.

The above problem areas caused cracking and delamination in the PTB and pyrolytic graphite exit cone, copper tungsten nut, and graphite inlet.

The recommendations to insure a reliable orifice performance for a 120 sec motor test included the following major design changes.

1. Change the orifice materials, processes and grain orientation and simplify the orifice design; the new materials to be more erosion resistant and not subject to spalling or chunking while subjected to differential heating and pressure forces around a 360 deg circumference.
2. Move the valve leg support cutout holes out and increase the insulation sleeve thickness to insure better support at the throat subassembly outer edge.
3. Provide a more heat resistant adhesive bond along the orifice material interfaces and provide a positive connection between the throat and the insulation sleeve.

The condition of the three failed and one survived orifices demands a significant improvement to the existing design without going to a new concept which would involve a development program.

Thus, the preliminary design selected for the orifice includes only three materials and five rings instead of the initial six materials and six rings. The initial orifice exit cone materials (PTB and pyrolytic graphite) were replaced by one ring of regraphitized graphite cloth phenolic. The throat and nut rings now use the same 2 percent thoriated tungsten material and forging process. The inlet Graphite 90 ring is now replaced with a ring of regraphitized graphite cloth phenolic.

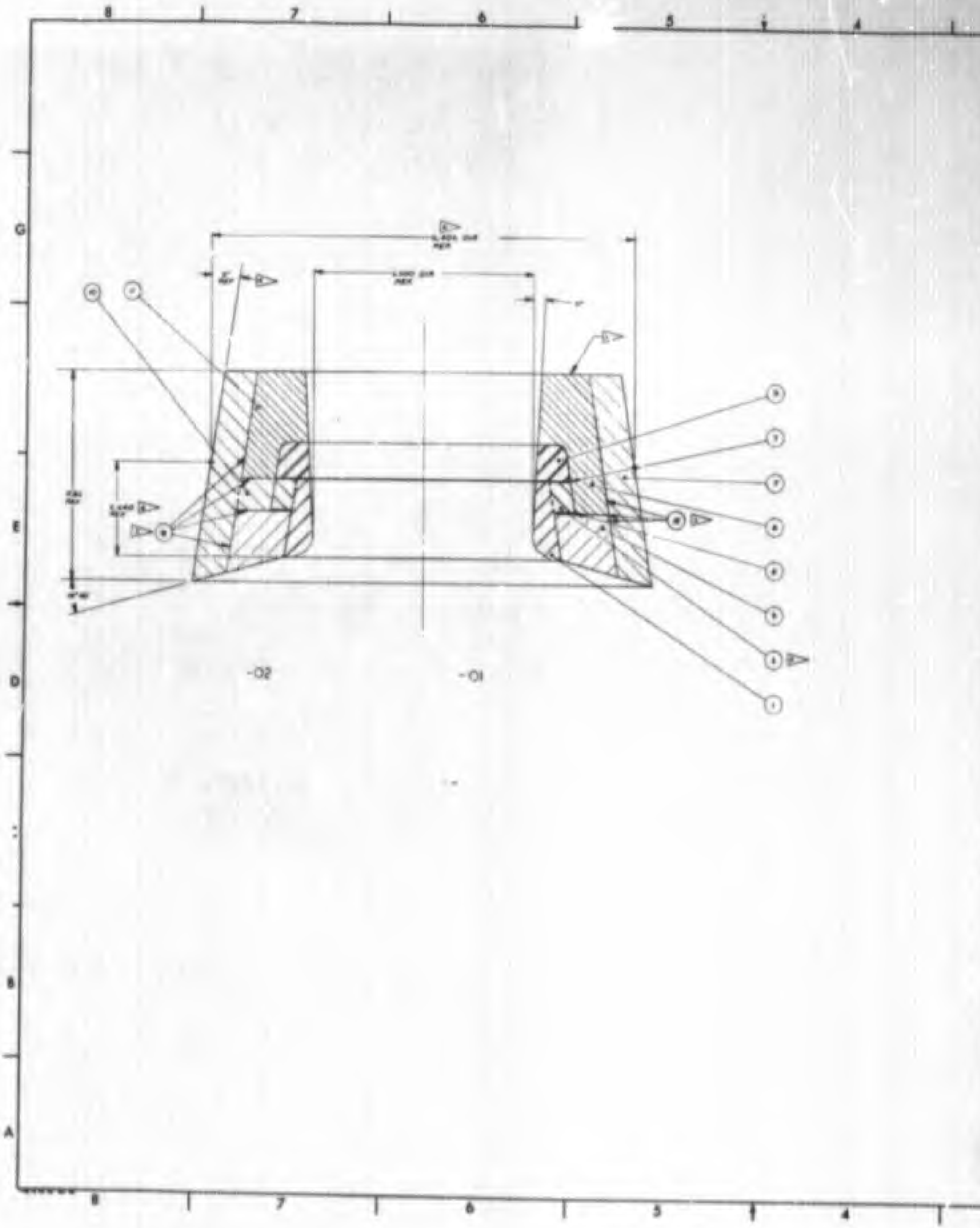

A

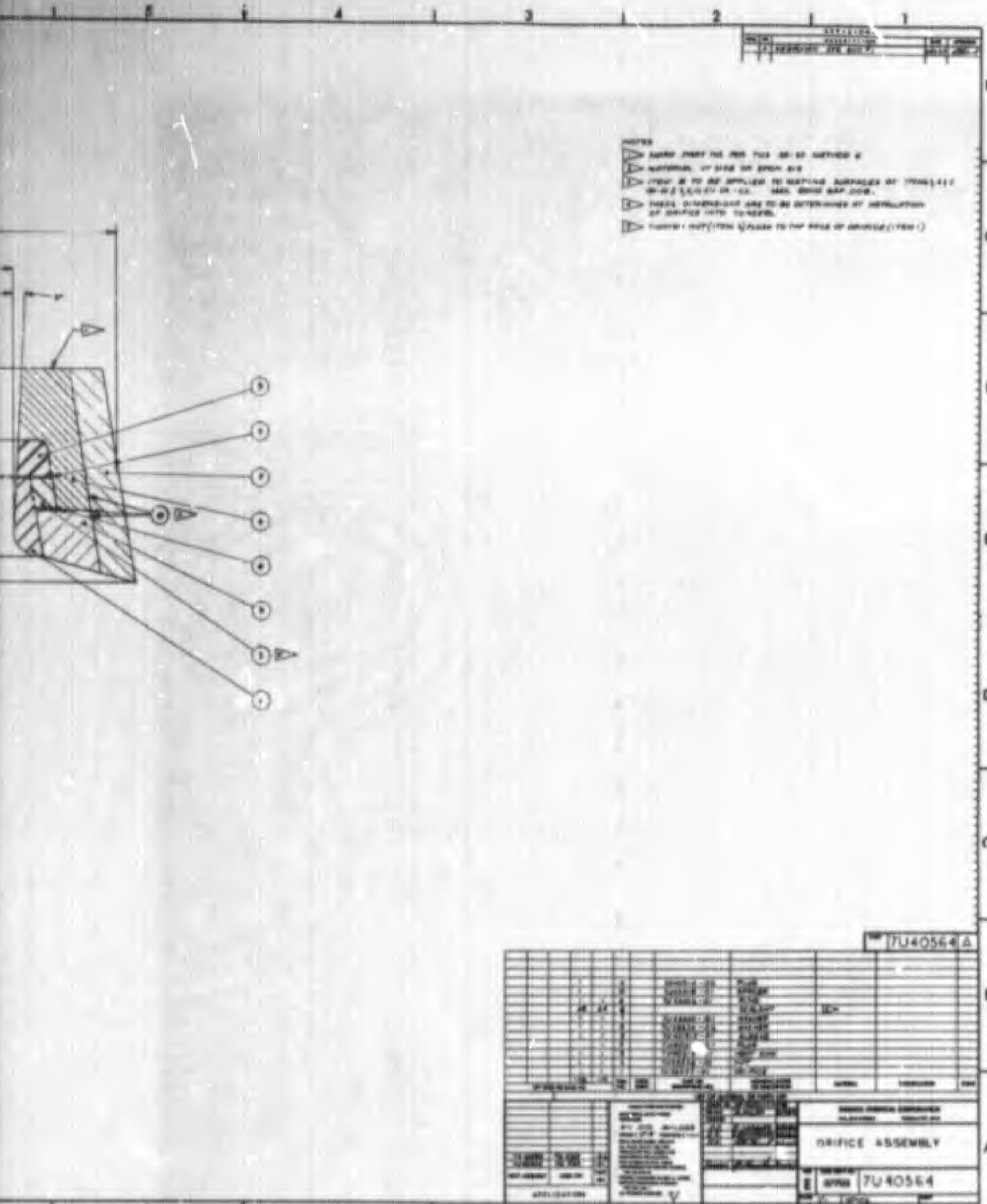

Figure 1. TU-520.04 Current Orifice Design

B

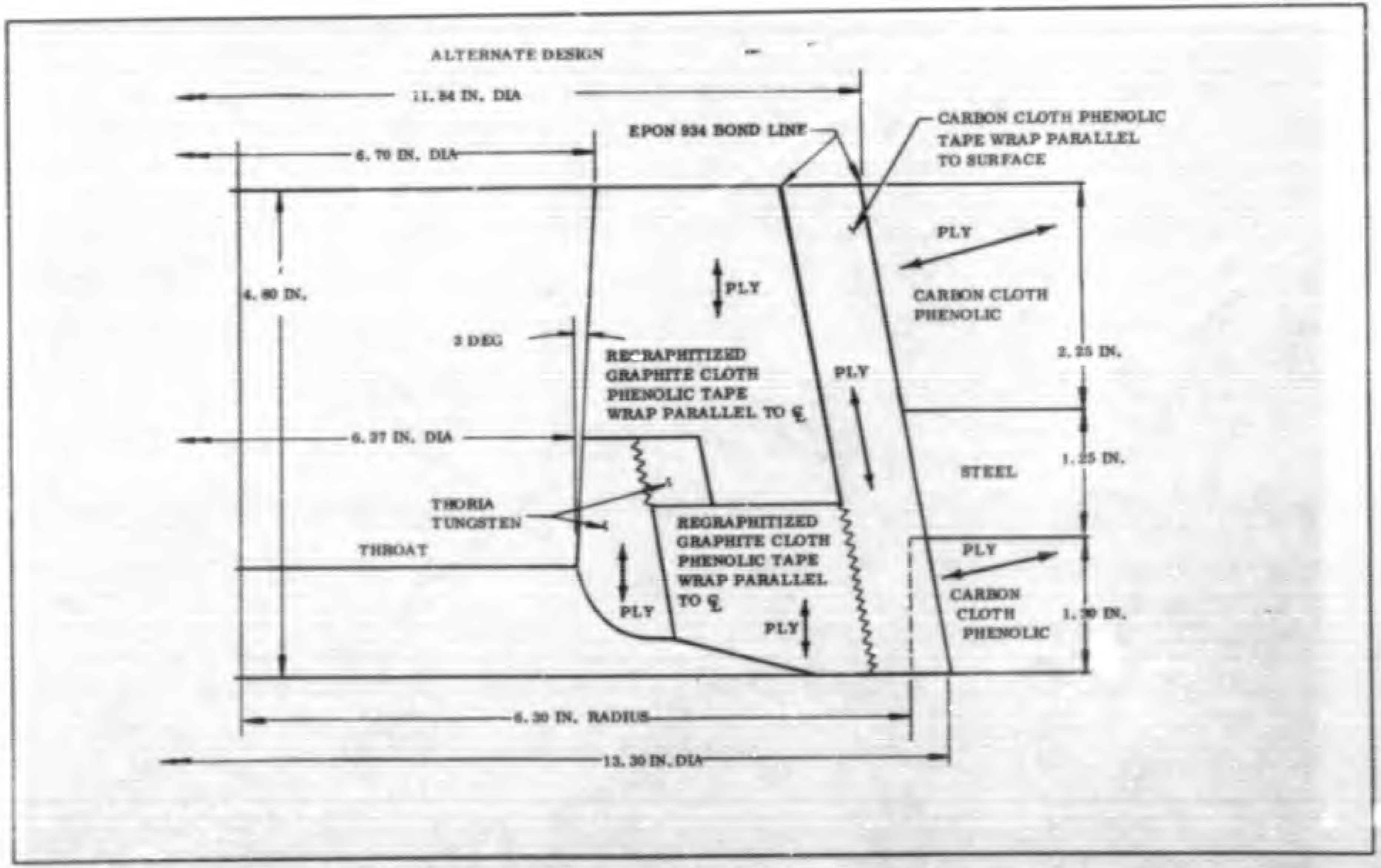

Figure 2. Improved Orifice Design

BLANK PAGE

SECTION II

DESIGN, FABRICATION, AND POST-TEST EVALUATION

A. DESIGN

The main design function of the orifice port acting with the pintle valve was to meter gas into the nozzle exit cone and create side force loads. The second design function was to maintain port cavity shape when the port is open or closed and subjected to steep unsymmetrical thermal gradients, a large range of unsymmetrical pressures, nozzle compression unsymmetrical membrane loads, and a pintle valve seating load.

The current design to meet these functional requirements is shown in Figure 1. The tungsten ring provides a noneroding, stable, high strength at temperature material and a hard, stiff, distribution point for the pintle load into the circular, curved, center hole, composite material plate. The graphite inlet, the pyrolytic graphite forward exit cone, the PTB aft exit cone and the carbon cloth sleeve maintain the shape of the orifice port cavity and nozzle exit cone walls while supporting the hot gas temperature and pressure. In addition, the carbon cloth sleeve insulates the nozzle structural steel shell.

A tungsten-copper nut was threaded to the tungsten throat and seated on the Graphite 90 inlet to form the throat subassembly. The large inlet pressure area of the throat subassembly provides a large seating load during pintle retraction and port open duty cycles.

Concentric conical rings of the orifice materials with the apex pointed toward the nozzle centerline were used to transmit the large pintle load (15,000 lb) and the chamber pressure loads (630 psi and 75,000 to 95,000 lb) through the port orifice to the nozzle conical steel shell by wedge action. In addition, the port orifice fills the hole in the steel conical shell and supports the nozzle unsymmetrical hoop and axial compression loads.

All four orifice ports were identical in design except for PTB aft exit cone material. Orifice port 3 used a long PTB billet that allowed it to be the support for both the tungsten nut and the pyrolytic graphite ring. Orifice ports 1, 2, and 4 used a short PTB billet which allowed it to support only the pyrolytic graphite ring. Three carbon cloth phenolic, tape wrapped parallel-to-centerline rings were fabricated by Thiokol Chemical Corporation to provide support for the tungsten nut.

The current orifice design (Figure 1) must maintain the orifice port wall aerodynamic shape while subjected to exhaust gas temperature and pressure, pintle actuator loads, and nozzle compression loads.

Three basic load conditions are shown in the following sketch and in Figure 3 for port 3, the first port to fail. Load condition P_B was not investigated, since the maximum retract load when opening was zero during the first 45 sec and the resulting condition is less severe than A and C conditions. The other three ports also show zero retract load when opening.

Each load condition is applied to four surfaces 360 deg in circumference; the inlet, orifice, nozzle exit, and the boundary.

The inlet surface shows the same gas temperature and pressure upstream and downstream. During port open, the gas pressure will be the same for the up and downstream surfaces, but differ from a port closed pressure.

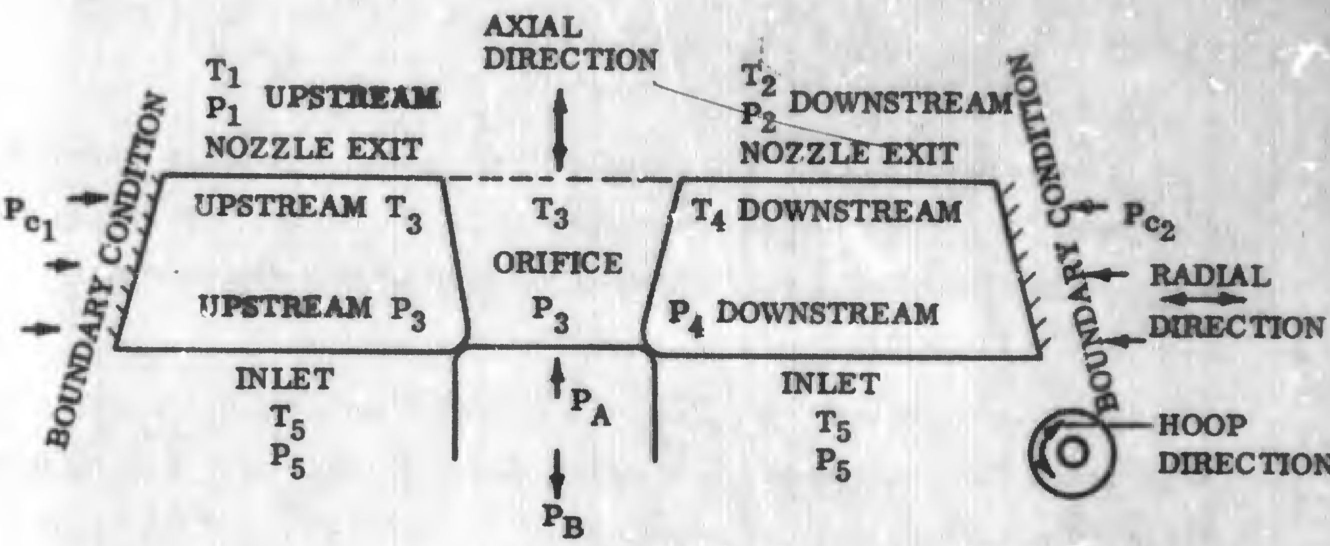

The orifice wall reflects a constant gas temperature, while the pressure around the port upstream and downstream differ. During a port open condition, the gas temperature and pressure increase uniformly around the circumference.

The nozzle exit cone wall surface shows the same gas temperature during open and closed port duty cycles. The pressure increases during port open condition due to hot gas injection shock waves and varies in magnitude around the port.

At the boundary conditions on the nozzle shell away from the port plug, the axial direction was fixed with the radial direction free to move while loaded with the nozzle compression loads. An alternative boundary condition fixed both the axial and radial directions.

The identifying terms for the loaded surfaces is indicated below.

T = gas temperature	P_A = extend pintle load
P_1 = gas pressure	P_B = retract pintle load
	P_c = nozzle loads

The loads are applied simultaneously on all four surfaces to determine the stress levels in each material. No attempt was made to apply the loads incrementally one at a time except for the application and release of the pintle actuator load.

B. FABRICATION

Fabrication of the orifice port starts with the receipt of preshaped material billets ready for final machining. The major material billets, listed in Table I, are purchased from the material supplies and fabricators with the indicated grain or ply orientation (Table II).

After machining and fitting operations on each material billet, the port orifice is ready for final assembly. The inlet, throat, nut and spacer form the throat subassembly by threading the nut onto the throat ring and seating it on the rubber spacer and graphite. The forward and aft exit cone rings and spacer are bonded to the throat subassembly, forming the liner subassembly. The insulation sleeve is then bonded to the inner subassembly, completing the port assembly, as indicated below.

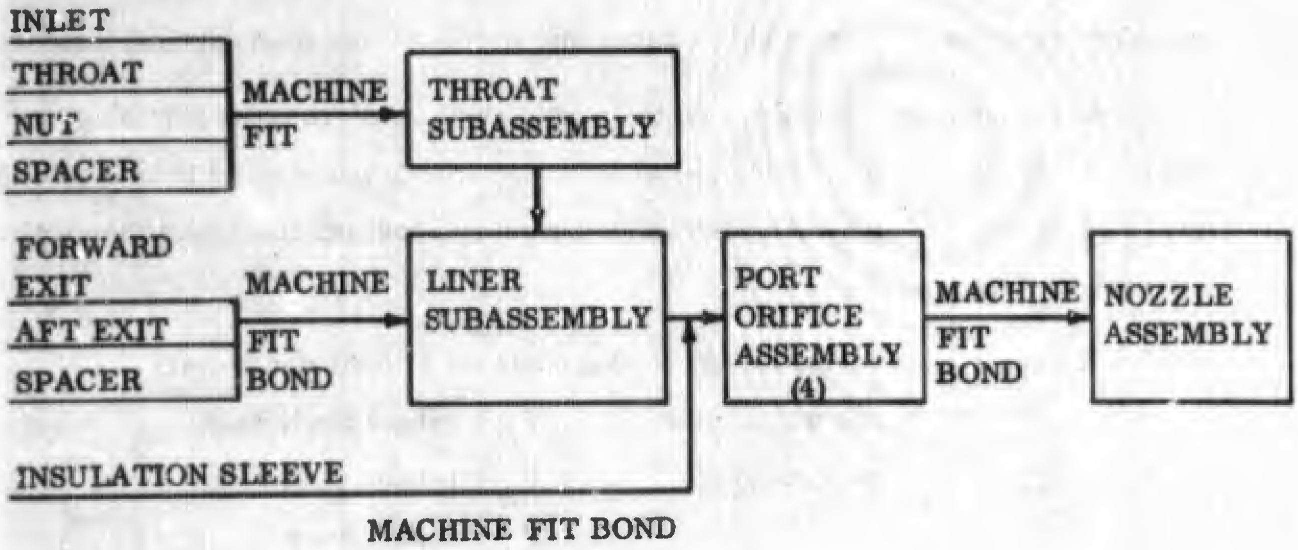

TABLE II

MATERIAL SUPPLIERS AND FABRICATORS

Item	Material	Grain or Ply Orientation	Material Supplier	Material Fabricator
Inlet	Graphite 90	Parallel to Orifice Centerline	Great Lakes Carbon	Carborundum
Throat	Thoria Tungsten	Parallel to Orifice Centerline	General Electric	Carlton, Taylor Forge
Fwd Exit	Pyrolytic Graphite	Perpendicular to Orifice Centerline	Pyrogenics	Pyrogenics
Aft Exit	PTB-Graphite Fiber Phenolic	Perpendicular to Orifice Centerline	Union Carbide	Union Carbide
Nut	Copper Tungsten	Perpendicular to Orifice Centerline	General Electric	General Electric
Insulation	Carbon Cloth Phenolic	Parallel to Orifice Centerline	U. S. Polymeric	Thiokol Chemical
Spacers	Rubber	Isotropic	Thiokol Chemical	Thiokol Chemical

The orifice assembly is then fitted, machined and bonded into the conical holes in the side of the submerged nozzle wall. When the final inside and outside diameters of the submerged nozzle are machined, the orifice port is flush with the nozzle walls except for the recessed inlet. Photographs of a pretest machined orifice port inlet and a pintle valve assembly orifice port are shown in Figures 4 and 5, respectively.

C. POST-TEST EVALUATION

The post-test evaluation includes interpretation of the test data (movies, photographs, instrumentation, erosion, and hardware inspection) and the Manufacturing-Quality Control planning process sheets to determine the modes and times of failure during the first 45 sec when orifice 3 was lost.

1. HARDWARE EXAMINATION

A visual examination of the pretest condition of the port and the immediate nozzle area around the port is provided by a series of photographs. Figures 6 thru 8 show the machined, installed port in the nozzle OD and the port-pintle valve-nozzle assembly. Figures 9, 10 and 11show the machined, installed port in the exit and the complete nozzle, valve, closure assembly.

The post-test condition of the components is shown in photographs. Figures 12 thru 15 show four views of the one surviving port, valve 1 after test. Note the valve, pintle and leg, and orifice port erosion patterns on the upstream side.

The nozzle and orifice port 1 exit cones are shown in Figures 16 thru 19. Note the characteristic teardrop erosion downstream of port 1, the loss of all the pyrolytic graphite and PTB orifice port exit cone material and the Graphite 90 inlet cracks.

The burnthrough around the nozzle and case circumference and locally in the aft closure after port 2, 3, and 4 ejection is shown in Figures 20 thru 22. A cross section view of the dissected nozzle through port 1 and through a plane 45 deg away from the port is shown in Figures 22 thru 24.

Components from port 1 that remained in place during the motor test are shown in Figure 25 (inlet graphite face: note three radial cracks), Figure 26 (carbon cloth phenolic insulation sleeve) and Figure 27 (tungsten throat and nut). Note the erosion at valve leg holes in the carbon cloth insulation sleeve. Gas leakage through the remaining orifice throat submerged assembly occurred at the leg hole cutout and at the graphite radial cracks.

Component parts from the four hot gas ports were found in the fields immediately around the test bay. Figure 28 shows ring segments of inlet graphite from the other three ports. Figure 29 shows the pieced together segmented and layered section of the port exit cone PTB material. Figure 30 shows small segments of the ports 2, 3, and 4 carbon cloth ring and sleeve and tungsten nut. Figures 31 and 32 show the 360 deg intact throat tungsten rings from ports 2 and 3. The tungsten throat ring for port 4 and the pyrolytic rings on all four ports have not been found. Note the port 2 throat ring eroded locally at interface with the pyrolytic graphite ring.

An evaluation of the post-tested hardware indicates that the orifice port 2, 3 and 4 failure initiated the burnthrough of the nozzle, aft closure and case, and the failure of the exit cone.

A preliminary conclusion based on visual examination of the post-tested hardware indicates that the PTB chunked out in partial ring and layer segments, as shown below. Layer I came out in ring segments, starting with segment (1) on the downstream face. As the last segments (3 and 4) of layer I were leaving the first segments (1 and 2) of layer II were ready to chunk. This chunking parallel to the grain direction continued until all the port aft exit PTB material was gone and allowed the pyrolytic graphite forward exit cone to be ejected. The pyrolytic graphite was probably ejected with PTB layer III.

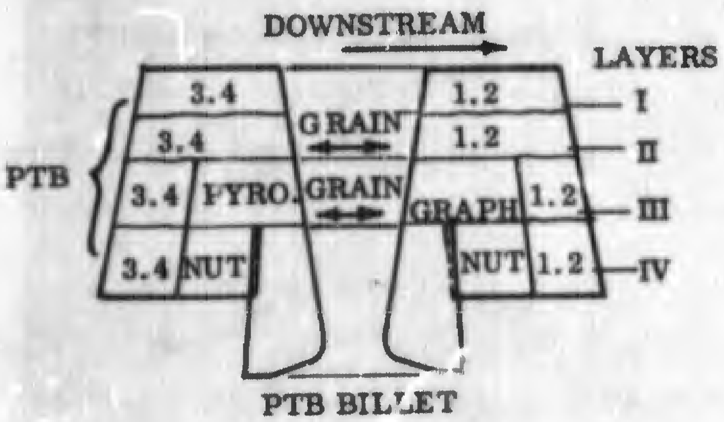

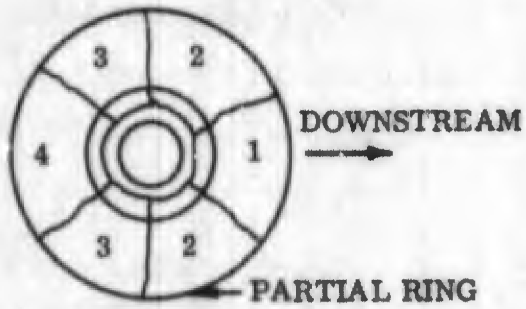

All four ports were identical, except for the PTB material area. Ports 1, 2 and 4 used short PTB billets (layers I, II, III) with carbon cloth phenolic (tape wrapped parallel to orifice centerline) filling in layer IV. Port 3 used a long PTB billet and did not need a carbon cloth phenolic ring filler. The failure of the carbon cloth phenolic (3) was probably due to a combination of erosion and fracture, as evidenced by the few recovered sections and shown in Figure 32.

Probably on ports 2, 3 and 4 the throat and nut were pushed through the cracked graphite after the PTB and pyrolytic graphite rings were ejected. The graphite ring was probably lost at, or shortly after, the tungsten ejection. The carbon cloth insulation sleeve was eroded out or lost when the pintle valve assembly was pushed through the enlarged orifice port after the three legs were burned through.

The surviving port orifice 1 remained closed after its first duty cycle (t = 33 sec) and lost only its PTB, pyrolytic graphite, and the carbon cloth phenolic filler ring. At t = 80 sec, the second scheduled open duty cycle, it remained closed due to the loss of electrical and hydraulic control lines. At the end of the static test the tungsten throat and nut had been pushed up the graphite support ramp about 0.5 in., indicating the throat failure mode.

2. PORT PERFORMANCE

Three ports were lost during the motor static firing (2, 3 and 4) with the fourth port (1) remaining in the motor. Erosion dimensions were taken for port 1, with the other three ports showing only the eroded hole radii.

Port 1 erosion, shown in two planes 90 deg to each other (Figures 33 and 34) shows the upstream, lateral and downstream erosion. The inlet erosion depth varied from 0.10 to 0.20 in. with some cocking of the inlet graphite on the downstream side after the test. The tungsten throat and nut rings were pushed up the graphite support ramp an estimated 0.5 in. while still welded to the extended pintle valve. At the port exit plane, the erosion depth varied from 0.48 in. upstream, to 1.39 to 1.40 in. laterally, to 2.44 in. downstream.

Ports 2, 3 and 4 erosion are shown in Figures 35 thru 37 with the maximum upstream eroded radius varying from 10.5 to 12.00 in., and the downstream erosion radius varying from 5.10 to 6.25 inches. Port 3 was open the longest after throat ejection and shows the largest upstream erosion radius (12.00 in.) and the complete unbonding locally of the nozzle carbon cloth insulation liner from the steel shell.

A comparison of port loads, duty cycle times, and failure times is presented in Table III. The pintle actuator extend stall load against the port orifice varied from 15,000 to 16,000 pounds. The pintle actuator retract load was zero when the port was just opening, assisted by a 3,390 to 4,410 lb chamber pressure load on a small segment of the pintle front face at the outside diameter. The initial port failures (throat ring lost) occurred from 35.74 to 77.50 seconds. The total actual valve open time up to 140 sec varied from 7.60 sec (port 1) to 113.24 sec (port 3). The open time includes open time before and after initial port failure. For ports 2, 3 and 4, the total actual valve open time before failure is 12.45, 8.98 and 5.70 sec, respectively.

The total side force created during open port conditions varied from 34,000 to 44,000 lb, as required by the duty cycle.

TABLE III

ORIFICE PORT PERFORMANCE SUMMARY

Performance Items	Port 1	Port 2	Port 3	Port 4
End Test Condition	Survived	Failed	Failed	Failed
Orifice Tungsten Throat Loss Time (sec)	--	65.76	35.74	77.50
Valve Tungsten Shell Loss Time (sec)	--	98.43	--	--
Valve Loss Time (sec)	--	106.56	55.56	116.50
Total Actual Valve Open Time (sec) to 140 Sec*	7.0	86.69	113.24	75.45
Total Programed Valve Open Time (sec) to 140 Sec	39.0	54.00	58.00	42.00
Total Actual Valve Open Time Before Failure (sec)	--	12.45	8.98	5.70
Maximum Actuator Extend Load (lb)	16,000	16,000	15,000	16,000
Maximum Actuator Retract Load (lb) (when pintle opens orifice port)**	0	0	0	0
Maximum Side Force (lb)	44,000	47,000	34,000	38,500

*TU-520.04 Motor Performance

	Predicted	Actual
Web Time (sec)	122.5	Approximately 95.0
Action Time (sec)	123.5	Approximately 140.0

**Chamber pressure on pintle front face between 7 in. contact diameter and 7.5 in. pintle diameter provides an unseating load when valve extend oil pressure drops to zero. The chamber pressure load is 3,390 lb at 600 psia and 4,410 lb at 780 psia. However, the pintle position transducer follows the input signal closely during the open events of the duty cycle, indicating the pressure is not unsticking the pintle-orifice interface, but assisting actuator retract pressure in pushing back the pintle face.

3. PHOTOGRAPHIC COVERAGE

The test bay was ringed with 10 cameras operating at speeds from 24 to 400 ft/sec and located from 50 to 2,500 ft away from the test bay. The sketch below indicates the location of the cameras. The chart indicates the camera speed and distance from the test motor.

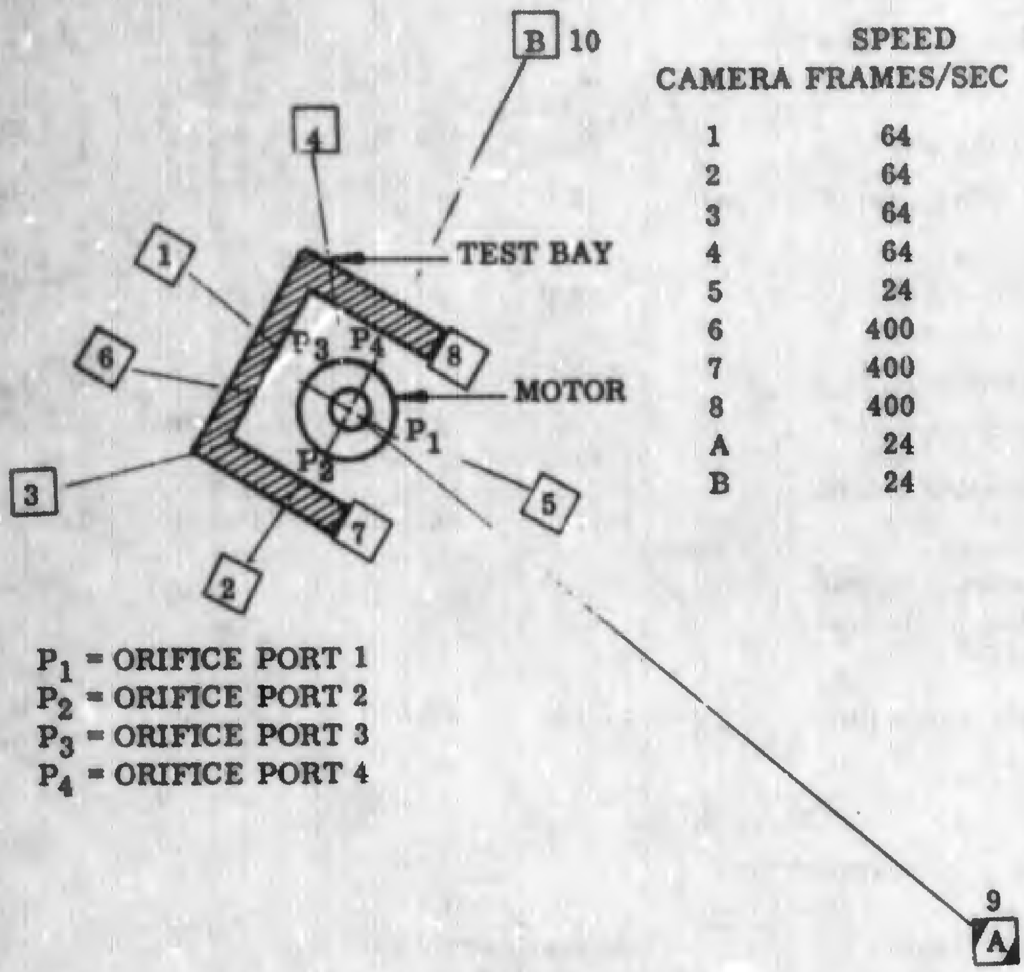

CAMERA	SPEED FRAMES/SEC	DISTANCE FT
1	64	50
2	64	100
3	64	100
4	64	100
5	24	100
6	400	50
7	400	50
8	400	50
A	24	2,500
B	24	1,250

P_1 = ORIFICE PORT 1
P_2 = ORIFICE PORT 2
P_3 = ORIFICE PORT 3
P_4 = ORIFICE PORT 4

The movie film viewing was confined to the first 45 sec and the bright objects leaving the nozzle were identified by size, time and direction. Cameras 6, 7, and 8, (50 ft from the nozzle and 400 fps) were used to establish the baseline data for objects leaving the nozzle. Cameras No. 1, 2, 3 and 4 (50 to 100 ft from the nozzle and 64 fps) were used as backup data.

Tables IV thru X. show the raw data taken from the movie viewing. Generally, for the first 20 sec, the sparks and small bright objects were seen leaving from the

TABLE IV

CAMERA 6 BRIGHT OBJECTS

Time	Object Size				Port Side Leaving Nozzle			
(sec)	Spark	Small	Medium	Large	P1	P2	P3	P4
18.2		X				X		
18.6		X				X		
18.8		X				X		
19.2		X				X		
29.7				X		X		
33.4		X				X		
33.5				X		X		
33.5			X					X
34.1		X				X		
35.7		X						X
39.9		X						X
43.2		X						X
43.7		X				X		
43.8		X				X		
43.9			X			X		
44.2			X					X
44.6		X				X		
44.8		X						X
46.3		Exit Cone Lost						

TABLE V

CAMERA 7 BRIGHT OBJECTS

Time (sec)	Object Size: Spark	Small	Medium	Large	Port Side Leaving Nozzle: P1	P2	P3	P4
7.4	X				X			X
13.9	X				X			X
15.7		X				X	X	
17.7		X				X	X	
18.0			X			X	X	
18.1		X				X	X	
18.2		X				X	X	
18.4		X				X	X	
18.4		X			X			X
18.5		X			X			X
18.5		X				X	X	
18.6		X				X	X	
18.7	X					X	X	
18.9		X				X	X	
18.9		X			X			X
19.0	X					X	X	
19.1	X					X	X	
19.3			X			X	X	
19.4		X				X	X	
19.5		X			X			X
19.5			X			X	X	
19.6		X				X	X	
19.7			X			X	X	
19.8		X				X	X	
19.9		X				X	X	
20.0		X				X	X	
20.1		X				X	X	
20.1			X			X	X	

TABLE V (Cont)

CAMERA 7 BRIGHT OBJECTS

Time	Object Size				Port Side Leaving Nozzle			
(sec)	Spark	Small	Medium	Large	P1	P2	P3	P4
20.2		X				X	X	
20.4		X				X	X	
20.5		X				X	X	
20.8		X				X	X	
20.9		X				X	X	
21.0		X	X			X	X	
21.2		X				X	X	
21.3			X			X	X	
22.1		X				X	X	
22.2		X				X	X	
22.4		X				X	X	
22.8		X				X	X	
23.3		X				X	X	
30.6			X	X	X	X	X	X
30.7		X			X	X	X	X
31.0		X				X	X	
33.8		X				X	X	
34.2		X				X	X	
34.4		X			X			X
34.5		X			X	X	X	X
34.5			X			X	X	
34.8		X			X	X	X	X
34.9		X			X	X	X	X
35.0		X				X	X	
35.1		X			X			X
35.2				X	X			X
36.2		X				X	X	

TABLE V (Cont)

CAMERA 7 BRIGHT OBJECTS

Time	Object Size				Port Side Leaving Nozzle			
(sec)	Spark	Small	Medium	Large	P1	P2	P3	P4
36.3		X			X			X
36.4		X			X	X	X	X
36.7		X			X			X
36.9		X			X			X
39.0		X			X			X
39.1		X				X	X	
40.0		X			X			X
40.1		X				X	X	
40.7		X			X			X
40.8		X				X	X	
40.9		X			X			X
41.2		X			X	X	X	X
41.7		X				X	X	
41.9		X				X	X	
42.0		X			X			X
42.2		X			X			X
42.3		X				X	X	
42.7		X				X	X	
42.8			X			X	X	
42.9		X			X			X
43.2		X			X			X
43.7		X			X	X	X	X
44.2		X			X	X	X	X
44.6		X			X			X
44.8		X			X			X
47.8		Exit Cone Lost						

TABLE VI

CAMERA 8 BRIGHT OBJECTS

Time	Object Size				Port Side Leaving Nozzle			
(sec)	Spark	Small	Medium	Large	P1	P2	P3	P4
1.7		X			X	X		
4.2		X			X	X		
9.0	X						X	X
14.0	X						X	X
16.6	X						X	X
17.4	X						X	X
18.7	X						X	X
18.8		X					X	X
19.0		X					X	X
19.1		X					X	X
19.3		X			X	X	X	X
19.4		X					X	X
19.7		X			X	X	X	X
19.8		X			X	X	X	X
19.9		X					X	X
20.1		X					X	X
20.2		X			X	X	X	X
20.2			X				X	X
20.4		X			X	X	X	X
20.7		X			X	X		
20.8		X					X	X
21.0		X					X	X
21.1		X					X	X
21.3		X					X	X
21.4		X			X	X		
21.9		X					X	X
22.2		X			X	X		

TABLE VI (Cont)

CAMERA 8 BRIGHT OBJECTS

Time	Object Size				Port Side Leaving Nozzle			
(sec)	Spark	Small	Medium	Large	P1	P2	P3	P4
22.3	X				X	X	X	X
23.0		X			X	X		
23.1	X						X	X
23.4		X					X	X
23.8		X					X	X
23.9		X					X	X
24.2	X						X	X
24.3		X					X	X
29.3	X						X	X
29.5		X					X	X
29.8		X					X	X
31.1		X			X	X	X	X
34.9		X			X	X		
35.1		X			X	X		
35.3		X			X	X	X	X
35.3				X			X	X
35.5		X			X	X		
35.7		X			X	X		
35.9		X			X	X		
36.1		X	X	X	X	X		
36.3		X			X	X		
36.5		X			X	X		
36.9		X			X	X	X	X
37.3		X			X	X		
37.5		X			X	X		
37.7		X			X	X		
37.9		X			X	X		

TABLE VI (Cont)

CAMERA 8 BRIGHT OBJECTS

Time	Object Size				Port Side Leaving Nozzle			
(sec)	Spark	Small	Medium	Large	P1	P2	P3	P4
38.1		X			X	X	X	X
38.3		X			X	X		
39.1		X			X	X		
39.5		X			X	X		
39.7		X			X	X		
39.8		X			X	X		
40.1		X			X	X		
40.2		X			X	X		
40.3		X			X	X		
41.6		X			X	X		
41.8		X			X	X		
42.0		X			X	X		
42.6		X			X	X		
43.1		X			X	X		
43.9		X			X	X		
44.0		X			X	X		
44.2		X			X	X		
44.3		X			X	X		
44.4		X			X	X		
44.5		X			X	X		
48.3		Exit Cone Failure						

TABLE VII

CAMERA 1 BRIGHT OBJECTS

Time	Object Size				Port Side Leaving Nozzle			
(sec)	Spark	Small	Medium	Large	P1	P2	P3	P4
19.6	X					X		
20.3	X					X		
20.7	X					X		
21.4	X					X		
21.8	X					X		
31.4		X				X		
35.1	X					X		
35.4	X							X
35.4		X				X		
36.1		X				X		
43.9	X					X		
44.5	X							X
49.2	Exit Cone Lost							

TABLE VIII

CAMERA 2 BRIGHT OBJECTS

Time	Object Size				Port Side Leaving Nozzle			
(sec)	Spark	Small	Medium	Large	P1	P2	P3	P4
4.2	X				X			
16.1	X						X	
26.9			X				X	
30.3		X					X	
31.2	X				X		X	
34.4	X						X	
35.5	X						X	
35.8				X	X			
37.7	X						X	
39.7	X				X			
40.3	X				X			
40.8	X				X			
41.3	X				X			
42.1	X				X			
42.6	X				X			
43.2	X				X			
44.2	X				X			
47.61	Out of Film							

TABLE IX

CAMERA 3 BRIGHT OBJECTS

Time (sec)	Object Size Spark	Small	Medium	Large	Port Side Leaving Nozzle P1	P2	P3	P4
15.2		X					X	X
29.4		X			X	X		
33.2		X					X	X
33.8		X			X	X		
33.9			X		X	X		
35.4	X						X	X
35.6	X				X	X		
37.4	X				X	X		
38.4	X				X	X		
39.2	X				X	X		
39.8	X				X	X		
40.3		X			X	X		
41.7		X			X	X		
43.6	X				X	X		
46.0	Exit Cone Leaves							

TABLE X

CAMERA 4 BRIGHT OBJECTS

Time (sec)	Object Size: Spark	Small	Medium	Large	Port Side Leaving Nozzle: P1	P2	P3	P4
34.1		X					X	X
34.8			X		X	X		
47.0	Exit Cone Lost							

2 and 3 port quadrants of the nozzle. Over the next 25 sec, objects were still leaving the nozzle on the 2 and 3 quadrants, but an increasing number of objects were seen leaving from the 1 and 4 quadrants.

Figure 38 shows the erratic speed (frames/sec) of camera 8 per foot of developed film. Using the Figure 38 curve, the times for departing bright objects were modified and agree closely with the other cameras on the time of exit cone failure.

After viewing the movie film, locating and identifying hardware in the field surrounding the test bay, and timing departure of the hardware, it is believed that large and medium objects generally left the nozzle 180 deg away from the originating port. The small and "spark" objects are thought to have been ejected in the same quadrant as the originating port.

Figures 39 (cameras 6, 7, and 8) and 40 (cameras 1 thru 4) classify the size and departure time of each bright object into the quadrant of the nozzle from which the bright object departed. In some camera coverage (7 and 8, for example) due to the angle of coverage it is only possible to identify the closest two quadrants; thus the bright object is plotted in both quadrants. The plots represent the number of objects seen leaving the nozzle by seven cameras versus time. A bright, large object could be seen by seven cameras and plotted seven times. The tables provide good indications of trends of object size and departure time. In Figure 39, small objects are seen to leave the nozzle as early as 1.7 sec and continue to leave the nozzle over the first 45 sec time span. Sparks and small objects predominate for the first 18 sec, then medium size objects depart from 2 and 3 quadrants with the large size objects starting to leave at 30 sec from 2 and 3 quadrants. Large objects leave quadrants 1 and 4 at 33.5 seconds.

The departing objects are clustered in time spans and port quadrants corresponding to the hot gas duty cycle open time events. Port 2 (1/4) open (5.9 to 10.6 sec), port 3 full open (15.8 to 24.7 sec), port 4 full open (28.6 to 34.4 sec), port 1 full open (32.5 to 40.2 sec) and port 3 open full throughout the test after the throat insert was lost at 35.7 seconds.

Figure 39 (cameras 6, 7 and 8) illustrating bright objects departure at 50 ft and 400 fps presents a more detailed sequence of failure than cameras (1 thru 4) at 100 ft and 64 fps (Figure 40). The objects appear larger and more objects are observable leaving the motor with the closeup cameras. However, the general trend of departing objects clustered at port open conditions and increasing in size with motor firing and open port operating time is also noted in the distant cameras (Figure 40). The earliest departing objects are comparable between sets of cameras, 1.7 sec for the close cameras and 4.2 sec for the distant cameras.

4. INSTRUMENTATION DATA

The major types of instrumentation included chamber pressure, motor thrust, motor side force, valve position, valve actuator pressure, hydraulic system pressure, valve cavity pressure, and valve support plate strain. The most significant instrument in ascertaining failure time and mode was the chamber pressure and pintle valve position transducers vs time as plotted in Figure 41.

After the initial pressurization of the motor, the initial interface of the throat orifice and pintle tungsten shells is dependent on material volume change with temperature, pintle actuation loads, and the gradual shifting of the tungsten in the orifice and valve.

The pressure trace (Figure 41) is normal up to 35.74 sec, when orifice 3 ejected. Pressure decreases are shown during the opening and closing of Ports 2, 3, 4, and 1. The pintle position indications for each of the four orifice port-pintle valve interfaces are also plotted. The plus and negative output position transducer reading indicates movement away from or towards the nozzle centerline, respectively, as sketched on the following page.

Figure 41 shows the chamber pressure and the four valve-orifice interface movements vs motor test time. For the first 12.5 sec, all ports are closed and the interface movement is dependent on material thermal size change, chamber pressure and pintle load. From 12.5 to 45 sec, all four ports open once and close. The interface position is discontinuous during open port condition. The position of the interface becomes more positive after closing due to higher heating rates during port-open and the shifting of materials in the orifice and valve assemblies.

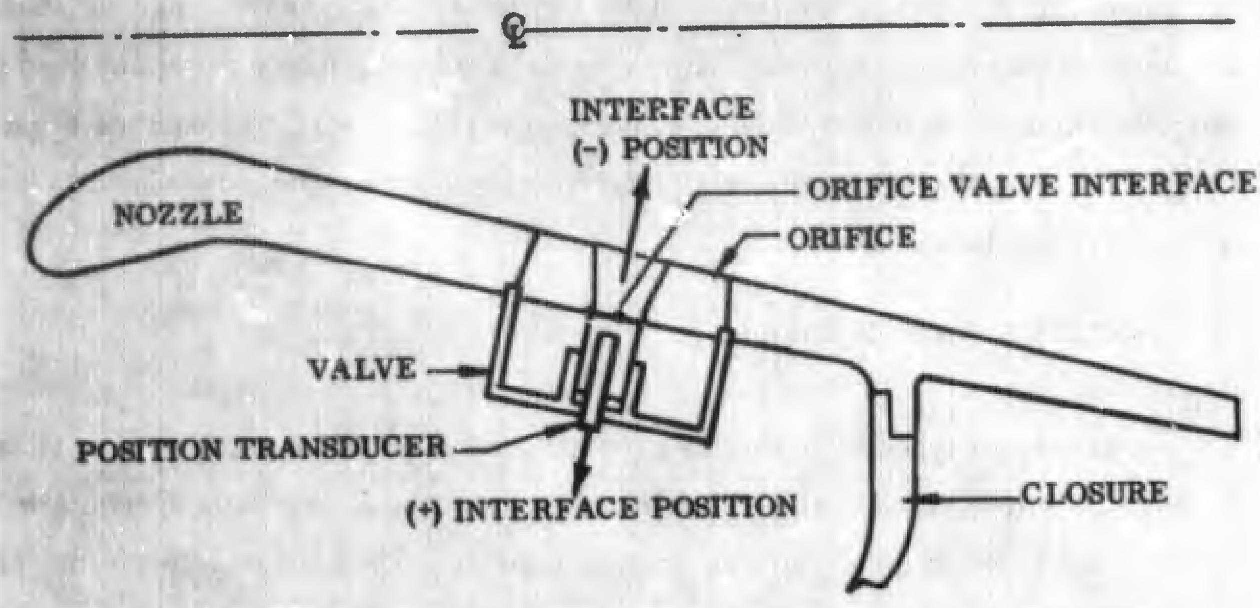

Orifice valve 2 opens first and after closing, the interface continues to move positively away from the nozzle. The interface movement is +0.008 in. closed, open, +0.075 to +0.158 in. closed. Orifice valve 3 opens and closes with the orifice valve interface moving in a negative position into the nozzle centerline and through its initial t=0 position. The interface movement is +0.007 closed, open, +0.081 to -0.0015 in., to +0.050 in. at t=35.6 throat ejection. Valve orifices 1 and 4 open and close with a large relative interface movement (+0.033 in. closed, open, +0.245 to +0.190 in. closed) at t=45 sec, orifice valve 1, 2, and 4 are intact and show a large positive interface reading, while orifice valve 3 has failed after showing a reverse interface movement (-) into the nozzle centerline. Orifice 3 probably lost a significant amount of material during, and shortly after, its open port condition, allowing the interface to move opposite to the other three identical orifice valve designs.

To locate the initial failure time, Figure 41 was magnified in the time scale t=0 to t=16 seconds. The resulting plot (Figure 42) shows the failed orifice valve 3 interface moving out (+) at the fastest rate until t=5 sec. Then orifice valve 3 growth rate flattens out, with the interface growth (+) of orifice valve 1, 2, and 4 continuing to high positive values.

The interface movement of the two orifice valve ports in subscale motor 2 (TU-521.02) is shown in Figure 43. Early in the test, both valves were open and then alternating open position to 19.2 sec when a third auxiliary nonmodulated port was opened with a burst disc. Gas flow was only through the orifice port. Orifice valve 3 was open four times in the first 45 sec with the port closed interface movement varying from +0.040 in. at t=5.1 sec to +0.150 in. at t=22.1 sec after open cycle to 0.095 in. at t=45 sec after open cycle. Orifice valve 4 was open three times in the first 45 sec with the port closed interface movement varying from +0.175 in. at t=16.5 sec after open cycle to +0.104 in. at t=40.6 sec prior to opening. Both orifices 3 and 4 were successful; though material cracks or delamination were noticeable in the PTB, pyrolytic graphite, tungsten nut and graphite after the 96.6 sec webtime motor test.

Based on valve feedback transducer data, an initial failure time appears to be t=5.0 based on Figure 42 , the major failure occurring during and shortly after the first open duty cycle.

5. FABRICATION DATA

During port fabrication, manufacturing and quality control process sheets indicate the problems associated with semifinished materials billets and final assembly.

The evaluation of the four orifice ports and the surrounding nozzle material includes (1) inspection of the material quality control logs and fabrication shop travelers, and (2) tests of postfired material specimens.

Each port had a test firing valve number, orifice serial number, and manufacturing dash number, as shown below:

Valve No.*	Orifice S/N	Part No.
1	2	7U40564-02
2	1	7U40564-02
3	4	7U40564-01
4	3	7U40564-02

*The valve number is also used to identify the orifice in this report.

An evaluation of the quality control logs and material inspection before assembly indicates that the materials were satisfactory, except a circumferential crack in orifice 3 finished PTB ring (Ref Table XI, Figure 44) at the thin large diameter end. The billet was accepted on an MRB action due to the location of the crack with respect to the heated inside diameter surface and the consideration of the material irregularity as a precrack in an area normally subjected to cracking during the test. While this crack did not initiate failure, it probably contributed to the complete loss of the PTB material. The pyrolytic rings showed some outside diameter surface delaminations and tool marks before final machining which were eliminated during final machining.

The carbon cloth phenolic sleeves were specified to be cured at 200 psi, but only one of the four rings was autoclaved to 200 psi. The other three sleeves were hydroclave cured at 1,000 psi. Material performance should be improved with a higher pressure cure; thus no MRB action was taken. The final assembly sequence as illustrated by Figures 44 , 45 and 46 of the failed orifice 3 was completed successfully for all four valve ports.

An evaluation of the nozzle quality control log, Table XII for the materials immediately around the four valve orifices indicated the materials tested out at acceptable levels for strength, density, and cure indicators (acetone extraction, volatile content, resin content) except the inside and outside carbon cloth phenolic liners (items 9 and 13 The acetone extraction percentage was higher than specificatio (1.78 to 4.75 percent) to (0.50 to 1.00 percent) indicating an incomplete cure of the debulked and hydroclave cured liners. However, since the other indicators (resin content, volatile content,

TABLE XI

ORIFICE ASSEMBLY MATERIAL REVIEW*

Drawing	Name	Material	Valve 1	Valve 2	Valve 3	Valve 4	Comments
7U39937	Orifice	2% Thoria Tungsten	OK	OK	OK	OK	--
7U39936	Nut	20% Copper-Tungsten	OK	OK	OK	OK	--
7U40913	Heat Sink	Graphite 90	OK	OK	OK	OK	--
7U40914	Plug	PTB-01	NID**	NID**	MRB Action	NID**	Circumferential Crack***
		-02	OK	OK	NID**	OK	
7U40915	Sleeve	Carbon Cloth Phenolic FM5063	OK	OK	OK	OK	One sleeve autoclave cured, three rings hydroclave cured, tapewrapped parallel to centerline.
7U39930	Washer	Neoprene-01	OK	OK	OK	OK	--
		-02	OK	OK	OK	OK	--
7U39932	Ring	Pyrographite	OK	OK	OK	OK	Outside diameter surface irregularities on unmachined rings.
7U40916	Spacer	Carbon Cloth Phenolic FM5063	OK	OK	NID**	OK	Autoclave cured, tape wrapped parallel to centerline.

*Final assembly of four orifices showed no anomalies.

**NID - Not included in orifice design.

***Crack was in thin machined section away from heated surface in a plane perpendicular to orifice centerline and 7.8 in. around circumference.

TABLE XII

NOZZLE MATERIAL REVIEW

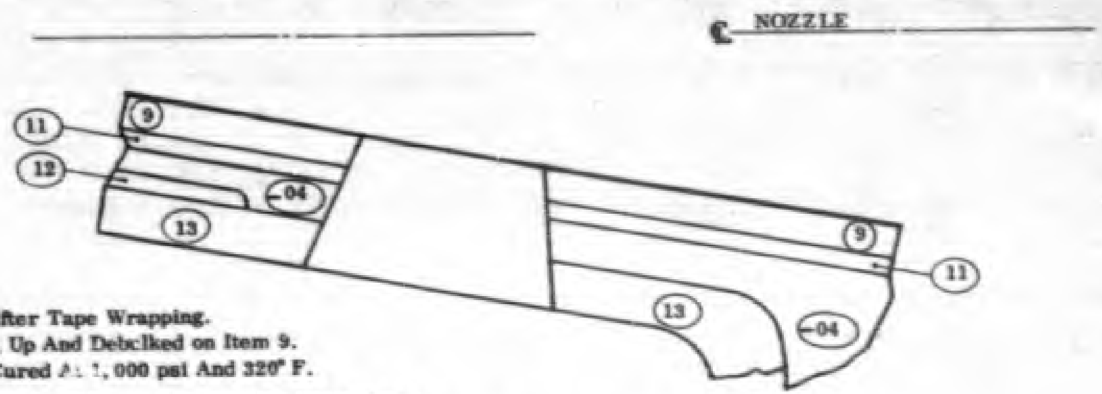

NOTES:

1. Item 9 Was Debulked After Tape Wrapping.
Then Item 11 Was Laid Up And Debulked on Item 9.
Items 9 And 11 Were Cured At 1,000 psi And 320° F.

2. Acetone Extraction is High, Indicating Incomplete Resin Cure.
However, as Other Properties Appear Normal, Material Was Judged Satisfactory.

3. All Components Satisfactory.

PART NO.	MATERIAL	CURE	FABRICATION	INTER LAMINAR SHEAR (PSI)	ACETONE EXTRACTION (%)	SPECIFIC GRAVITY	VOL CONTENT (%)	RESIN CONTENT (%)	COMPRESSION STRENGTH (PSI)	COMPRESSION MODULUS (PSI)
13	FM5063 CARBON CLOTH PHENOLIC	1,000 PSI 320° F	TAPE WRAP PARALLEL TO NOZZLE ℄	2,805	1.78 (2)	1.49	0.293	35.62	27,400	2.04×10^6
9	(1) FM5063 CARBON CLOTH PHENOLIC	DEBULK 1,000 PSI 180° F	TAPE WRAP PARALLEL TO NOZZLE ℄	2,374	4.75 (2)	1.48	0.385	35.12	26,897	2.11×10^6
11	(1) MX4600 GLASS CLOTH PHENOLIC	DEBULK 15 PSI 70° F	LAYUP PARALLEL TO 9 OD	3,929	0.217	2.17	0.223	16.90	57,100	3.95×10^6
12	MX4600 GLASS CLOTH PHENOLIC	1,000 PSI 320° F	TAPE WRAP PARALLEL TO NOZZLE ℄	—	0.094	2.09	0.593	20.83	68,180	3.74×10^6
-04	STEEL	—	ROLL AND WELD, FORGING	AVG TENSILE YIELD = 150,666 PSI AVG TENSILE ULT. = 168,666 PSI			AVG ELONGATION = 12.3% AVG REDUCTION IN AREA = 46.3%			

strength, and density) met the material specifications, the liners were accepted for final assembly.

To further evaluate the orifice materials, samples were selected from the test fired rings of PTB and graphite 90 for compression tests at room temperature and the tungsten throat and nut for photomicrographs. No pyrolytic graphite rings were found from any of the four orifice ports to evaluate. No tests were conducted on the carbon cloth insulation sleeve.

The results of the PTB material tests are shown in Table XIII. The test specimens were taken from the gas exposed surface and the surface back of the tungsten nut exposed to thermal gradients. The test fired material showed lower density and ultimate compression strength than the good virgin material at room temperature as expected. A further comparison of subscale 2 (TU-521.02) PTB successful material to TU-521.02 fullscale failed material indicated higher densities and lower strength of the failed specimens compared to the successful specimens. Lower time exposure at elevated temperatures for the failed parts, accounts for the differences in material properties. To verify the compression strength, a final test of virgin material was tested at 3500°F to double check the test fired material and to be used in the structural analysis of the orifice port. The reported compression strength was 3,870 psi at 3500°F.

The test results of the inlet graphite 90 material specimens indicate a narrow range of density and compressive strength variations (Table XIV). The good specimen test data out of a subscale and fullscale motor test brackets the failed specimen test data, indicating equal material quality. The good virgin unfired specimen test data show a lower density than the fired specimens and a lower compression strength than two out of the three fired specimens. These data agree with the vendor strength and density versus temperature curves showing increased strength and density with higher temperature.

The test data do point out that the good and failed specimens were of comparable quality and the reason for poor performance of the TU-520.04 orifice valves cannot be attributed to a change of graphite and PTB material processing and quality.

TABLE XIII

ORIFICE MATERIAL TESTS
PTB-AFT EXIT

SPECIMEN

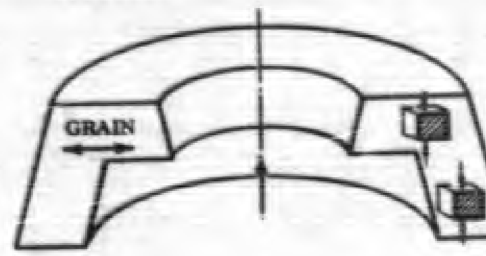

NOTE:

1. [3] Number Indicates Number of Test Specimens.

	UPPER SPECIMENS	BULK DENSITY (GR/CC AT RT)	ULTIMATE COMPRESSION (AG) (PSI AT RT)		LOWER SPECIMENS	BULK DENSITY (GR/CC AT RT)	ULTIMATE COMPRESSION (AG) (PSI AT RT)
A.	PORT 4 TU-521.02 SUBSCALE MOTOR GOOD FIRED SPECIMEN	1.17 [2]	4,300	1.	PORT 4 TU-521.02 SUBSCALE MOTOR GOOD FIRED SPECIMEN	1.17 [3]	3,691
B.	NO PORT IDENTIFICATION FAILED FIRED SPECIMEN TU-520.04 FULL SCALE MOTOR	1.27 [2]	4,040	2.	NO PORT IDENTIFICATION FAILED FIRED SPECIMEN ERODED SURFACE TU-520.04 FULL SCALE MOTOR	1.22 [3]	3,350
C.	GOOD VIRGIN MATERIAL VENDOR DATA	1.40	15,122	3.	NO PORT IDENTIFICATION FAILED FIRED SPECIMEN NO ERODED SURFACE TU-520.04 FULL SCALE MOTOR	1.26 [3]	3,833
				4.	GOOD VIRGIN MATERIAL VENDOR DATA	1.40	15,122

TABLE XIV

ORIFICE MATERIAL TESTS OF GRAPHITE 90 INLET

SPECIMEN

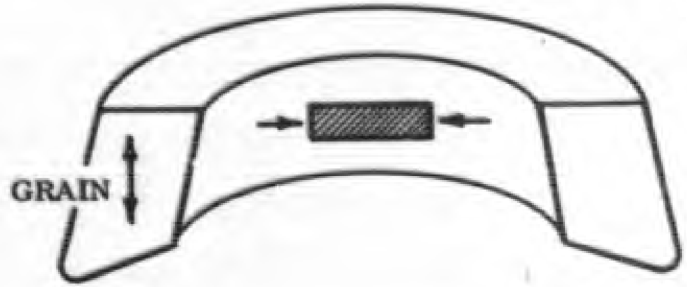

NOTE:

1. 3 INDICATES NUMBER OF TEST SPECIMENS

	SPECIMEN SOURCE	WATER DISPLACEMENT DENSITY (GR/CC) AT ROOM TEMPERATURE	ULTIMATE COMPRESSION (PSI) AT ROOM TEMPERATURE (AGAINST GRAIN)
A.	NO. 4 PORT OF TU-521-02 SUBSCALE MOTOR SURVIVED FIRED SPECIMEN	1.94 [3]	8,330
B.	NO. 1 PORT OF TU-520-04 FULL SCALE MOTOR SURVIVED FIRED SPECIMEN	1.99 [3]	8,765
C.	NO PORT IDENTIFICATION TU-520.04 FULL SCALE MOTOR EJECTED FIRED SPECIMEN	1.95 [3]	8,675
D.	GOOD VIRGIN MATERIAL VENDOR DATA	1.91	8,400

Photomicrographs at 250 magnification were taken of the tungsten throat and nut from different orifices to verify the quality of the tungsten received and used throughout the program. Four different throat rings--three from the fullscale TU-520.04 motor and one from the subscale TU-521.02--were compared to each other (Figures 47 thru 53) with no significant anomalies noted between throat rings. Figure 47 shows the six mounted specimens and their origin in the throat or nut rings.

Specimen 1 (Figure 48) selected from the survived orifice 1 throat at the thread is compared to specimen 2 (Figure 49) selected from the ejected orifice 2 at the thread--both from the full scale TU-520.04 motor. The plated surface of specimen 1 indicates uniform dispersion of the 2 percent thoria throughout the forged tungsten throat. For the etched surfaces, the main difference is the larger grain size of the ejected tungsten specimen. Locally in this area, the tungsten shell exhibited erosion (Figure 31). The local erosion resulting from a shifted or cocked throat and gas leakage would indicate high heating rates and cause larger grain growth than specimen 1. However, both specimens indicate no anomalies that would reject the tungsten material.

Specimen 3--selected from the ejected orifice 3 throat plane of the full scale TU-520.04--was compared to specimen 4 from the survived port 4 throat plane of the TU-521.02 subscale motor. No appreciable grain growth difference is noted and no voids or cracks are apparent. Both specimens are of similar acceptable forged tungsten material.

Specimen 5--selected from the survived orifice 4 nut of the TU-521.02 subscale--is compared to specimen 6--selected from the survived orifice 1 nut on the full scale TU-520.04. The nut is composed of 20 percent copper and 80 percent tungsten evenly dispersed throughout the two rings, as noted in the polished surface photomicrographs. The grain size has enlarged in specimen 6 due to higher heating rate in the cavity when all surrounding material (PTB, pyrolytic graphite) is ejected from the motor. Figure 26 shows a raised tungsten-copper material bubble on the upstream leg side. However, both specimens indicate no anomalies that would reject the copper-tungsten material.

6. SUMMARY

A review of the orifice hardware and performance, the movies and instrumentation, and orifice manufacturing and quality control reports indicates the following.

1. Initial orifice failure started at 5.0 sec, probably with the ejection of small layered ring segments of PTB in the orifice exit cone.
2. First major orifice failure occurred during and immediately after the first orifice 3 open duty cycle, t=25.0 seconds.
3. Orifice 3 PTB exhibited a circumferential pretest crack. The crack did not initiate PTB material failure, but did contribute to the total loss of the PTB and throat tungsten ejection. Other orifice materials satisfied specifications and quality control inspection.
4. The throat subassembly shifts axially, or cocks, during and after the first orifice open duty cycle as noted by one sided throat erosion (orifice 2, Figures 31 and 32), eroded configuration of orifice 1 and large plus interface movements of orifice valve after orifice open duty cycle (Figure 41) not accounted for by material thermal size change.
5. Valve leg holes cut out of the orifice after assembly to the nozzle, contribute locally to the erosion of the carbon cloth insulation sleeve and cause graphite radial cracks around the local leg hole area.

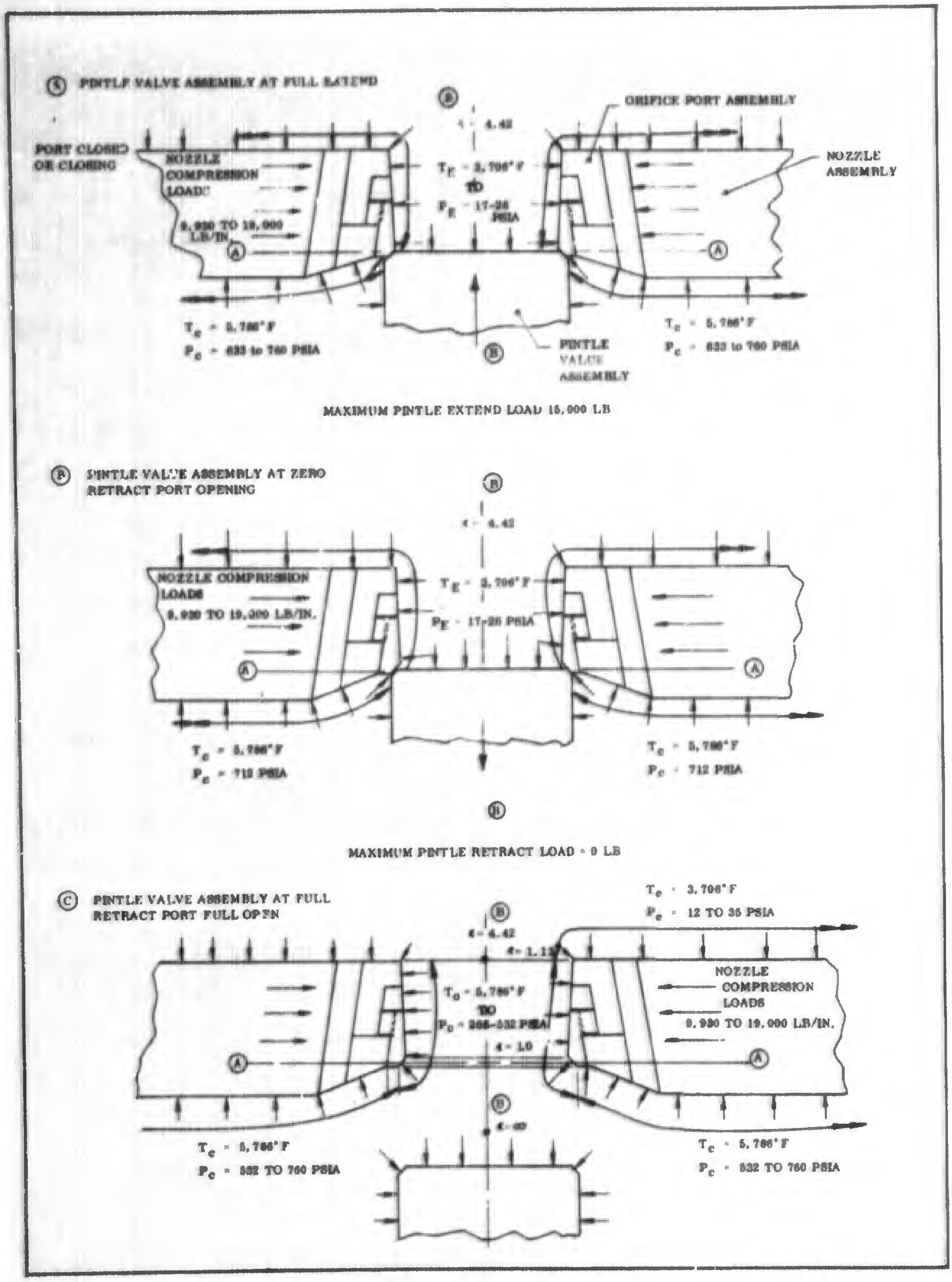

Figure 3. Orifice Port 3 Load Conditions

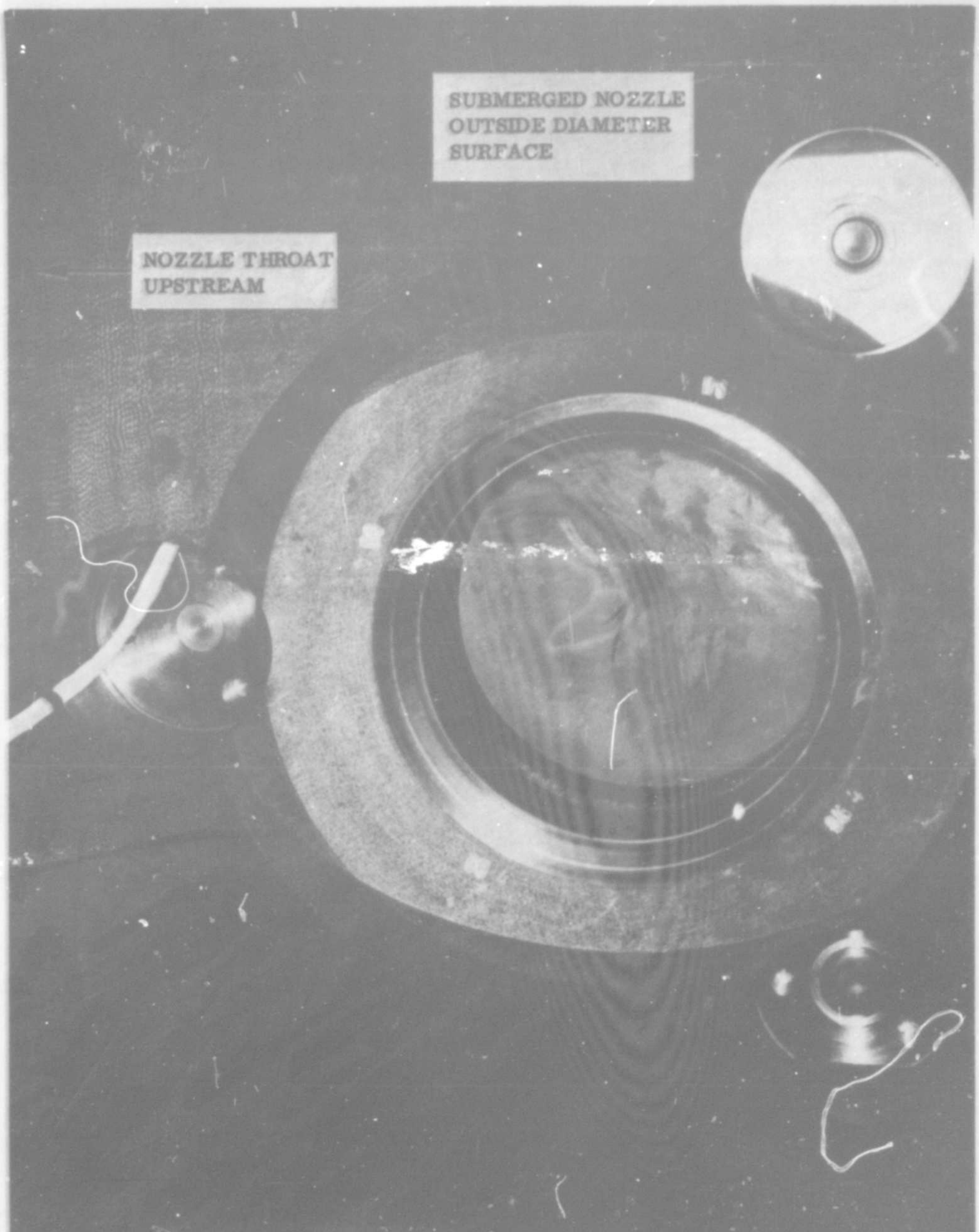

Figure 4. Pretest Machined Orifice Port 3 Inlet

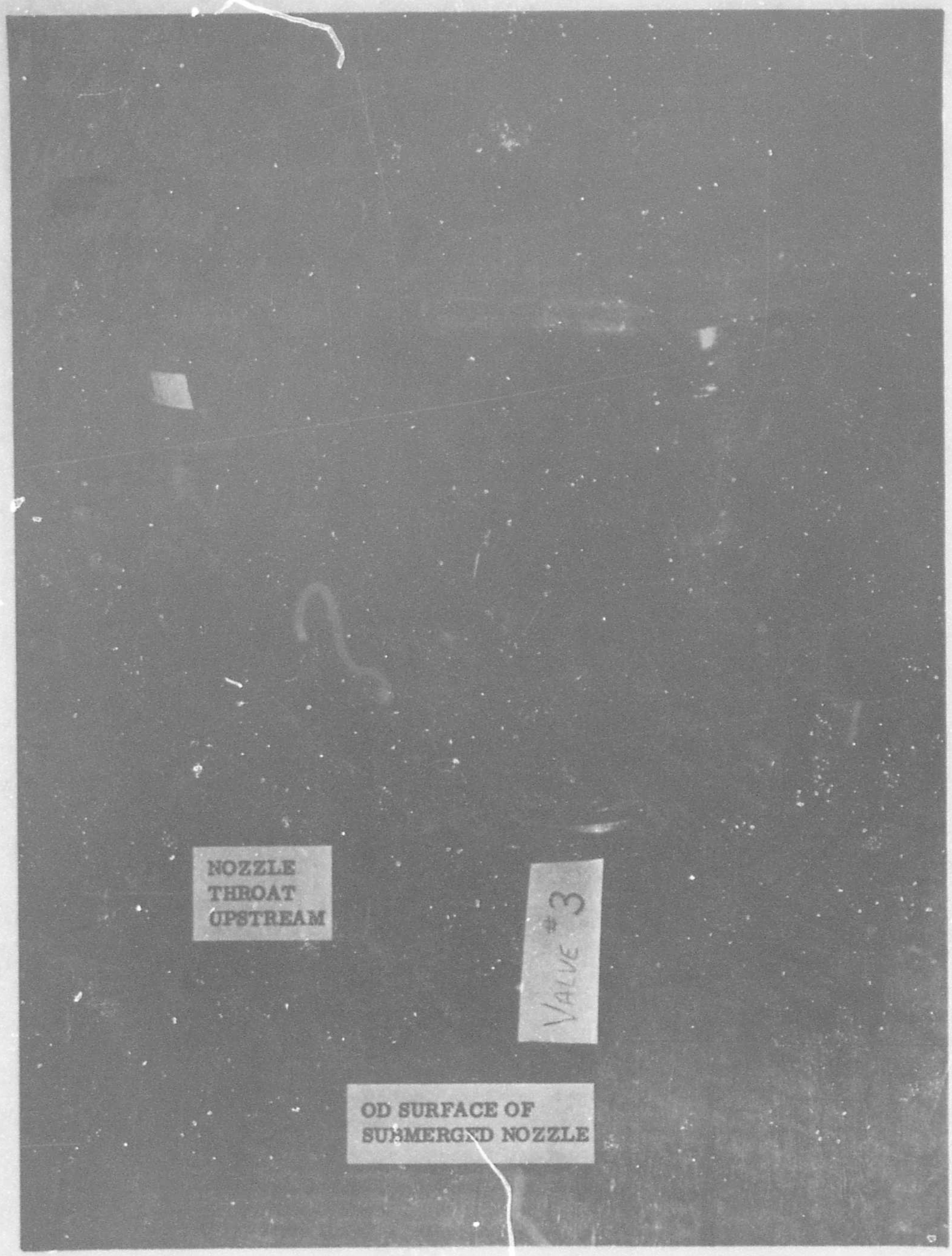

Figure 5. Pintle Valve Assembly 3 Orifice Port

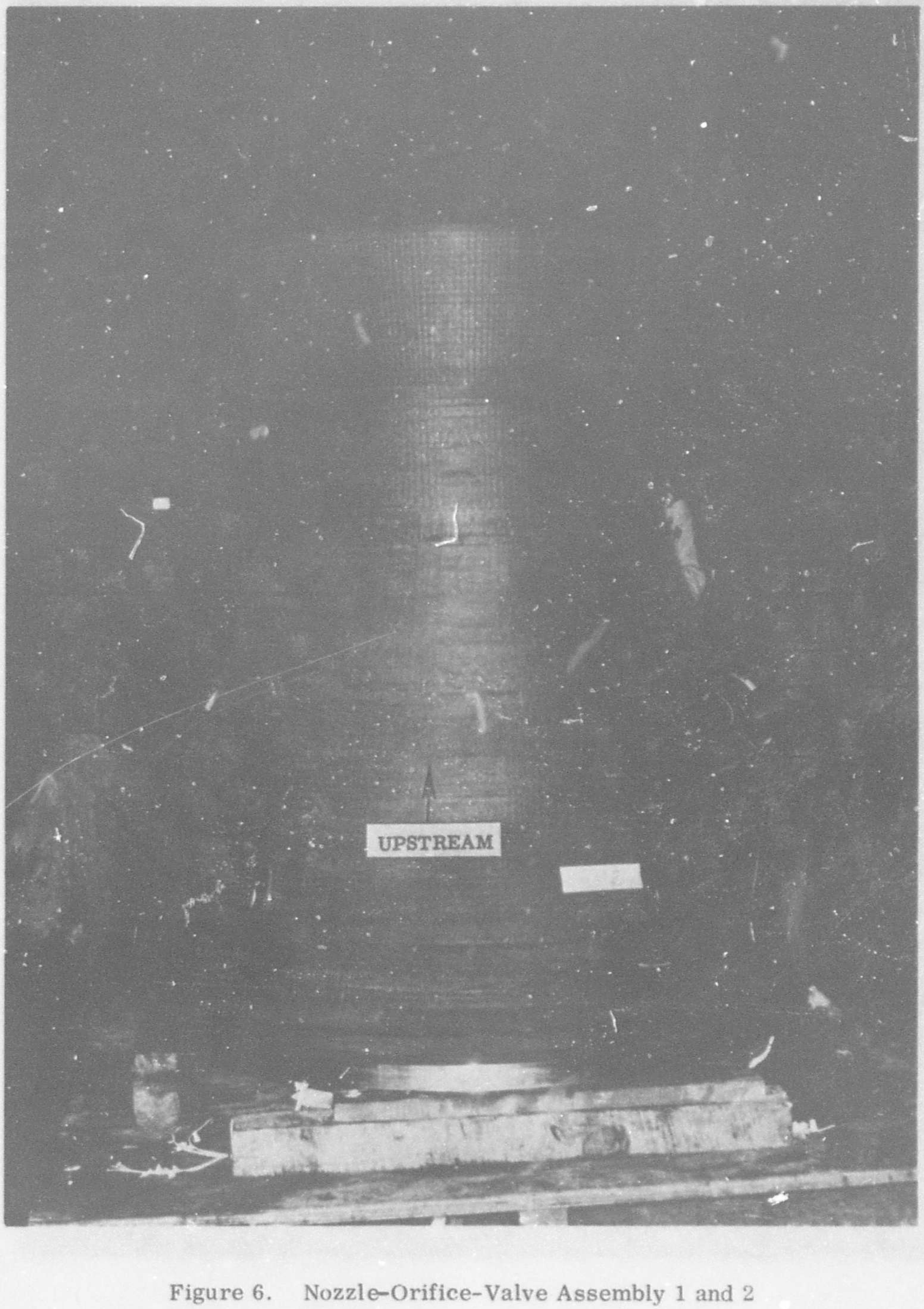

Figure 6. Nozzle-Orifice-Valve Assembly 1 and 2

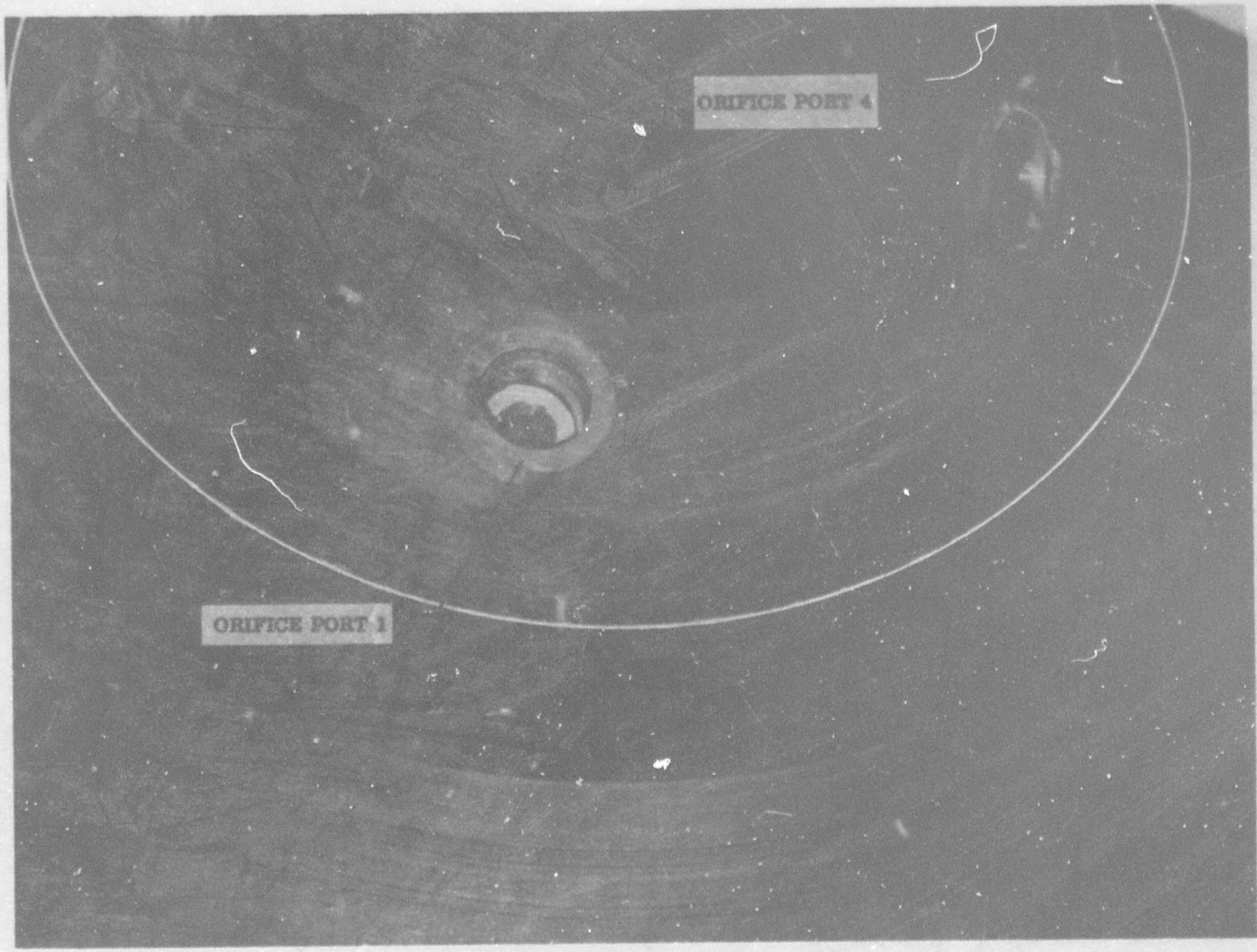

Figure 7. Orifice Ports 1 and 4 in Nozzle Exit Cone

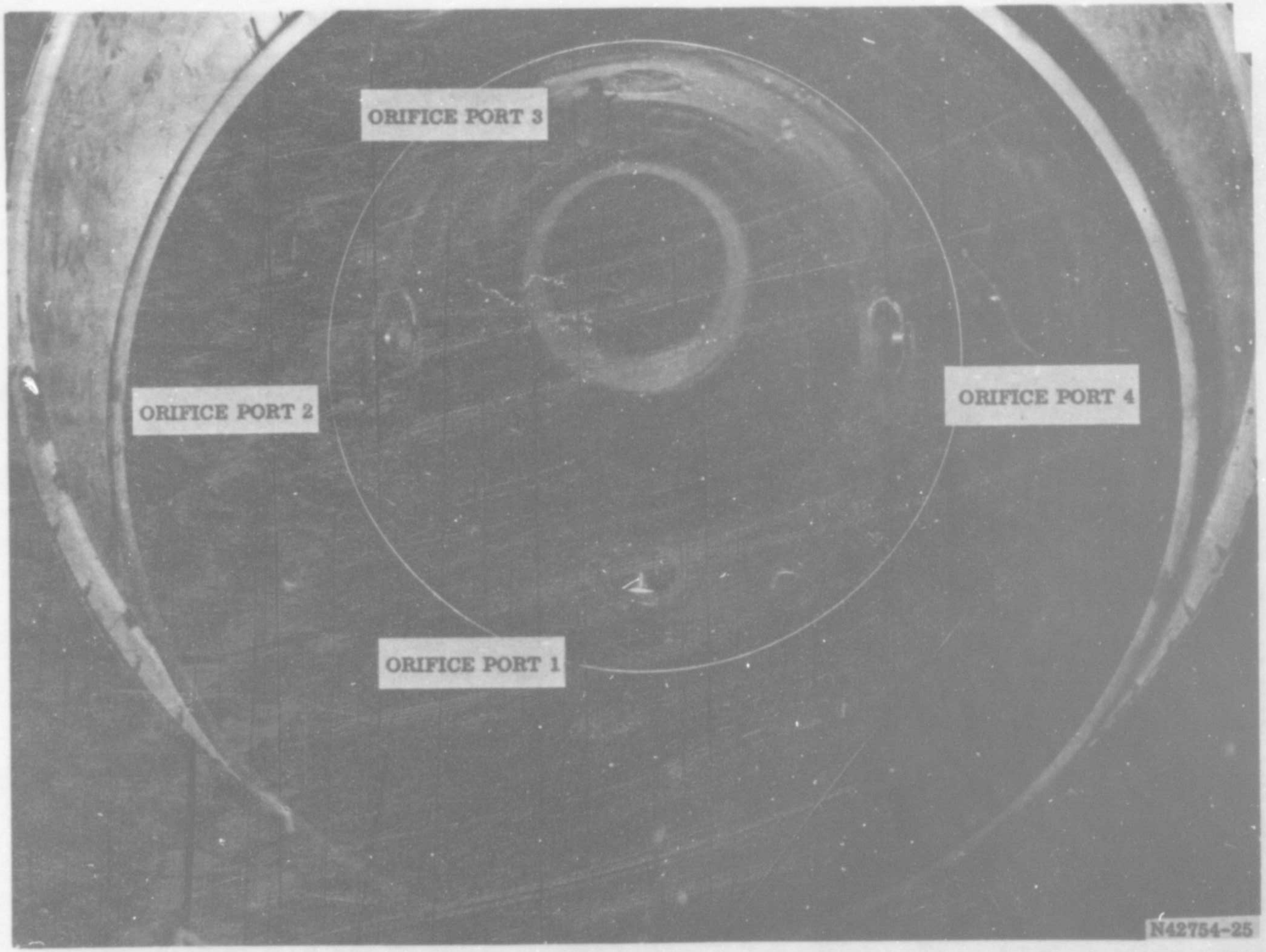

Figure 8. Four Orifice Ports in Nozzle Exit Cone

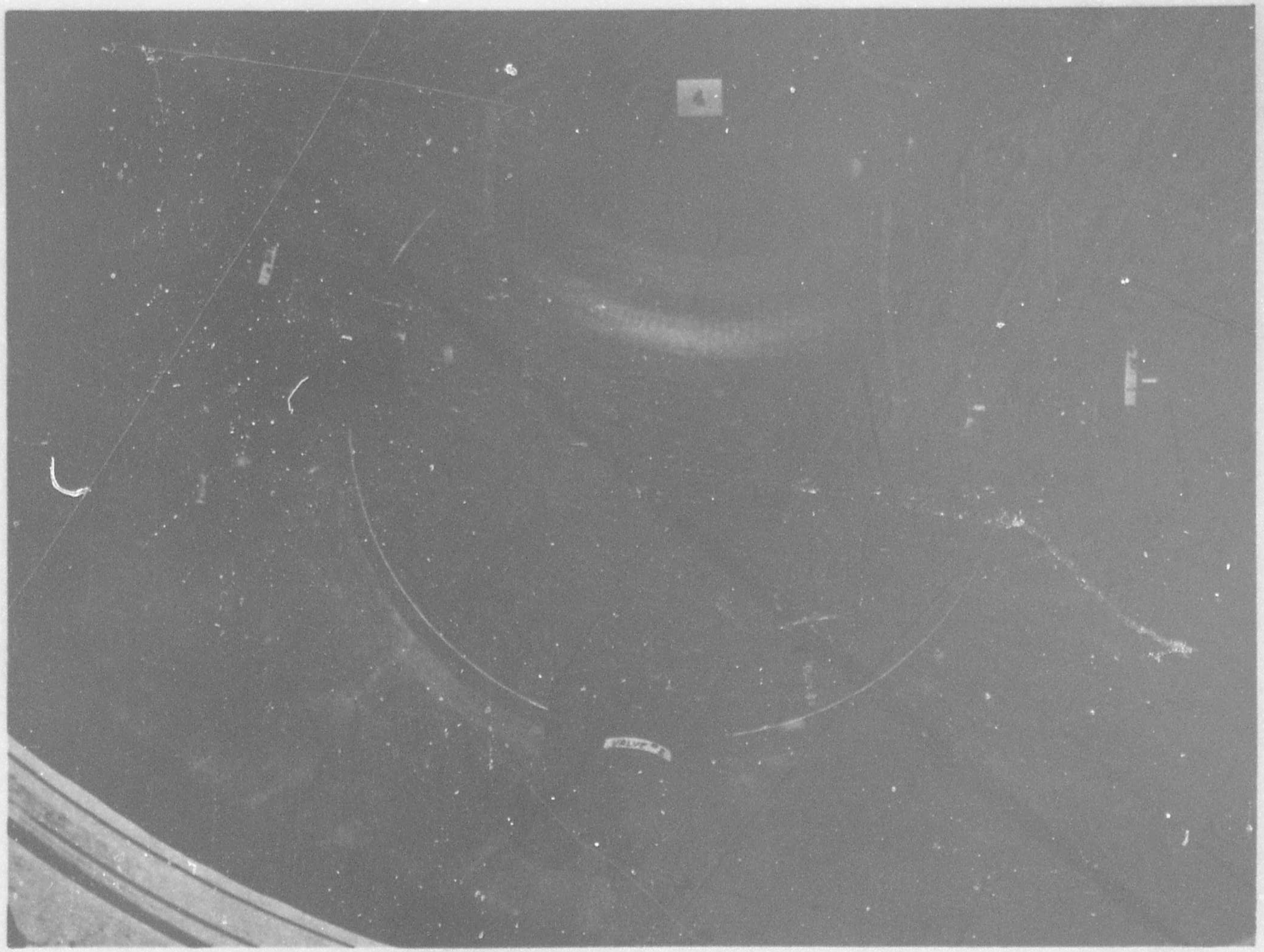

Figure 9. Nozzle-Orifice-Valve-Aft Closure Assembly

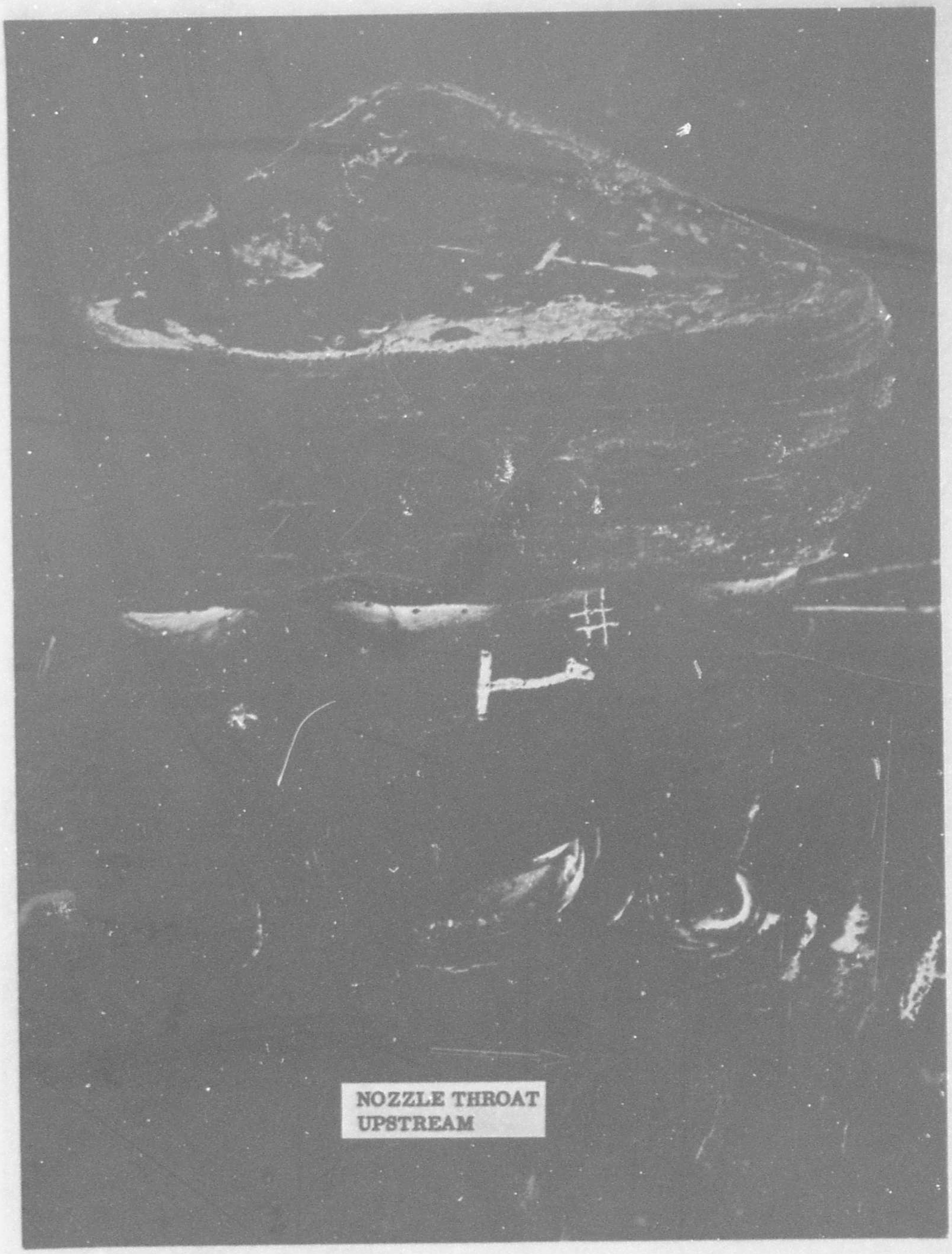

Figure 10. Post-Test Orifice Valve 1

Figure 11. Valve 1 After Test

Figure 12. Valve and Orifice 1 After Test

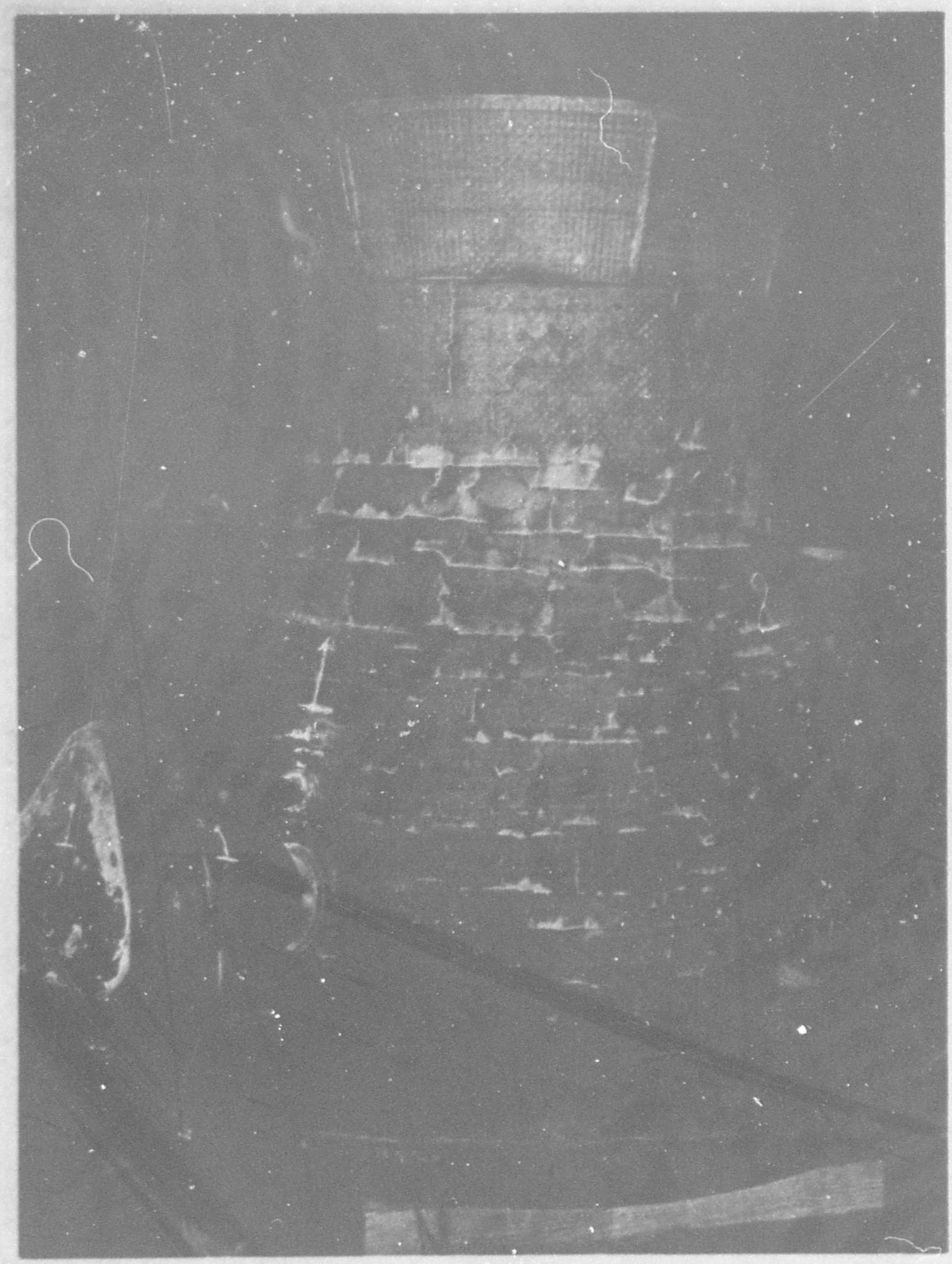

Figure 13. External View of Nozzle Submerged Section and Valve 1

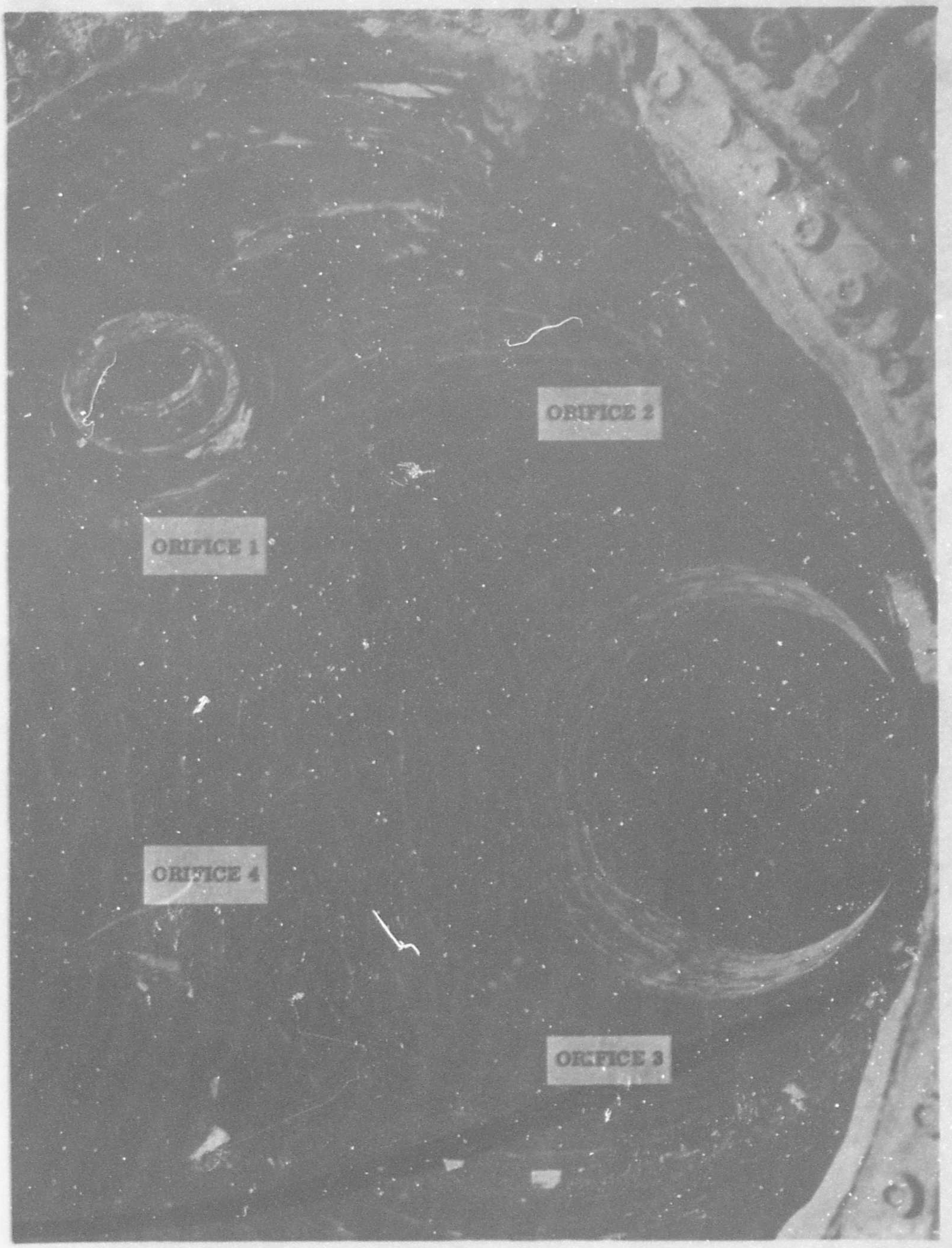

Figure 14. Nozzle-Orifice Ports Erosion at Exit Cone

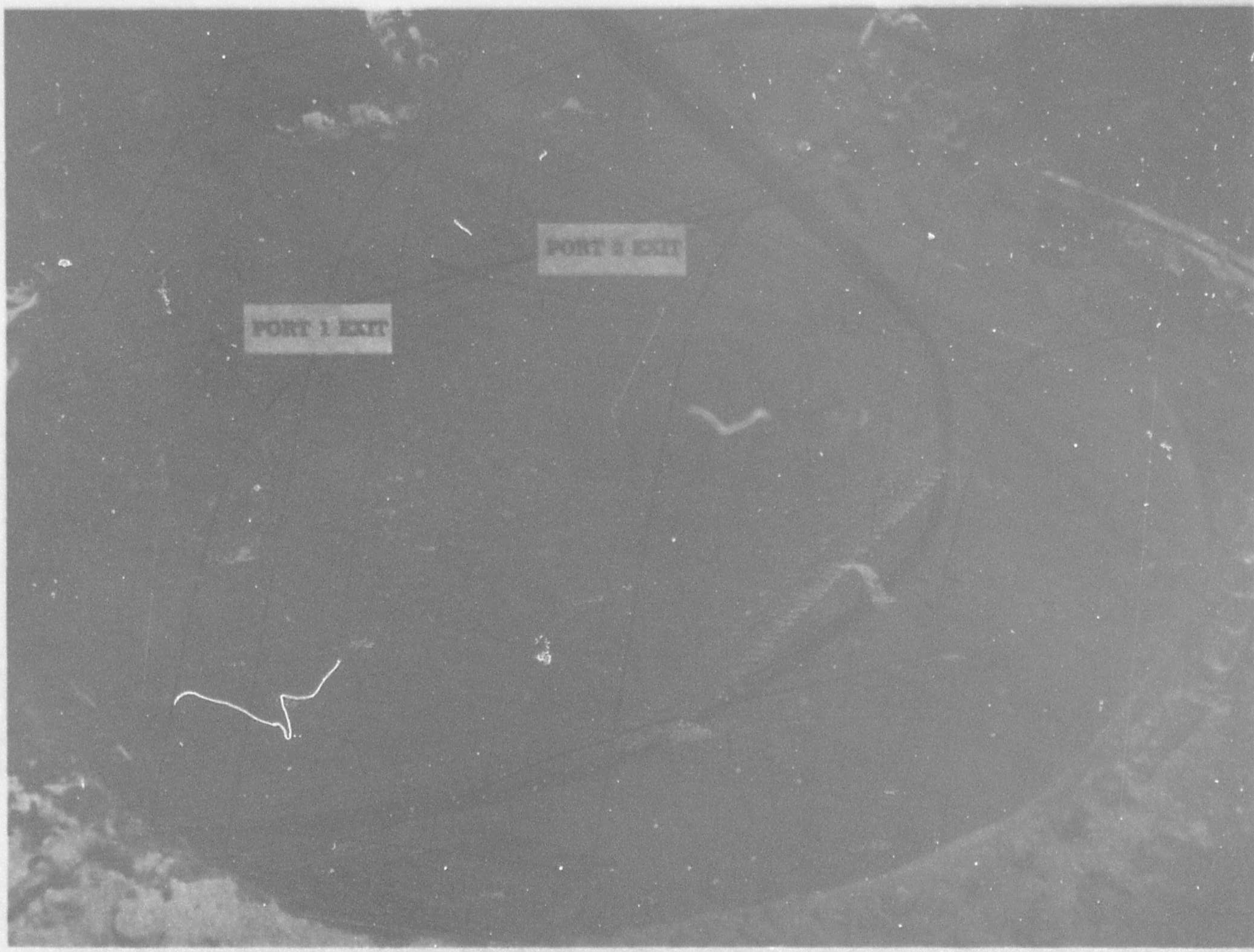

Figure 15. Orifice Ports 1 and 2 Erosion

Figure 16. Post-Test Nozzle Exit Cone, Port Orifice 1

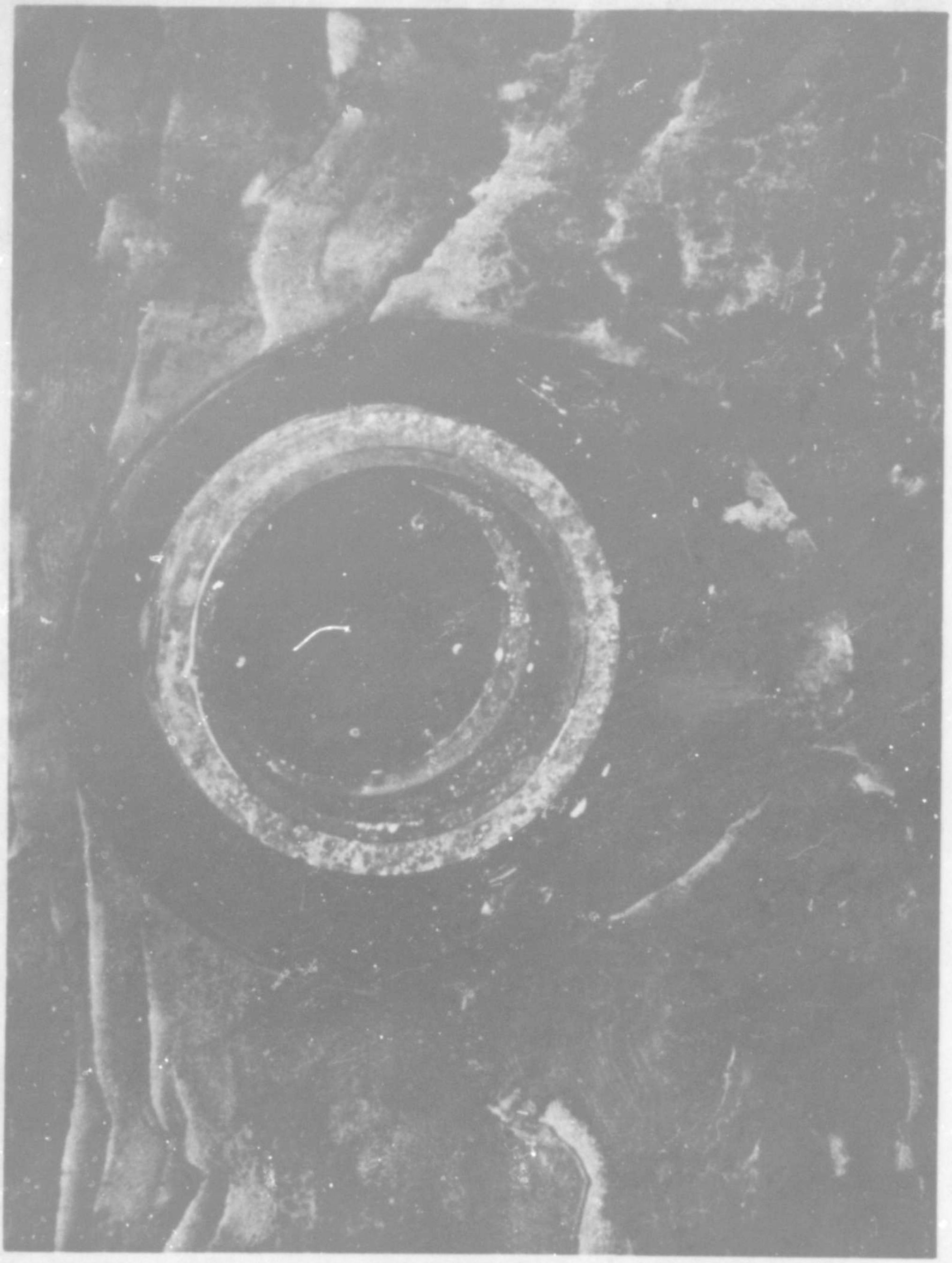

Figure 17. Post-Test Pintle Orifice, Port 1

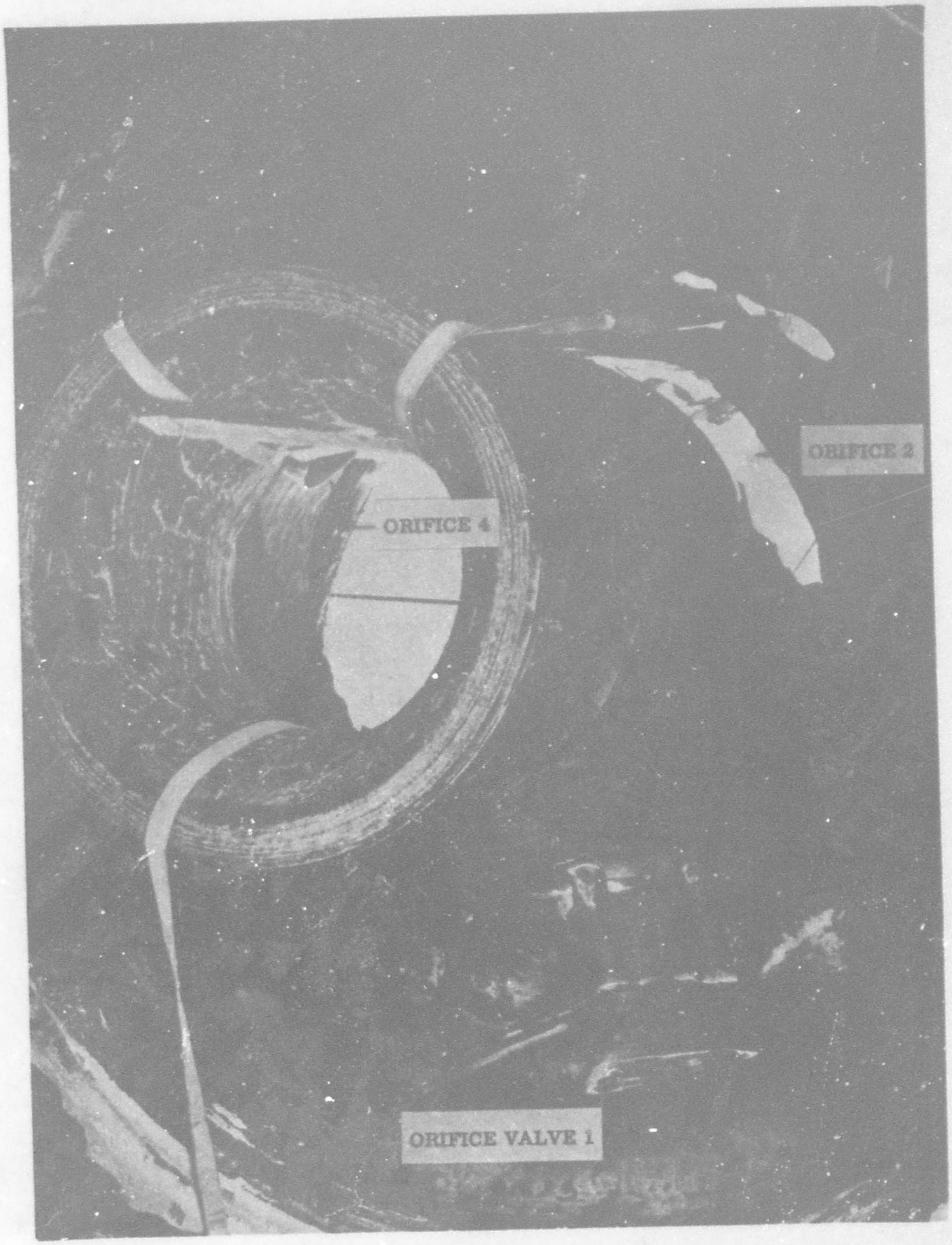

Figure 18. Port 1 Nozzle Burnthrough

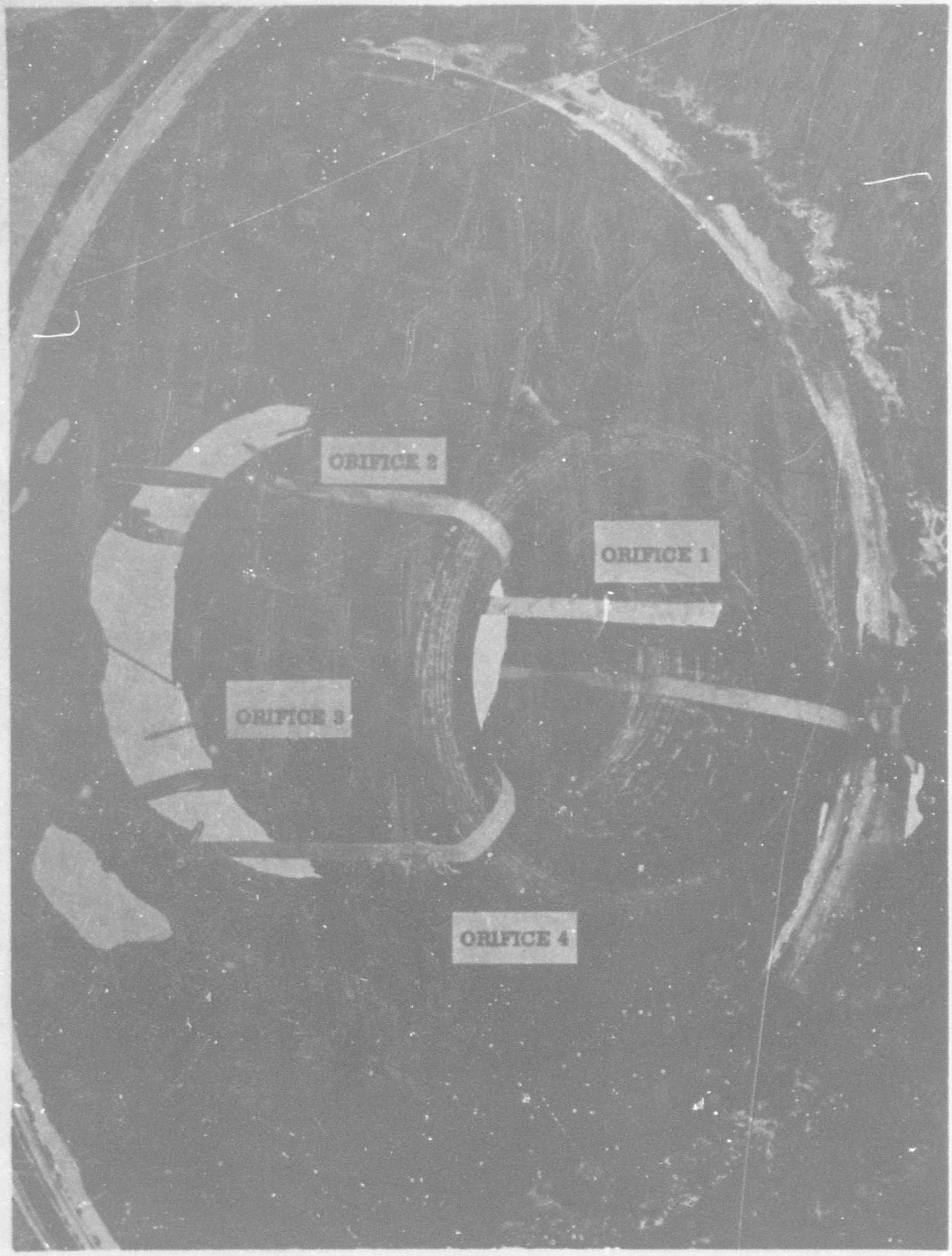

Figure 19. Nozzle-Case Closure Burnthrough

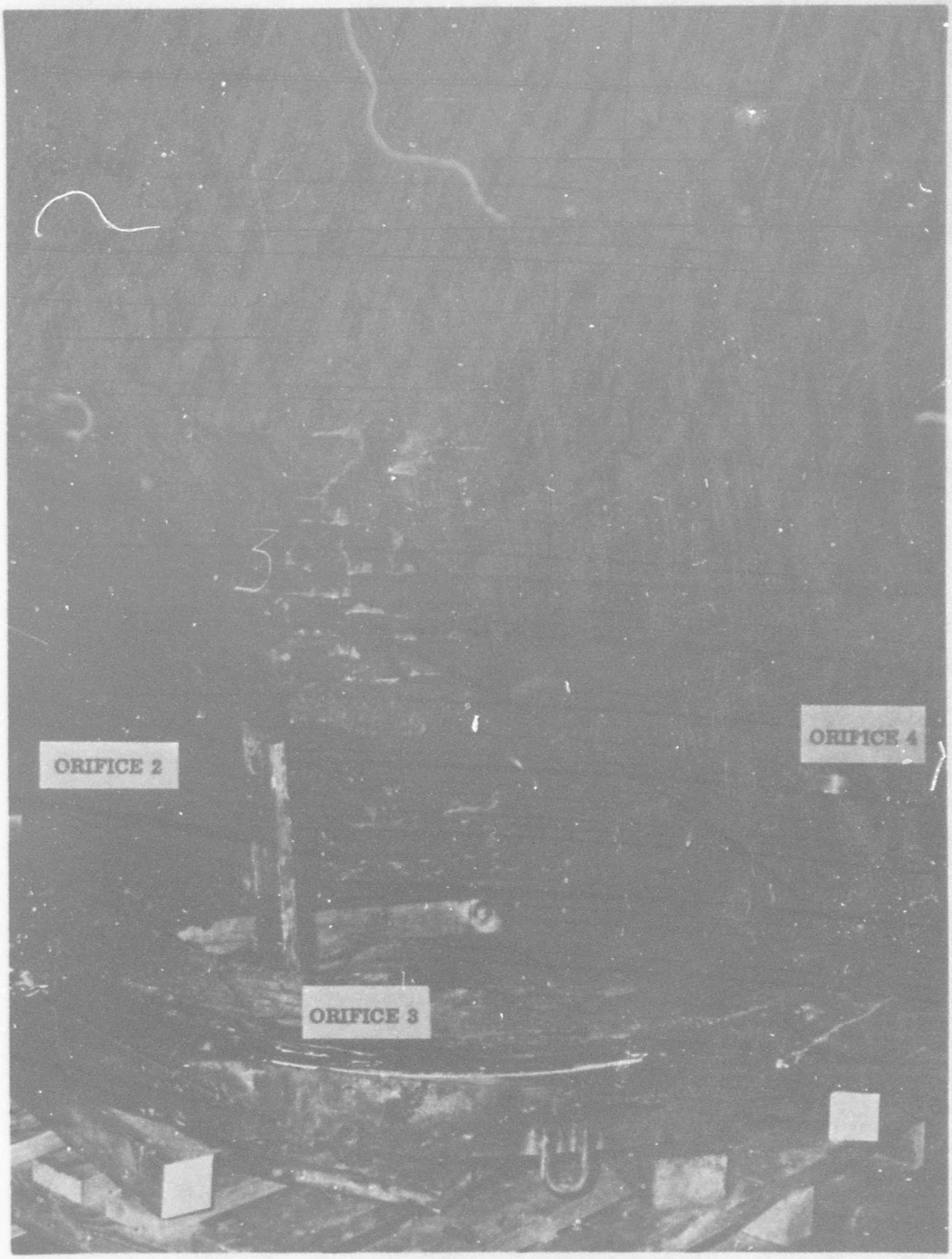

Figure 20. Nozzle Burnthrough, Ports 2, 3, and 4

Figure 21. Submerged Nozzle Cross Section at Port 1

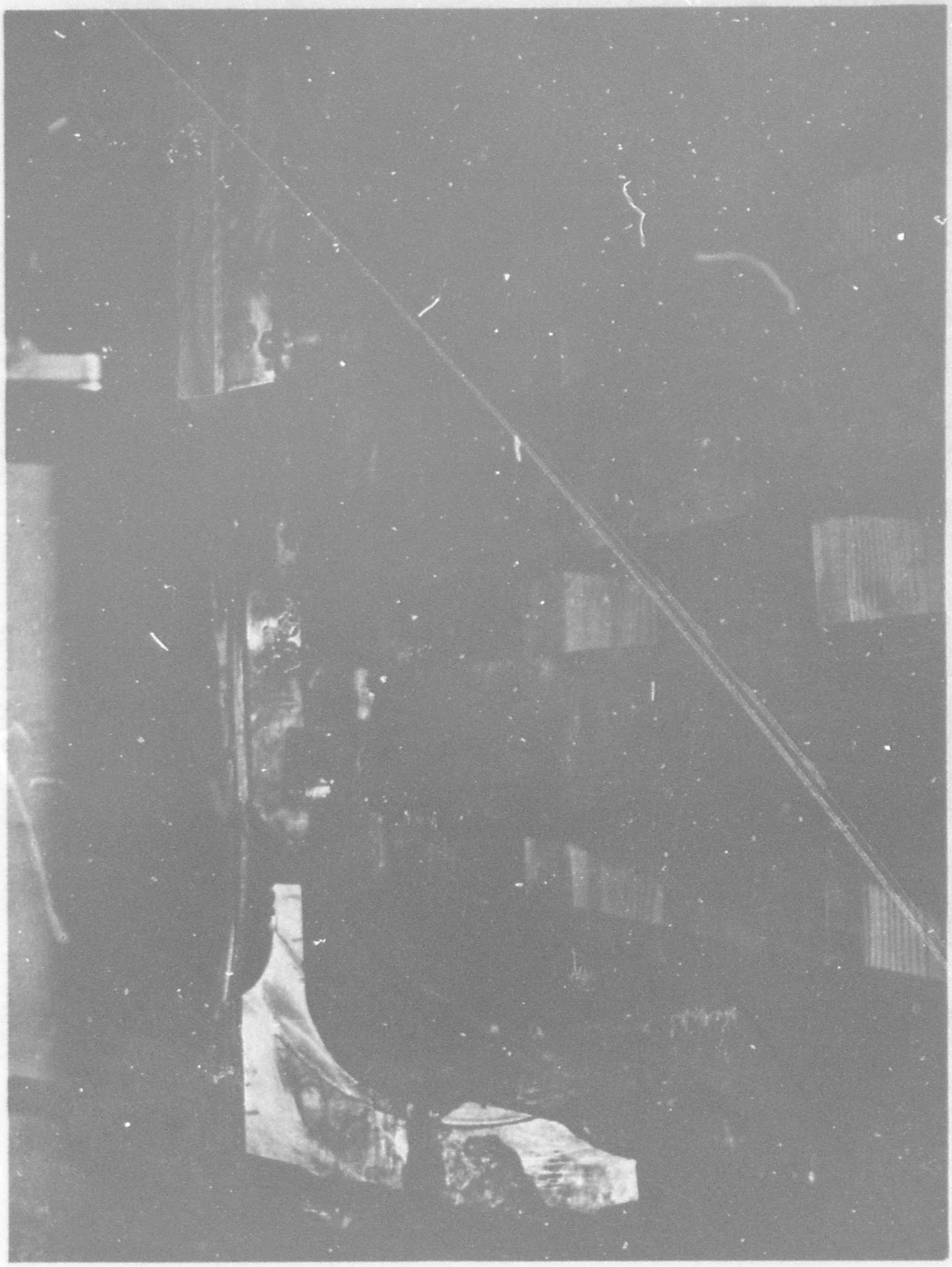

Figure 22. Port 1 Cross Section

Figure 23. Submerged Nozzle Cross Section 45 Deg Away From Port 1

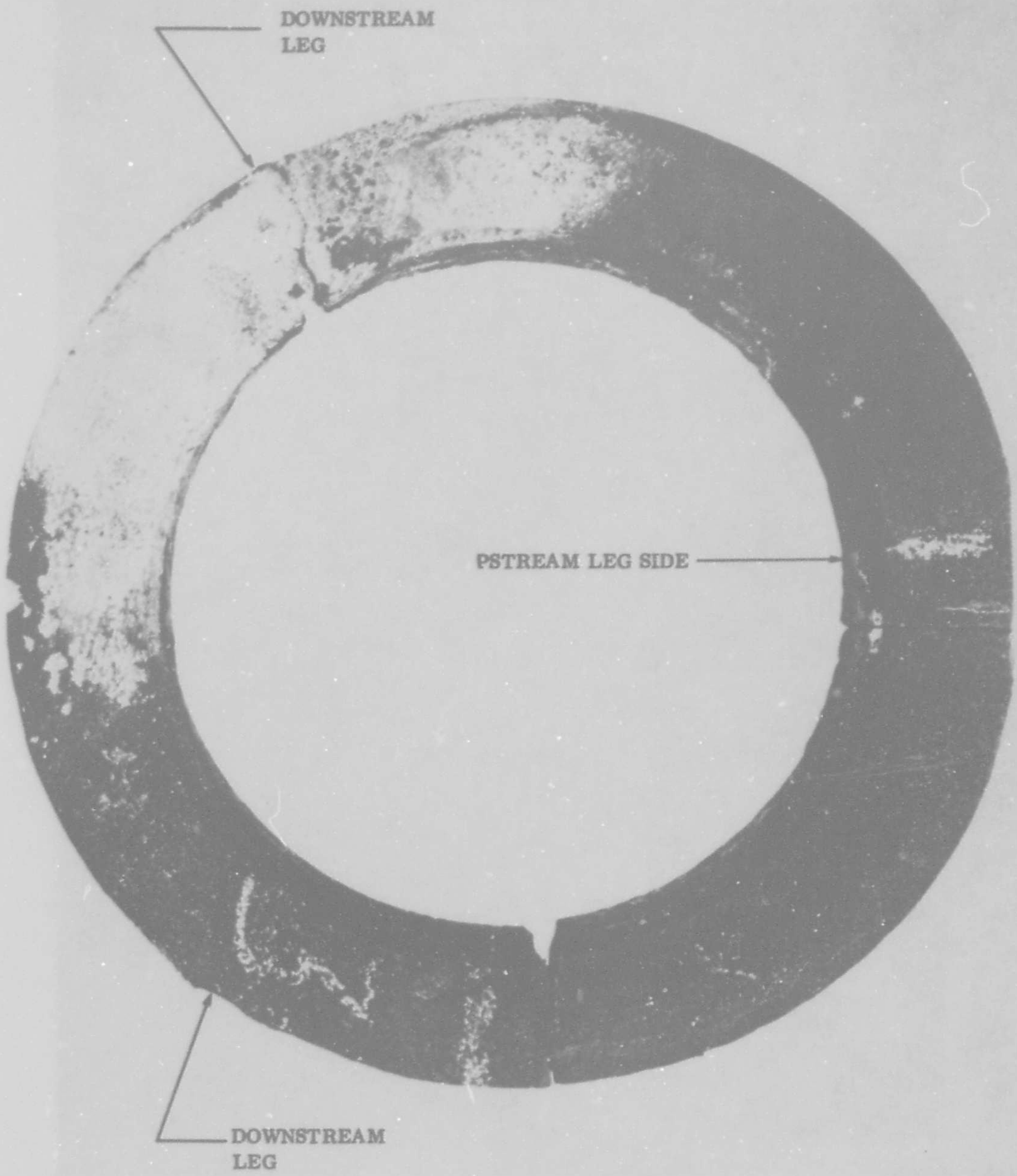

Figure 24. Port 1 Graphite - Inlet Face

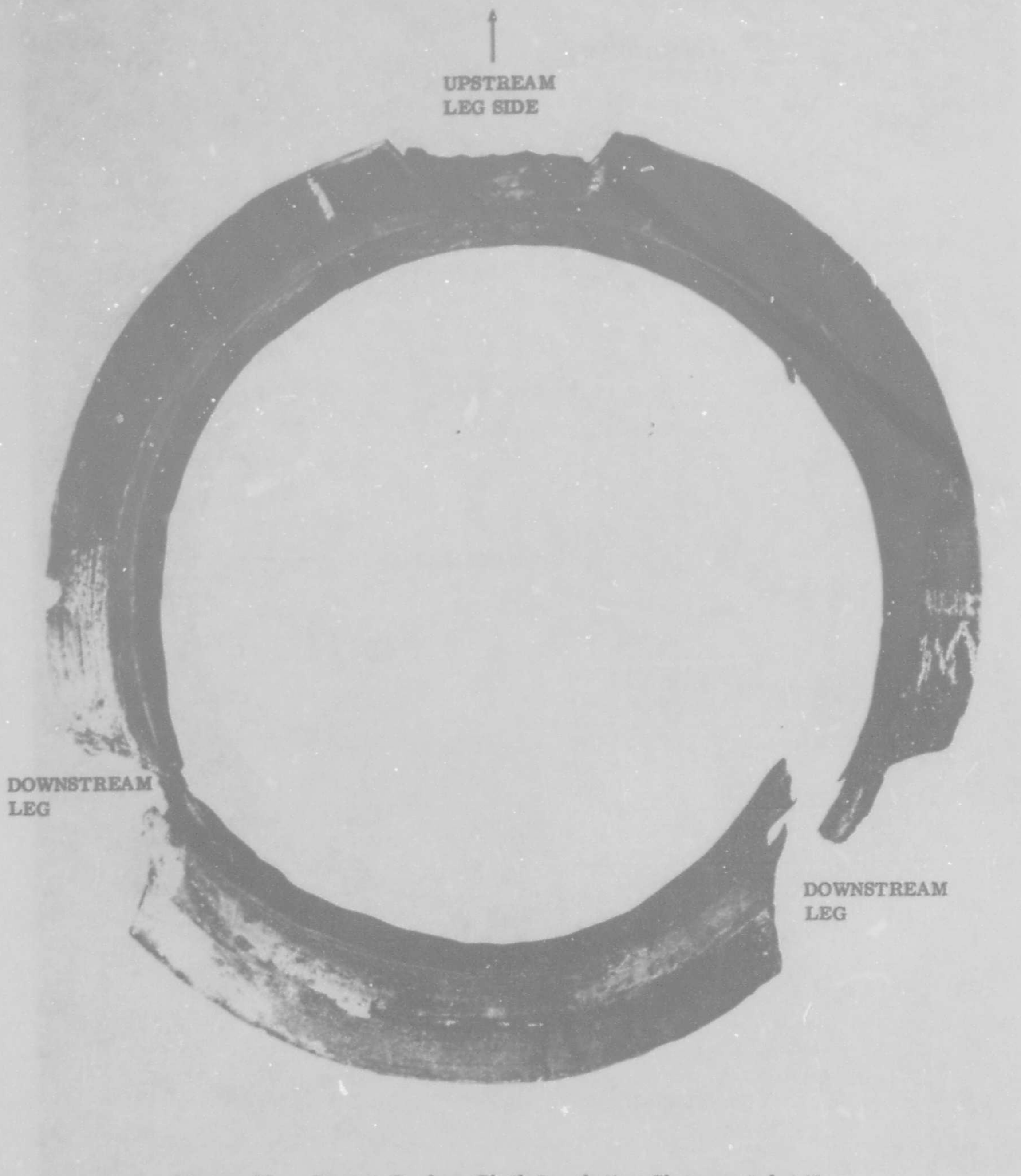

Figure 25. Port 1 Carbon Cloth Insulation Sleeve - Inlet Face

Figure 26. Port 1 Tungsten Throat and Retention Nut - Exit Cone Face

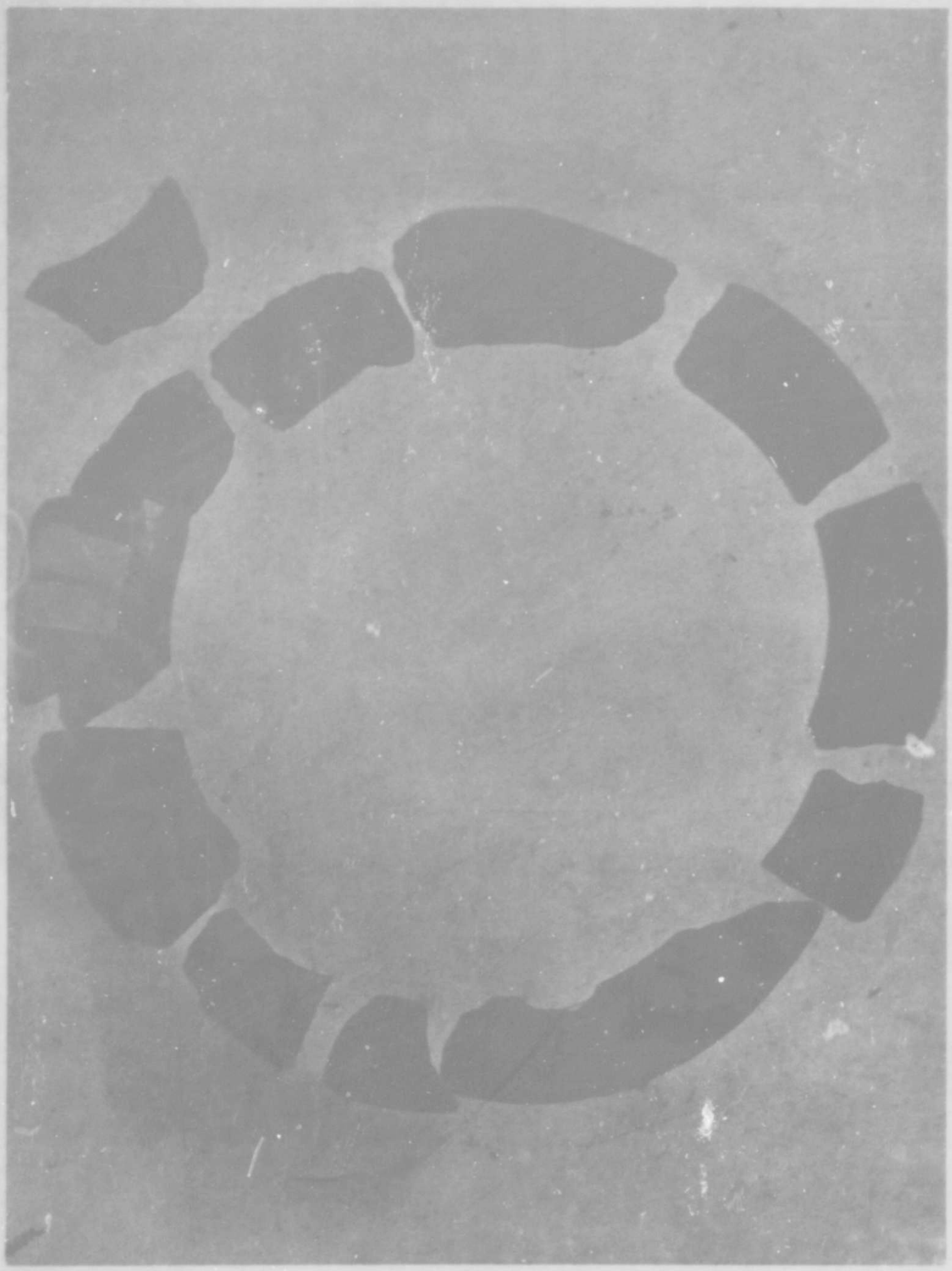

Figure 27. Port Inlet Graphite Ring Segments

Figure 28. Port Exit Cone PTB Ring Segments

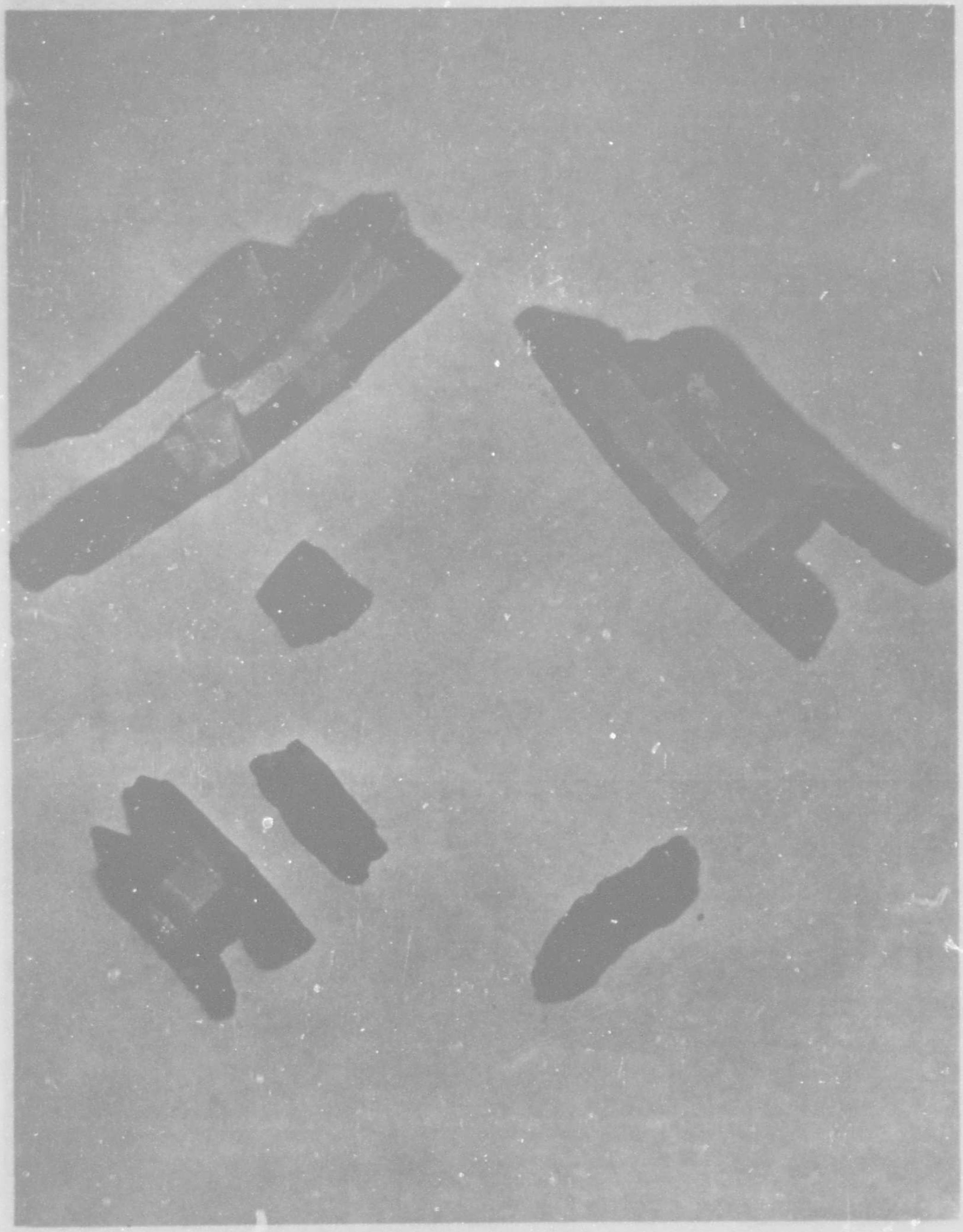

Figure 29. Port Exit Cone PTB Ring and Layer Segments

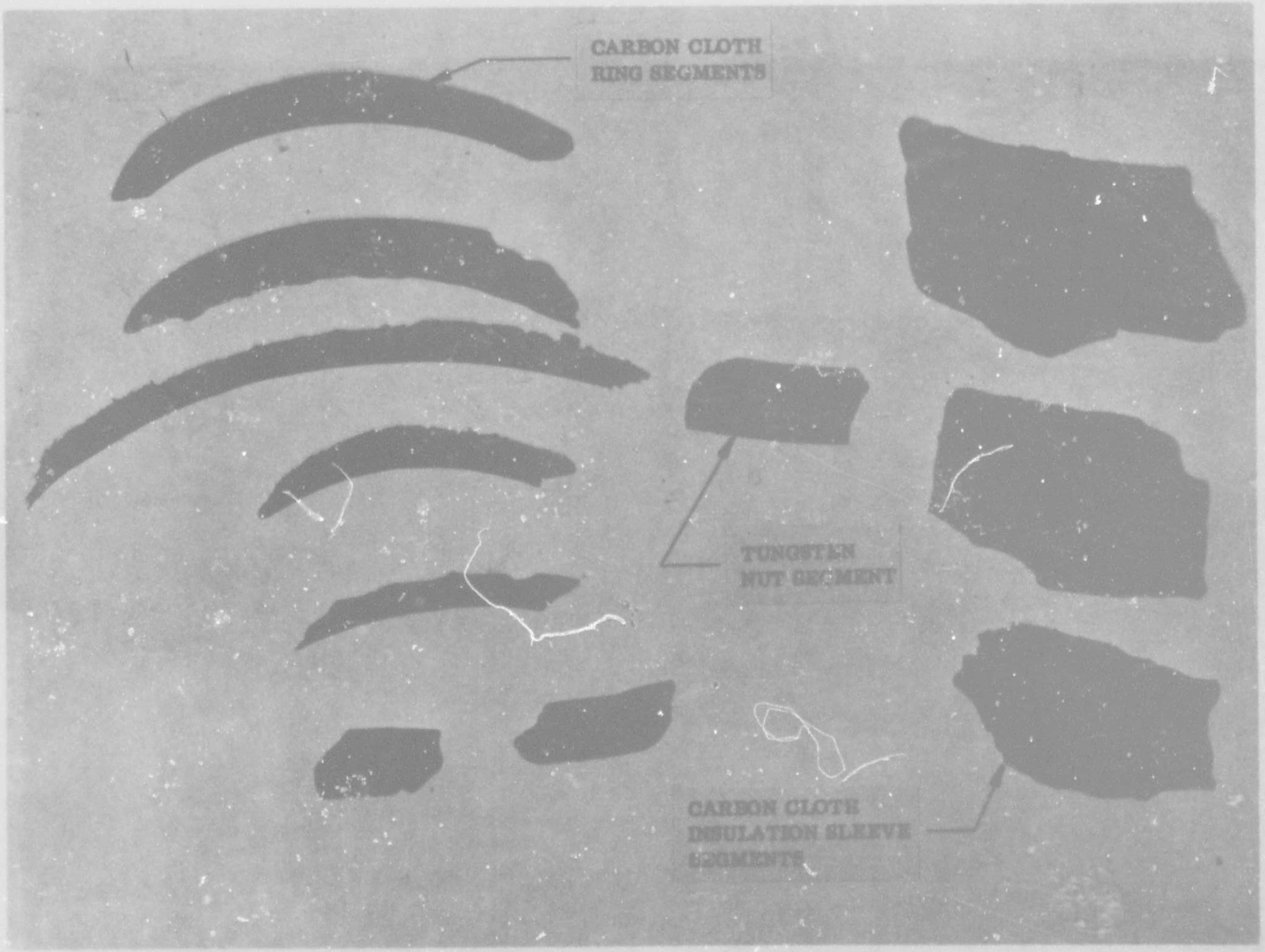

Figure 30. Post-Test Port Components

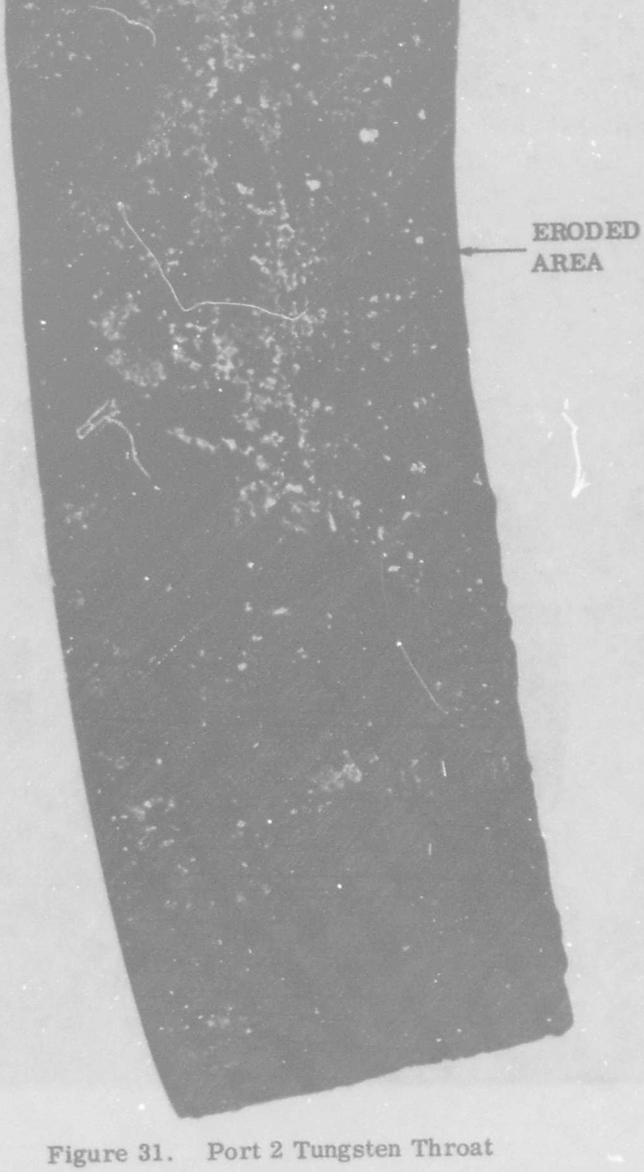

Figure 31. Port 2 Tungsten Throat

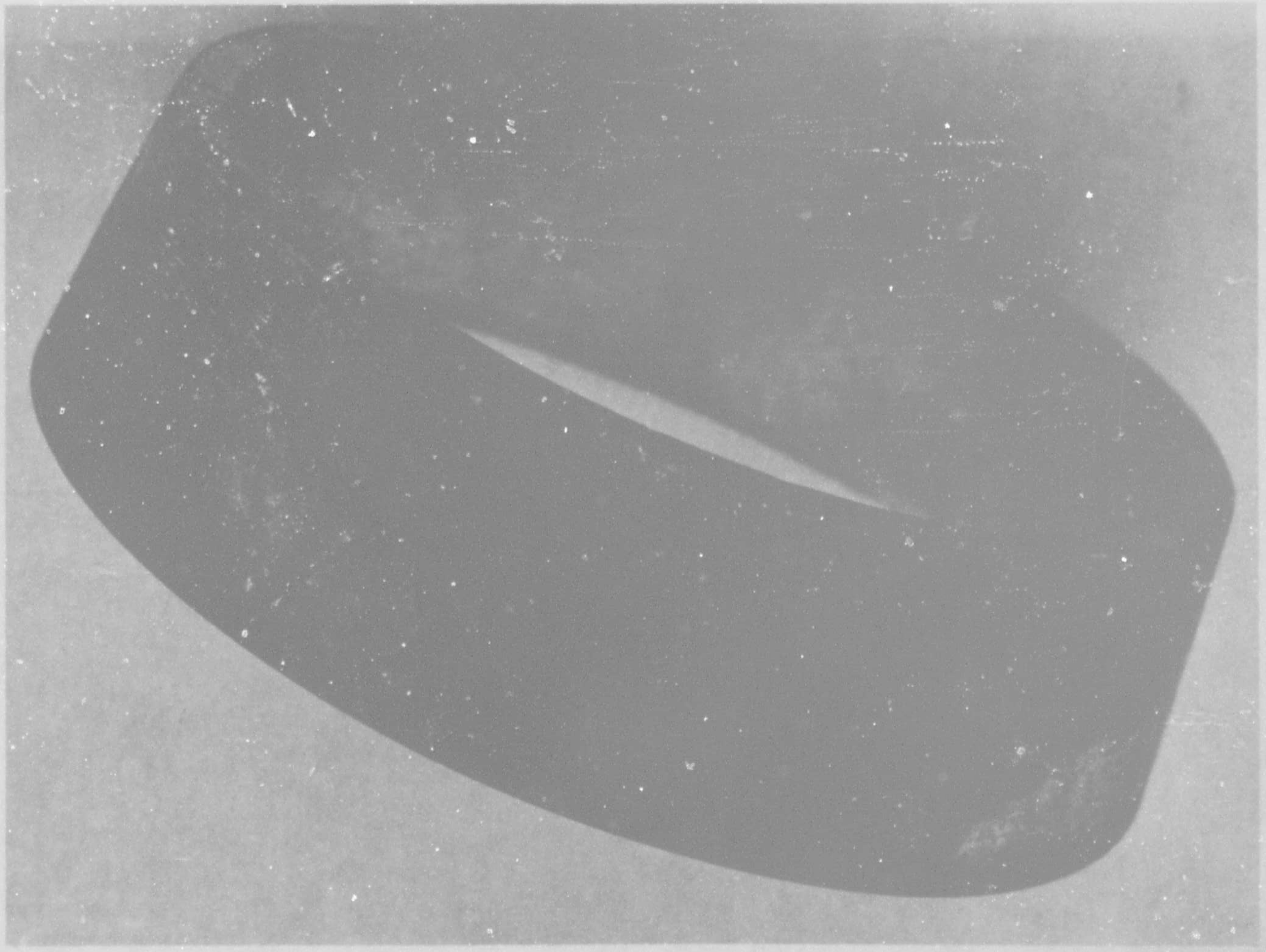

Figure 32. Port 3 Tungsten Throat

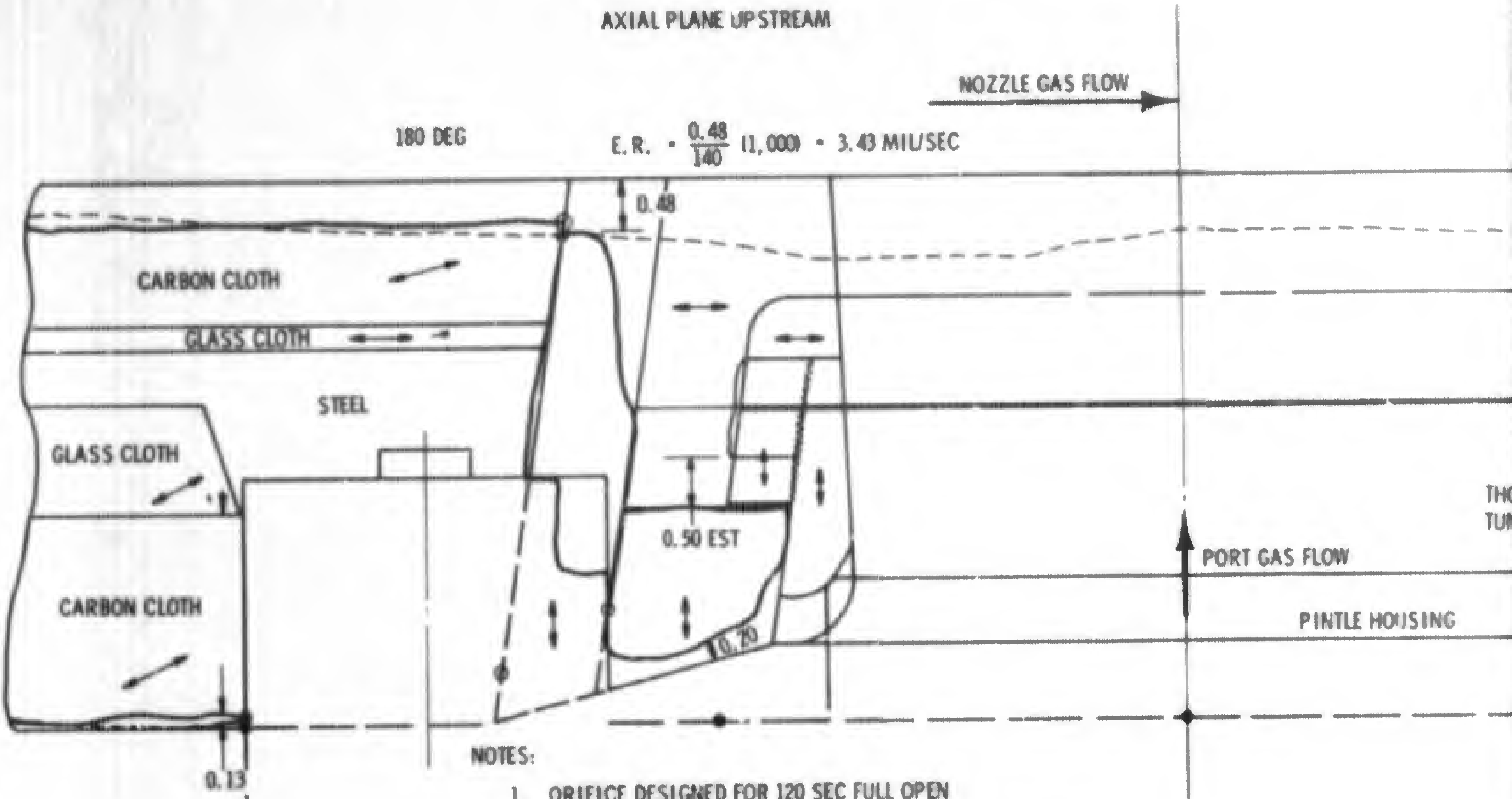

NOTES:

1. ORIFICE DESIGNED FOR 120 SEC FULL OPEN
2. MOTOR ACTION TIME = 140.00 SEC
3. <u>ACTUAL DUTY CYCLE DATA</u>
   VALVE OPEN 7.6 SEC   VALVE CLOSED 132.4 SEC
   AVERAGE MOTOR PRESSURE DURING VALVE OPEN: 683 PSIA
   AVERAGE MOTOR PRESSURE DURING VALVE CLOSED: 401 PSIA
4. MATERIAL GRAIN OR PLY ORIENTATION
5. PROPELLANT - CURED CP GRAIN - TP-H1077 = TP-H1011
6. PINTLE LOADING: MAX ACTUATOR EXTEND - 16,000 LB; MAX ACTUATOR RETRACT - 6,000 LB
7. <u>ACTUAL PORT ORIFICE DUTY CYCLE</u>
   CLOSED 0.00 - 32.65 SEC   PRESSURE RANGE 600 - 780 PSIA
   OPEN 32.65 - 40.20 SEC   PRESSURE RANGE 670 - 730 PSIA
   CLOSED & LEAKING 40.20 - 140.00 SEC   PRESSURE RANGE 670 - 75 PSIA
8. PROGRAMED SIDE FORCE - MAX = 44,000 LB
9. PINTLE AND ORIFICE WERE WELDED TOGETHER AND THE PORT LEAKING THROUGH CRACKS AND ERODED AREAS AT THE END OF STATIC TEST

EROSION LINE KEY

—— 0 DEG THRU

— — 45 DEG AWA

A

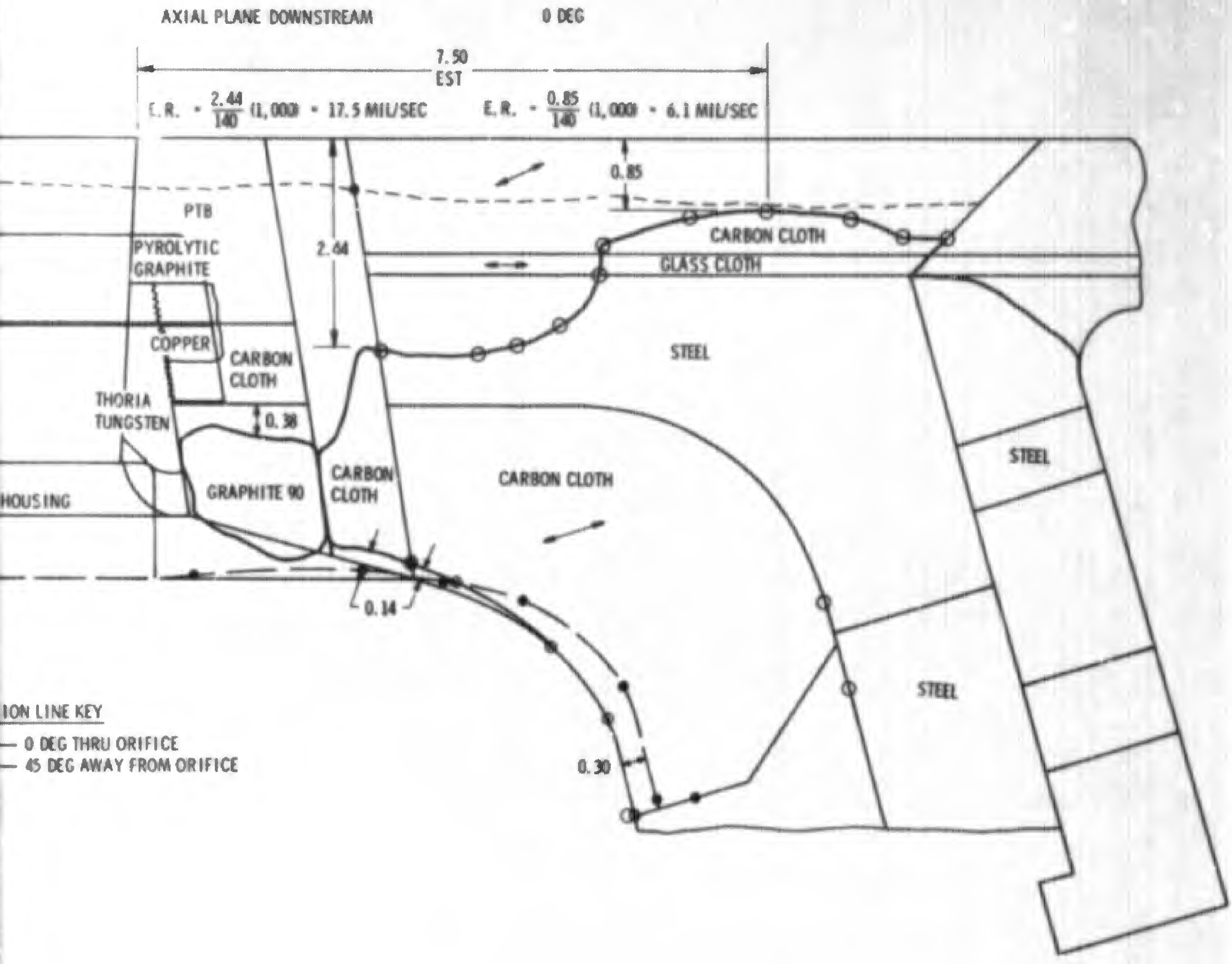

Figure 33. Orifice Port 1 Erosion (0 to 180 Deg Plane)

B

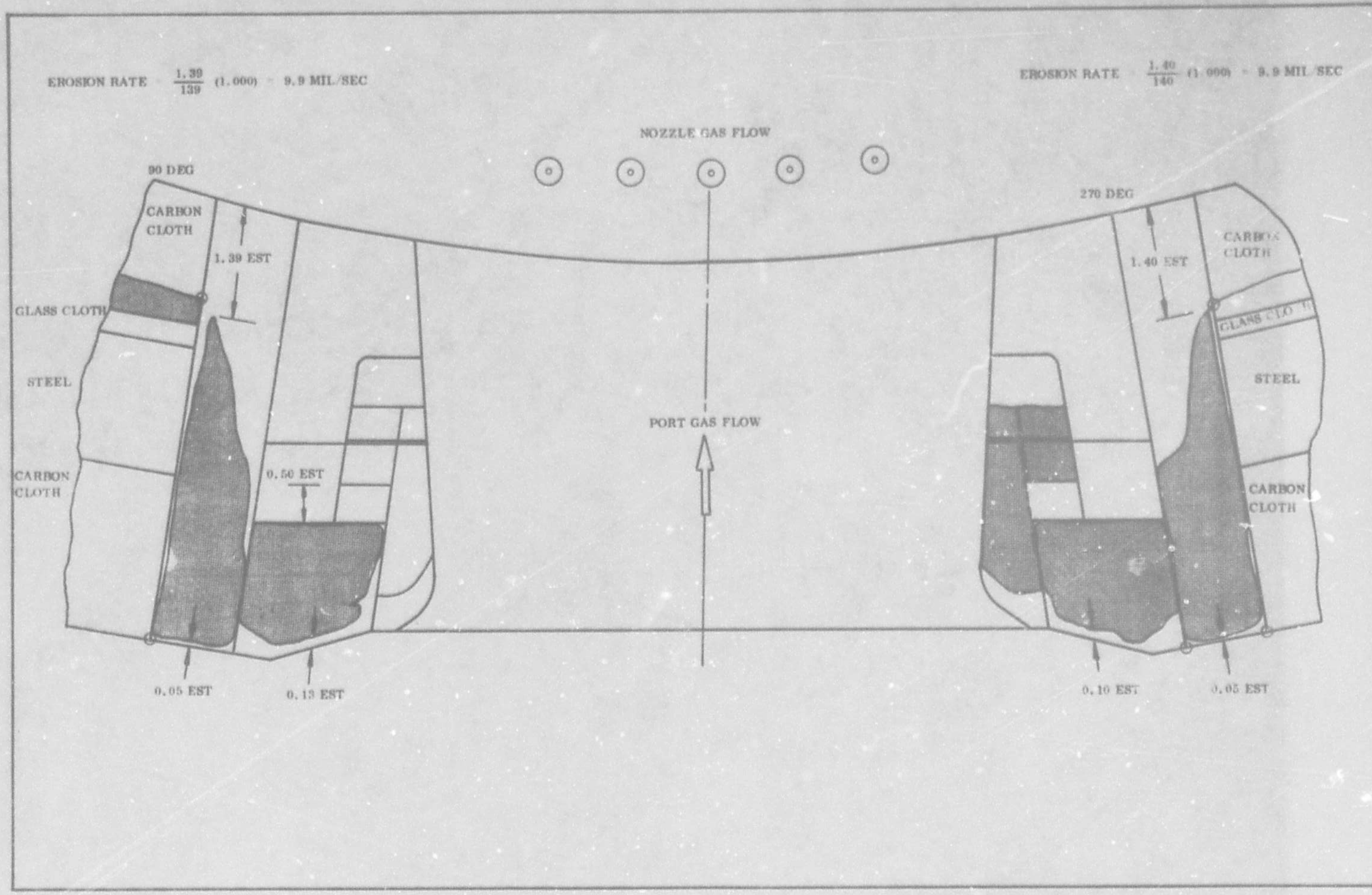

Figure 34. Orifice Port 1 Erosion (90 to 270 Deg Plane)

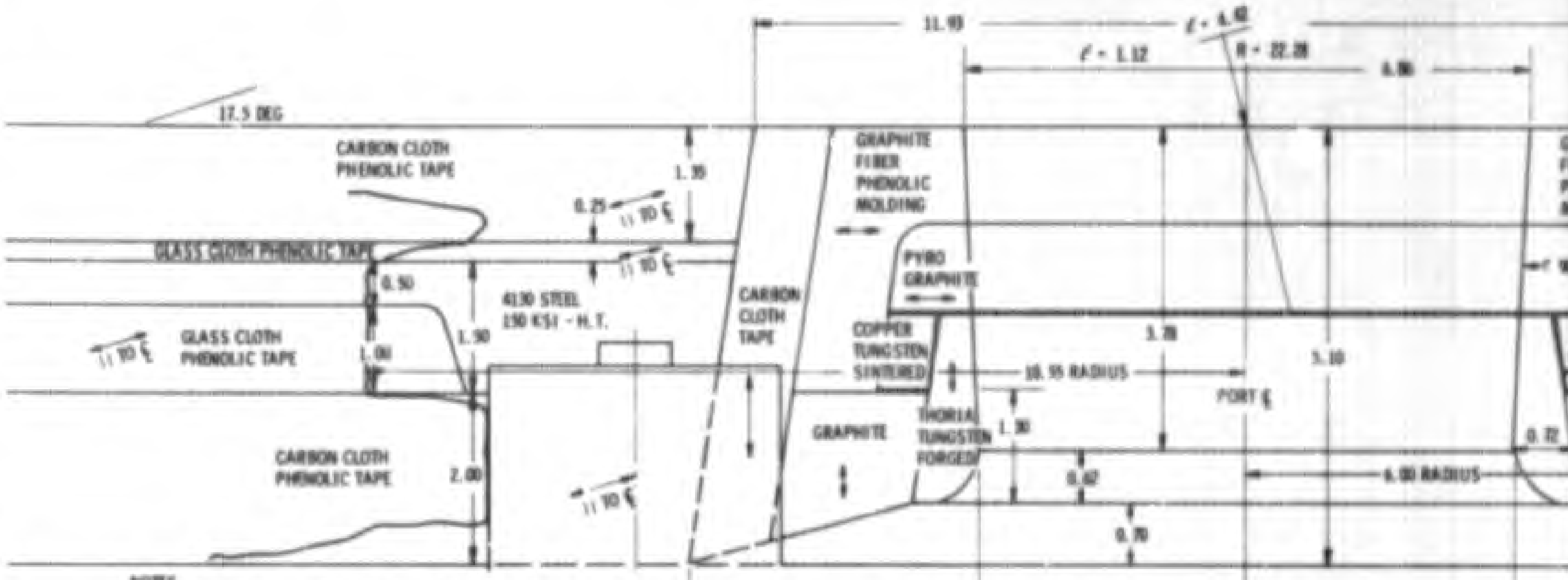

NOTES:

1. ORIFICE DESIGNED FOR 120 SEC FULL OPEN
2. MATERIAL GRAIN OR PLY ORIENTATION AS SHOWN
3. PROPELLANT-CURED CP GRAIN - TP-H1077 * TP-H1011
4. MOTOR ACTION TIME * 140 SEC
5. ACTUAL PINTLE LOADING — MAX ACTUATOR EXTEND - 16,000 LB; MAX ACTUATOR RETRACT - 5,600 LB
6. ACTUAL TVC DUTY CYCLE
   - CLOSED (0.00 - 5.90) SEC
   - OPEN (5.90 - 10.60) SEC
   - CLOSED (10.60 - 45.60) SEC
   - OPEN (45.60 - 53.35) SEC
   - CLOSED (53.35 - 65.76) SEC
   - OPEN (65.76 - 140.00) SEC
7. ACTUAL TVC DUTY CYCLE DATA
   - VALVE OPEN - 86.69 SEC VALVE CLOSED - 53.31 SEC
   - PORT TUNGSTEN THROAT RING LOST AT 65.76 SEC
   - PINTLE TUNGSTEN SHELL LOST AT 98.43 SEC
   - PINTLE VALVE LOST AT 106.56 SEC
   - VALVE - 12.45 SEC
     - TWO EVENTS
   - MAXIMUM ACTUAL SIDE FORCE - 47,000 LB

A

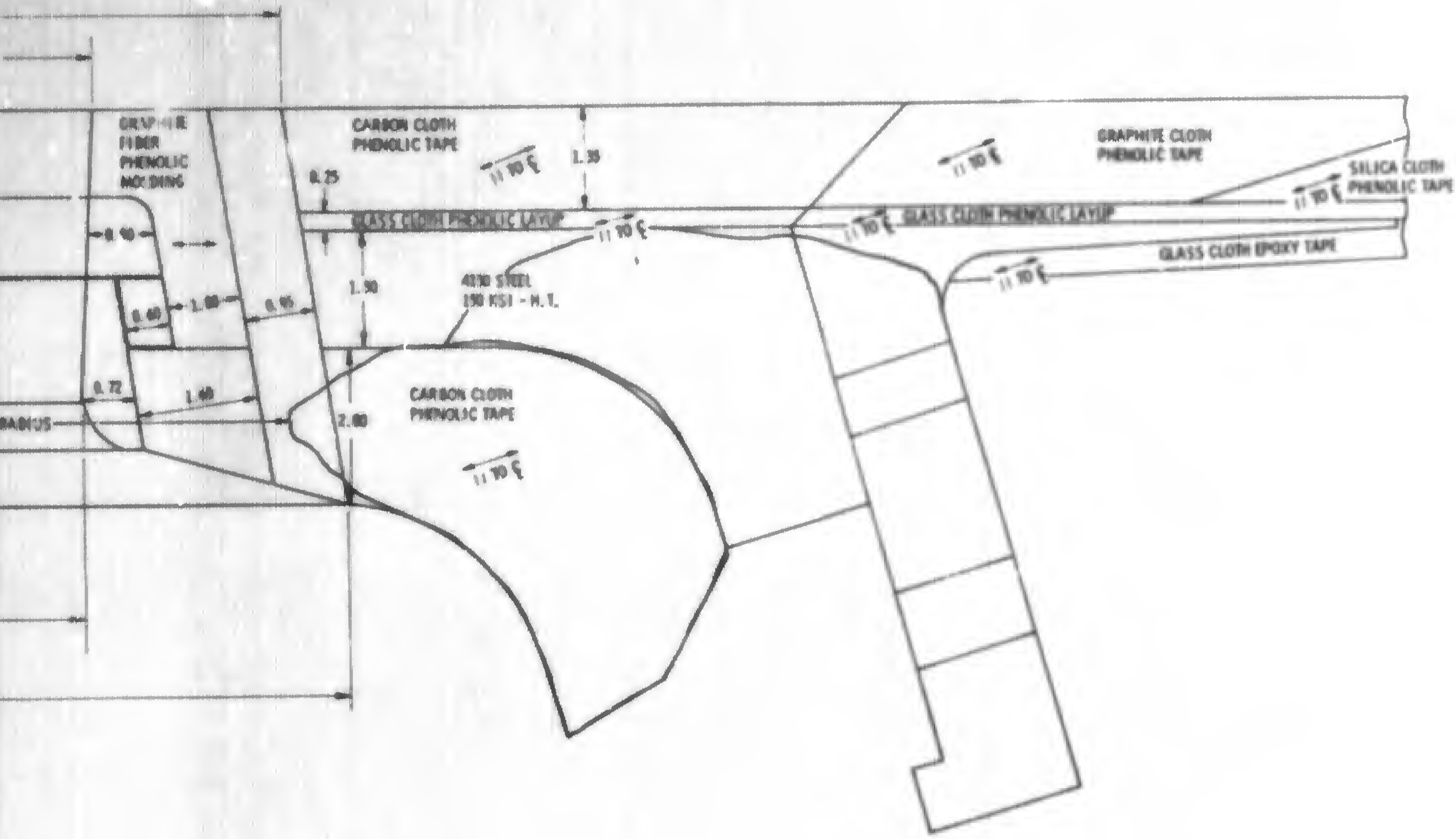

Figure 35. Orifice Port 2 Erosion

B

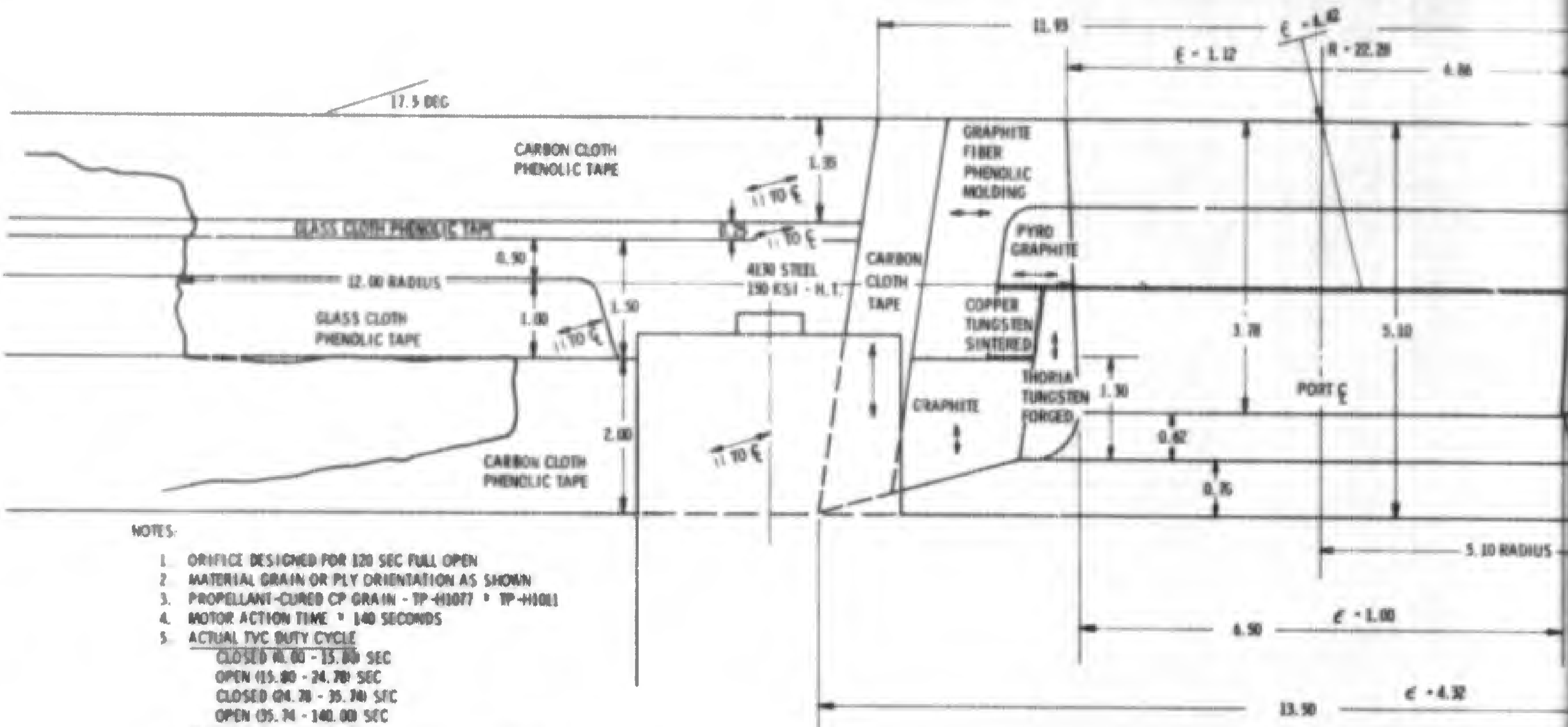

NOTES:

1. ORIFICE DESIGNED FOR 120 SEC FULL OPEN
2. MATERIAL GRAIN OR PLY ORIENTATION AS SHOWN
3. PROPELLANT-CURED CP GRAIN - TP-H1077 * TP-H1011
4. MOTOR ACTION TIME * 140 SECONDS
5. ACTUAL TVC DUTY CYCLE
   - CLOSED (0.00 - 15.80) SEC
   - OPEN (15.80 - 24.78) SEC
   - CLOSED (24.78 - 35.74) SEC
   - OPEN (35.74 - 140.00) SEC
6. ACTUAL DUTY CYCLE DATA
   - VALVE OPEN 113.24 SEC VALVE CLOSED 26.76 SEC
   - PORT TUNGSTEN THROAT RING LOST AT 35.74 SEC
   - PINTLE VALVE LOST AT 55.50 SEC
   - PINTLE SUPPORT PLATE LOST AT 55.56 SEC
   - VALVE OPEN BEFORE FAILURE - 8.98 SEC
   - ACTUAL PINTLE LOAD: MAX ACTUATOR EXTEND - 15,000 LB; MAX ACTUATOR RETRACT - 0 LB
   - ACTUAL SIDE FORCE MAXIMUM - 34,000 LB

A

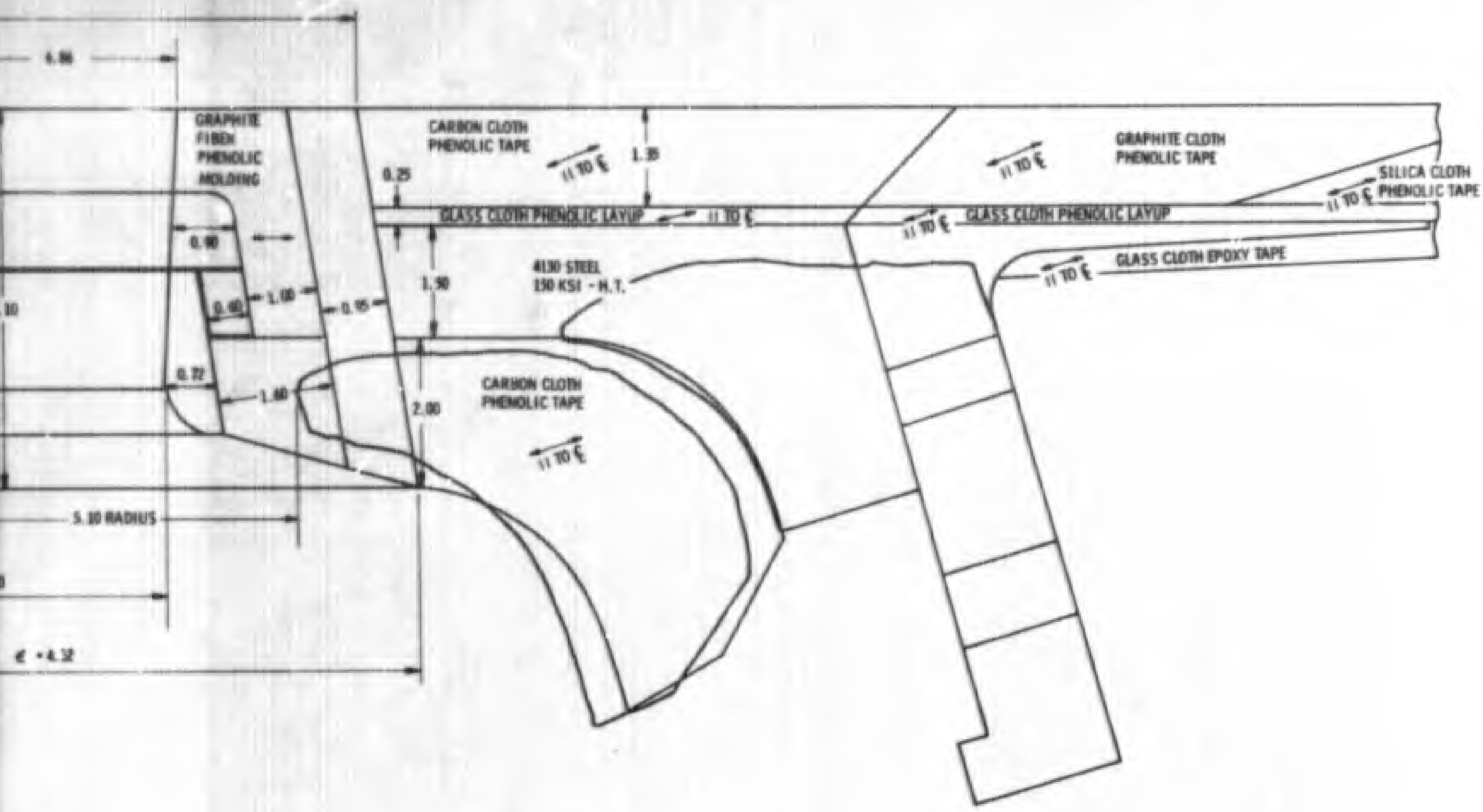

Figure 36. Orifice Port 3 Erosion

B

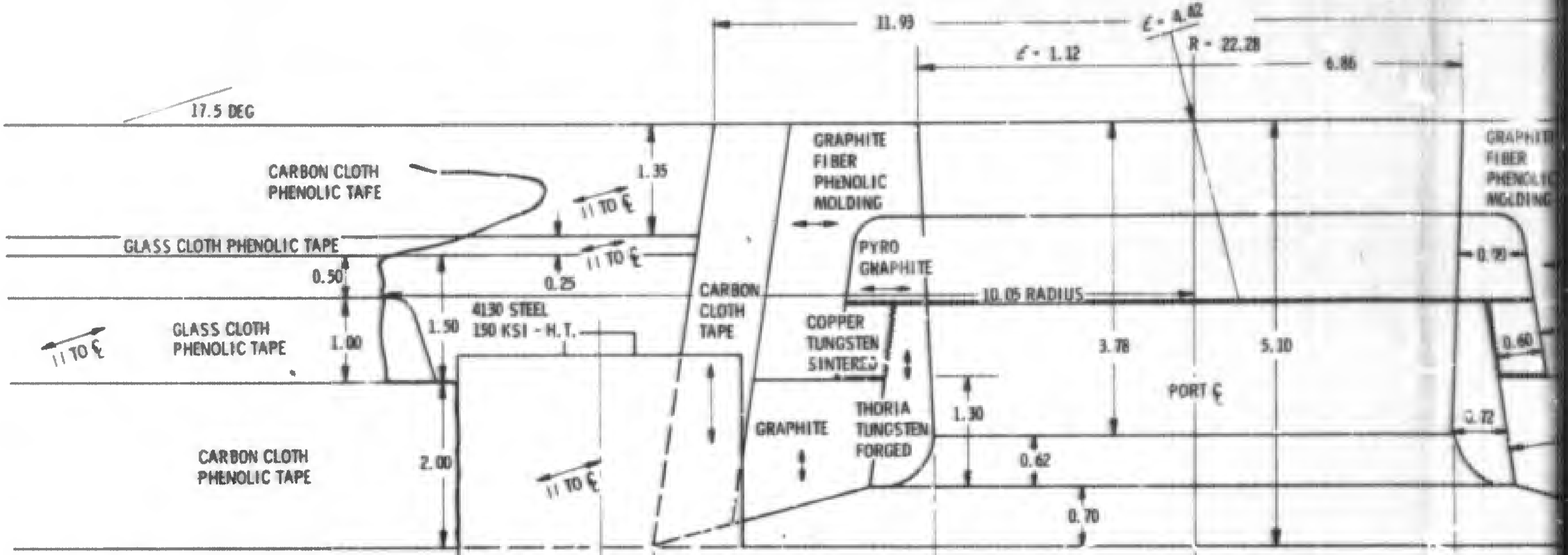

NOTES:

1. ORIFICE DESIGNED FOR 120 SEC FULL OPEN
2. MATERIAL GRAIN OR PLY ORIENTATION AS SHOWN
3. PROPELLANT-CURED CP GRAIN - TP-H1077 = TP-H1011
4. MOTOR ACTION TIME = 140 SEC
5. ACTUAL TVC DUTY CYCLE
   - CLOSED - (0.00 - 28.80) SEC
   - OPEN - (28.80 - 34.50) SEC
   - CLOSED - (34.50 - 70.25) SEC
   - OPEN - (70.25 - 140.00) SEC
6. ACTUAL DUTY CYCLE DATA
   - VALVE OPEN 75.45 VALVE CLOSED 64.55 SEC
   - PORT TUNGSTEN THROAT RING LOST AT 77.50 SEC
   - PINTLE VALVE DROPS INTO MOTOR AT 116.5 SEC
   - VALVE OPEN BEFORE FAILURE - 5.70 SEC
   - ACTUAL PINTLE LOAD | MAX ACTUATOR EXTEND - 15,000 LB / MAX ACTUATOR RETRACT - 5,800 LB
   - ACTUAL SIDE FORCE MAX - 38,500 LB

A

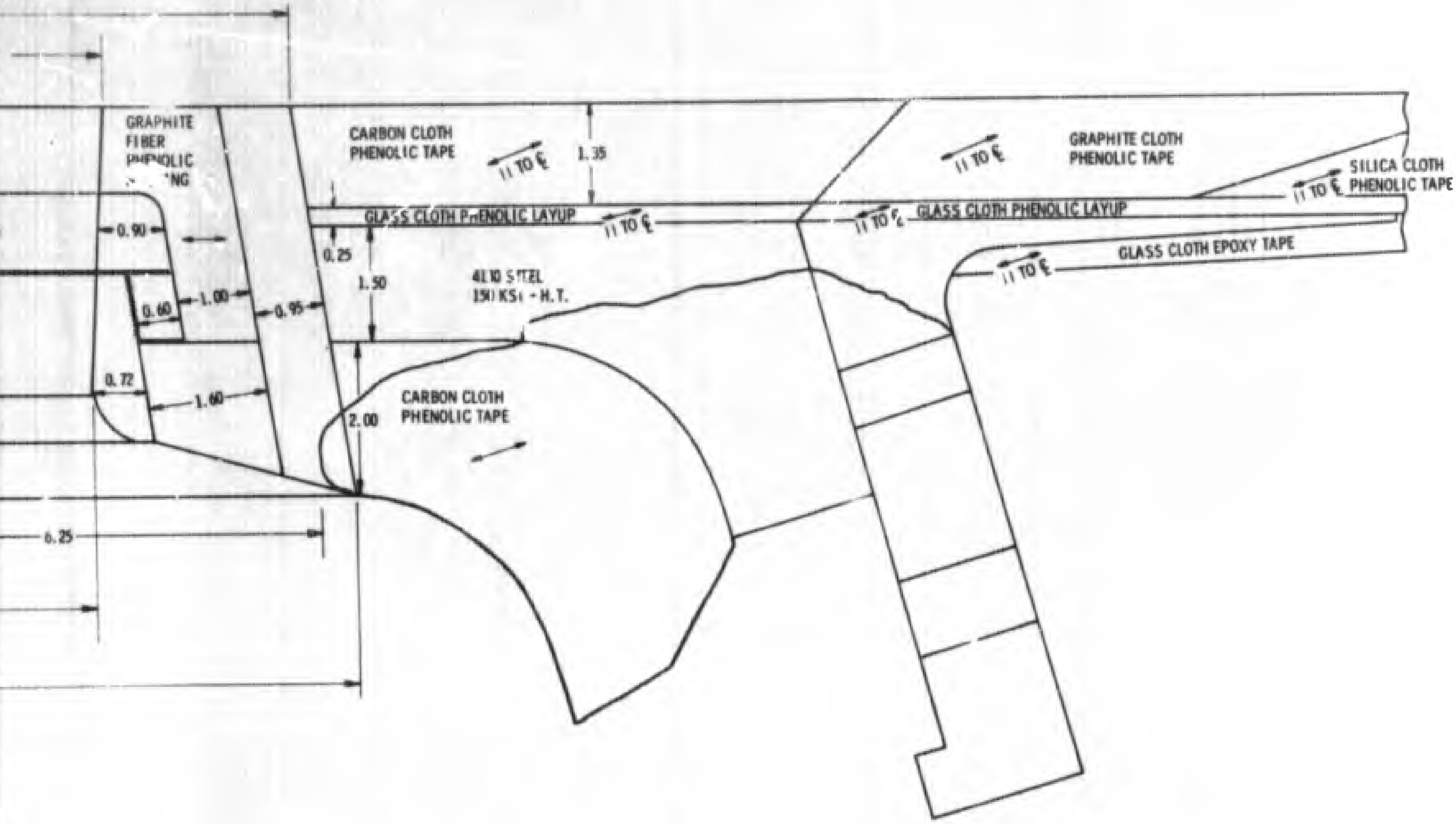

Figure 37. Orifice Port 4 Erosion

B

CAMERA COMPARISON AT EXIT CONE FAILURE

CAMERA NO.	TIME (SEC)	FRAME/SEC	CAMERA NO.	TIME (SEC)	FRAME/SEC
6	46.3	400	1	49.2	64
7	47.8	400	2	47.61	64 (FILM OUT)
8	48.3	271	3	46.00	64
			4	47.00	64

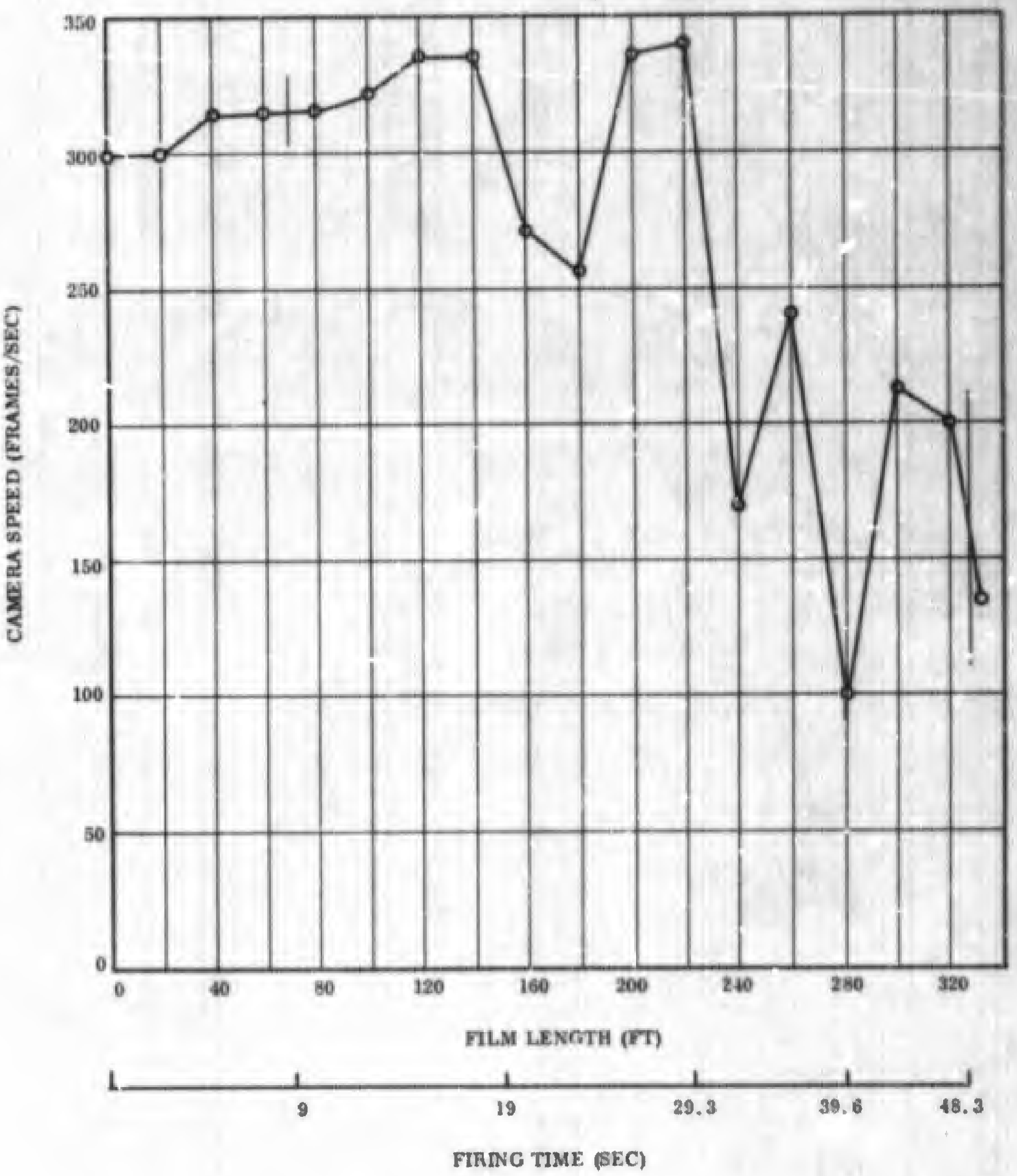

Figure 38. Camera 8 Speed vs Film Length and Firing Time

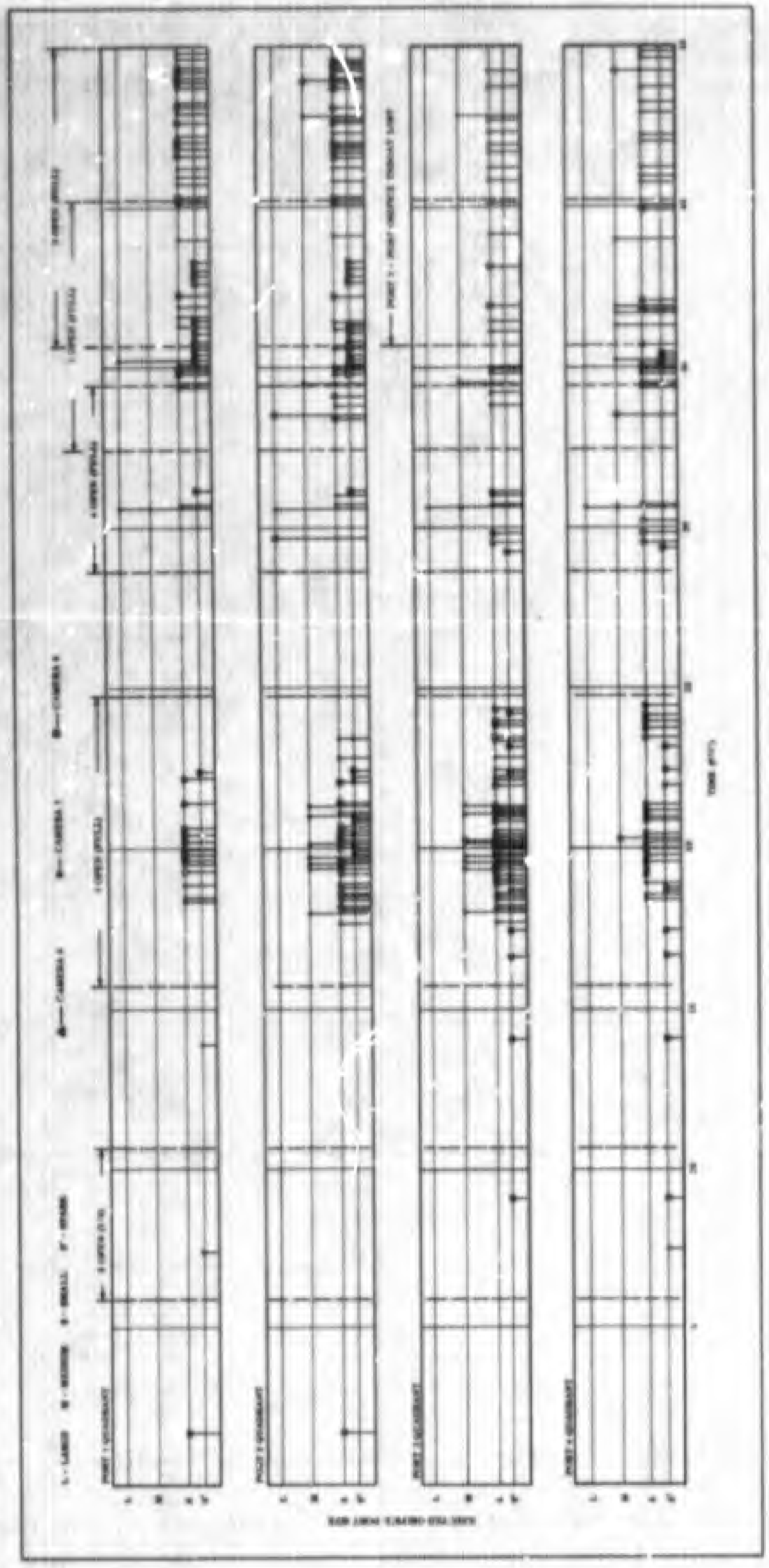

Figure 39. Motion Picture Analysis, Cameras 6 thru 8

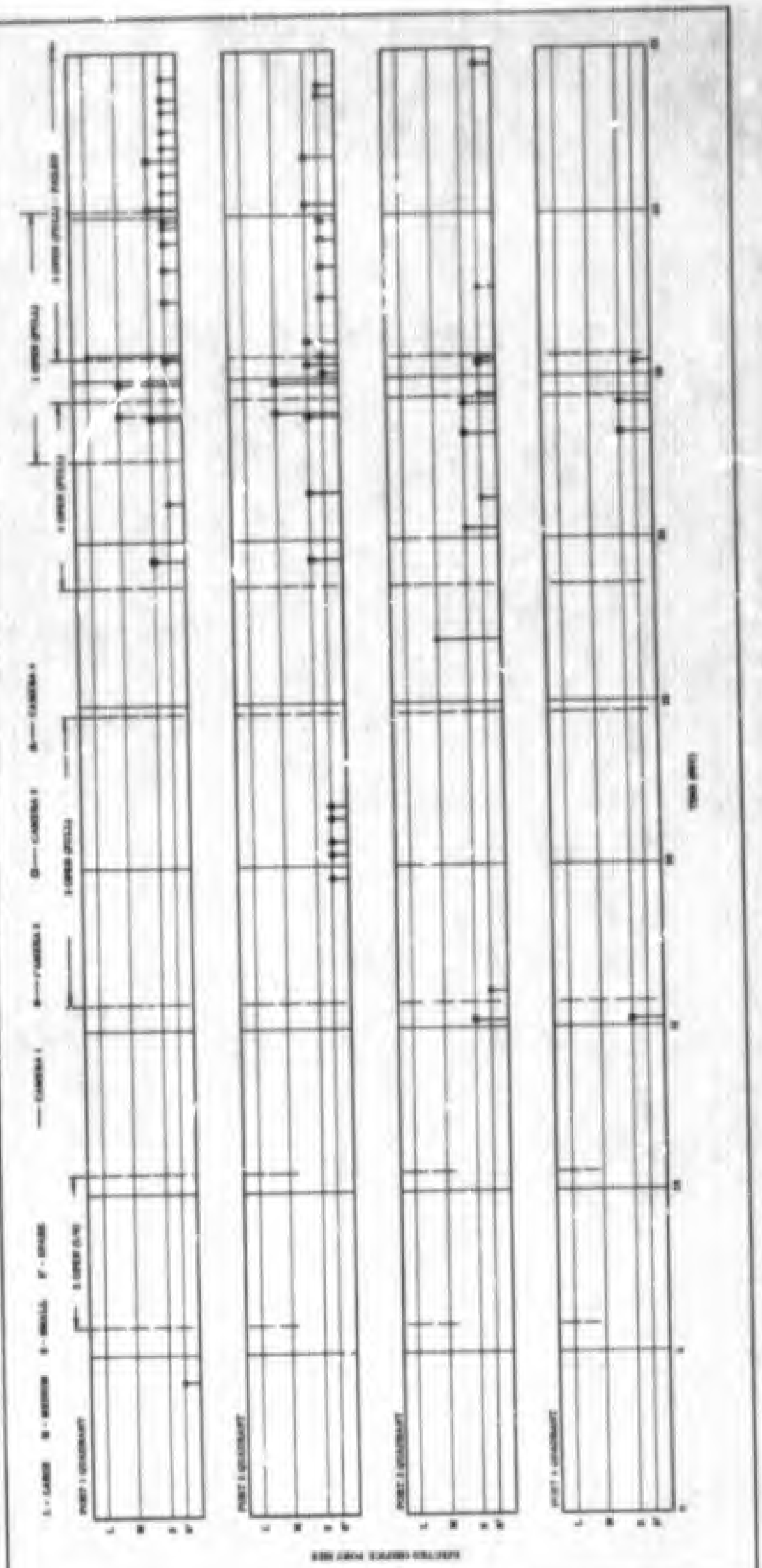

Figure 40. Motion Picture Analysis, Cameras 1 thru 4

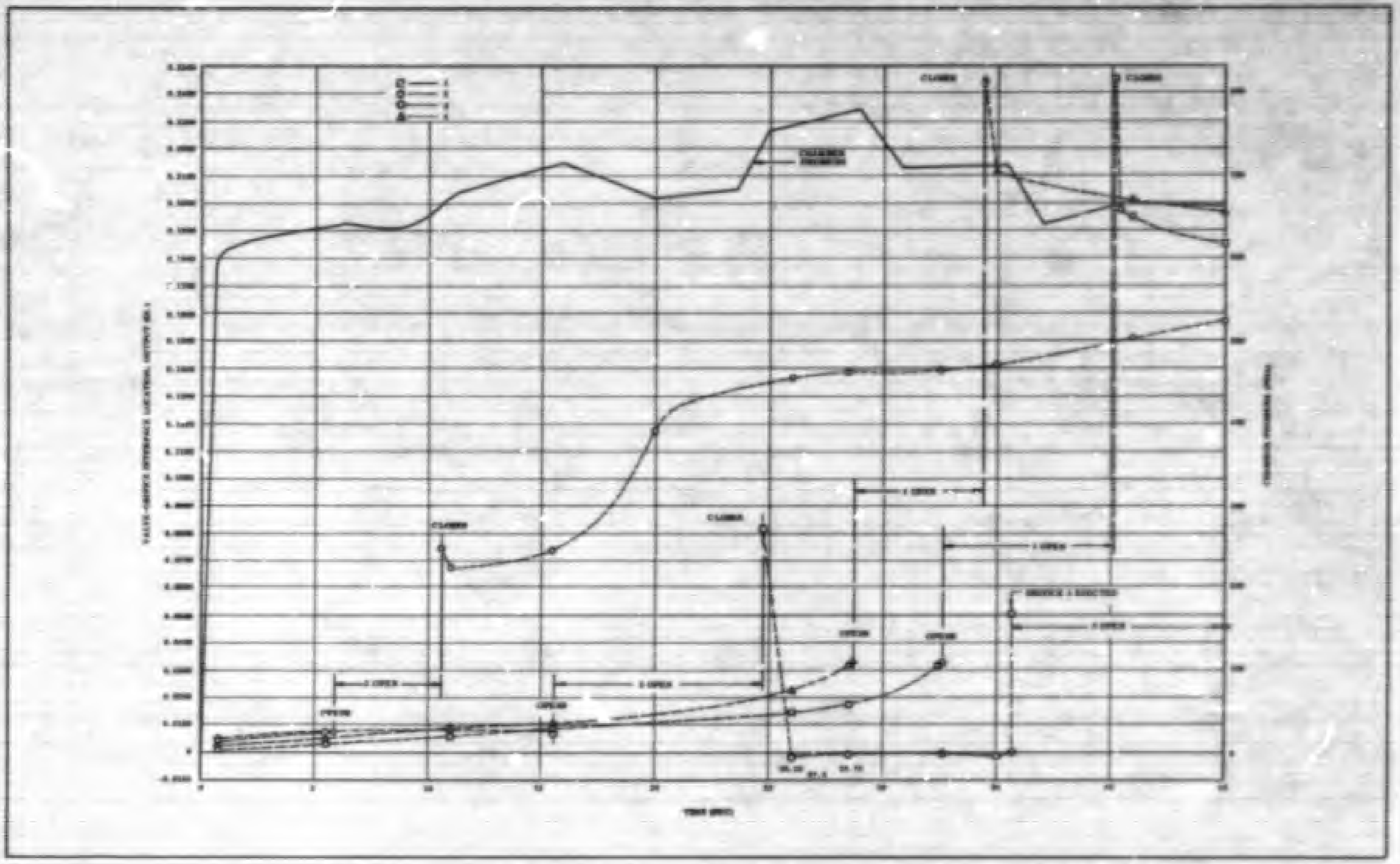

Figure 41. Valve-Orifice Interface Location and Chamber Pressure vs Time

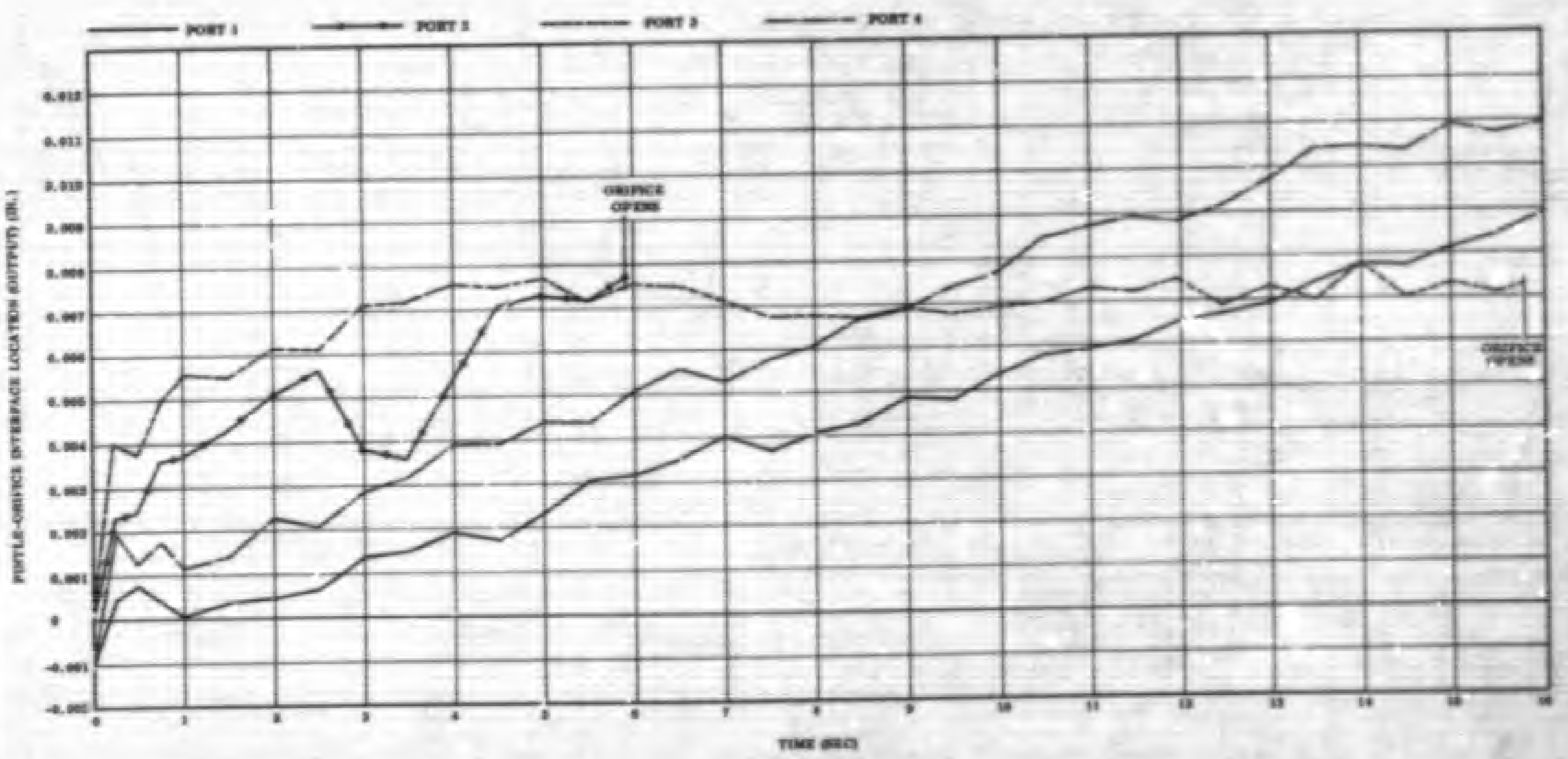

Figure 42. Valve-Orifice Interface Location vs Time, at 0 to 16 Sec

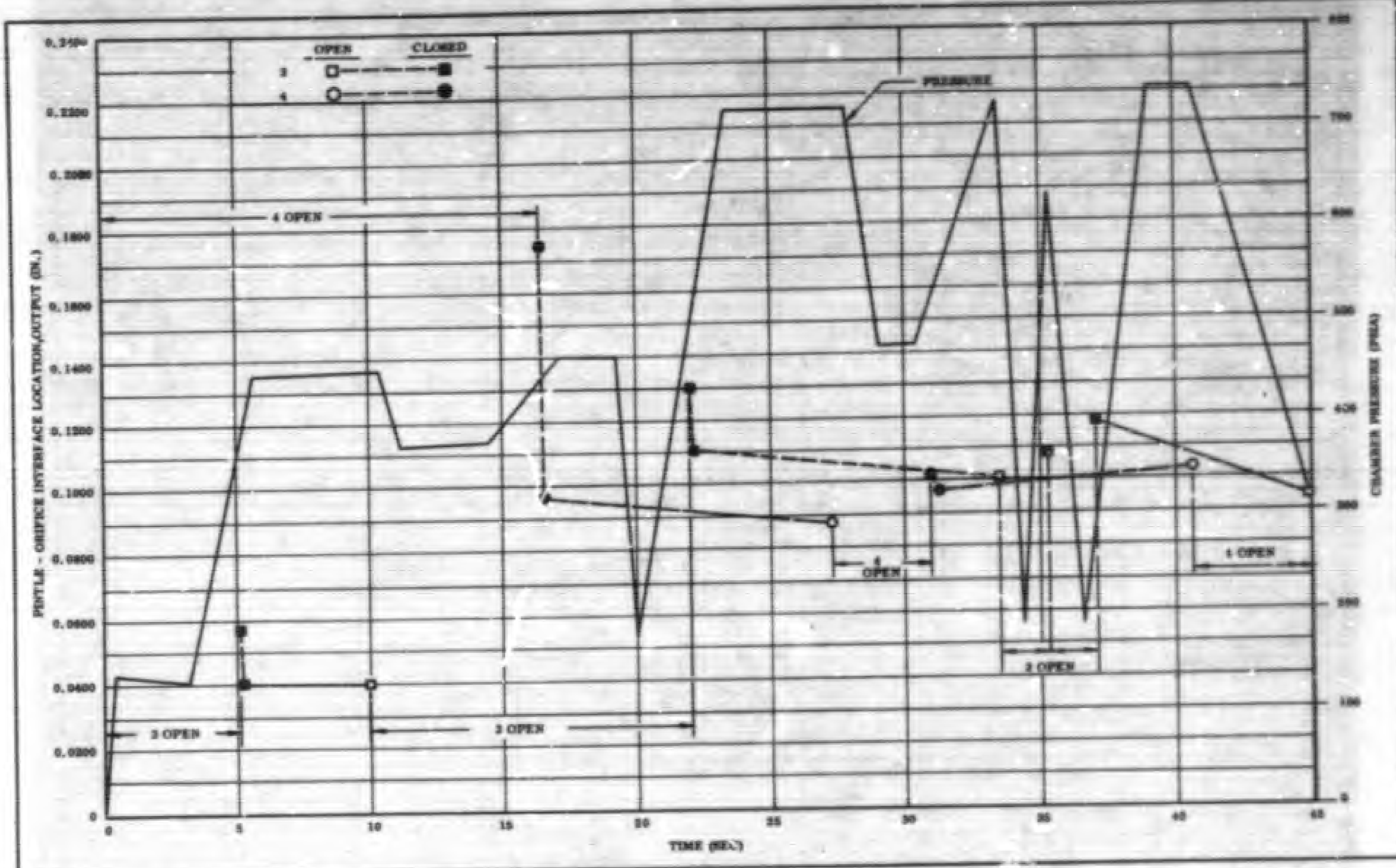

Figure 43. TU-521.02 Motor Orifice-Valve Interface and Chamber Pressure vs Time

Figure 44. Orifice 3 Components

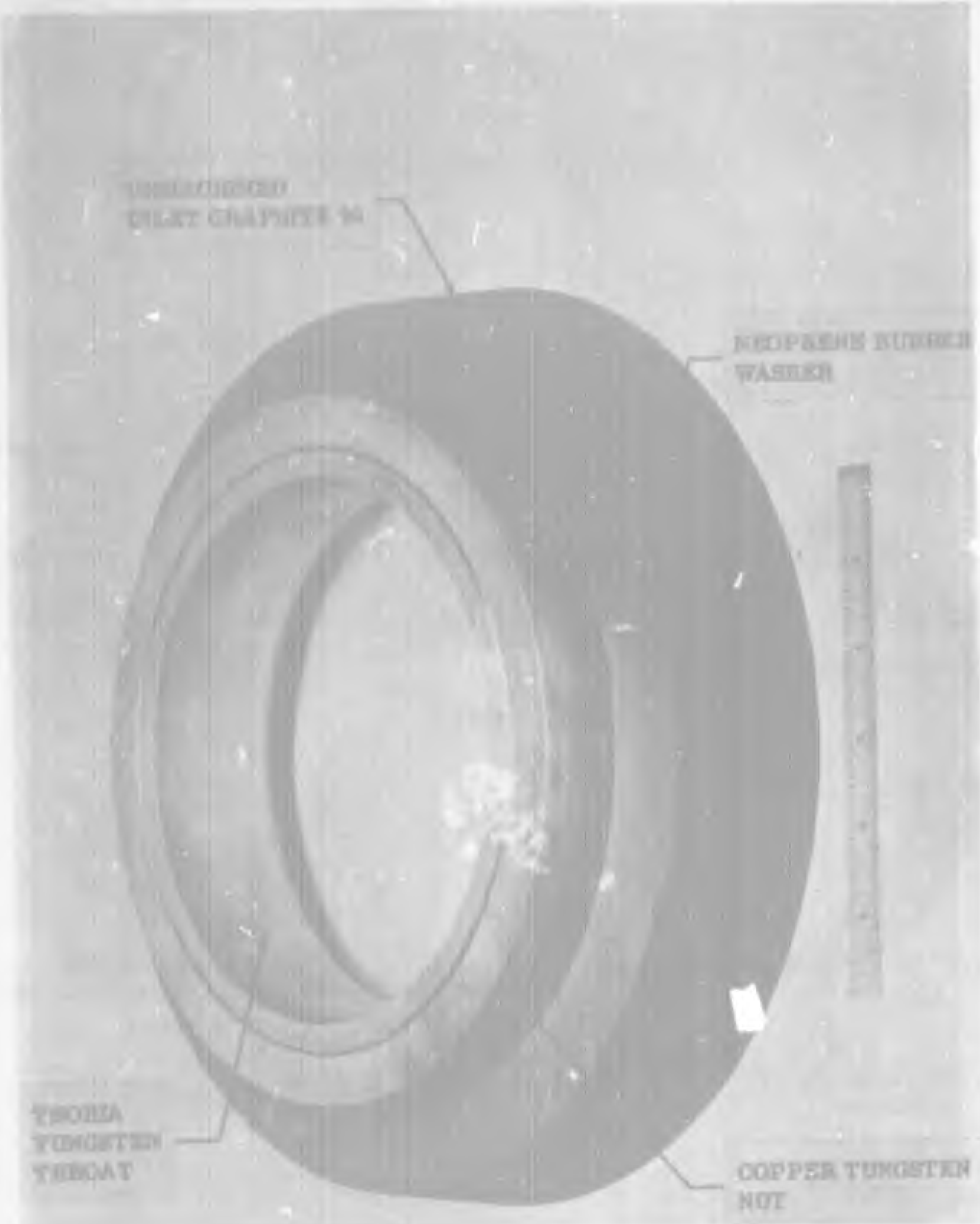

Figure 45. Orifice 5 Throat Subassembly - Forward View

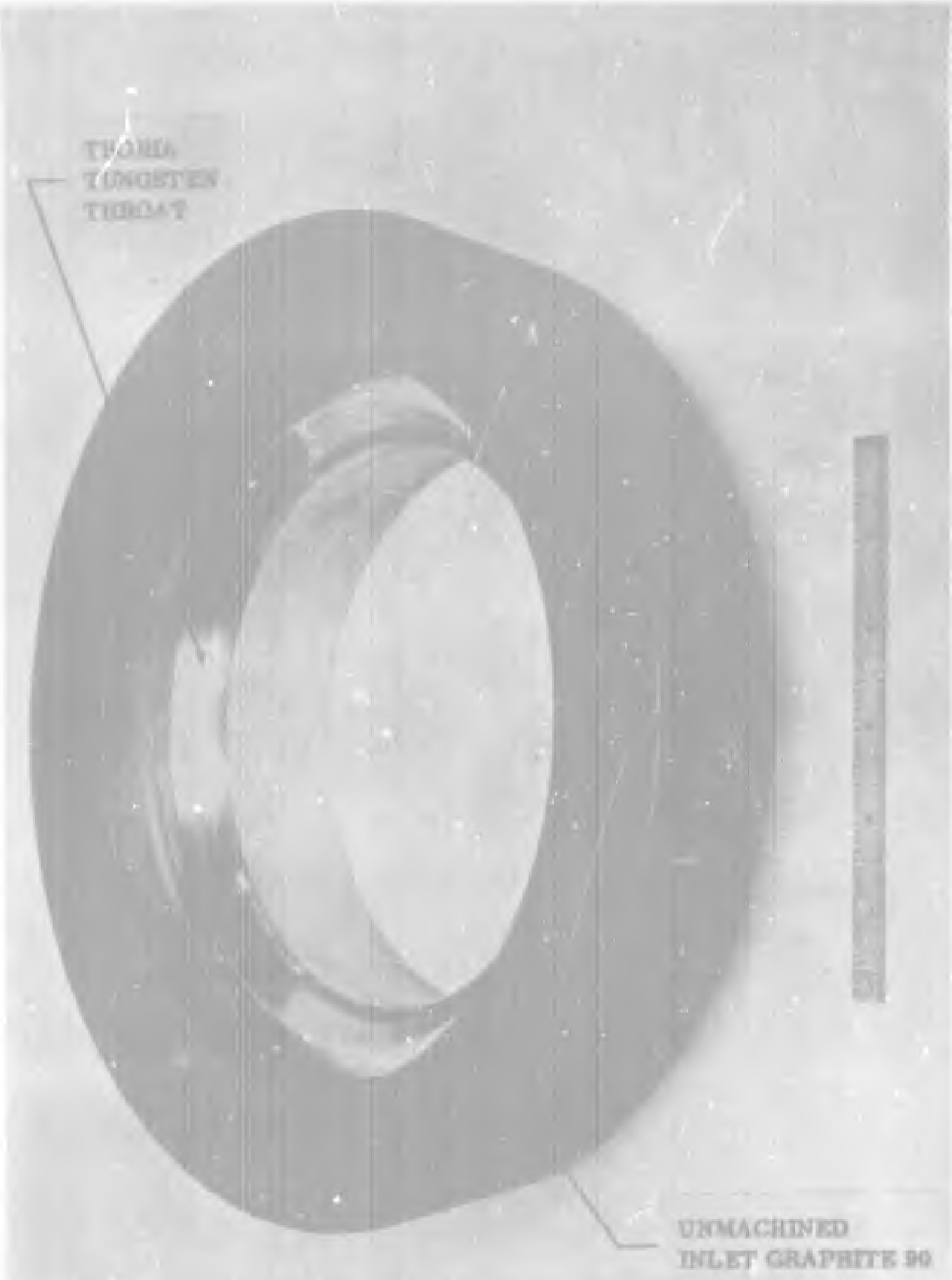

Figure 46. Orifice 3 Throat Subassembly - Aft View

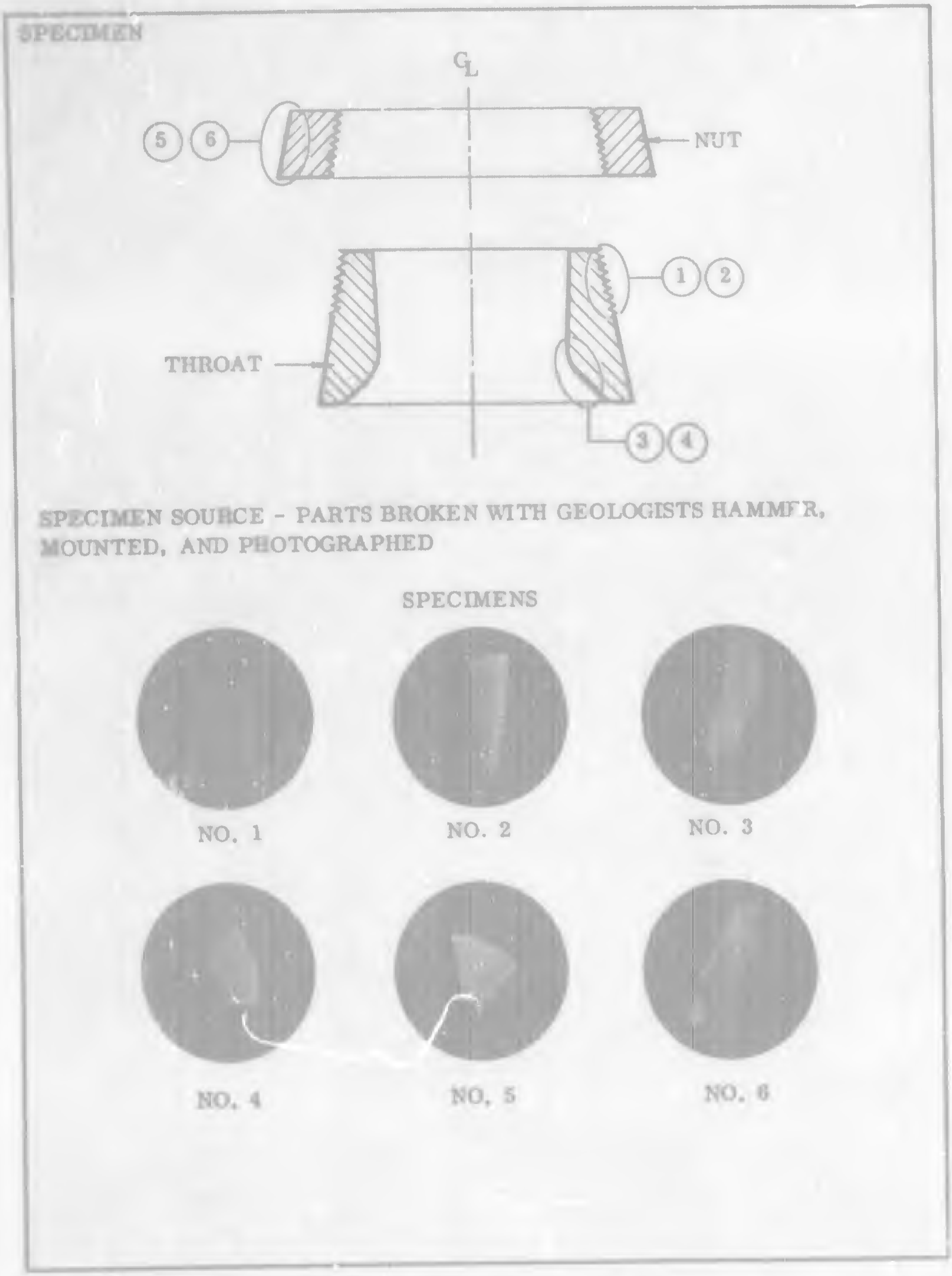

Figure 47. Orifice Tungsten Photomicrographs - Specimen Location

ETCHED SURFACE

POLISHED SURFACE

TU-520.04 FULL SCALE MOTOR
SURVIVED THROAT ORIFICE 1
2% THORIATED - TUNGSTEN SPECIMEN AT THREAD
MAGNIFICATION - 250

Figure 48. Orifice Tungsten Photomicrographs - Specimen 1

ETCHED SURFACE

TU-520.04 FULL SCALE MOTOR
EJECTED THROAT, ORIFICE 2
2% THORIATED - TUNGSTEN SPECIMEN AT THREAD
MAGNIFICATION - 250

Figure 49. Orifice Tungsten Photomicrographs - Specimen 2

ETCHED SURFACE

TU-520.04 FULL SCALE MOTOR
EJECTED THROAT, ORIFICE 3
2% THORIATED - TUNGSTEN SPECIMEN AT THROAT
MAGNIFICATION - 250

Figure 50. Orifice Tungsten Photomicrographs - Specimen 3

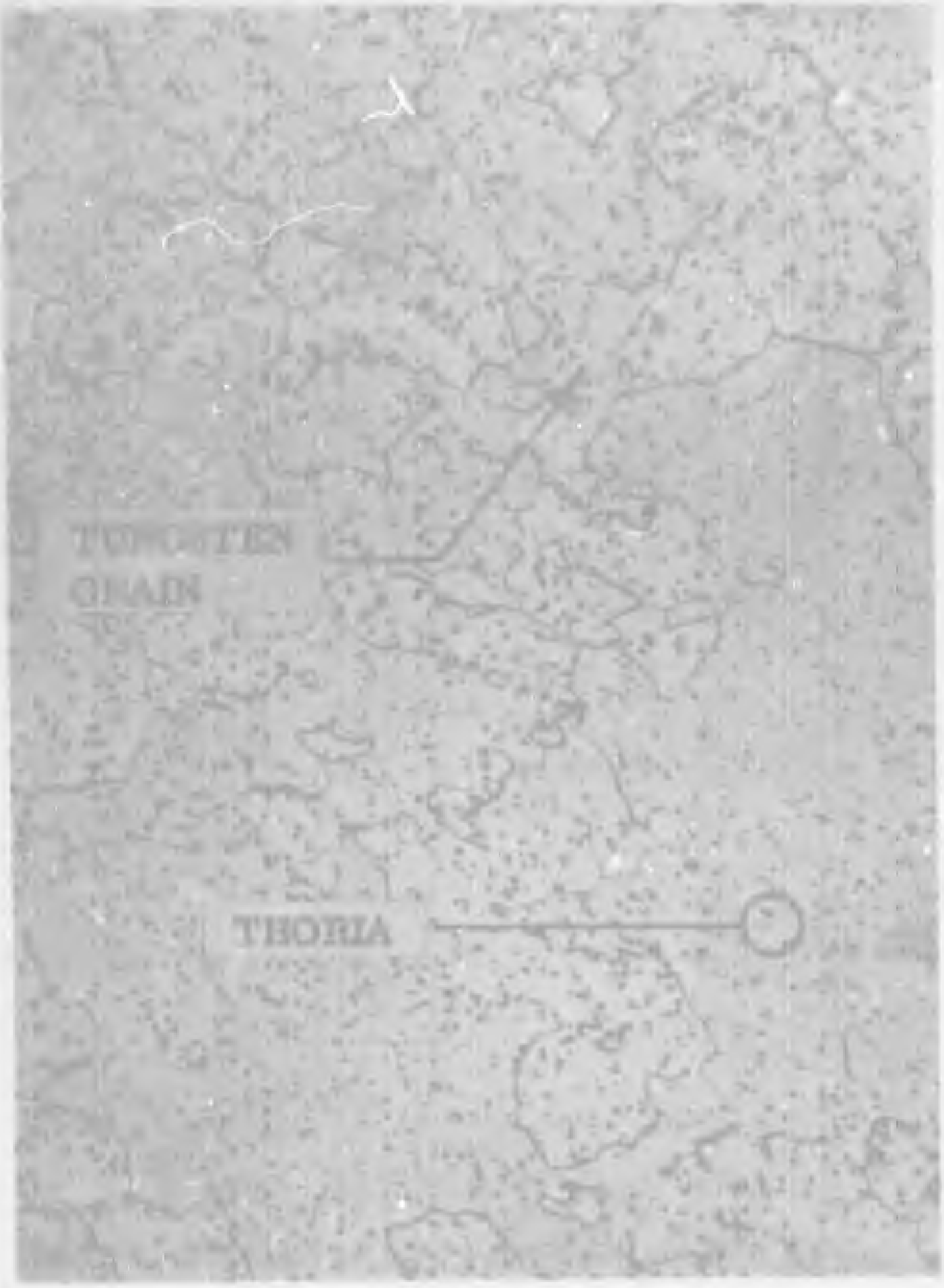

ETCHED SURFACE

TU-521.02 SUBSCALE MOTOR
SURVIVED THROAT ORIFICE 4
2% THORIATED - TUNGSTEN SPECIMEN AT THROAT
MAGNIFICATION - 250

Figure 51. Orifice Tungsten Photomicrographs - Specimen 4

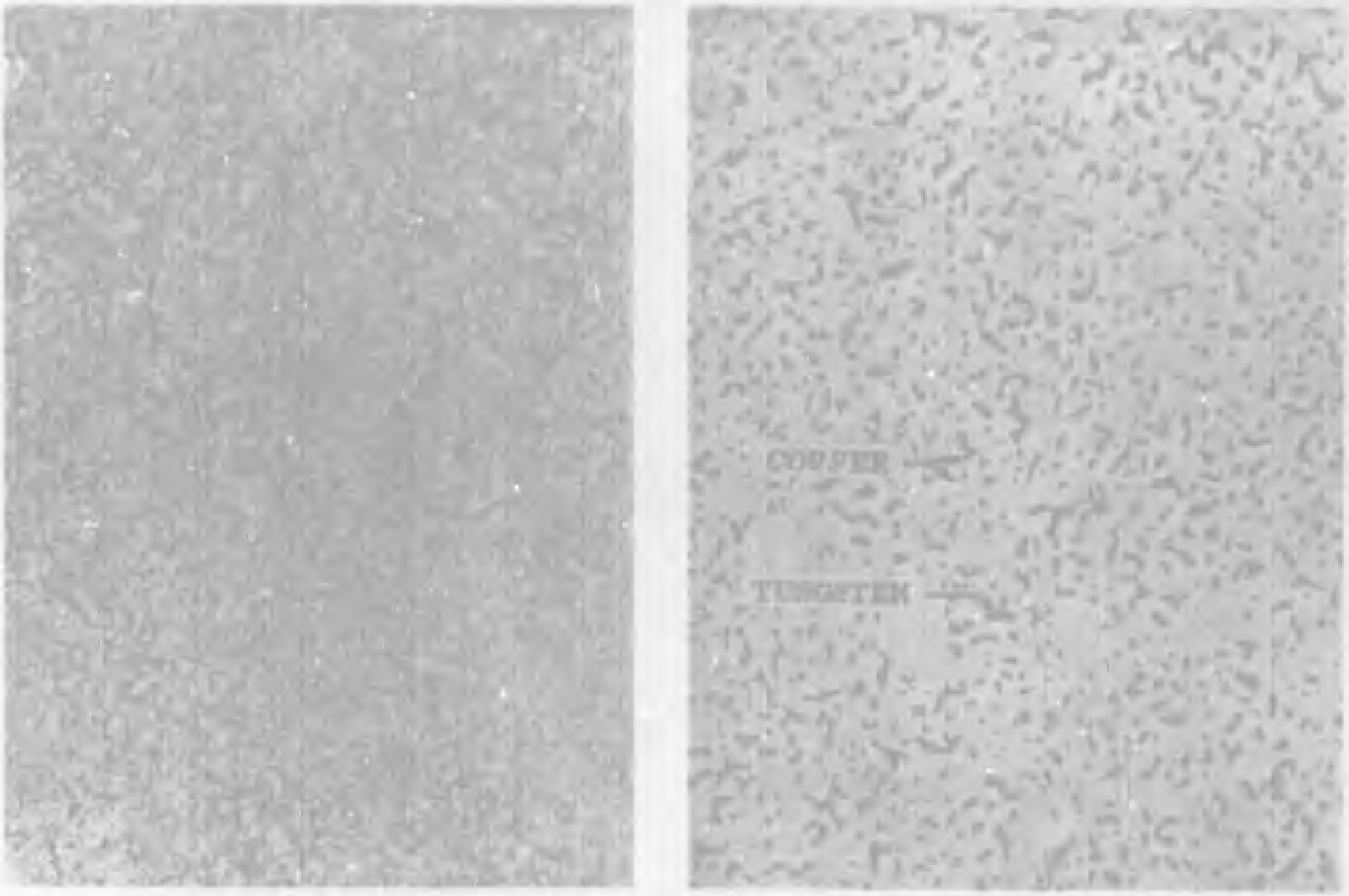

ETCHED SURFACE

POLISHED SURFACE

TU-520.02 SUBSCALE MOTOR
SURVIVED NUT FROM ORIFICE 4
20% COPPER - 80% TUNGSTEN SPECIMEN AT OUTSIDE DIAMETER SURFACE
MAGNIFICATION - 250

Figure 52. Orifice Tungsten Photomicrographs - Specimen 5

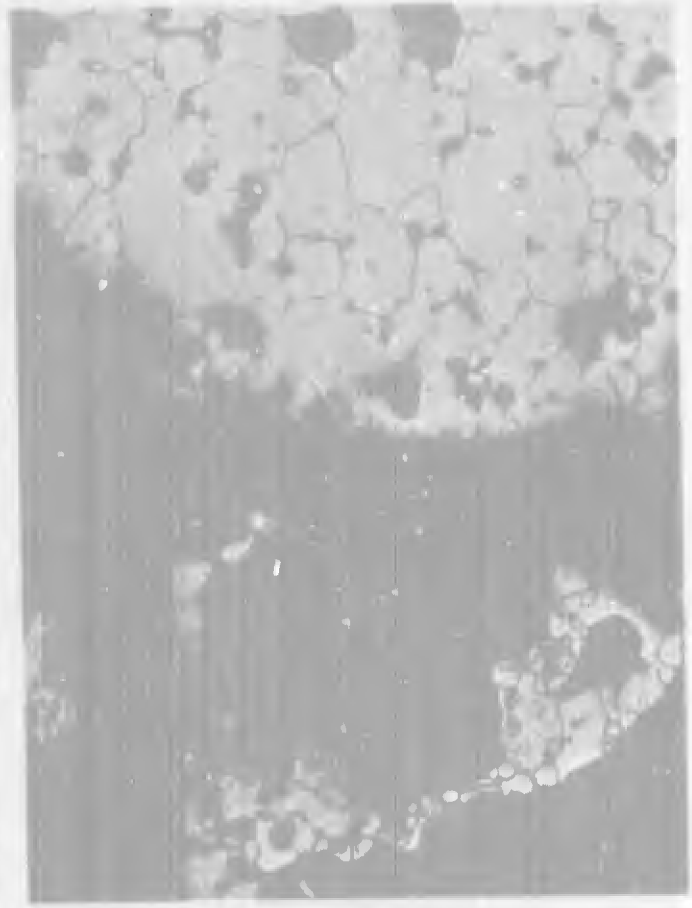

POLISHED SURFACE

AWAY FROM OUTSIDE DIAMETER SURFACE

ETCHED SURFACE

NUT OUTSIDE DIAMETER SURFACE AT BUBBLE OF COPPER-TUNGSTEN

TU-520.04 FULL SCALE MOTOR
SURVIVED ORIFICE 1 NUT
20% COPPER - 80% TUNGSTEN SPECIMEN
MAGNIFICATION - 250

Figure 53. Orifice Tungsten Photomicrographs - Specimen 6

SECTION III

FAILURE ANALYSIS

To provide an analysis model of the TU-520.04 orifice a number of limitations were necessary. These limitations and the reasons therefore are listed below:

Limitation	Reason
1. Selection of port 3 for analysis	1. First port to fail
2. Analysis time span of 45 seconds	2. Orifice 3 throat insert lost at 35.7 seconds
3. Material loss limited to predicted erosion	3. Actual material loss rate vs time unknown
4. Use of port 3 duty cycle for analysis	4. To agree with port under analysis
5. Symmetrical heating and loads on orifice	5. Limitations of thermo and structural computer programs
6. Current material properties where possible	6. Cost to obtain additional properties prohibitive to this program scope
7. Twenty-two inch diameter port and orifice analysis area $\geqq$ 1.5 orifice outside diameter	7. Includes orifice-nozzle erosion area and limits effects of boundary conditions on orifice materials
8. Analysis area is a symmetrical circular flat plate with a hole in the middle	8. Limitations of thermal and structural computer programs

With these limitations and the analysis model defined, an initial failure time of 5 seconds (closed) and a major failure time of 25.0 and 25.1 seconds (port open, port closed) was established.

Three separate disciplines, aerodynamics, thermodynamics and stress analyses provide outputs that are mutually required to determine the overstressed regions of the orifice and provide a basis for the orifice port redesign.

The aerodynamic analysis, including cold flow simulation model static test data and the evaluation and use of industry research papers on similar problems, provides a cross check for the theoretical flow and pressure patterns in and around the orifice cavity. Final adjustment of theoretical flow and pressure patterns with cold flow simulation data and other industry static test data is input to the computer, and provides a final wall pressure and heat transfer coefficient upstream, down-stream, and cross stream of the orifice centerline for the orifice inlet, orifice and nozzle exit cone at three separate times, 0, 16, and 25 seconds per the eroded orifice shape.

For the thermodynamic and structural analysis a two-dimensional (radial length and axial width) common element orifice grid is drawn (Figure 54). For structural analysis the elements close to the orifice wall are divided in half for a more accurate stress and deflection output. The basic input includes the location of each element corner or center node with respect to the orifice and nozzle reference plane and the material physical and thermal properties.

The thermodynamics two-dimensional computer model inputs heat transfer coefficients and erosion along the three walls for the thermal gradients through the elements in the analyses area for the upetream and downstream walls at five seconds. An evaluation of the thermal gradients for the upstream and downstream planes showed that the downstream walls exhibited higher wall temperatures and erosion on the weaker materials. Based on this evaluation the downstream plane was established as the critical plane to be assumed for the symmetrical orifice computer model. Inputting erosion at 16 and 25 seconds into the orifice computer model by eliminating elements or nodes, thermal gradients were provided at 16, 25, and 25.1 seconds.

The structural analysis using the common orifice element grid further subdivided at the orifice wall inputs the wall pressure, element temperatures, valve seating loads, and boundary loads or conditions into the orifice computer model to provide the axial and radial-stress and deflection and the shear and hoop stress for each element. Comparing the actual to allowable stress at temperature for each node indicates the overstressed elements are located in the downstream plane.

A. AERODYNAMIC ANALYSIS

Using the results of an extensive literature survey of similar aerodynamic problems, a theoretical model was used to simulate the actual orifice open and closed conditions. Using a subscale submerged nozzle and orifice cavity model, cold flow studies were made to simulate full scale nozzle and orifice conditions. A correlation of simulation model data, static test data, and theoretical predictions allows for the adjustment of the theoretical model to the actual flow and pressure conditions. Since the orifice cavity changes shape with erosion, empirical predictions are required based on previous Thiokol-Wasatch-AFRPL Static Tests for upper stage HGTVC, and Lockheed Jet Pipe HGTVC static tests for large motors, to alter the theoretical model shape with motor static test time. The computer output provides the pressure and heat transfer coefficient around and in the orifice cavity at 0, 16, and 25 seconds.

1. LITERATURE SURVEY

A literature survey was made to uncover applicable test data for flow in cavities. The desired flow conditions in the cavity are the wall Mach numbers and heat transfer coefficients.

The investigation began with a survey of publications in the Thiokol Library through an Information Retrieval Request under the general topic, "Aerodynamic Interaction" (270 references). Two other literature searches conducted were the National Aeronautics and Space Administration Literature Machine Search under "Supersonic Flow," two parts (1480 references), and the Defense Document Center Report Bibliography Search on "Supersonic Flow" (500 references).

These sources were supplemented by a search of current publications, for the recent years, from the Index of Papers published in the American Institute of Aeronautics and Astronautics (published annually); Index of Papers published in the

Journal of Spacecraft and Rockets (published annually); Transactions of the American Society of Mechanical Engineers (published quarterly): Journal of Heat Transfer, Journal of Basic Engineering, Journal of Applied Mechanics; Technical Abstract Bulletin (published semimonthly); Applied Science and Technology Index (published quarterly); Scientific and Technical Abstract Reports (published semimonthly); Classified Scientific and Technical Abstract Reports (published semimonthly); and Business Periodicals Index (published semiannually).

In addition, bibliographies on similar subject matter, recently conducted, were reviewed. These include a Bibliography of Bibliographies, A Report Bibliography prepared by D. D. C. (March 1965); Report Bibliography prepared by the Air Force Rocket Propulsion Laboratory (December 1966); An Aerosonics Bibliography prepared by the University of California at Los Angeles (April 1965); A Review of Separated and Reattaching Flows with Heat Transfer prepared by the International Journal of Heat and Mass Transfer (June 1967); and Transverse Jet Experiments and Theories, a Survey of the Literature prepared by the U.S. Army Missile Command at Redstone Arsenal (June 1967).

The literature survey is divided into four parts as follows:

1. Reports on Flow and Heat Transfer in a Cavity,
2. Reports on Flow and Heat Transfer Behind Rearward Facing Steps,
3. Reports on Flow and Heat Transfer in Front of Forward Facing Steps,
4. Reports on Generally Related Flow and Heat Transfer Effects.

Item 1 consists of an identification of the document and authors, a summation of the contents, and extraction of the data and/or theory presented. Items 2 and 3 present only the summation of contents, and item 4 presents limitations of contents relative to the investigation.

Documents not fully reviewed from the literature survey and still probably applicable to the investigation are listed without numerical reference at the end of the section.

a. Reports on Flow and Heat Transfer in a Cavity

(1) Rhudy, J. P., and Magnan, J. D., Turbulent Cavity Flow Investigation at Mach Numbers 4 and 8, AEDC-TR-66-73, von Karman Gas Dynamics Facility, Arnold Engineering Development Center, June 1966.

Investigations of turbulent flow over a cavity in an aerodynamic surface at M-4 and 8 with Re = 8.0×10^6 and 11.0×10^6 respectively. Wall-to-free-stream stagnation temperature ratio is at 0.4 and 0.8 and at 0.75. Ratio of initial boundary-layer thickness to cavity depth was approximately 0.2. Surface pressure and temperature measurements and flow field surveys of pilot and static pressures and total temperature were made. Results showed that the recirculating fluid temperature was not less than 0.7 times the free stream stagnation temperature despite decrease of the wall temperature to 0.4 the free-stream value. Compressible-flow experimental velocities correlated well with theoretical profiles. A linear relation between velocity and total temperature is adequate to describe the total temperature variation across the mixing layer. The mixing zone similarity parameter was near 12 regardless of Mach number or wall-to-free-stream stagnation temperature ratio.

(2) Mills, R. D., On the Transfer of Heat in a Cavity at High and Low Speeds, R and M No. 3428, Ministry of Aviation, Aeronautical Research Council, London, July 1964.

Discussion on transfer of heat between a fluid and a cavity in a solid surface over which it flows. Using a closed inner boundary layer concept, a (constant pressure) integral condition is derived specifying the net flux of heat through the cavity at all Mach numbers. Velocity and temperature profiles are obtained as functions of Mach number and Prandtl number, while heat-transfer coefficients are developed in terms of these parameters.

(3) Fox, J., Surface Pressure and Turbulent Airflow in Transverse Rectangular Notches, NASA TN D-2501, Lewis Research Center, November 1964.

(4) Baron, M. L. and Mathews, A. T., "Diffraction of a Pressure Wave by a Cylindrical Cavity in an Elastic Medium," Journal of Applied Mechanics, 28, September 1961, pp 347-54.

(5) Sparrow, E. M., Albers, L. U., and Excert, E. R. G., "Thermal Radiation Characteristics of Cylindrical Enclosures," Journal of Heat Transfer, 84, February 1962, pp 73-81.

(6) Morrisette, E. L., "Effect of Mass Injection into a Cavity on Hypersonic Boundary-Layer Transition," AIAA Journal, 4, August 1966, pp 1488-90.

(7) Filetti, E. G. and Cays, W. M., "Heat Transfer in Separated, Reattached, and Redevelopment Regions Behind a Double Step at Entrance to a Flat Duct," Journal of Heat Transfer, 89, May 1967, pp 163-68.

(8) Schubert, G., "Viscous Incompressible Flow over Wall Projections and Depressions," AIAA Journal, 5, February 1967, pp 373-75.

(9) Emery, A. F., Sadunas, J. A., and Loll, M., "Heat Transfer and Pressure Distribution in Open Cavity Flow," Journal of Heat Transfer, February 1967, pp 103-08.

(10) Haugen, R. L. and Dhanak, A. M., "Heat Transfer in Turbulent Boundary-Layer Separation Over a Surface Cavity," Journal of Heat Transfer, pp 1-6.

(11) Charwat, A. F., Roos, J. N., Dewey, F. C., and Hitz, J. A., "An Investigation of Separated Flows - Part I: The Pressure Field," Journal of the Aerospace Sciences, June 1961, pp 457-70.

The article describes an investigation of several types of separated regions such as blunt-base wakes and cavities formed with cutouts in the boundaries and ahead of or behind two-dimensional steps in supersonic (Mach numbers 2 to 4) and subsonic flow. The conditions for the existence, the geometry, and the pressure field are described in this paper.

A second article (to be published) will describe investigations of the internal flow and the heat transfer across such separated regions.

It is found that there is a maximum (critical) ratio of the length of the separated free-shear layer to the depth of the depression of the boundary beyond which the cavity collapses, leaving mutually independent separated regions at each protrusion. This critical length changes greatly upon laminar-turbulent transition in the oncoming boundary layer; in either laminar or turbulent flow it is approximately independent of Mach and Reynolds numbers. A semiempirical correlation predicting the conditions under which the flow will span a depression of arbitrary depth is proposed.

Detailed pressure distributions along the boundaries of a cavity (in turbulent flow) are presented as a function of the ratio of the cavity length to the critical length, which is found to be the pertinent similarity parameter. For short notches ($L/L_{cr} < 0.5$) the impact pressure due to the reversal of the inner portion of the shear layer at recompression tends to thicken the shear layer and a type of boundary layer-free stream interaction patterns the pressure field. The pressure in the cavity is nearly constant and can be higher than free-stream. In long notches ($L/L_{cr} > 0.5$) the shear layer bends inward at separation and curves back gradually ahead of the recompression point. The cavity-pressure variation is pronounced and the recovery pressure at reattachment is small. The variation of the drag coefficient on Mach number reflects the change from one to the other mechanism of recompression.

Detailed surveys of the Mach number distributions in a blunt-body wake and the mixing region behind its throat, as was in the shear layer spanning a cutout in a wall, are presented and analyzed. It is found that, in general, the assumptions of the simple supersonic-wake models which rely on a principle of steady flow with mass conservation in the cavity are not adequate in cavities in which there is recompression against a boundary.

Results show the influence of the thickness of the initial boundary layer (in the range of 0.3 to 3 times the notch depth).

(12) Charwat, A. F., Dewey, C. F., Roos, J. N., and Hitz, J. A., "An Investigation of Separated Flows - Part II: Flow in the Cavity and Heat Transfer," Journal of the Aerospace Sciences, 28, July 1961, pp 513-27.

The first portion of this paper describes studies of the internal structure of the separated flow in a notch at a free-stream Mach number of 3. Observations include: flow visualization, spark-Schlieren pictures of the fluctuations of the free shear layer, and diffusion of heat from sources placed in the separated region. The second part describes measurements of local heat transfer to the wall.

The external Mach number, the length-to-depth ratio of the cavity, the ratio of the oncoming boundary layer thickness to the notch depth (in the turbulent flow region), the thermal-to-momentum thickness ratio of the boundary layer and, finally, the geometry of the internal boundary of the separated region is varied as systematically as possible. On the basis of these observations, a simple model of the flow in and the heat transfer to the separated region is formulated.

(13) Spee, B. M., Wind Tunnel Experiments on Unsteady Cavity Flow at High Subsonic Speeds, AGARD Fluid Dynamics Panel, Conference Proceedings No. 4, Separated Flows, Part 2, Belgium, May 1966, pp 947-74.

(14) Korst, H. H., Dynamics and Thermodynamics of Separated Flows, AGARD Fluid Dynamics Panel, Conference Proceedings No. 4, Separated Flows, Part 2, Belgium, May 1966, pp 701-46.

(15) Bales, E. L., On Heat Transfer Within and Across Nearly Circular Cavities Including the Effects of Variable Wall Temperature and Mass Bleed, 1967 University of Illinois Ph.D. Thesis.

(16) Ellis, B. K., and Ryan, H. S., Drag Resulting from Separated Flow Induced by Surface Cavities at a Mach Number of 3.74, Test Report All 9, The David W. Taylor-Model Basin, Aerodynamics Laboratory, November 1964.

(17) Thomke, G. L., Separation and Reattachment of Supersonic Turbulent Boundary Layer Behind Downstream Facing Steps and Over Cavities, SM-43062, Douglas Missile and Space Systems Division, March 1964.

(18) Spee, B. M., Wind Tunnel Experiments on Unsteady Cavity Flow at High Subsonic Speeds, Discussions Following the Presentation of Papers at the AGARD Fluid Dynamics Specialists Meeting on "Separated Flows" (AGARD Conference Proceedings No. 4) Supplement, Belgium, 1966.

(19) Smith, G. L., Vortex Flow and Erosion in Rocket Nozzles Due to Warm-Gas Injection for Thrust Vector Control, NASA TN D-3241, Langley Research Center, February 1966.

(20) Sparrow, E. M., Jonsson, V. F., Lundgren, T. S., and Chen, T. S., "Heat Transfer and Forces for Free-Molecule Flow on a Concave Cylindrical Surface," Journal of Heat Transfer, 86, February 1964, pp 1-11.

(21) Lin, S. H., and Sparrow, E. M., "Radiant Interchange Among Curved Specularly Reflecting Surfaces-Application to Cylindrical and Conical Cavities," Journal of Heat Transfer, 86, May 1965, pp 299-307.

(22) Centrolanzi, F. J., Heat Transfer to Blunt Bodies Having Cavities to Promote Separation, NASA TN D-1975, July 1963.

(23) Morrison, D. F., and Sheppard, L. M., "Hole Size Effect on Hemisphere Pressure Distributions," Australian Royal Aeronautical Society Journal, 71, April 1967, pp 317-19.

(24) Burggraf, O. R., A Model of Steady Separated Flow in Rectangular Cavities at High Reynolds Number, Heat Transfer and Fluid Mechanics Institute Proceedings, June 1965, pp 190-229.

(25) Fox, J., Flow Regimes in Transverse Rectangular Cavities, Heat Transfer and Fluid Mechanics Institute Proceedings, June 1965, pp 230-47.

(26) Seban, R. A. and Fox, J., Heat Transfer to the Air Flow in a Surface Cavity, Proceedings of the 1961-1962 Heat Transfer Conference, 1963, pp 426-31.

(27) Nielsen, W. C., A Theoretical and Experimental Investigation of the Acoustic Response of Cavities in an Aerodynamic Flow, Tecnnical Report No. WADD-61-75, Flight Dynamics Laboratory, March 1962.

b. Reports on Flow and Heat Transfer Behind Rearward Facing Steps

(1) Smith, H. E., The Flow Field and Heat Transfer Downstream of a Rearward Facing Step in Supersonic Flow, ARL 67-0056, Aerospace Research Laboratories, Office of Aerospace Research, March 1967, Ph.D. Paper Under ARL Project No. 7063.

(2) Crawford, D. R., Supersonic Separated Flow Downstream of a Backward Facing Step, AS-67-9, College of Engineering, University of California, May 1967, Under Ph.D. Paper Under AFOSR Grant 268-67.

(3) Scherberg, M. G., Explorations of Supersonic Shear Flow Over a Cavity, Paper Presented at Proceedings of the Ninth Israel Annual Conference on Aviation and Astronautics Nelo at Tel Aviv and Haifa, February 1967, ARL Report.

(4) Roshko, A. and Thomke, J., "Observations of Turbulent Reattachment Behind an Axisymmetric Downstream-Facing Step in Supersonic Flow," AIAA Journal, June 1966, pp 975-80.

(5) Sfeir, A., Supersonic Flow Separation on a Backward Facing Step, Report No. AF-66-18, Division of Aeronautical Sciences, University of California, ME Thesis, December 1966, Under AFOSR Grant 268-66.

(6) Baum, E., An Interaction Model of a Supersonic Laminar Boundary Layer on Sharp and Rounded Backward Facing Steps, BSD-TR-67-181, Advanced Research Projects Agency, Space and Missile Systems Organization (AFSC), July 1967. ARPA Contract No. AF 04(694)-992.

(7) Rom, J., Seginer, A., and Kronzon, J., The Flow Field in the Turbulent Supersonic Near Wake Behind a Two-Dimensional Wedge-Flat Plate Model, TAE Report No. 54, Department of Aeronautical Engineering, Technicon-Israel Institute of Technology Haifa, August 1966, Under ARL Contract AF61(052)-576.

(8) Donaldson, I. S., "On the Separation of a Supersonic Flow at a Sharp Corner," AIAA Journal, 5 June 1967, pp 1086-88.

(9) Scherberg, M. G. and Smith, H. E., Experimental Study of the Flow Structure and Heat Transfer for a Rearward Facing Step in Supersonic Flow, Paper Presented at the Proceedings of the 8th Israel Annual Conference on Aviation and Astronautics Held at Tel Aviv and Haifa, Israel, February 1966, Aerospace Research Laboratories Report ARL-66-0164, February 1966.

(10) Rom, J. and Victor, J., Base Pressure Behind Two-Dimensional and Axially-Symmetric Backward Facing Steps in a Turbulent Supersonic Flow, TAE Report No. 31, Department of Aeronautical Engineering, Technicon-Israel Institute of Technology, Haifa, December 1963, Under ARL Contract AF 61(052)-576.

(11) Thommen, H. V. and Magnus, J., Numerical Calculation of Separated Flow Fields, AGARD Fluid Dynamics Panel, Conference Proceedings No. 4, Separated Flow, Part 1, Belgium, May 1966, pp 187-205, General Dynamics Paper.

(12) Charwat, A. F. and Der, J., Studies of Laminar and Turbulent Free Shear Layer with a Finite Initial Boundary Layer at Separation, AGARD Fluid Dynamics Panel, Conference Proceedings No. 4, Separated Flows, Part 1, Belgium, May 1966, pp 207-40, Under NSF Grant No. GP2350.

(13) Adamson, T. C., The Effect of Transport Properties on Supersonic Expansion Around a Corner, Report No. 4613-120-T Willow Run Laboratories, University of Michigan, May 1966, Under ARPA Contract SD-91.

(14) Rom, J., Near Wake Flow Studies in Supersonic Flow, TAE Report No. 38, Department of Aeronautical Engineering, Technicon-Israel Institute of Technology, Haifa, March 1965, Under ARL Contract AF 61(052)-576.

(15) Ginoux, J. J., Effect of Mach Numbers on Streamwise Vortices in Laminar Reattaching Flows, Technical Note No. 26, von Karman Institute for Fluid Dynamics, Rhode-Saint Genese, Belgium, July 1965, Under Contract NR AF EOAR 65-11.

(16) Scherberg, M. G., and Smith, H. E., Experimental Study of the Flow Structure and Heat Transfer for a Rearward Facing Step in Supersonic Flow,

Paper Presented at Proceedings of the 8th Israel Annual Conference on Aviation and Astronautics held at Tel Aviv and Haifa, February 1966, ARL Report.

(17) Rom, J., Analysis of the Near Wake Pressure in Supersonic Flow Using the Momentum Integral Method, TAE Report No. 35, Technicon-Israel Institute of Technology, Haifa, September 1964, Under ARL Contract AF 61(052)-576 .

(18) Khosla, P. K., Flow of Radiating Gas Past a Corner, PIBAL Report No. 981, Department of Aerospace Engineering and Applied Mechanics, Polytechnic Institute of Brooklyn, June 1966, Under ONR Contract No. NONR 839(34).

(19) Tani, I., Experimental Investigation of Flow Separation Over a Step, University of Tokyo.

Recently, Korst and Chapman, Kuehn and Larson independently put forward a simple method of predicting the base pressure by dividing the flow into the dissipative "cavity" flow region wherein the pressure is assumed to be constant and a reattachment zone wherein the compression is assumed to be such that not much total pressure is lost along the dividing streamline.

It appears from these theoretical investigations that the most essential and intriguing part of the problem is concerned with the mixing process between the dissipative cavity flow and the non-dissipative main flow. This kind of interactive mixing occurs equally at subsonic speeds, but no ad hoc measurement seems to have been made at subsonic speeds.

In view of these circumstances, the investigation described in this paper was undertaken by determining at subsonic speeds the distribution of surface pressure and that of mean and fluctuating velocities in the separated flow over a backward-facing step. The work was conducted with the financial support of the Ministry of Education by the Scientific Research Fund.

(20) Donaldson, J. C. and Myers, A. W., Investigation of the Separation and Reattachment of Flow Downstream of a Two-Dimensional Rearward Facing Step at Mach Numbers 2.5 and 3.5, AEDC-TR-65-223, von Karman Gas Dynamics Facility, Arnold Engineering Development Center, November 1965.

(21) Rom, J. and Seginer, A., "Laminar Heat Transfer to a Two-Dimensional Backward Facing Step from the High-Enthalpy Supersonic Flow in the Shock Tube," AIAA Journal, 2, February 1964, pp 251-55.

(22) Rom, J., Supersonic Flow Over Two-Dimensional and Axially Symmetric Backward Facing Steps, TAE Report No. 33, Department of Aeronautical Engineering, Technicon-Israel Institute of Technology, Haifa, March 1964, Under ARL Contract AF 61(052)-576.

(23) George, A. R., Hypersonic Flow Over a Wedge with Upstream Non-Uniformities and Variable Wedge Angle, Report No. 695, Gas Dynamics Laboratory, Princeton University, December 1964, Under AF-AFOSR Grants 112-63 and 112-63A.

(24) Roshko, A., and Thomce, G. J., Flow Separation and Reattachment Behind a Downstream-Facing Step, Report No. SM-4 3056, Douglas Missile and Space Systems Division, Paper No. 1 on Results of Research and Development Studies by the Douglas Aerophysics Laboratory Staff During Fiscal Year 1963, January 1964, pp 1-43.

c. Reports on Flow and Heat Transfer in Front of Forward Facing Steps

(1) Zukoski, E. E., "Turbulent Boundary-Layer Separation in Front of a Forward-Facing Step," AIAA Journal, 5, October 1967, pp 1746-53.

(2) Gillette, W. B., Separation Measurements of Supersonic Turbulent Boundary Layers Over Compression Corners, Report No. DRL-543, Defense Research Laboratory, University of Texas, Austin, July 1966, Under APL/JHU Subcontract 181471.

(3) Speaker, W. V., and Ailman, C. M., Static and Fluctuating Pressures in Regions of Separated Flow, AIAA Paper No. 66-456, Presented at 4th Aerospace Sciences Meeting Held at Los Angeles, California, June 1966, Douglas Aircraft Company.

(4) Rogers, E. W. E., Berry, C. J. and Davis, B. M., An Experimental Investigation of the Interaction Between a Forward-Facing Step and a Laminar

Boundary Layer in Supersonic, Low-Density Flow, N.P.L. Aero Report 1139, Aerodynamics Division, National Physical Laboratory, England, January 1965.

(5) Halprin, R. W., Step Induced Boundary-Layer Separation Phenomena, AIAA Journal, 3, February 1965, pp 357-59.

(6) Revell, J. D., and Gleason, R. E., Turbulent Wall Pressure Fluctuations Under Separated Supersonic and Hypersonic Flows, Technical Report AFFDL-TR-65-77, Flight Dynamics Laboratory, Air Force Systems Command, August 1965.

(7) Williams, J. C., On the Upstream Length of Turbulent-Boundary Layer Separation, AIAA Journal, 3, December 1965, pp 2347-48.

(8) Kistler, A. L., Surface Pressure Fluctuations Produced by Attached and Separated Supersonic Boundary Layers, Report 458, Presented at AGARD Specialists Meeting Held at Rhode-Saint-Genese, Belgium, April 1963, Yale University Study.

(9) Love, E. S., Base Pressure at Supersonic Speeds on Two-Dimensional Airfoils and on Bodies of Revolution With and Without Fins Having Turbulent Boundary Layers, NACA TN 3819, Langley Aeronautical Laboratory, January 1957.

d. Reports on Generally Related Flow and Heat Transfer Effects

(1) Waltrup, P. J., Hall, D. G., and Schetz, J. A., "Flowfield in the Vicinity of Cylindrical Protuberances on a Flat Plate in Supersonic Flow," Journal of Spacecraft and Rockets, 5, January 1968, pp 127-28.

(2) Bossel, H. H., Inviscid and Viscous Models of the Vortex Breakdown Phenomenon, Report No. A567-14, College of Engineering, University of California, Berkeley, August 1967, Under NSF Grant No. GK-1297.

(3) Rom, J., and Seginer, A., Laminar and Transitional Heat Transfer in the Two-Dimensional Separated Flow Behind a Sharp Protruding Leading Edge, TAE Report No. 71, Department of Aeronautical Engineering, Technicon-Israel Institute of Technology, Haifa, July 1967, Under ARL Contract F61052-67-C-0033.

(4) Sieker, W. D., Protuberance Heating Test Program, DAC Report SM-47497, Missile and Space Systems Division, Douglas Aircraft Company, Huntington Beach, February 1966, Under NASA Contract NAS7-101.

(5) Westkaemper, J. C., "Step-Induced Boundary-Layer Separation Phenomena," AIAA Journal, 4, June 1966, pp 1147-48.

(6) Miller, W. H., Pressure Distributions on Single and Tandem Cylinders Mounted on a Flat Plate in Mach Number 5.0 Flow, Report DRL-538, Defense Research Laboratory, University of Texas, Austin, June 1966, Under APL/JHU Subcontract 181471.

(7) Kwan, L. S., Vortex Phenomena in a Conical Diffuser, AIAA Paper No. 66-426 Presented at 4th Aerospace Sciences Meeting Held at Los Angeles, June 1966, TRW Systems Report.

(8) Richmond, J. K., and Goldstein, R., "Fully Developed Turbulent Supersonic Flow in a Rectangular Channel," AIAA Journal, August 1966, pp 1331-36.

(9) Anderson, W. J., Supersonic Wind Tunnel Tests of Wavy Walled Cylinders, ARL 65-203, Aerospace Research Laboratories, October 1965.

(10) Leining, R. B., The Use of Probes for Rocket Thrust Vector Control, Report P. Dev 4045, Allegany Ballistics Laboratory, Hercules Powder Company, March 1963 CLASSIFIED

(11) Deissler, R. G., "Turbulent Heat Transfer and Temperature Fluctuations in a Field with Uniform Velocity and Temperature Gradients," International Journal of Heat and Mass Transfer, 6, 1963, pp 257-70.

(12) Gessner, F. B., and Jones, J. B., "A Preliminary Study of Turbulence Characteristics of Flow Along a Corner," Journal of Basic Engineering, 83, December 1961, pp 657-62.

(13) Stratford, B. S., and Neale, M. C., Some Tests with Trapped Vortices in Supersonic Flow, C. P. No. 716, Aeronautical Research Council, Ministry of Aviation, London, September 1960.

(14) McLean, F. E., and Rennemann, C., Supersonic Flow Past Nonlifting Bumped and Indented Bodies of Revolution, NACA TN 3744, Langley Aeronautical Laboratory, September 1956.

(15) Chapman, D. R., Kuehn, D. M., and Larson, H. K., Investigation of Separated Flows in Supersonic and Subsonic Streams with Emphasis on the Effect of Transition, NACA TN 1356.

(16) Klebanoff, P. S., and Kiehl, Z. W., Some Features of Artificially Thickened Fully Developed Turbulent Boundary Layers with Zero Pressure Gradient, NACA TN 2475, National Bureau of Standards, October 1951.

(17) Laufer, J., Investigation of Turbulent Flow in a Two-Dimensional Channel, CIT Report 1053, Guggenheim Aeronautical Laboratory, California Institute of Technology, Pasadena, September 1949.

2. THEORETICAL FLOW CONDITIONS IN VALVE CLOSED CAVITY

The structural and thermal analysis of the orifice requires the net pressure loads on each orifice component, a longitudinal pressure profile, 90 deg pressure profile, heat transfer coefficient longitudinal and transverse, and erosion rates along these two planes (Figure 55).

a. Nozzle Flow--The first portion of the analysis was to calculate the flow in the nozzle assuming the valve was closed and the orifice did not affect the nozzle flow. A one-dimensional equilibrium thermodynamic run was made by the computer and a tape record of these properties was used as input to the axisymmetric characteristics run to define the gas flow conditions along the nozzle wall. The characteristics that intersect the wall just forward and aft of the port are given in Table XIII. The real gas wall Mach number along with the one-dimensional and ideal gas Mach numbers are shown in Figure 56 . The Mach number differences for three techniques are not large at the orifice. The static pressures from the real gas analysis and the convective heat transfer coefficient from a turbulent boundary layer analysis are presented in Figure 57 . These data define the inviscid flow field above the orifice and the boundary layer ahead of the orifice.

b. Analytical Analysis of Reattachment--When the valve is closed the orifice is a separated flow area. The primary nozzle flow does not go into the orifice and the velocities are induced by a viscous mixing with the free stream flow and a dissipation by viscous drag on the walls of the orifice. This recirculation is shown in Figure 58 . The regions of the mixing zone and its coordinate system are shown in Figure 58.

The calculation of the mixing zone results in

similarity parameter	$\sigma = 19.17$
Crocco number	$Ca = 0.5505$

TABLE XV

HOT GAS VALVE 120 IN. REAL GAS FLOW CONDITIONS - NOZZLE EXIT CONE
(Case 1)

Line	Point	Description	R Mach Angle	X Pressure	M Density	Theta Temperature	Entropy Velocity
34	18		0.83879E 01 0.24587E 02	0.34028E 02 0.85424E 04	0.24034E 01 0.11252E 02	0.32324E 01 0.44517E 04	0.0 0.71893E 04
34	19		0.87555E 01 0.24478E 02	0.34722E 02 0.83608E 04	0.24134E 01 0.11041E 02	0.34944E 01 0.44407E 04	0.0 0.72117E 04
34	20		0.90904E 01 0.24375E 02	0.35351E 02 0.81900E 04	0.24230E 01 0.10842E 02	0.37480E 01 0.44302E 04	0.0 0.72331E 04
34	21		0.93814E 01 0.24283E 02	0.35894E 02 0.80381E 04	0.24317E 01 0.10664E 02	0.39796E 01 0.44207E 04	0.0 0.72524E 04
34	22		0.96135E 01 0.24207E 02	0.36324E 02 0.79144E 04	0.24388E 01 0.10519E 02	0.41719E 01 0.44129E 04	0.0 0.72683E 04
34	23		0.97672E 01 0.24156E 02	0.36609E 02 0.78315E 04	0.24437E 01 0.10422E 02	0.43030E 01 0.44075E 04	0.0 0.72790E 04
34	24		0.98217E 01 0.24137E 02	0.36709E 02 0.78017E 04	0.24454E 01 0.10387E 02	0.43503E 01 0.44056E 04	0.0 0.72829E 04
34	25		0.11070E 02 0.23719E 02	0.38978E 02 0.71427E 04	0.24860E 01 0.96095E 03	0.54270E 01 0.43613E 04	0.0 0.73719E 04
31	26		0.13523E 02 0.22981E 02	0.43276E 02 0.60508E 04	0.25613E 01 0.83016E 03	0.72975E 01 0.42791E 04	0.0 0.75338E 04
34	27		0.17054E 02 0.22053E 02	0.49151E 02 0.48156E 04	0.26634F 01 0.67873E 03	0.96858E 01 0.41685E 04	0.0 0.77461E 04
34	28		0.21775E 02 0.21007E 02	0.56551E 02 0.36881E 04	0.27895E 01 0.53583E 03	0.12329E 02 0.40458E 04	0.0 0.79876E 04
34	29	Wall	0.28061E 02 0.19963E 02	0.65818E 02 0.27348E 04	0.29290E 01 0.41107E 03	0.15003E 02 0.39126E 04	0.0 0.82417E 04

The Percent Change in Mass Flow is = 0.331752E 01

Pressure Integration Results

Force X	Force Y	Torque Z	Deflection X	Deflection Y
-0.85776E 08	0.0	-0.0	-0.29630E 07	0.0

TABLE XV (Cont)

HOT GAS VALVE 120 IN. REAL GAS FLOW CONDITIONS - NOZZLE EXIT CONE
(Case 1)

Line	Point	Description	R Mach Angle	X Pressure	M Density	Theta Temperature	Entropy Velocity
33	18		0.99014E 01 0.26080E 02	0.28239E 02 0.11222E 05	0.22747E 01 0.14311E 02	0.64511E 01 0.45931E 04	0.0 0.68937E 04
33	19		0.10301E 02 0.25952E 02	0.28854E 02 0.10980E 05	0.22851E 01 0.14039E 02	0.66564E 01 0.45816E 04	0.0 0.69181E 04
33	20		0.10673E 02 0.25827E 02	0.29445E 02 0.10746E 05	0.22954E 01 0.13775E 02	0.68709E 01 0.45703E 04	0.0 0.69422E 04
33	21		0.11010E 02 0.25711E 02	0.29969E 02 0.10530E 05	0.23051E 01 0.13530E 02	0.70825E 01 0.45597E 04	0.0 0.69647E 04
33	22		0.11300E 02 0.25607E 02	0.30419E 02 0.10338E 05	0.23138E 01 0.13513E 02	0.72785E 01 0.45501E 04	0.0 0.69849E 04
33	23		0.11531E C2 0.25523E 02	0.30774E 02 0.10184E 05	0.23209E 01 0.13138E 02	0.74430E 01 0.45423E 04	0.0 0.70014E 04
33	24		0.11683E 02 0.25466E 02	0.31008E 03 0.10081E 05	0.23257E 01 0.13021E 02	0.75560E 01 0.45370E 04	0.0 0.70125E 04
33	25		0.11736E 02 0.25446E 02	0.31091E 02 0.10045E 05	0.23274E 01 0.12960E C2	0.75969E 01 0.45351E 04	0.0 0.70164E 04
33	26		0.12956E 02 0.24990E 02	0.32949E 02 0.92340E 04	0.23671E 01 0.12051E 02	0.85435E 01 0.44916E 04	0.0 0.71072E 04
33	27		0.15325E 02 0.24191E 02	0.36463E 02 0.78891E 04	0.24403E 01 0.10490E 02	0.10239E 02 0.44112E 04	0.0 0.72715E 04
33	28		0.18671E 02 0.23198E 02	0.41233E 02 0.63620E 04	0.25336E C1 0.86770E 03	0.12472E 02 0.43038E 04	0.0 0.74856E 04
33	29	Wall	0.23072E 02 0.22126E 02	0.47202E 02 0.49067E 04	0.26550E 01 0.69005E 03	0.15003E 02 0.41775E 04	0.0 0.77291E 04

The Percent Change in Mass Flow is = 0.165435E 01

Pressure Integration Results

Force X	Force Y	Torque Z	Deflection X	Deflection Y
-0.82813E 06	0.0	-0.0	-0.28196E 07	0.0

then

$$\eta_\infty = \frac{\sigma Y_\infty}{l_j} = 0.5217; \qquad Y_\infty = 0.1872 \text{ in.}$$

for a slope of 1°34'

and

$$\eta_D = \frac{\sigma Y_D}{l_j} = 0.2469; \qquad Y_D = 0.0866 \text{ in.}$$

for a slope of 44'

and

$$\varphi_D = \frac{U_D}{U_\infty} = 0.6365; \qquad U_D = 4{,}863 \text{ ft/sec}$$

$$k = \frac{\eta_M - \eta_\infty}{2\,\eta_M} = 0.4130; \qquad \eta_M = 2.998$$

$$Y_M = \frac{\eta_M\, l_j}{\sigma} = 1.076 \text{ in.}$$

then the

slope of the dividing streamline

$$= \arctan\left(\frac{Y_M - Y_D}{l_j}\right)$$

$$= 8°12'$$

with a reattachment point

0.99 in. into the cavity

c. Cavity Flow Conditions--The flow Mach number in the cavity was calculated theoretically by a momentum exchange computer program. The program computes the cavity Mach number by balancing the frictional momentum loss on the walls with the viscous transfer of momentum from the free stream.

By this analysis the cavity flow Mach number is 0.44. This was assumed constant throughout except at reattachment areas or in separated areas. A cavity flow Mach number of between 0.42 and 0.55 was measured in the cold flow tests so the theoretical calculation was confirmed.

The flow conditions near the stagnation point are quite difficult to measure so several semi-empirical techniques were used to define these flow conditions*. The solution for the incompressible momentum equation and energy equation on a cylinder results in

$$St = 0.570\left(\frac{C_p \mu}{k}\right)^{-0.6} \left(\frac{\beta D}{U}\right)^{-0.5} \left(\frac{DU\rho}{\mu}\right)^{-0.5}$$

where St = Stanton number

$\frac{C_p \mu}{k}$ = Prandtl number

$\frac{DU\rho}{\mu}$ = Reynolds number

D = diameter of curvature

β = velocity gradient at the stagnation point

U = free stream velocity

for the incompressible solution ($\beta D/U$) = 4.0 but it is corrected by the compressible effects to give

$$(\beta D/U) = 2.5$$

for

$$M = 2.6$$

then

γ = 1.18

U_∞ = 7,640 ft/sec

μ = 60×10^{-6} lbm/ft sec

Pr = 0.85

Re = 2.11×10^{6}

C_p = 0.435 Btu/lbm °F

*Turbulent Flow and Heat Transfer, Vol V of High Speed Aerodynamics and Jet Propulsion, Princeton University Press, 1959.

then

$$St = 0.000682$$

and

$$h = St\, C_p\, \rho\, U$$

$$= 0.0654 \text{ Btu/ft}^2 \text{ sec °R}$$

and

$$h/C_p = 0.15 \text{ lbm/ft}^2 \text{ sec}$$

because of the discontinuity at the stagnation point

$$M = 0$$

$$h/C_p > 0$$

an artificial value of Mach number was assumed for $H/C_p = 0.15$ based on other data for standard nozzle inlets. The assumed value was

$$M_{stag} = 0.05$$

The Mach number gradient away from the stagnation point was back calculated from $\beta D/ U = 2.5$

$$\beta = 1{,}790 \text{ ft/sec/in.}$$

or

$$\frac{\partial M}{\partial l} = 0.526 \frac{1}{\text{in.}}$$

The Mach number and total pressure gradients are shown near the reattachment point in Figure 59 and shown relative to the orifice in Figure 60.

d. Cavity Convective Heat Transfer Coefficients--Because the boundary layer program does not allow a variable total pressure, the analysis was run in steps of 74 psia. At the end of each step, the boundary layer was restarted with the previous section's momentum thickness and the next increment of total pressure and the proper Mach number gradient.

The resulting heat transfer coefficients are shown in Figure 61 for the downstream side of the orifice. The gas flow streamline continues down the wall, across the floor of the cavity, and up the upstream wall so the boundary layer was developed along this streamline. Because of the sharp corners where the wall and floor meet, the boundary layer was restarted at these two locations. These data are shown in Figures 61 and 62.

3. COLD FLOW TEST STUDY IN VALVE CLOSED CAVITY

Because the flow in the cavity cannot be predicted by conventional analysis, i.e., the flow is not axisymmetric or inviscid; a cold flow simulation study was developed to determine flow conditions in the orifice while closed.

a. Test Description -- The basic model was from a previous study on orifice and pintle flow conditions during injection*. A cross section of the model through the injection orifice is shown in Figure 63 . The pintle tip was bonded into the injection orifice at the proper depth to simulate the depth to diameter ratio of the TU-520 orifice. The pressure taps were not hooked up on the pintle tip and orifice walls. Stipples of lampblack and kerosene were applied in the orifice to determine wall flow directions. The inlet total pressure was increased to 100 psig to flow the nozzle full past the injection orifice then dropped, the orifice was then inspected, and photos were taken of the smear patterns. These measurements of flow direction were taken on a perpendicular to centerline orifice. It was located at an X/L=0.5 on a 8:1 expansion ratio nozzle with a 17.5 degree cone. The free stream Mach number for air is 2.84 on tests 2 and 3.

Tests 4 and 5 were for a different orifice configuration. A new pintle tip and orifice were built and installed in a different location on the nozzle. The orifice was at a free stream Mach number of 2.6 with a diameter of 1 inch. The orifice centerline is perpendicular to the nozzle wall as in the TU-520.

A stepped insert was also built to simulate the orifice geometry with the PTB missing. This was also installed in the old orifice perpendicular to centerline.

Figure 63 shows the Mach number probe in the center of the pintle tip and the eight static pressure taps on the pintle tip.

---

*TWR-846, Cold Flow Studies Submerged Hot Gas Valve Program Wing V Production Support by Thiokol Chemical Corporation, February 1965.

b. Test Results -- The first tests were for the perpendicular to centerline orifice. Two similar runs, runs 2 and 3, were made on this configuration and the data are shown in Figures 64 thru 75 . The arrow and D indicate nozzle flow direction and orifice downstream edge. Figure 65 shows the backflow along the base of the cavity (pintle tip). Figures 68 and 72 show the flow down the downstream wall, the split and separation near the floor of the cavity.

The data for the perpendicular to wall orifice configuration which matches the TU-520 orifice is given in Figures 76 thru 82. The cold flow data for test 4 is given in Figure 83 and Table XVI. The pressure variation along the floor of the cavity is shown in Figure 84. From the circumferential pressure variation in Figure 83, a computer program matches this pressure curve to calibration curves developed previously to compute the Mach number in the bottom of the cavity which equaled between 0.42 and 0.55 depending on which calibration curve was used. This large uncertainty was because the calibration had been made for Mach numbers below 0.2. The value used in the analysis was 0.5.

The pressure distribution on the floor of the cavity shows a pressure decay from reattachment up to the center of the floor of the orifice then no change on the forward half of the orifice.

The data for the perpendicular to centerline orifice with a stepped insert to simulate the orifice geometry with the PTB missing is shown in Figures 85 thru 90. The stipples applied to the orifice show the wall flow directions as illustrated in Figure 91 . The smear patterns from the cold flow analysis shows an apparent secondary circulation has been set up on the end of the pyrolytic graphite insert and would cause increased heating there.

TABLE XVI

COLD FLOW PRESSURE DATA, BOTTOM OF CAVITY

Tap	Value at Bottom of Cavity	Pressure (Hg)	Pressure (psia)	P/P_T
1	62.85	--	--	--
2	50.80	13.41	6.587	0.1005
3	52.50	15.11	7.422	0.1132
4	53.45	16.06	7.887	0.1203
5	51.15	13.76	6.759	0.1031
6	51.20	13.81	6.783	0.1035
7	51.40	14.01	6.882	0.1050
8	50.85	13.46	6.612	0.1009
9	50.60	13.21	6.489	0.0990
10	53.20	15.81	7.766	0.1185
11	39.15	--	--	--
12	26.25	12.56	6.169	0.0941
13	26.60	12.91	6.341	0.0967
14	26.75	13.06	6.415	0.0979
15	27.05	13.36	6.566	0.1001
16	26.95	13.26	6.513	0.0974
17	26.35	12.66	6.218	0.0949

P_T = 108 psig = 65.555 psia

4. ORIFICE MOTOR TEST DATA CORRELATION

Because of the difficulty in predicting the flow environment in the cavity, the past data on nozzle erosion was scalable to the orifice. The data which was considered was from

1. The TU-453 orifice,
2. The TU-454 orifice,
3. The Lockheed TRW L-73-156 in. HGSITVC S/N 3, S/N 4, S/N 103, and S/N 104.

After reviewing the configuration and test conditions of these motors, only the TU-453 was close enough to scale adequately. The injection is perpendicular to the wall and at a free stream Mach number of 2.52 (one-dimensional area ratio of 3.6). The cavity length/height = 0.5 which is much lower than the injection orifice of the TU-520 (L/H = 1.6).

The data was evaluated by the following procedure:

1. The viscous drag program was used to calculate the cavity flow Mach number for the uneroded and eroded configuration of the four ports.
2. The velocity and total pressure variation from the reattachment point was calculated for the TU-453 orifice.
3. The boundary layer was calculated in the longitudinal plane.
4. The erosion depth was scaled from the erosion profiles and the erosion predicted for the valve open was subtracted. The erosion rate was then determined from the valve closed time interval.

5. The theoretical erosion rate $\left[\dot{\epsilon}_t = (h/C_p)\ \beta\, 12{,}000/\rho\right]$ was plotted versus the measured erosion rate in Figure 92. The data from port 1 was not used because some pieces of the insert apparently chunked out and all material loss was not due to erosion. The data from port 3 was used as most representative of the TU-453 orifices.

The theoretical curve in Figure 92 represents the erosion data except near the reattachment area. It was speculated the erosion near the reattachment area is increased by high boundary layer shear forces removing the char and/or mechanical erosion by the condensed phases in the rocket exhaust. The assumption of chemical erosion controlled by diffusion of the oxidizing species into the graphite wall and reacting to form carbon monoxide could be affected by the conditions near the stagnation point and thus alter the controlling factors in the chemical reaction.

The details of this problem were not investigated except to insure the adequacy of the present aero-thermo analysis on the orifice (maximum time = 25 seconds). Where greater depths of erosion are predicted the theoretical prediction could be in even greater error.

5. EROSION EFFECT ON CAVITY FLOW

a. Cavity Flow Conditions at 16 Sec--The next step in the analysis was to calculate the eroded configuration of the orifice at t = 16 seconds, the time at which the valve opens.

From the convective heat transfer coefficient for the 0 sec configuration (Figure 61) and the erosion prediction curve (Figure 92) the eroded profile of Figures 93 and 94 were calculated. The erosion on the downstream wall did not affect the reattachment region so the heat transfer curve did not change at 16 seconds. The only curve which would change is the downstream side while the port is open. The erosion would cause the flow to go supersonic and lower the heat transfer coefficient. This summarizes the condition at 16 sec for the valve closed and the valve open.

b. Cavity Flow Conditions at 25 Sec--Between 16 sec and 25 sec the valve is held open. The next step in the analysis was to compute the flow conditions, erosion profile, and heat transfer coefficient at 25 seconds. From the port open heat transfer coefficients at 16 sec the erosion rate was calculated and the 25 sec eroded profile calculated. An axisymmetric boundary layer for one-dimensional Mach numbers was computed for the upstream and downstream halves of the orifice with the predicted profile. The results did not vary enough to require a recalculation of the erosion but the new heat transfer coefficient should be used in the thermal analysis. The eroded profile, Mach No. and convective heat transfer coefficient profiles are shown in Figures 95, 96 and 97. The conditions after 25 sec, valve closed, have been shifted down into the cavity to account for the erosion effect.

c. Flow Conditions in the Nozzle--The flow in the nozzle during hot gas injection was not analyzed in detail but enough conditions were developed to obtain a heat transfer coefficient downstream for the valve open and closed.

The valve closed conditions was an extension of the analysis to the lip of the orifice. At the corner the total pressure is up to free stream and the Mach number is 0.6. While turning the corner the boundary layer would separate and reinitiate about 1/2 inch downstream. The flow was assumed to reach free stream Mach number in about 5 inches. The upper curve of Figure 98 represents the boundary layer calculation of this heat transfer coefficient. This is considerably higher than the free stream heat transfer coefficient shown in Figure 57.

The injection flow conditions in the nozzle are shown in Figure 99 and are based on the model by J. W. Mitchell*. Based on the Mach numbers along the separated area aft of the injection orifice, the viscous mixing program was used to compute the Mach number along the wall. This was then used to compute the total pressure in the separated area as the static pressure equals that outside the separated area and the boundary layer heat transfer coefficients were calculated. These data are shown in Figure 98 and are quite close to those in the unperturbed flow.

The upstream and 90 deg sides convective heat transfer coefficient during port open is shown in Figure 100 reflecting higher values than shown for the normal undisturbed upstream wall port closed as shown in Figure 57.

An alternative approach was also used for structural pressure loads on the orifice. The "k" performance factor was calculated in Table XVII for port 3 full open between t = 21-23 seconds. A composite axial pressure distribution along the nozzle exit cone is obtainable from Fluidyne tests of secondary gas injection pressure profiles in a conical nozzle for Edwards Air Force Base.** The data were retained in its coefficient form and corrections of the resultant profile were made

---

*An Analytical Study of a Two-Dimensional Flow Field Associated with Sonic Secondary Injection into a Supersonic Stream by J. W. Mitchell Vidya TN 9166-TN-2, March 1964.

**TWR-755 "Technical Note on Induced Pressure Profiles in an 8:1-17.5 Degree Conical Nozzle During Secondary Gas Injection, September 1964, Unclassified. AF 04(611)-9075 "Model Tests of Secondary Injection Thrust Vector Control on 17 1/2 Degree Conical Nozzles, May 1964. Unclassified.

TABLE XVII

ORIFICE 3 PERFORMANCE AT 21 TO 23 SEC, OPEN DUTY CYCLE

Omniaxial: (Single Port Injection)

The TVC side force loads are presented as acting normal to the nozzle exit cone axis.

From: Test Data-(Using Port 3)

16 - 21 Sec Port Opening	Load Cell at	17,000
21 - 23 Sec Port Open	Load Cell at	17,000
23 - 25 Sec Port Closing	F Side =	34,000

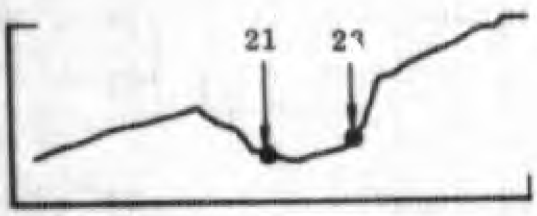

Uncorrected	Corrected	Vacuum
338,000	386,000	433,000 at 21 sec
355,000	405,000	445,000 at 23 sec

$$\text{Vacuum } \frac{F\ \text{Side}}{F\ \text{Axial}} = \frac{34,000}{433,000} = 0.78521 \text{ sec } \tau = 4.49 \text{ deg TVC at 21}$$

$$\frac{34,000}{445,000} = 0.076404 \text{ sec } \tau = 4.37 \text{ deg TVC at 23}$$

Axial Flow Rate, $\dot{W}_a$ = 1,679.8 lb/sec (at 16 →25 sec)

Injectant Flow Rate, $\dot{W}_s$ = 105.0 lb/sec (maximum at 21 →23 sec)

$$\text{Using: } \frac{\text{Injectant Flow Rate}}{\text{Axial Flow Rate}} = \frac{\dot{W}_s}{\dot{W}_a} = 0.0625$$

$$\text{From: } \frac{F\ \text{Side}}{F\ \text{Axial}} = K\,\frac{\dot{W}\ \text{Side}}{\dot{W}\ \text{Axial}}$$

$$K = \frac{F_s/F_a}{\dot{W}_s/\dot{W}_a} = \frac{0.0785 - 0.0764}{0.0625} \approx \begin{matrix}(16 \rightarrow 21 \text{ sec})\\ 1.256 \rightarrow 1.222\end{matrix}$$

for the proper hot flow specific heat ratio and nozzle exit cone geometry. Injector valve orientation was similar and force and flow ratio values were matched.

An axial and lateral plane through the orifice port shows the TVC side force and the axisymmetrical' nozzle pressure load distribution as a lb/in. load normal to nozzle wall for a one inch width of nozzle wall.

6. VALVE OPEN FLOW

The flow conditions in the orifice while the valve was open were computed one-dimensionally and without the boundary layer displacement thickness. The small error induced by these assumptions was within the accuracies required for the thermal and erosion analysis. The data are included with the valve closed data.

The orifice inlet Mach number and heat transfer coefficient when the port is open* is shown in Figure 100.

---

*Based on Cold Flow Studies Submerged Hot Gas Valve Program Wing V Production Support by Thiokol Chemical Corporation, February 1965.

B. THERMODYNAMIC ANALYSIS

1. ORIFICE PORT

The nozzle injection port thermal analysis for TU-520.04 motor was run using the computer program S-3148 "Two-Dimensional Axisymmetric Transient Temperature Production Program."

The program was used to determine preliminary and final thermal gradients through the orifice analytical model at 5, 16, 16.1, 25 and 25.1 seconds. The data input includes element location with respect to reference axes in the common orifice model grid and material thermal-physical properties taken from the Thiokol Insulation Materials Design Data Book (TWR-2462, Revision A).

The computer operation is a series of discrete steps. (1) The program is run from 0-16.0 sec with time (t) = 0 heat transfer coefficients orifice closed and no wall erosion. (2) At 16.1 sec the 16.0 sec heat transfer coefficients for orifice open and eroded and 16.0 sec wall erosion are inputed and the program allowed to run from 16.1 to 25.0 seconds. Erosion is simulated by dropping elements from the input data. (3) At 25.1 sec, the 25.0 sec heat transfer coefficients orifice closed and eroded and 25.0 sec wall erosion are inputed and the program run from 25.1 to 35.0 seconds. Elements are eliminated from the input data to simulate erosion.

The aerodynamic analysis provided the heat transfer coefficients and erosion for the three orifice wall surfaces as indicated in the following sketch for the input to thermodynamic programs.

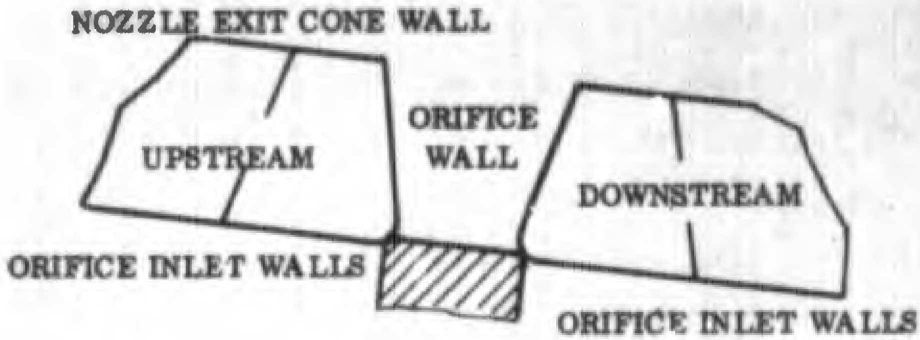

Aerodynamic Erosion and Heat Transfer Coefficient Input	Thermodynamic Analysis Preliminary		Thermodynamic Analysis Final	
Nozzle Exit Cone Wall				
Upstream				
Closed t = 0, 16, 25	Figure	57	Figure	57
Open t = 16, 25	Figure	57	Figure	100
Downstream				
Closed t = 0, 16, 25	Figure	57	Figure	98
Open t = 16, 25	Figure	57	Figure	98
Orifice Wall				
Upstream				
Closed t = 0, 16, 25	Figures	93,96	Figures	93,95
Open t = 16, 25	Figures	93,95	Figures	93,95
Downstream				
Closed t = 0, 16, 25	Figures	61, 93	Figures	93,95
Open t = 16, 25	Figures	93, 95	Figures	93,95
Orifice Inlet Wall				
Upstream				
Closed -t = 0, 25	Radiation Heating		Radiation Heating	
Open t = 16, 25	Figure	101	Figure	101
Downstream				
Closed t = 0, 25	Radiation Heating		Radiation Heating	
Open t = 16, 25	Figure	101	Figure	101

The preliminary thermal gradients were determined for the upstream and downstream orifice planes. Each plane environment was assumed all around the 360 deg orifice in separate thermal analyses at times 5, 16, 16.1, 25, 25.1 seconds. At each time, the two planes are shown together in Figures 102 thru 107. The preliminary thermal gradients were used to determine the critical orifice plane to assume around the 360 deg orifice analyses model.

At all five times, whether open or shut, the downstream edge has higher orifice, nozzle exit cone temperatures and erosion due to gas stagnation at downstream orifice wall. The upstream tungsten has higher temperatures consistently due to the reversal of gas flow in the orifice cavity across the pintle valve face to the upstream tungsten face and turn 90 deg up the upstream orifice cavity wall, as indicated in the sketch below.

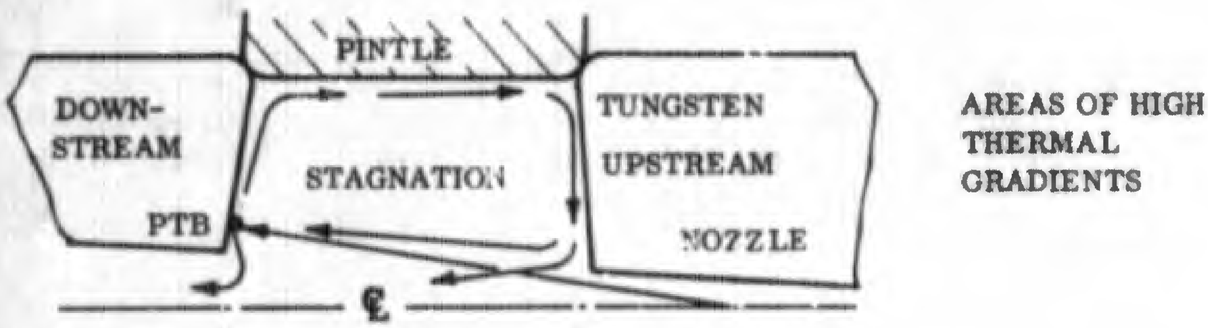

Since the tungsten shell is the most reliable material at elevated temperatures and the PTB material is the least characterized of all orifice materials, the downstream plane was selected to be used all around the ring for the axisymmetrical final thermodynamic analysis.

The final thermal gradients at the downstream orifice plane at t = 5, 16, 16.1, 25, and 25.1 seconds are shown in Figures 108 thru 113.

The comparison of the preliminary and final thermal gradients at t = 5.0 seconds is shown in the following sketch.

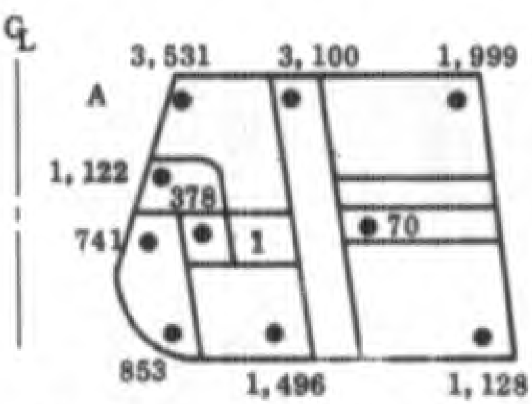

PRELIMINARY THERMAL GRADIENTS DOWNSTREAM

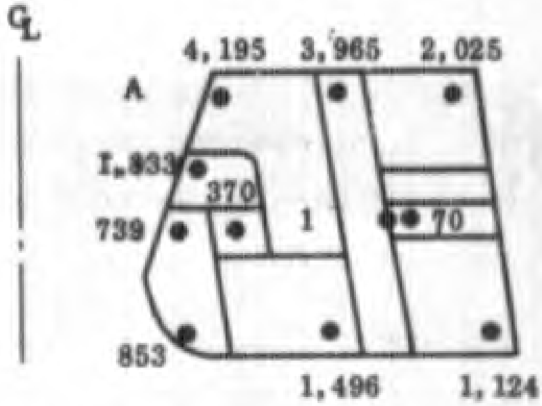

FINAL THERMAL GRADIENTS DOWNSTREAM

NOTES: A MATERIAL 1 IS CARBON CLOTH PHENOLIC LIKE PARTS 1, 2, AND 4 IN THE PRELIMINARY THERMAL GRADIENTS, WHILE MATERIAL 1 IS PTB IN THE FINAL THERMAL GRADIENTS AS PART 3 WAS FABRICATED.

B THE FINAL NOZZLE WALL AND ORIFICE WALL HEAT TRANSFER COEFFICIENTS ARE HIGHER THAN USED IN THE PRELIMINARY THERMODYNAMIC ANALYSIS. THIS IS REFLECTED IN THE HIGHER FINAL WALL TEMPERATURES AROUND POINT A .

NOTES: A Material 1 is carbon cloth phenolic like parts #1-#2-#4 - in the preliminary thermal gradients, while material 1 is PTB in the final thermal gradients as part #3 was fabricated.

B The final nozzle wall and orifice wall heat transfer coefficients are higher than used in the preliminary thermodynamic analysis. This is reflected in the higher final wall temperatures around point A .

2. VALVE LEGS

The area where the valve leg interfaced with the orifice and nozzle components was analyzed to determine if excessive temperatures might have been a contributing factor to the failure of valve, orifice, or nozzle components.

The leg-nozzle-orifice interface was analyzed using a two-dimensional, axisymmetric transient temperature prediction program. The analysis was conducted subject to the actual duty cycle experienced by valve 3. The legs were considered to be heated by radiation when the valve was closed and by convection and radiation with the valve open. Erosion was not considered in the analysis.

The material thermal properties were taken from the Thiokol Insulation Materials Design Data Book (TWR-2462, Revision A). The emissivity of the materials was assumed to be 0.80.

The heat transfer coefficients which were used in these analyses were obtained from an aerodynamic analysis of the valves. The applicable heat transfer coefficients are shown in Figures 114 and 115. Since the heat transfer coefficient varies around the leg, the highest value, 0.515, given in Figure 11 of TWR-1978 Report was used. The heat transfer coefficient used for the seat between the legs was 0.21.

Figure 116 shows the materials and nodal configuration which was evaluated. Figures 117 thru 121 present the results of these analyses. Examination of these figures indicates that no thermal problem existed at the time when orifice 3 indicated failure by slipping.

C. STRESS ANALYSIS

A structural analysis for the stress and strain distribution in the orifice port was achieved using Computer Program 53112, a two-dimensional, orthotropic axisymmetric finite element analyses.

The input included element temperatures, material properties and loads. The common orifice element network was also used for the structural analysis. The inputed thermal gradients used the preliminary thermal gradients at t = 5.0 sec for the downstream orifice plane, with the final thermal gradients used at t = 25.0 and 25.1 sec analysis of downstream plane. Material properties include Poisson's ratio, coefficient of linear thermal expansion and Young's modulus. The loads include the pintle actuator stall load, wall gas pressure, nozzle axial and hoop membrane uniform load.

The boundary conditions at the edge of the nozzle-orifice analysis area was considered fixed axially and free to move radially with nozzle uniform loads. An alternative boundary condition of fixed-axially and radially was used to show the difference in the element stresses and deflections.

Due to the extensive amount of analyst time to input nodal temperatures, location, material properties and loads only one location plane (downstream) was analyzed at times 5.0 sec, pintle valve closed, 25.0 sec pintle valve open and 25.1 sec pintle valve closed.

The output includes nodal center stresses in the radial, axial and hoop directions and nodal corner radial and axial movement.

1. METHOD OF ANALYSIS

The finite element approach to structural analysis problems has provided a means by which accurate solutions may be obtained for the state of stress in complex axial symmetric two-dimensional (axial length and radial thickness) structures which have orthotropic elastic properties.

The technique involved has been programed for the computer and requires input of a description of element geometry, orthotropic material properties, boundary conditions and loadings. The output lists the displacements, stresses and strains at various points throughout the section being studied.

The direct stiffness method is utilized in the program and is applicable to both articulated and continuum structures subject to static or dynamic loadings.

For continuum problems the region of interest is approximated by a set of simple subregions called finite elements which are simple geometric shapes (triangular or rectangular). Within each element, the displacement field is assumed to have the form of a polynomial in the coordinates. The assumed displacement function in an element can be related to the displacement of the corners of the element. These corners are called nodal points. The required functional for the region can be calculated as a quadratic function of the nodal point displacements. Thus, the minimization of the functional is reduced to the solution of algebraic equations in the unknown point displacements. These equations are the stiffness relations for the body and the coefficient matrix is called the stiffness matrix. The resulting structural stiffness relation is then modified to account for any specified displacement or loads and the resulting system is solved for nodal point displacements. The strain and the stress fields are inferred from the calculated values of the nodal point displacements.

This technique was applied to a section or region of the TU-520.04 HGSITVC nozzle orifice (Figure 122).

Figure 123 is a schematic view of the way the orifice cross section was subdivided into finite trapezoidal elements for the purpose of analysis. The number of each element is designated by the number of the lowest boundary node (I, J), where I denotes the row, and J denotes the column. The grid structure was chosen in such a manner that normal grid lines fall on natural material boundaries and to coincide with thermal analysis elements. The coordinates of each node point are input into the program.

There are many loading conditions which can be used. Each element within the system can be loaded with pressure and/or shear loading on any of its four sides, as well as a body force within the element if required.

The boundary conditions imposed on the orifice downstream cross section are as follows:

1. <u>5 sec condition with pintle valve closed</u> (Figure 123)
   a. 26 psig static pressure on inside orifice boundary wall,
   b. The freestream pressure on the nozzle exit cone wall,
   c. 633 psig chamber pressure on the orifice inlet wall,
   d. Pintle valve stall load of 15,000 lb on tungsten orifice valve seat.
   e. Two boundary conditions were investigated
      1) Axial and radial nodes fixed
      2) Axial nodes fixed and radial nodes free except for steel which has 12,000 lb/in. uniform load. The uniform load simulates the average hoop and axial nozzle load around the orifice. The eight material elements J (9-12) to I (11, 15) were changed to PTB from carbon cloth phenolic to simulate orifice 3.
   f. No adhesive bond lines were inputed into finite element model. Materials considered to blend into each other.
2. <u>25 second condition with pintle valve open</u> (Figure 124)
   a. 760 psig chamber pressure on orifice inlet wall varying downward as pressure flows thru the orifice.

b. The freestream pressure plus side load pressure on the nozzle exit cone wall.

c. The orifice movement on the outside boundary nodes was fixed and a radial load inward was applied on the node of the materials to simulate hoop or axial load in the nozzle. The load was applied on all materials and was divided by ratio of modulus and thickness to each of the materials (Table XVIII). An alternate boundary condition was axial and radial nodes fixed.

d. No adhesive bond lines were inputed into finite element model. Materials considered to blend into each other.

3. <u>25.1 sec condition with pintle valve closed</u> (Figure 125).

a. 26 psig static pressure on the orifice wall.

b. The freestream pressure on the nozzle exit cone wall.

c. 760 psig chamber pressure on the orifice inlet wall.

d. Pintle valve stall load of 15,400 lb on the tungsten valve seat.

e. The axial movement on the outside boundary nodes was fixed and a radial load inward was applied on the node of each of the materials to simulate hoop or axial load in the nozzle. An alternate boundary condition was axial and radial nodes fixed.

f. No adhesive bond lines were inputed into finite element model. Materials considered to blend into each other.

TABLE XVIII

ORIFICE EQUIVALENT STEEL LOAD AT BOUNDARY CONDITION

Distribution of Nozzle Radial Load to Orifice Boundary Conditions

Equivalent Steel Thickness

$$t_s = \frac{E_c}{E_s} t_c$$

Carbon Cloth:

$$= \frac{0.64 \times 10^6}{29 \times 10^6} \times 0.15 = 0.0033$$

$$t_s = \frac{1.4 \times 10^6}{29 \times 10^6} \times 0.2 = 0.0096$$

$$t_s = \frac{2.7 \times 10^6}{29 \times 10^6} \times 0.2 = 0.0186$$

$$t_s = \frac{2.65 \times 10^6}{29 \times 10^6} \times 0.3 = 0.0274$$

$$t_s = \frac{2.65 \times 10^6}{29 \times 10^6} \times 0.5 = 0.0456$$

Glass:

$$t_s = \frac{1.5 \times 10^6}{29 \times 10^6} \times 0.25 = 0.0129$$

Carbon Cloth:

$$t_s = \frac{2.65 \times 10^6}{29 \times 10^6} \times 0.4 = 0.0365$$

$$t_s = \frac{2.65 \times 10^6}{29 \times 10^6} \times 0.45 = 0.0411$$

$$t_s = \frac{2.7 \times 10^6}{29 \times 10^6} \times 0.5 = 0.0465$$

$$t_s = \frac{0.3 \times 10^6}{29 \times 10^6} \times 0.65 = 0.0067$$

Total	0.2482 in.
Steel =	1.5000
Total =	1.7482 in.

Equivalent Steel Loads

P = 760 - 20 = 740 psi

$$\sigma_2 = \frac{P \times R}{\cos 15 \text{ deg}} = \frac{740 \times 24.8}{\cos 15 \text{ deg}} = 19{,}000 \text{ lb/in.} \quad \text{use } 14{,}000 \text{ lb/in.}$$

$$\sigma_1 = \frac{P\,(R^2 - R_t^2)}{2\,R \cos 15 \text{ deg}} = \frac{740\,(27.5^2 - 10.65^2)}{2 \times 24.8 \cos 15 \text{ deg}} = 9{,}930 \text{ lb/in.}$$

2. LITERATURE SURVEY

Orthotropic material properties were obtained from a literature search of 15,000 industry documents and published Material Suppliers Data. Applicable material properties were plotted versus temperature. The properties inputed into the computer program include coefficients of thermal expansion, Young's Modulus, Poisson's Ratio, compressive, tensile and shear strength. The individual material sources are as indicated.

A <u>Graphite 90</u>: The extruded graphite ring properties were obtained from the following sources (Figures 126 thru 129).

1. "Final Development Laboratory Report on Elevated Temperature Testing of Graphite for Reliability Improvement Program," Thiokol Chemical Corporation, Wasatch Division, Report WGT-132, 16 Dec 1964, R. E. Corder.
2. "Some Parameters of the Mechanical Behavior of Graphites," Southern Research Institute, F. J. Digesu, C. D. Pears, paper presented to American Ceramic Society Meeting, Los Angeles, California, November 1963.
3. Carborundum Company, Graphite Products Division, Engineering Material Data Book.

B <u>2% Thoria-Tungsten</u>: The forged tungsten ring properties were obtained from the following sources (Figures 130 thru 135):

1. General Electric Company, Engineering Material Data Book.
2. "The Engineering Properties of Tungsten and Tungsten Alloys," DMIC Report 191, 27 Sep 1963, Battelle Memorial Institute.

3. Lockheed Aircraft Corporation, Missiles and Space Division Report 2-36-61-1, Section 8 - Tungsten.

4. "High Temperature Tensile Tests of Tungsten Nozzle Insert Forgings." Thermatest Laboratories Inc, 13 June 1962, b. L. Joseph, R. L. Zaitz.

5. Tensile Properties of Commercially Pure Tungsten Sheet, H. S. Parichanium, H. Leggett, C. L. Harmsworth, SAE Paper 520A, April 1962.

6. Data obtained from Walter K. Brinn, General Electric Company, Cleveland, Ohio.

7. Tensile Properties of Molybdenum and Tungsten from 2,500 to 3,700°F, R. W. Hall, P. F. Sikora, NASA-Lewis Research Center, February 1959.

8. Shear Strength, Fansteel Tungsten Manufacturing Data.

9. "Refractory Metals and Alloys," Metallurgical Society Conferences, Detroit, Michigan, May 1960, Interscience Publishers.

10. "Report on the Mechanical and Thermal Properties of Tungsten and TZM Sheet Produced in the Refractory Metal Sheet Rolling Program." Part I, Southern Research Institute, Birmingham, Alabama, August 1966, AD-638-631, Bureau of Naval Weapons.

11. "Development of Dispersion Strengthened Tungsten Base Alloys," AFML-TR-65-407, Part II, November 1966, Westinghouse Lamp Division, H. G. Sell, W. R. Morcom, G. W. King.

The development of the t = 5.0 and 25.0 sec 2% thoria tungsten modulus curve requires special mention. An elastic modulus curve (E) vs temperature is shown in Figure 130 with the stress-strain curves vs temperature in Figure 131.

The throat tungsten is divided into 6 columns and 6 rows for the common element stress grid. At 5 sec a one-dimensional thermal mechanical stress is run between columns 14 and 15 and rows 1 thru 6 in the tungsten and to row 25 in the carbon cloth (see sketch). The element J (14 and 15), I (1 and 2) is overstressed to -66,685 psi, 0.0014 in./in. strain at 1,573°F with the elastic curve. From the physical appearance of the survived orifice 1 and ejected orifices 2 and 3, it is apparent that the tungsten does not fail only the surrounding material. The material in the first element has gone plastic and requires a suitable adjustment to the elastic curve. The subsequent stress used for a 0.0014 in /in. strain at 1,573°F from Figure 131 is 17,500 psi as shown in Figure 130. Other similar adjustments are made at 2,000 and 3,000°F for the same strain of 0.0014 in./inch. The revised 5.0 sec tungsten modulus curve is used for the t = 5.0 sec two-dimensional finite element analysis.

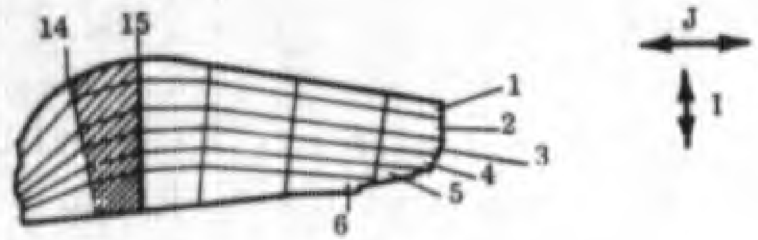

At t = 25.0 sec all I rows 1 thru 6 are overheated (3,728 to 5,498°F) and the one-dimensional (radial) stresses are calculated for column J (14 and 15) and column I rows 1-6-25 using three different tungsten modulus curves, A , B , and C . The stress vs modulus curve is plotted for the six overheated throat elements using three modulus curves (Figure 133). Each of the six element curves (1 thru 6) has three points of E vs σ corresponding to the three modulus allowable curves at temperatures. Knowing the temperature of each element and the maximum allowable plastic stress (Figure 131). At that temperature, the maximum allowable strain is read off the curve. The modulus is calculated $\left(\epsilon = \frac{\sigma_R}{\text{strain}} \quad \frac{\text{psi}}{\text{in./in.}}\right)$. A new modulus at each element and temperature level is calculated and plotted (x) on the element line (Figure 133) and connected. The final modulus valve and temperature at each element is transposed to Figures 132 and 130 for the final t = 25 sec curve allowable.

C 20% Copper-Tungsten: The pressed and sintered copper-infiltrated tungsten ring properties were obtained from the following sources (Figures 130, 134, and 135).

1. Teledyne Corporation, Wah Chang Albany Division: Infiltrated Tungsten, Engineering Material Data Book, January 1968.
2. Atlantic Research Corp: Study of Tungsten Rocket Nozzles, E. L. Olcott, June 1965, No Number-4356(00) (x)-5252, U.S. Naval Research Laboratory.
3. Teledyne Corporation, Wah Chang Albany Division: Infiltrated Tungsten, Engineering Material Data Book, January 1967.

The coefficient of thermal expansion, Poisson's Ratio are assumed the same as thoriated tungsten. For the modulus at elevated temperatures, the thoriated tungsten is ratioed down to copper infiltrated tungsten by a factor of 27/57-moduli numbers. The shear strength is assumed to be 0.60 (ultimate tensile strength 80,000) = 48,000 psi.

D Pyrolytic Graphite: The vapor deposited plate properties were obtained from the following sources (Figures 136 thru 139).

1. Raytheon: Pyrolytic Graphite - an Initial Assessment, C. A. Klein, July 1962, Report R-63.
2. Southern Research Institute: Some Parameters of the Thermal Conductivity of Pyrolytic Graphite, C. D. Pears, J. G. Allen, presented at Thermal Conductivity Conference, October 1964.
3. Jet Propulsion Lab.: Tensile Properties of Pyrolytic Graphite to 5,000°F, W. V. Kotlensky, H. E. Martens, Report 32-71, March 1961.
4. Raytheon: Summary Report on Pyrolytic Graphite, Report S-527, March 1963, Contract NOw-60-0409-C (FBM), CONFIDENTIAL.

5. Lockheed Aircraft Corporation: Pyrolytic Graphite - Its High Temperature Properties, Sunnyvale, W. Bradshaw, J. R. Armstrong, March 1963, ASD-TDR-63-195.
6. General Electric Missile and Space Division: Mechanical Properties of Pyrolytic Graphite, J. J. Gebhardt, J. M. Berry, R64SD26, April 1964.
7. Super-Temp Corporation: Engineering Material Data Book, October 1964.
8. Union Carbide Corporation, High Temperature Materials Division: Engineering Material Data Book, February 1962.
9. General Electric Corporation: Metallurgical Products, Engineering Material Data Book, July 1963.
10. Space Age Materials Corp, Pyrogenics Division: Engineering Material Data Book, September 1964.

E PTB-Graphitized Graphite Fiber Phenolic: The molded and regraphitized billet properties were obtained from the following sources (Figures 140 thru 142).

1. Thiokol Chemical Corporation, Wasatch Division: Memorandum "Physical Properties as Required by STW4-359A," Report No. F-66-200, September 1966, Union Carbide Corporation, Quality Control Test Data.
2. Research and Development on Advanced Graphite Materials, Vol 25, Physical Properties of Some Newly Developed Graphites WADD-TR-61-72, June 1963.
3. Thiokol Chemical Corporation, Wasatch Division: Development Laboratories - PTB Test Data - Compressive Tensile and Density at Room Temperature - Compressive Tensile at 3,500°F, July 1968.

The material mechanical properties vs temperature curve used to determine the overstressed PTB elements was Figure 141. Thiokol Wasatch test values at room and 3,500°F temperatures provide a revised material property curve showing good agreement at elevated temperatures but poor agreement at the lower temperature levels (Figure 142) Thus, additional PTB elements at the lower temperatures would show failure if the revised PTB material curves had been used.

F Carbon Cloth Phenolic: The tape wrapped and cured ring properties were obtained from the following sources (Figures 143-thru 145).

1. Aerojet-General Corporation: Evaluation of Low Cost Materials and Manufacturing Processes for Large Solid Rocket Nozzles, J. J. Warga, H. O. Davis, J. D. Eacetis, J. A. Lampman, AFRPL-TR-67-310, December 1967.
2. Aerospace Corp: New Technique for Mechanical Strength Testing of Rapidly Charred Ablation Materials, W. E. Welsh, Jr. and A. Ching, AIAA, October 1967.
3. The Boeing Company Aerospace Group: Thermal Properties of Ablative Chars, AF 33(615)-3804, December 1966.
4. Southern Research Institute: The Thermal and Mechanical Properties of Fine Ablative Reinforced Plastics from Room Temperature to 750°F, C. D. Pears, W. T. Engelke, J. Thornburgh, AFML-TR-65-133, April 1965.
5. HITCO - U.S. Polymeric Division: Engineering Material Data Book, 1967.
6. Fiberite: Engineering Material Data Book, 1967.

G Glass Cloth Phenolic: The laid-up and cured cone insulation properties were obtained from the following sources (Figures 146-and 147).

1. Plastics for Flight Vehicles, Part I Reinforced Plastics, MIL-HDBK-17, November 1959, Department of Defense.
2. HITCO, U. S. Polymeric Division: Engineering Material Data Book, 1967.
3. Fiberite: Engineering Material Data Book, 1967.

H 4130 Steel: The forged and welded plate assembly cone properties were obtained from the following source (Figures 148 and 149).

1. Metallic Materials and Elements for Aerospace Vehicle Structures, Department of Defense, MIL-HDBK-5A, February 1966.

I Neoprene Rubber: The cured sheet spacers properties were obtained from the following source (Figure 150).

1. Thiokol Chemical Corporation, Wasatch Division: Engineering Material Data Book, 1967.

J Epon 913-934: The cured adhesive bond properties were obtained from the following source (Figure 151).

1. Shell Chemical Corp: Engineering Material Data Book, 1967.

3. DISCUSSION

The finite element computer program uses the common element grid 12 elements long (25 nodal points) and 15 elements wide (16 nodal points).

The output includes: the radial, axial, and hoop stress at the midpoint of each element, the shear stress in planes parallel to the faces of the elements, the maximum and minimum principal stresses and all strains corresponding to the listed stresses. The displacements in the radial and axial directions are at the nodal points.

A negative sign by the radial, axial, and hoop stresses indicates a compressive stress. A negative shear stress indicates a shear as shown in the sketch below with the positive shear in the opposite direction along the element edges.

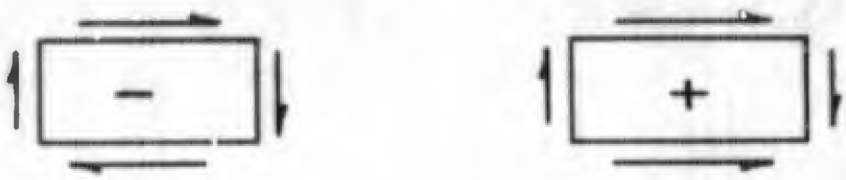

A minus sign by the displacement indicates movement inward for the radial and to the left for the axial.

For boundary condition A, axial fixed, radial free and loaded with nozzle uniform load, the element stresses and displacements are shown inside each element box. For t = 5.0 sec the four stresses and two displacements are shown in Figures 152 thru 157. The overstressed elements for each type of stress (radial, axial, hoop, shear) are shown inside the boxed areas. The allowable stress is obtained by determining the element temperature from the preliminary thermal gradient curves for t = 5.0 sec Figure 103 and then from the orifice material strength curves vs temperature, Figures 127 thru 129 Graph-I-tite G, Figures 134 and 135 tungsten, pyrolytic graphite Figures 138 and 139 PTB Figure 141, carbon cloth phenolic, Figure 145, glasscloth Figure 147, 4130 Figure 149 the allowable material stress is read off the curve. The overstressed element condition exists when the actual element stress is higher than the allowable element stress at the element temperature.

For t = 25.0 sec the four stresses and two displacements are displayed in Figures 158 thru 163 with the overstressed elements included in boxes. The elements temperature levels are shown in the final downstream thermal gradients for t = 25.0 sec (Figure 112).

At t = 25.1 sec closed the four stresses and two displacements are shown in Figures 164 thru 169 with the overstressed elements included in boxes. The elements temperature is shown in the final downstream thermal gradient at t = 25.1 sec, (Figure 113) the orifice material strength allowables are determined from the same figures as used for the t = 5.0 sec condition.

For boundary condition B, axial and radial edge fixed, no nozzle uniform load, the orifice material elements are evaluated at t = 5.0 and 25.1 second. The purpose of the different boundary condition is determined by the sensitivity of orifice material stresses to the boundary conditions. A summary of the applicable element figures for t = 5.0 and 25.1 sec conditions is listed below.

Condition B	Element Stresses and Displacements Overstressed Elements	Downstream Plane Element Temperature Profile	Downstream Plane Element Material Allowable Stress Curve
t = 5.0 sec	Figures 170 thru 175	Figure 103	Figures 127, 128, 129, 134, 135, 138, 139, 141, 145, 147, 149
t = 25.1 sec	Figures 176 thru 181	Figure 113	Figures (same as above)

A summary of the overstressed elements at each time interval t = 5.0, 25.0 and 25.1 sec by the four stresses with the boundary condition A is shown in Figures 182 thru 184. Those elements that are overstressed by all four stresses are enclosed in blocked areas. Neglecting the tungsten throat ring elements, where the material mechanical properties were adjusted to try to keep the actual stress equal to the allowable plastic stresses at a known strain level, the largest overstressed area exists within the PTB and pyrolytic graphite material. The PTB and pyrolytic overstressed area spreads even with elements dropped due to erosion, as the static firing time (open or closed) increases.

The overstressed element summary for boundary condition B at time intervals of t = 5.0 and 25.1 sec is shown in Figures 185 and 186. Again neglecting the tungsten ring the overstressed area is the largest in the PTB and pyrolytic graphite and increases in area with motor time. A comparison of the boundary condition A and B overstressed areas indicates a definite similarity between the two load conditions. Boundary condition on visual inspection is the more severe of the two conditions.

To summarize the percent of elements overstressed or eroded at each of the three times (t = 5, 25, 25.1) for boundary condition A for all the orifice and support materials, Ref Tables XIX thru XXIV.

Each element has four different types of stress: radial, axial, hoop and shear at three different times, 5, 25, 25.1 second. If any one stress is higher than the allowable, then on a preliminary examination basis it is considered a failed element. Thus the number of failed elements in each orifice material are taken from Tables XIX thru XXIV and listed below:

	Failed or Eroded Elements			Total	Percent of Overstressed and Failed Elements		
Material	5 sec Closed	25 sec Open	25.1 sec Closed	Material Elements	5 Sec	25 Sec	25.1 Sec
2% Thoria Tungsten	6	35	36	36	17	97	100
Graphite 90	4	2	6	32	13	6	19
20% Cu Tungsten	-	-	1	8	-	-	13
Pyrolytic Graphite	4	19	18	20	20	95	90
PTB	24	79	80	86	28	92	93

Since the tungsten throat is the last item to be ejected, is in excellent shape when recovered after being ejected, and the mechanical properties were adjusted during the orifice analysis to try to show an unfailed plastic stress condition, the next most questionable materials are the PTB and pyrolytic graphite orifice exit cones with 92 percent and 95 percent overstressed and failed elements at 25.0 second.

TABLE XIX

DOWNSTREAM ORIFICE THROAT - 2 PERCENT THORIA TUNGSTEN
(Percent of Overstressed and Eroded Elements)

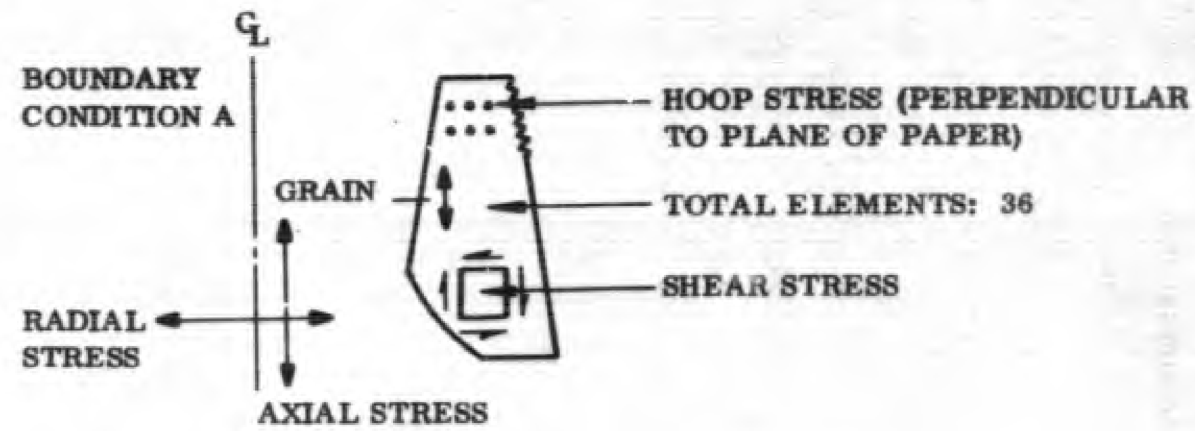

	t = 5.0 Sec (Closed)				t = 25.0 Sec (Open)				t = 25.1 Sec (Closed)			
Stress Type	Element Erosion	Over-stressed Elements	Total Lost Elements	Per-cent Total	Element Erosion	Over-stressed Elements	Total Lost Elements	Per-cent Total	Element Erosion	Over-stressed Elements	Total Lost Elements	Per-cent Total
Axial	--	3	3	8	--	--	--	--	--	--	--	--
Radial	--	--	--	--	--	--	--	--	--	--	--	--
Hoop	--	6	6	17	--	35	35	97	--	36	36	100
Shear	--	2	2	6	--	--	--	--	--	--	--	--
All Stresses	--	6	6	17	--	35	35	97	--	36	36	100

TABLE XX

DOWNSTREAM ORIFICE INLET - GRAPHITE 90
(Percent of Overstressed and Eroded Elements)

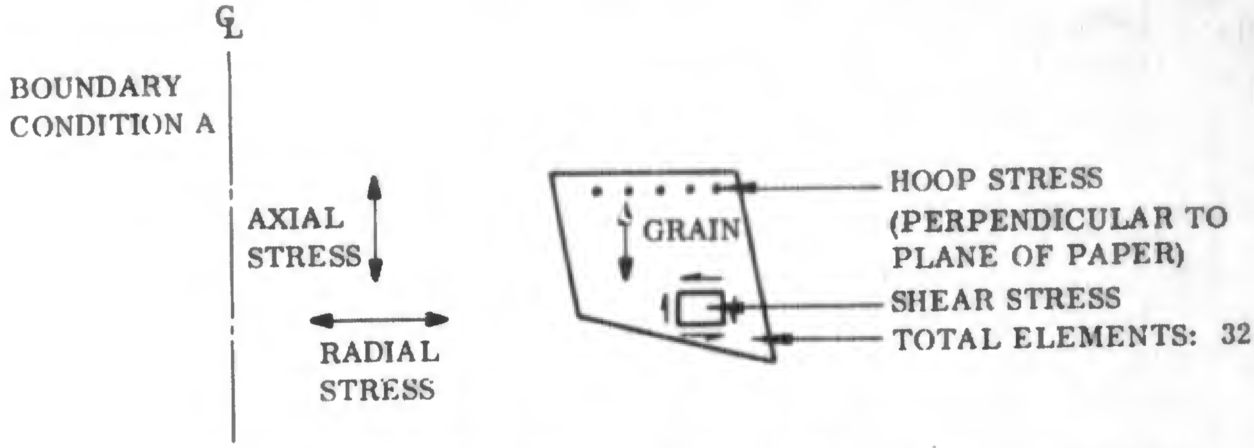

Stress Type	t = 5.0 Sec (Closed) Over-stressed Elements	t = 5.0 Sec (Closed) Percent Total	t = 25.0 Sec (Open) Over-stressed Elements	t = 25.0 Sec (Open) Percent Total	t = 25.1 Sec (Closed) Over-stressed Elements	t = 25.1 Sec (Closed) Percent Total
Axial	--	--	--	--	--	--
Radial	4	13	2	6	4	13
Hoop	--	--	--	--	2	6
Shear	--	--	--	--	--	--
All Stresses	4	13	2	6	6	19

TABLE XXI

DOWNSTREAM ORIFICE RETENTION NUT - 20 PERCENT COPPER - TUNGSTEN
(Percent of Overstressed and Eroded Elements)

BOUNDARY
CONDITION A

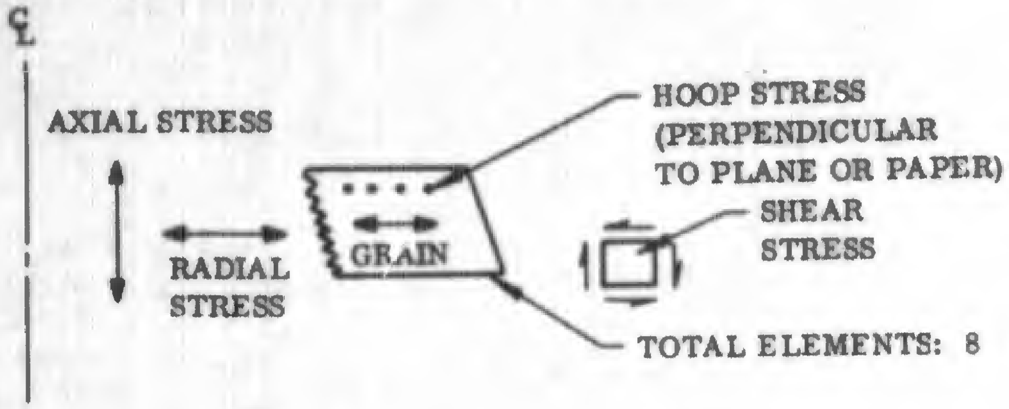

	t = 5.0 Sec (Closed)		t = 25.0 Sec (Open)		t = 25.1 Sec (Closed)	
Stress Type	Over-stressed Elements	Percent Total	Over-stressed Elements	Percent Total	Over stressed Elements	Percent Total
Axial	--	--	--	--	--	--
Radial	--	--	--	--	--	--
Hoop	--	--	--	--	1	13
Shear	--	--	--	--	--	--
All Stresses	--	--	--	--	1	13

TABLE XXII

DOWNSTREAM ORIFICE FORWARD EXIT CONE - PYROLYTIC GRAPHITE
(Percent of Overstressed and Eroded Elements)

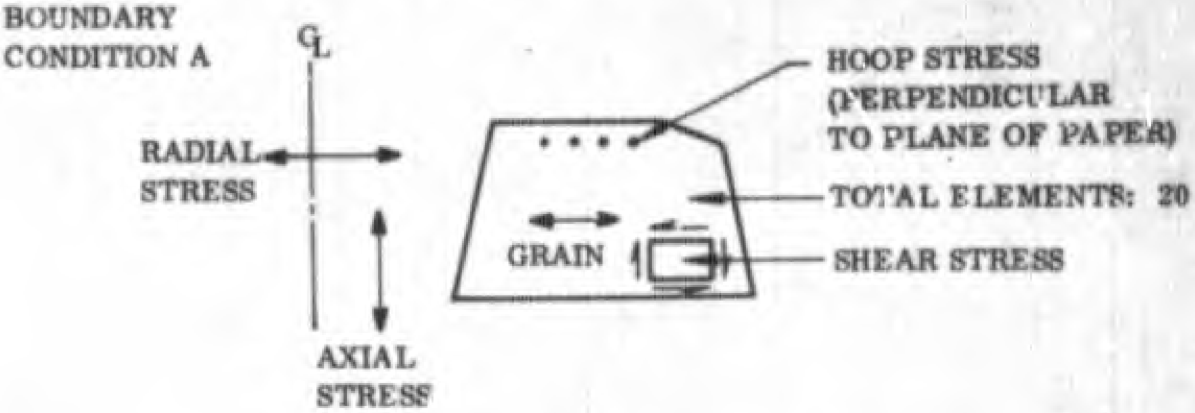

	t = 5.0 Sec (Closed)		t = 25.0 Sec (Open)		t = 25.1 Sec (Closed)	
Stress Type	Over-stressed Elements	Percent Total	Over-stressed Elements	Percent Total	Over-stressed Elements	Percent Total
Axial	3	15	3	15	3	15
Radial	1	5	8	40	4	20
Hoop	--	--	1	5	1	5
Shear	--	--	18	90	17	85
All Stresses	4	20	19	95	18	90

TABLE XXIII

DOWNSTREAM ORIFICE AFT EXIT CONE - PTB
(Percent of Overstressed and Eroded Elements)

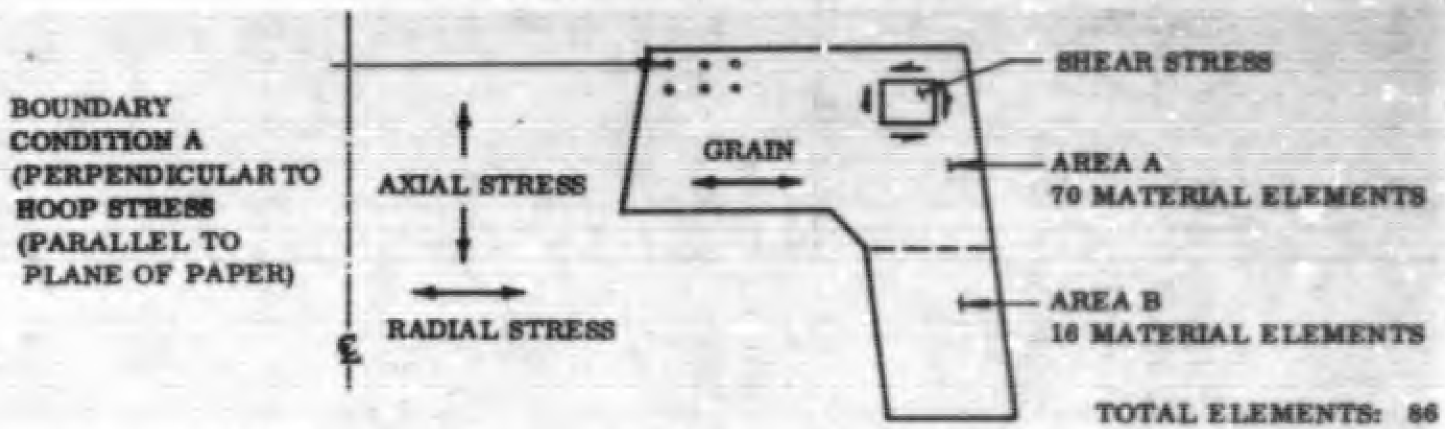

TOTAL ELEMENTS: 86

Stress Type	Location	t = 5.0 Sec (Closed) Elements Eroded	t = 5.0 Sec (Closed) Over-stressed Elements	t = 5.0 Sec (Closed) Total Lost Elements (Percent)	t = 25.0 Sec (Open) Elements Eroded	t = 25.0 Sec (Open) Over-stressed Elements	t = 25.0 Sec (Open) Total Lost Elements (Percent)	t = 25.1 Sec (Closed) Elements Eroded	t = 25.1 Sec (Closed) Over-stressed Elements	t = 25.1 Sec (Closed) Total Lost Elements (Percent)
Axial	A	0	6	9	24	25	70	36	22	83
	B	0	1	6	0	5	31	0	8	50
Radial	A	0	11	16	24	37	87	36	23	84
	B	0	0	—	0	6	38	0	5	31
Hoop	A	0	13	19	24	30	77	36	18	77
	B	0	0	—	0	0	—	0	1	6
Shear	A	0	12	17	24	35	84	36	25	87
	B	0	0	—	0	5	31	0	6	38
All Stresses	A	0	23	33	24	44	97	36	33	98
	B	0	1	6	0	11	69	0	11	69
	A + B	0	24	28	24	55	92	36	44	93

TABLE XXIV

OTHER ORIFICE AND SUPPORT MATERIALS
(Percent of Overstressed and Eroded Elements)

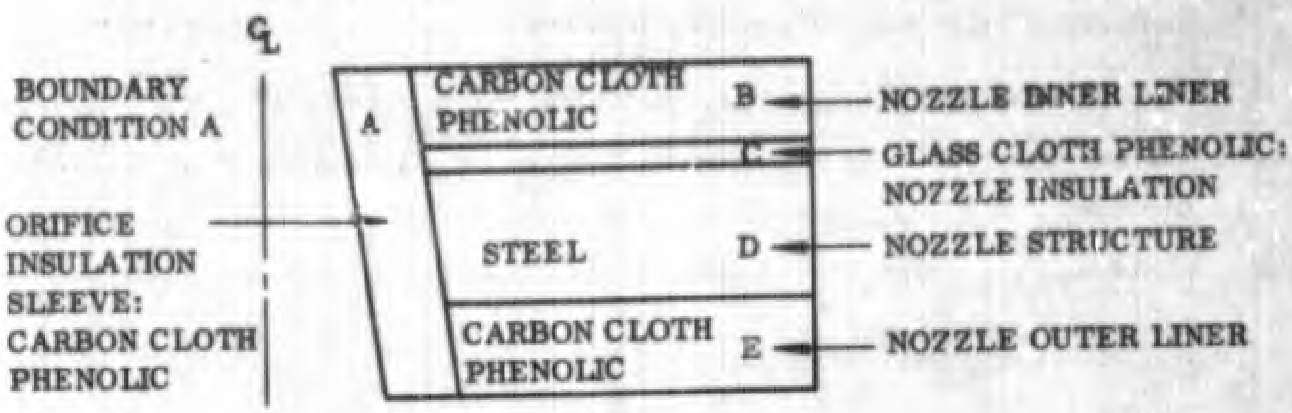

Stress Type	t = 5.0 Sec (Closed)	t = 25.0 Sec (Open)	t = 25.1 Sec (Closed)
Axial	None	None	None
Radial	None	None	None
Hoop	None	None	None
Shear	None	None	None

The movement of the orifice element edges or nodes points along the wall surfaces is taken from Figures 156, 157, 162, 163, 168, 169, at t = 5.0, 25.0 and 25.1 sec with boundary condition A and drawn on the orifice with a ten magnification. Figures 187 thru 189 shows the deflected and rotated orifice design without the carbon cloth insulation sleeve. The orifice is drawn with a 3/1 scale factor.

The orifice deflection and rotation is inward towards the nozzle centerline and rotates clockwise. The orifice analysis model for boundary condition A is a circular flat plate with a hole in the middle. The forces acting on the plate include pressure, pintle stall load, and nozzle uniform loads. The sketch below shows the plate, forces, support, deflection and rotation.

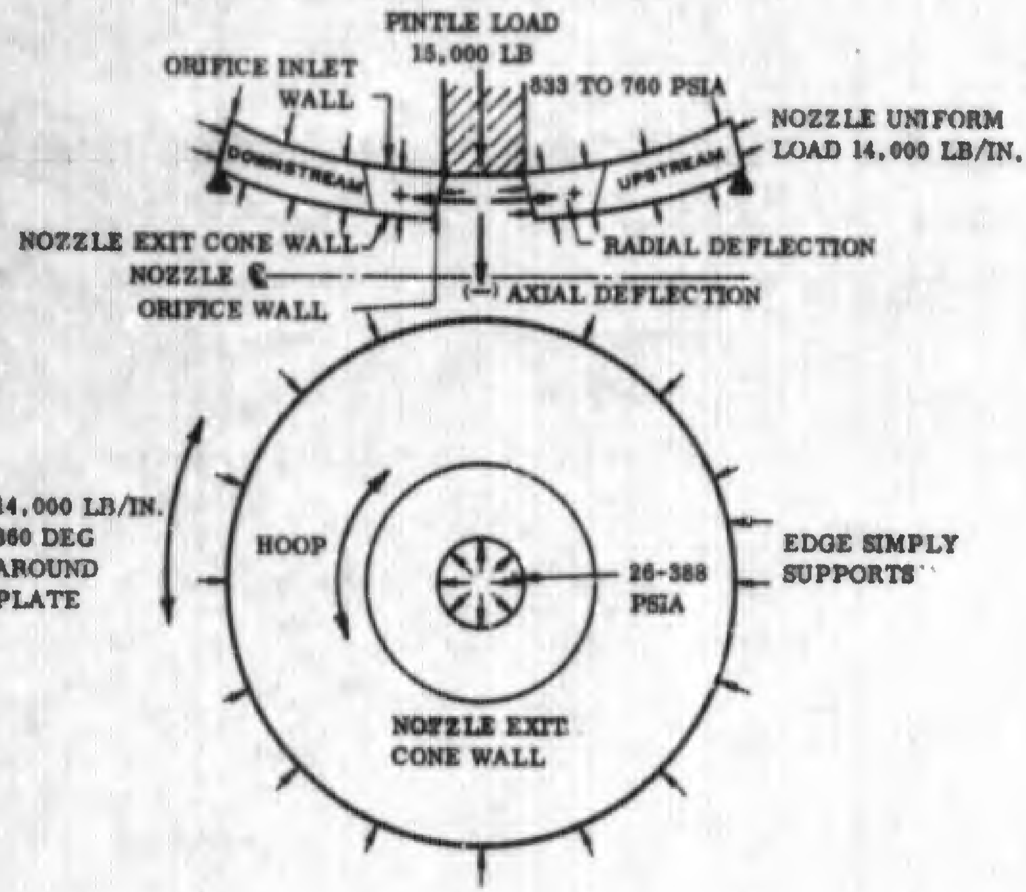

The tungsten throat ring during the 0 - 25.1 sec time interval is expanding axially and contracting radially. Axially the expansion at tungsten node point 16 is outward, overcoming the general orifice inward deflection. The tungsten orifice throat-valve pintle interface is forced outward and agrees with the valve feedback position transducer instrumentation. At tungsten node 9 the expansion is inward and follows the general orifice inward deflection. The tungsten throat is actually pushing the pyrolytic graphite inward as indicated by 8-9 node interface. The large overlap of points 8-9 is a limitation of the analytical model analysis. The rubber spacer burns out early in the test and the computer has no instructions to restrain the movements of 8 and 9 nodes to a common interface.

The PTB aft orifice exit cone is deflected inward towards the nozzle centerline by general orifice loading and tungsten, pyrolytic graphite ring expansion.

The five second orifice displacements and stresses would be larger if the final heat transfer coefficients had been used as shown on page 137. In addition at t = 5.0 and 25.1 sec the aerodynamic pressure inside the cavity is not truly represented by an average 20 psi internal pressure as shown in loading conditions (Ref Figures 123 and 125. The actual pressure distribution is represented by pressure profiles A and B (Ref Figures 59, 60, 83).

However a comparative picture of progressive material failure from t = 0 to t = 25.1 is presented in the following sketches. The real orifice design probably has more severe force and temperature environments than the analytical orifice model.

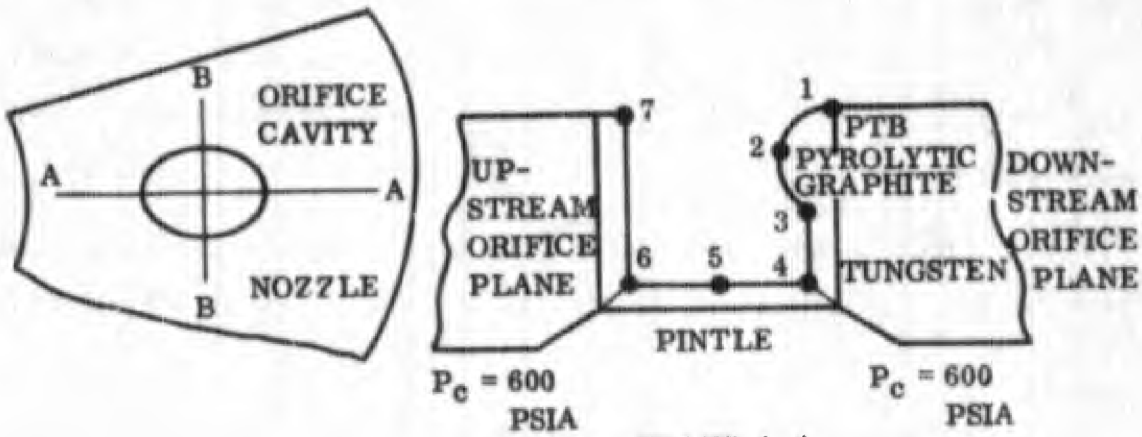

PLANE A-A

POINT	1	2	3	4	5	6	7
PRESSURE (PSIA)	26	330	26	27	27	27	27

POINT	1	2	3	4	5	6	7
PRESSURE (PSIA)	27	27	27	27	27	27	27

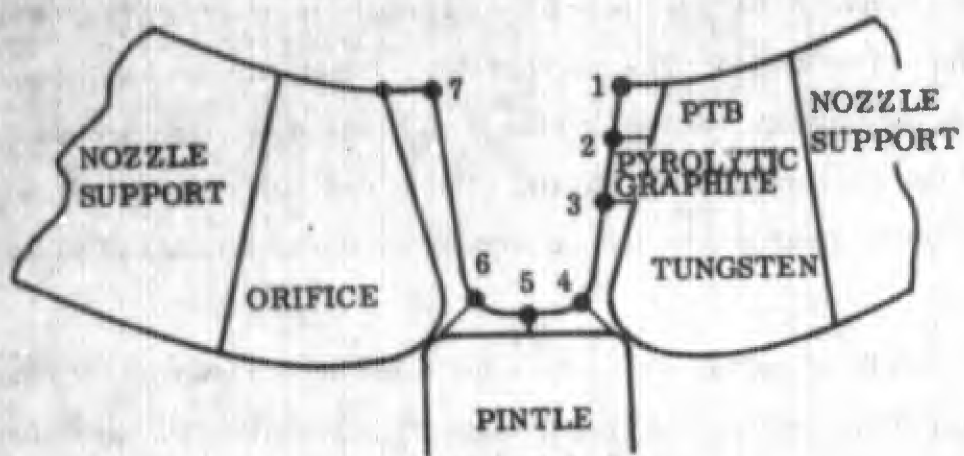

PLANE B-B

t = 0 SEC

The movement of the orifice element edges or node points along the orifice wall surfaces is taken from Figures 174, 175, 180, 181 at t = 5.0 and 25.1 sec with boundary condition B. The or fice is drawn at 3/1 scale and the deflections at 10/1 scale. Figures 190, 191 show the deflected and rotated orifice design without the carbon cloth insulation sleeve.

The orifice deflection and rotation is inwards towards the nozzle centerline and rotates clockwise similar to boundary condition A deflections and rotations, but smaller in actual numbers. The orifice analysis model for boundary condition B is also a circular flat plate with a hole in the middle but with a fixed, moment resistant, edge support. A sketch of the plate, forces, support, deflection and rotation is shown on the following page.

The fixed boundary condition B at the outer orifice, analysis model edge prevents the large deflections and rotations shown by the simple support boundary condition A.

The tungsten throat ring still expands axially while contracting radially. The expansion axially is outward at the orifice valve interface and inward at the pyrolytic graphite tungsten interface. The PTB and pyrolytic graphite again move inward as a result of plate deflection and tungsten thermal expansion.

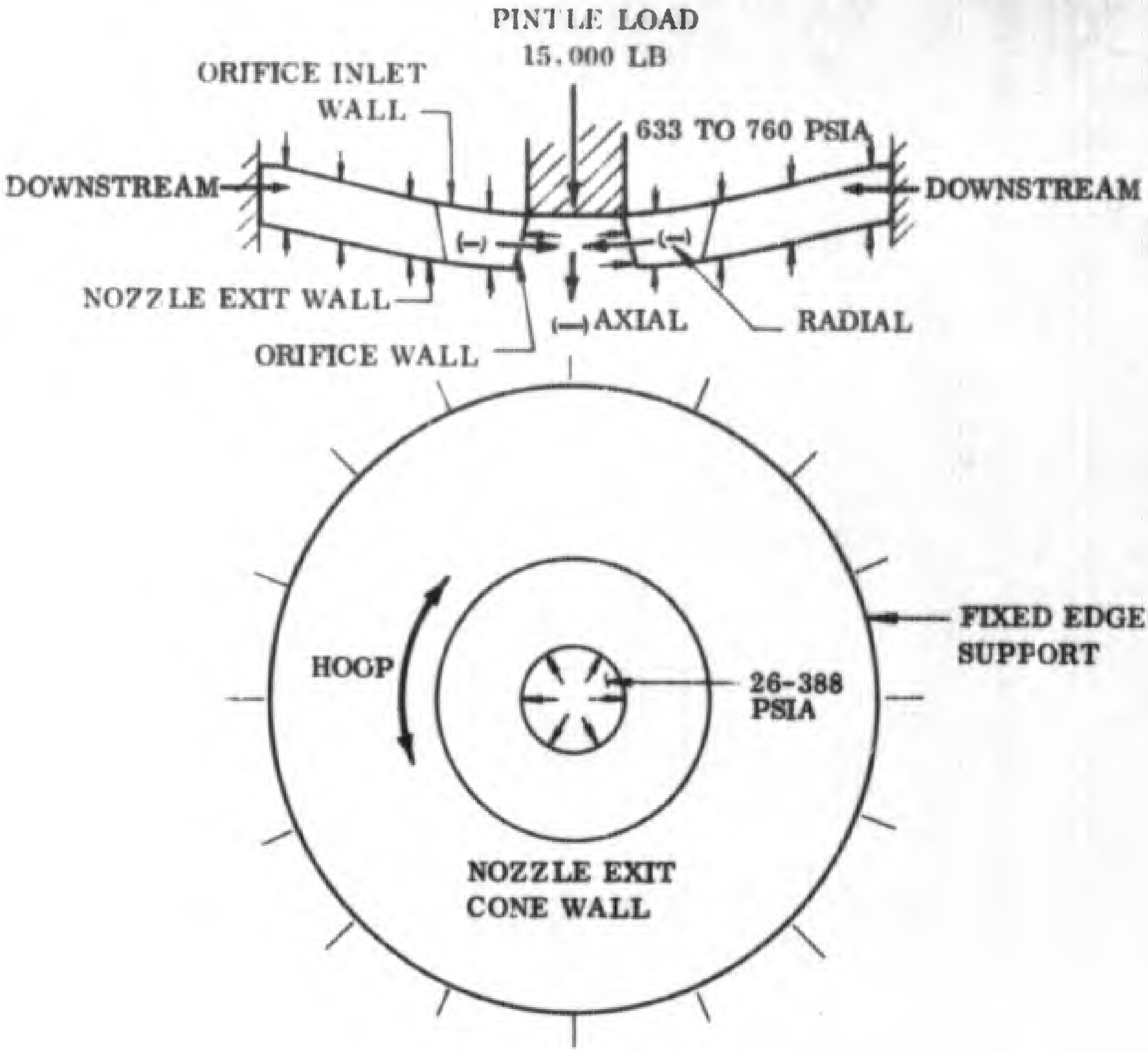

An effort is made to correlate the steel plate finite element stresses at the outer edge, for boundary conditions A and B and t = 5.0 sec when the material thermal gradients exert the smallest thermal stresses with the simple plate formula stresses from Formulas for Stress and Strain (Roark, McGraw Hill, 3rd Edition, 1954) as shown on the following page.

MAXIMUM STRESS AT OUTER PLATE SUPPORT *t = 5.0 sec

Boundary Condition	Radial Stress: Finite Element Analysis (psi)	Radial Stress: Circular Flat Plate Analysis (psi)	Hoop Stress: Finite Element Analysis (psi)	Hoop Stress: Circular Flat Plate Analysis (psi)
(A) Simple Support	-9196[1] Steel	-9350[5] Steel	-12,030[2] Steel	-12,100[5] Steel
(B) Fixed Support	-5,802[3] +1,679 Composite	-1,744[6] +1,744 Composite	-1,926[4] + 488 Composite	N/A[5] Composite

NOTES: [1]Ref Figure 152
[2]Ref Figure 154
[3]Ref Figure 170
[4]Ref Figure 172
[5]Flat plate analysis, parameters and load conditions

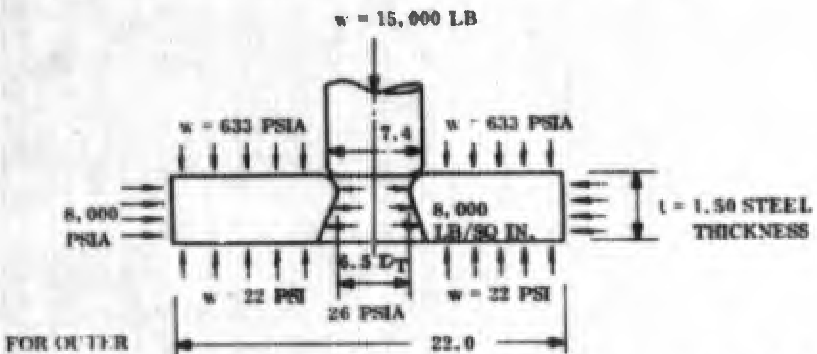

Radial and hoop stresses superimpose conditions 27, 28, Table XIX.
Condition 27 with 26 psi pressure has negligible effects on outer stresses.
The concentrated load and pressure load provide only shear stress at the simply supported OD surface.

[6]Flat plate analysis, parameters and load conditions

BOUNDARY CONDITION B

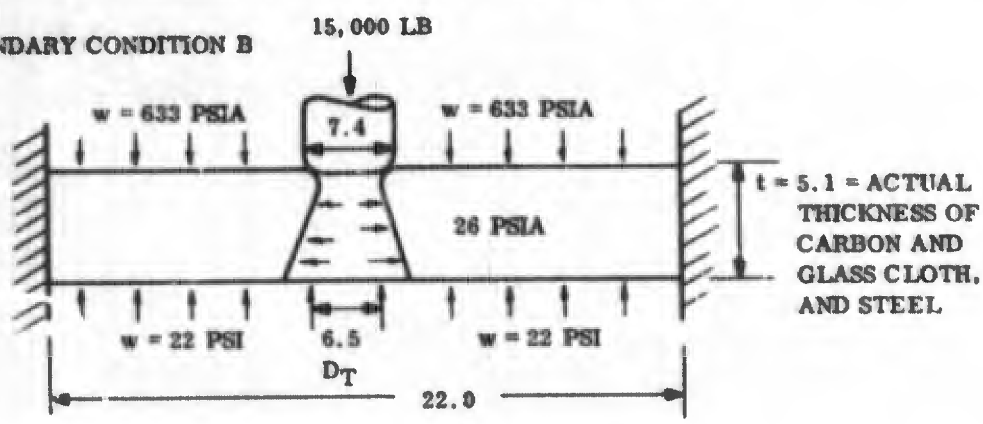

For outer edge radial and hoop stresses, superpose conditions 19, 20 Table XV, internal orifice cavity pressure effect on outside diameter stress is negligible, hoop stresses not available from handbook.

A comparison of the maximum stresses at the outer edge of the orifice analyses plate show excellent agreement for boundary condition A and fair agreement for boundary condition B. While this comparison does not confirm all the stresses in every material element it does show there is reasonable agreement between two different analysis methods at the outer boundary surface. Also in summary the actual boundary condition is somewhere between A and B conditions.

4. THROAT SUBASSEMBLY MOVEMENT

The valve pintle orifice throat interface movement during the TU-520.04 motor static test as reported by the valve position feedback transducer (Ref Figure 41) showed an outward position of + 0.25 in. at least + 0.15 in. more than thermal growth of the tungsten orifice throat valve pintle and the deflection of valve support would indicate. These maximum outward movements always occur after an open port duty cycle and is verified by Figure 43 , the subscale TU-521.02 orifice valve interface movement. The throat subassembly moves inward after the valve pintle stall load was applied, but never as low as the expected outward movement. The outward interface movement also seems to increase with motor static firing time.

The problem was approached from the standpoint of applied loads on the tungsten nut throat and graphite inlet at times t = 0.75 closed, 16.0 sec closed, 16.1 sec open, 25 sec open, 25.1 sec closed. The pressure and pintle loads and adhesive on the graphite outside diameter hold the throat subassembly in place with the nozzle uniform loads causing a wedge effect outward movement. A summary of all these loads is shown on the following pages.

Loads[1] (lb)	p = 633 psi t = 5.0 (sec/lb)	p = 712 psi t = 16.0 (sec/lb)	p = 712 psi t = 16.1 (sec/lb	p = 760 psi t = 25.0 (sec/lb)	p = 760 psi t = 25.1 (sec/lb)
. Inlet pressure[3]	- 42,500	-47,700	-41,200	+43,900	-51,000
. Pi[illegible] stall	- 15,000	-15,000	--	--	-15,000
. Adhesive allowable[2]	-153,000	-44,000	-44,000	--	--
. Nozzle wedge	+ 68,700	+77,500	+77,500	+82,500	+82,500
TOTAL	-141,800	-29,200	- 7,700	+38,600	+16,500

-Load is inward
+Load is outward

NOTES: [1]Thermal mechanical stress from inside orifice wall to outside wall also causes an outward movement by a wedge effect (9° ramp angle) which we are neglecting.

[2]The adhesive allowable is reduced by the temperature in the bond line. (Ref final thermal gradients, Figures 108 thru 113 and Epon 913 adhesive strength vs temperature Figure 151.)

[3]The inlet frontal pressure load is as shown:

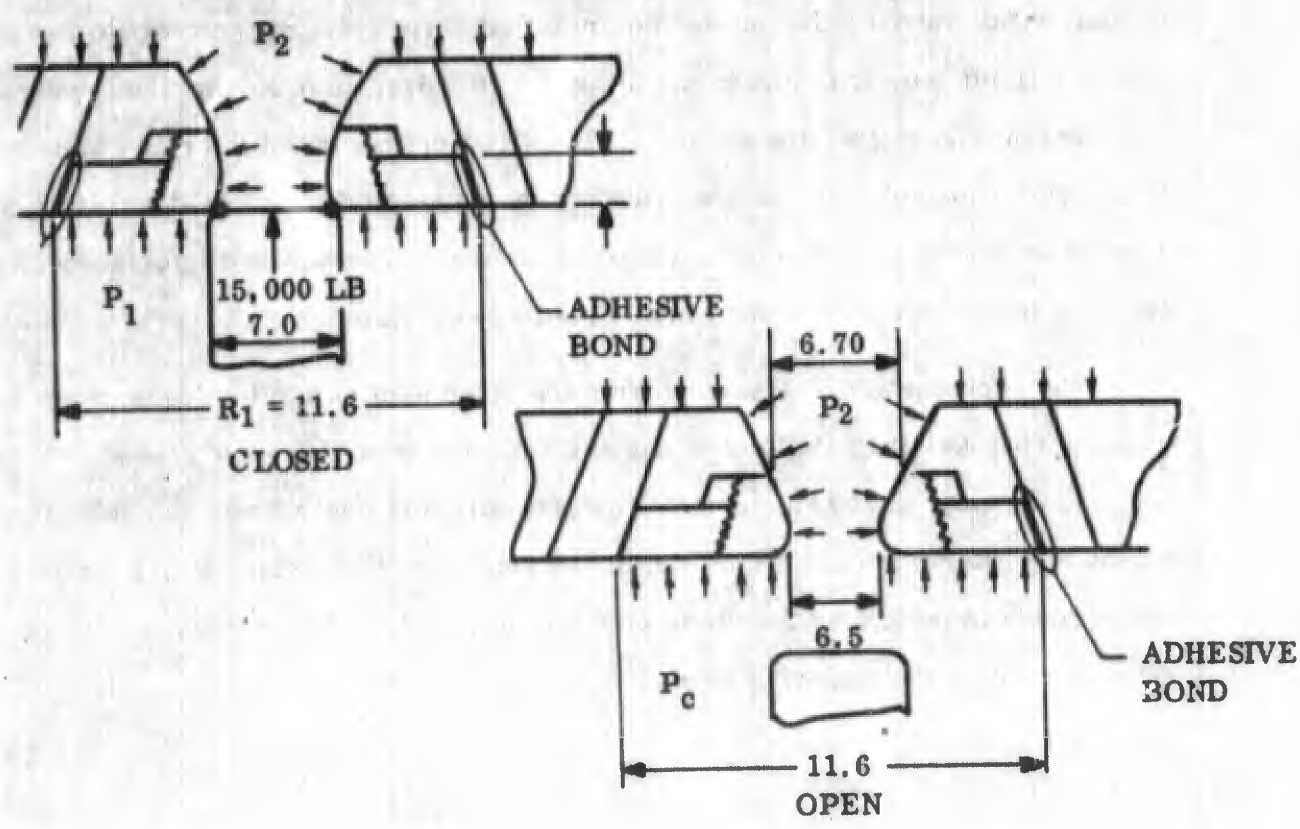

[4]The nozzle wedge effect loads are determined as illustrated.

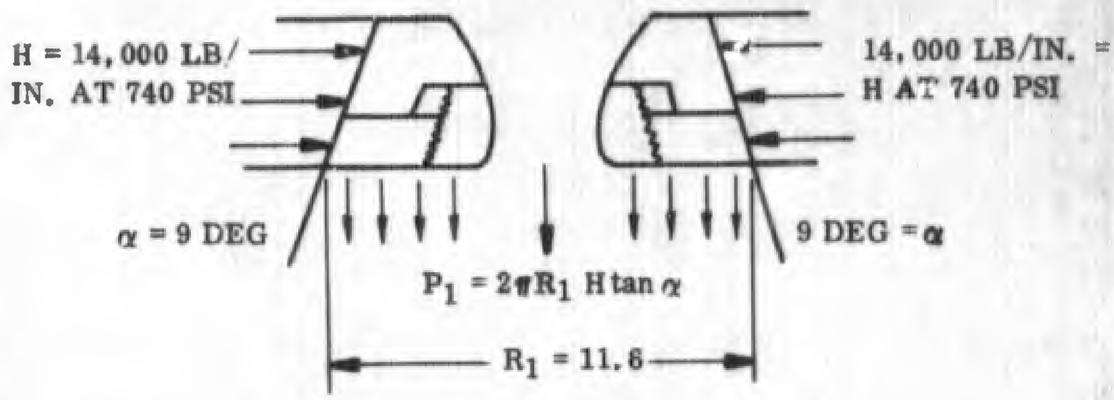

While the loads are only representative of the actual loads it does show a trend of loads that cause the throat assembly to be forced outward towards the valve pintle face. The condition is caused by the loss of the bond adhesive strength after 16.1 second. Notice that when the orifice closes at 25.1 sec the valve pintle load decreases the throat subassembly outward load but does not eliminate it. Thus the loads tend to support the actual interface movement as reported by the pintle valve transducer position feedback instrumentation. The outward interface reading is large at the end of duty cycle open and decreases with re-application of the pintle valve stall load but not enough to restore to the expected interface position of + 0.10 inch.

In a redesign effect some permanent connection of the throat subassembly to the insulation sleeve should be investigated to insure the stability of the throat.

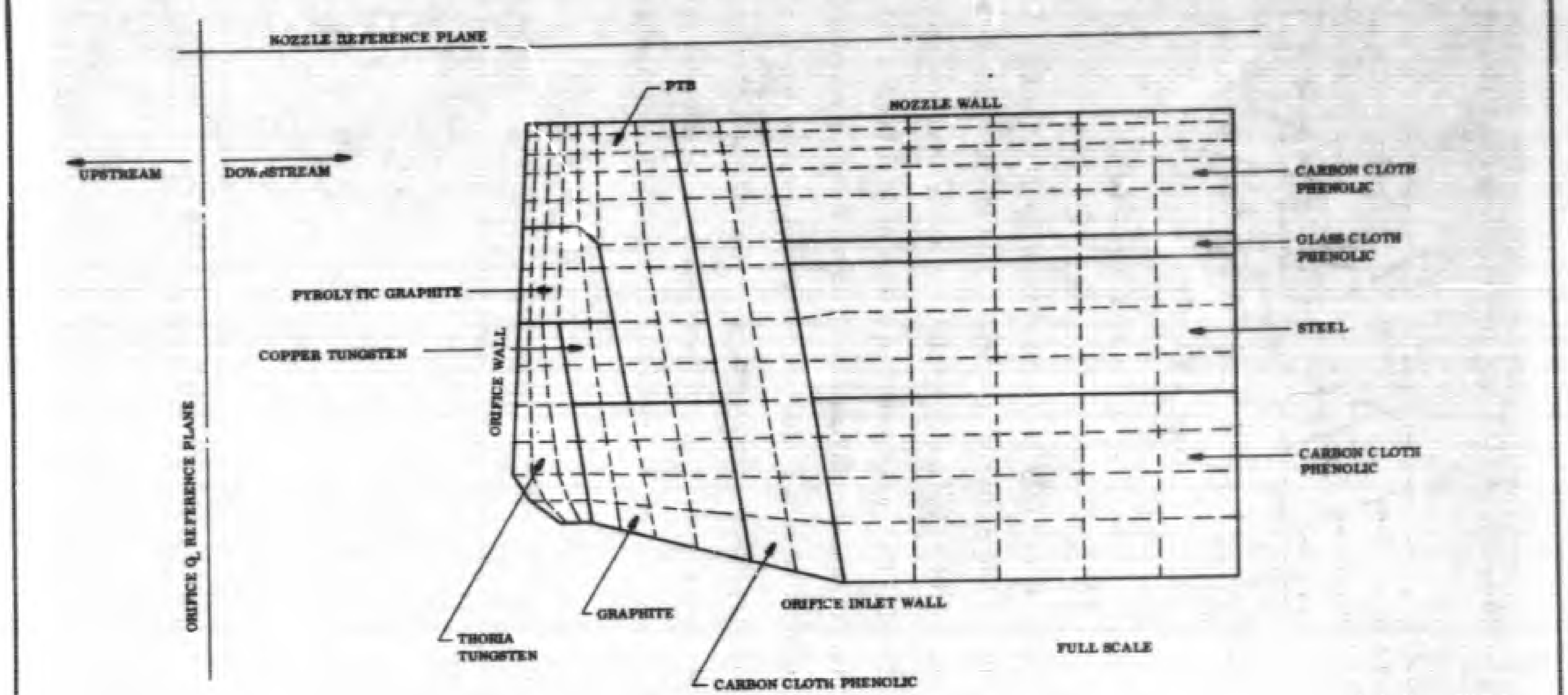

Figure 54. Orifice 3 Common Element Grid

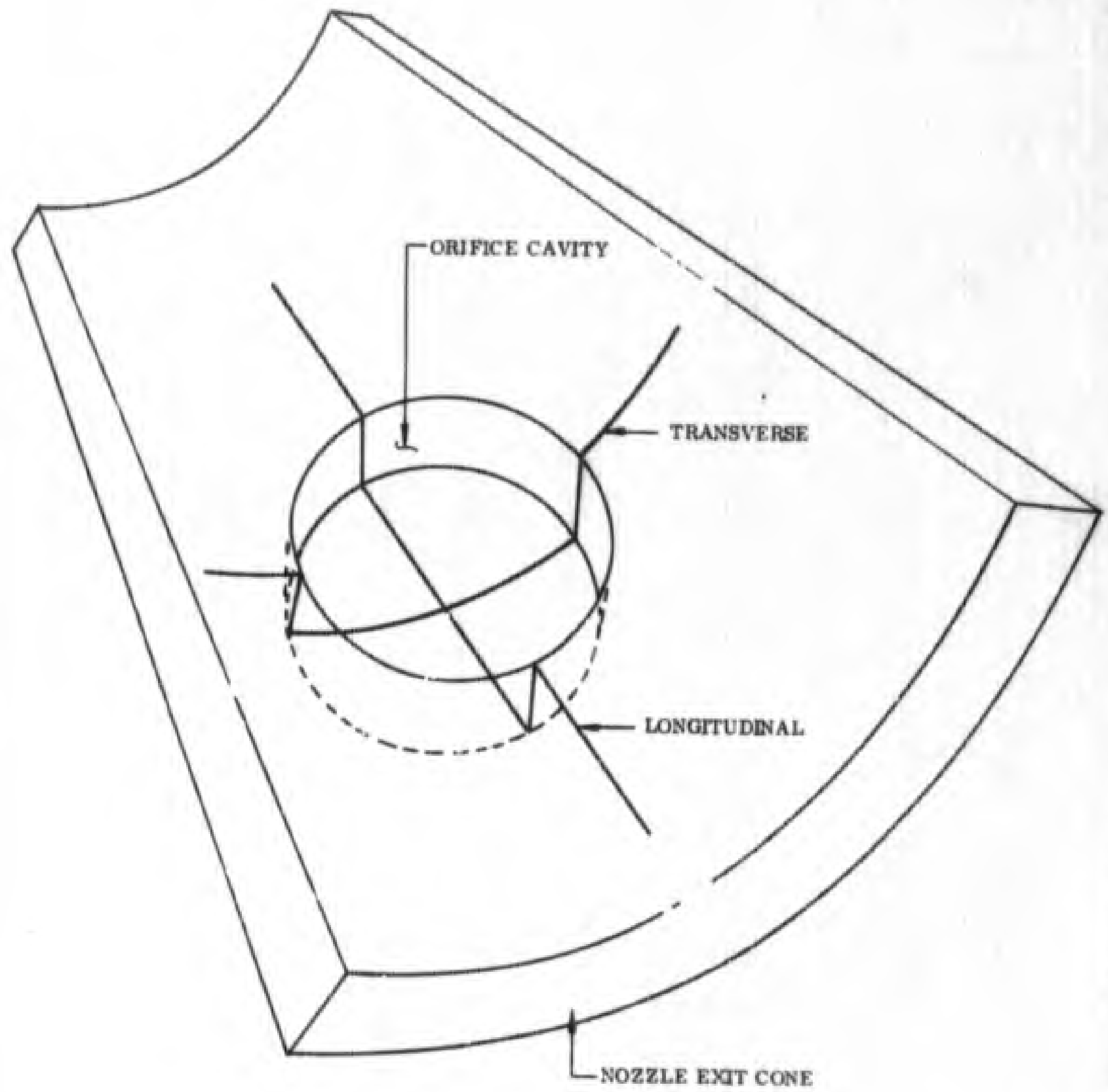

Figure 55. Plane of Gas Flow Conditions for Thermal Analysis

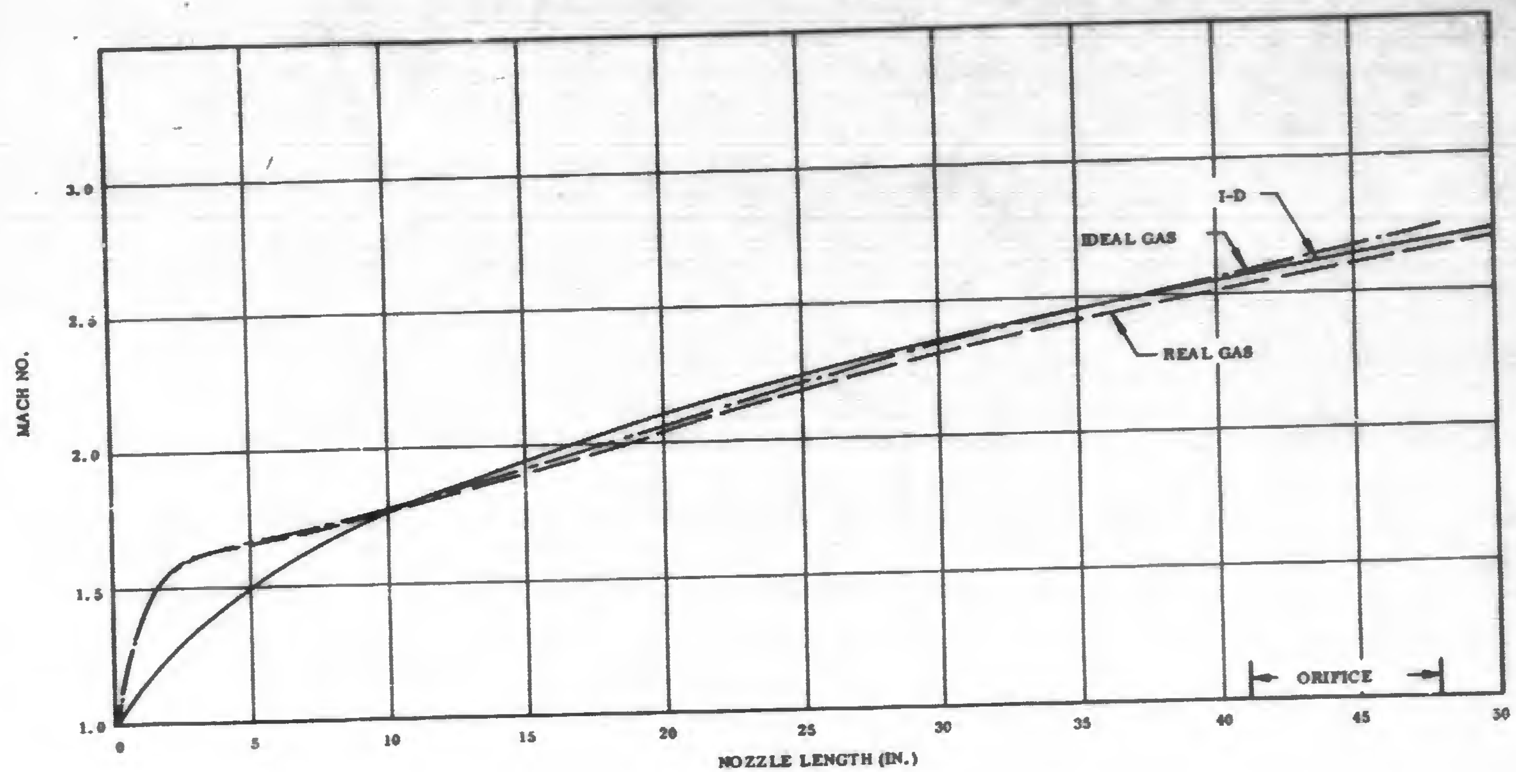

Figure 56. Nozzle Wall Mach Number

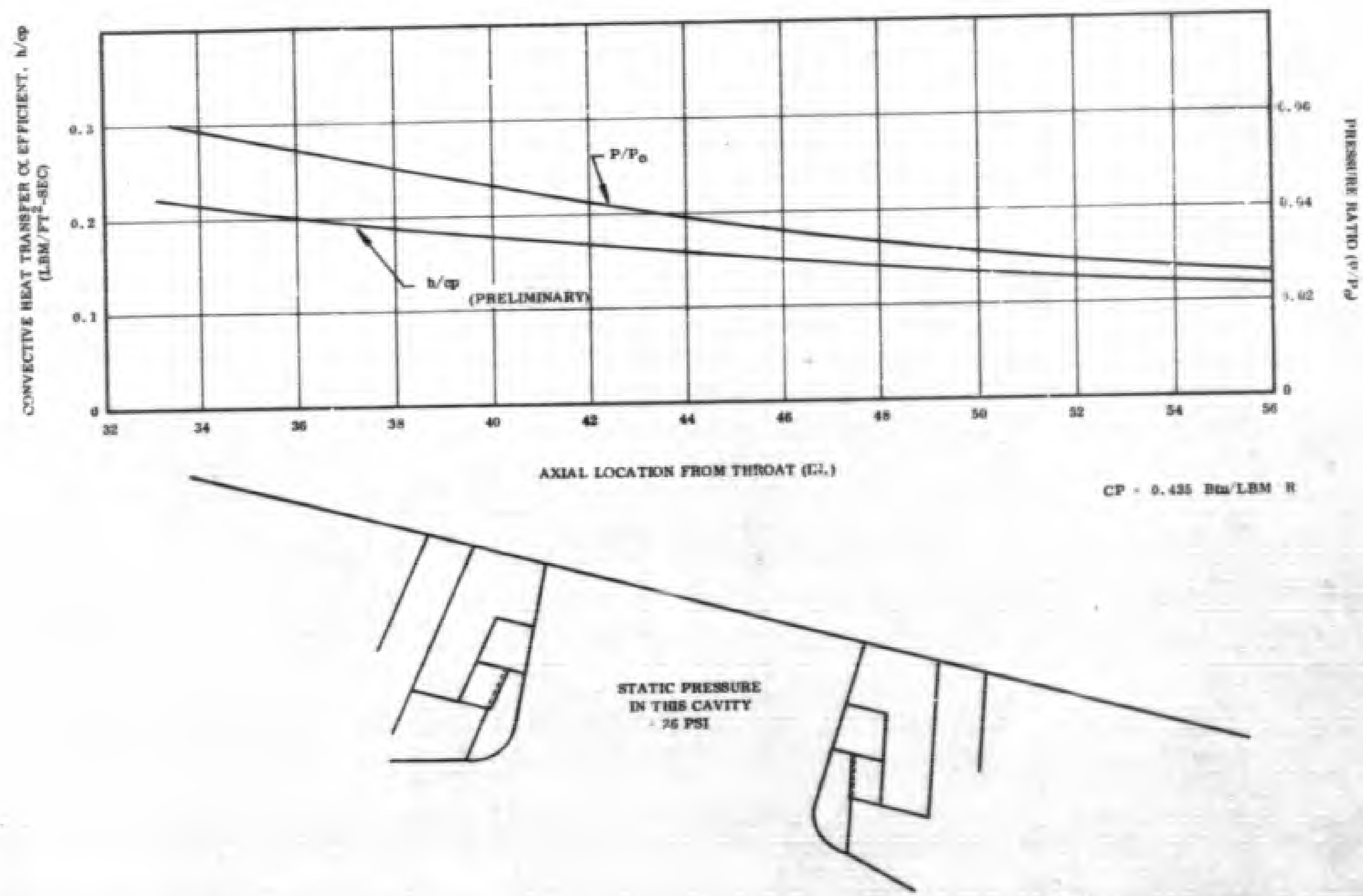

Figure 57. Nozzle Wall Pressure Ratio and Heat Transfer Coefficient

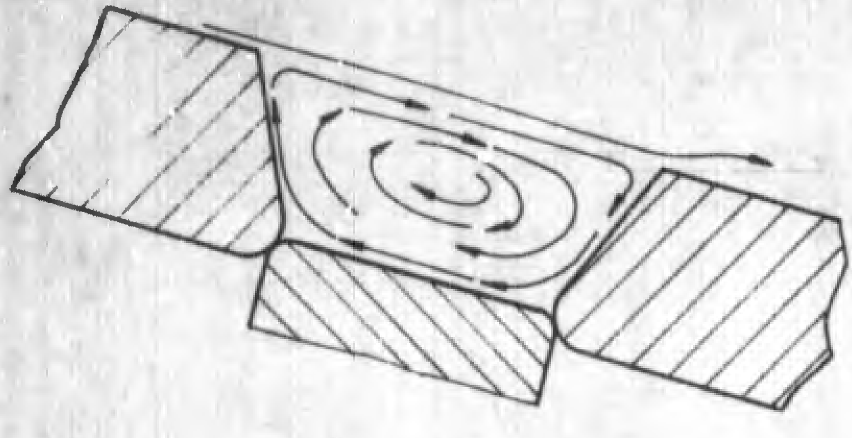

A. SEPARATED FLOW REGION

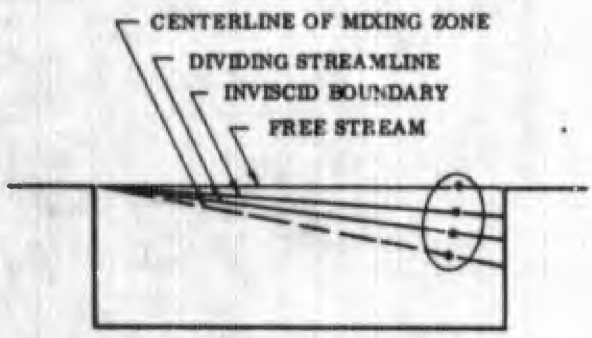

B. REGION OF FLOW IN THE SEPARATED REGION

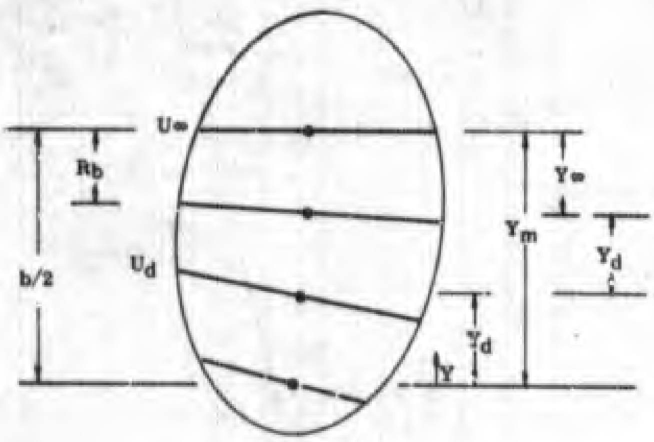

C. COORDINATE SYSTEM IN THE SEPARATED REGION

Figure 58. Flow in the Cavity

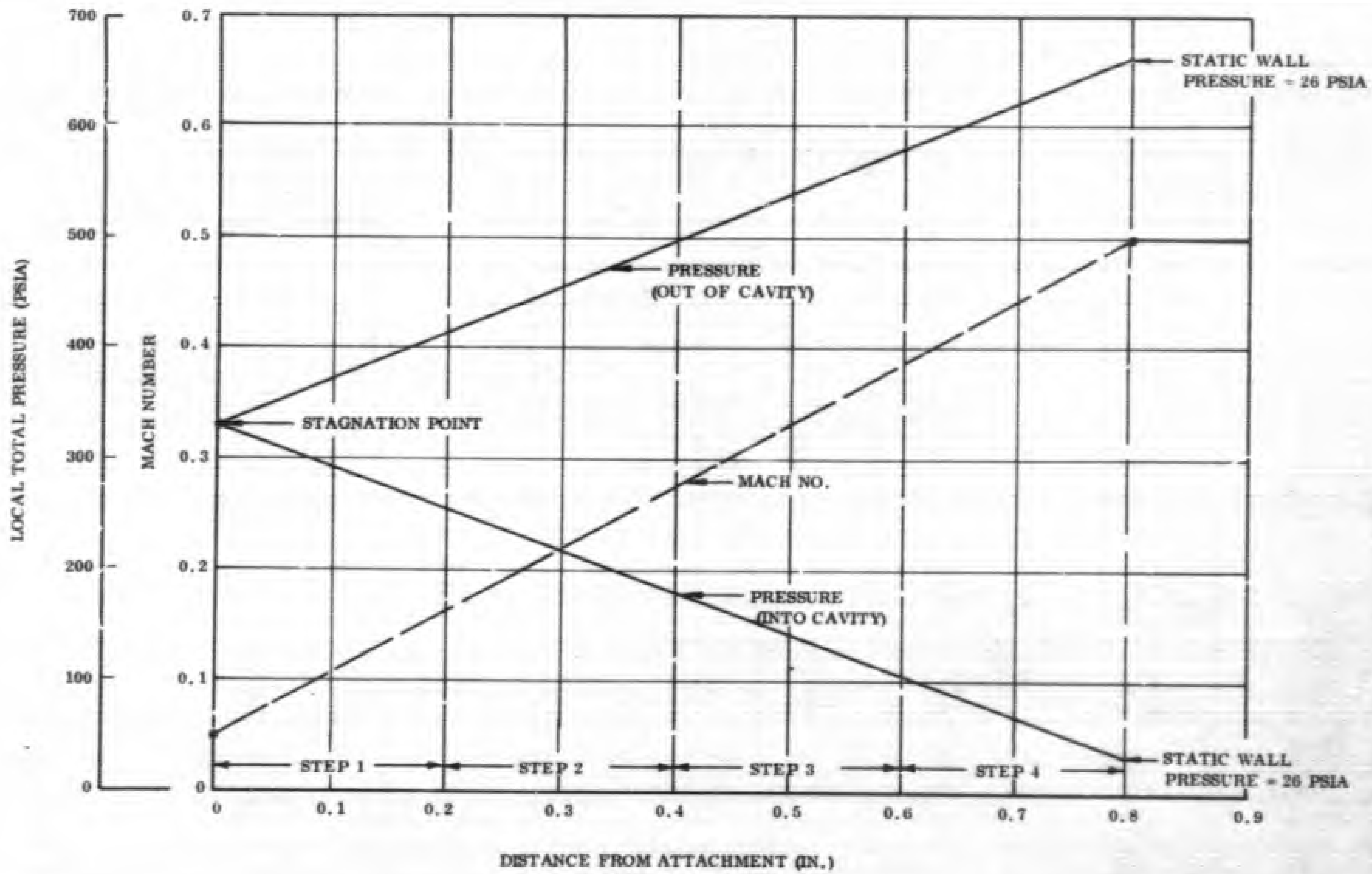

Figure 59. Stagnation Point Pressure and Mach Number Gradients

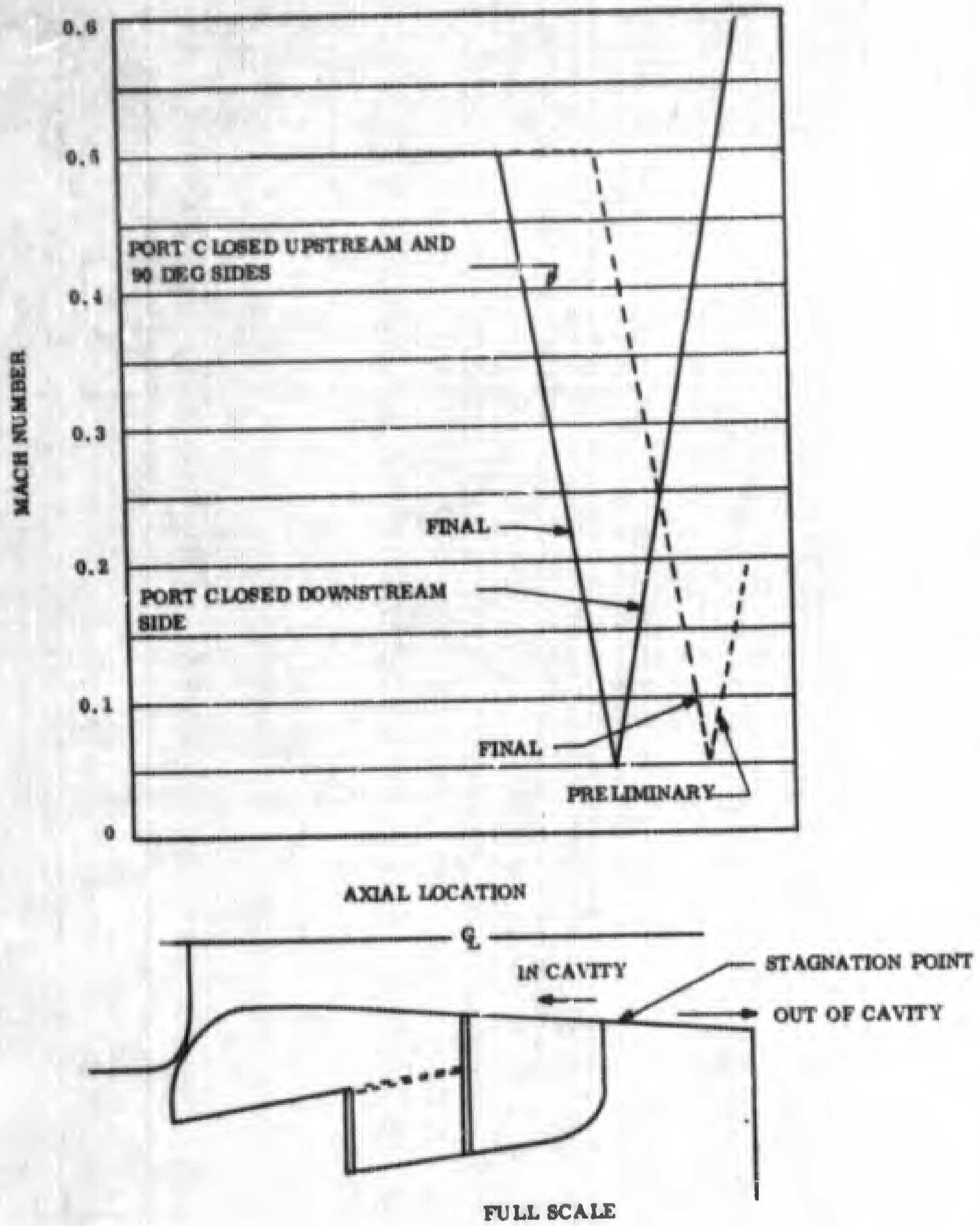

Figure 80. Mach Number vs Axial Location, Closed Cavity

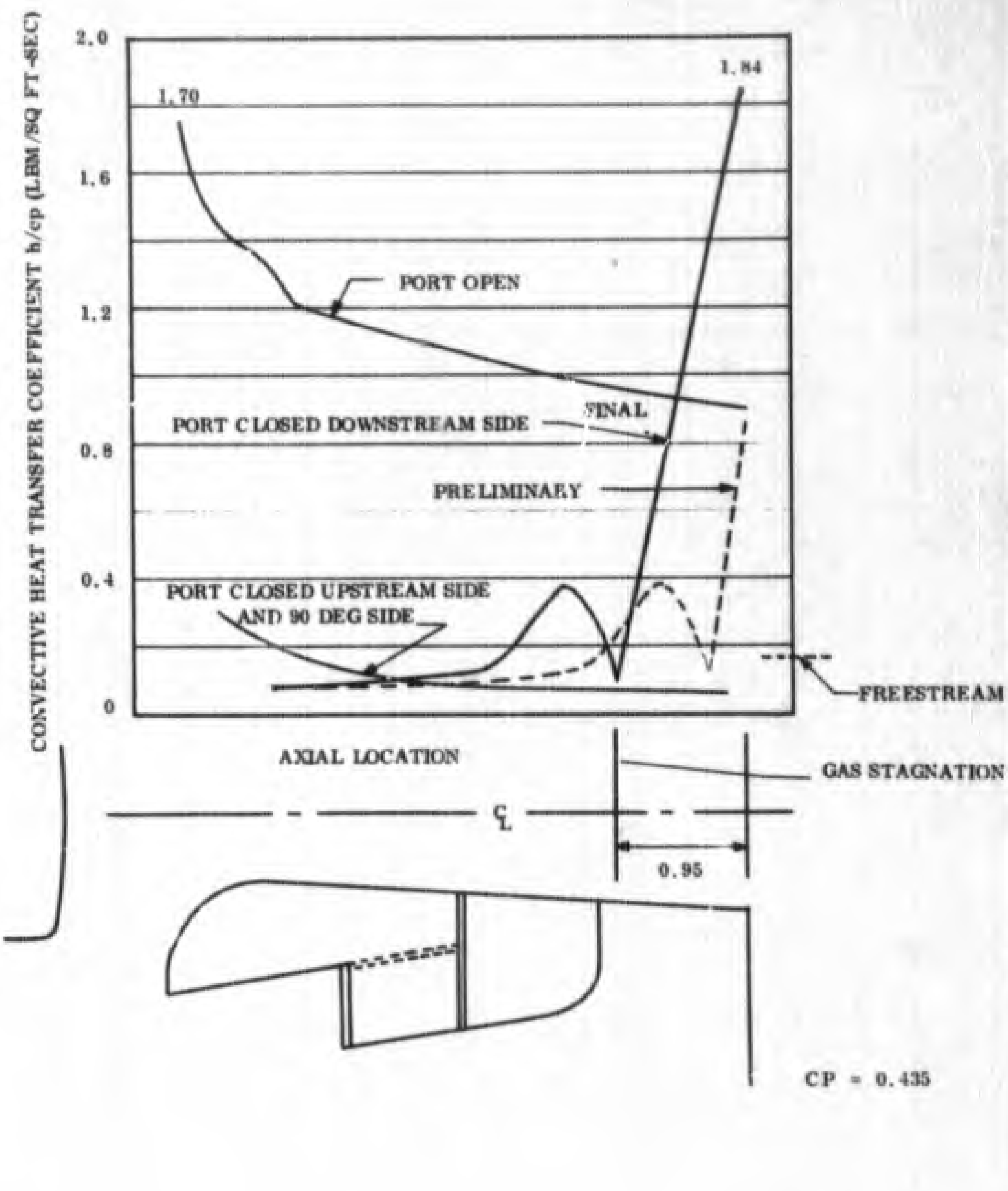

Figure 61. Port h/cp vs Axial Location, at 0 Sec, Port Open and Closed

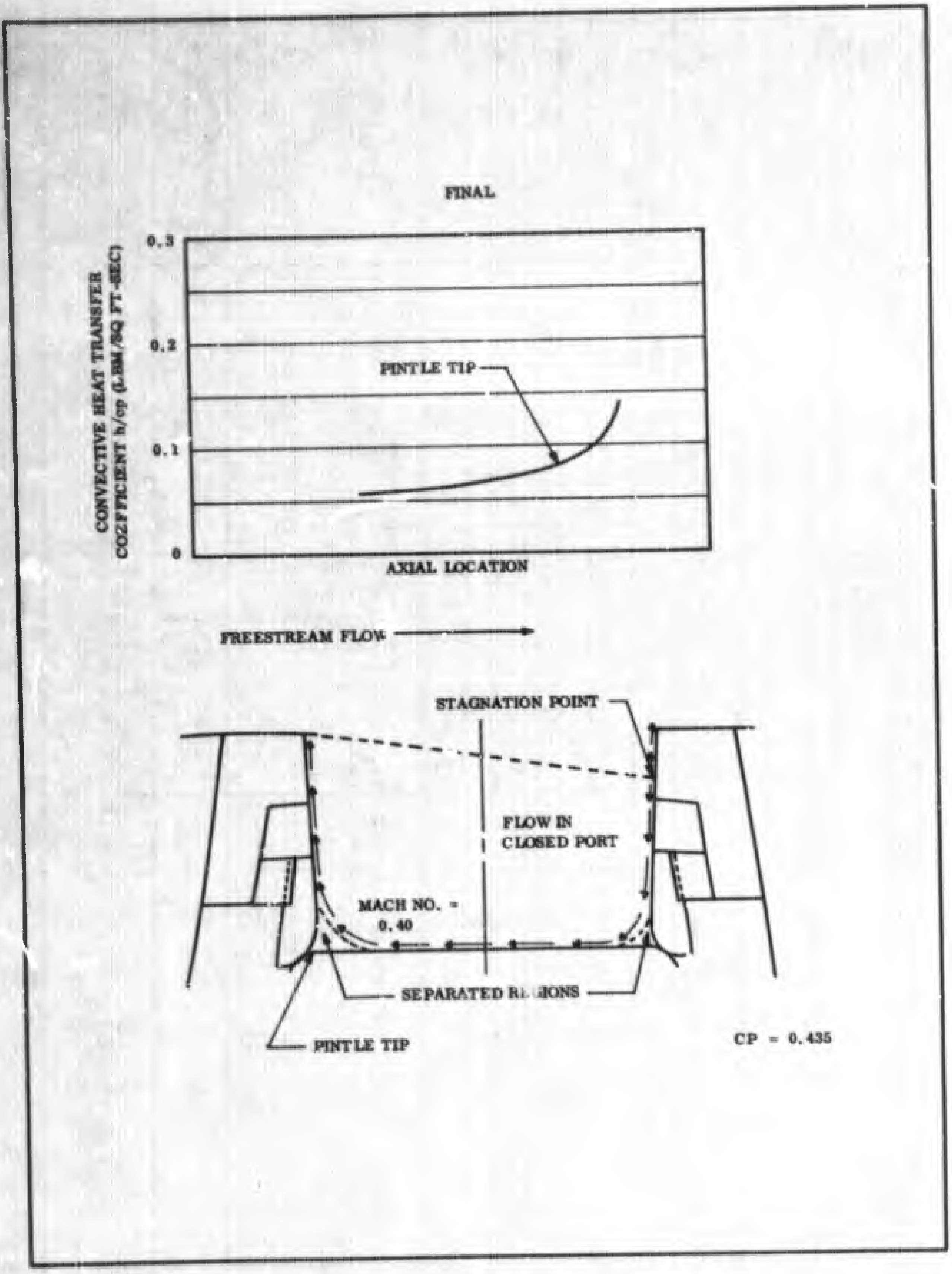

Figure 62. Pintle Valve h/cp vs Axial Location, Port Closed

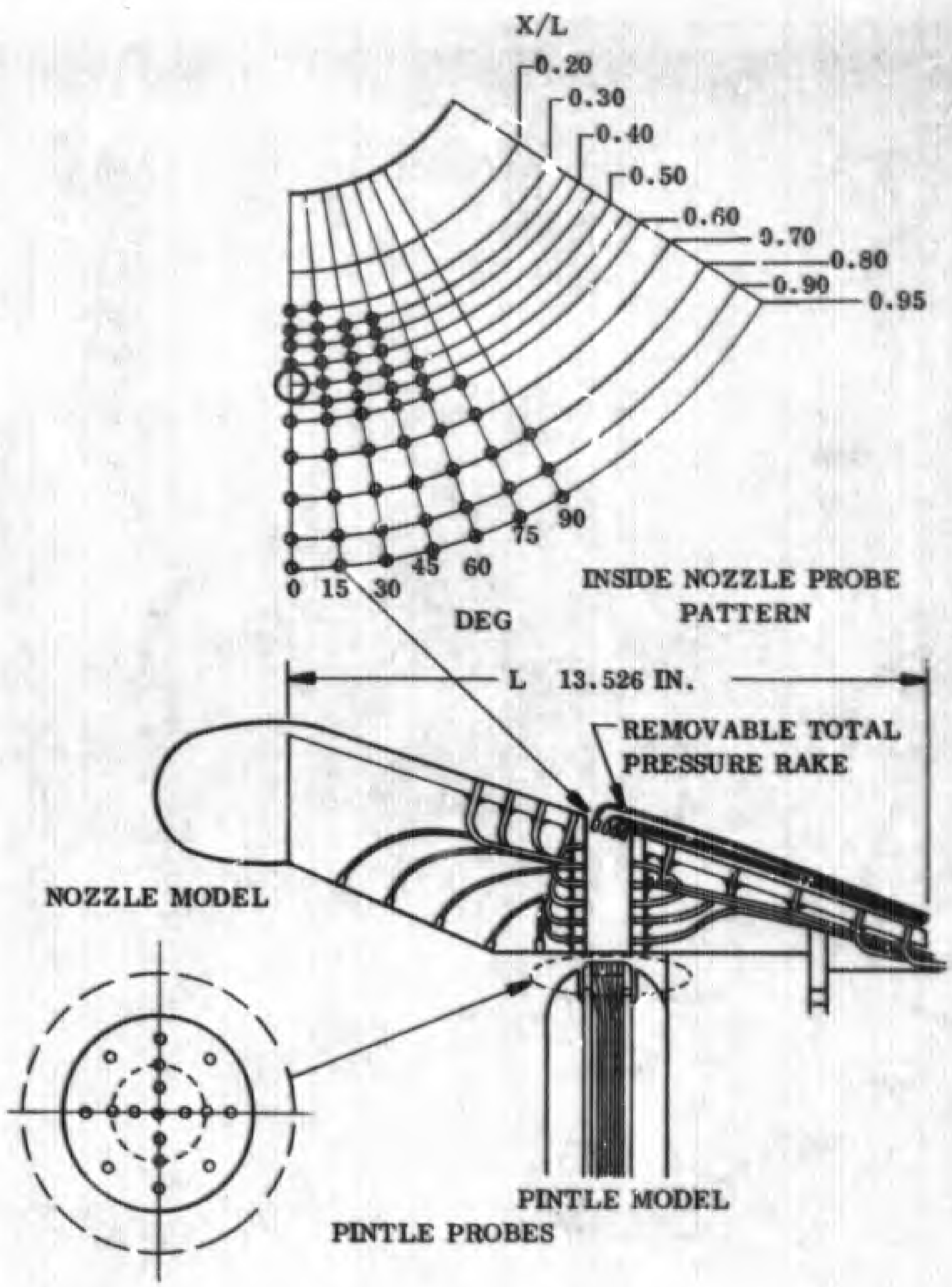

Figure 63. Cold Flow Test Model and Pressure Probe Locations

Figure 64. Orifice Smear Photo, Perpendicular to Centerline

Figure 65. Orifice Smear Photo, Perpendicular to Centerline

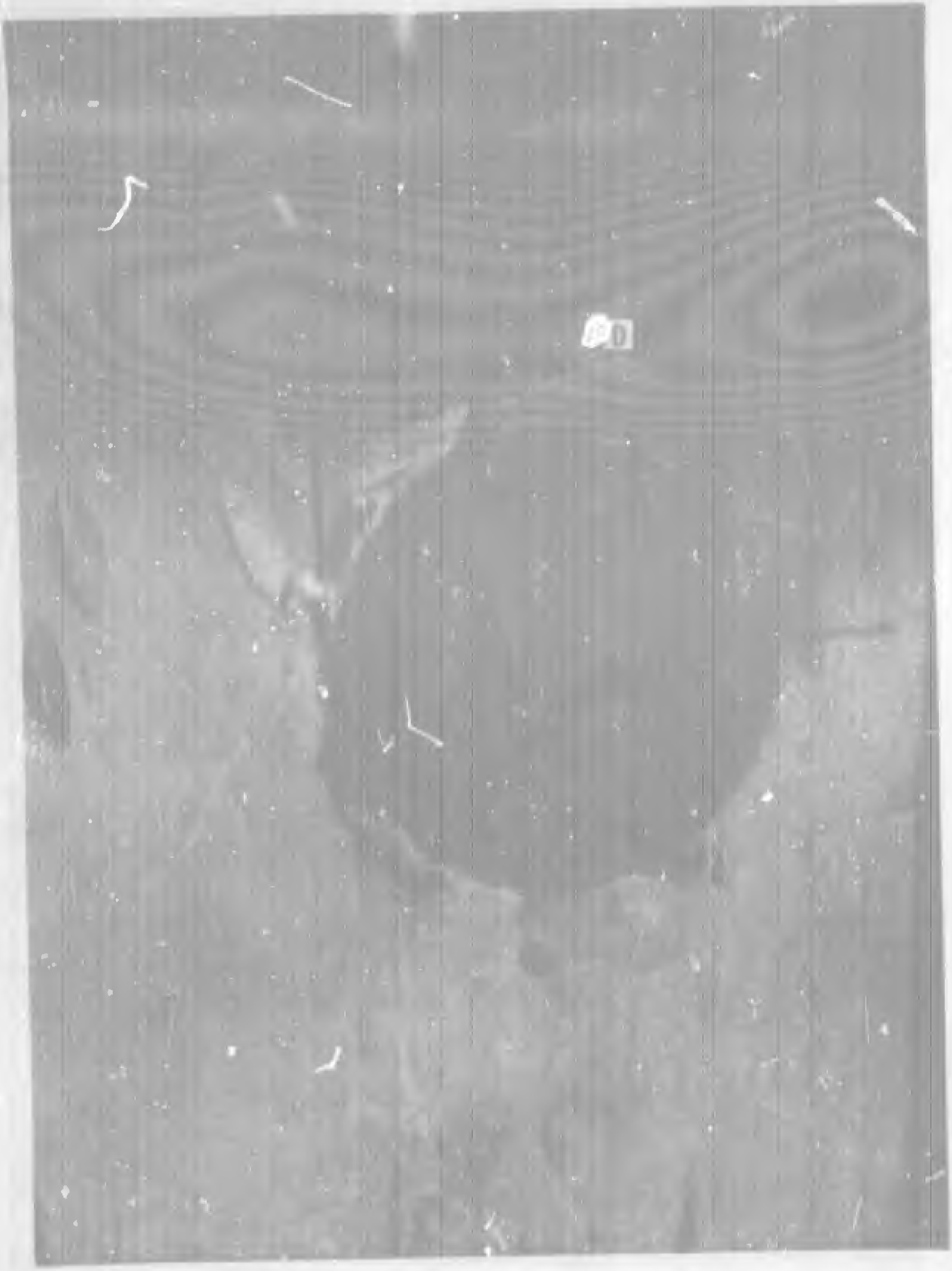

Figure 66. Orifice Smear Photo, Perpendicular to Centerline

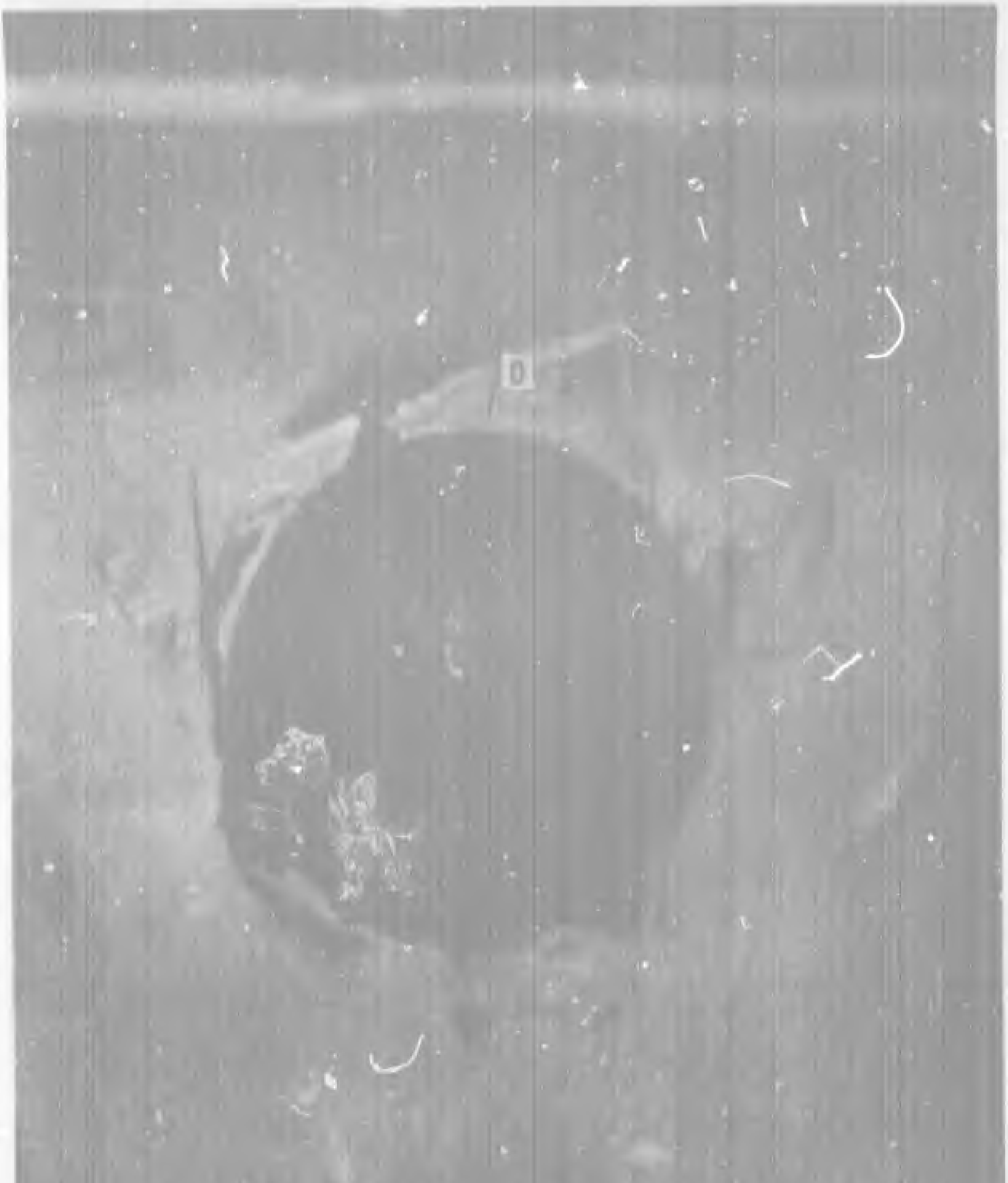

Figure 67. Orifice Smear Photo, Perpendicular to Centerline

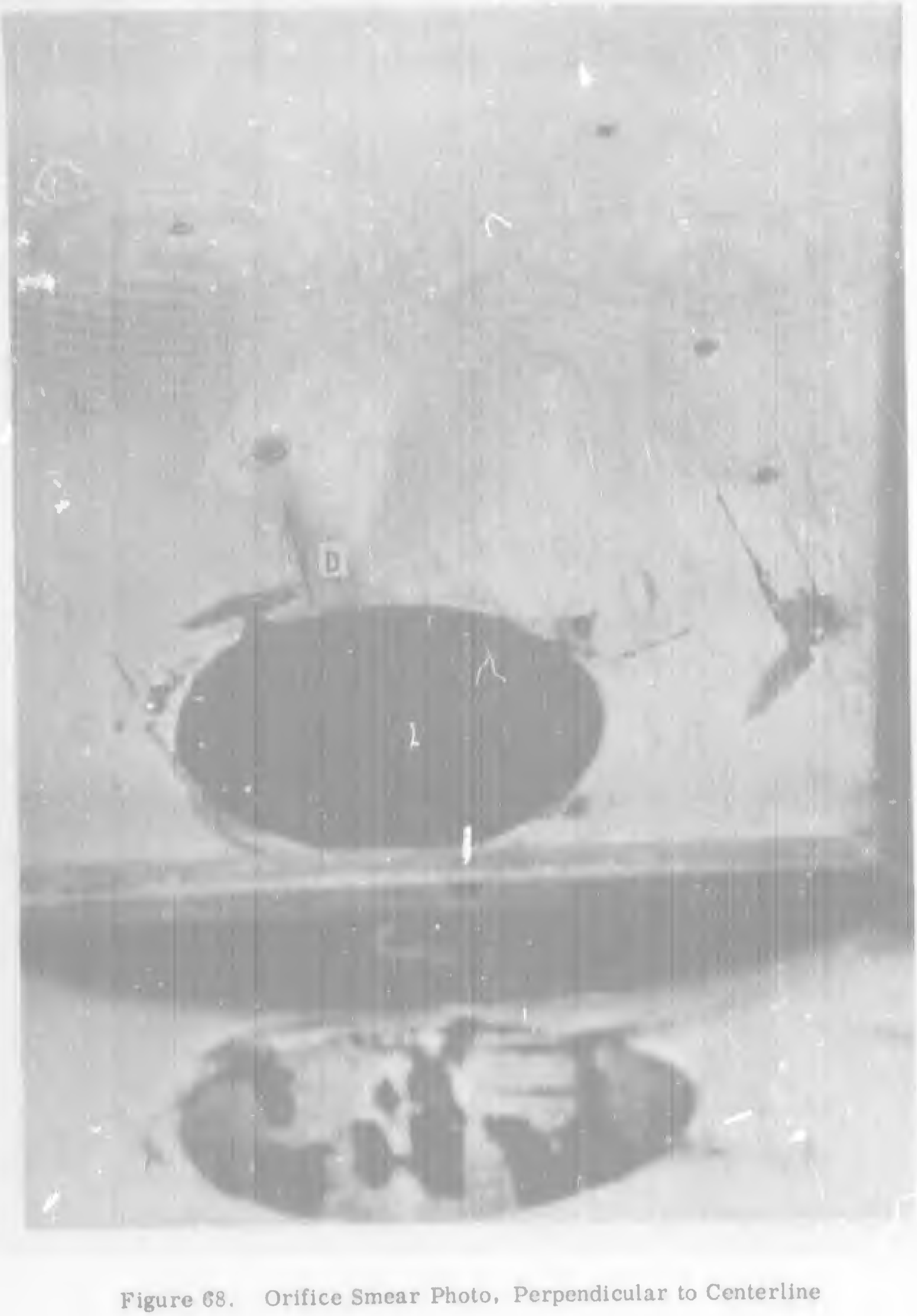

Figure 68. Orifice Smear Photo, Perpendicular to Centerline

Figure 69. Orifice Smear Photo, Perpendicular to Centerline

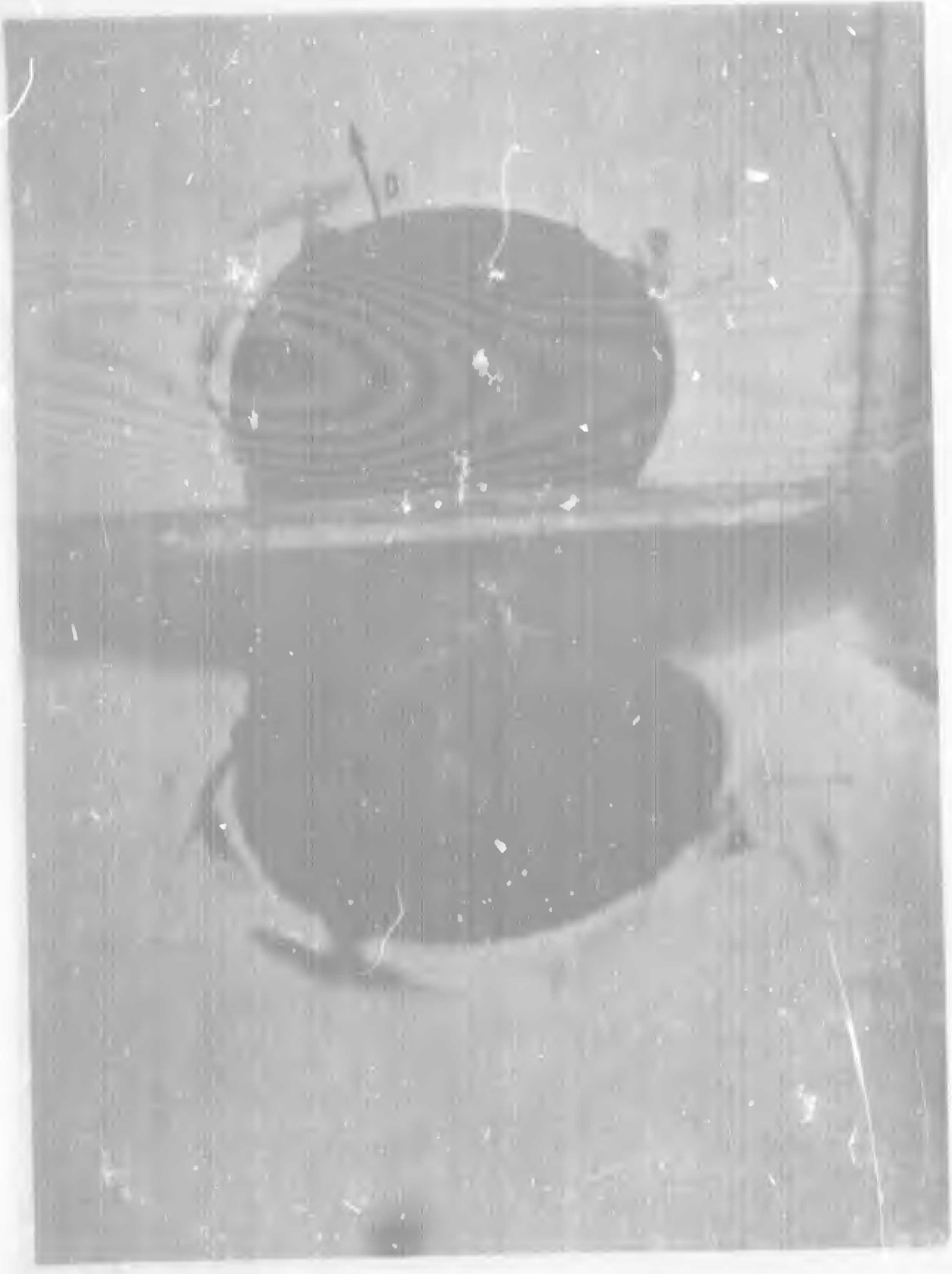

Figure 70. Orifice Smear Photo, Perpendicular to Centerline

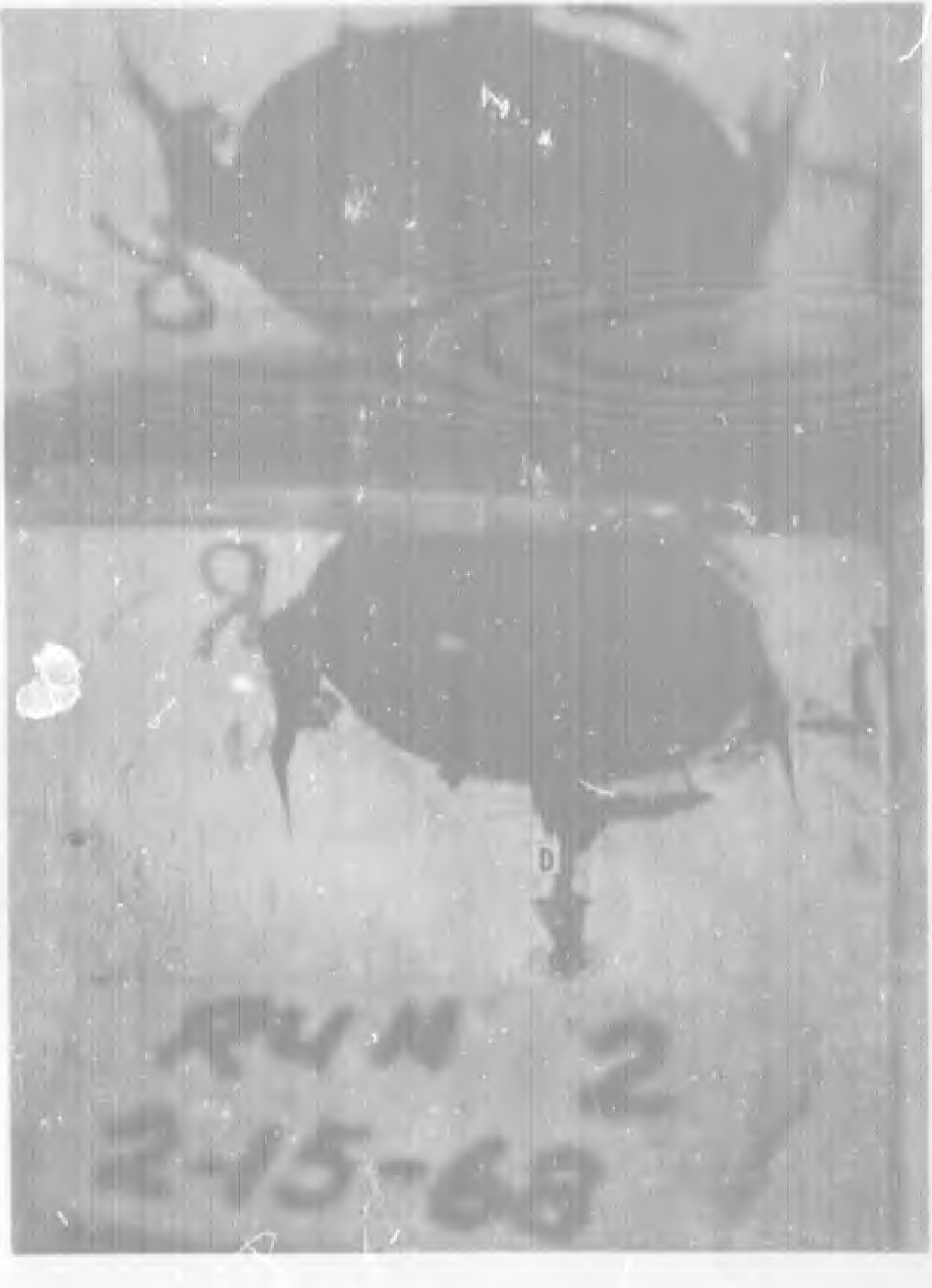

Figure 71. Orifice Smear Photo, Perpendicular to Centerline

Figure 72. Orifice Smear Photo, Perpendicular to Centerline

Figure 73. Orifice Smear Photo, Perpendicular to Centerline

Figure 74. Orifice Smear Photo, Perpendicular to Centerline

Figure 75. Orifice Smear Photo, Perpendicular to Centerline

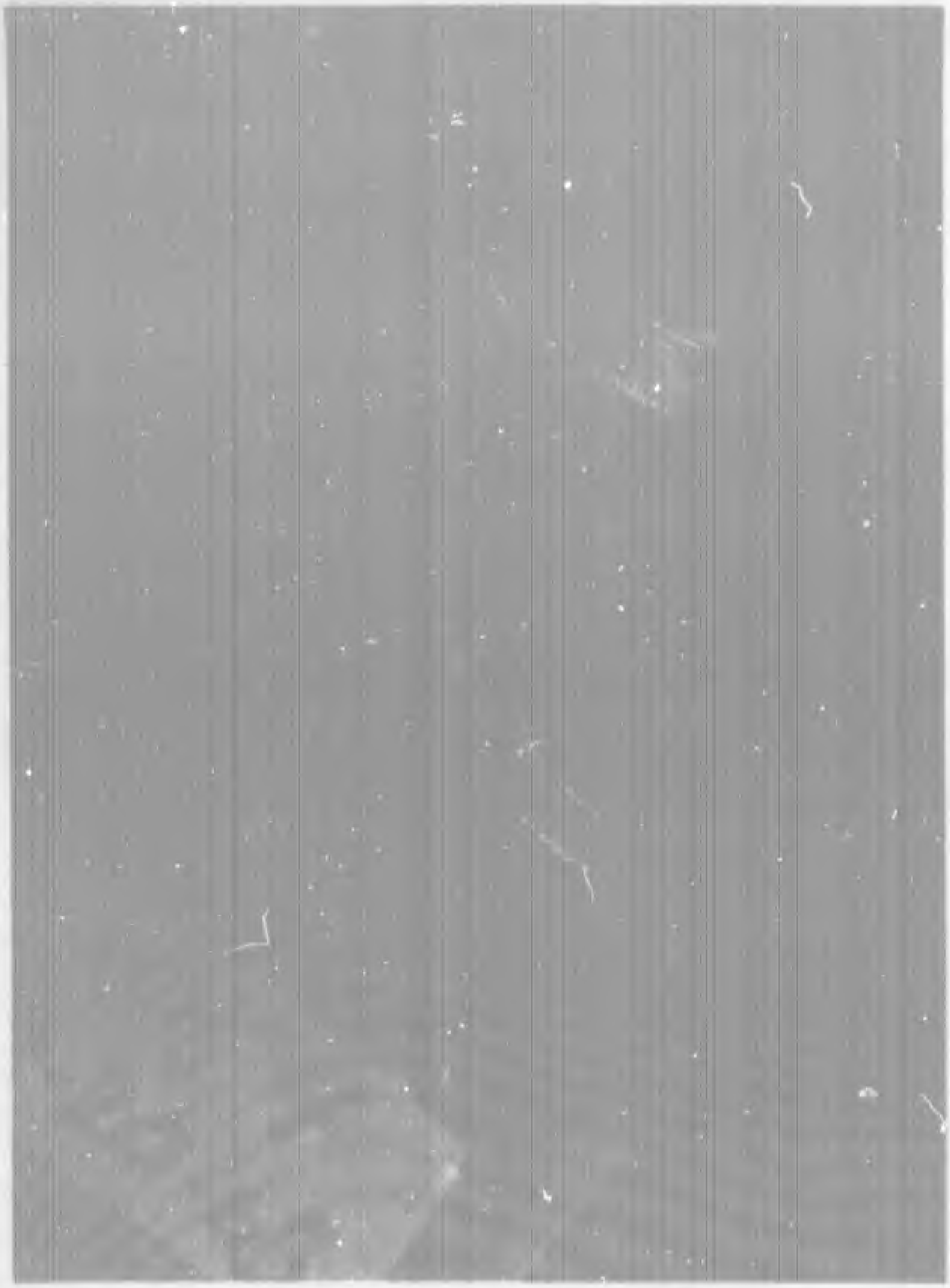

Figure 76. Orifice Smear Photo, Perpendicular to Wall

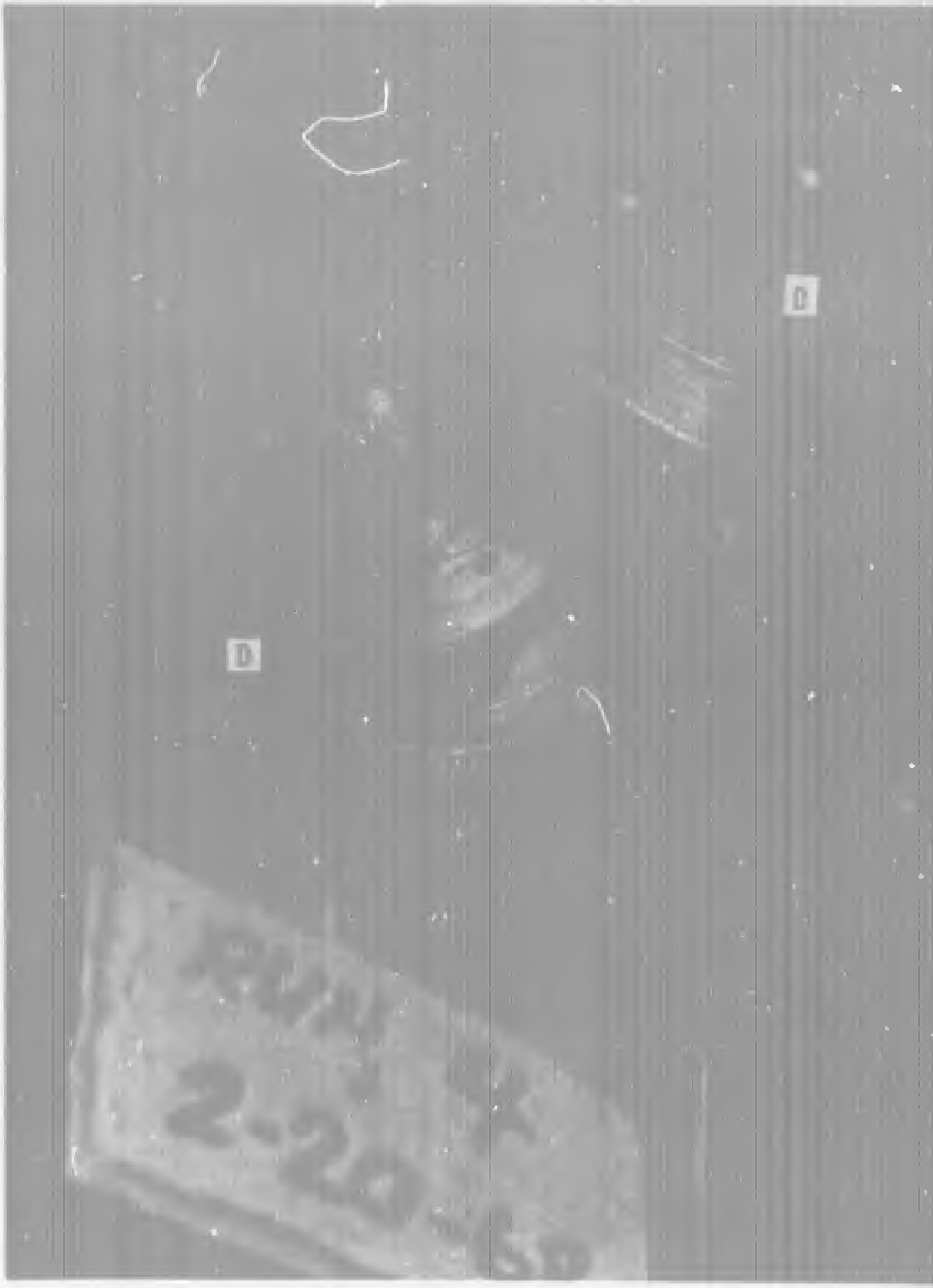

Figure 77. Orifice Smear Photo, Perpendicular to Wall

Figure 78. Orifice Smear Photo, Perpendicular to Wall

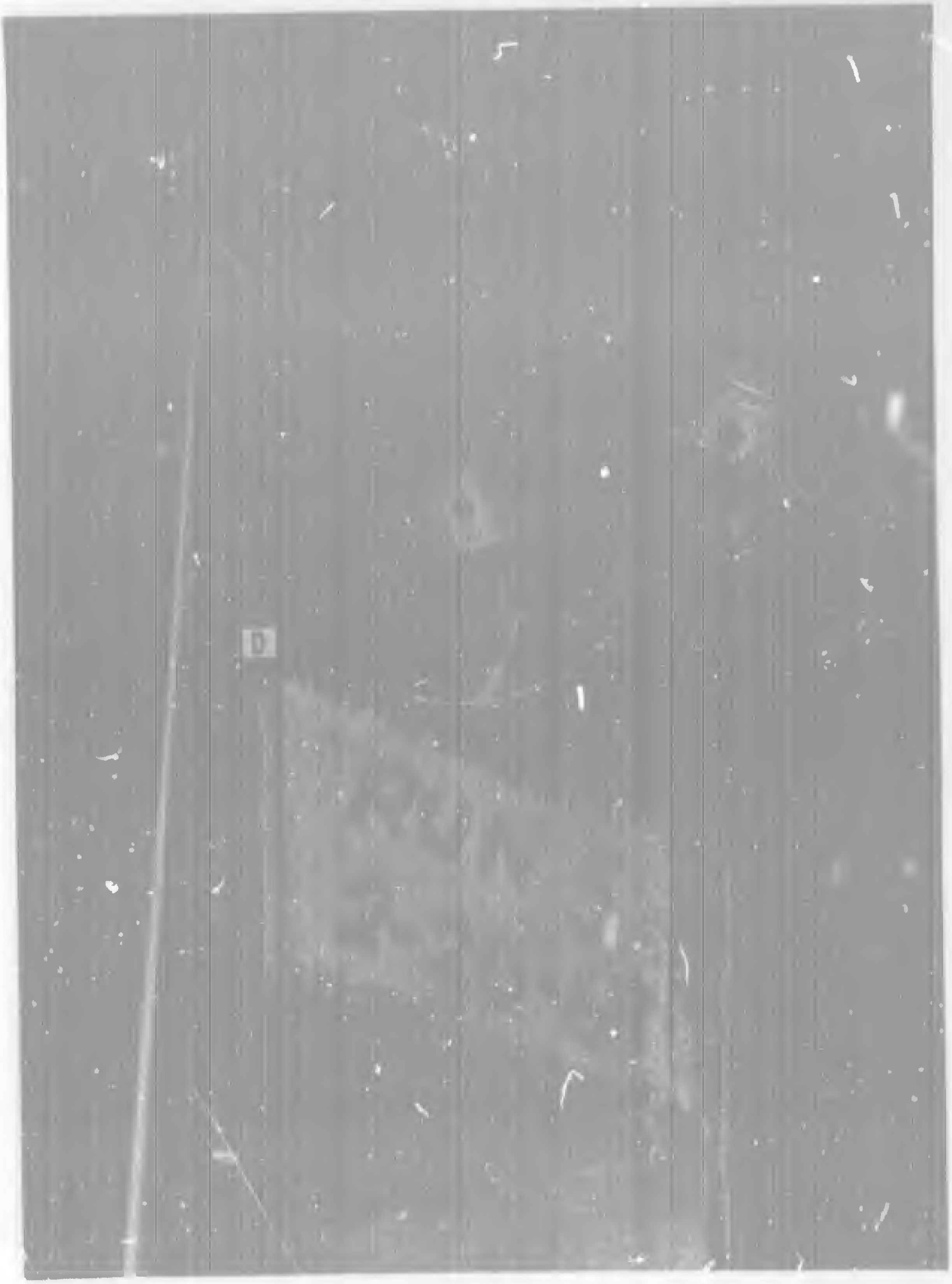

Figure 79. Orifice Smear Photo, Perpendicular to Wall

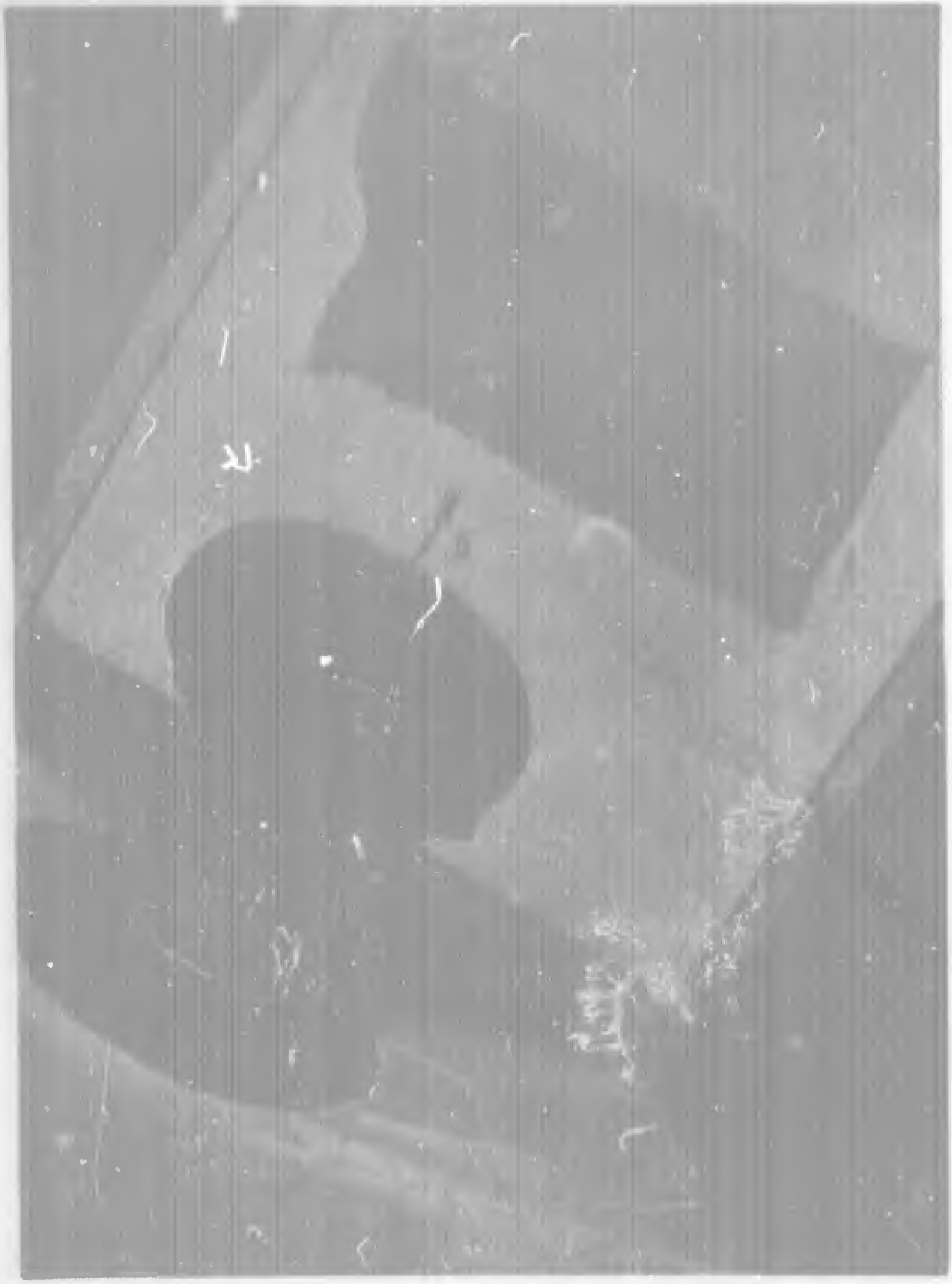

Figure 80. Orifice Smear Photo, Perpendicular to Wall

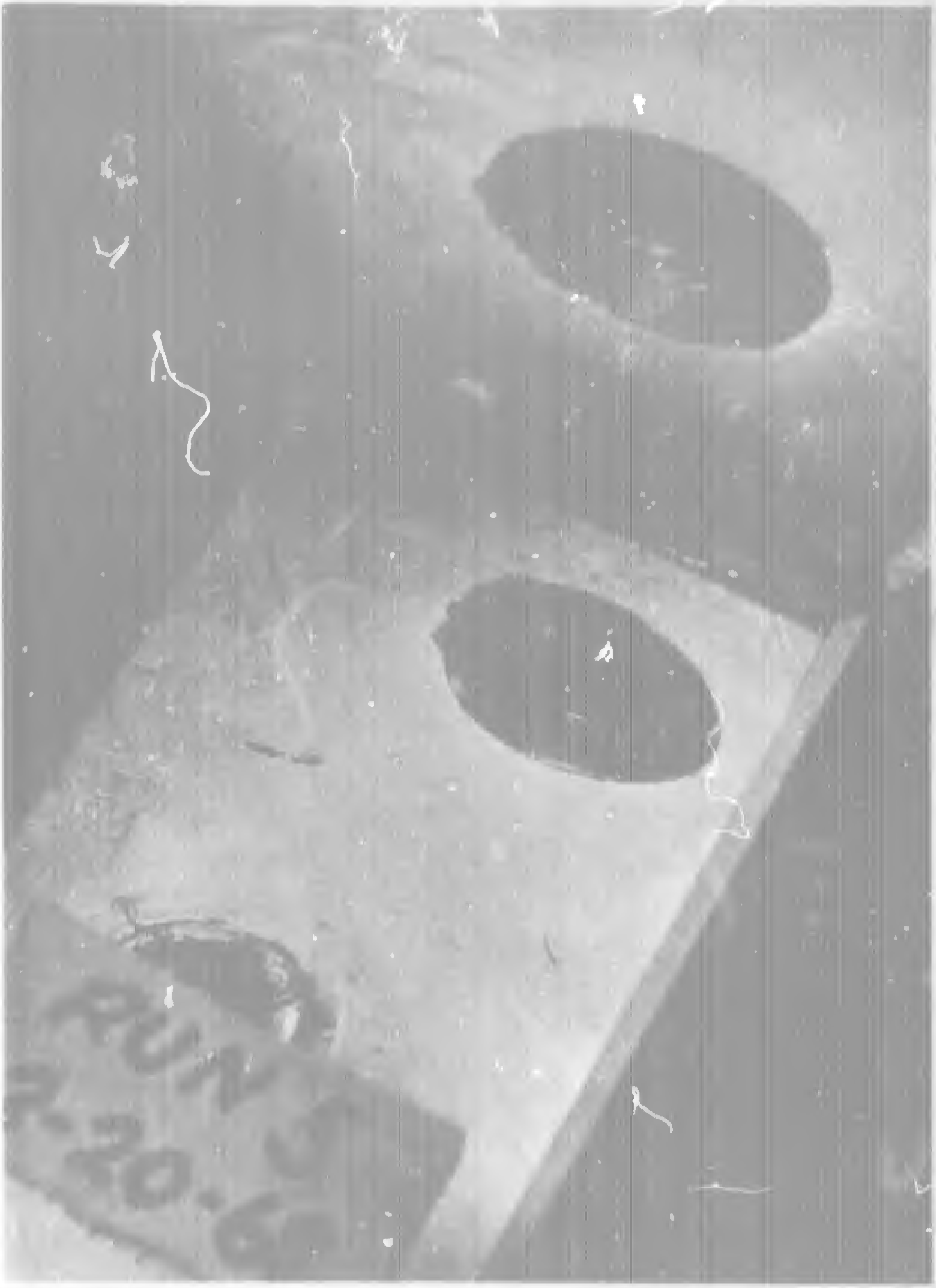

Figure 81. Orifice Smear Photo, Perpendicular to Wall

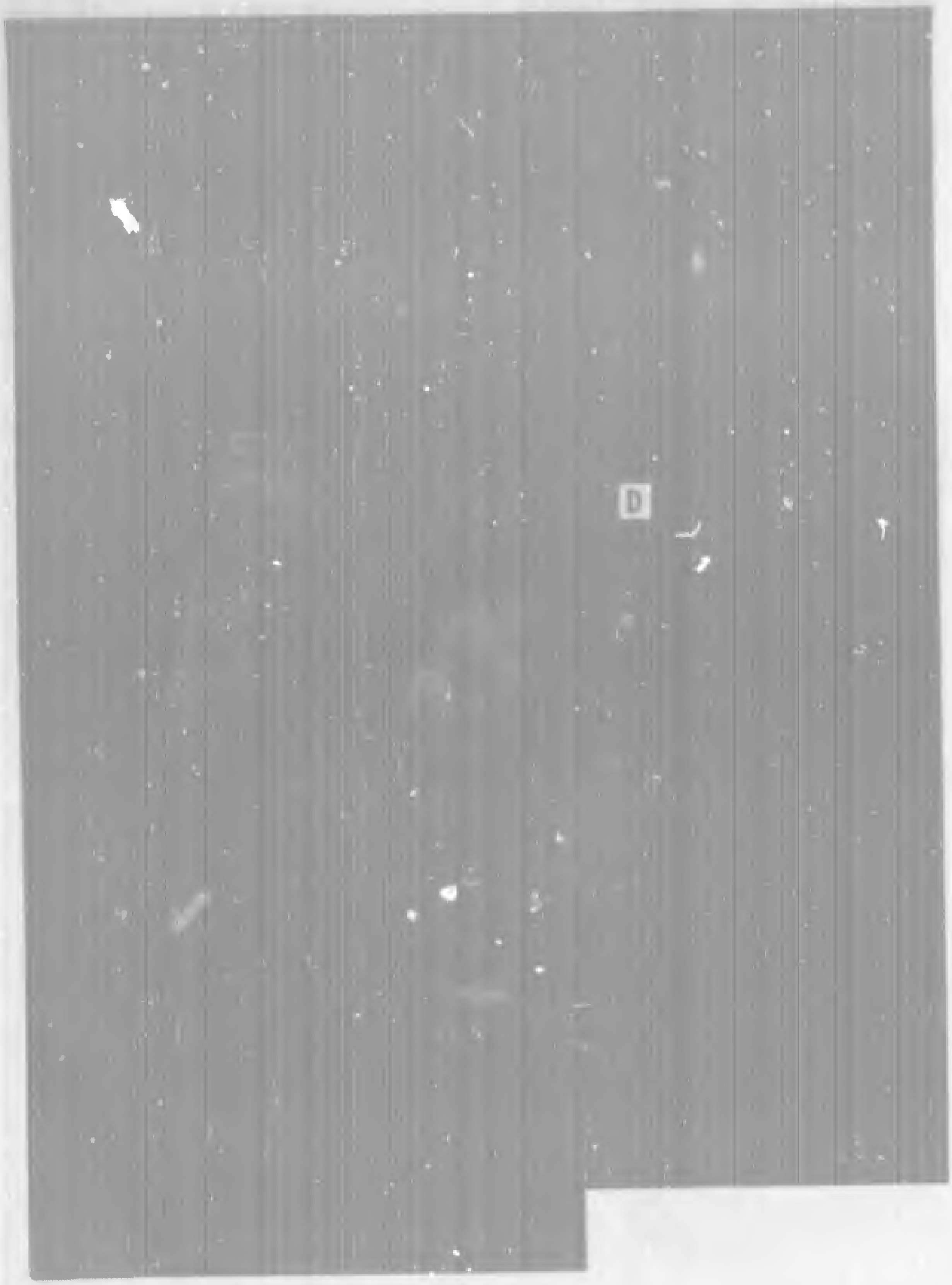

Figure 82. Orifice Smear Photo, Perpendicular to Wall

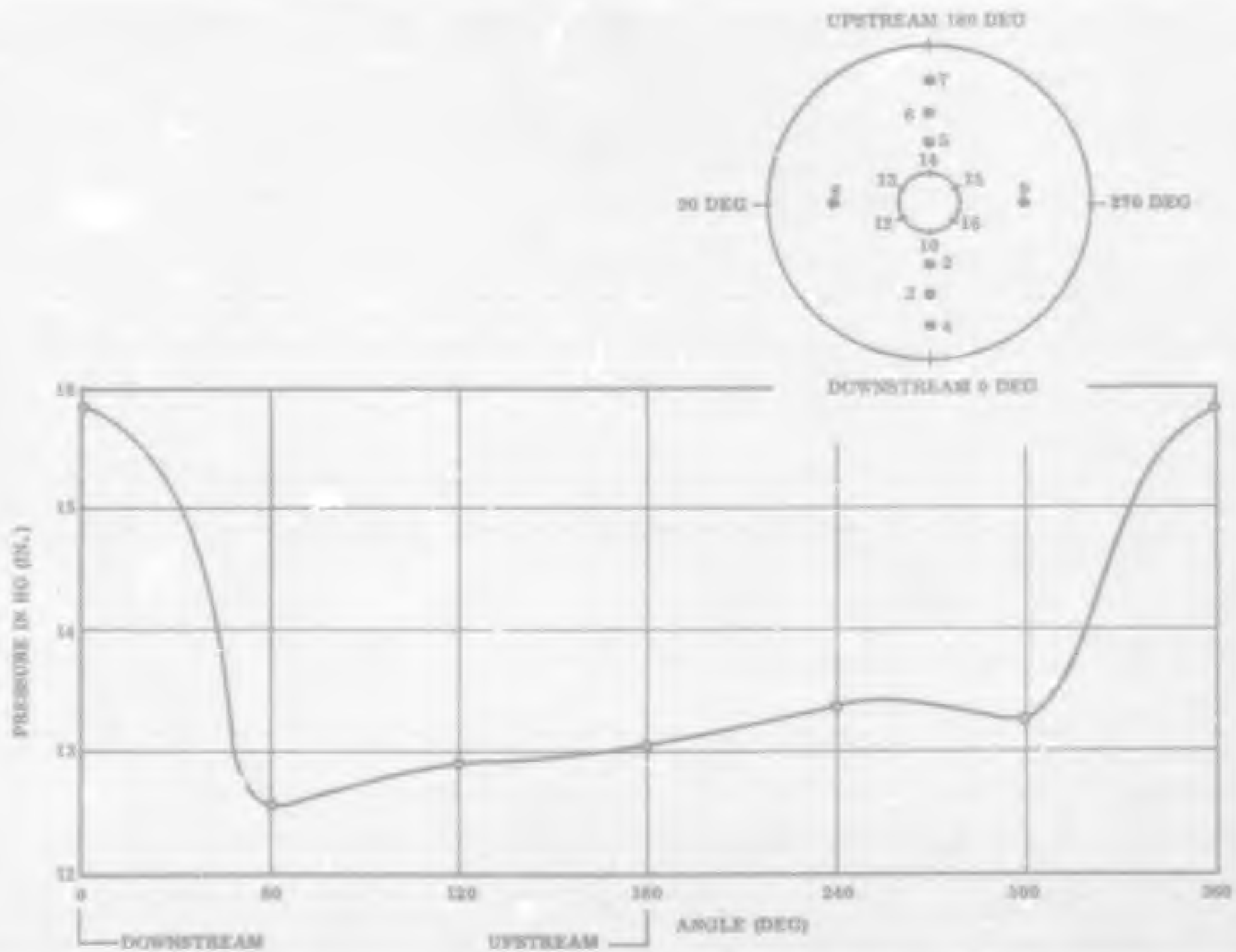

Figure 83. Cold Flow Pressure Data, Bottom of Cavity

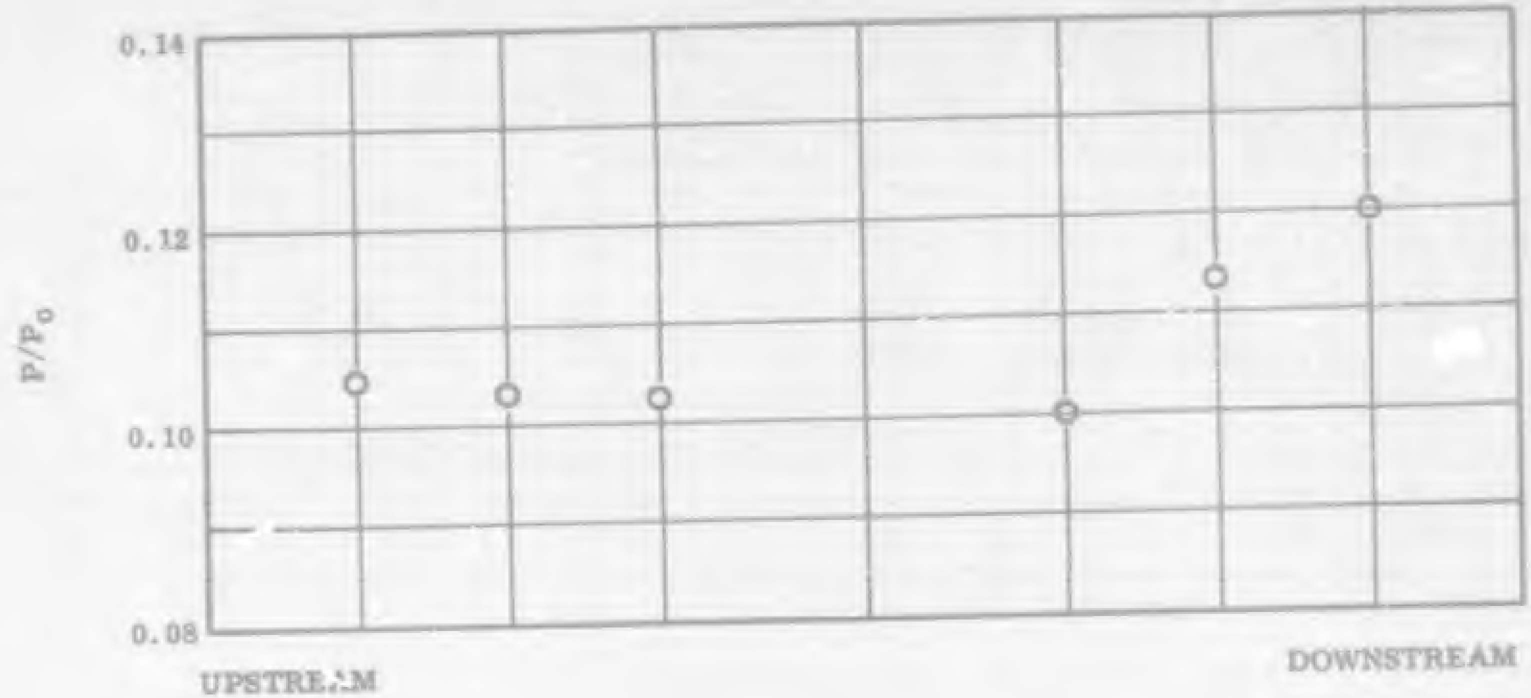

Figure 84. Cold Flow Pressure Ratio Data, Bottom of Cavity

Figure 85. Orifice Smear Pattern, Perpendicular to Centerline, for PTB Missing

Figure 86. Orifice Smear Pattern, Perpendicular to Centerline, for PTB Missing

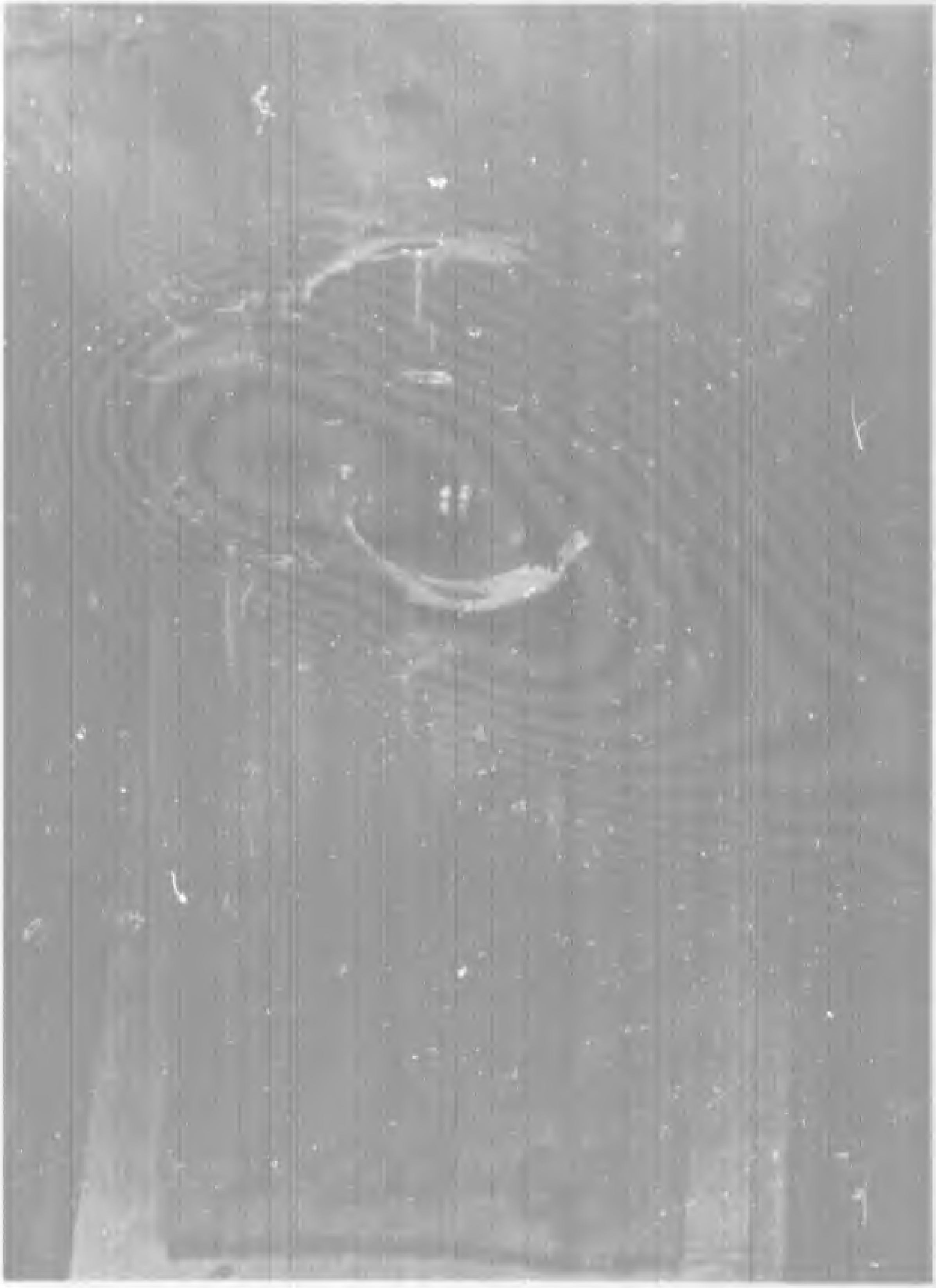

Figure 87. Orifice Smear Pattern, Perpendicular to Centerline, for PTB Missing

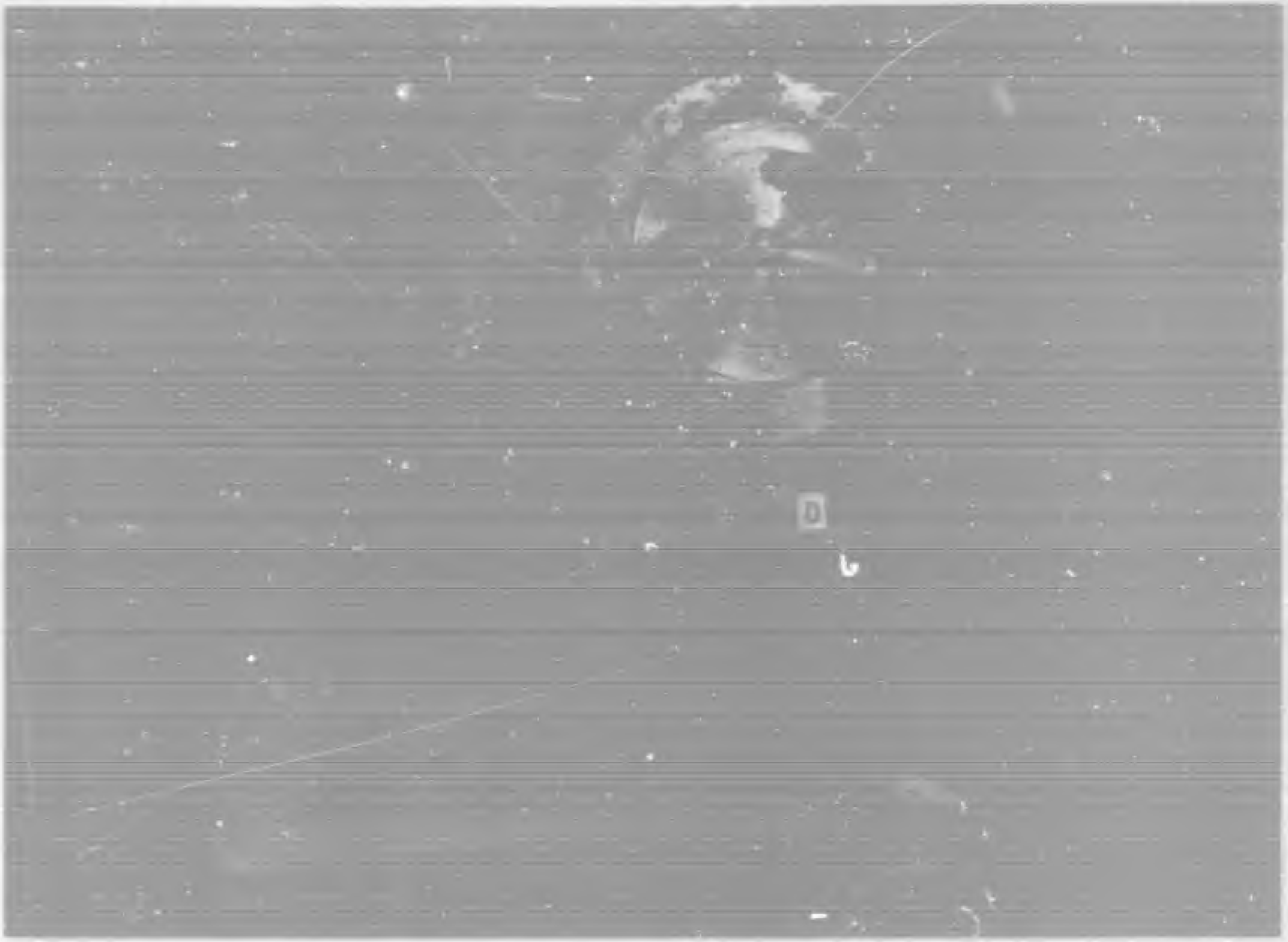

Figure 88. Orifice Smear Pattern, Perpendicular to Centerline, for PTB Missing

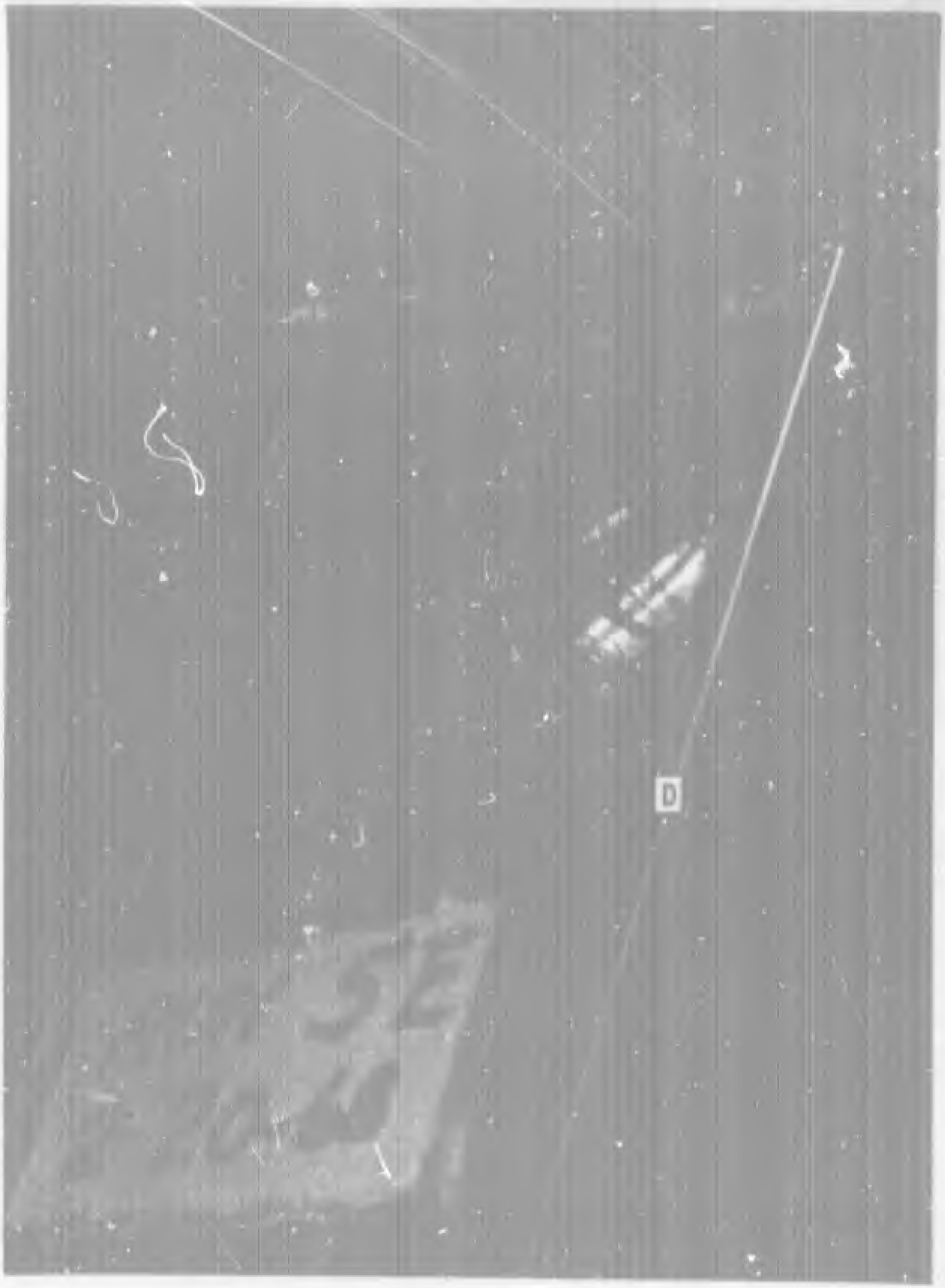

Figure 89. Orifice Smear Pattern, Perpendicular to Centerline, for PCB Missing

Figure 90. Orifice Smear Pattern, Perpendicular to Centerline, for PTB Missing

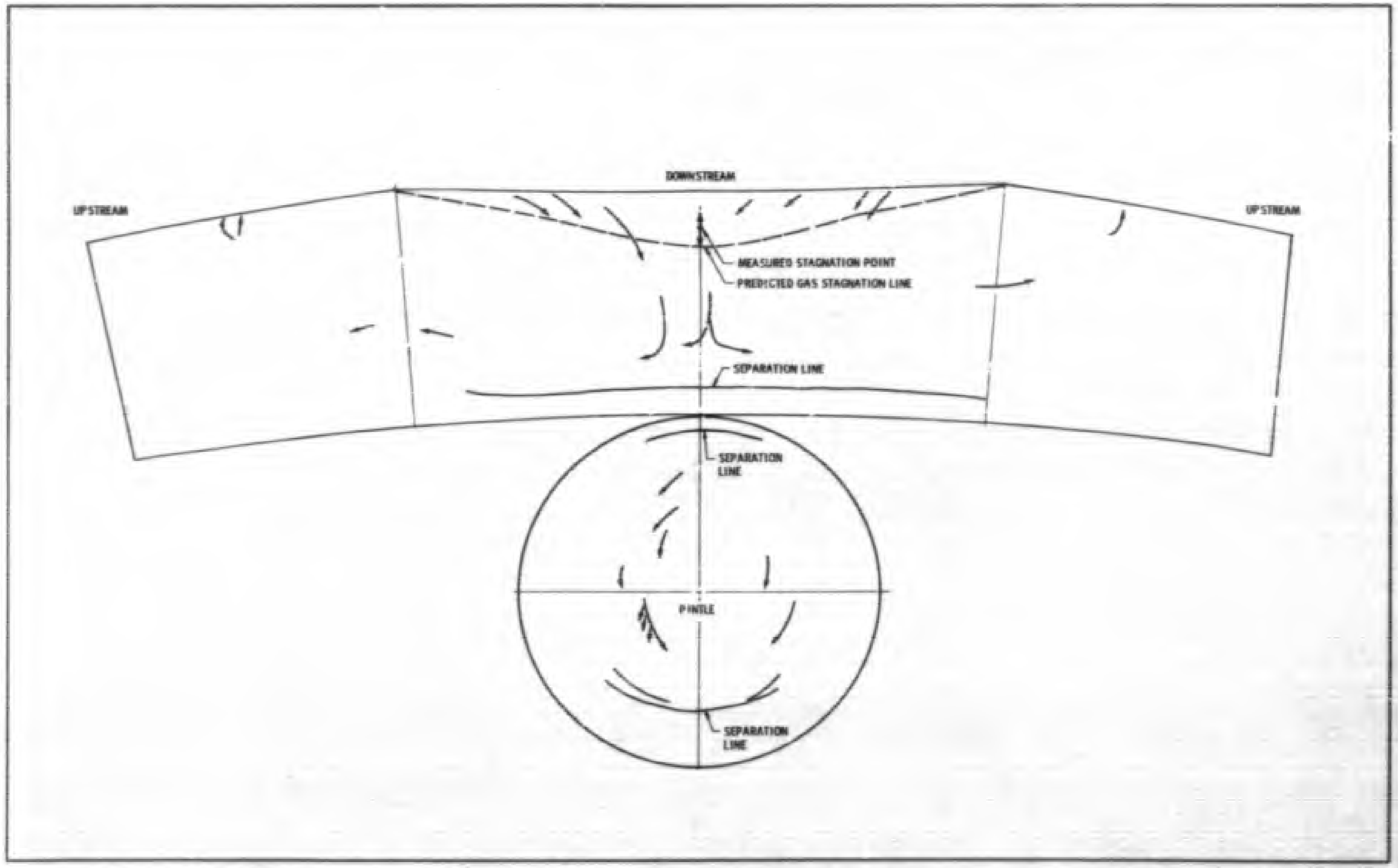

Figure 91. Summary of Cavity Flow Patterns

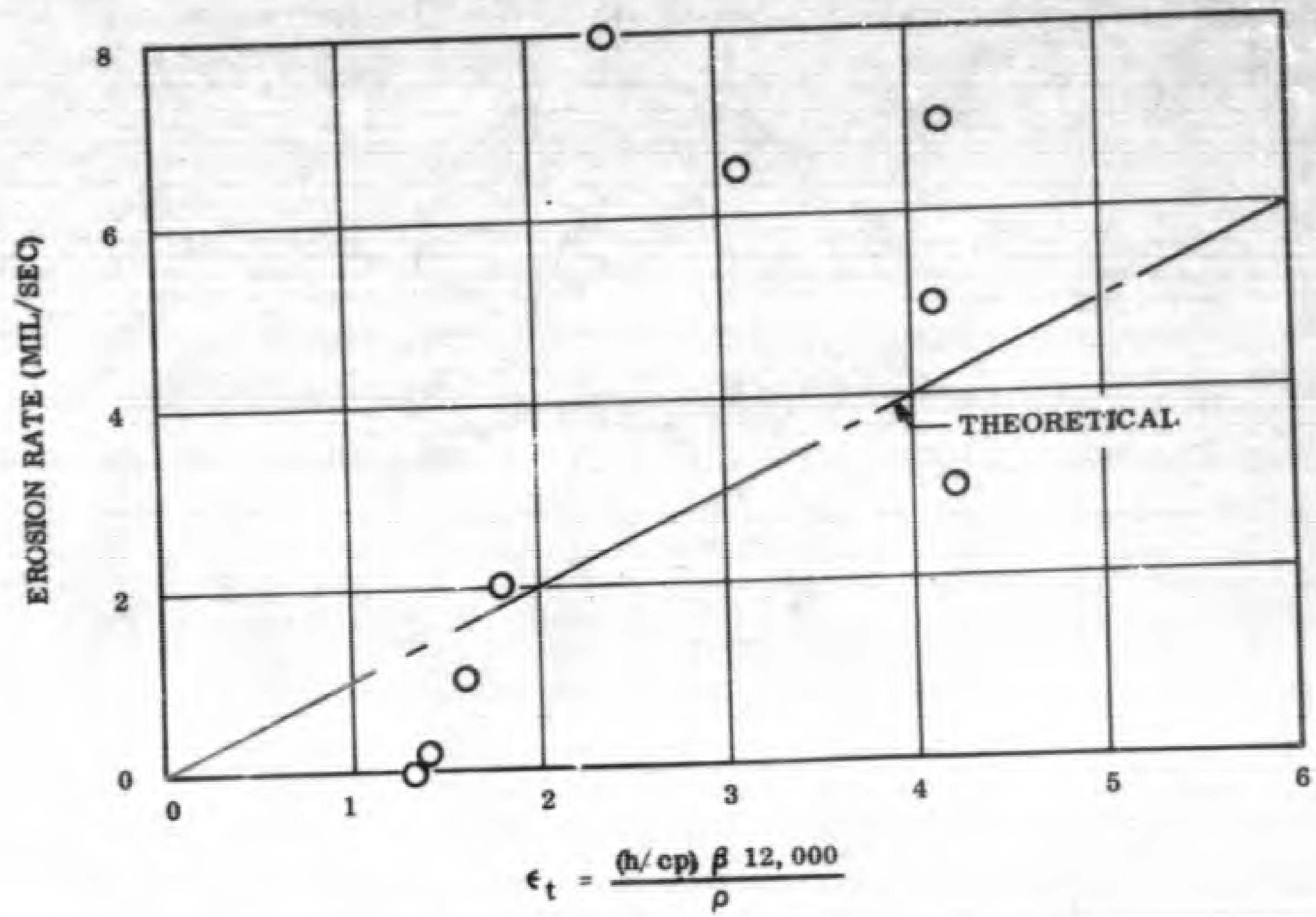

Figure 92. TU-453 Orifice Erosion Data, Port 3

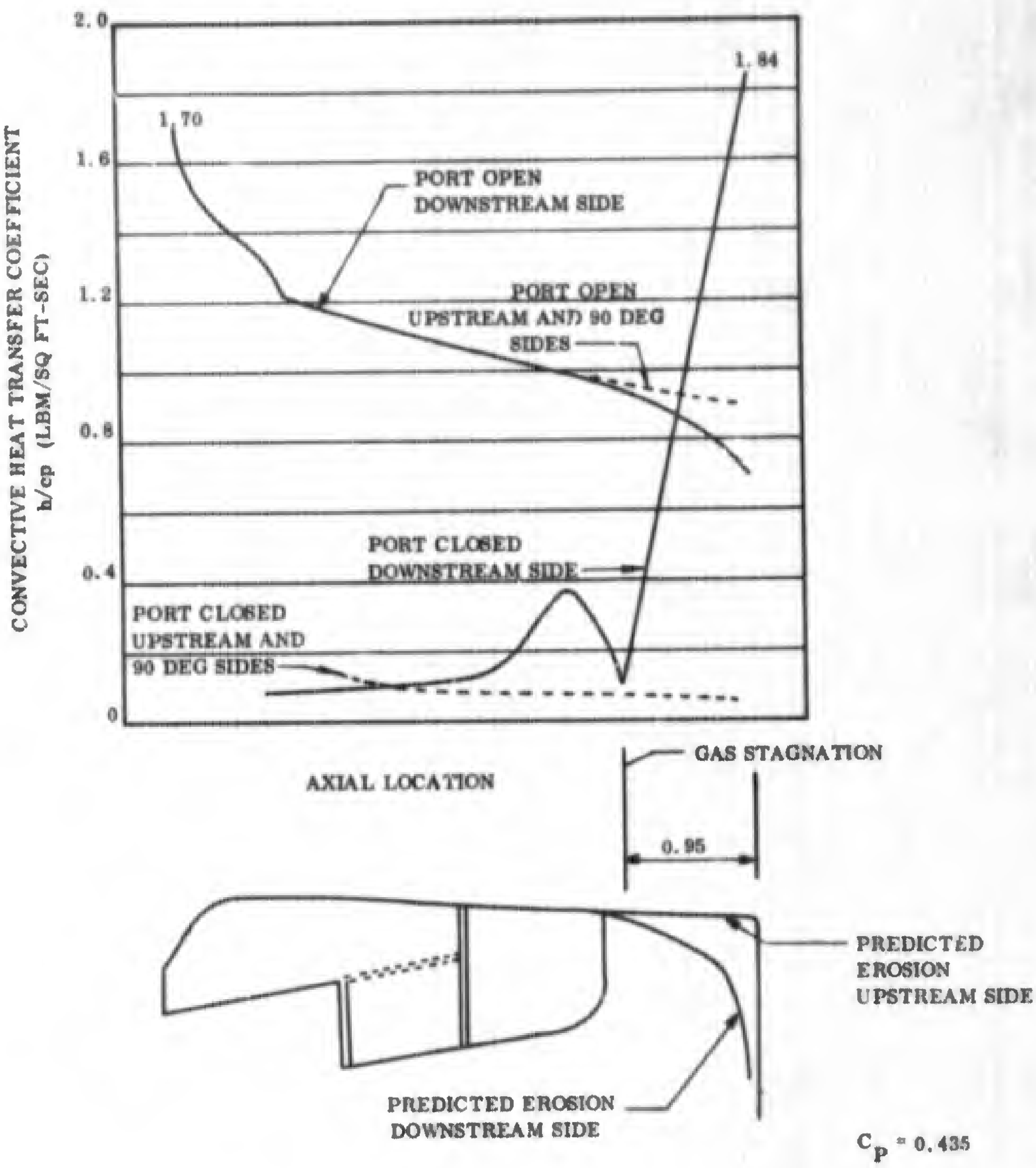

Figure 93. Orifice Wall h/cp vs Axial Location at 16 Sec - Final

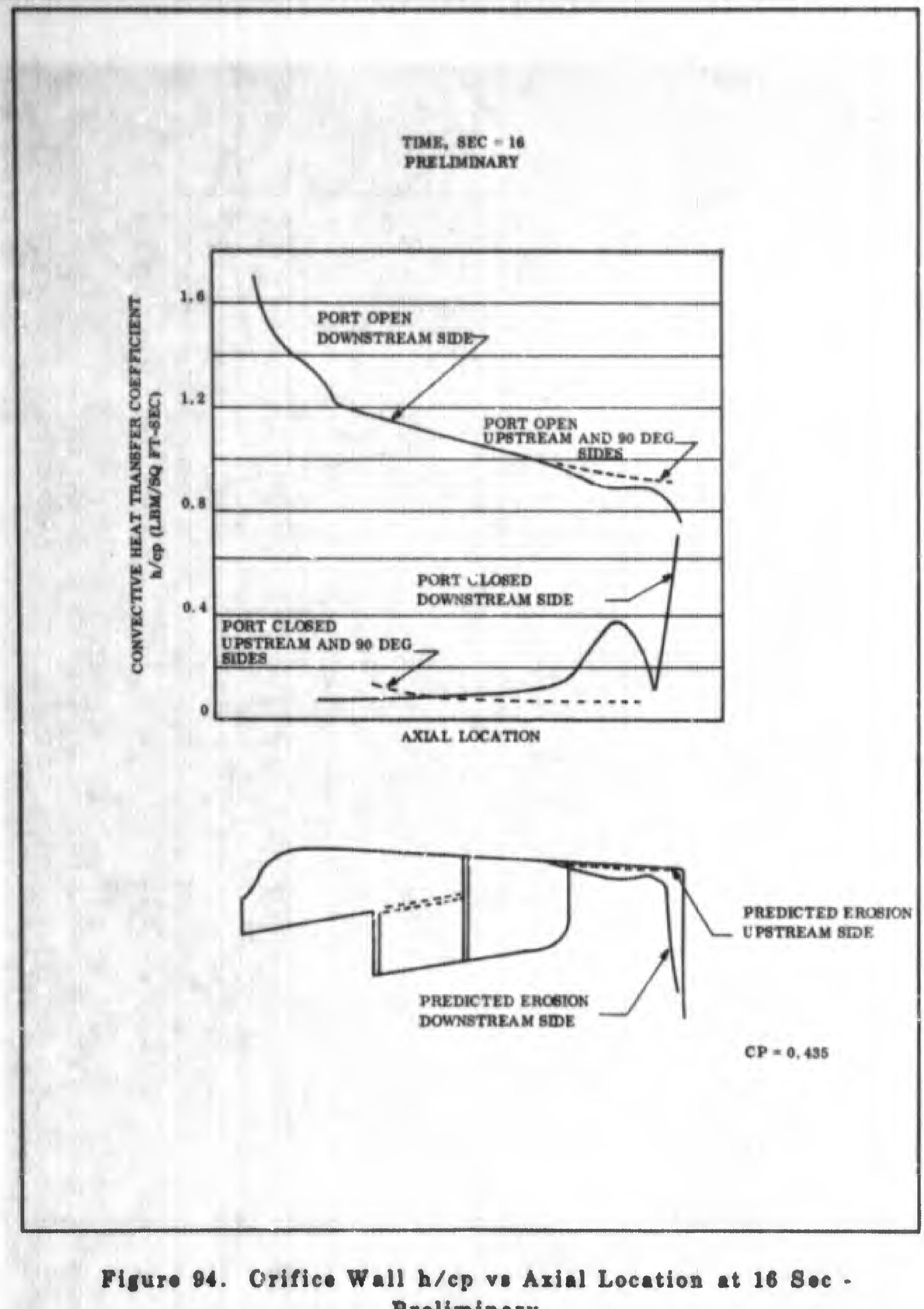

Figure 94. Orifice Wall h/cp vs Axial Location at 16 Sec - Preliminary

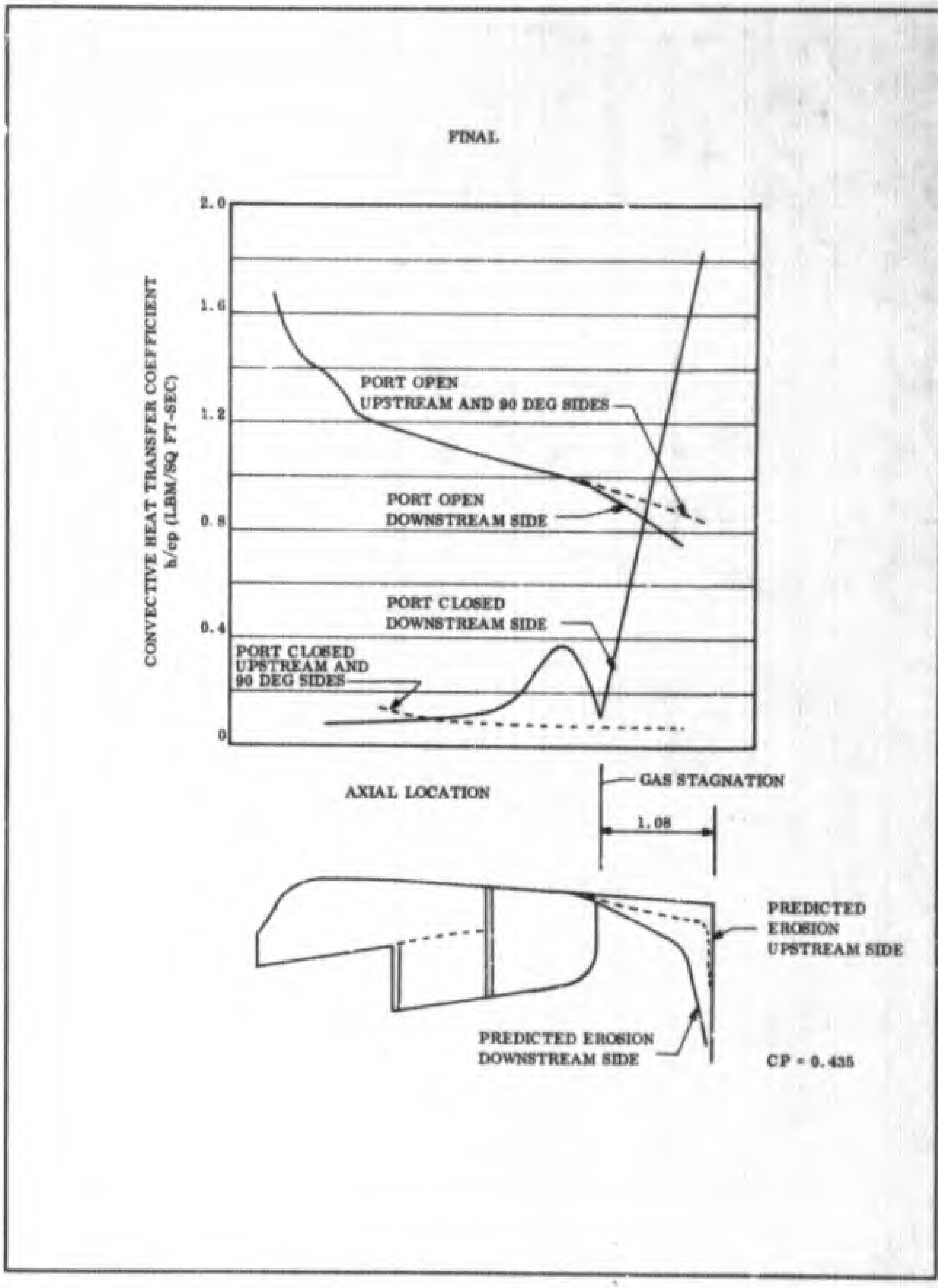

Figure 95. Orifice Wall h/cp vs Axial Location at 25 Sec - Final

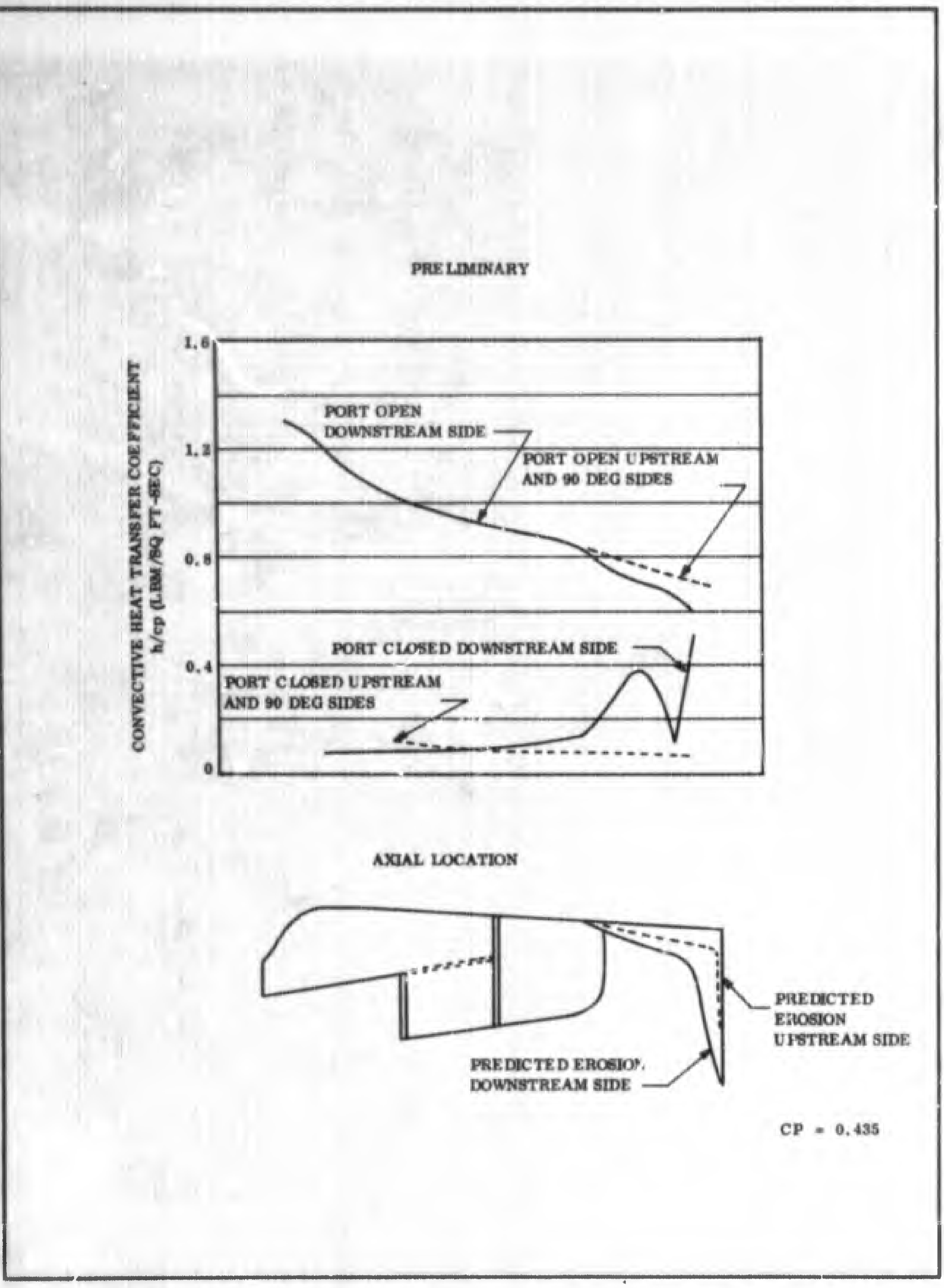

Figure 96. Orifice Wall h/cp vs Axial Location at 25 Sec - Preliminary

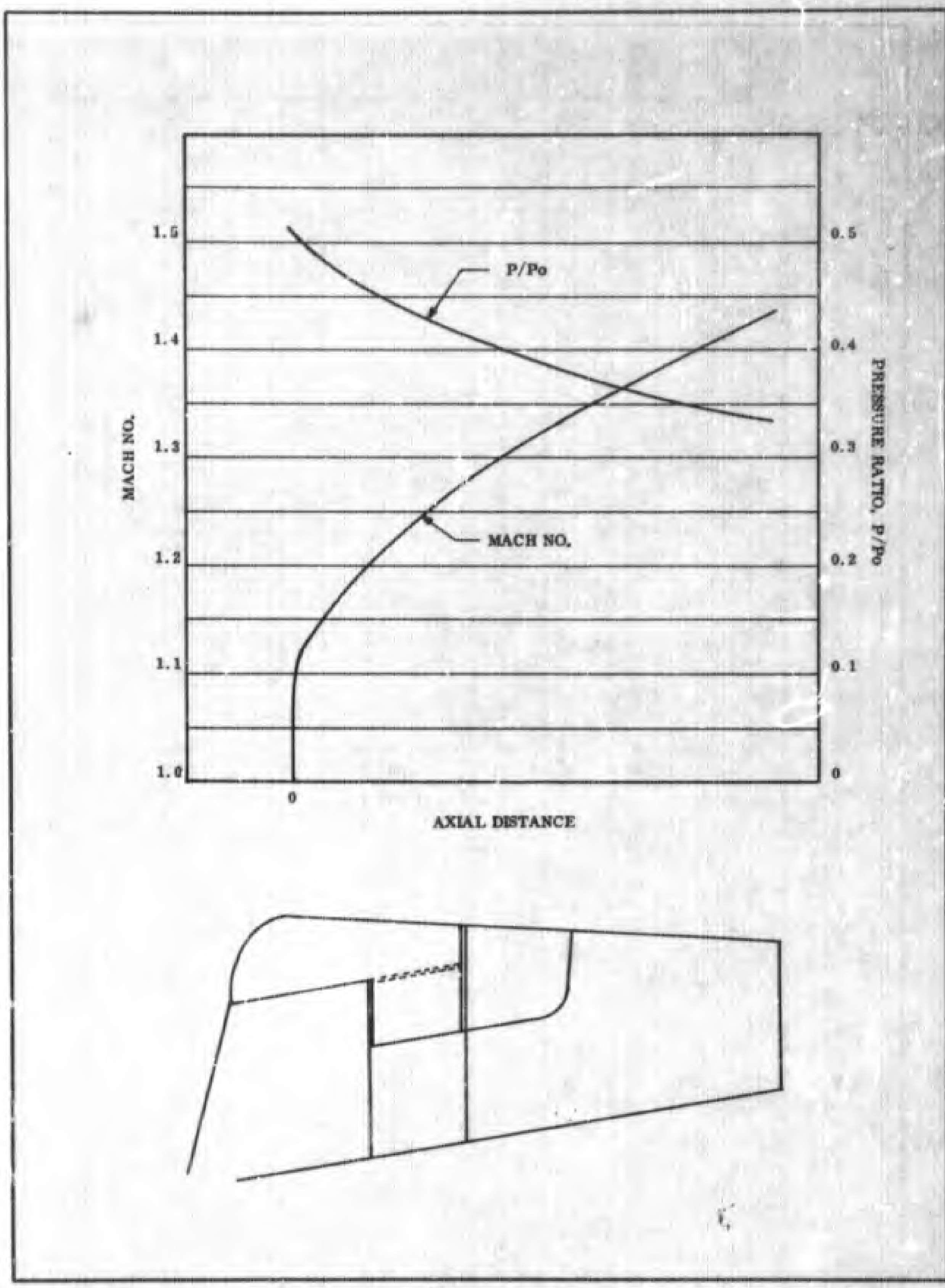

Figure 97. Orifice Wall Pressure Ratio and Mach Number - Port Open

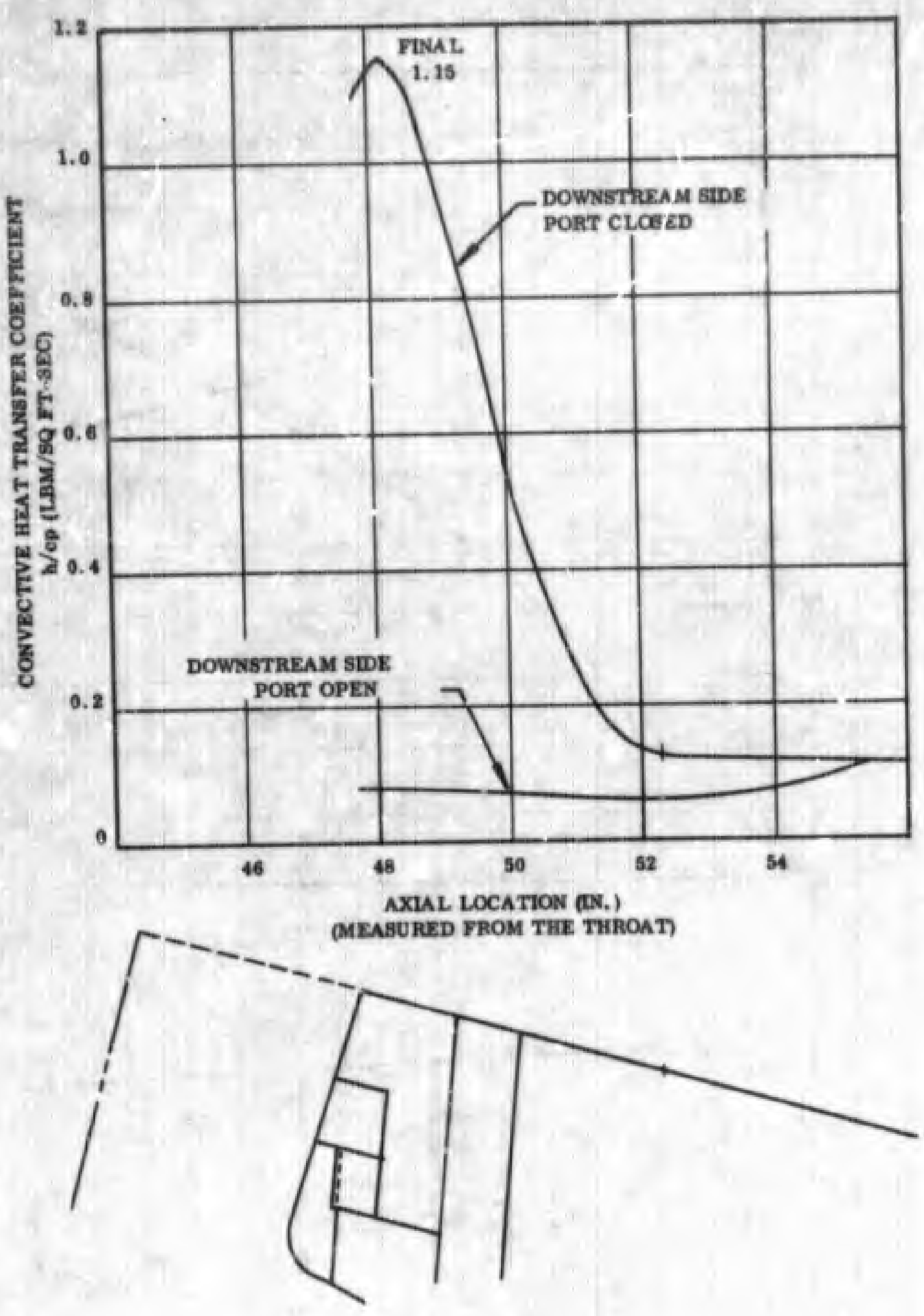

Figure 98. Downstream Nozzle Wall h/cp vs Axial Location - Port Open and Closed

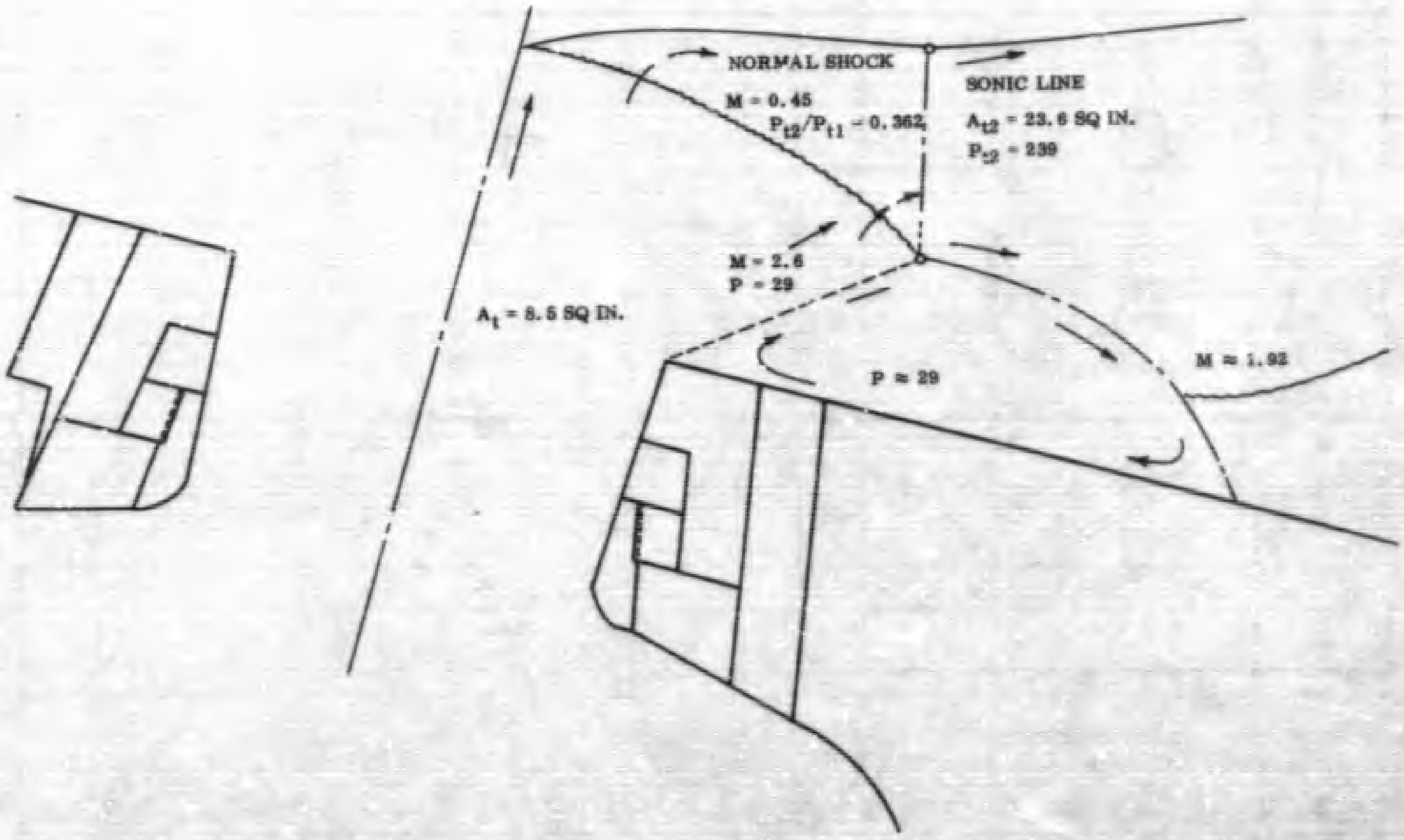

Figure 99. Injection Flow Conditions in the Nozzle

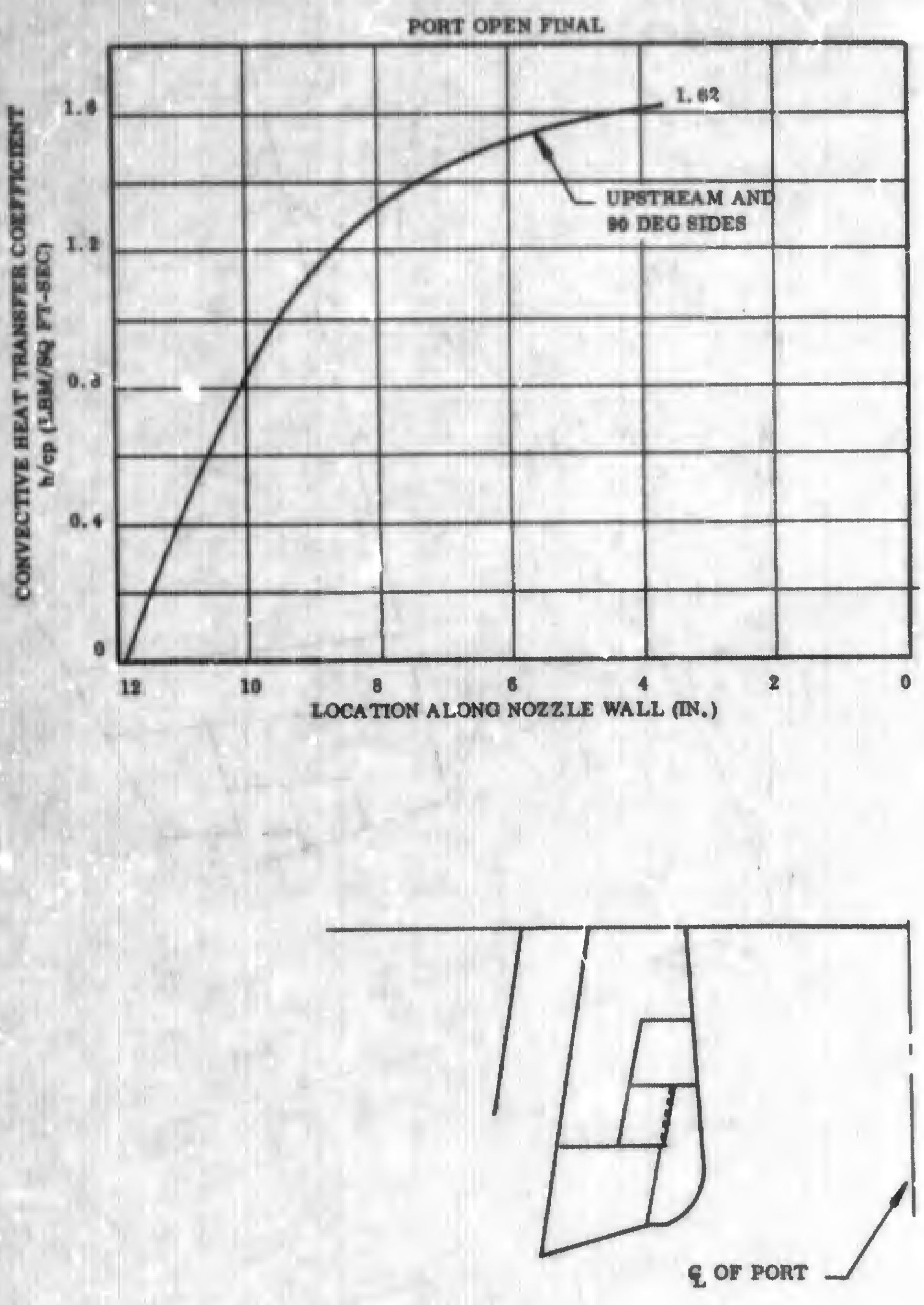

Figure 100. Upstream Nozzle Wall h/cp vs Axial Location - Port Open

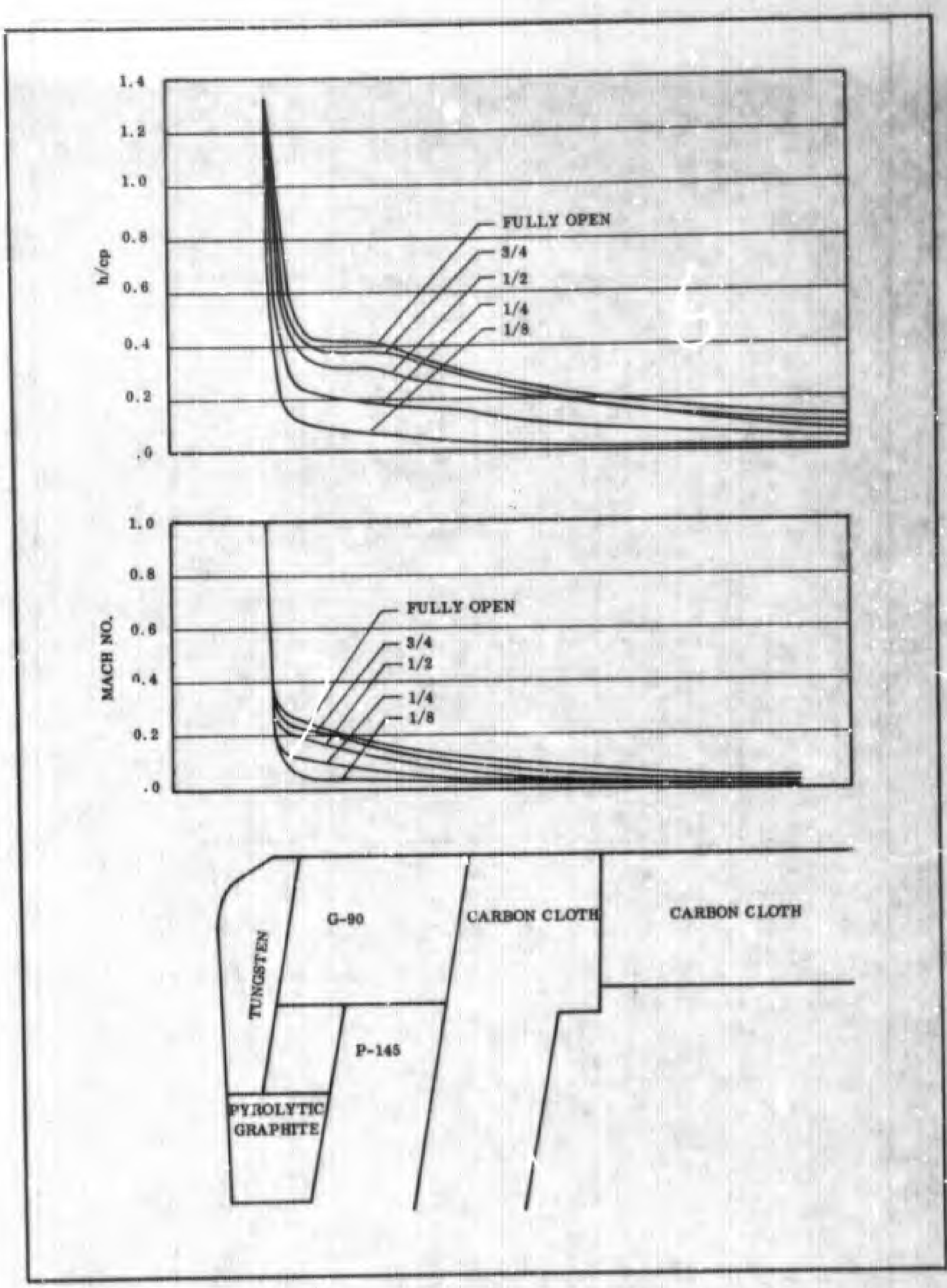

Figure 101. Inlet h/cp vs Axial Location - Port Open

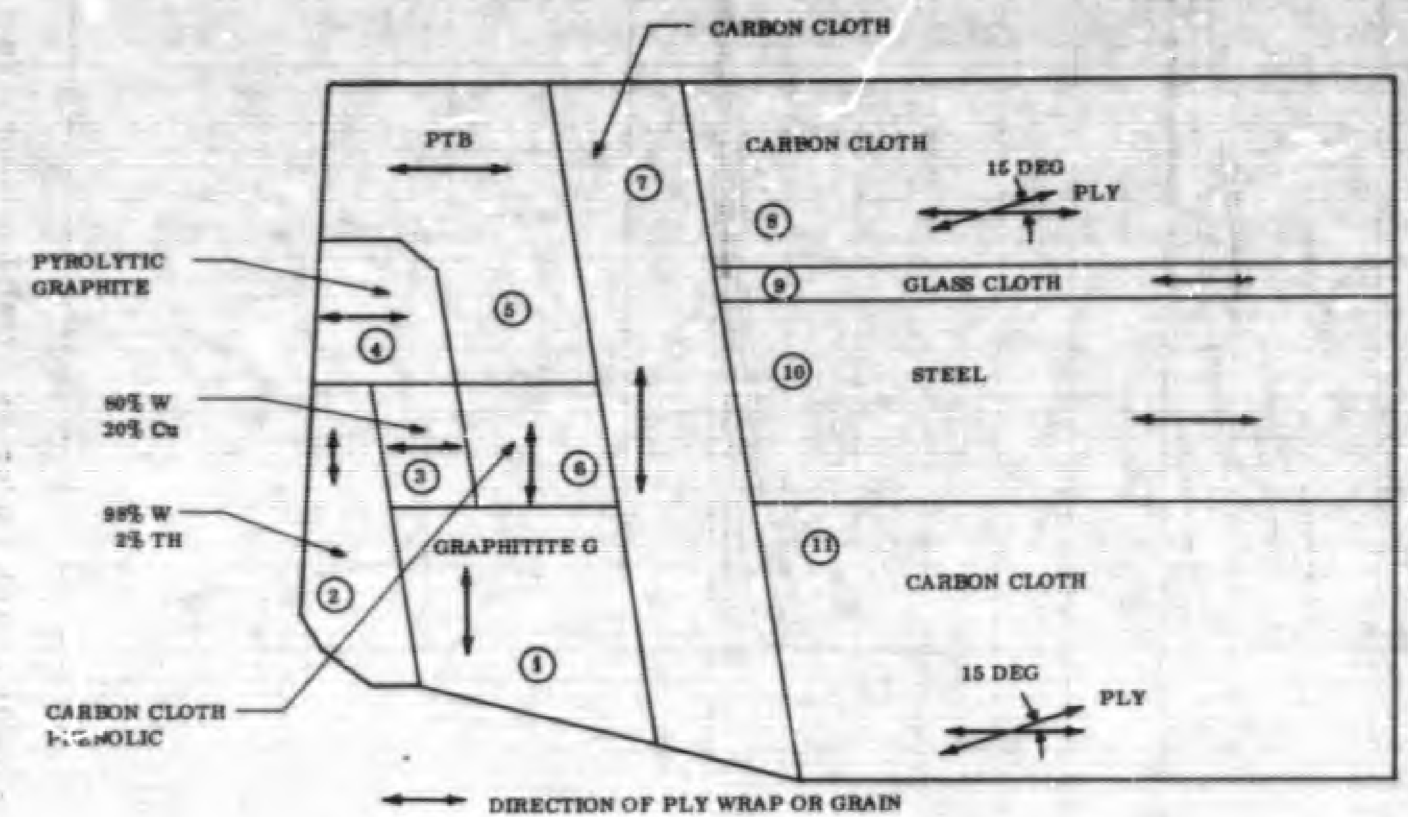

Figure 102. Preliminary Thermal Gradients - Element Material Identification

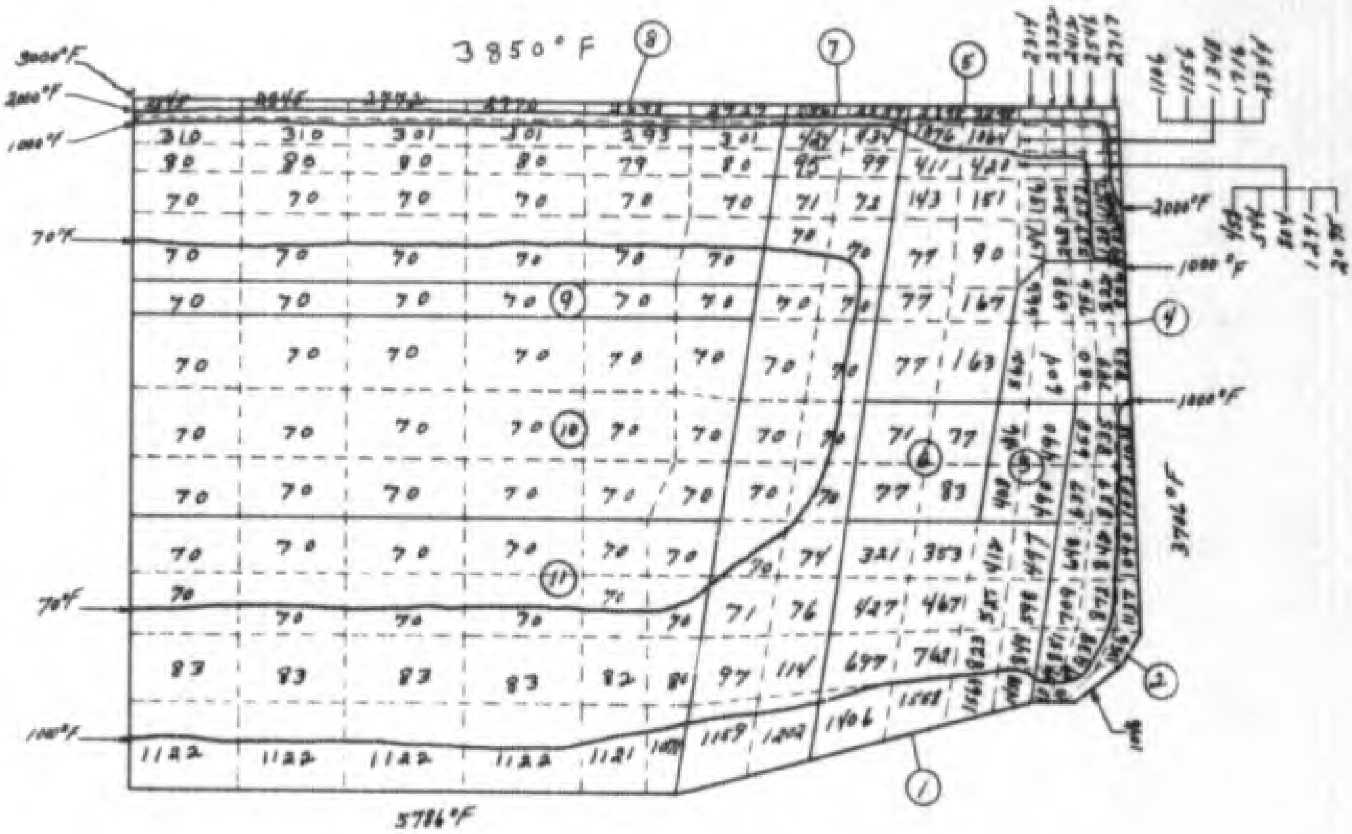
3850° F
3000°F
2000°F
1000°F
70°F
70°F
100°F
5786°F
3706°F
2000°F
1000°F
1000°F

A

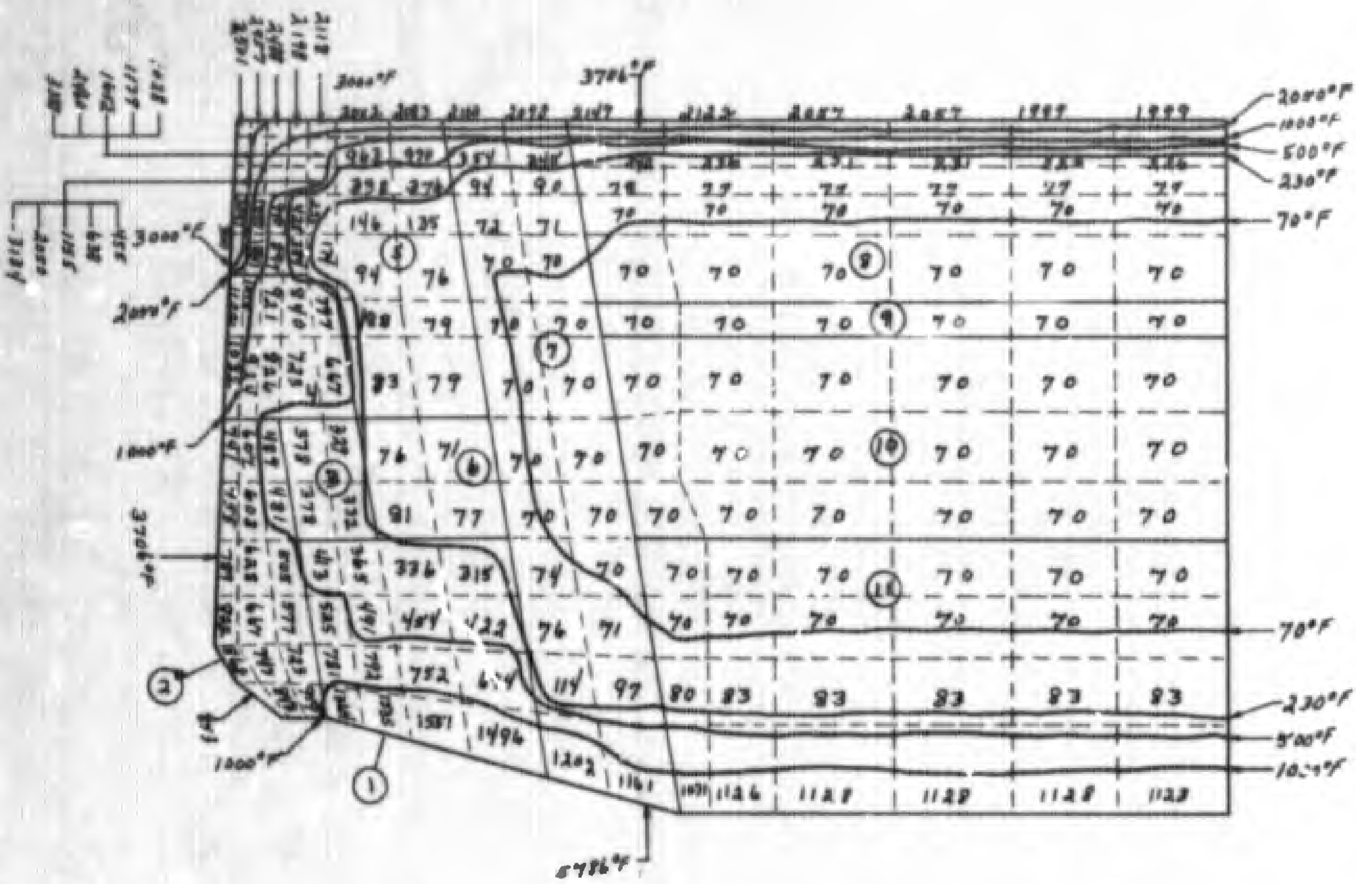

Figure 103. Preliminary Upstream and Downstream Thermal Gradients at 5 Sec

B

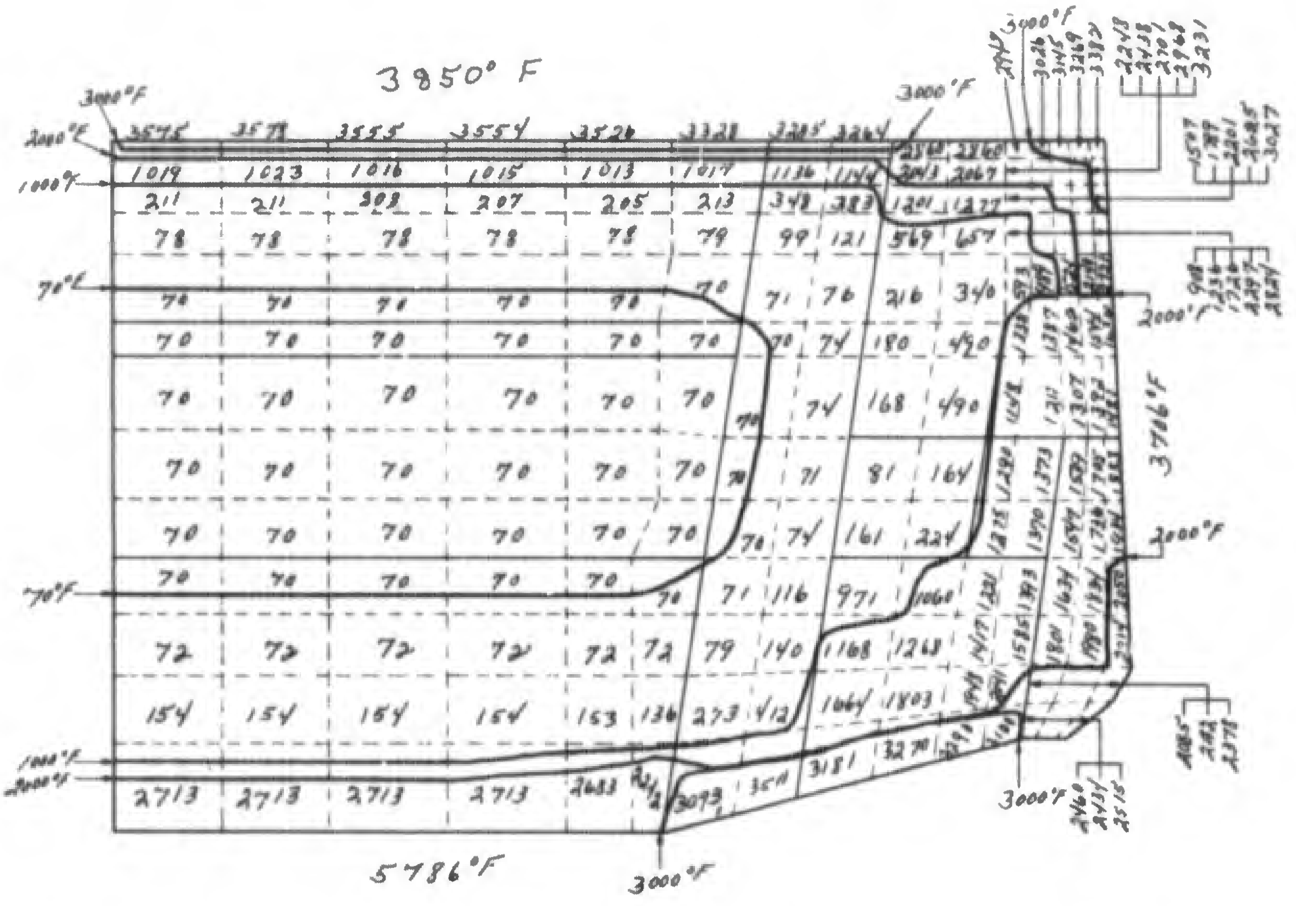

3850° F
3000°F
2000°F
1000°F
70°F
3000°F
2000°F
3786°F
3000°F
5786°F
3000°F

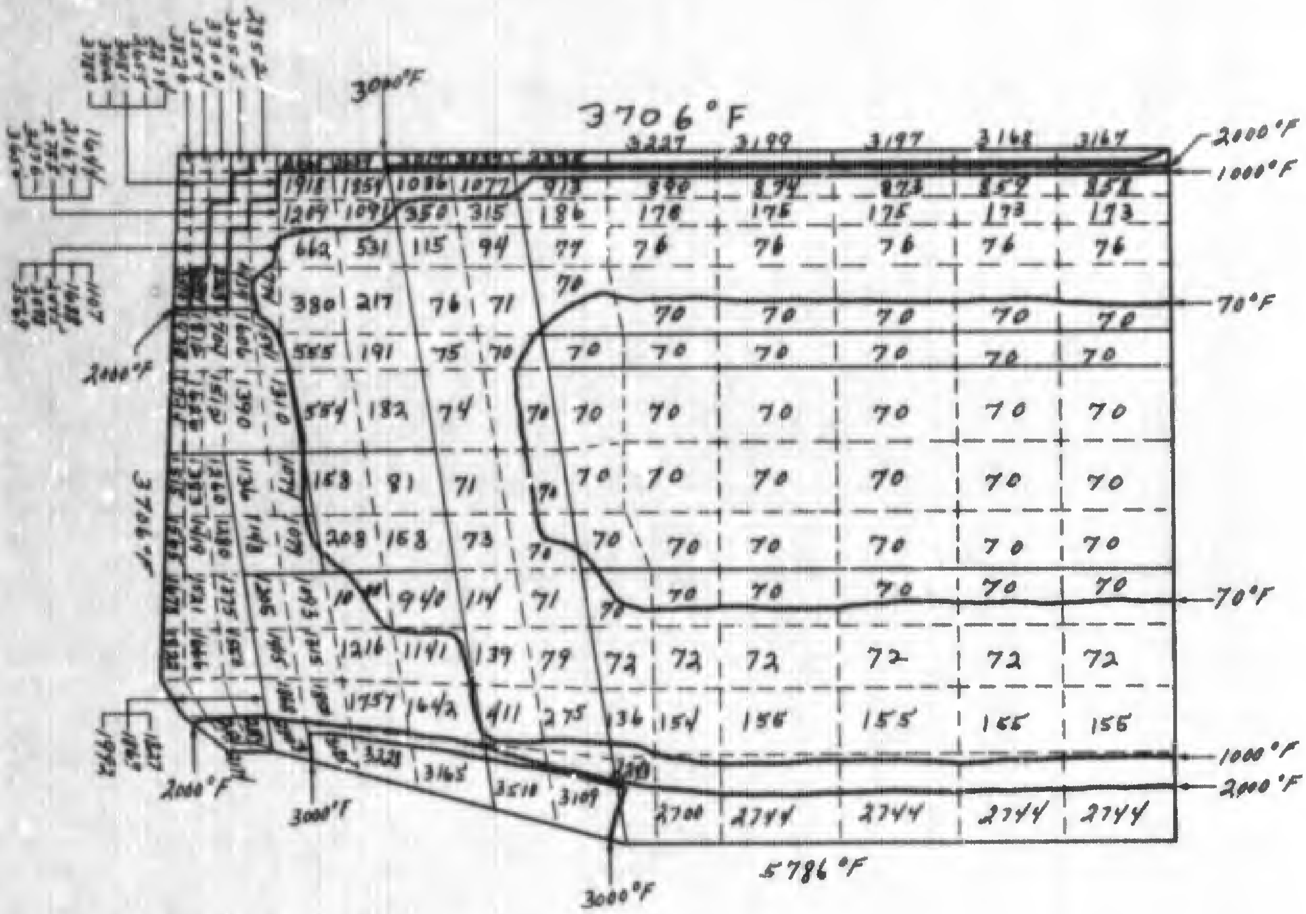

Figure 104. Preliminary Upstream and Downstream Thermal Gradients at 16.0 Sec

B

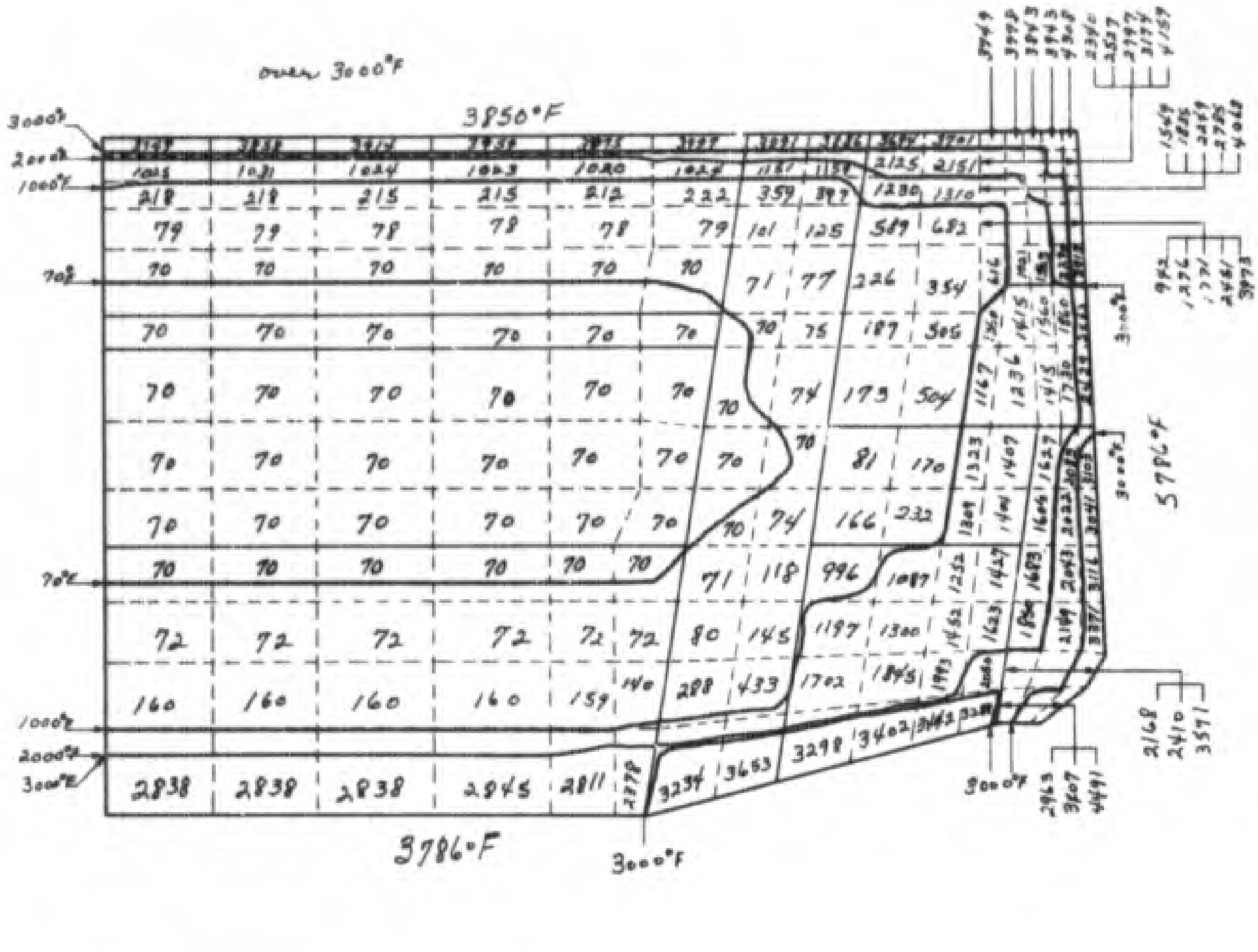
over 3000°F
3850°F
3000°F
2000°F
1000°F
70°F
3786°F

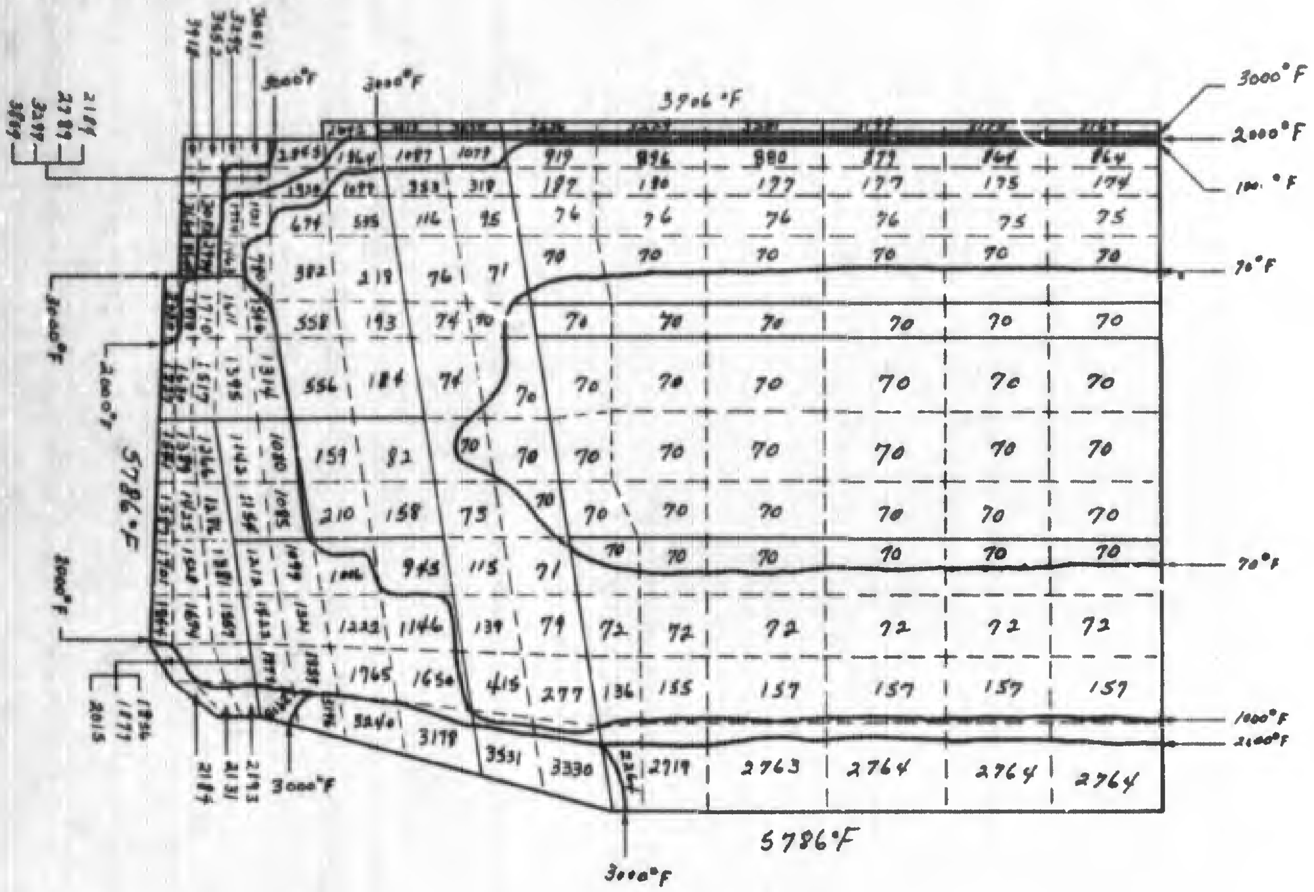

Figure 105. Preliminary Upstream and Downstream Thermal Gradients at 16.1 Sec

B

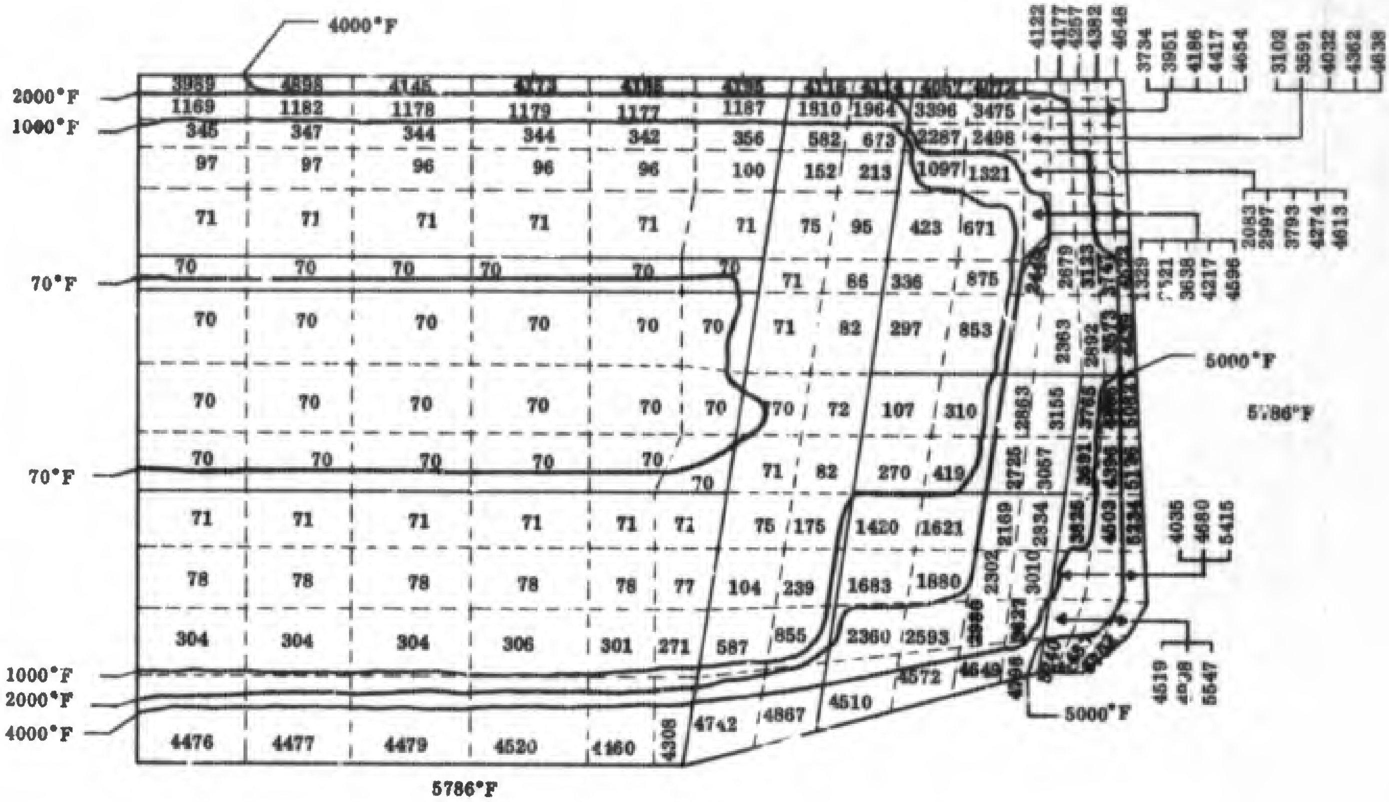
4000°F
2000°F
1000°F
70°F
70°F
1000°F
2000°F
4000°F
5000°F
5786°F
5000°F
5786°F

A

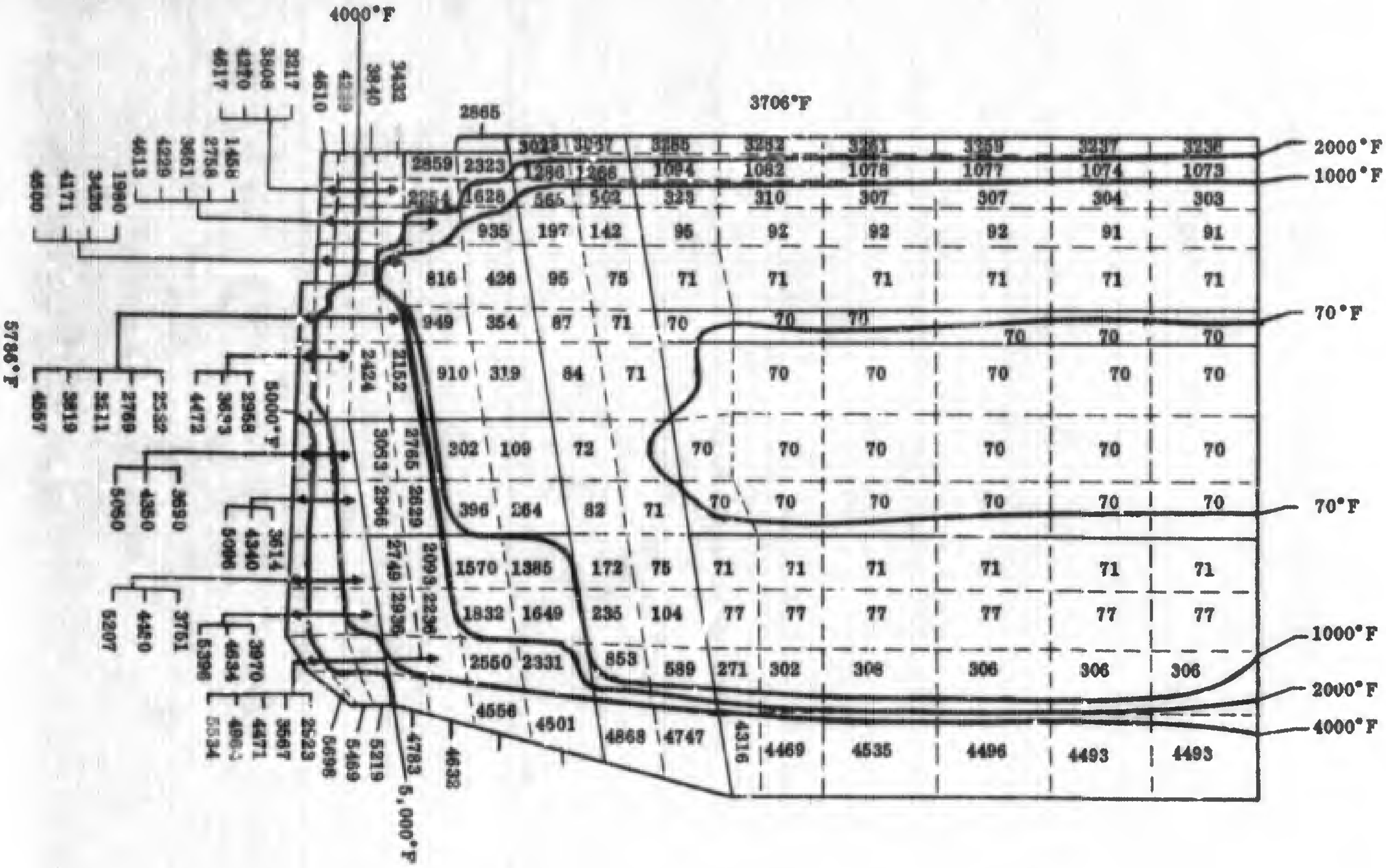

Figure 106. Preliminary Upstream and Downstream Thermal Gradients at 25.0 Sec

B

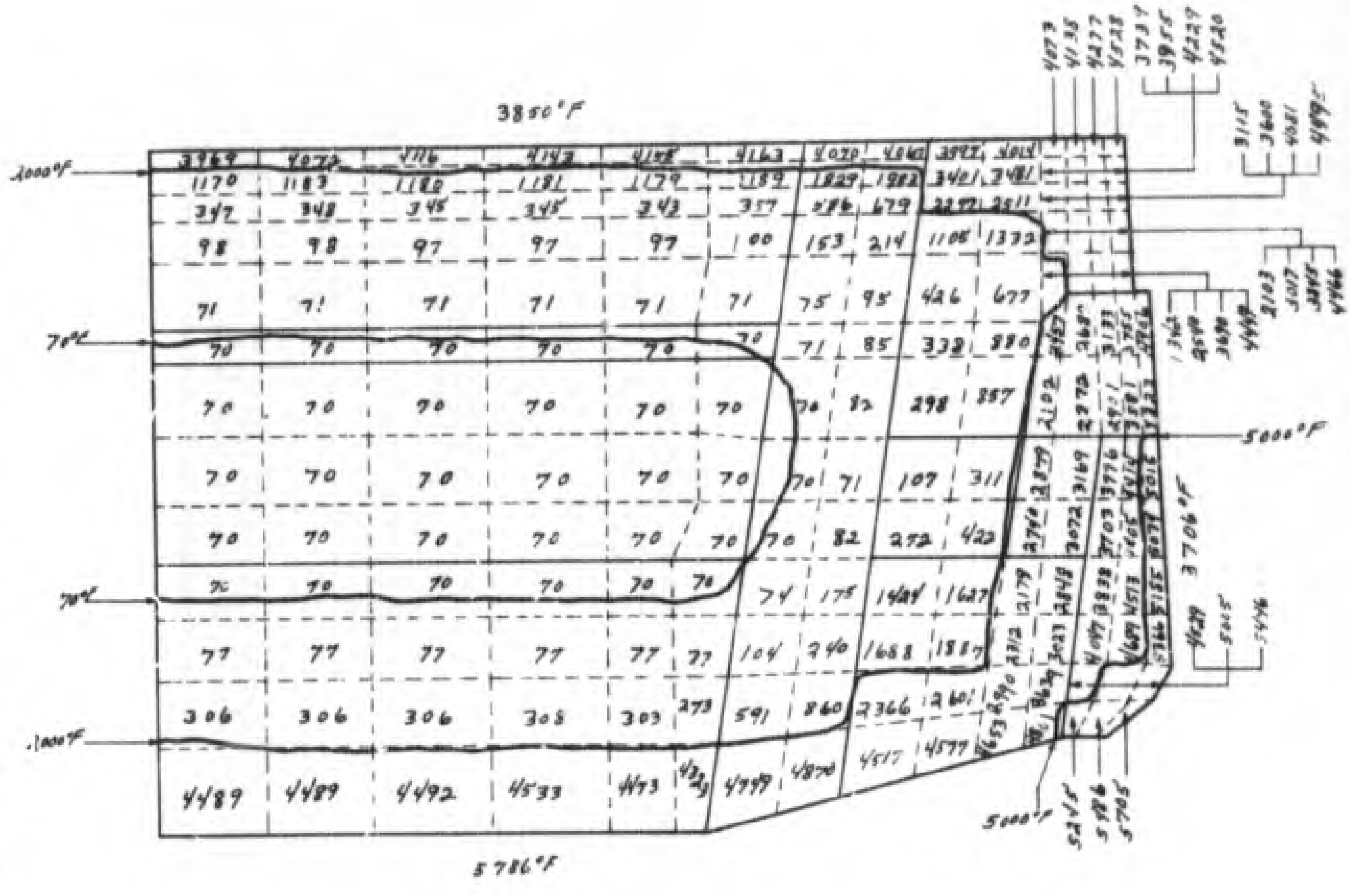

3850°F
1000°F
70°F
70°F
1000°F
5000°F
3706°F
5000°F
5786°F

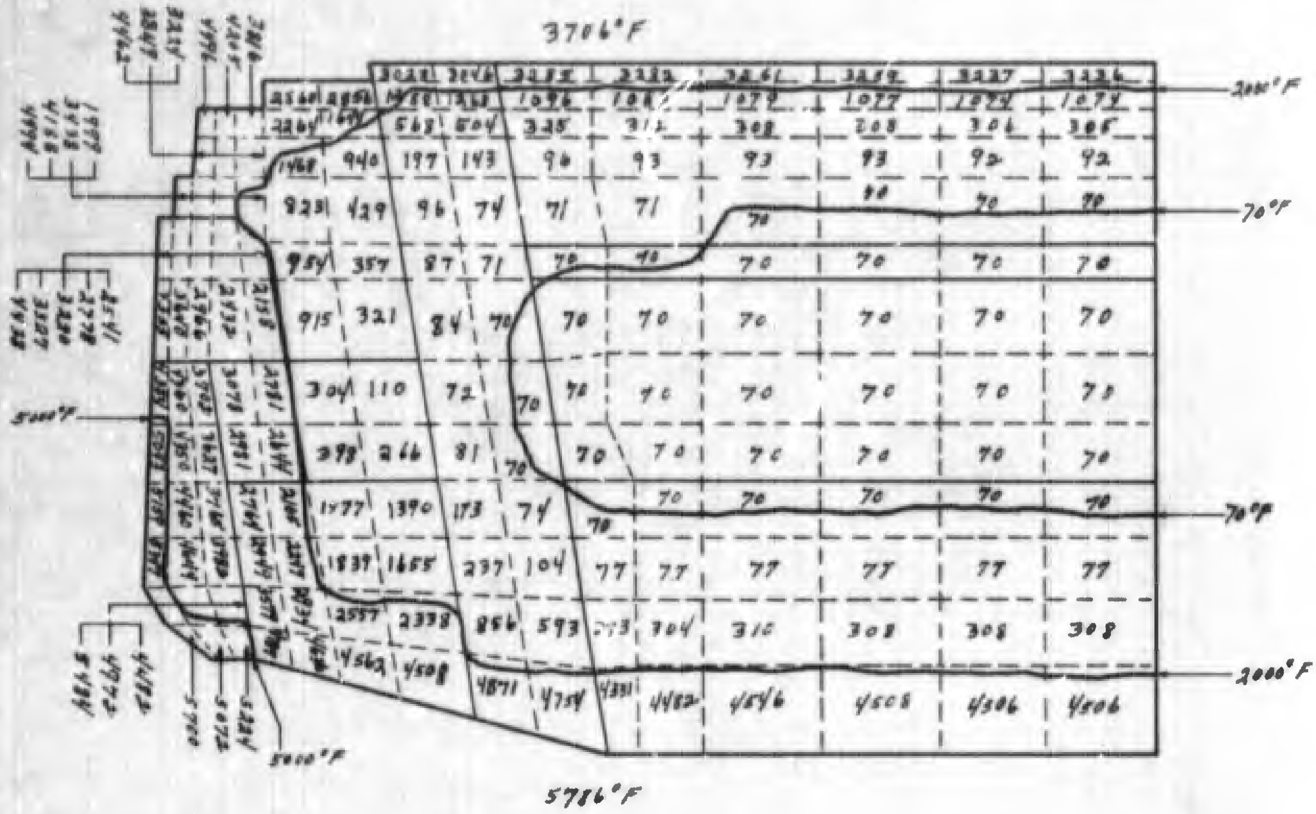

Figure 107. Preliminary Upstream and Downstream Thermal Gradients at 25.1 Sec

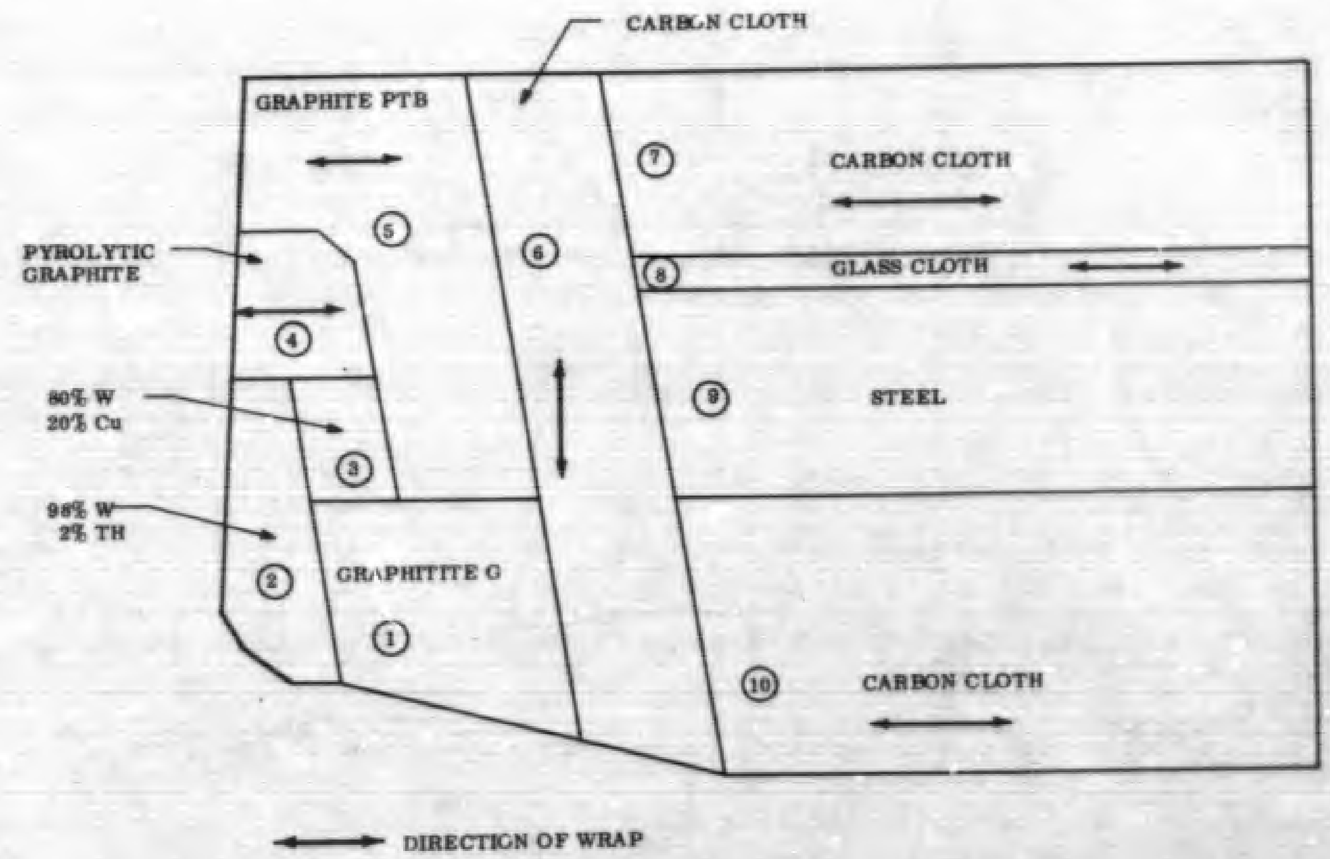

Figure 108. Final Thermal Gradients - Element Material Identification

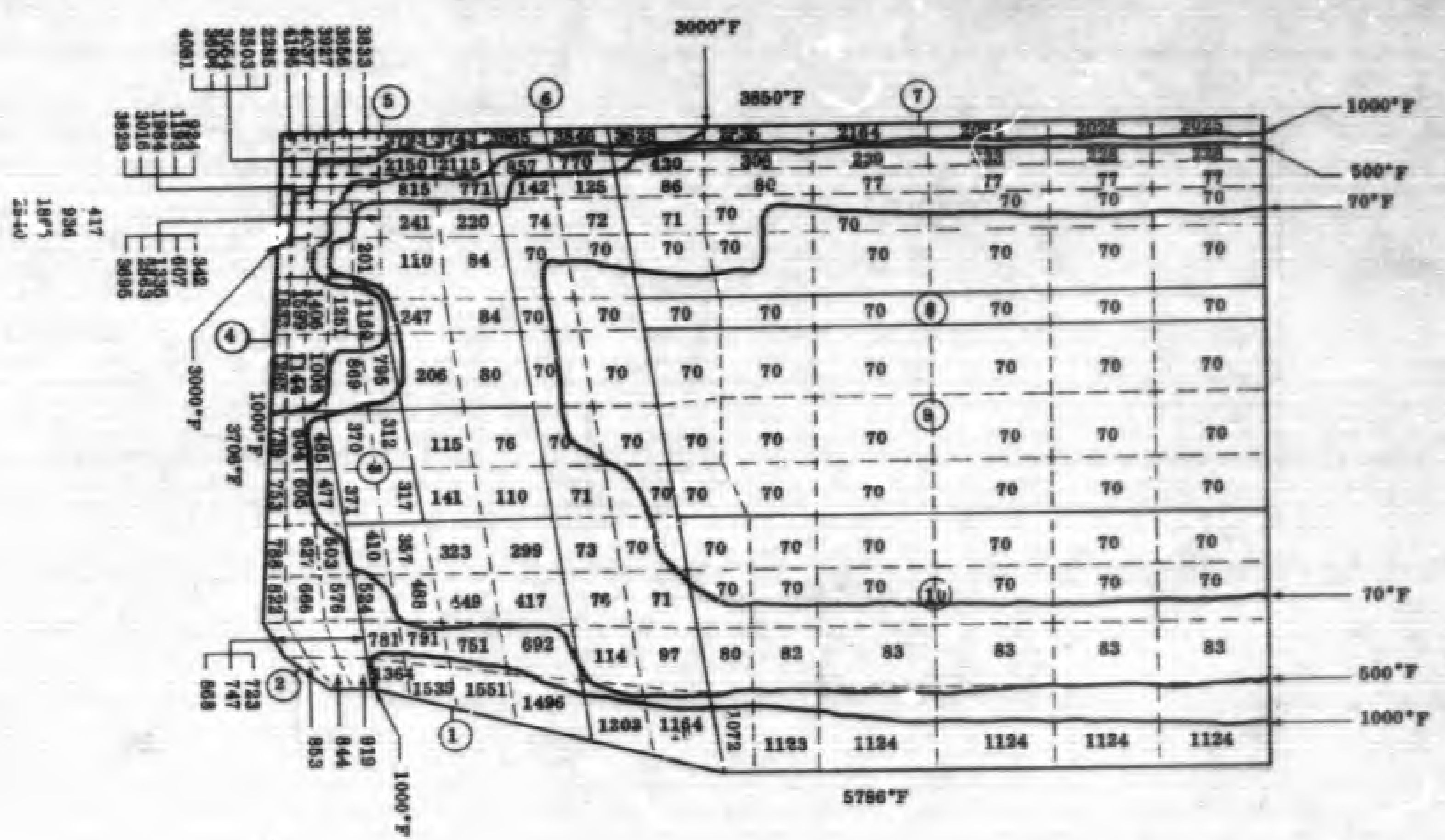

Figure 109. Final Downstream Thermal Gradients at 5 Sec

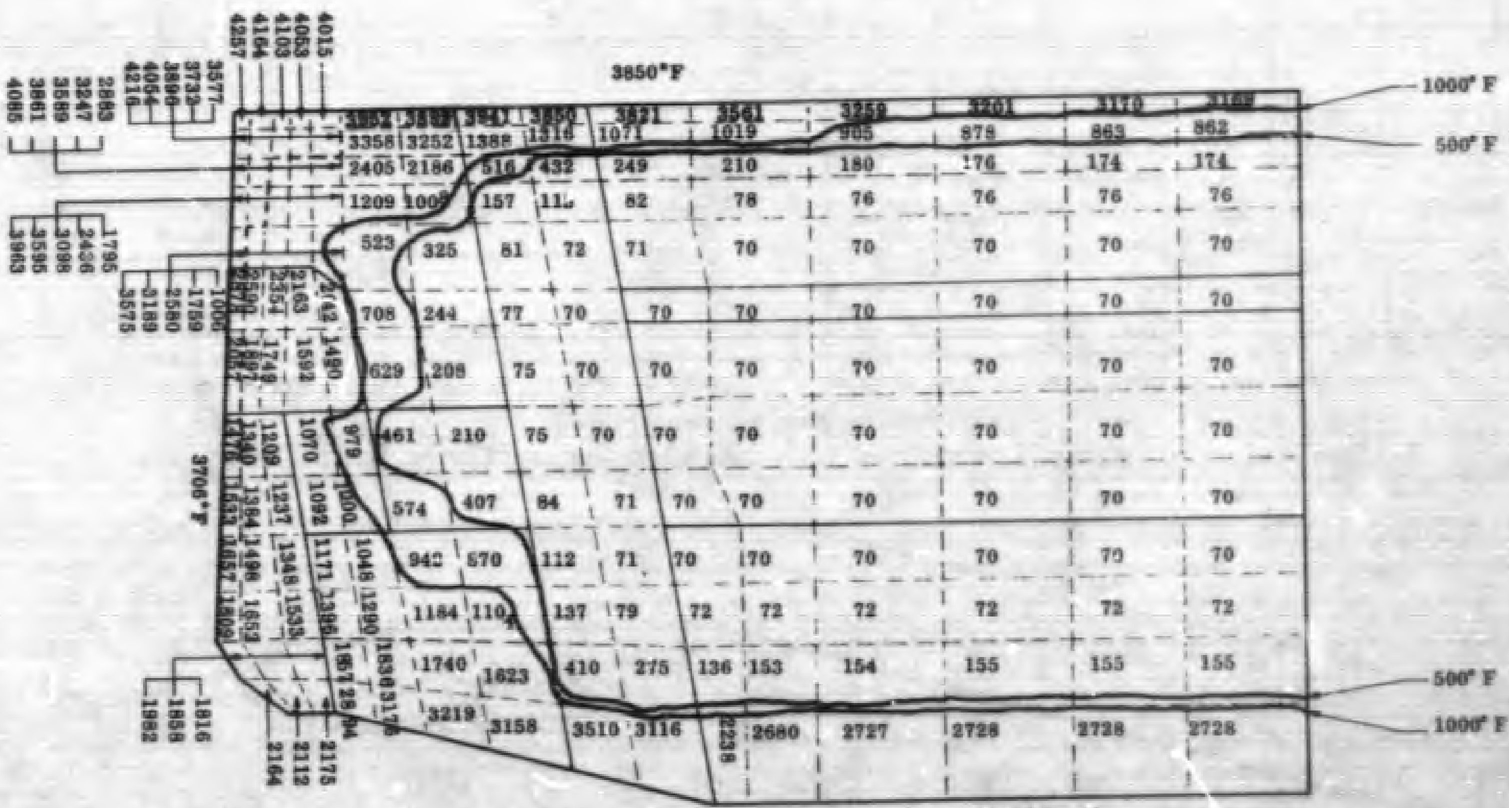

Figure 110. Final Downstream Thermal Gradients at 16.0 Sec

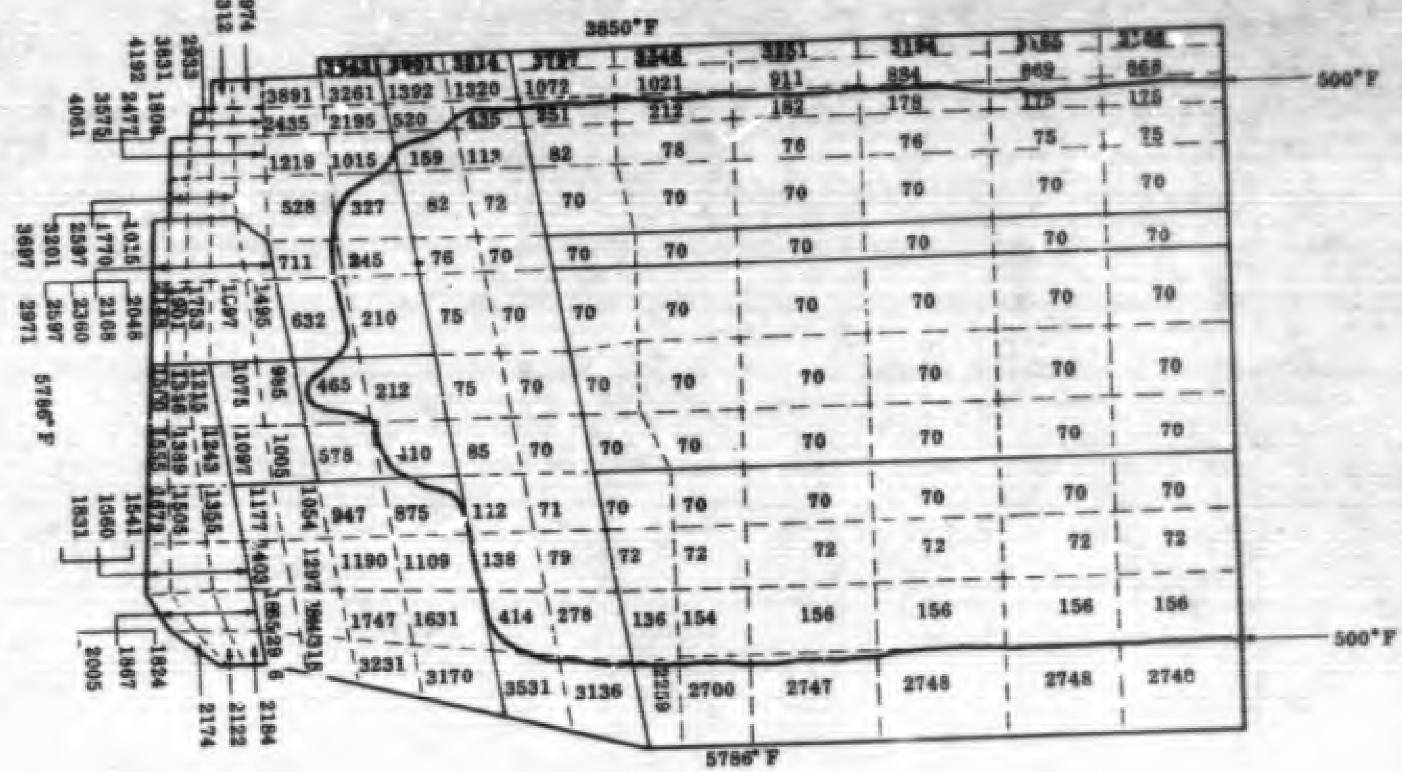

Figure 111. Final Downstream Thermal Gradients at 16.1 Sec

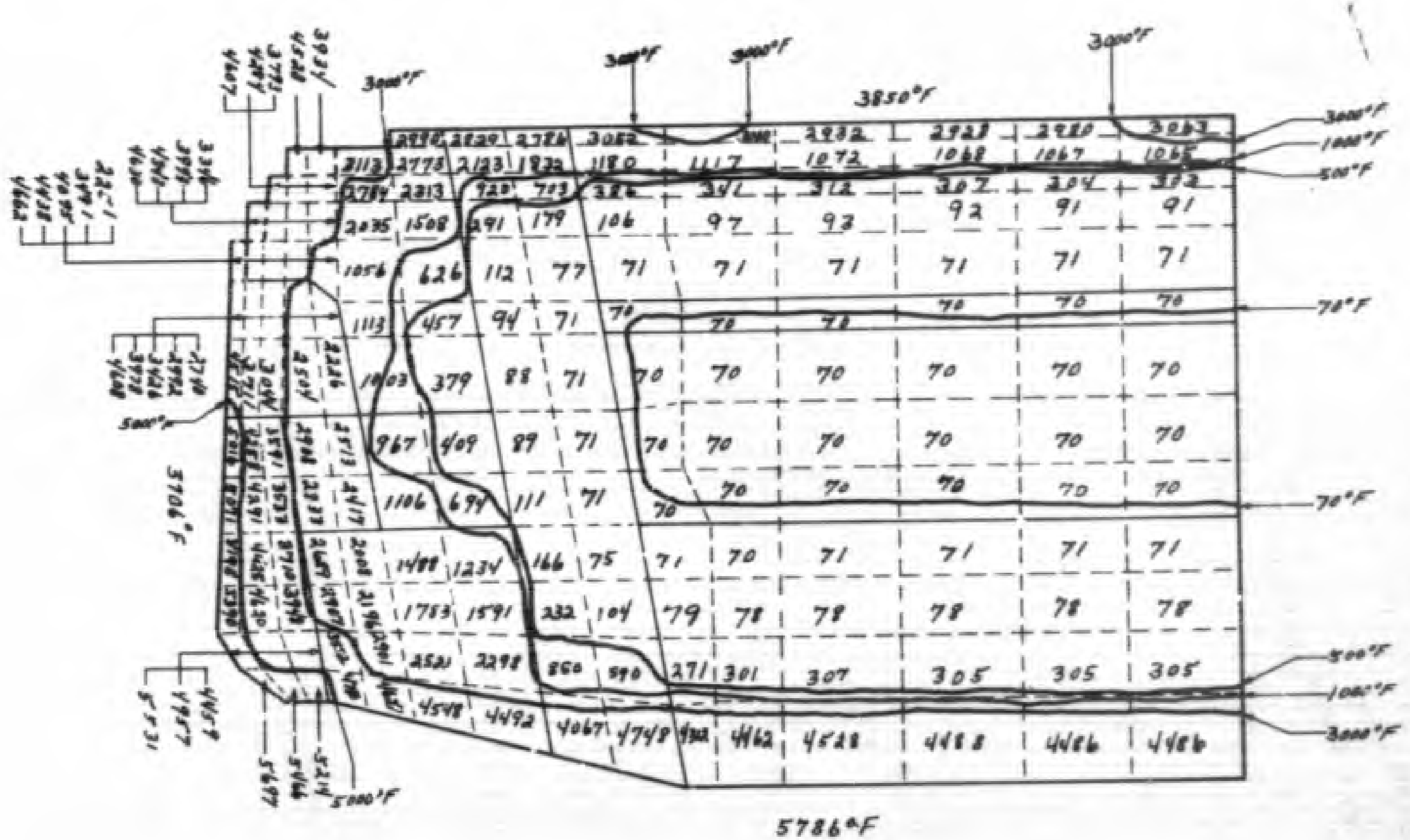

Figure 112. Final Downstream Thermal Gradients at 25.0 Sec

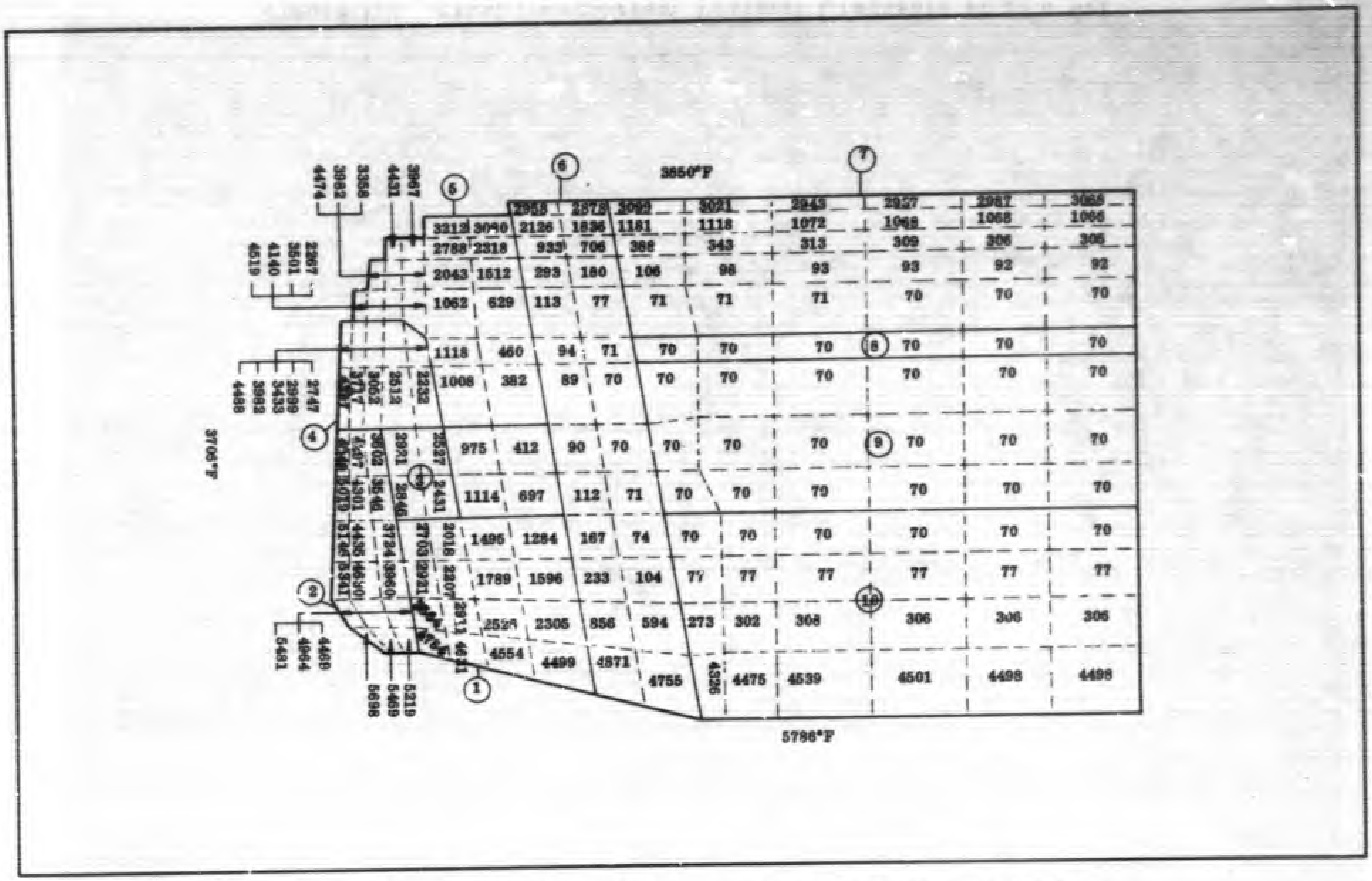

Figure 113. Final Thermal Gradients, Downstream at 25.1 Sec

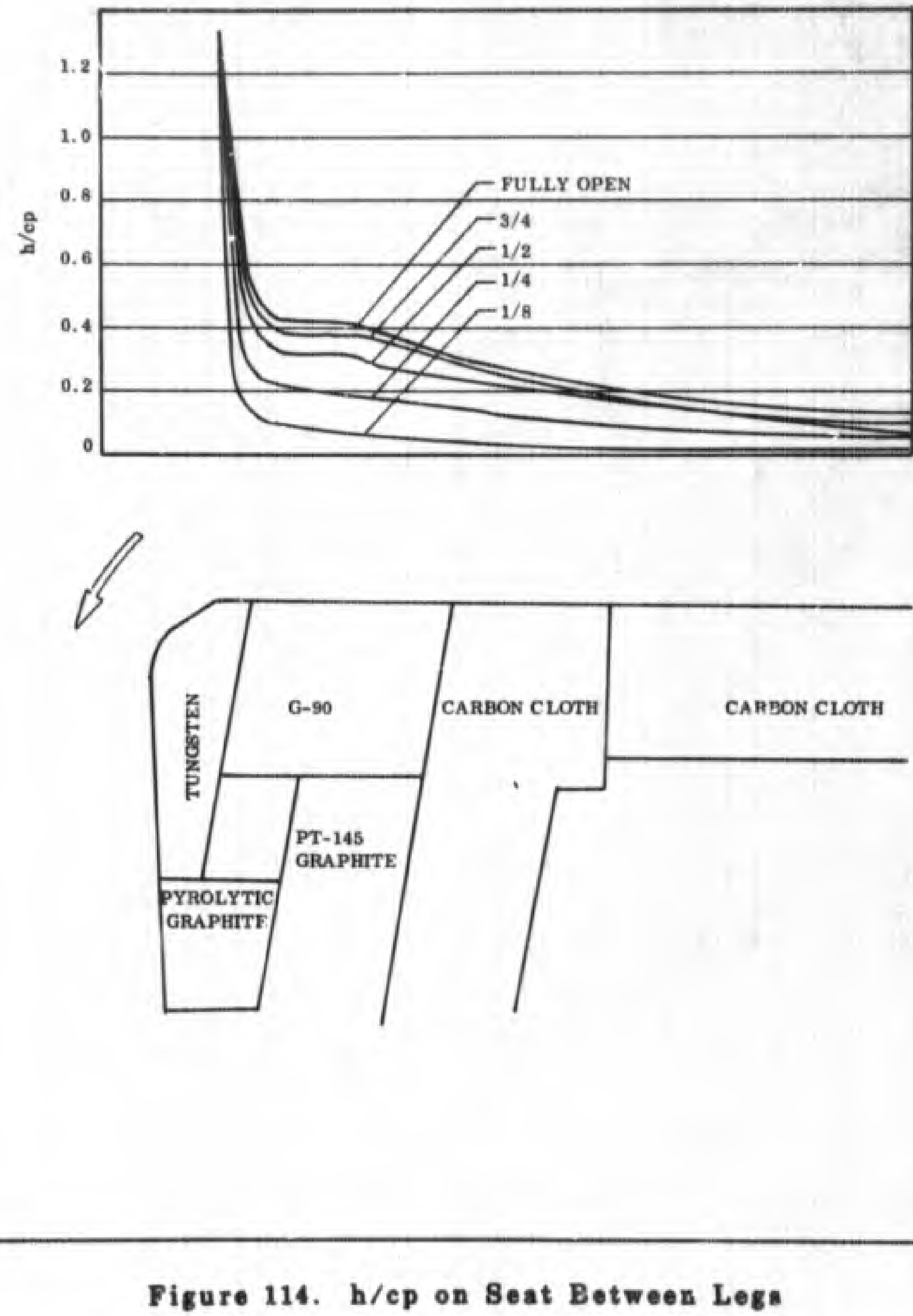

Figure 114. h/cp on Seat Between Legs

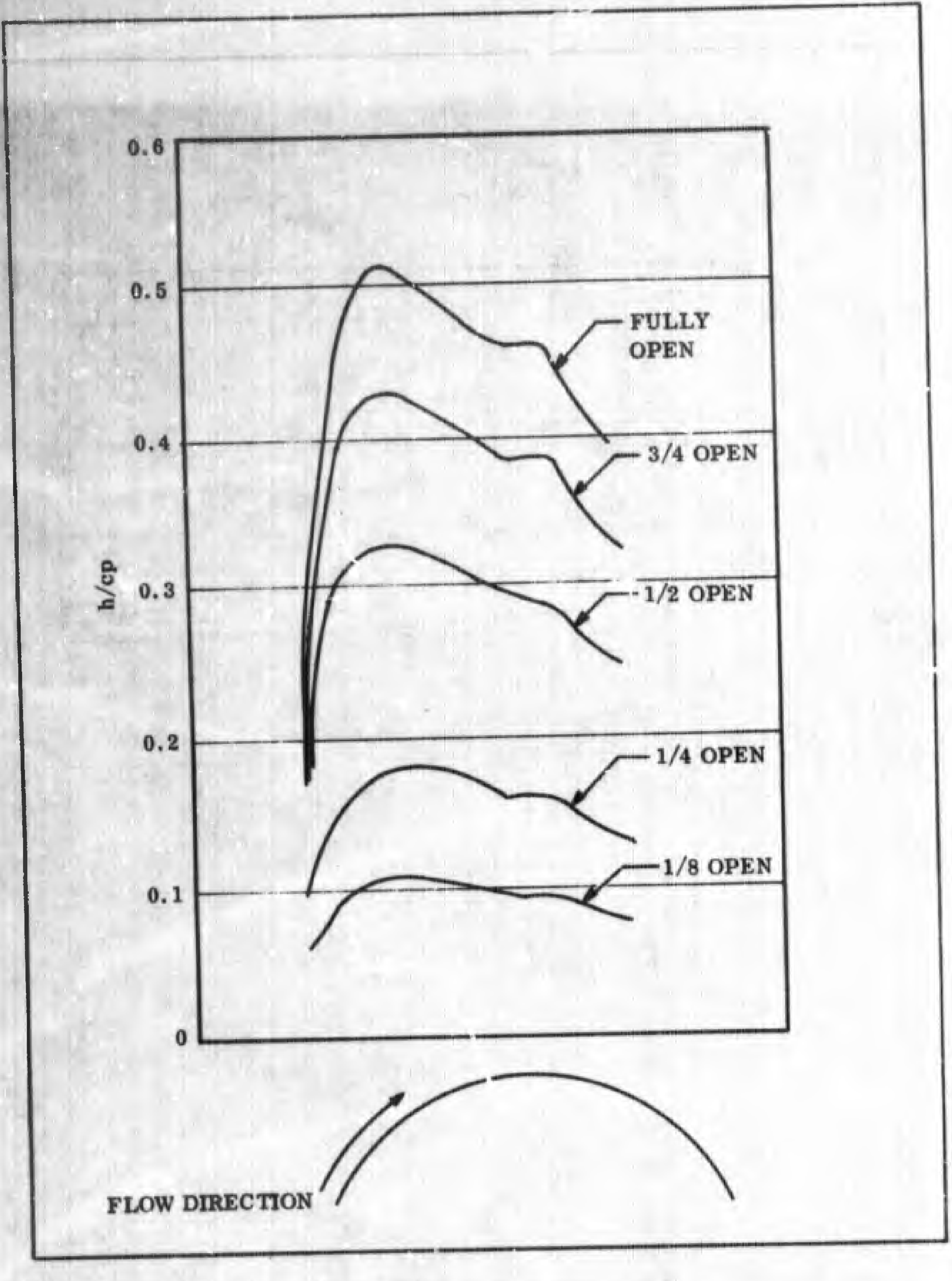

Figure 115. h/cp Around Support Leg

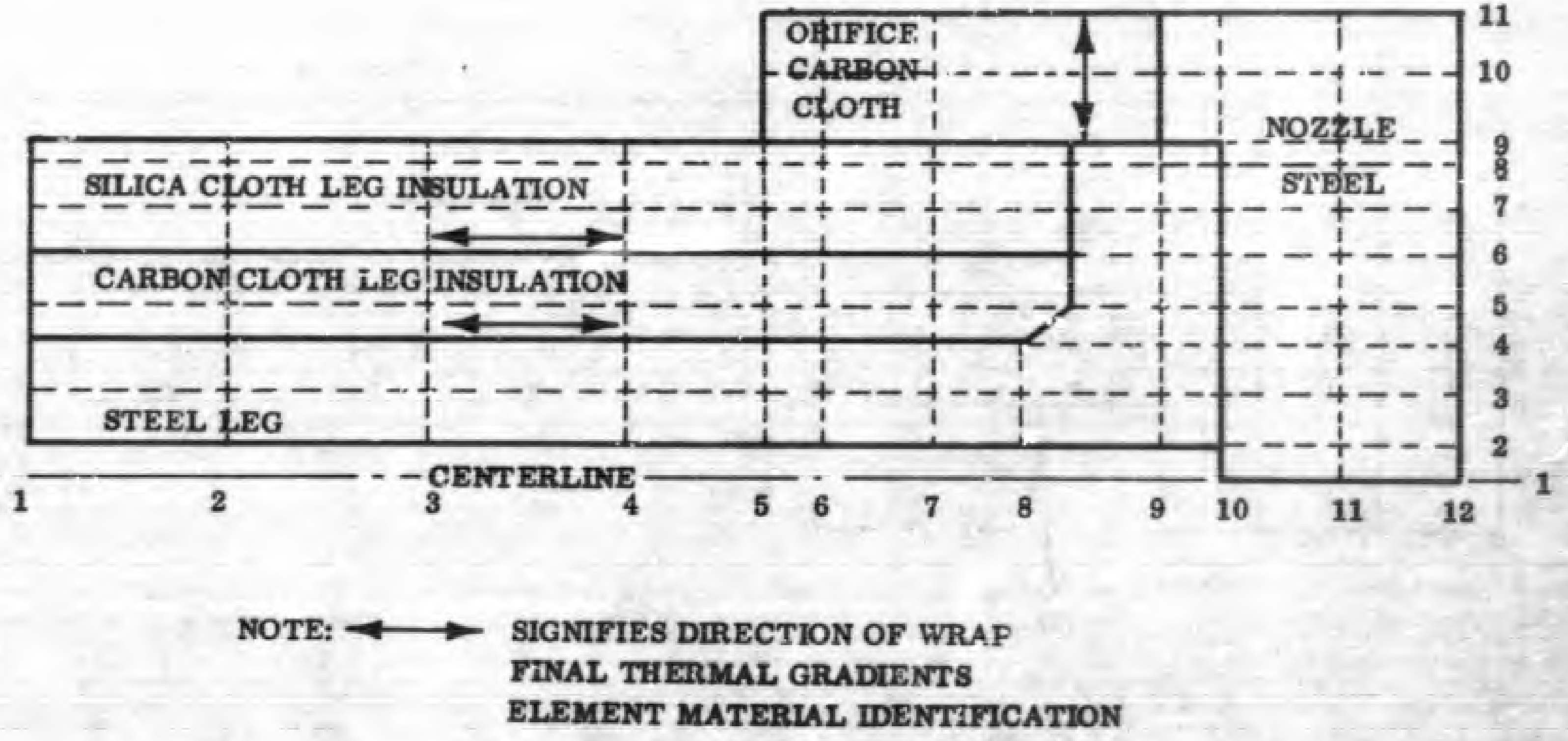

Figure 116. Final Thermal Gradients, Element Material Identification - Legs

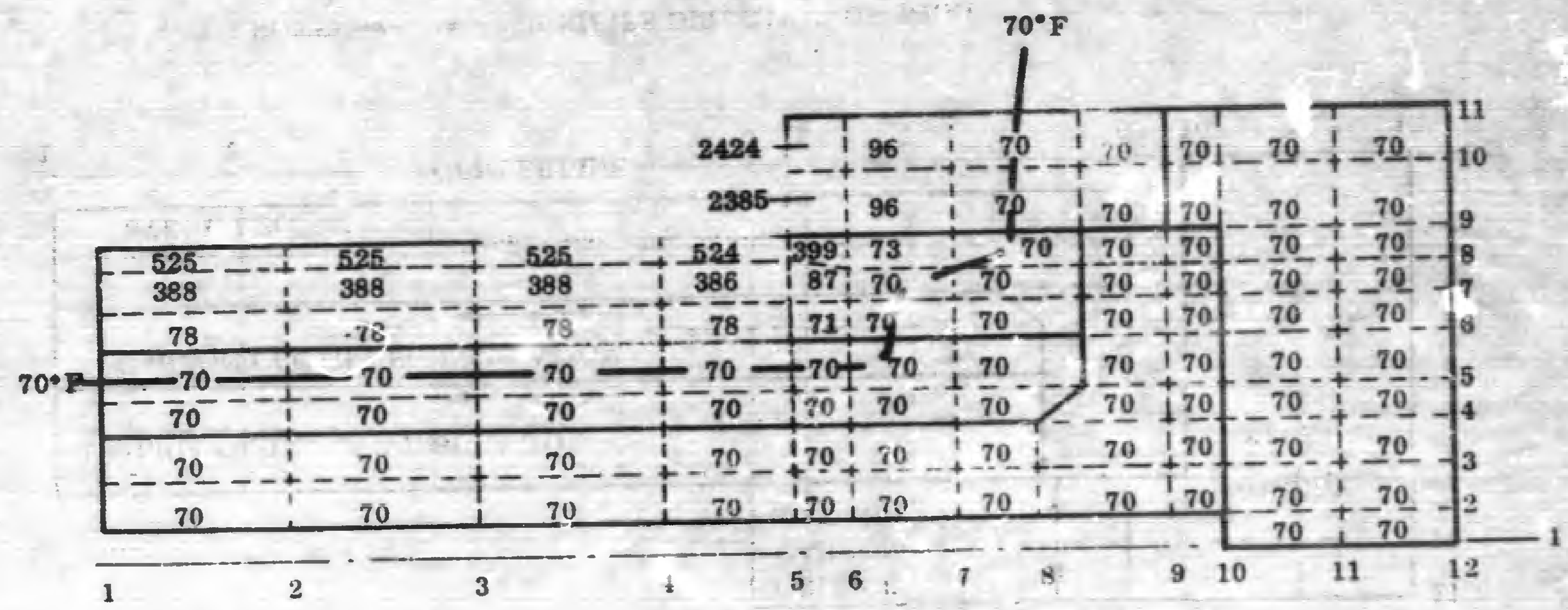

Figure 117. Leg Thermal Gradients at 5.0 Sec

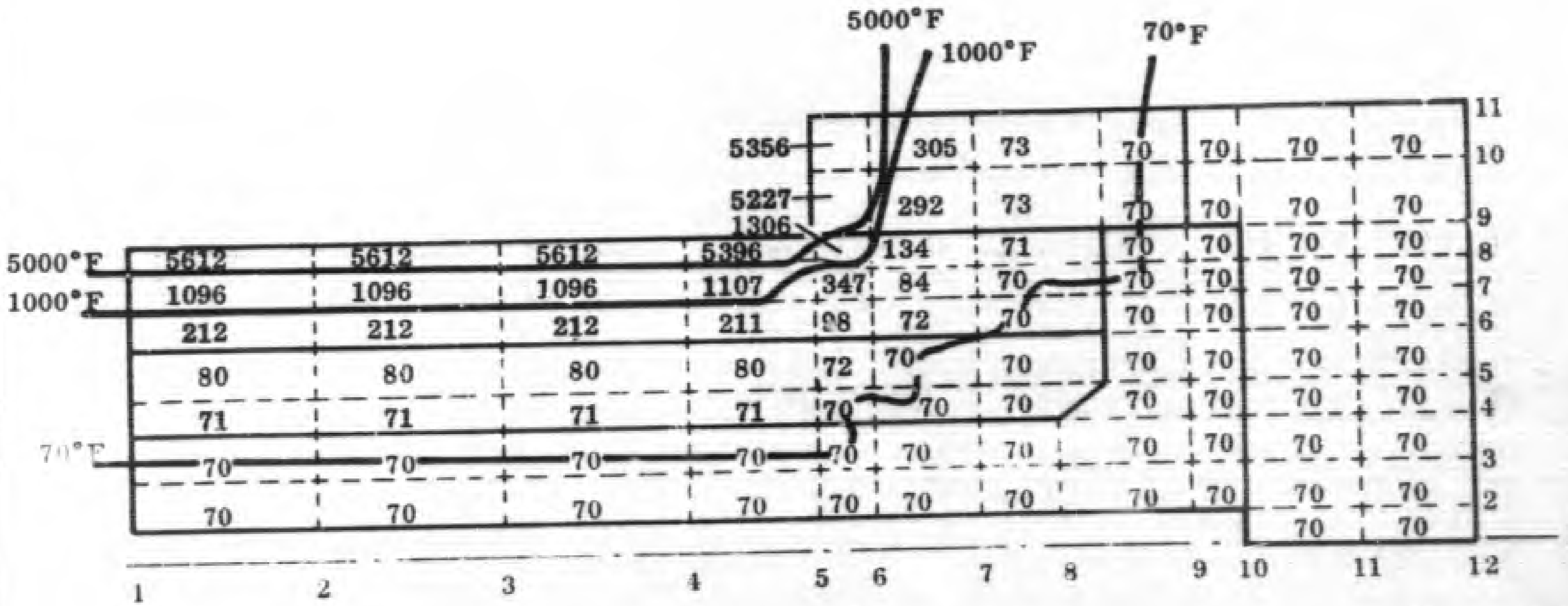

Figure 118. Leg Thermal Gradient at 16.0 Sec

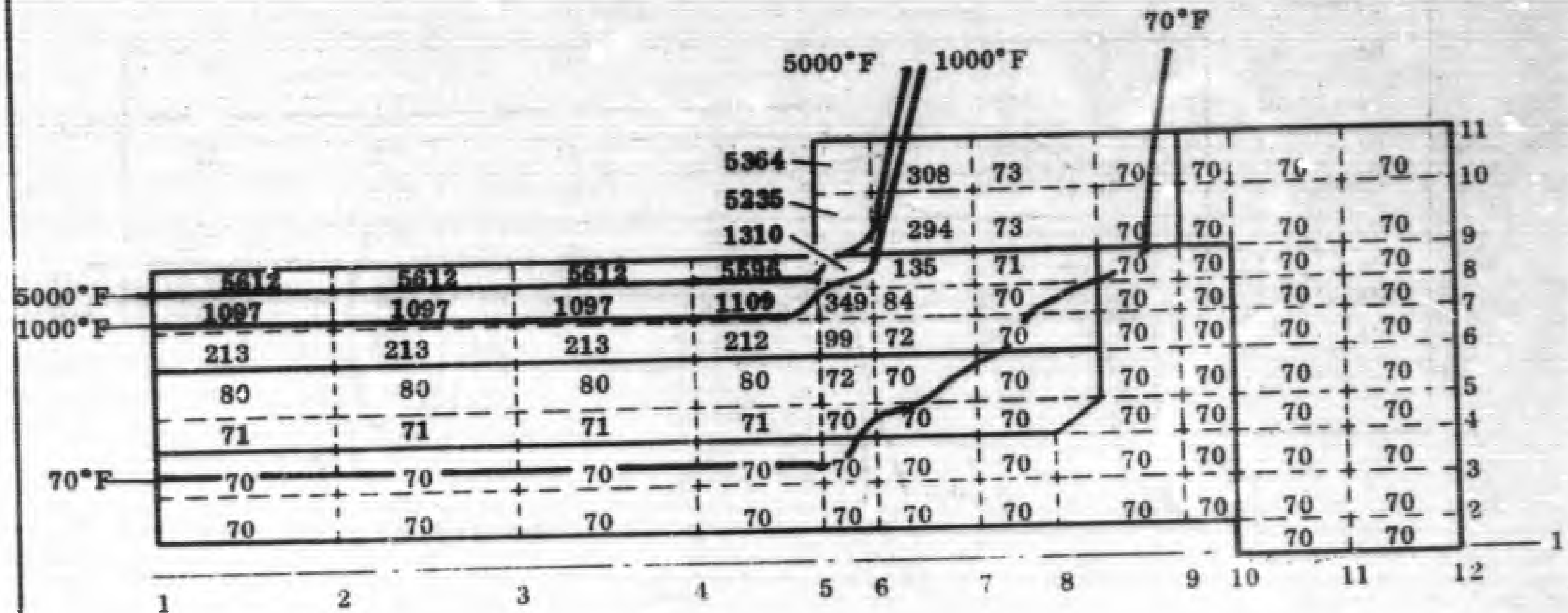

Figure 119. Leg Thermal Gradient at 16.1 Sec

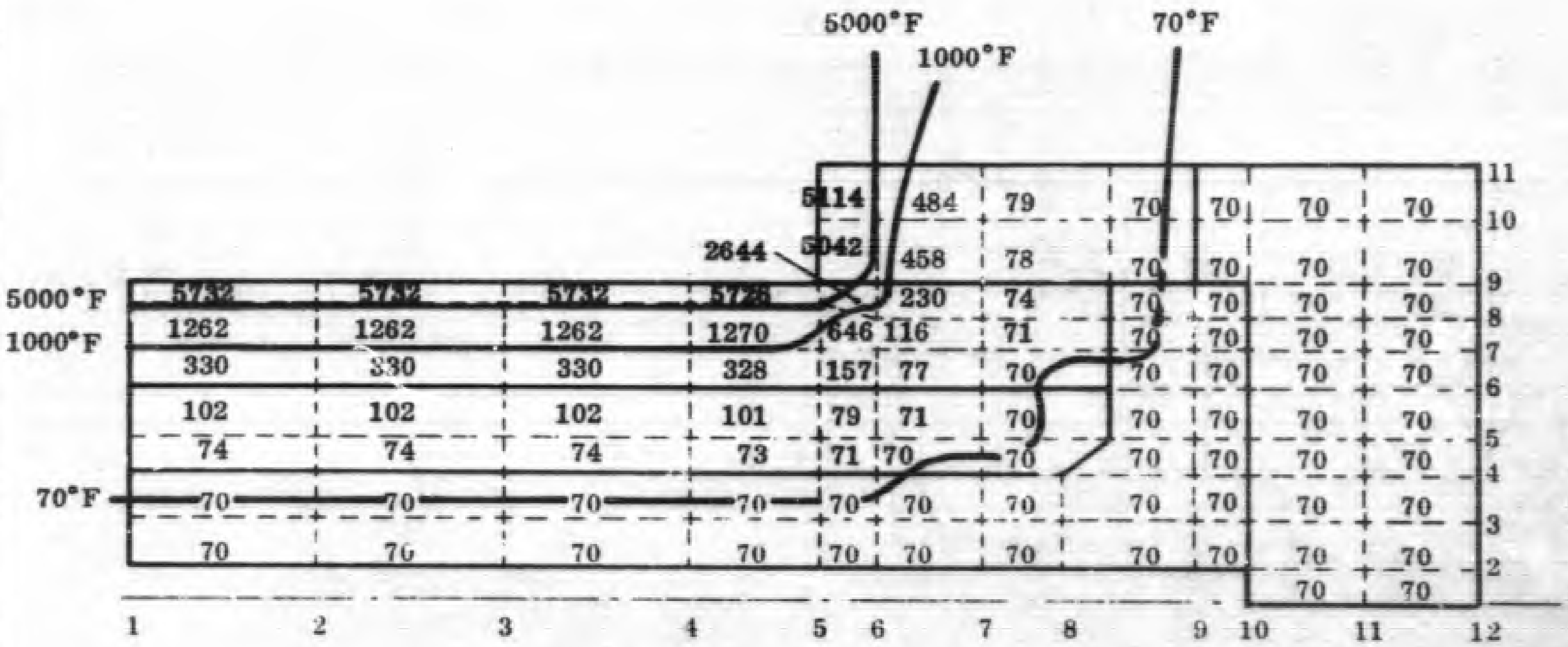

Figure 120. Leg Thermal Gradient at 25. 0 Sec

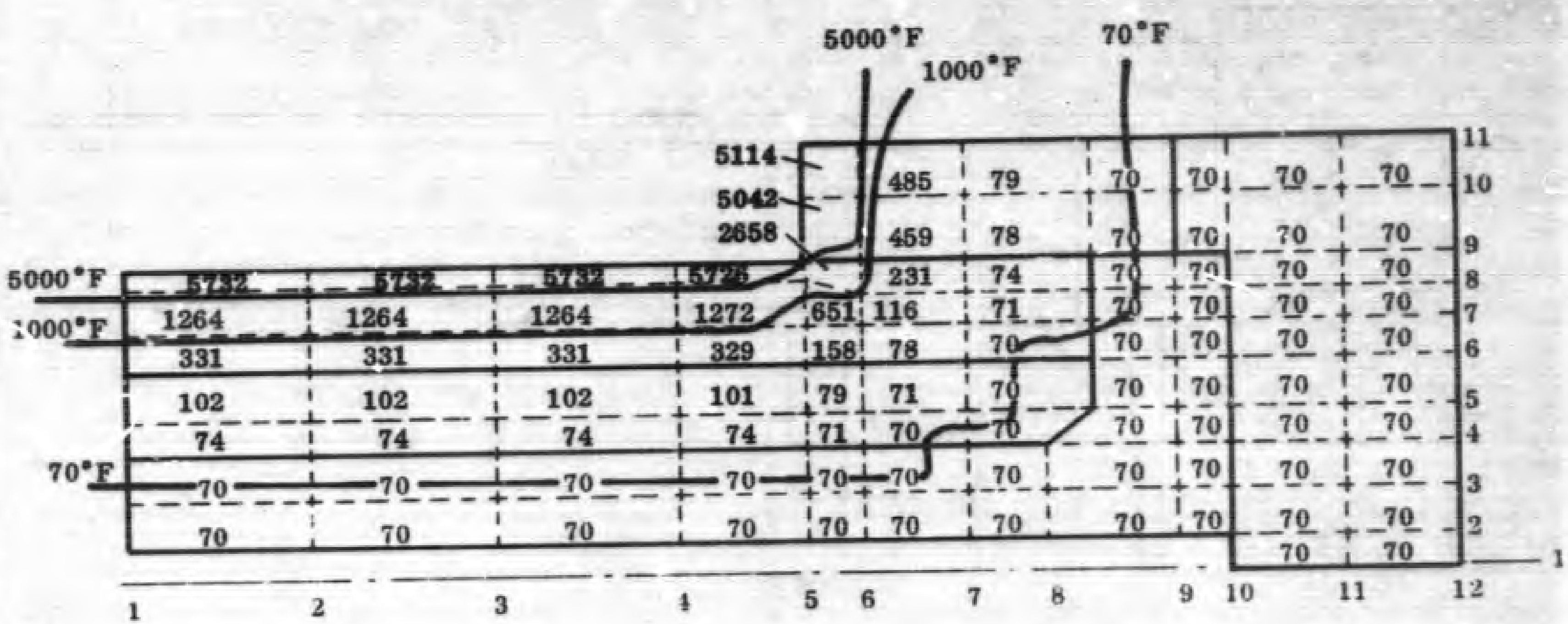

Figure 121. Leg Thermal Gradient at 25.1 Sec

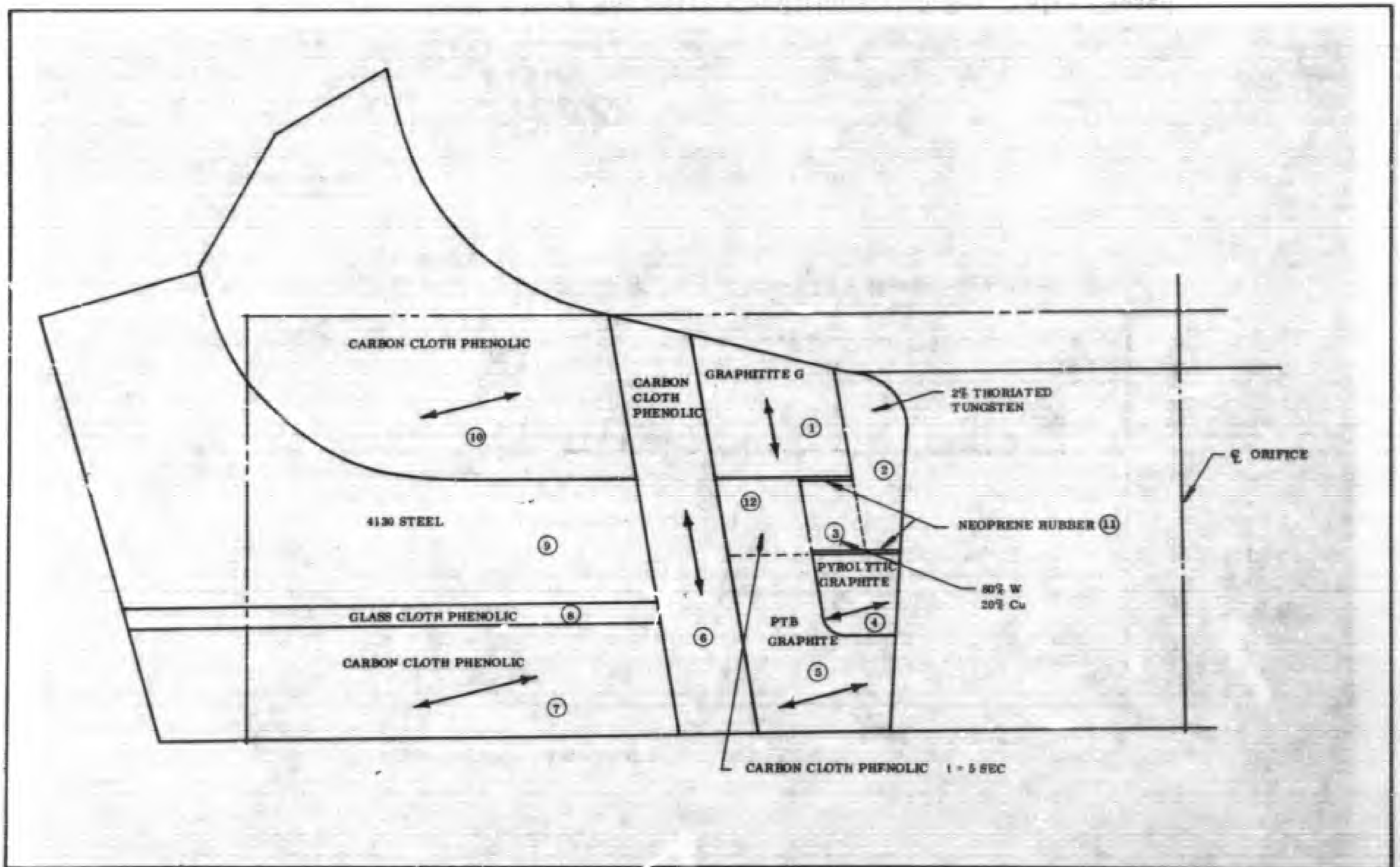

Figure 122. TU-520 HGSITVC Nozzle Section Analyzed

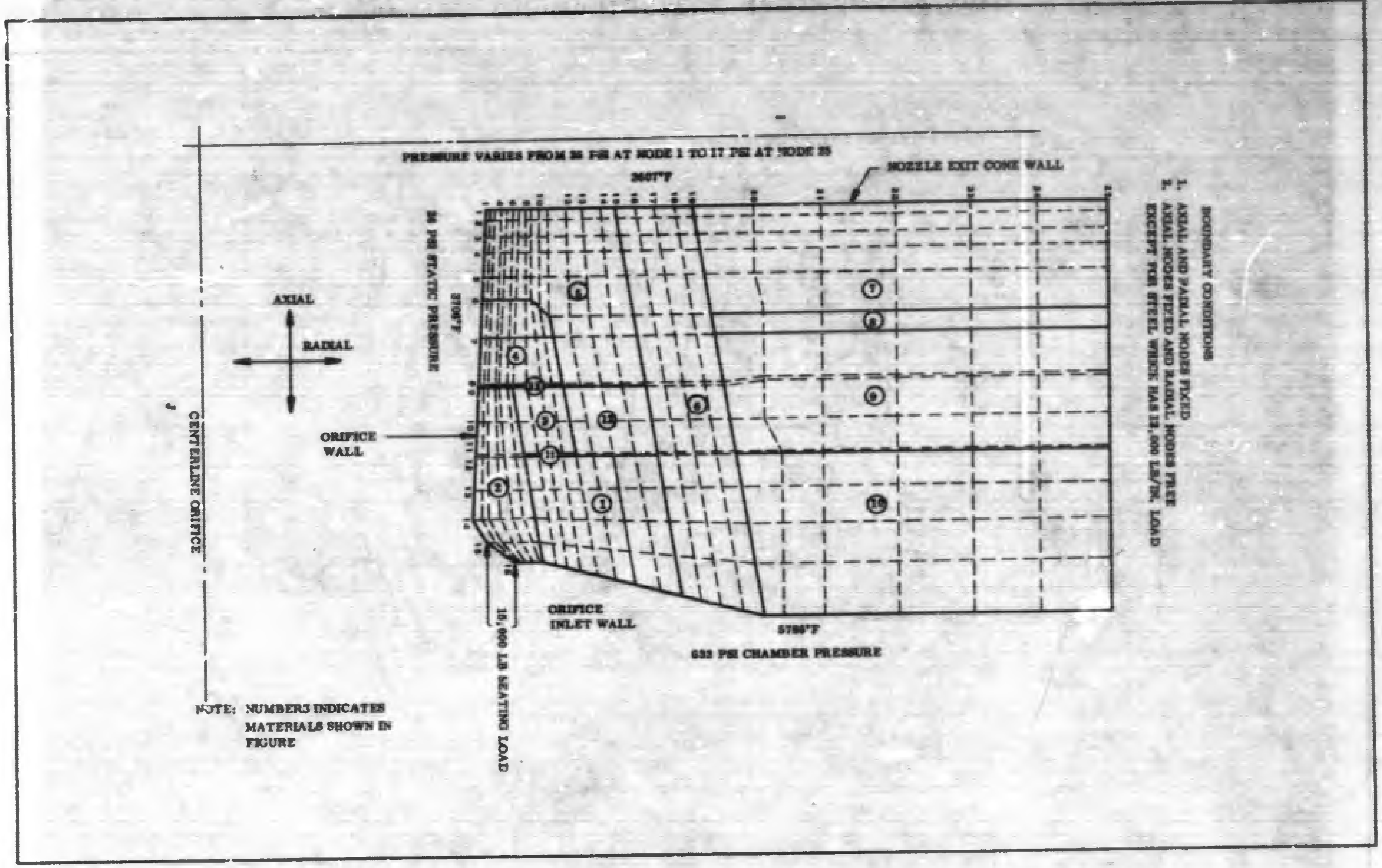

Figure 123. Orifice Port Boundary Conditions at 5 Sec, Valve Closed

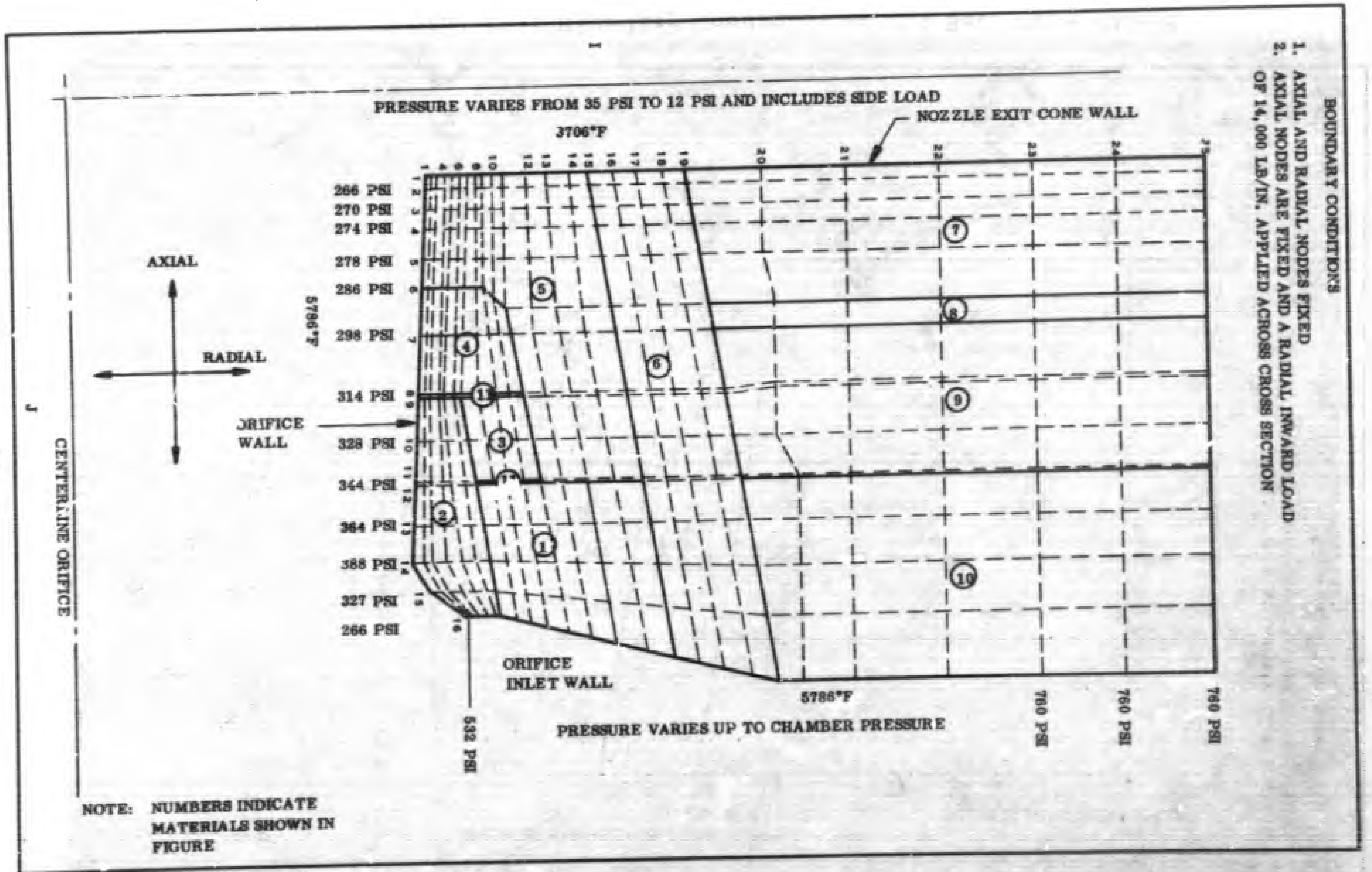

Figure 124. Orifice Port Boundary Conditions at 25.0 Sec, Valve Open

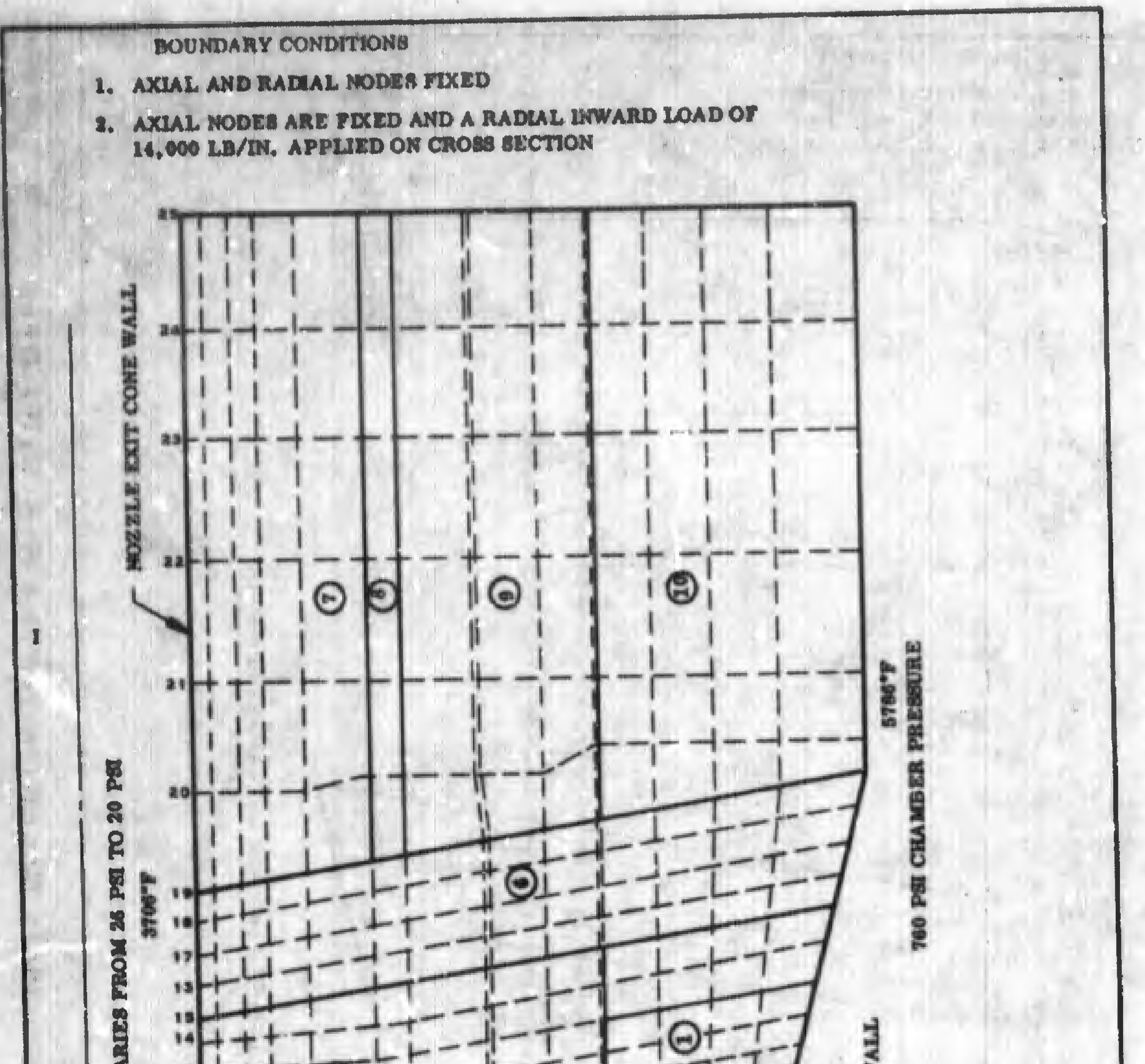

Figure 125. Orifice Port Boundary Conditions at 25.1 Sec, Valve Closed

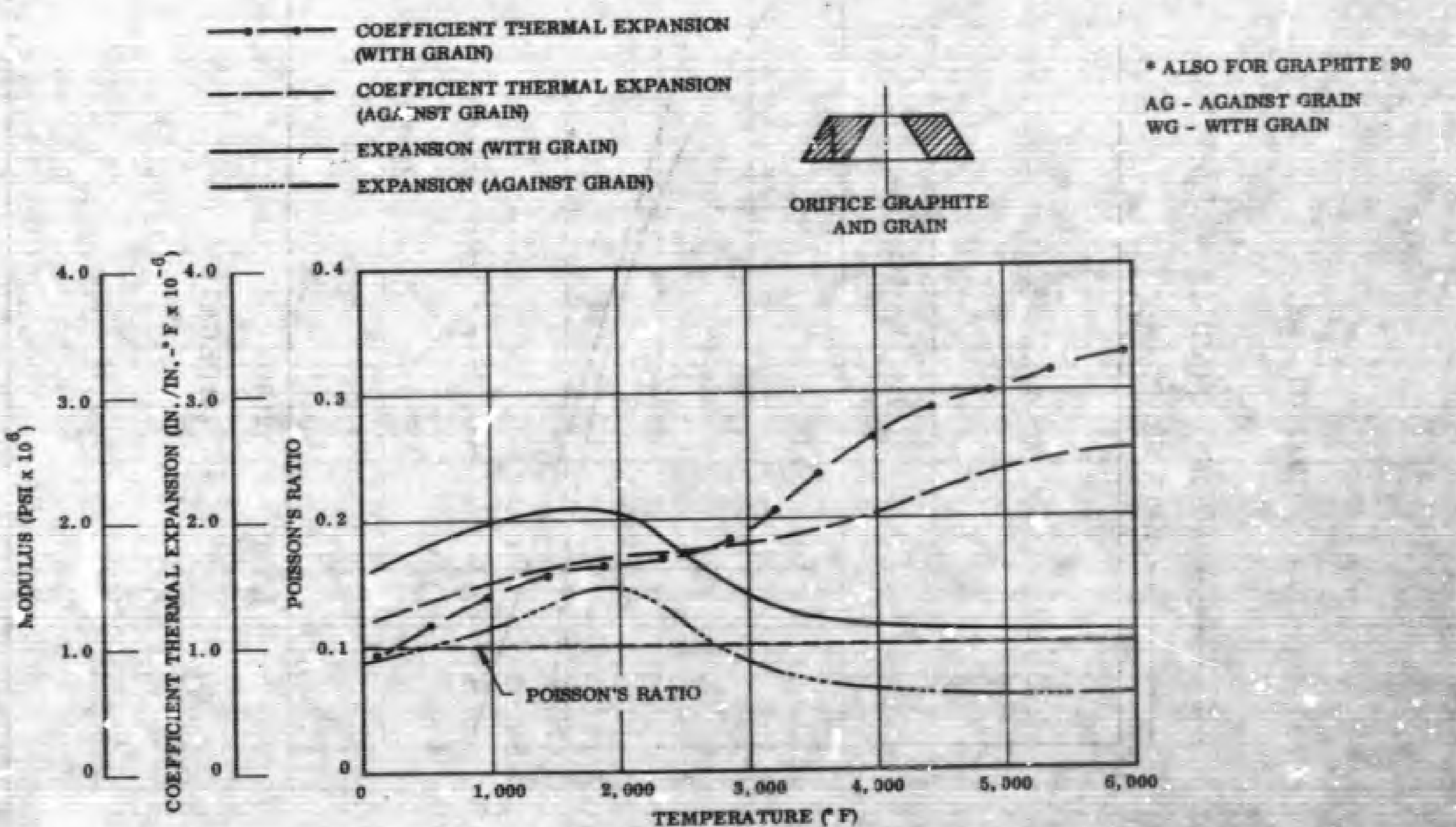

Figure 126. Graphite 90 CTE, E, Poisson's Ratio vs Temperature

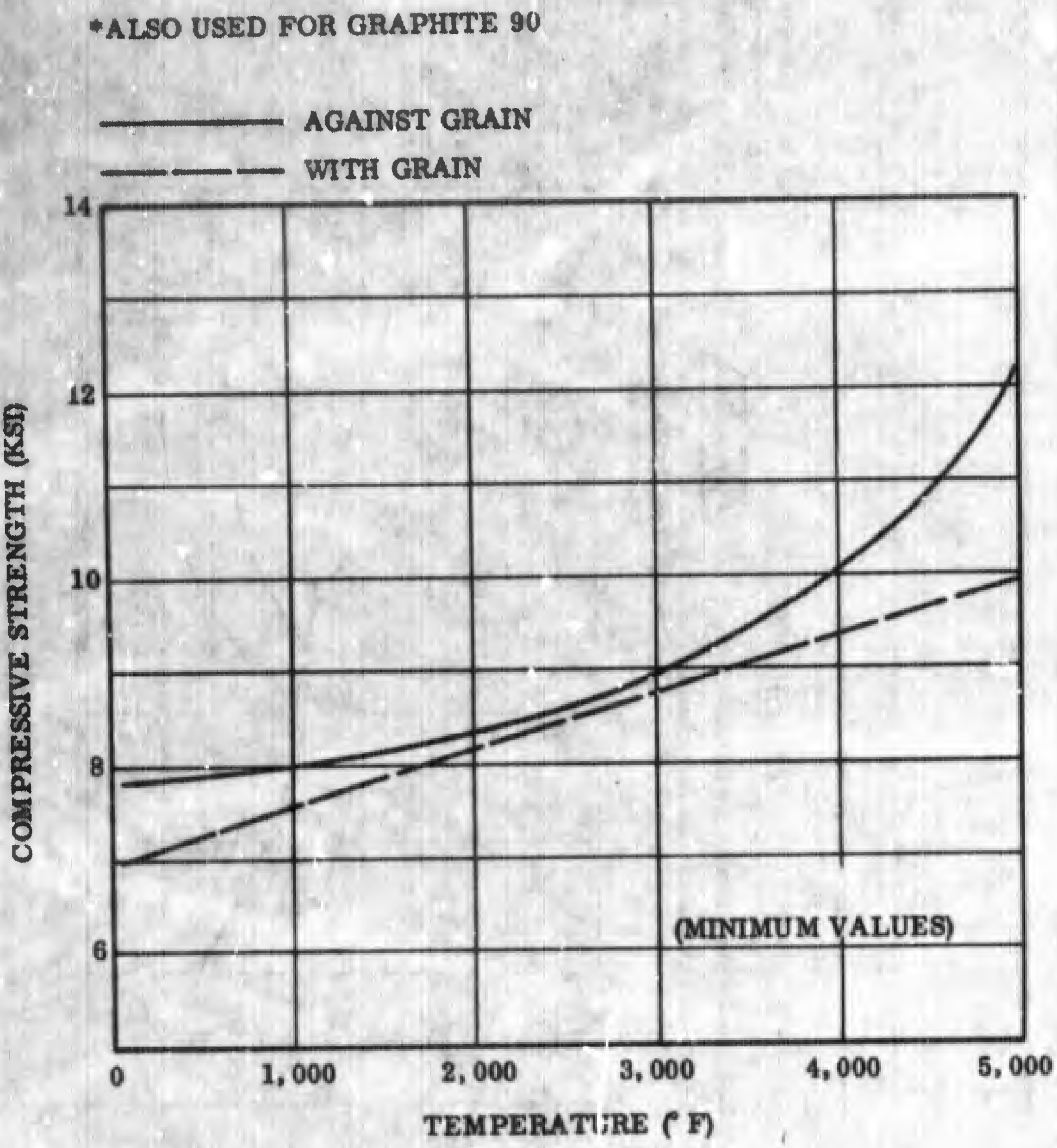

Figure 127. Graphite 90 Ultimate Compressive Strength vs Temperature

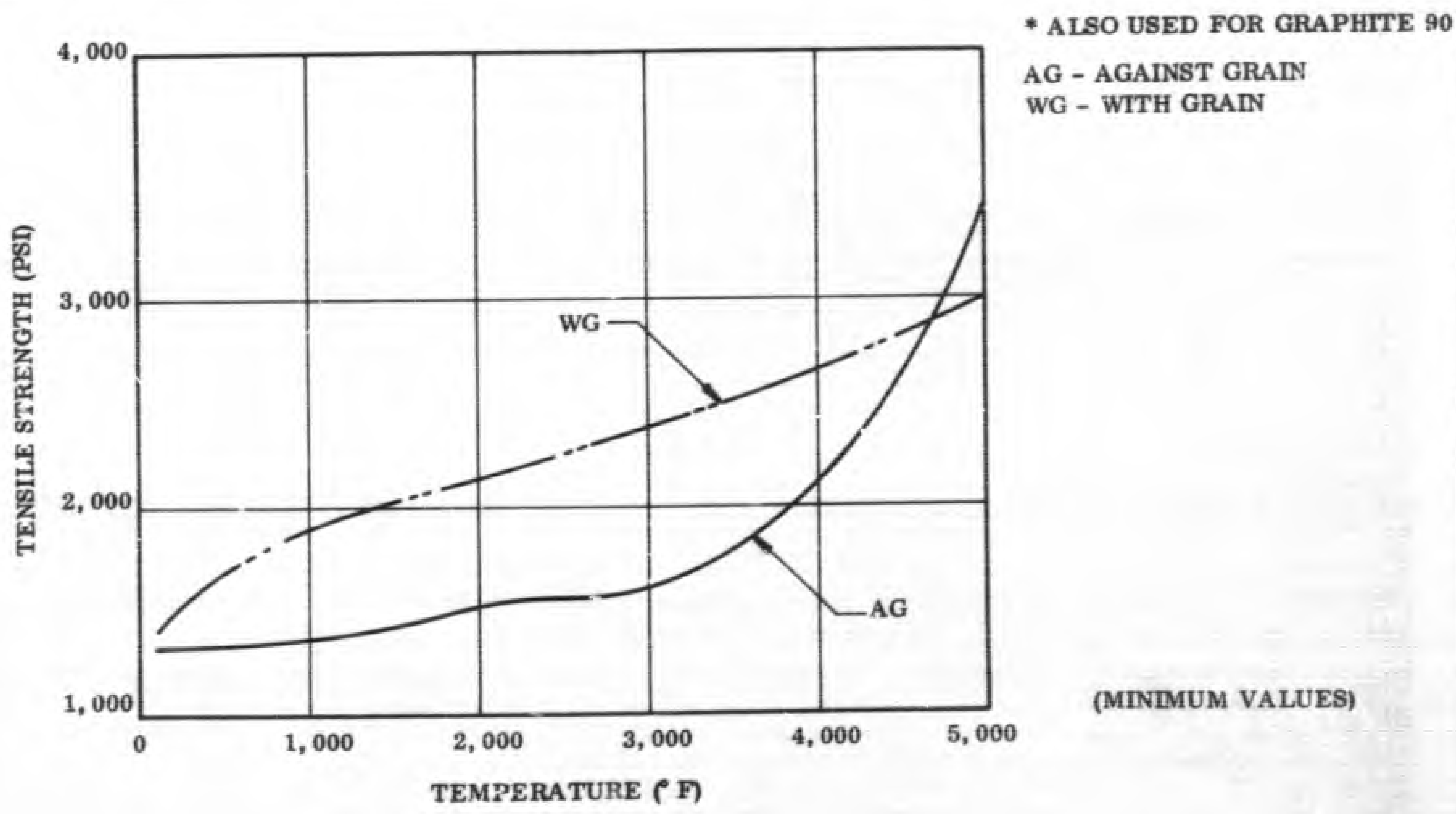

Figure 128. Graphite 90 Ultimate Tensile Strength vs Temperature

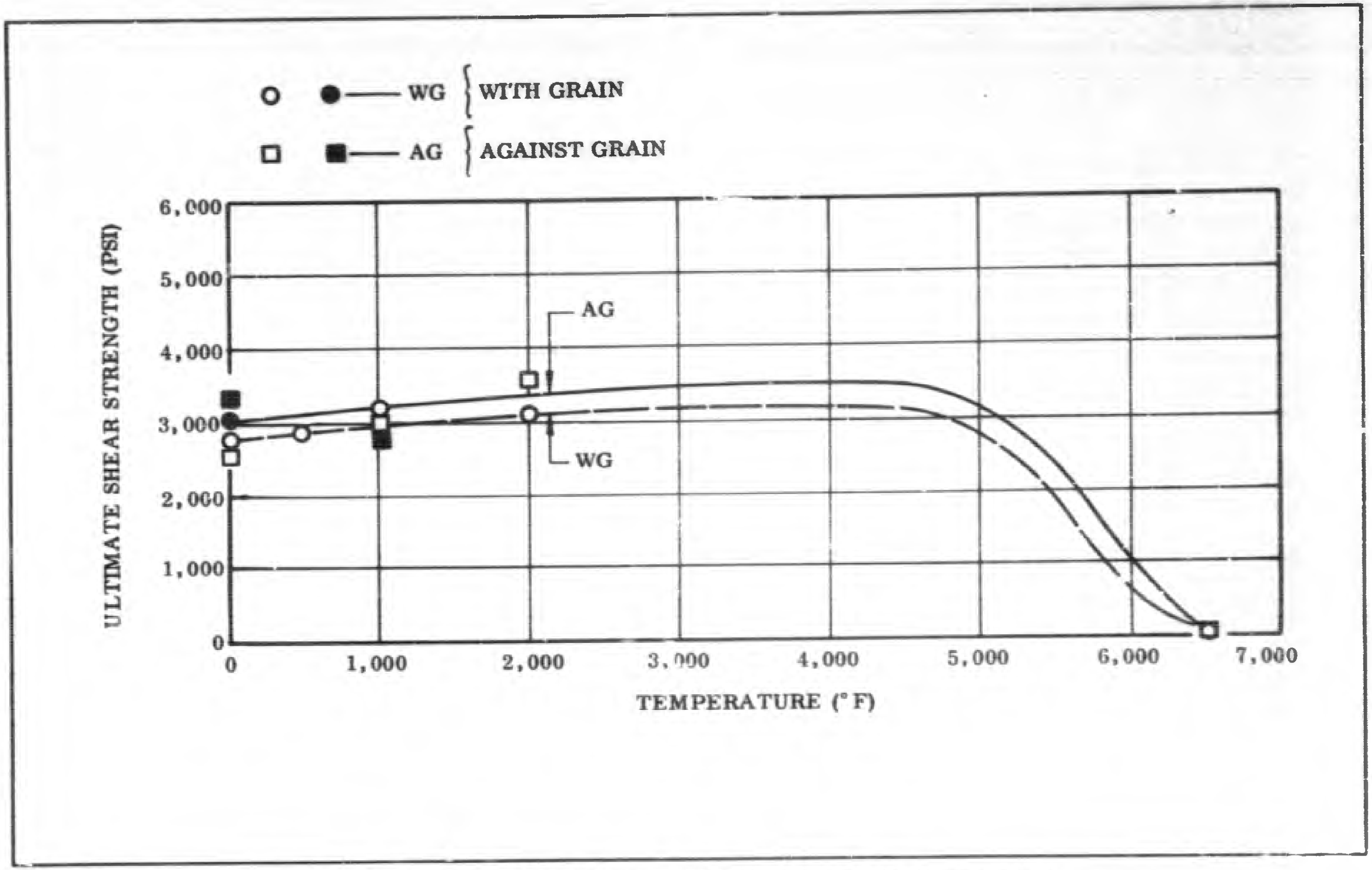

Figure 129. Graphite 90 Ultimate Shear Strength vs Temperature

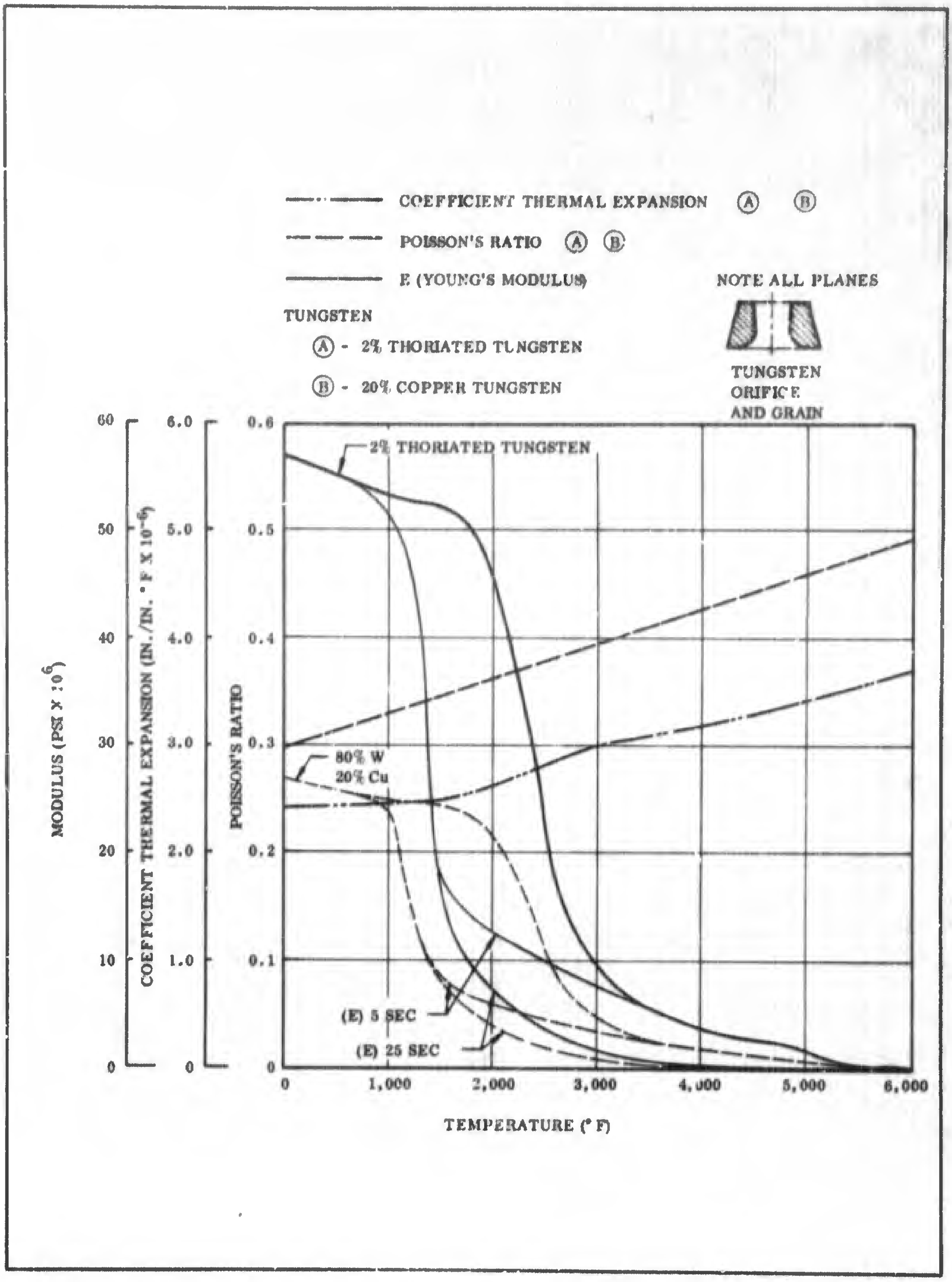

Figure 130. Tungsten CTE, E, Poisson's Ratio vs Temperature

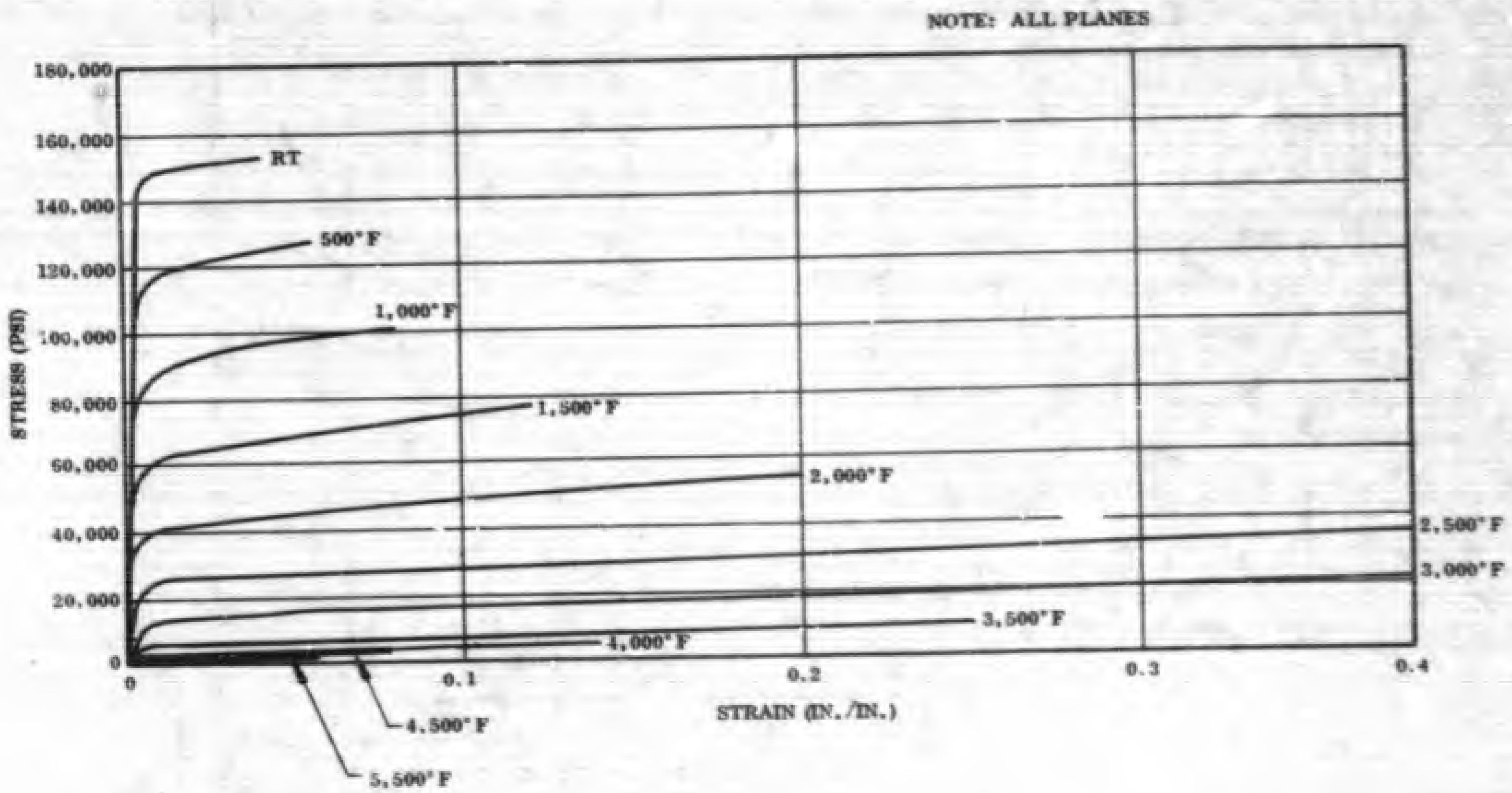

Figure 131. Two Percent Thoria-98% Tungsten, Stress-Strain Curves at Temperature

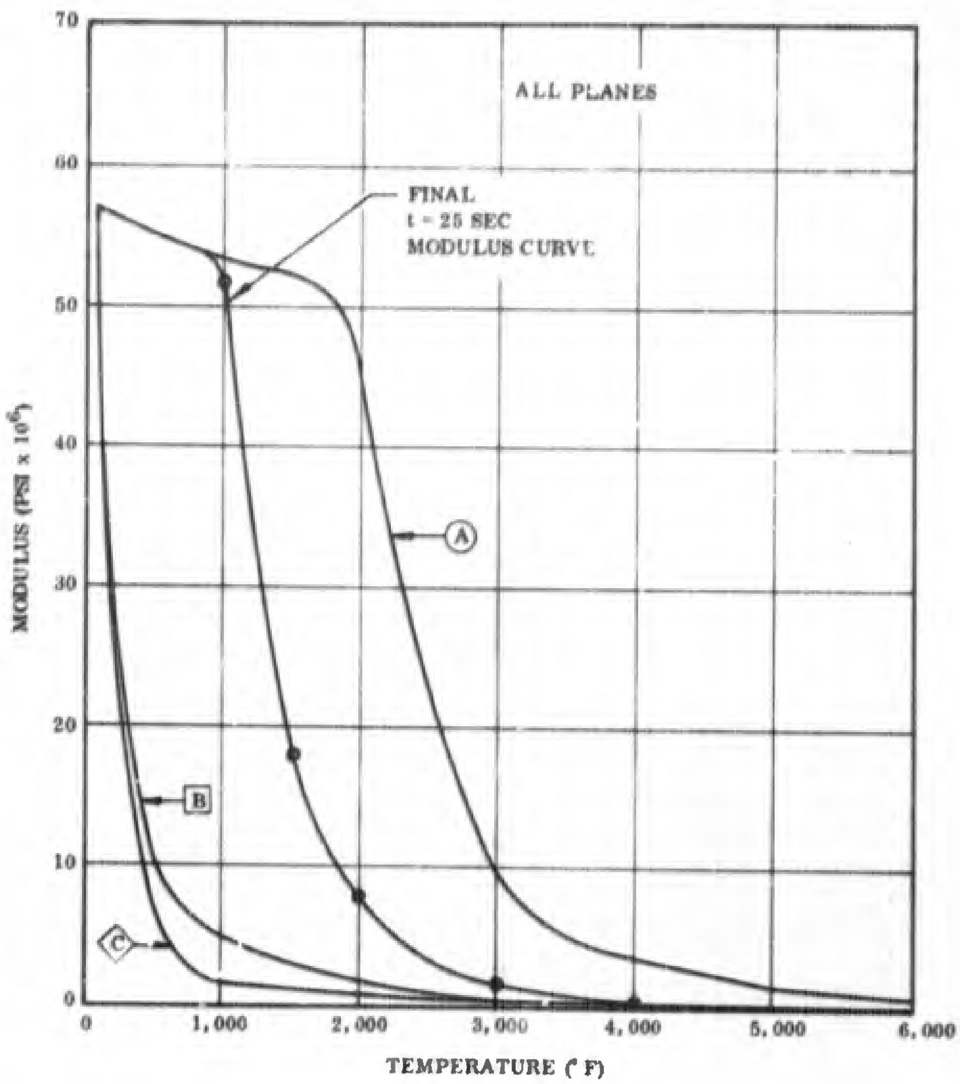

Figure 132. Two Percent Thoria-98% Tungsten, at 25 Sec Modulus vs Temperature

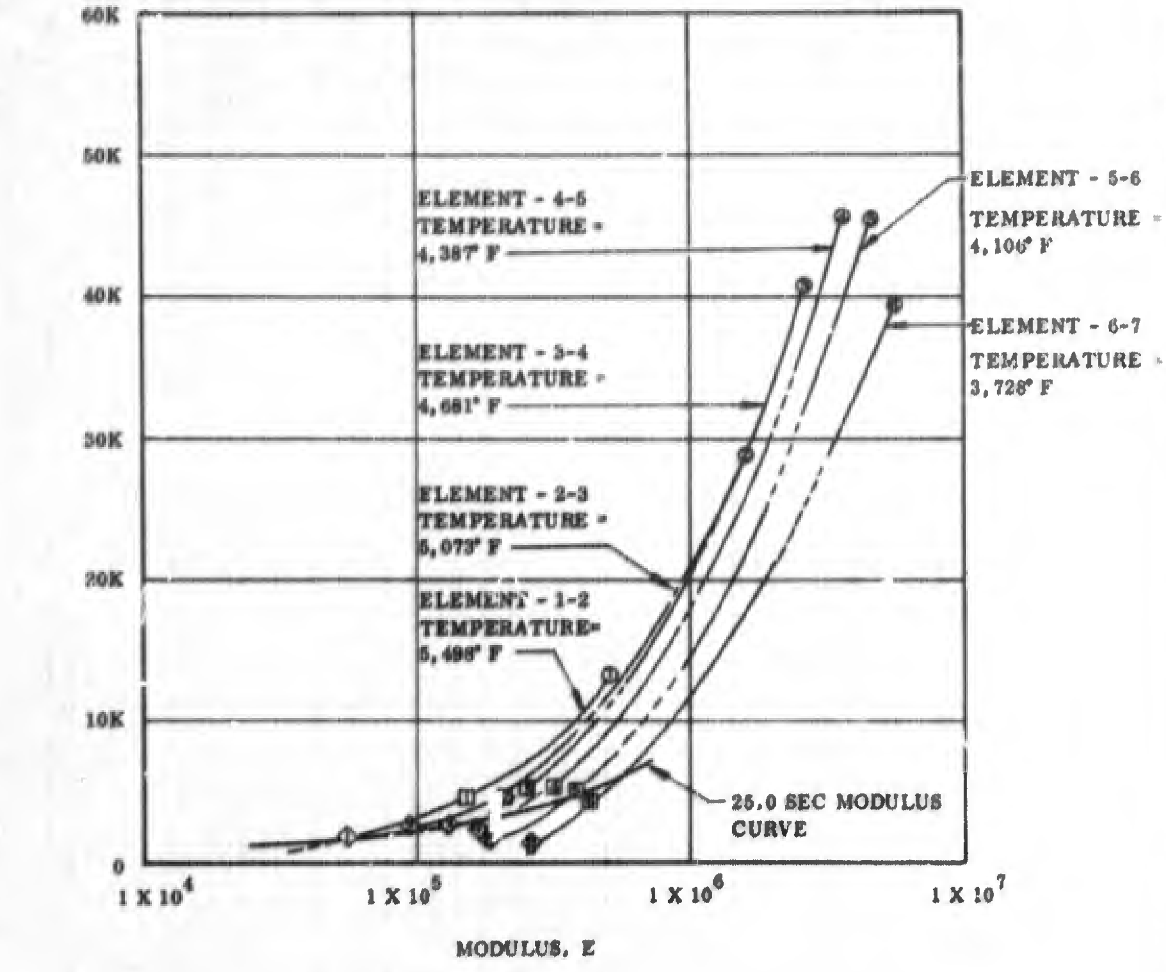

NOTE: ONE-DIMENSIONAL ANALYSIS

NOTE: ALL PLANES

Figure 133. Two Percent Thoria-98% Tungsten, at 25 Sec Modulus vs Stress

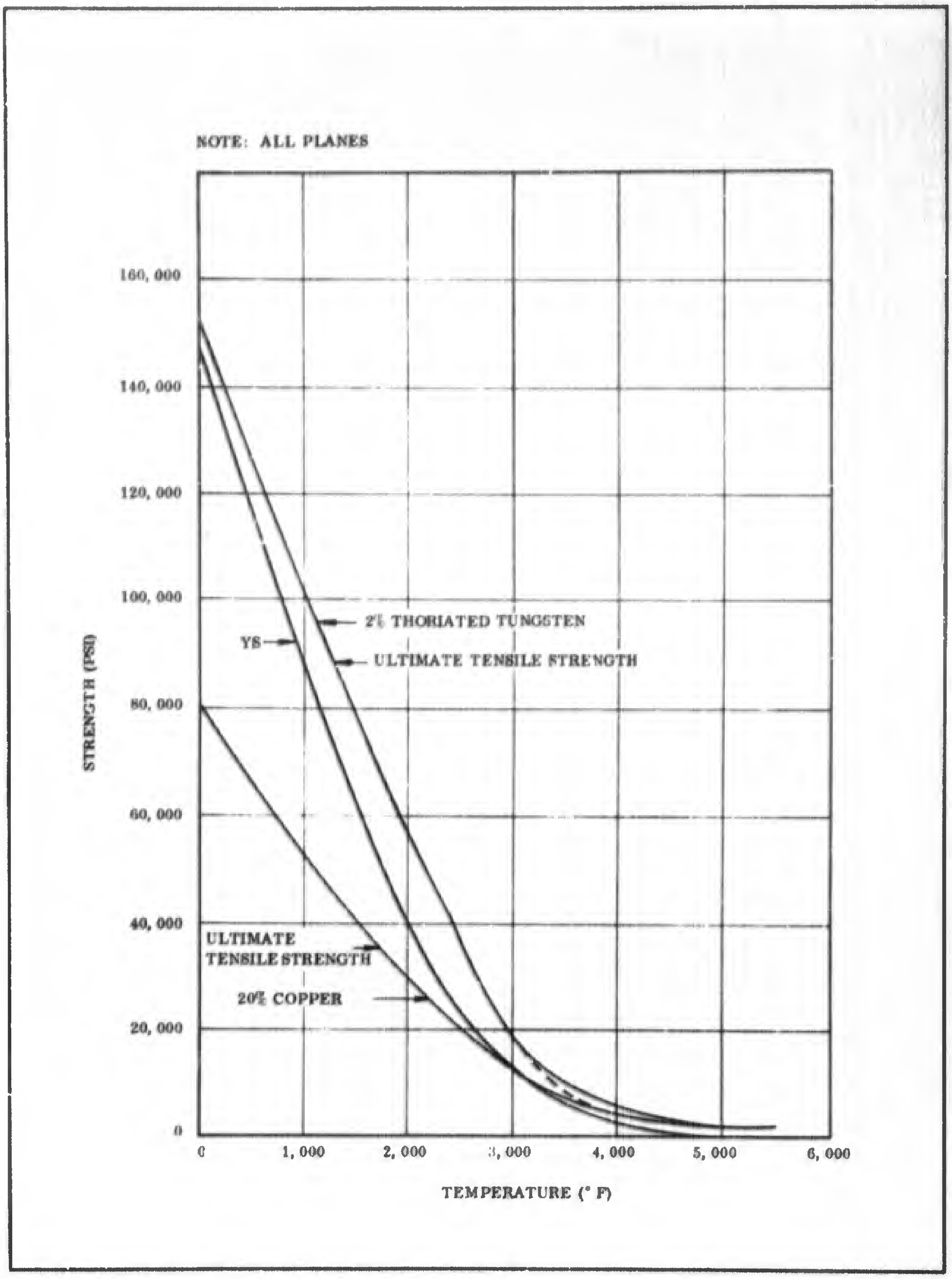

Figure 134. Tungsten, Ultimate and Yield Strength vs Temperature

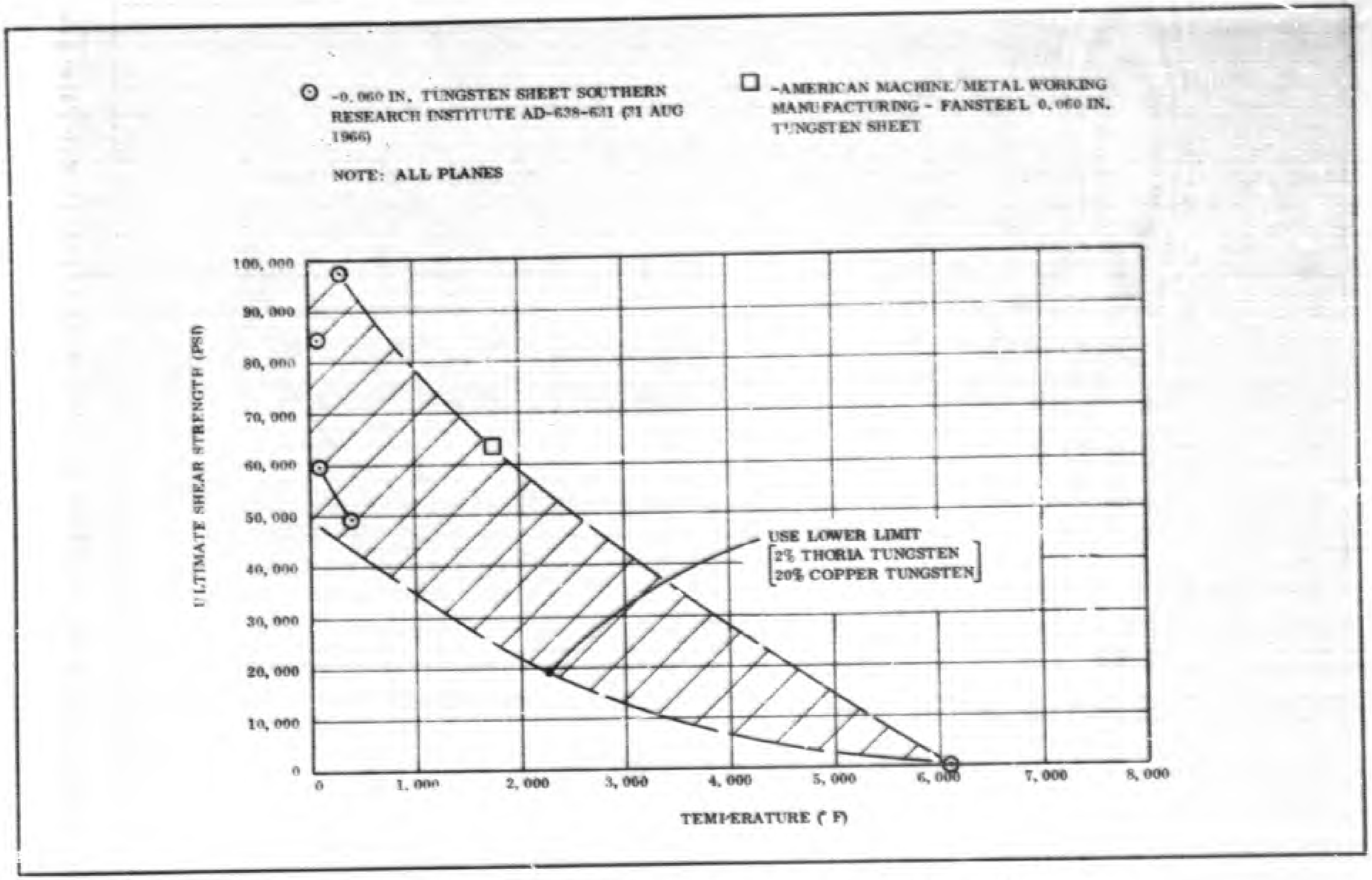

Figure 135. Tungsten, Ultimate Shear Strength

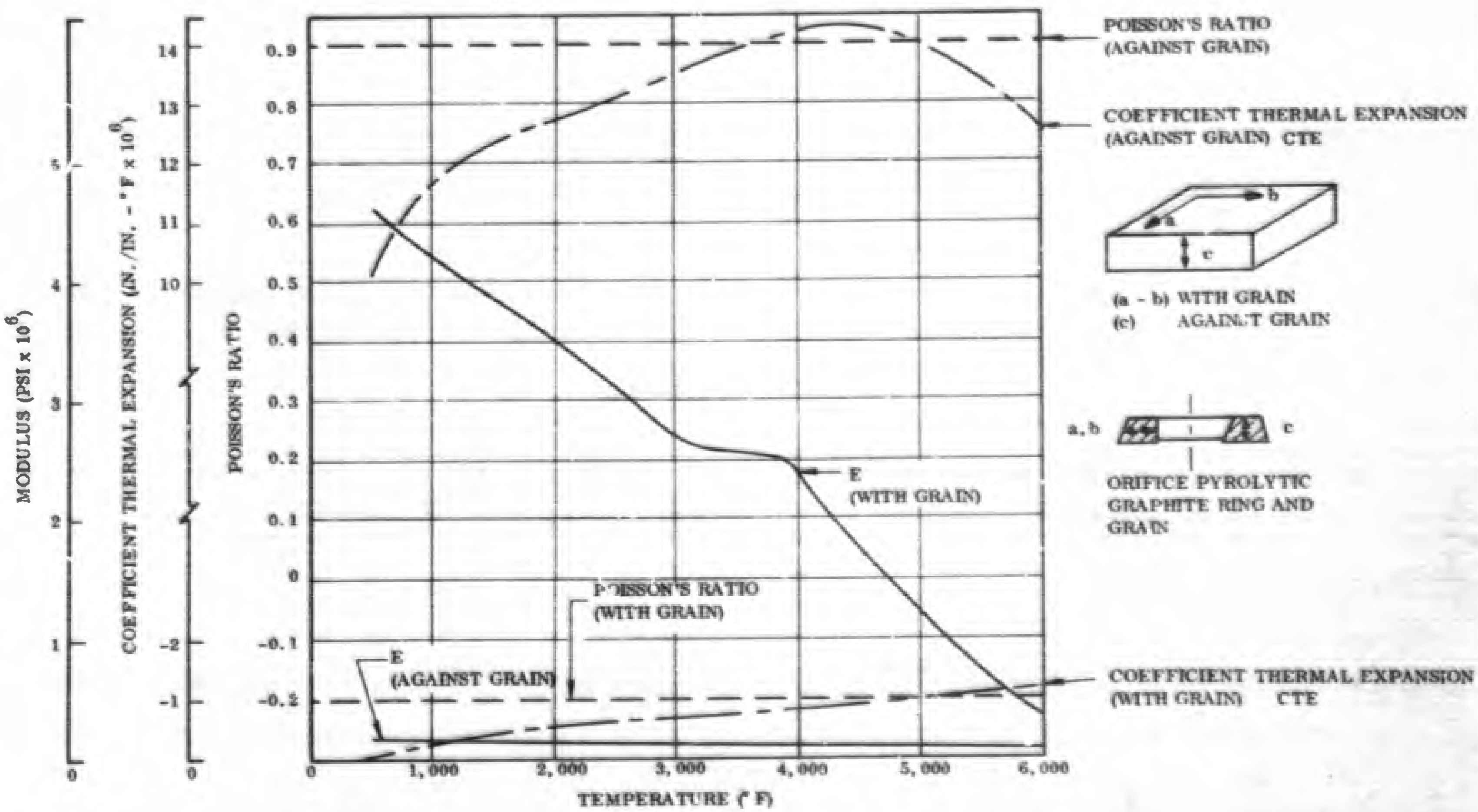

Figure 136. Pyrolytic Graphite, CTE, E, Poisson's Ratio vs Temperature, Tension Loaded

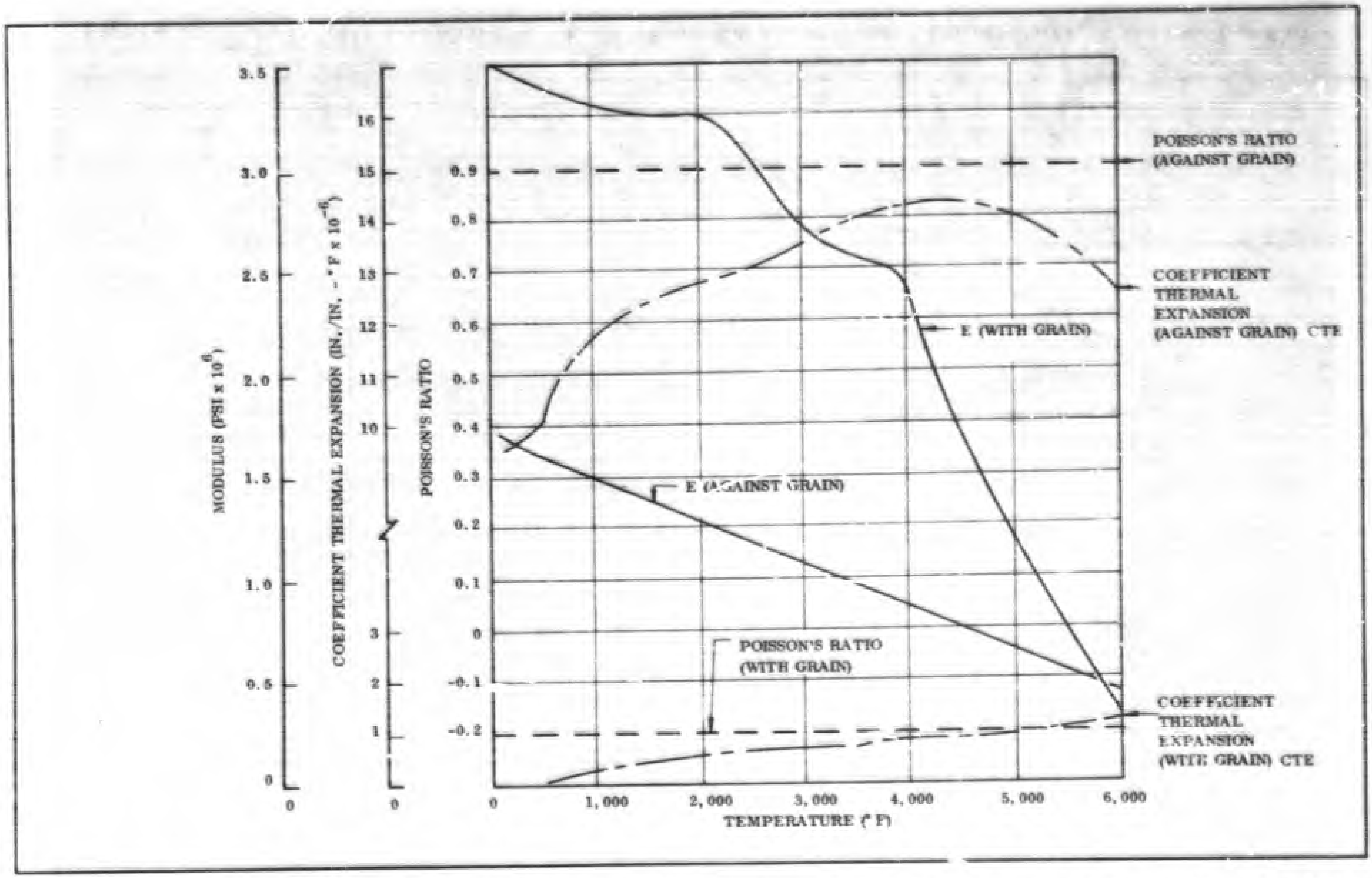

Figure 137. Pyrolytic Graphite, CTE, E, Poisson's Ratio vs Temperature, Compression Loaded

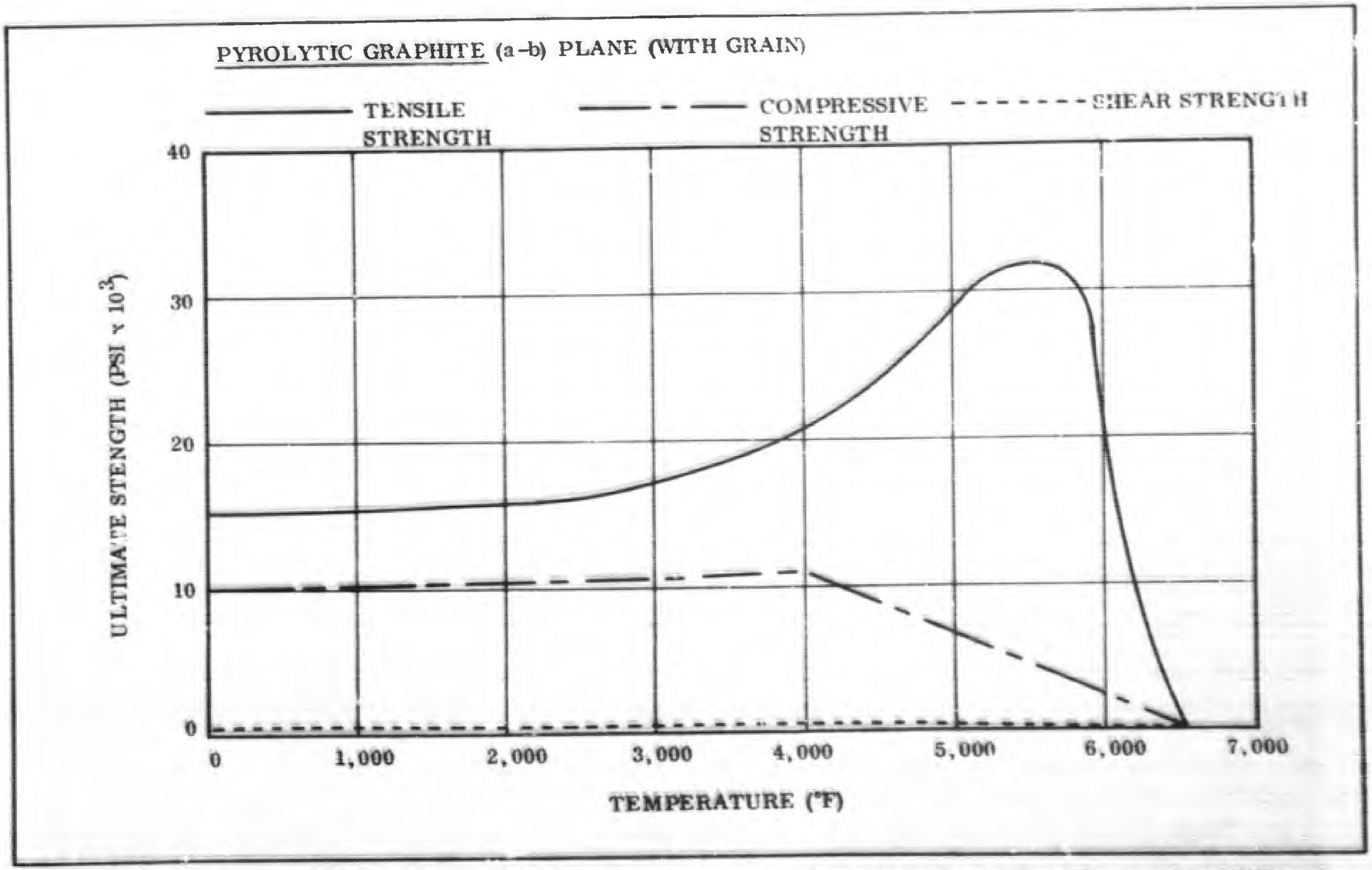

Figure 138. Pyrolytic Graphite, Ultimate Tensile, Compressive, Shear Strength vs Temperature (NG)

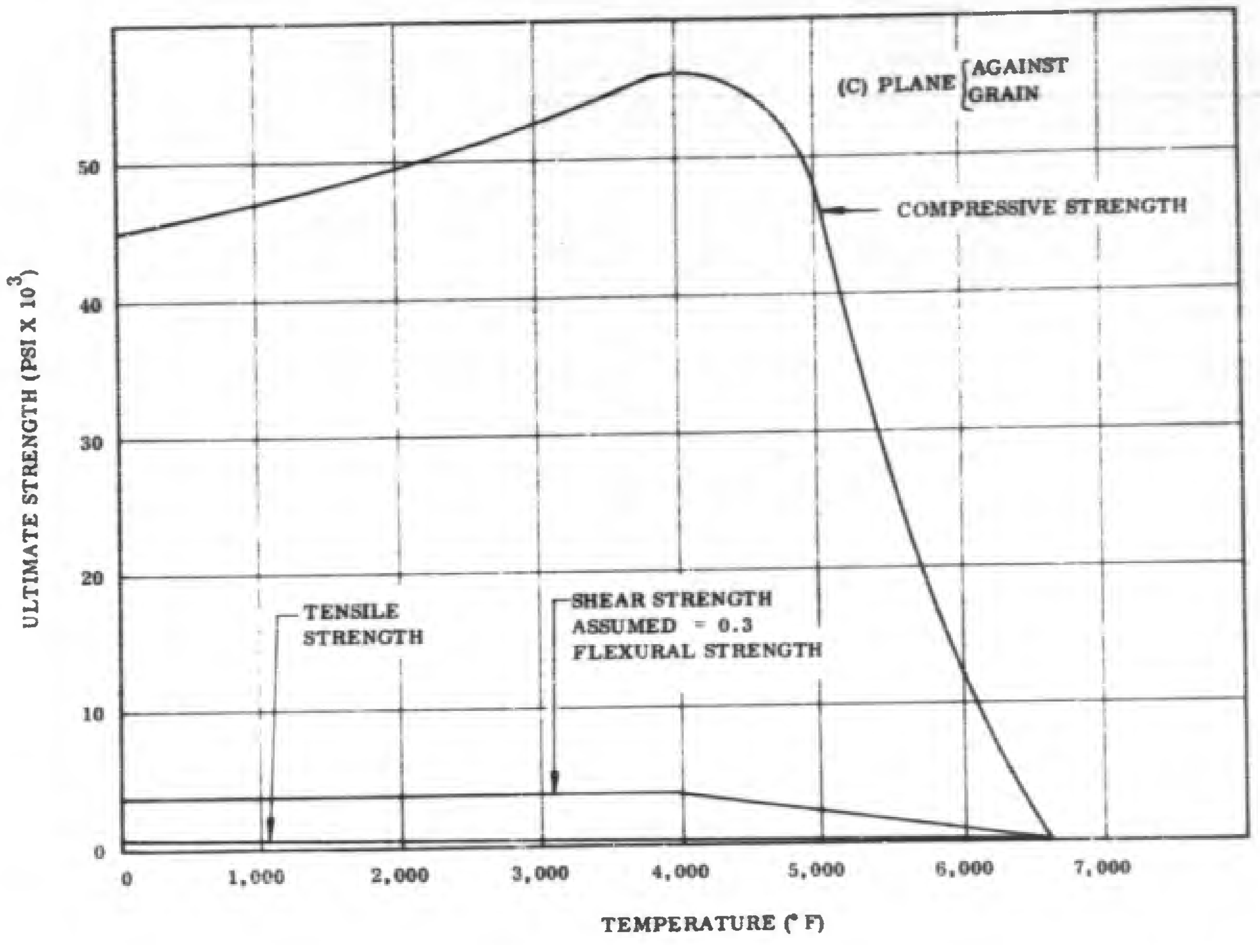

Figure 139. Pyrolytic Graphite, Ultimate Tensile, Compressive, Shear Strength vs Temperature (AG)

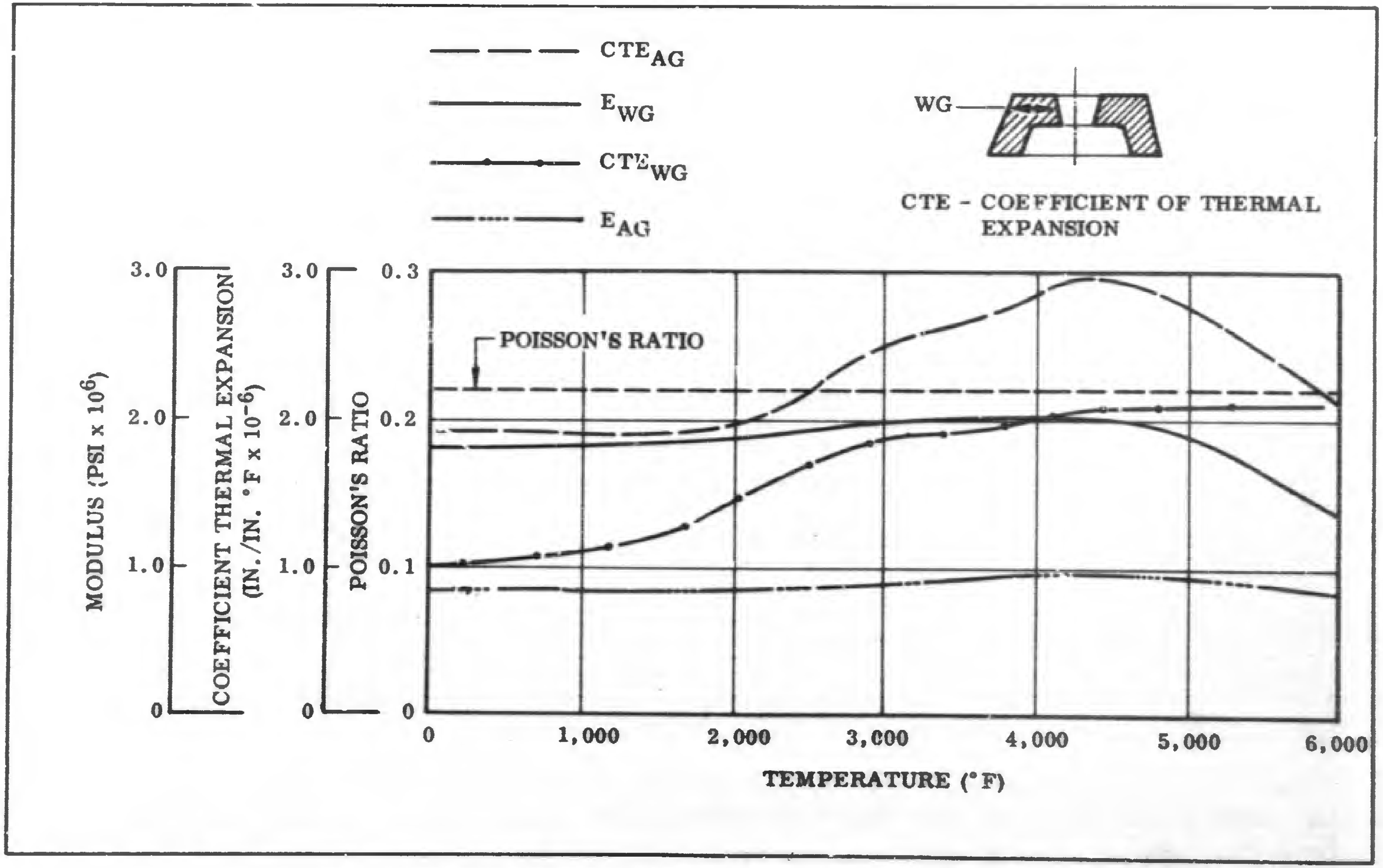

Figure 140. PTB CTE, Poisson's Ratio, E vs Temperature

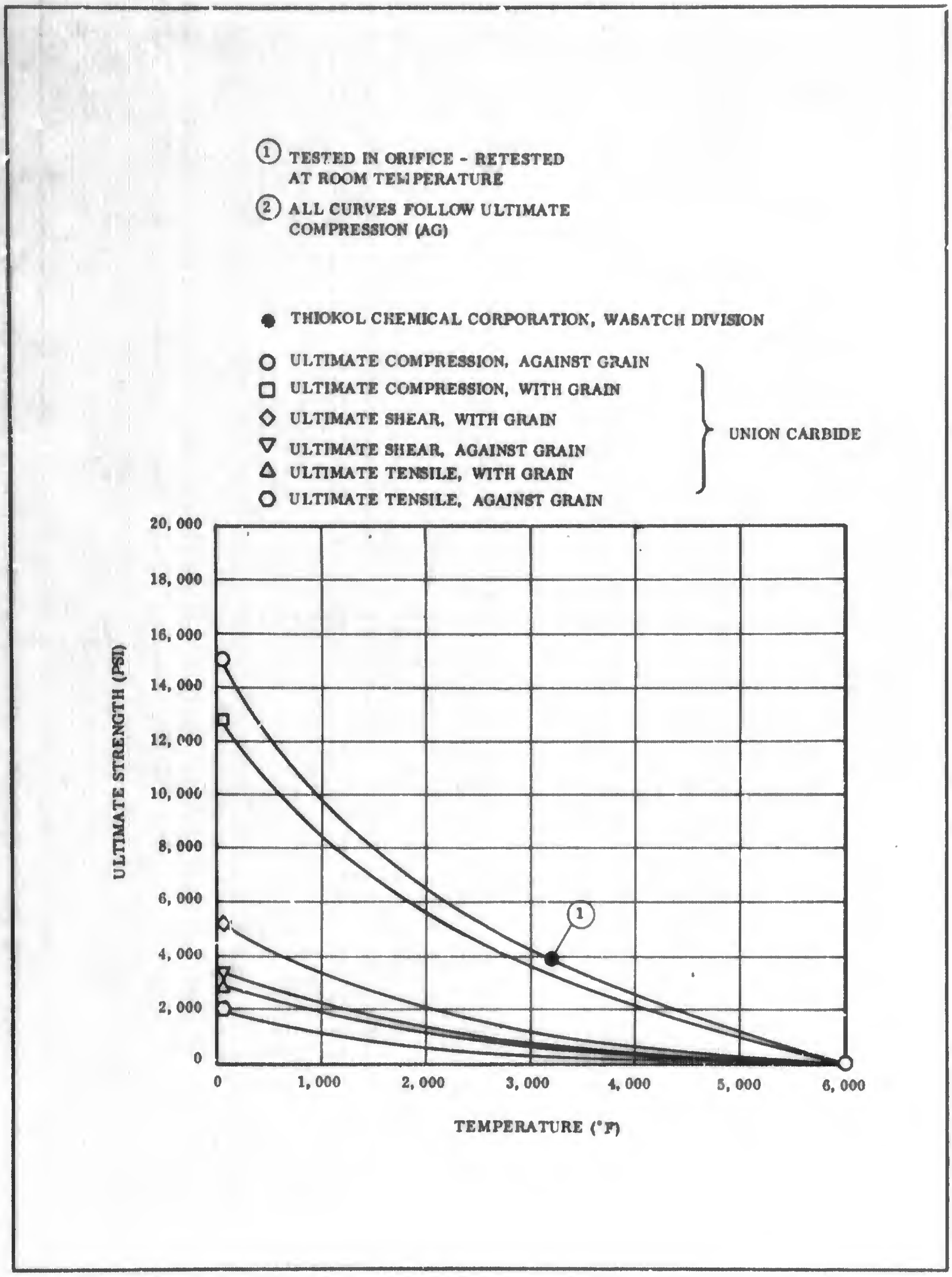

Figure 141. PTB Ultimate Tensile, Compressive and Shear Strength vs Temperature

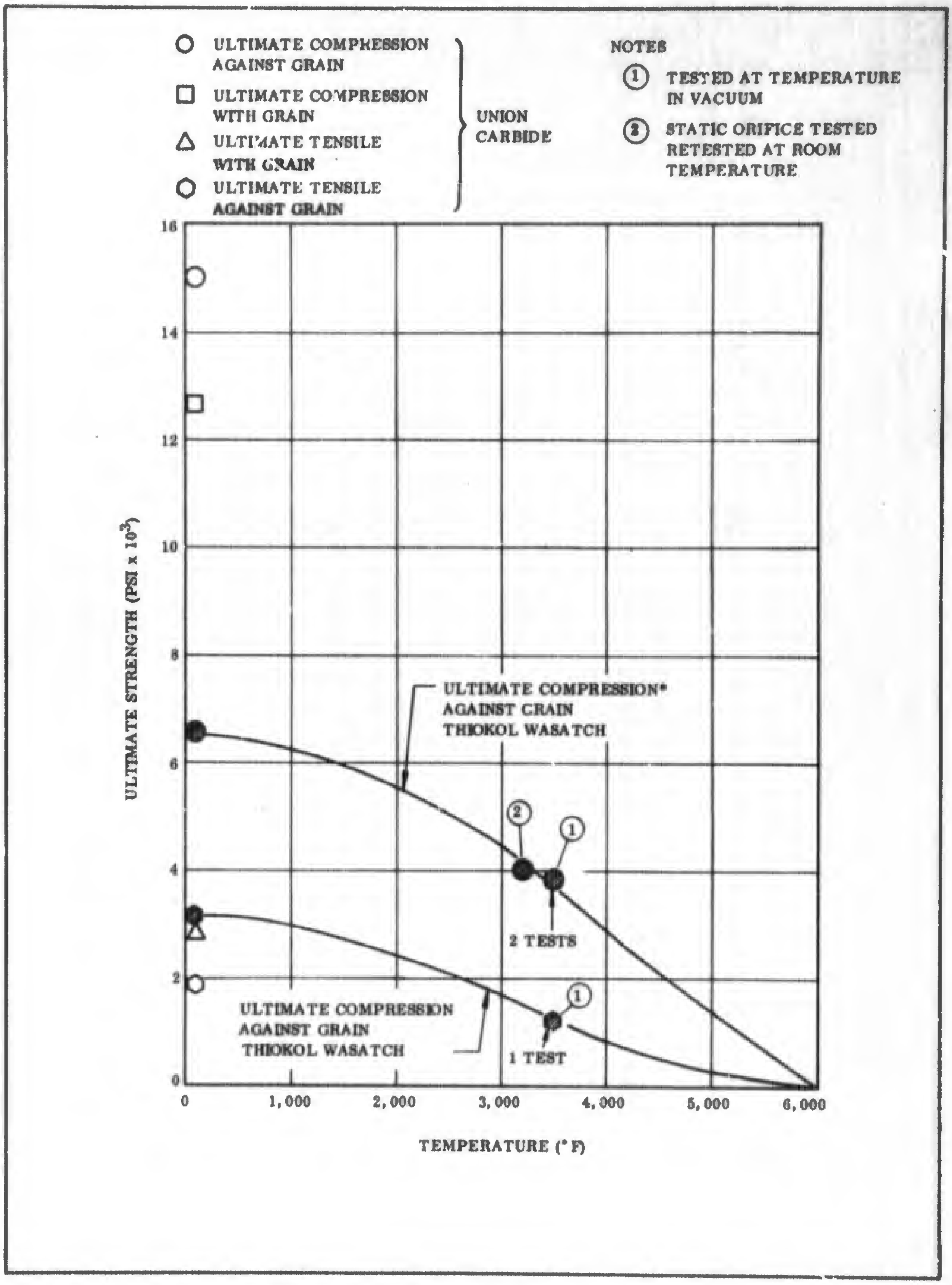

Figure 142. PTB Revised, Ultimate Tensile, Compressive and Shear Strength vs Temperature

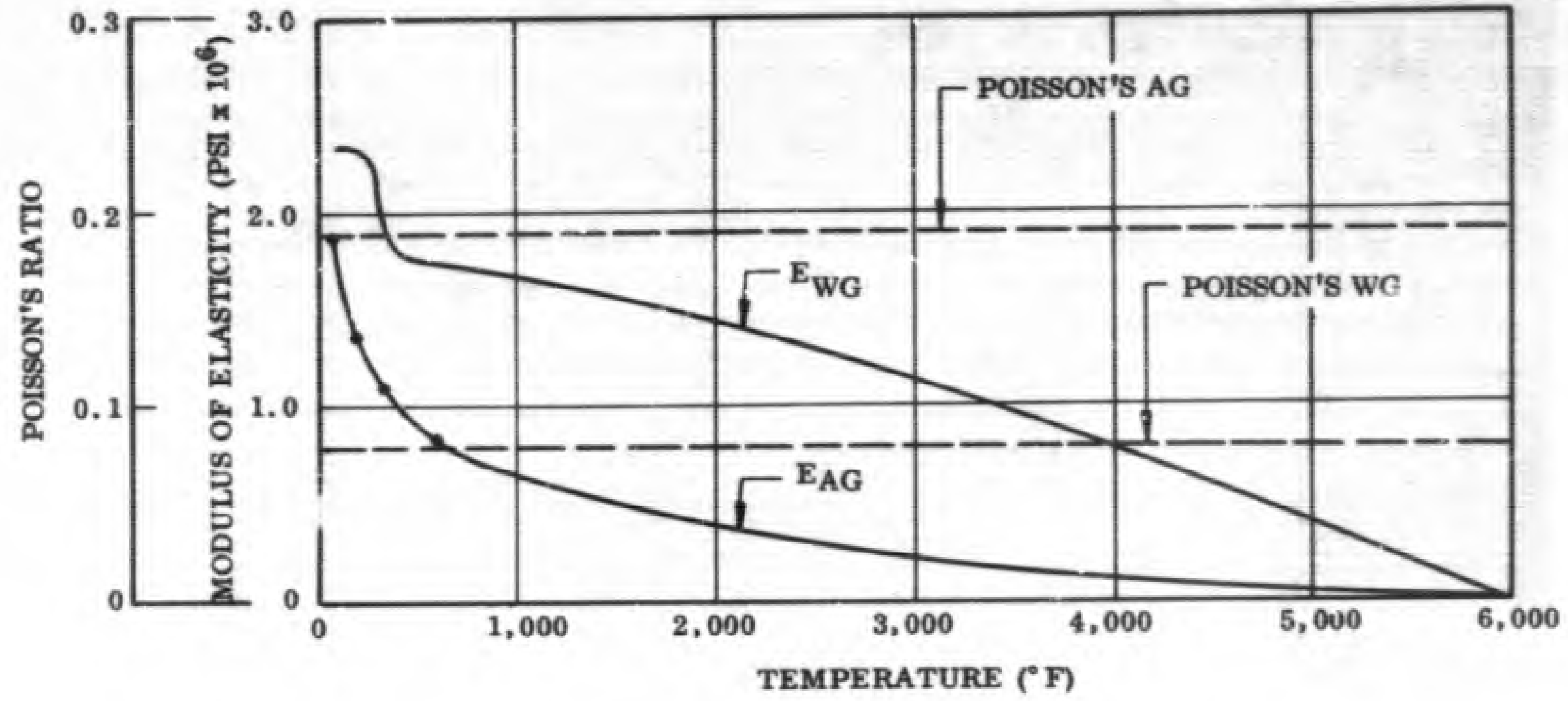

Figure 143. Carbon Cloth Phenolic, CTE, Poisson's Ratio, E vs Temperature - Compressive

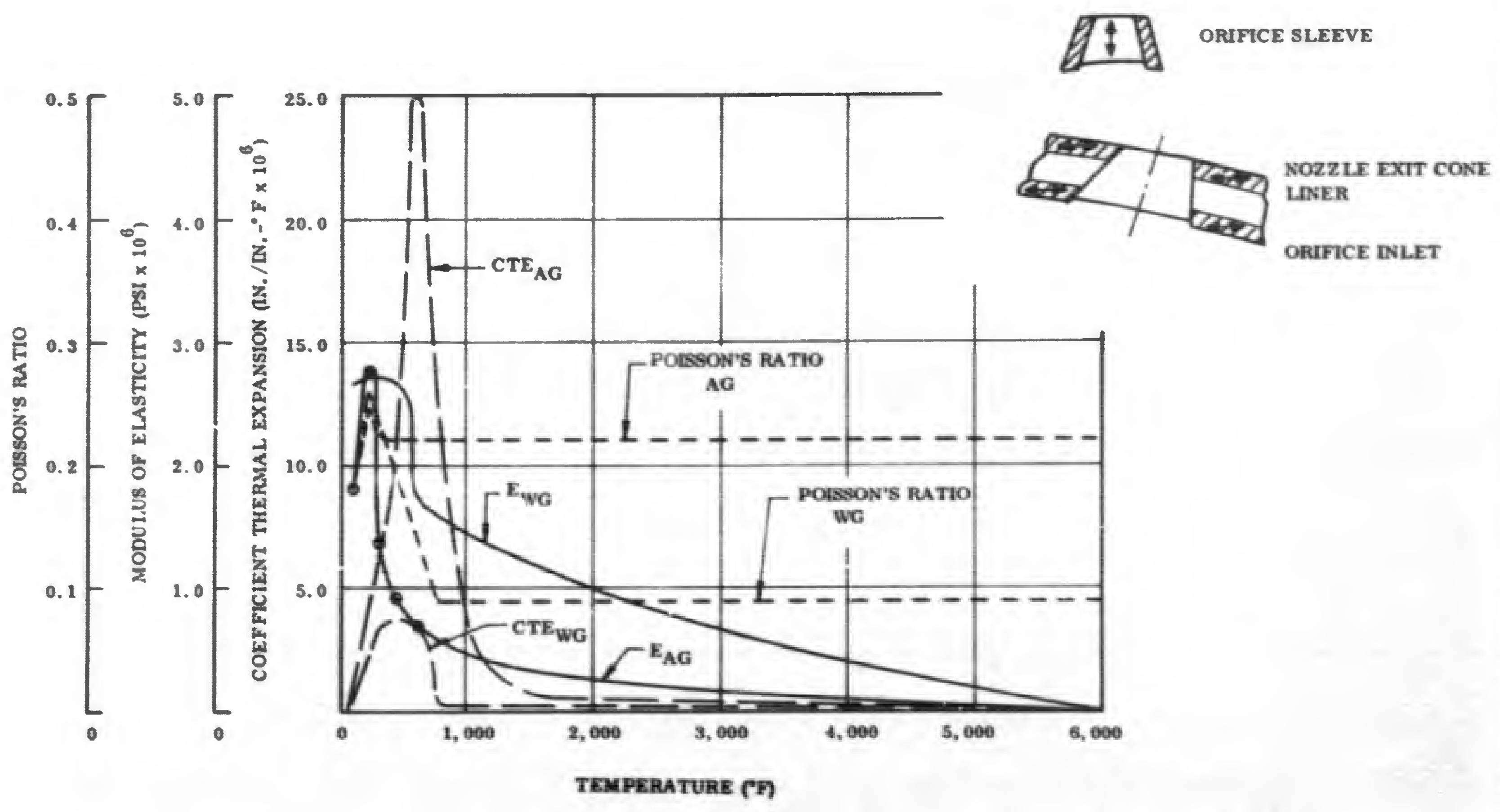

Figure 144. Carbon Cloth Phenolic, CTE, Poisson's Ratio, E vs Temperature - Tensile

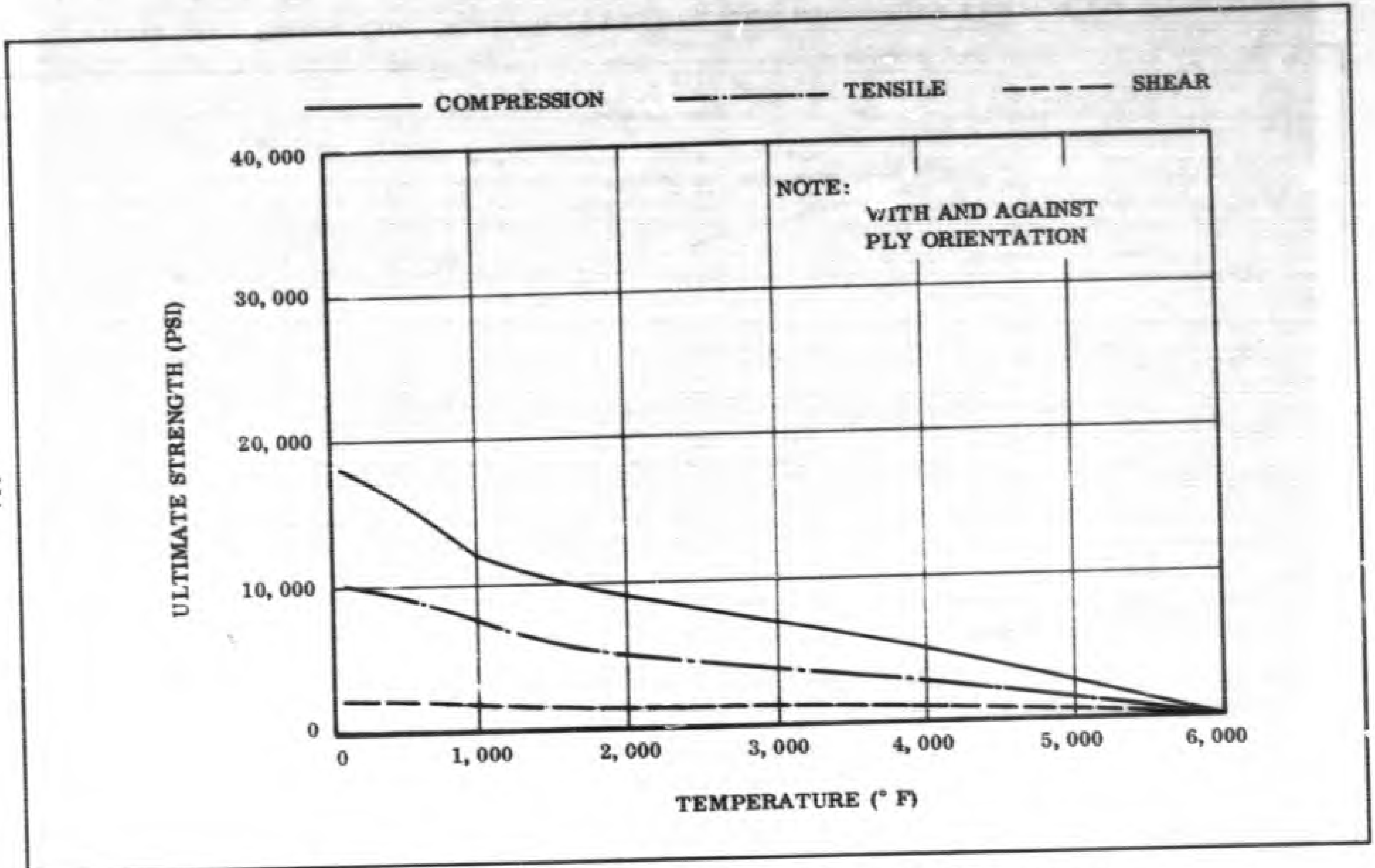

Figure 145. Carbon Cloth Phenolic, Ultimate Strength vs Temperature

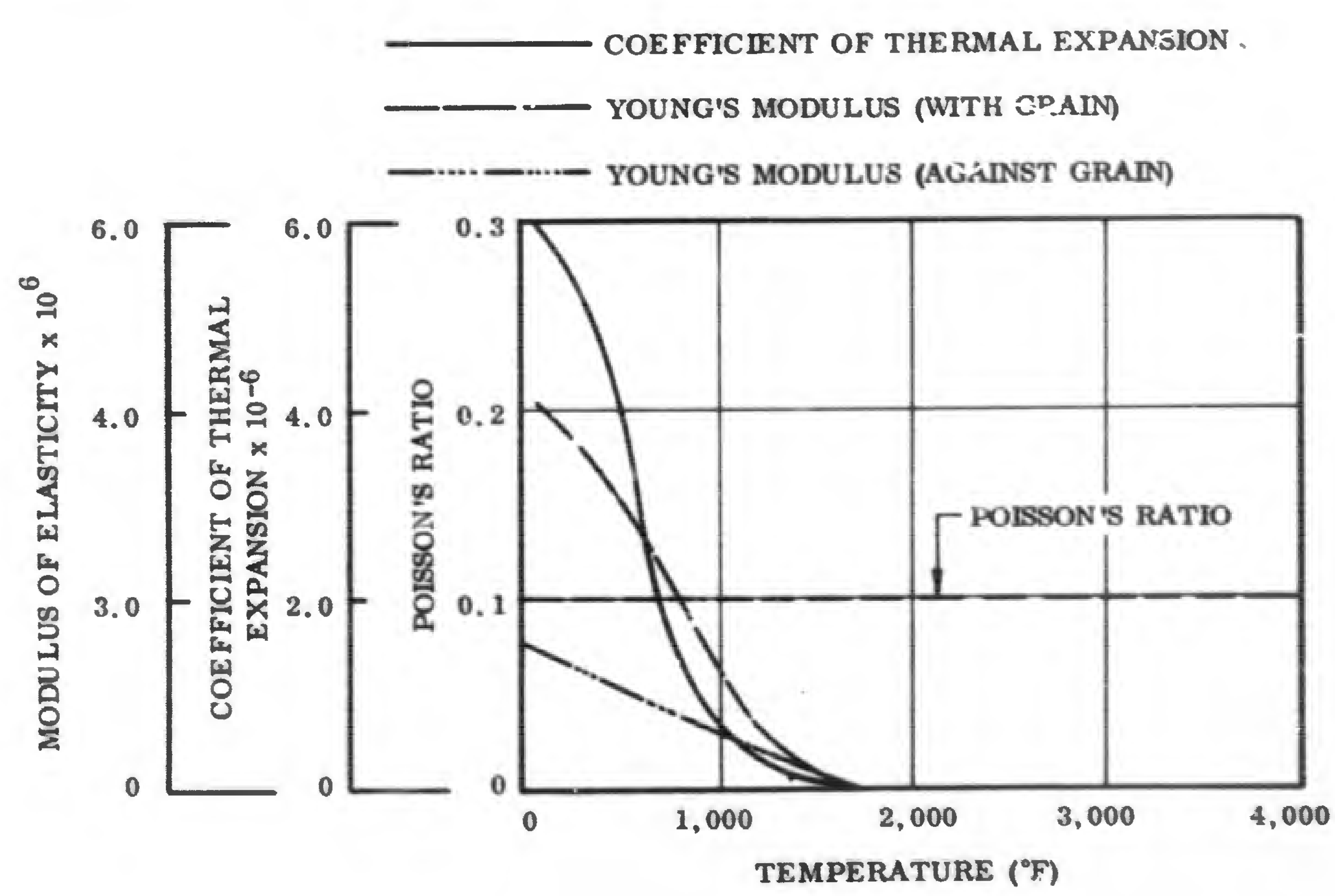

Figure 146. Glass Cloth Phenolic, CTE, Modulus, Poisson's Ratio vs Temperature

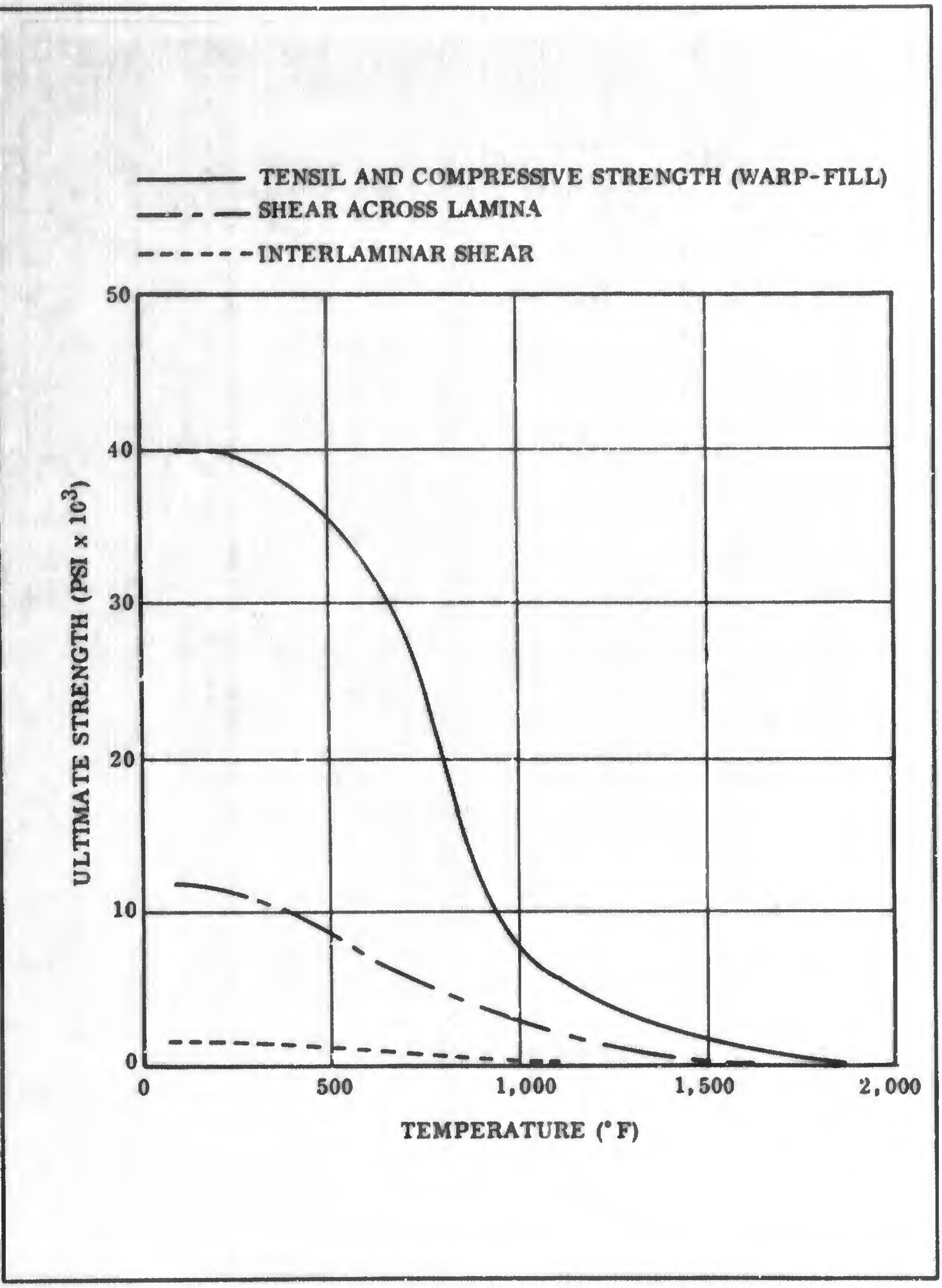

Figure 147. Glass Cloth Phenolic, Ultimate Tensile, Compressive, Shear Strength vs Temperature

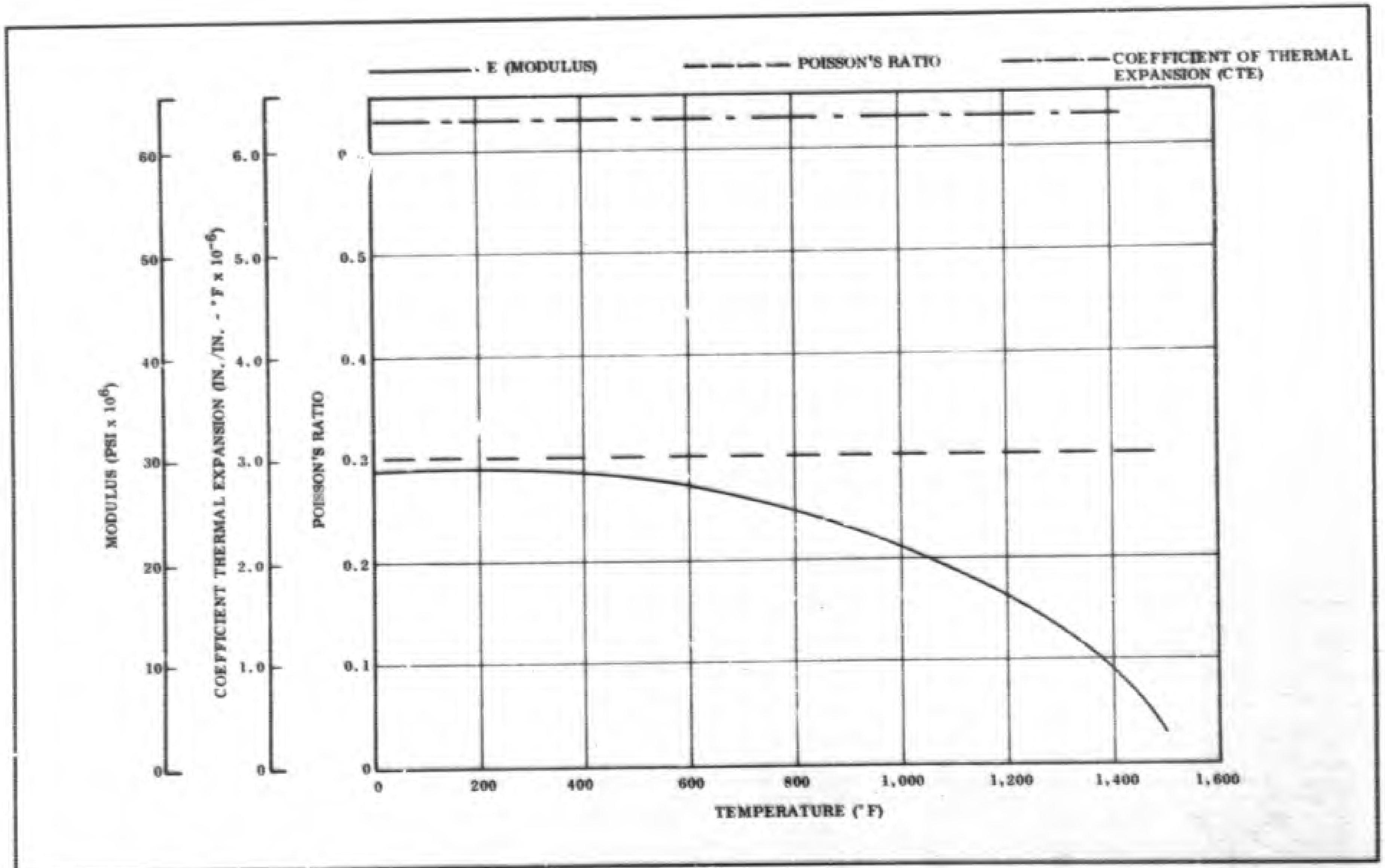

Figure 148. 4130 Steel, CTE, Modulus, Poisson's Ratio vs Temperature

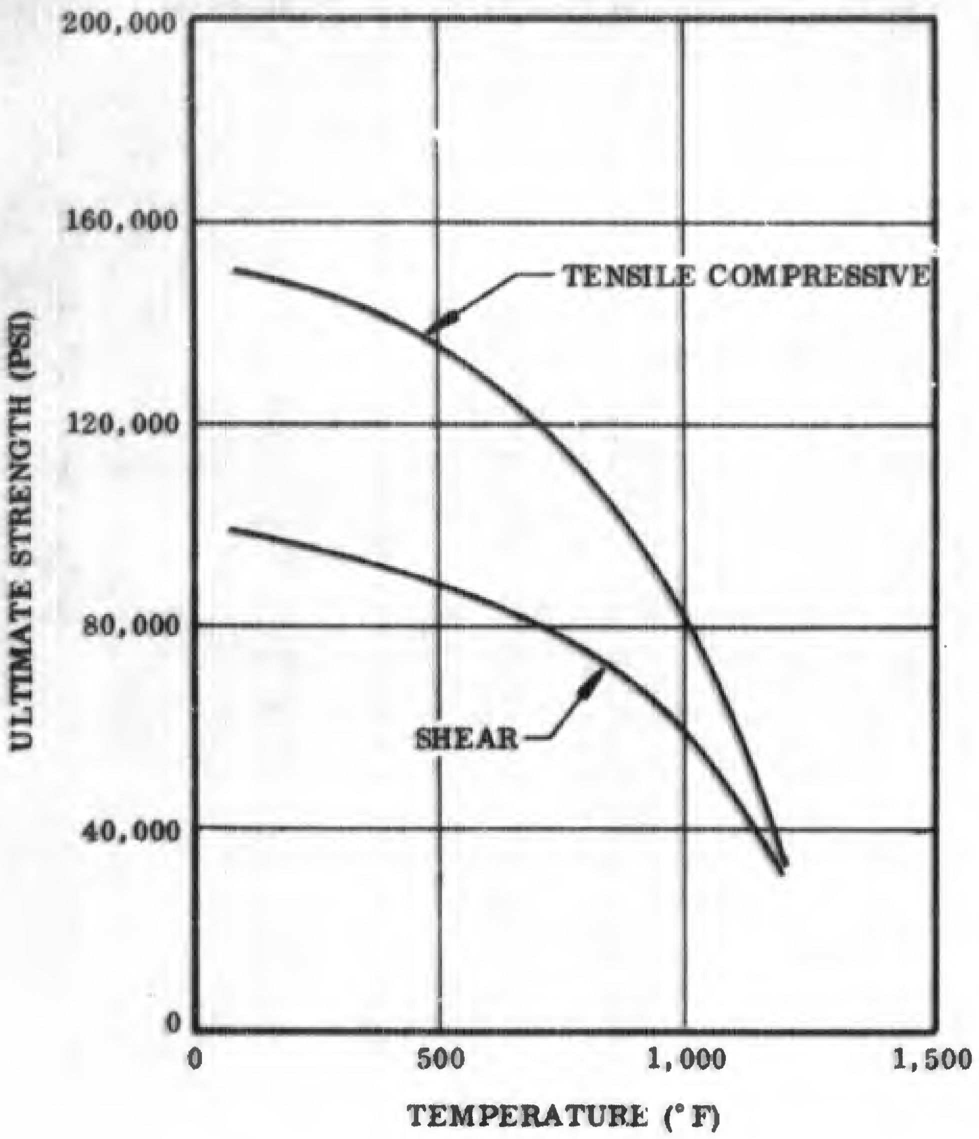

Figure 149. 4130 Steel, Ultimate Strength vs Temperature

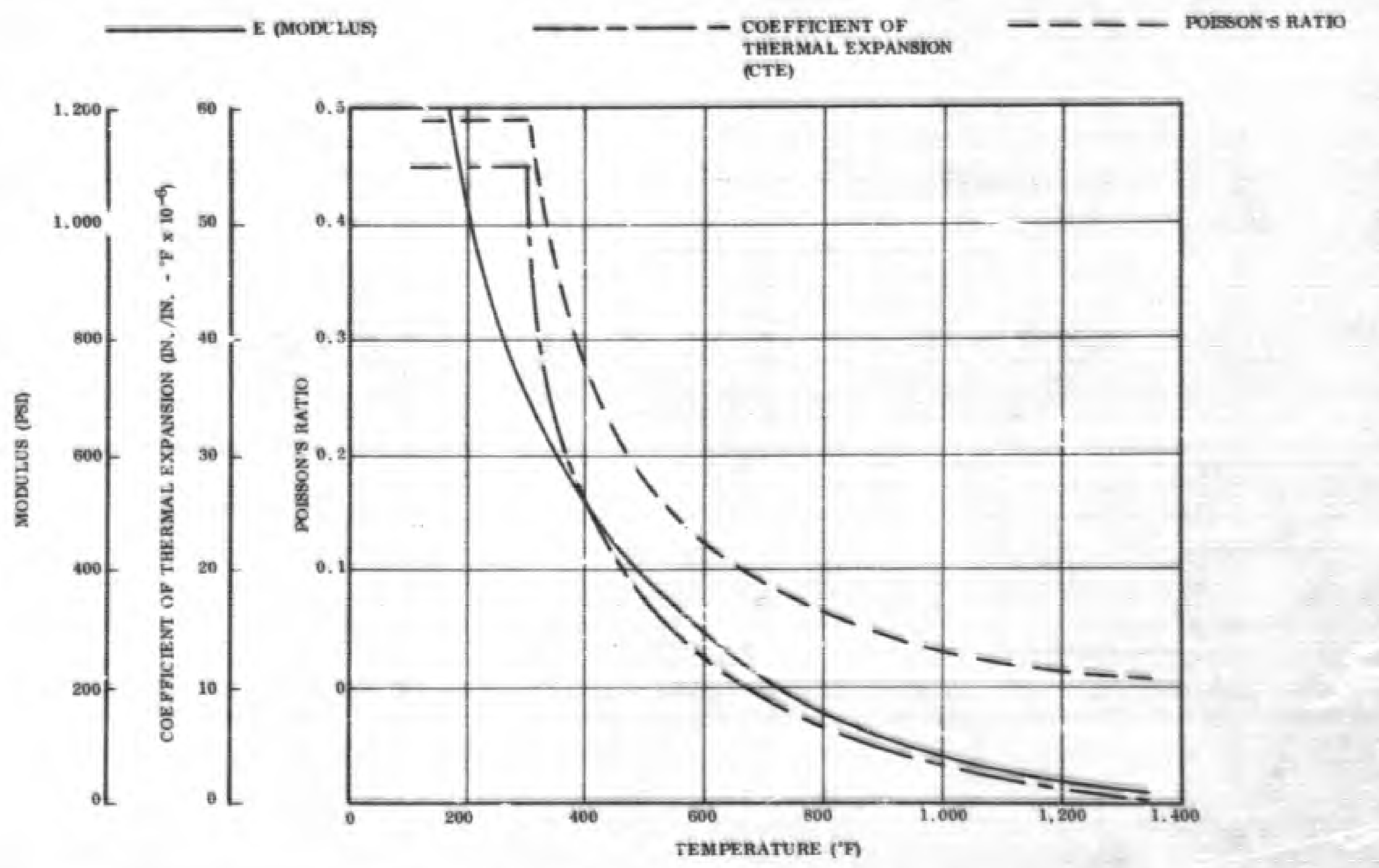

Figure 150. Neoprene Rubber, CTE, Poisson's Ratio, Modulus vs Temperature

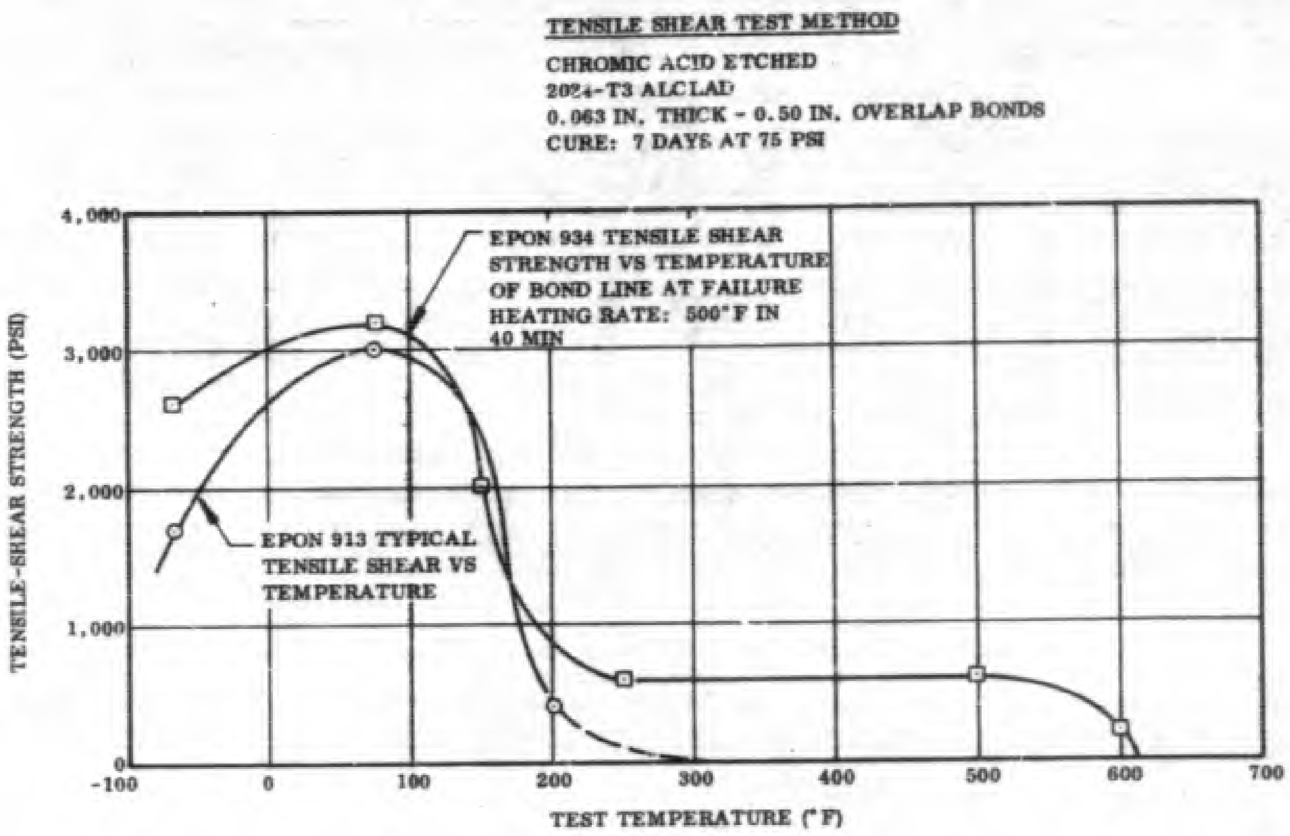

Figure 151. Epon 913 and 934, Typical Tensile-Shear Strength vs Temperature

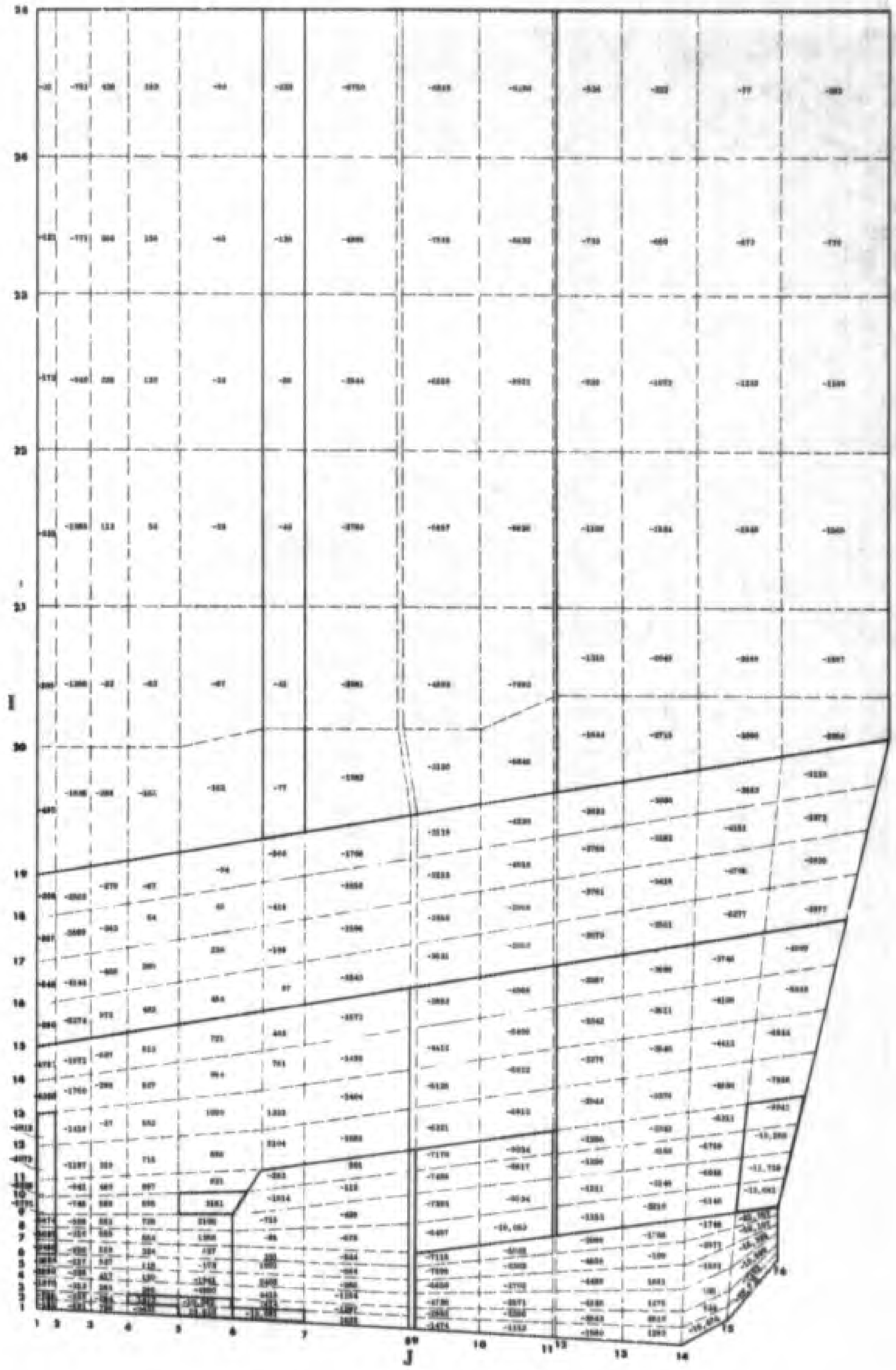

Figure 152. Boundary Condition A, Radial Stress at 5.0 Sec, Valve Closed

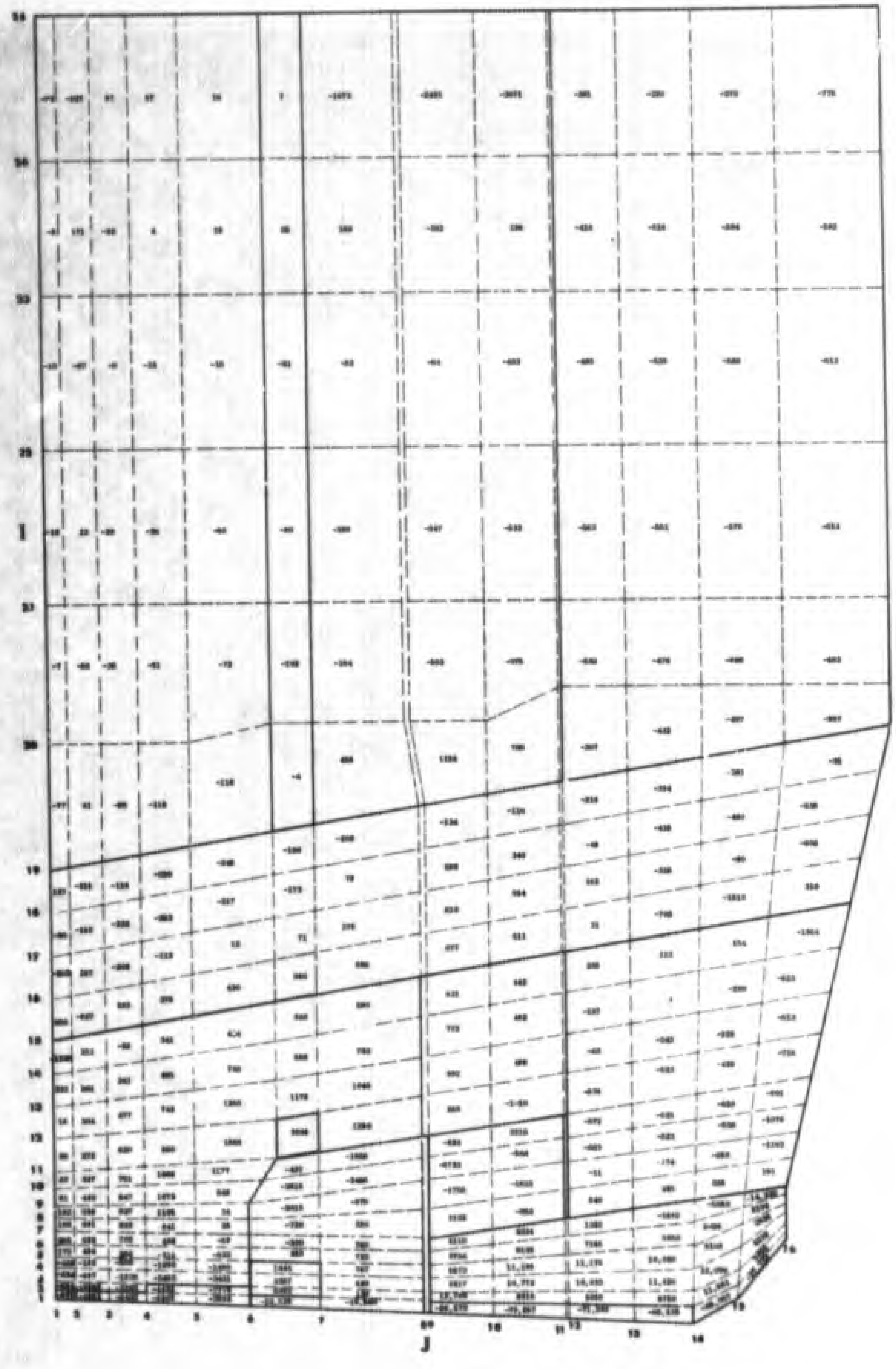

Figure 153. Boundary Condition A, Axial Stress at 5.0 Sec, Valve Closed

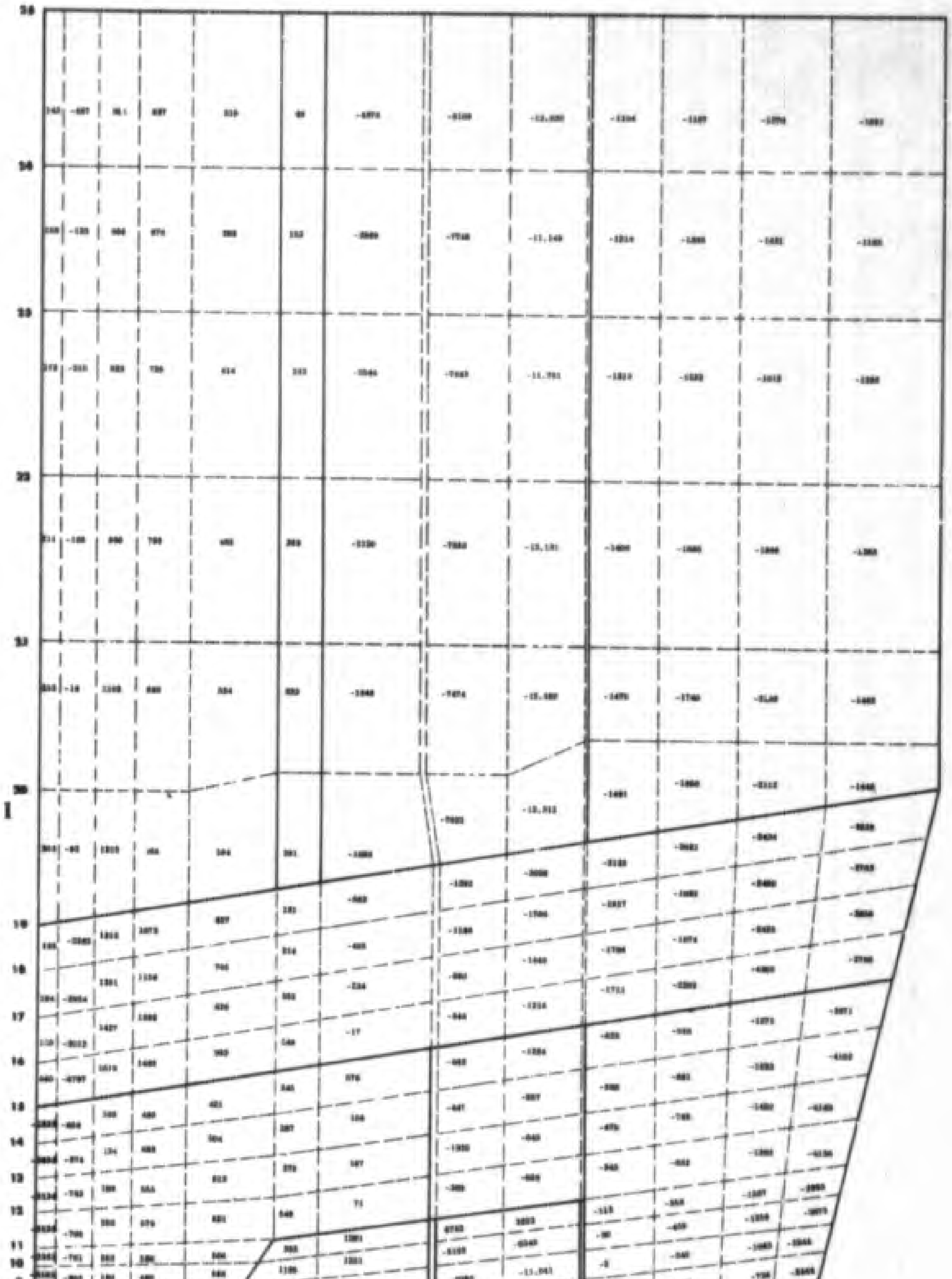

Figure 154. Boundary Condition A, Hoop Stress at 5.0 Sec, Valve Closed

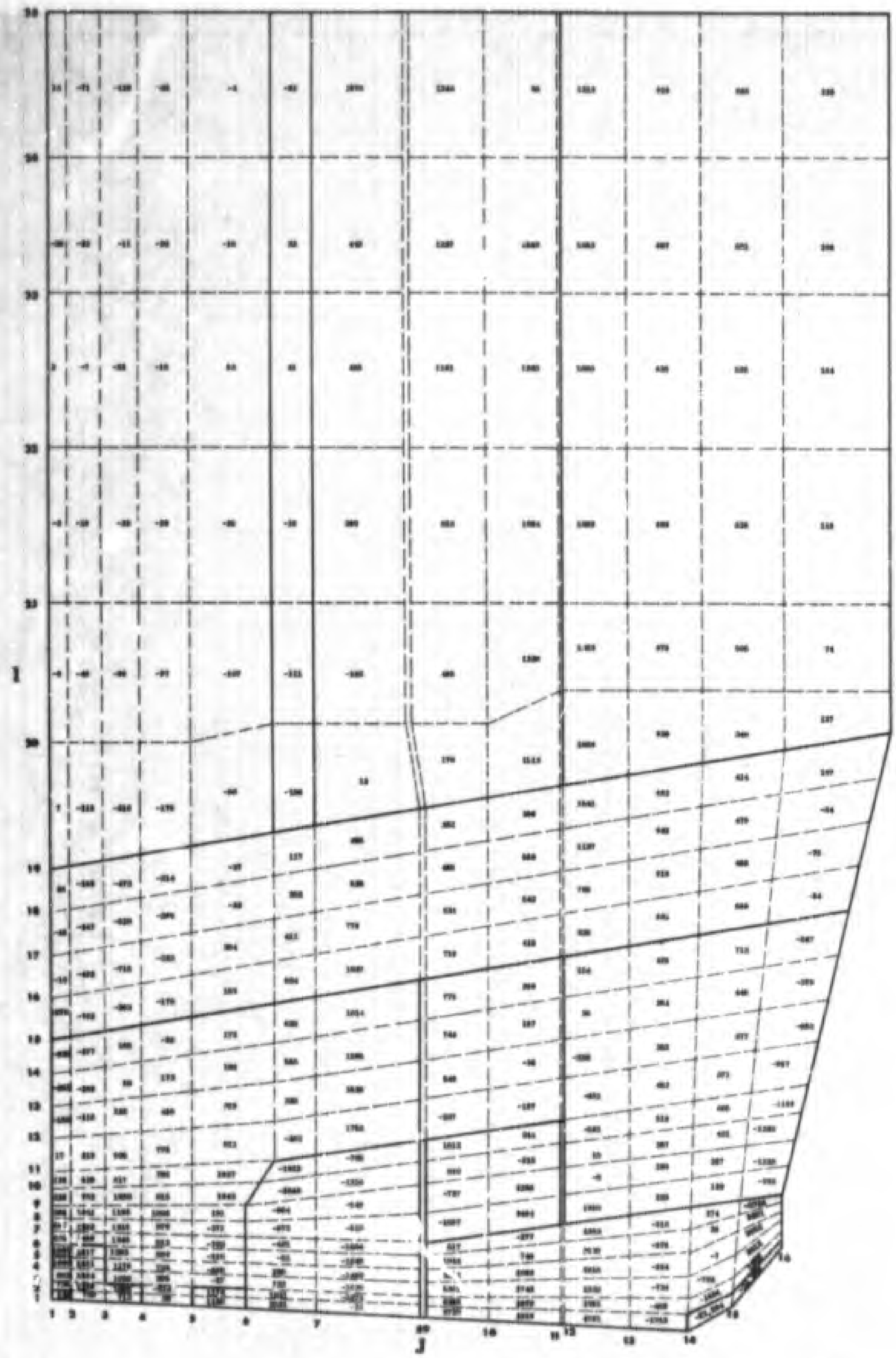

Figure 155. Boundary Condition A, Shear Stress at 5.0 Sec, Valve Closed

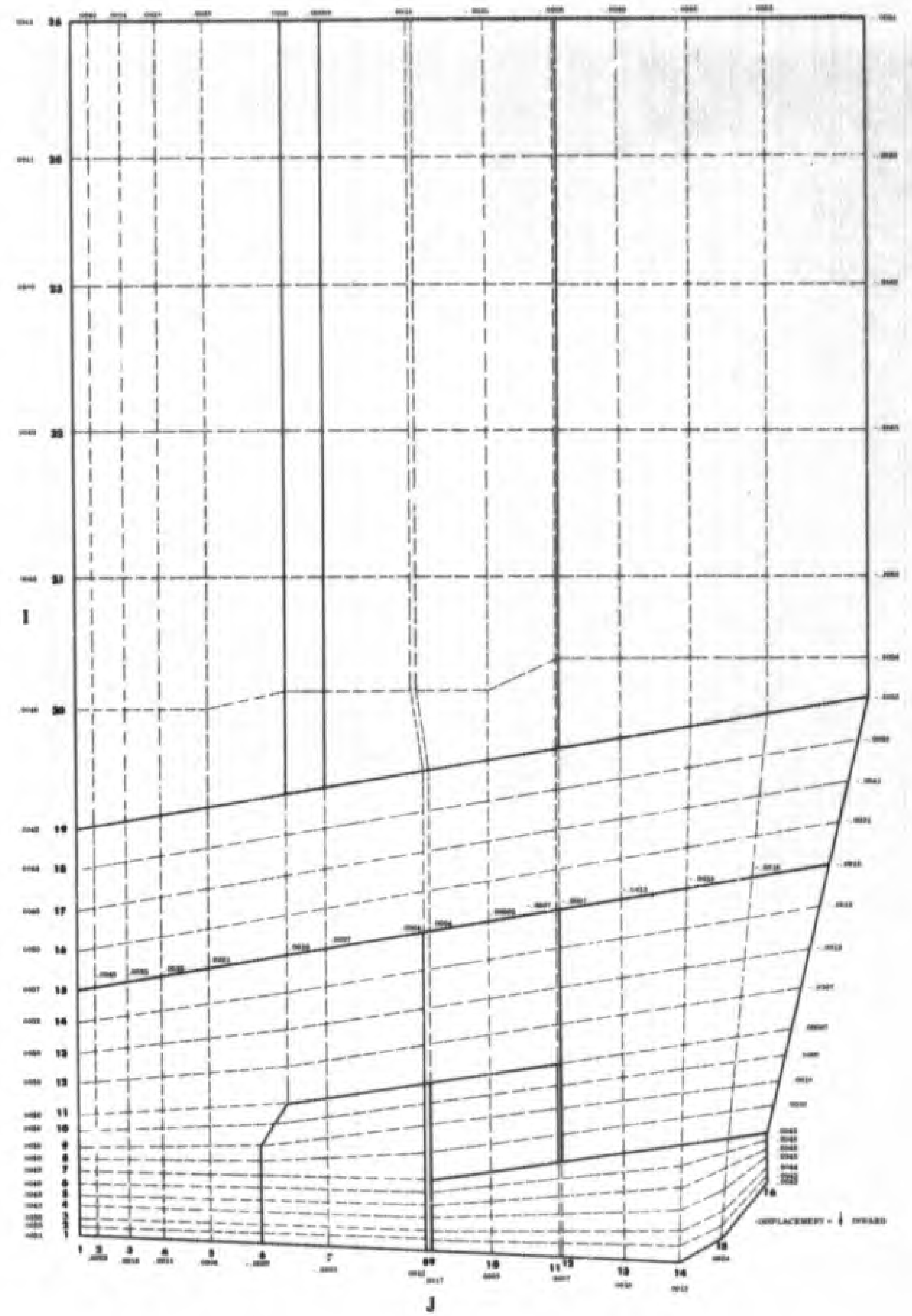

Figure 156. Boundary Condition A, Radial Displacements at 5.0 Sec, Valve Closed

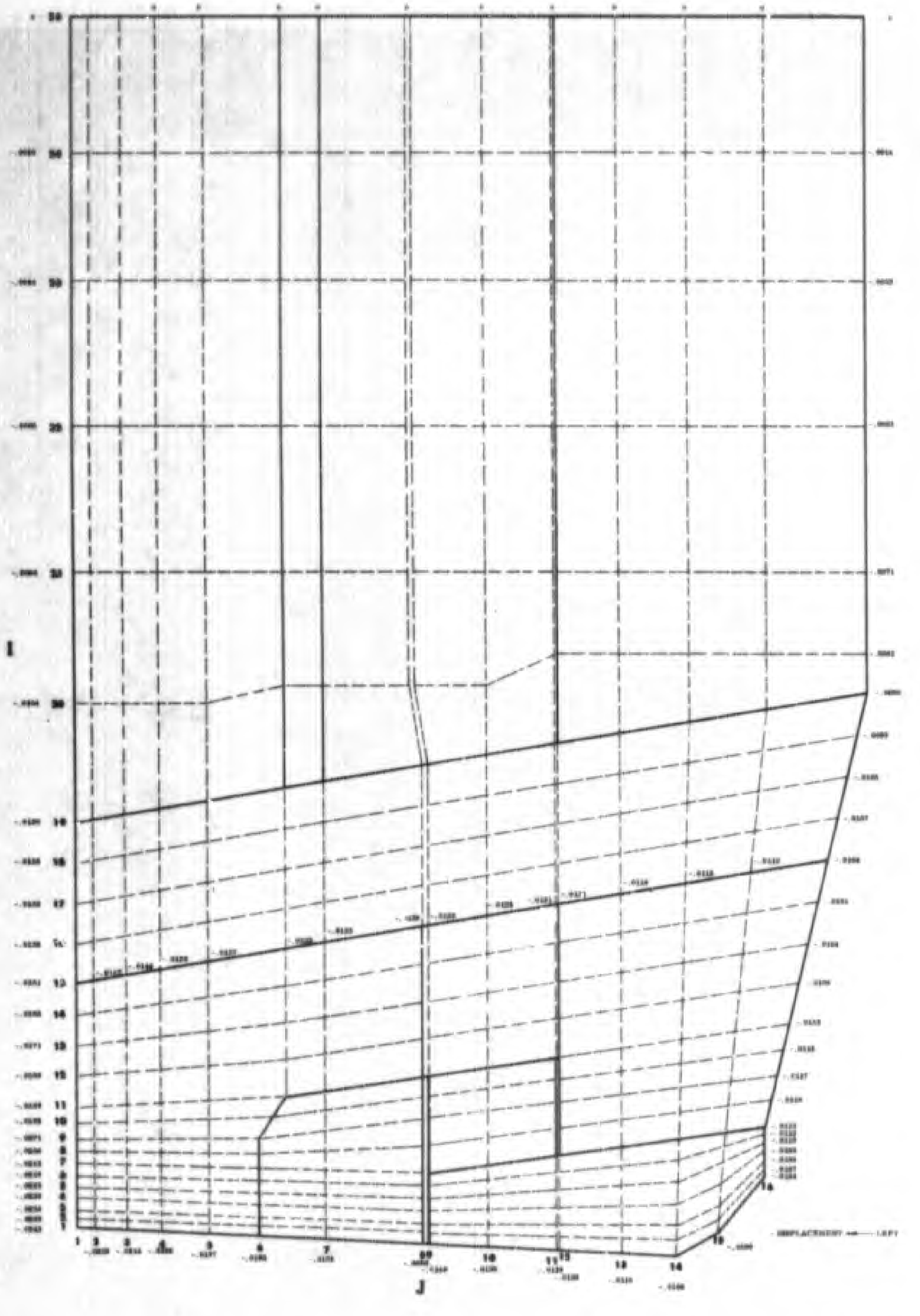

Figure 157. Boundary Condition A, Axial Displacements at 5.0 Sec, Valve Closed

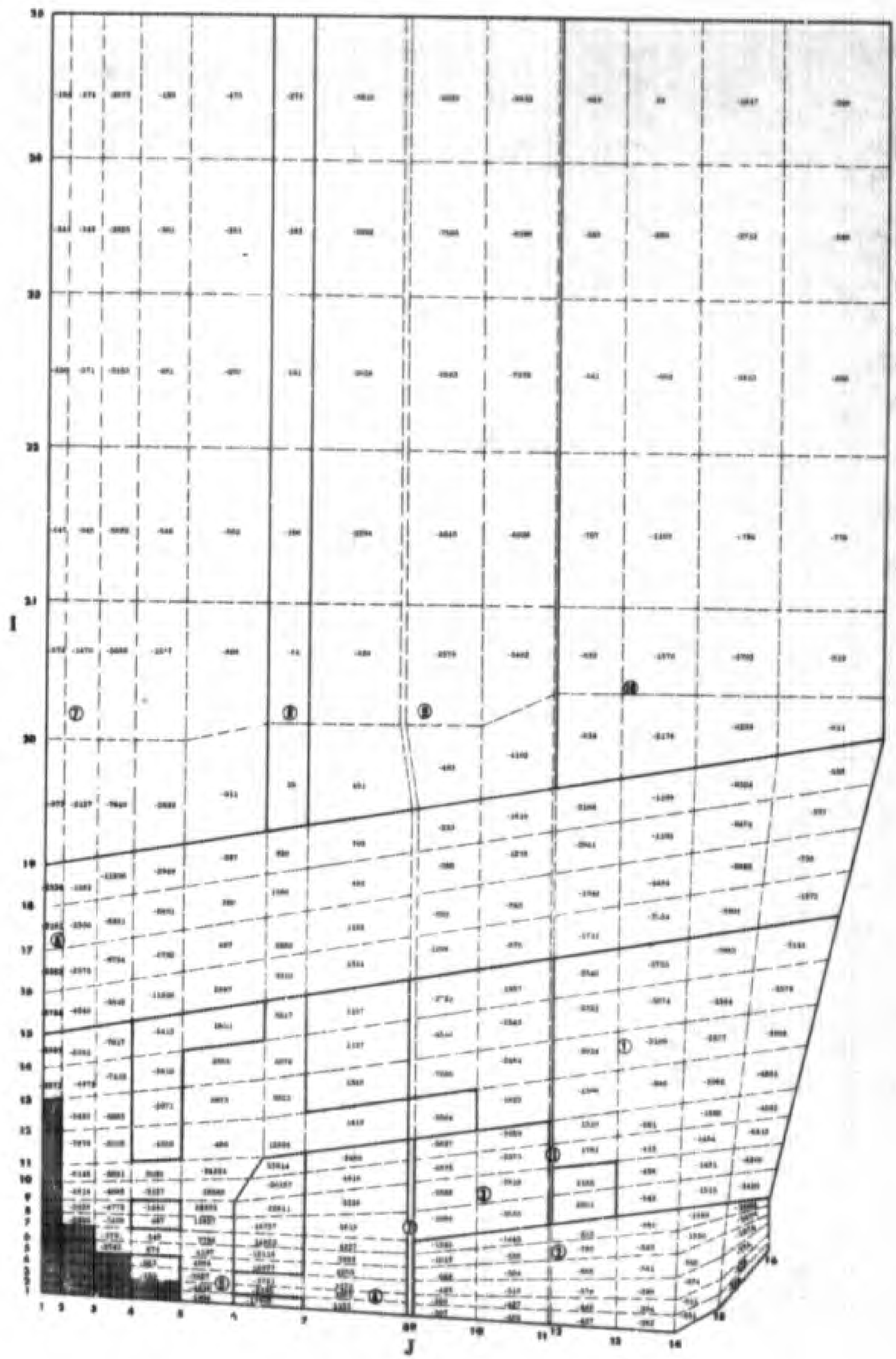

Figure 158. Boundary Condition A, Radial Stress at 25.0 Sec, Valve Open

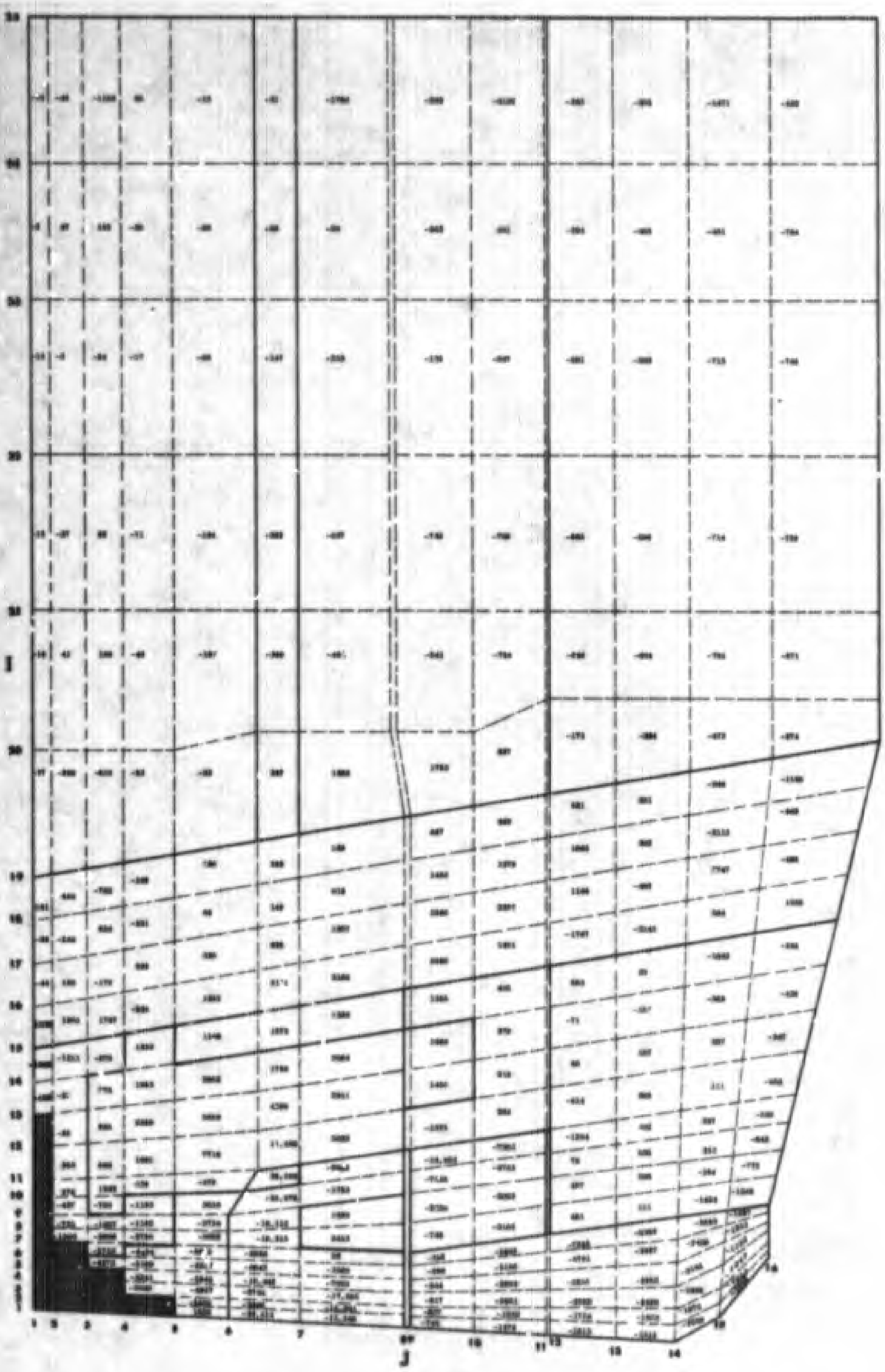

Figure 159. Boundary Condition A, Axial Stress at 25.0 Sec, Valve Open

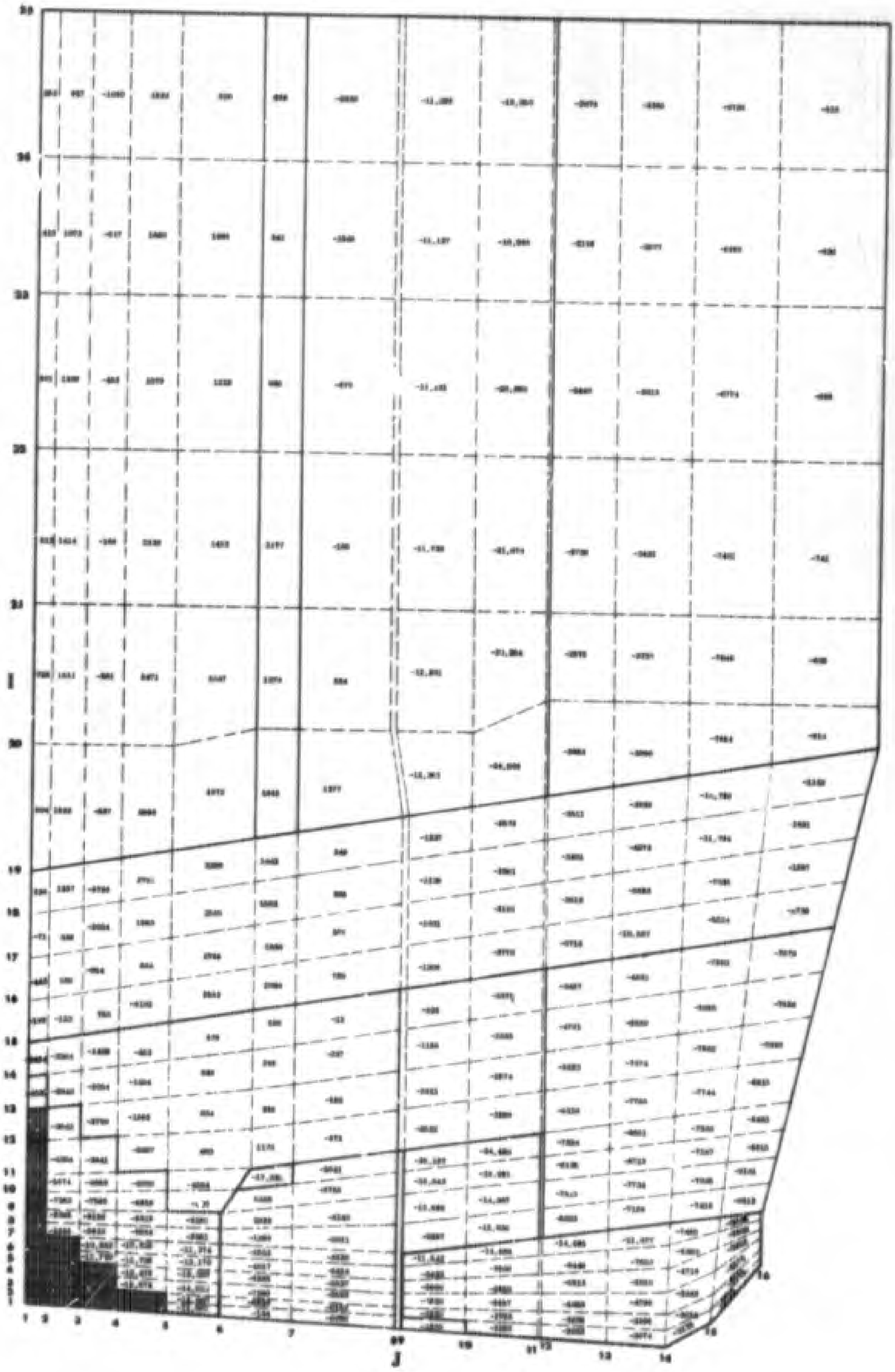

Figure 160. Boundary Condition A, Hoop Stress at 25.0 Sec, Valve Open

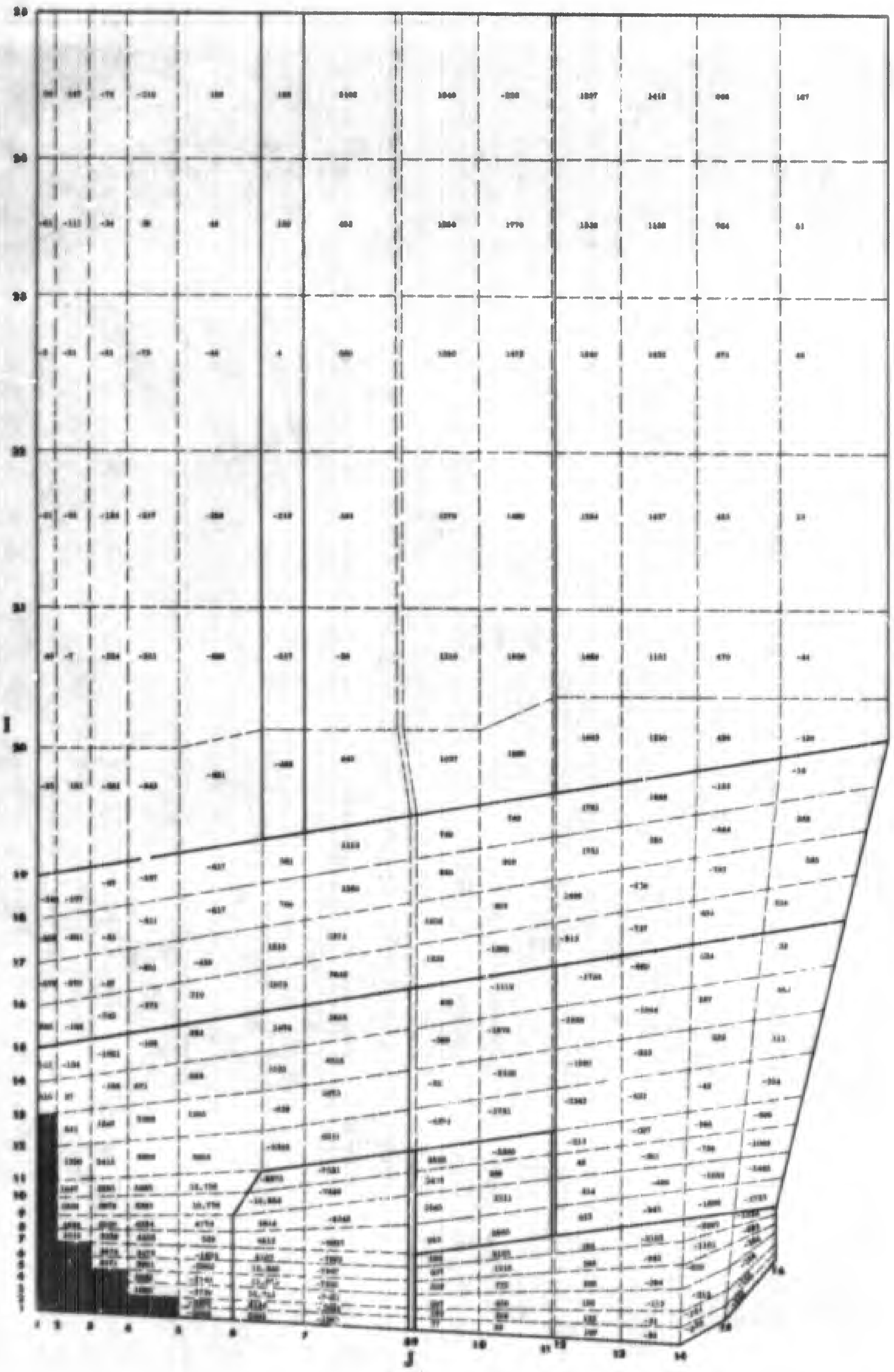

Figure 161. Boundary Condition A, Shear Stress at 25.0 Sec, Valve Open

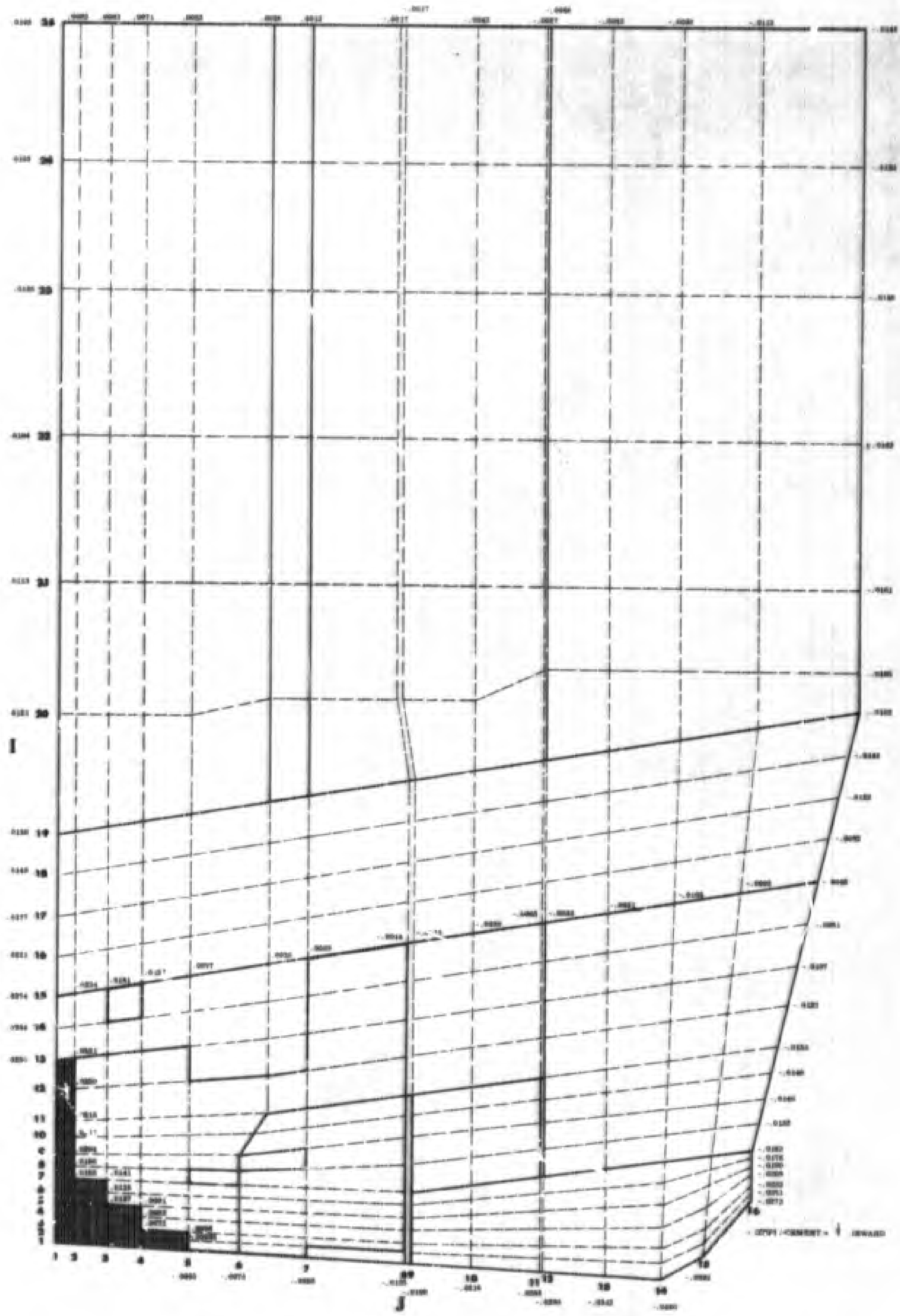

Figure 162. Boundary Condition A, Radial Displacements at 25.0 Sec, Valve Open

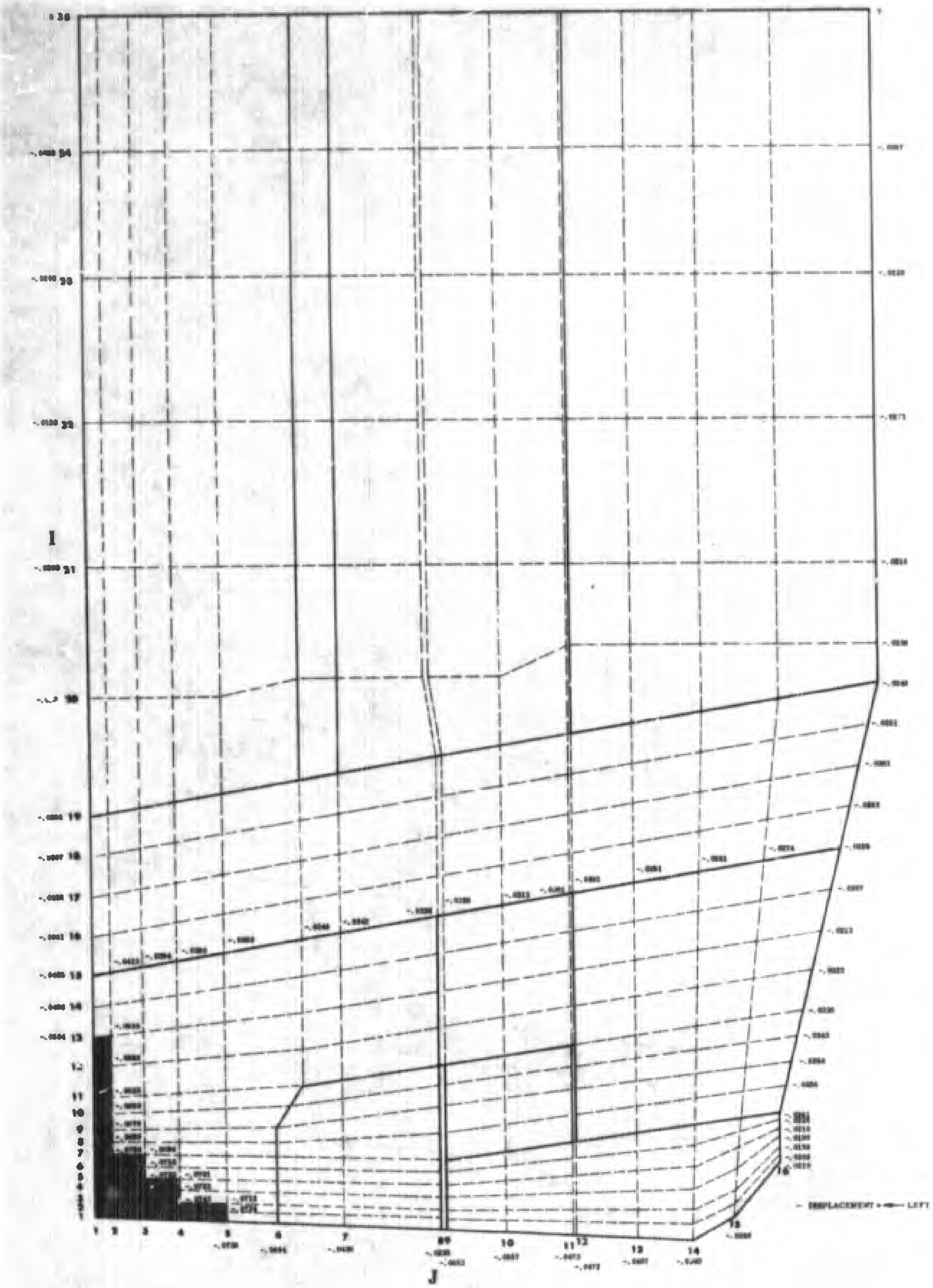

Figure 163. Boundary Condition A, Axial Boundary Displacements at 25.0 Sec, Valve Open

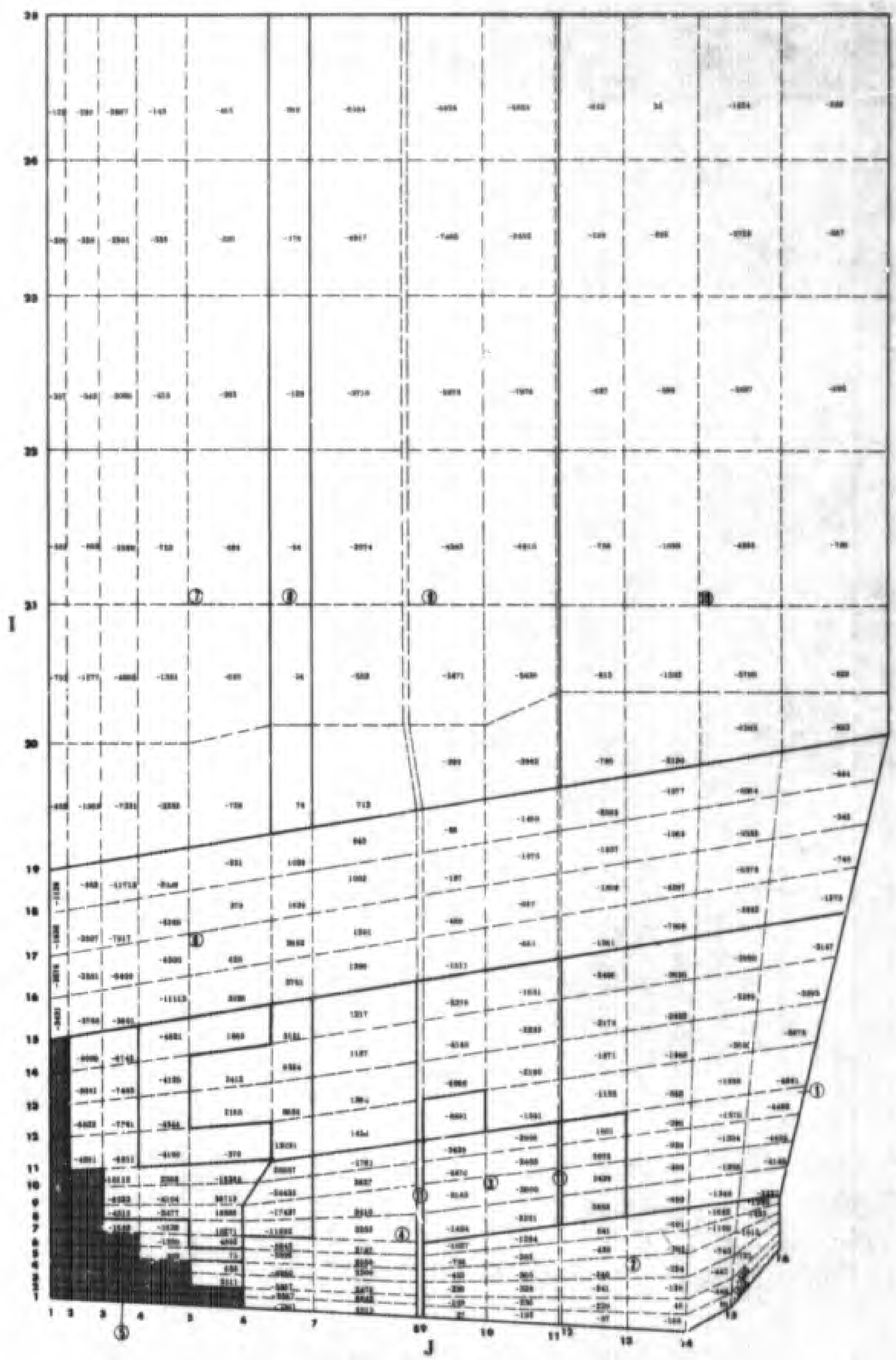

Figure 164. Boundary Condition A, Radial Stress at 25.1 Sec, Valve Closed

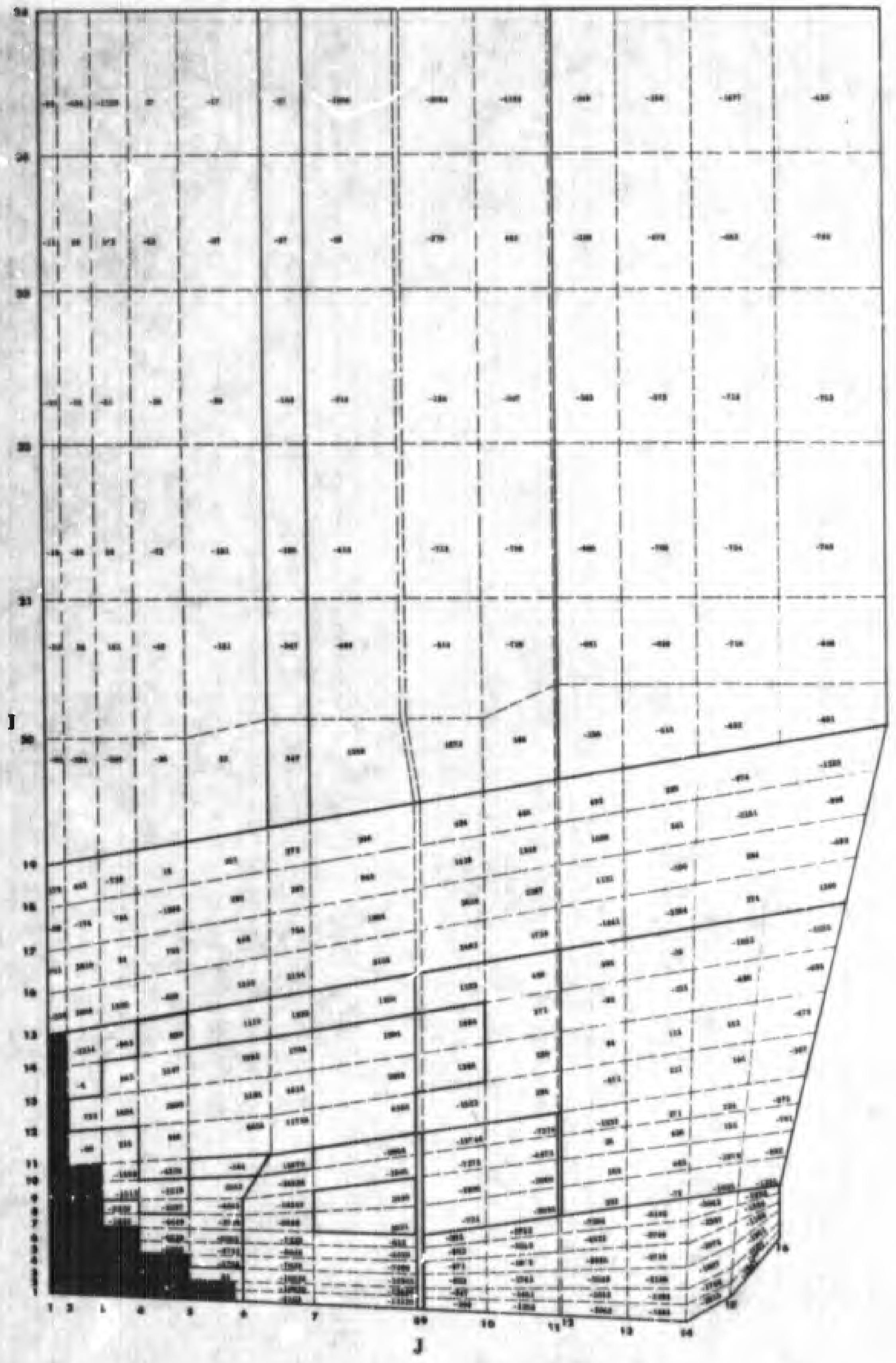

Figure 165. Boundary Condition A, Axial Stress at 25.1 Sec, Valve Closed

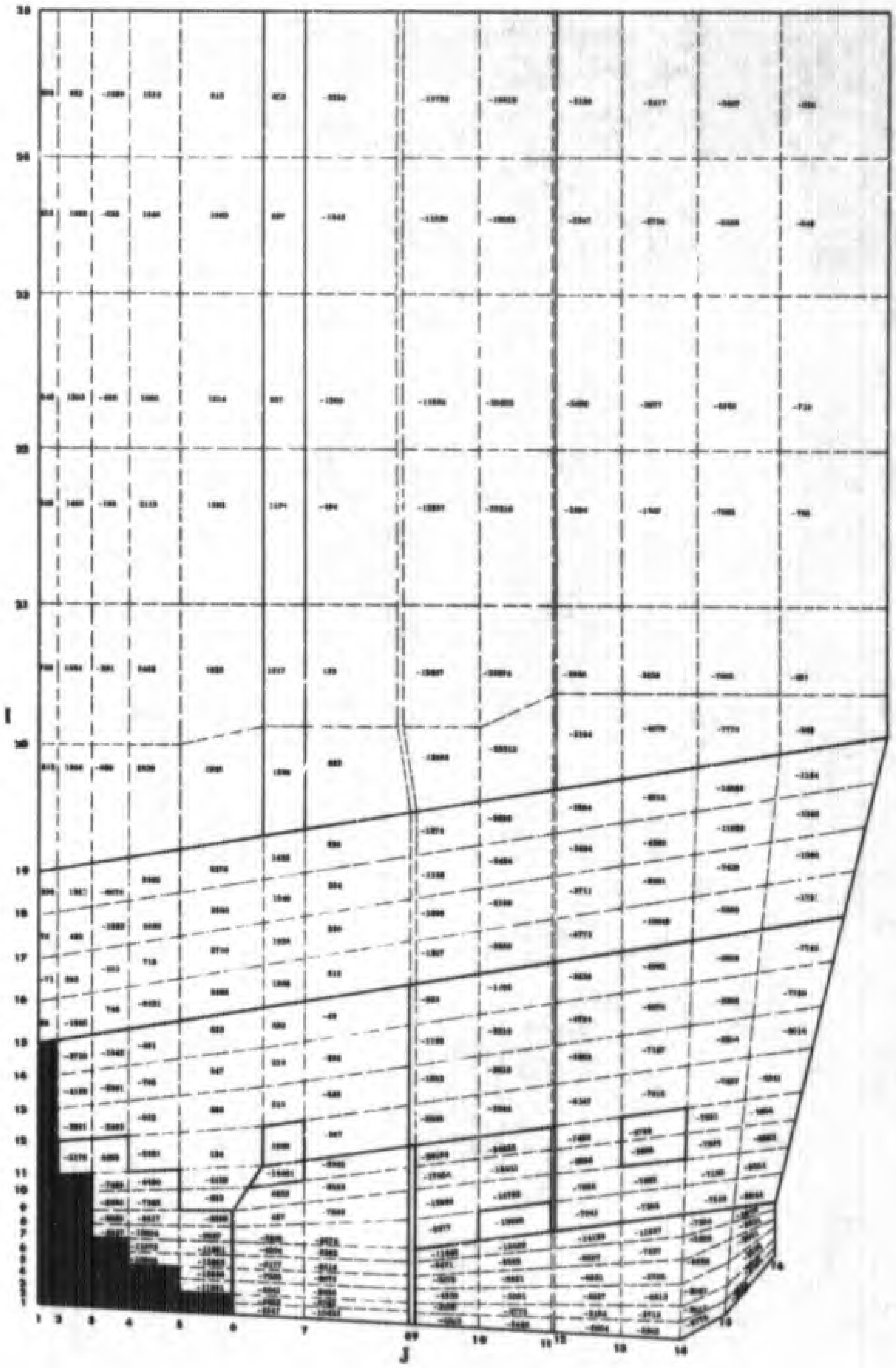

Figure 166. Boundary Condition A, Hoop Stress at 25.1 Sec, Valve Closed

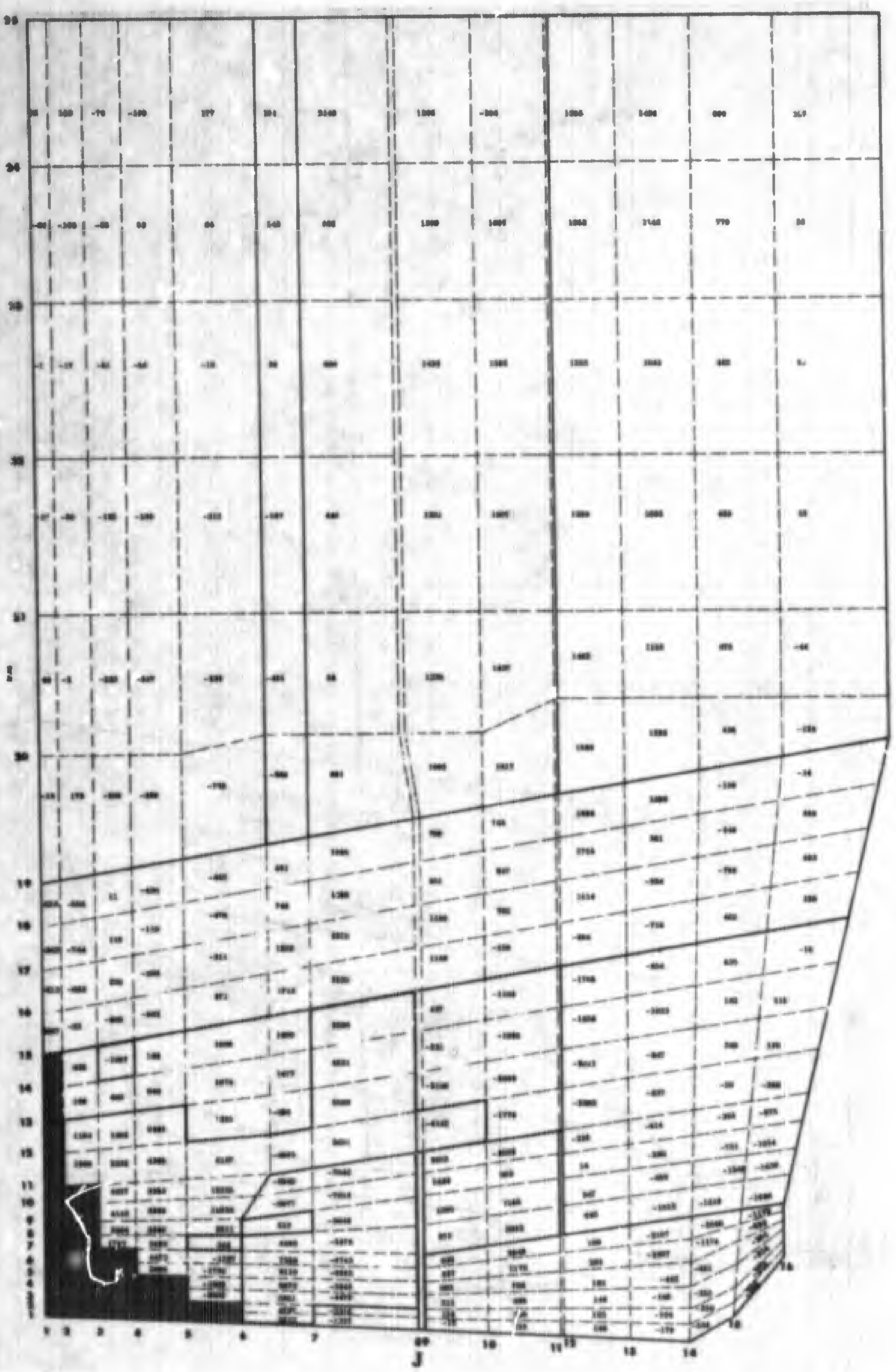

Figure 167. Boundary Condition A, Shear Stress at 25.1 Sec, Valve Closed

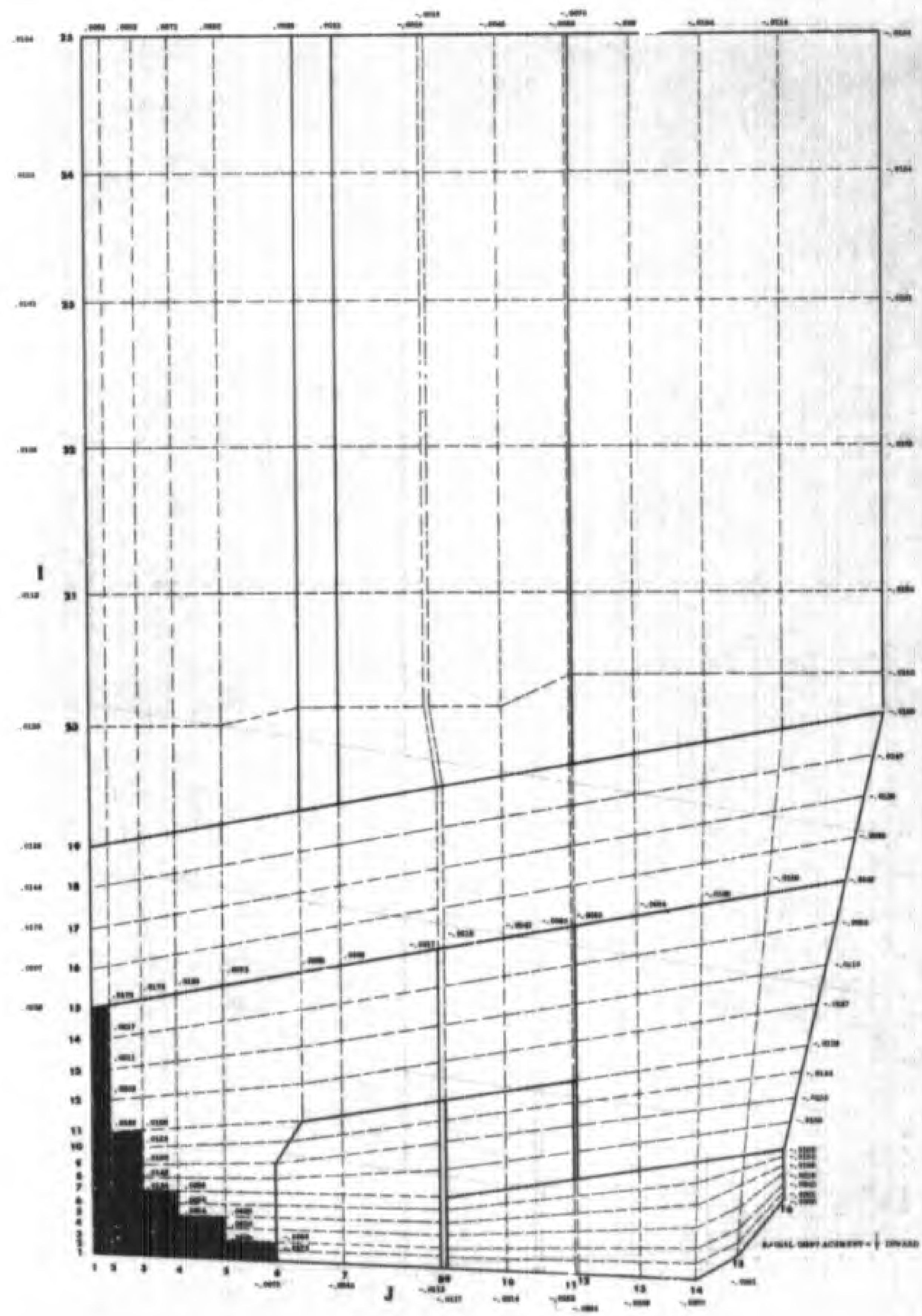

Figure 168. Boundary Condition A, Radial Displacements at 25.1 Sec, Valve Closed

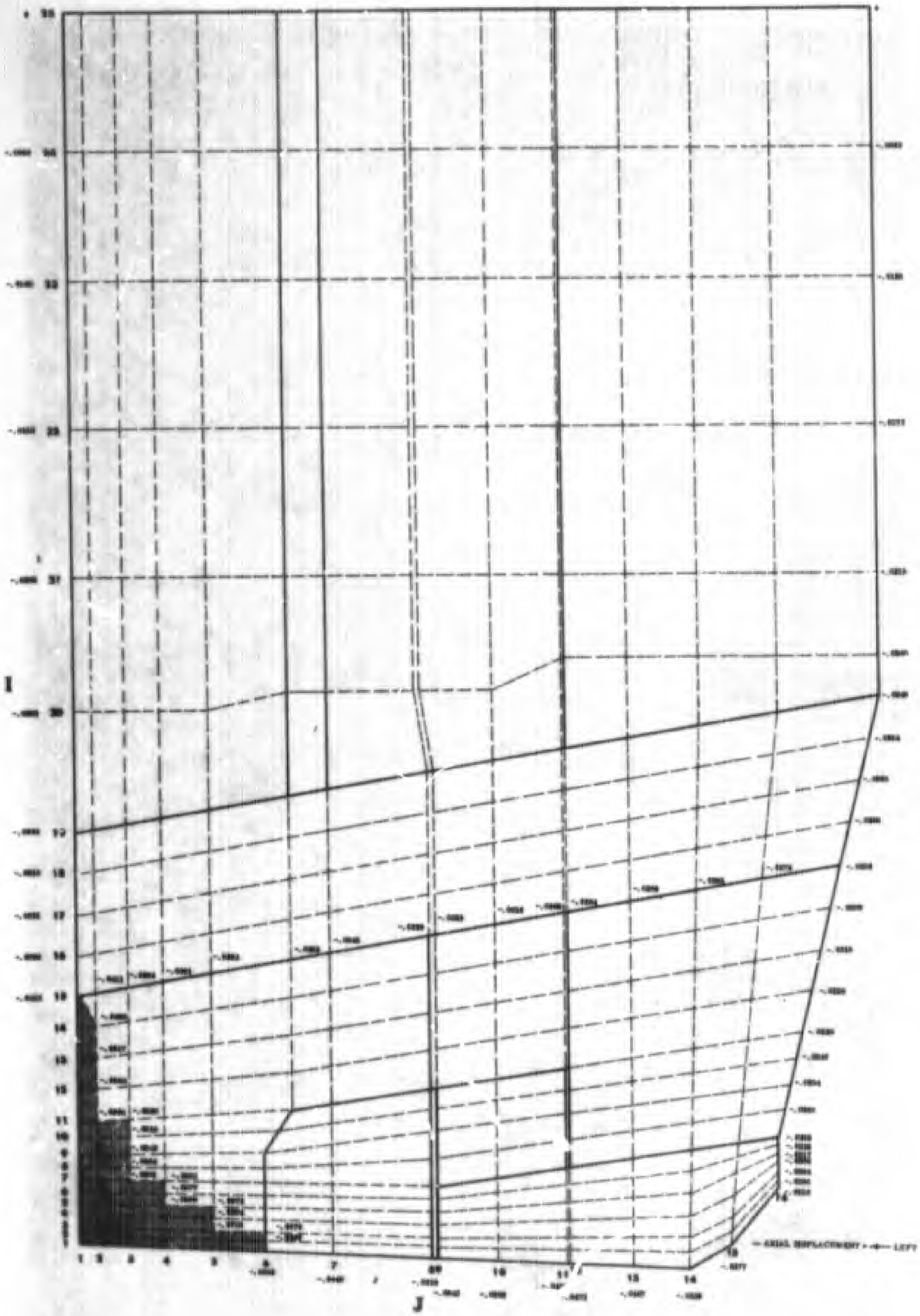

Figure 169. Boundary Condition A, Axial Boundary Displacements at 25.1 Sec, Valve Closed

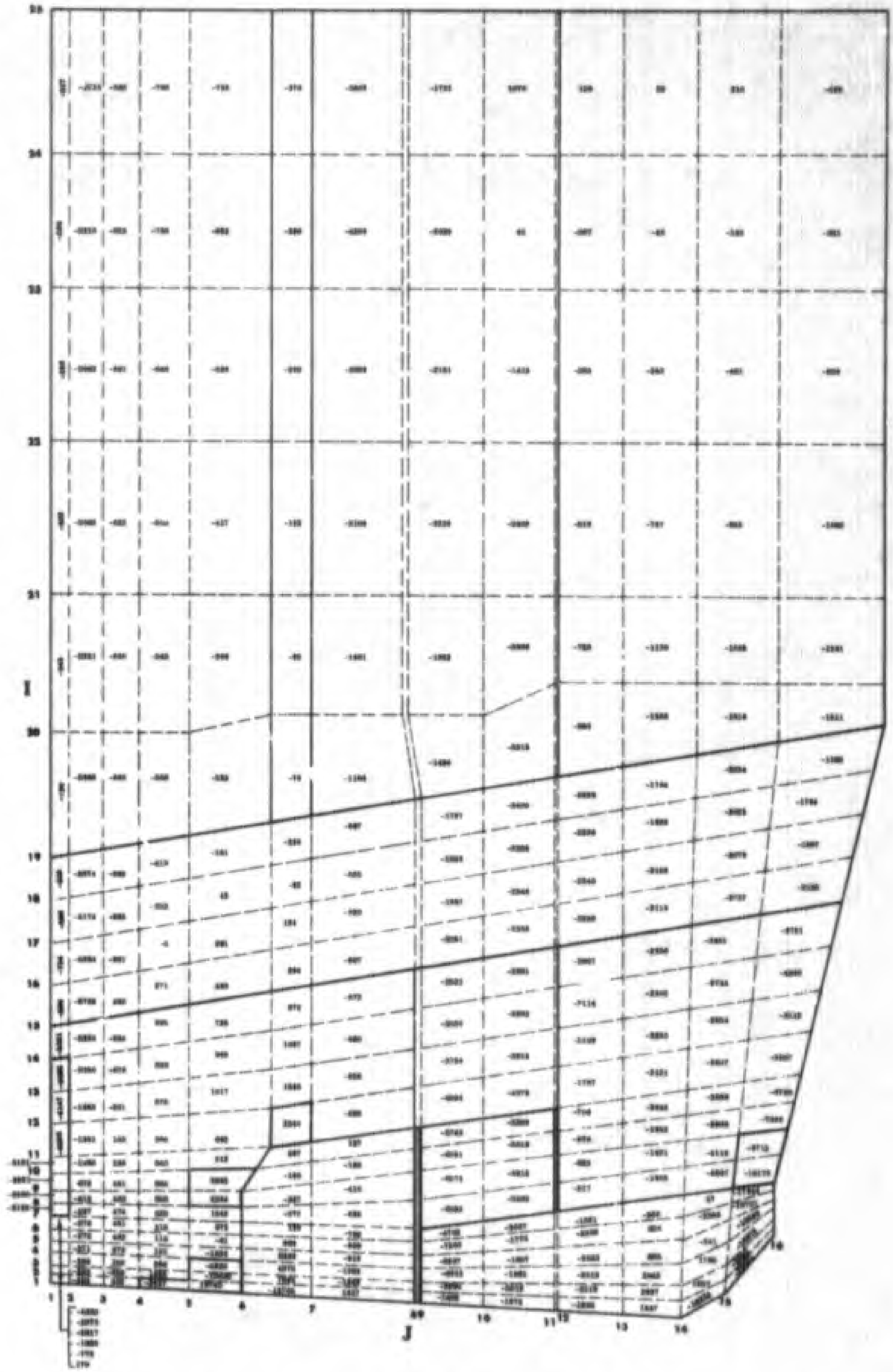

Figure 170. Boundary Condition B, Radial Stress at 5.0 Sec, Valve Closed

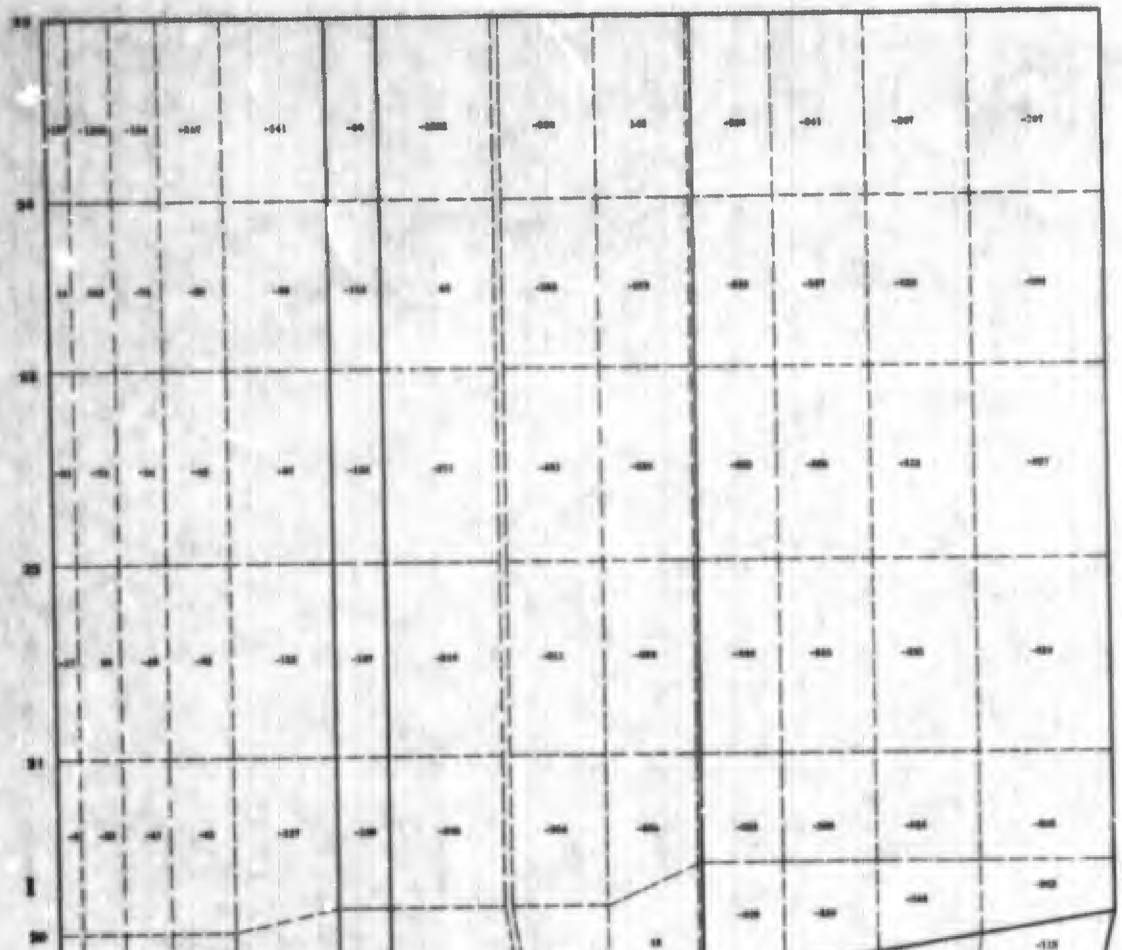

Figure 171. Boundary Condition B, Axial Stress at 5.0 Sec, Valve Closed

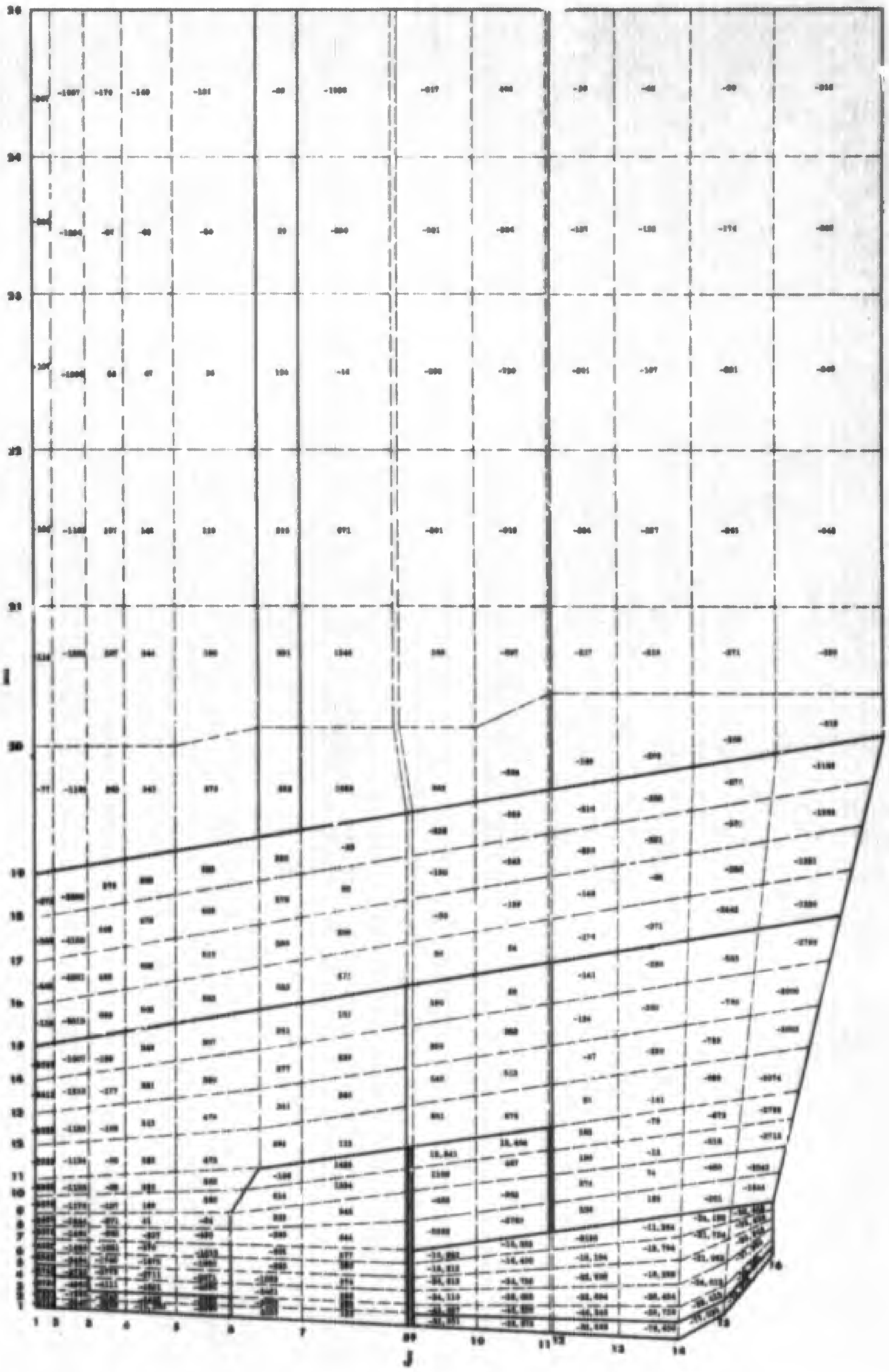

Figure 172. Boundary Condition B, Hoop Stress at 5.0 Sec, Valve Closed

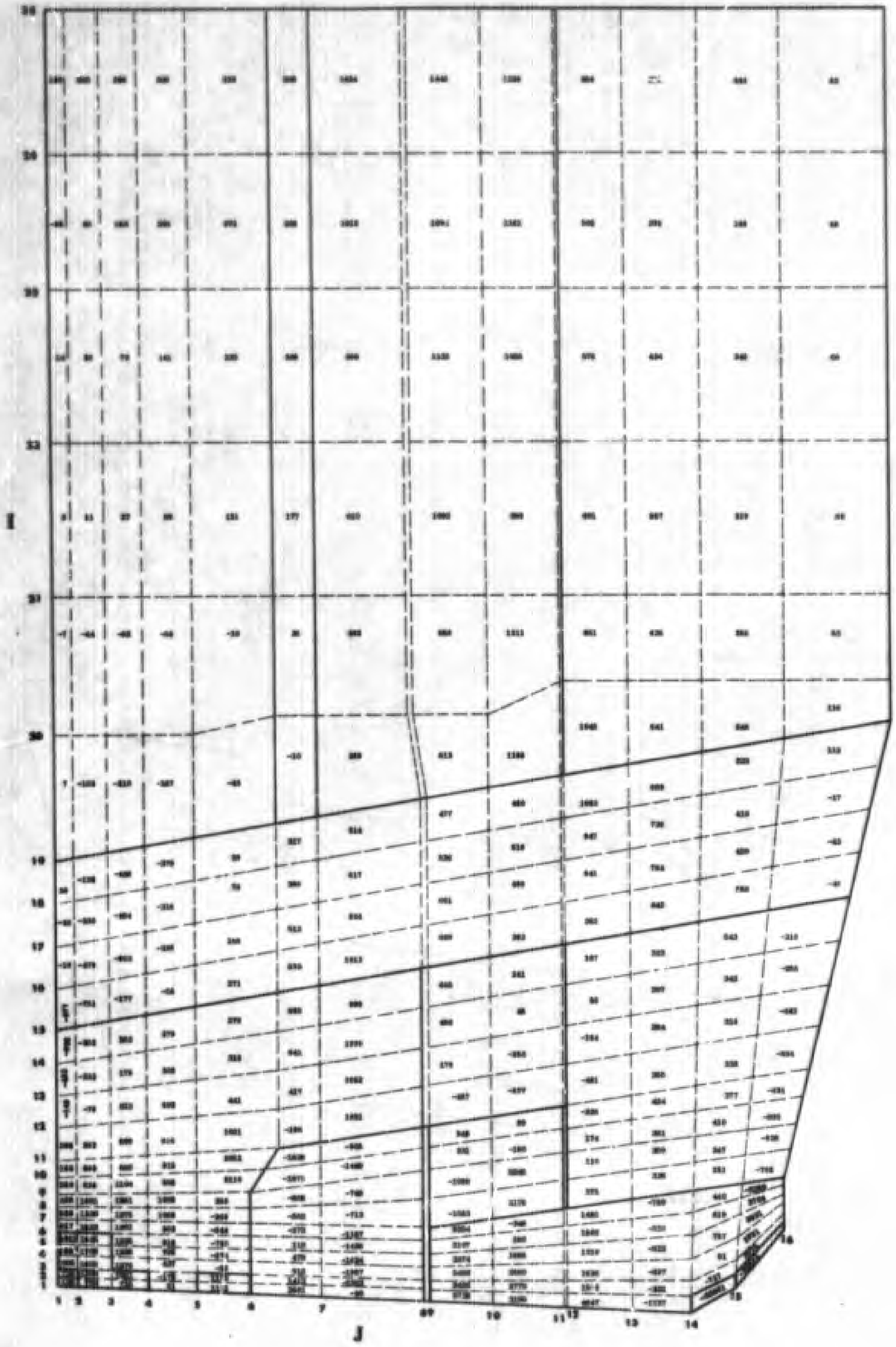

Figure 173. Boundary Condition B, Shear Stress at 5.0 Sec, Valve Closed

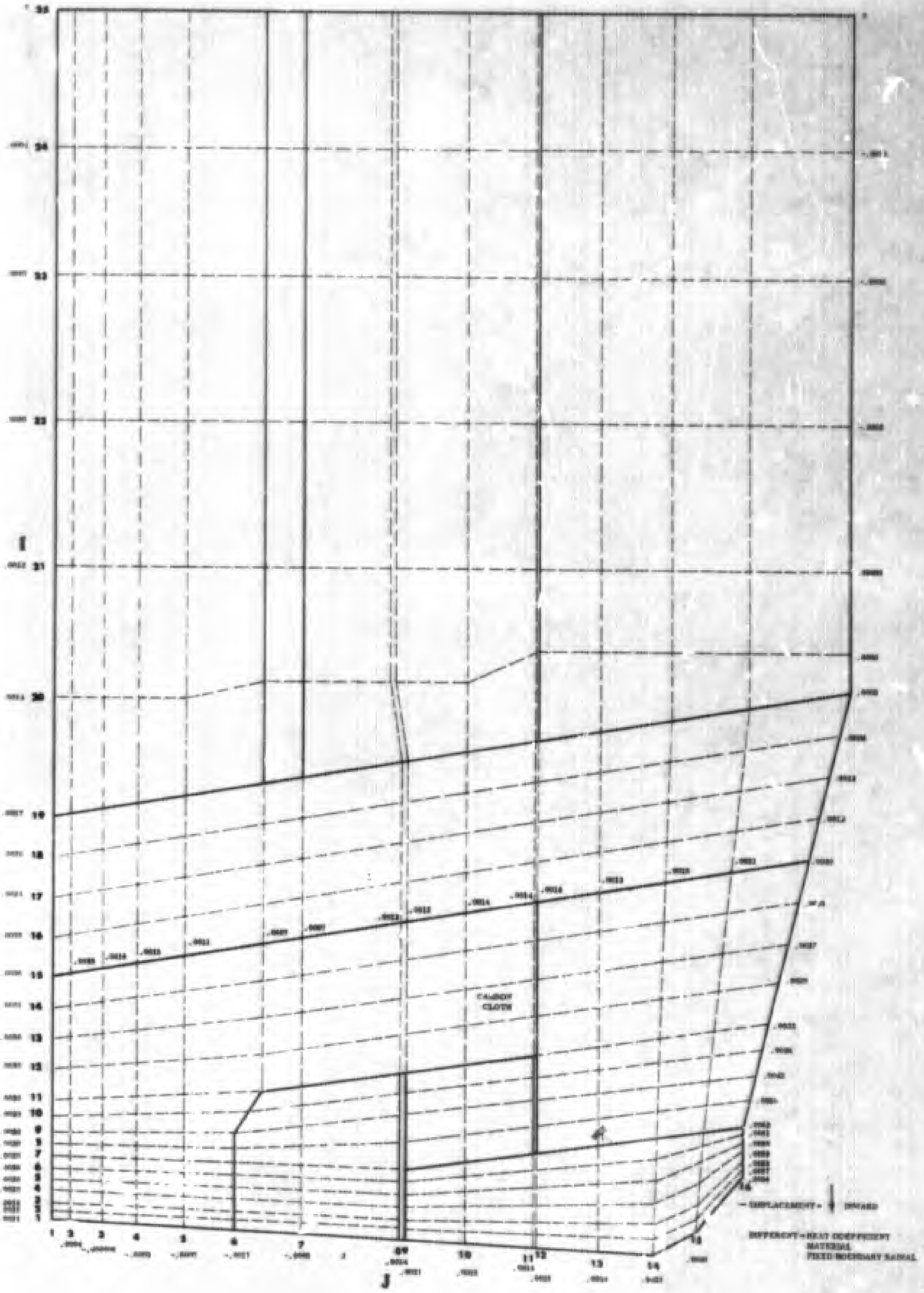

Figure 174. Boundary Condition B, Radial Displacements at 5.0 Sec, Valve Closed

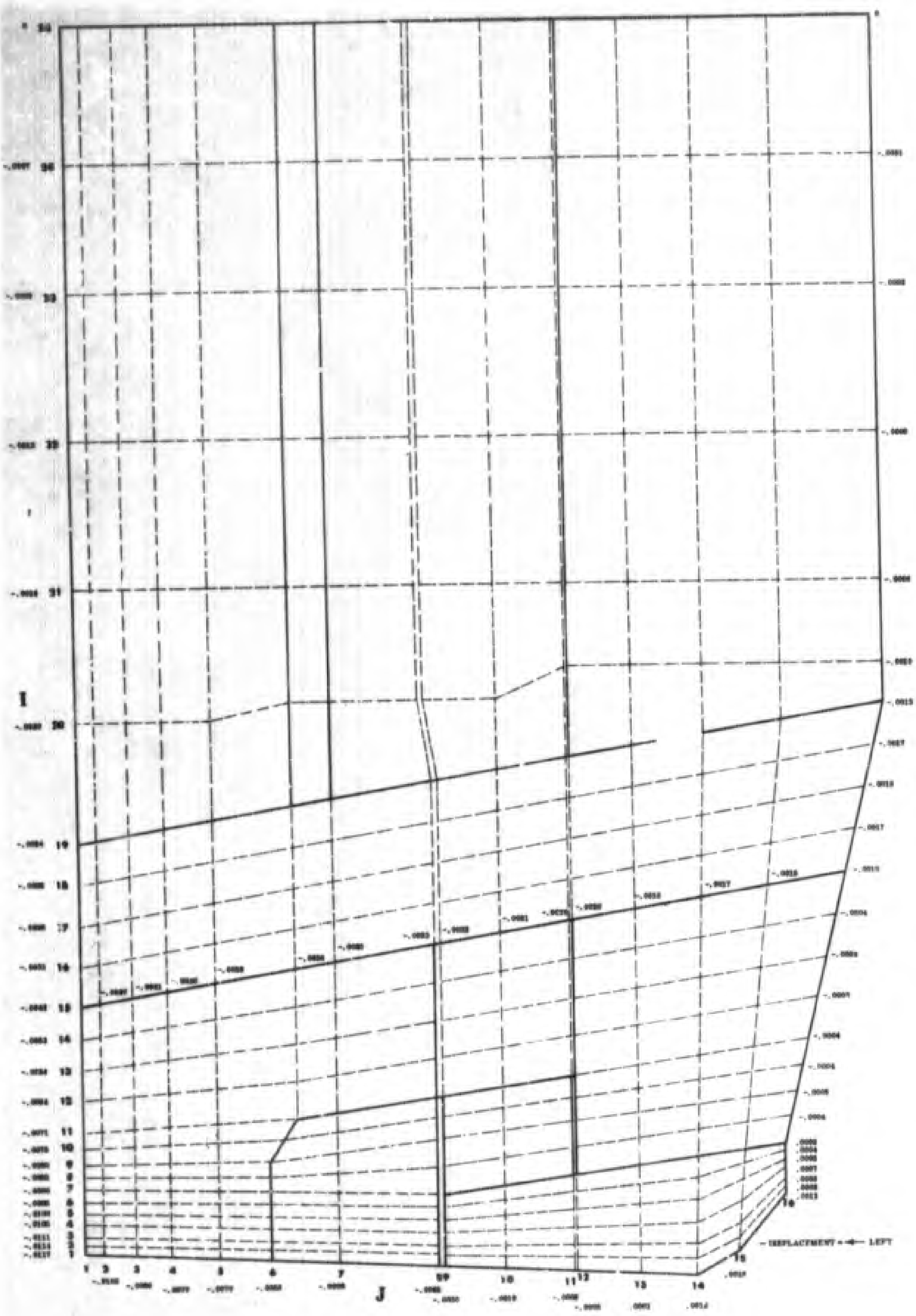

Figure 175. Boundary Condition B, Axial Displacements at 5.0 Sec, Valve Closed

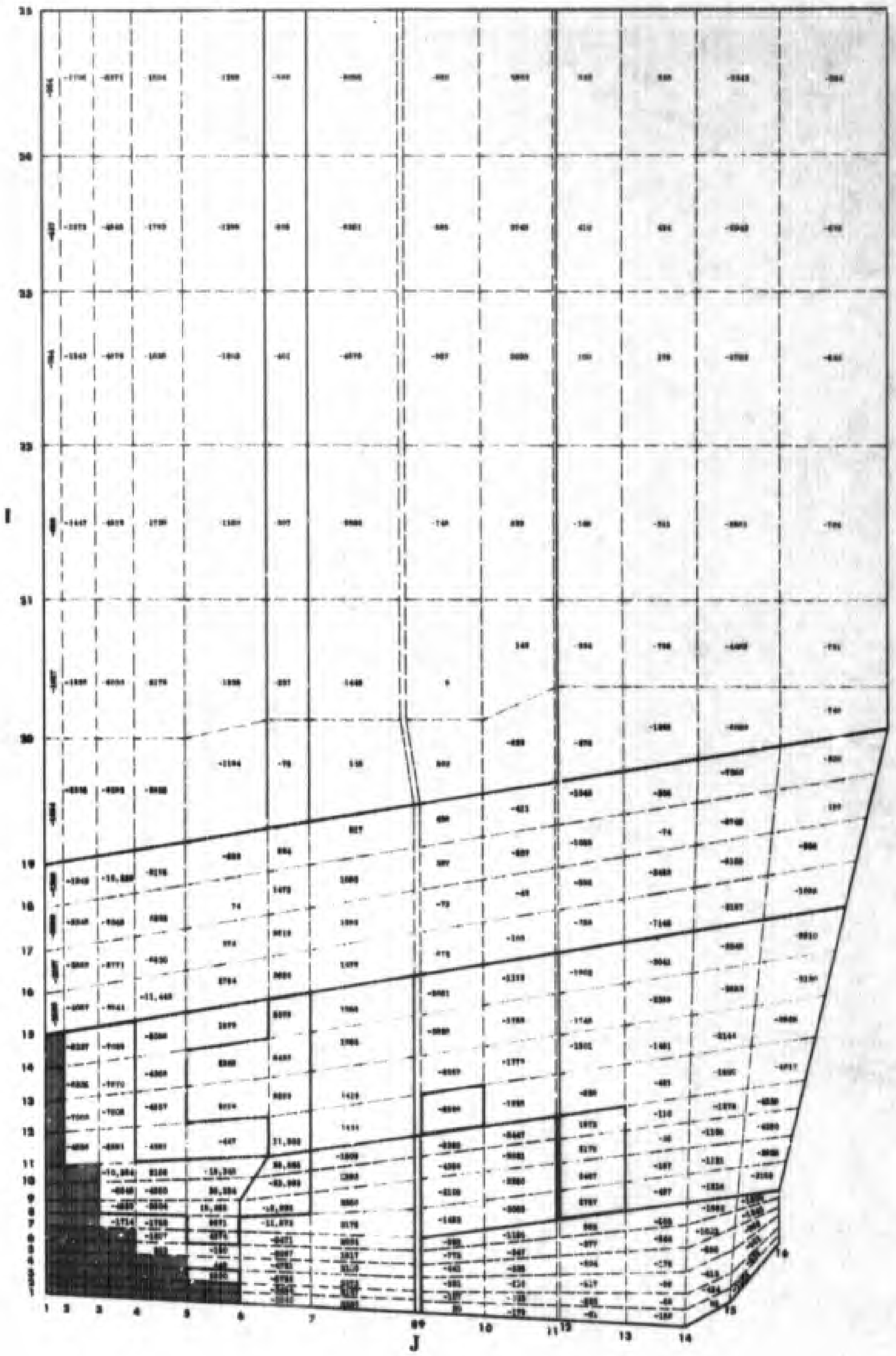

Figure 176. Boundary Condition B, Radial Stress at 25.1 Sec, Valve Closed

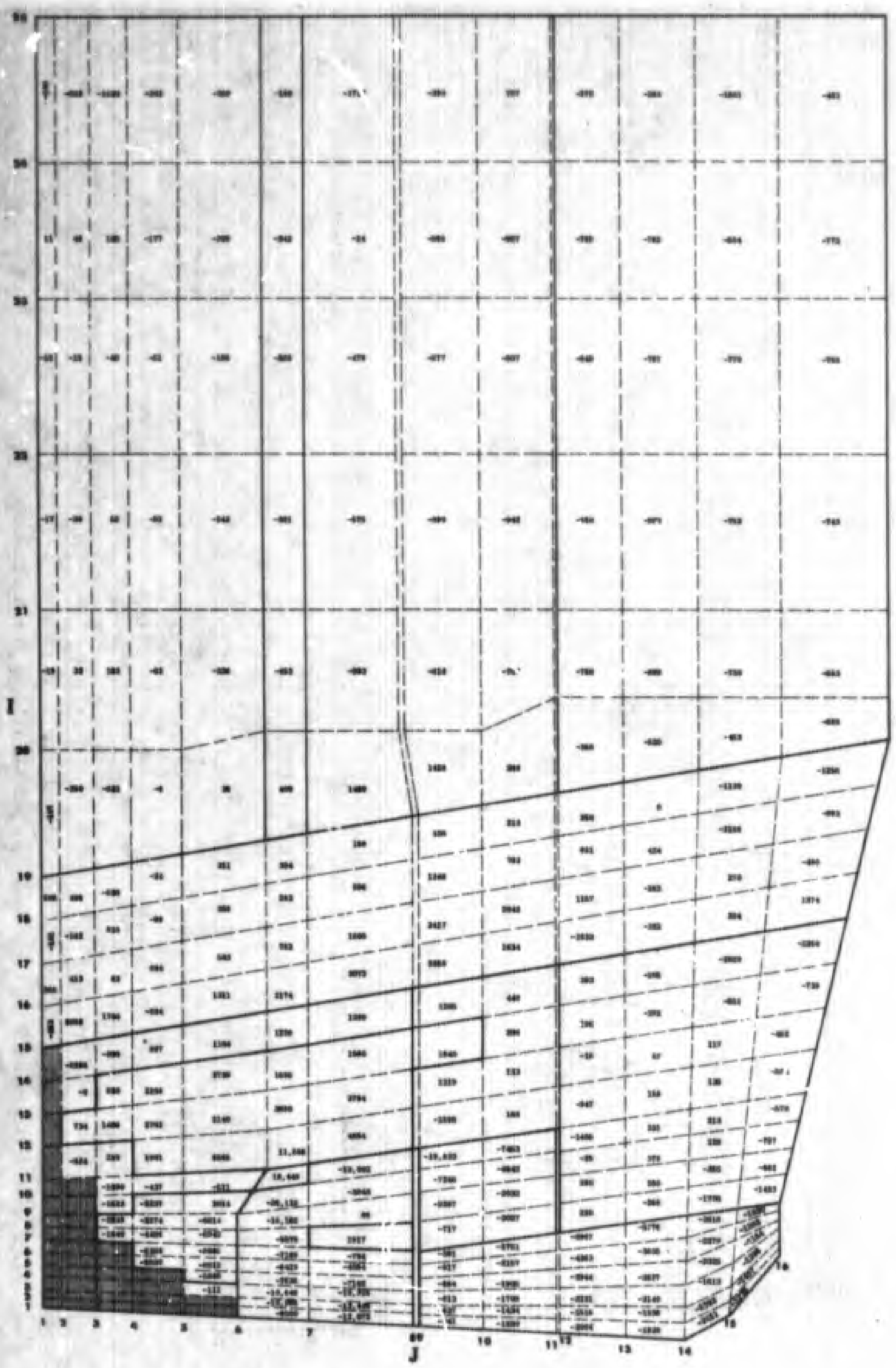

Figure 177. Boundary Condition B, Axial Stress at 25.1 Sec, Valve Closed

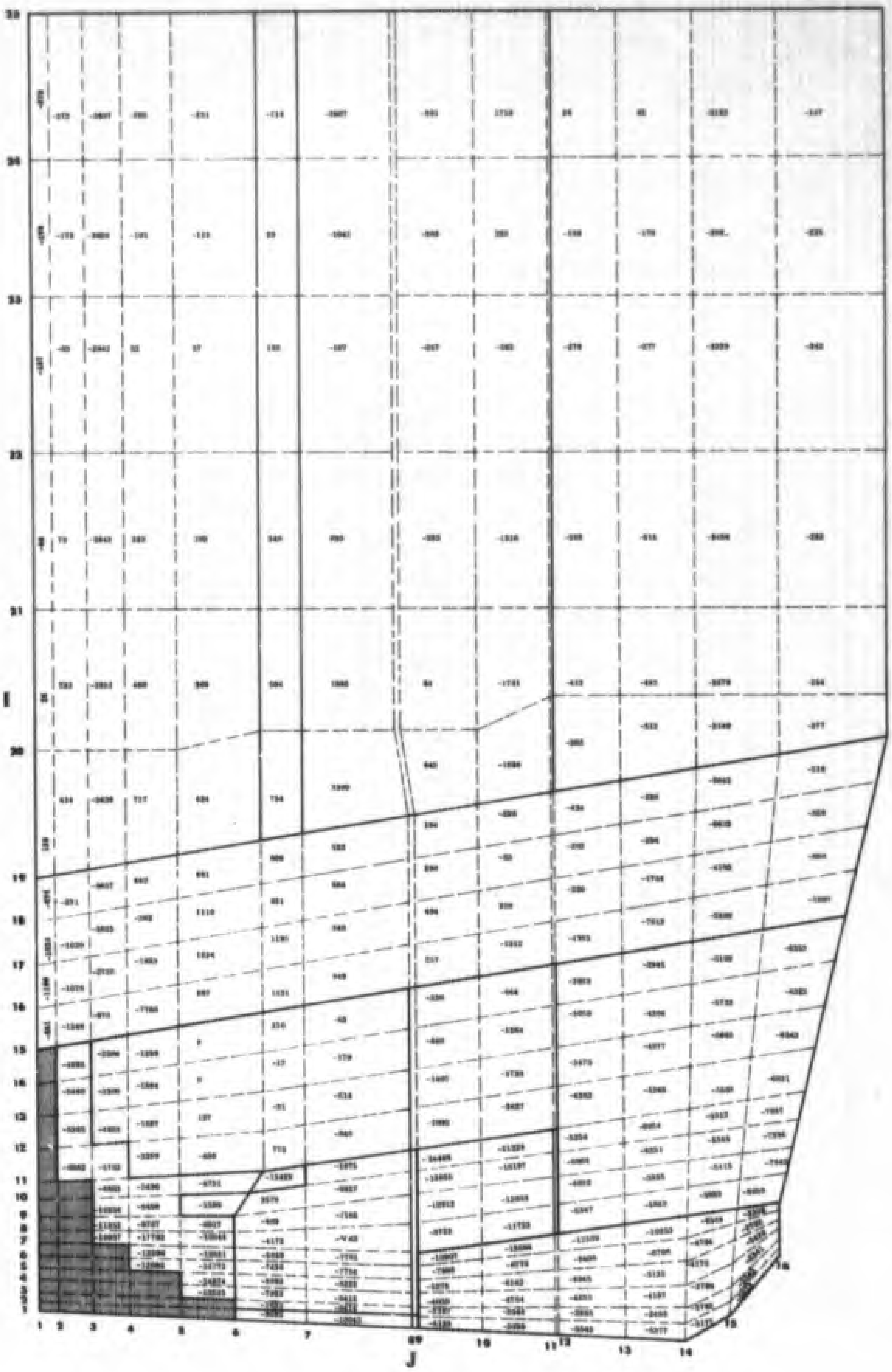

Figure 178. Boundary Condition B, Hoop Stress at 25.1 Sec, Valve Closed

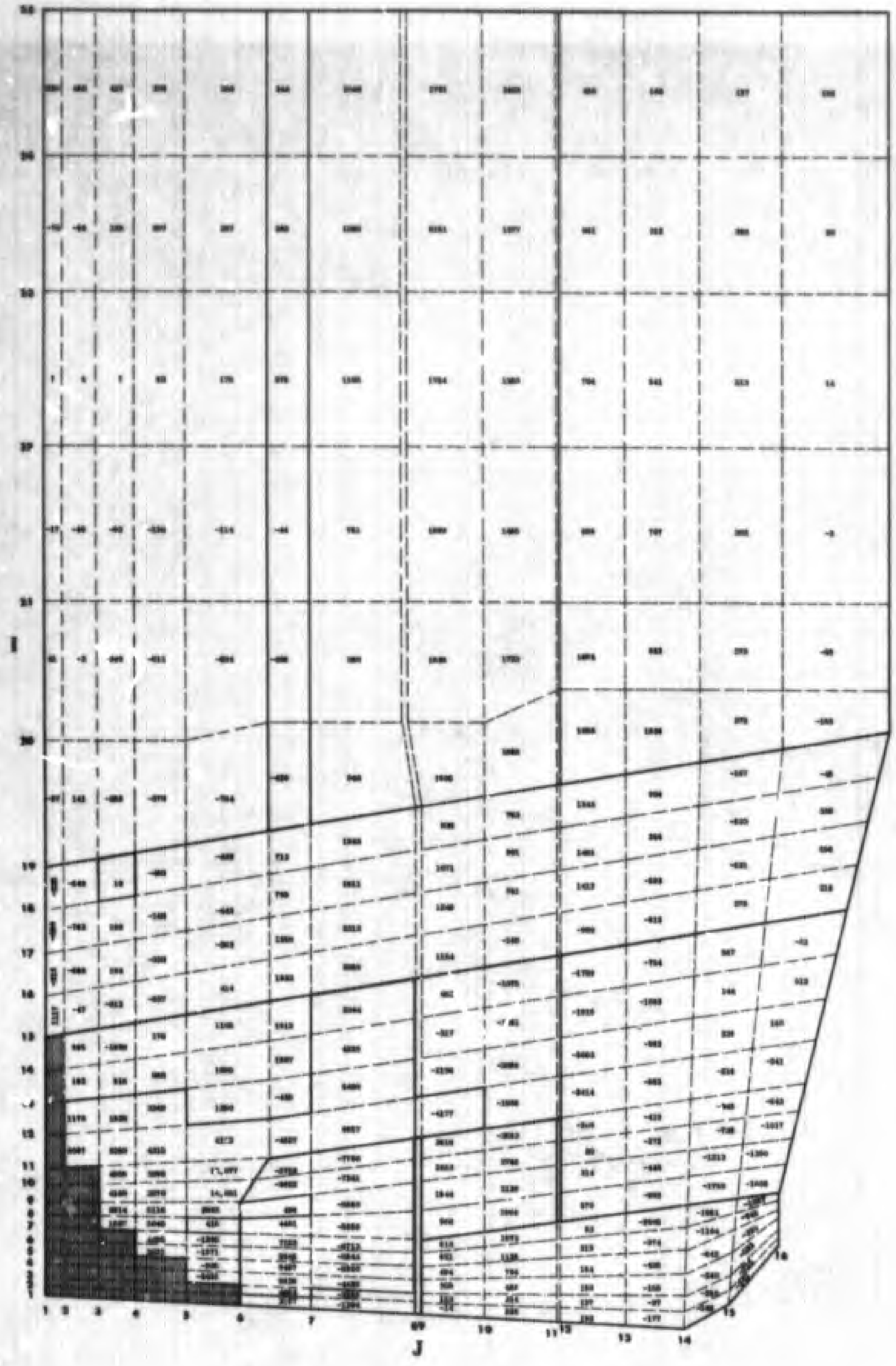

Figure 179. Boundary Condition B, Shear Stress at 25.1 Sec, Valve Closed

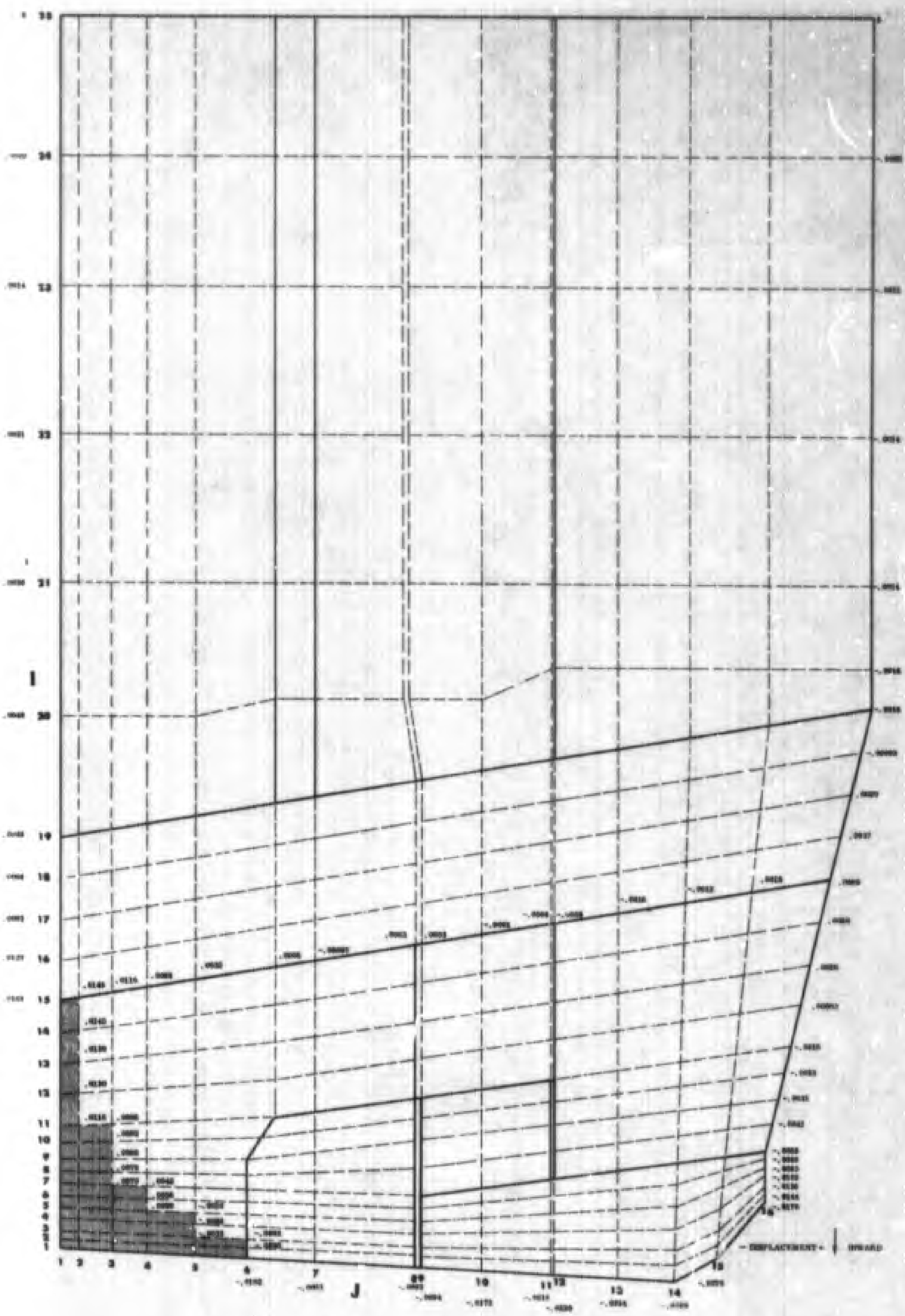

Figure 180. Boundary Condition B, Radial Displacements at 25.1 Sec, Valve Closed

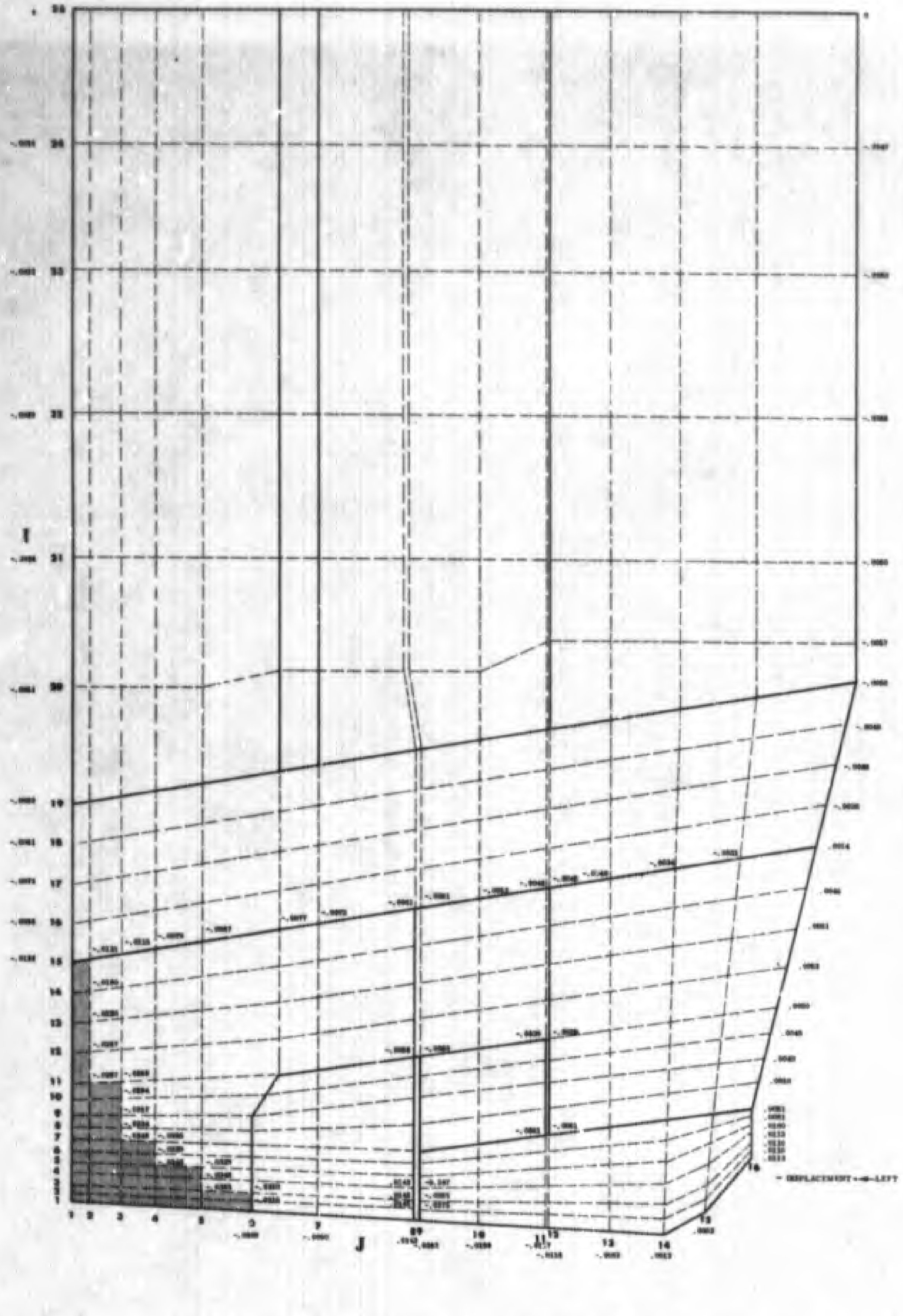

Figure 181. Boundary Condition B, Axial Displacements at 25.1 Sec, Valve Closed

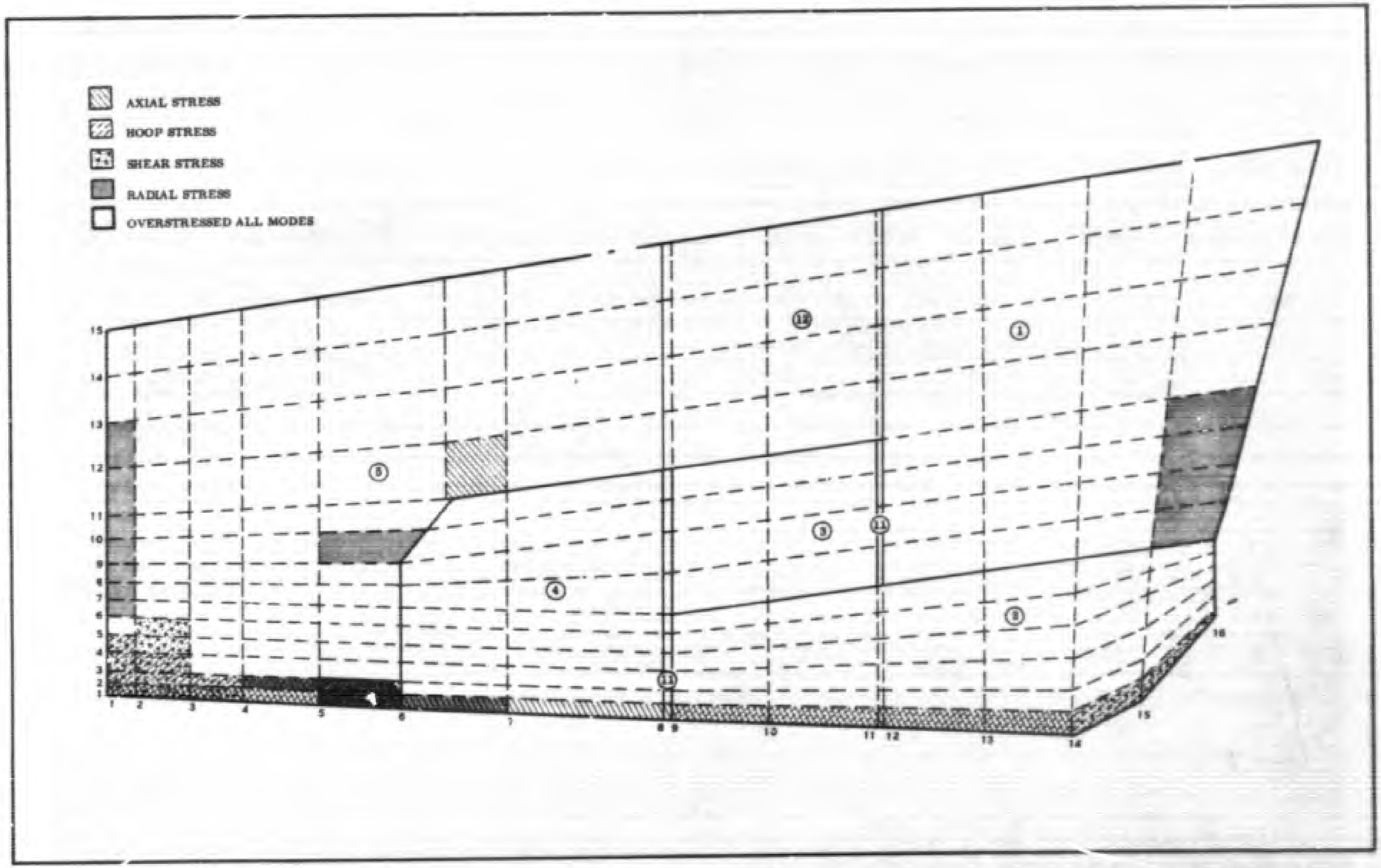

Figure 182. TU-520 HGSITVC, Overstressed Areas, Boundary Condition A at 5.0 Sec

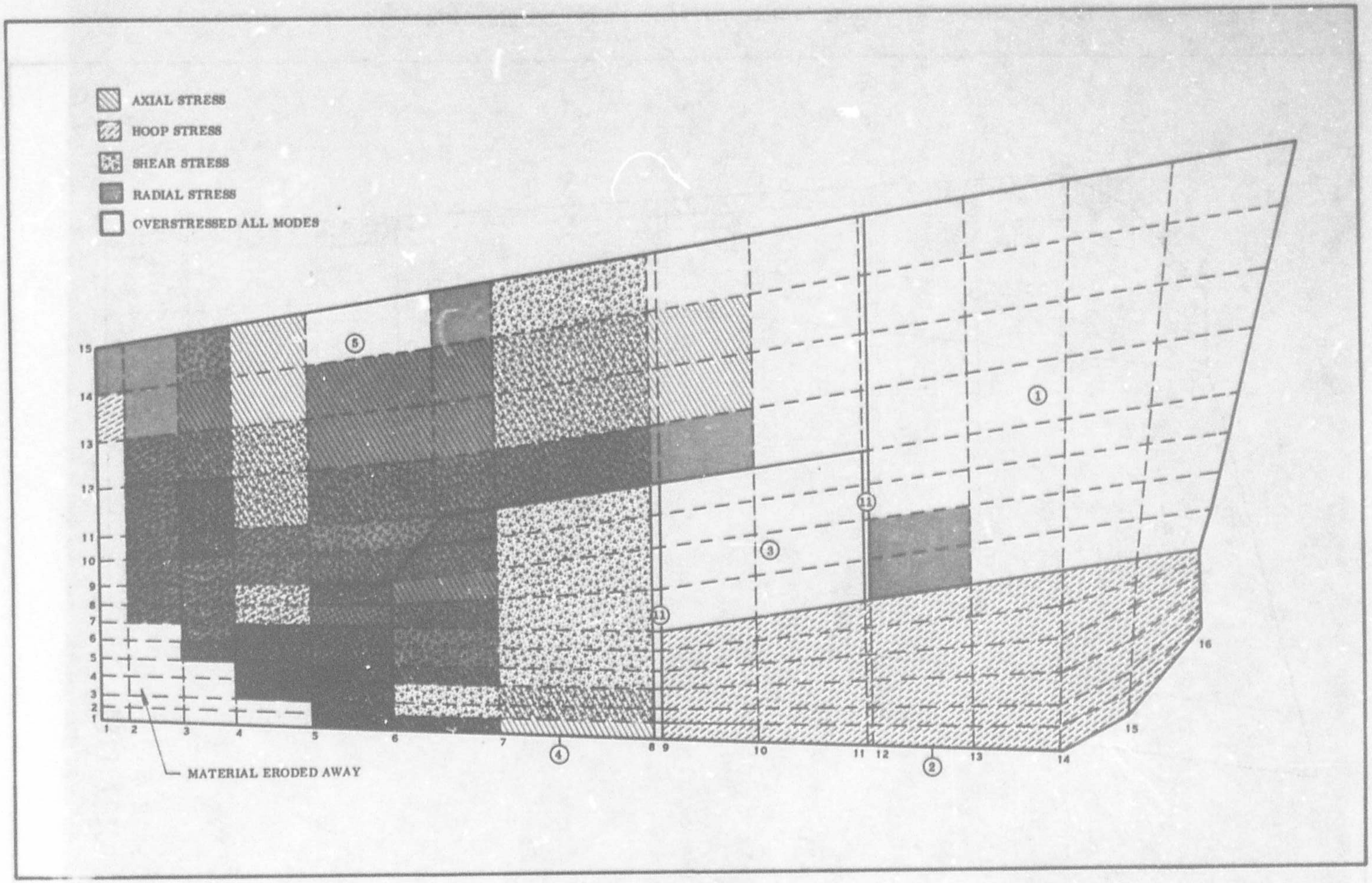

Figure 183. TU-520 HGSITVC, Overstressed Areas, Boundary Condition A at 25.0 Sec

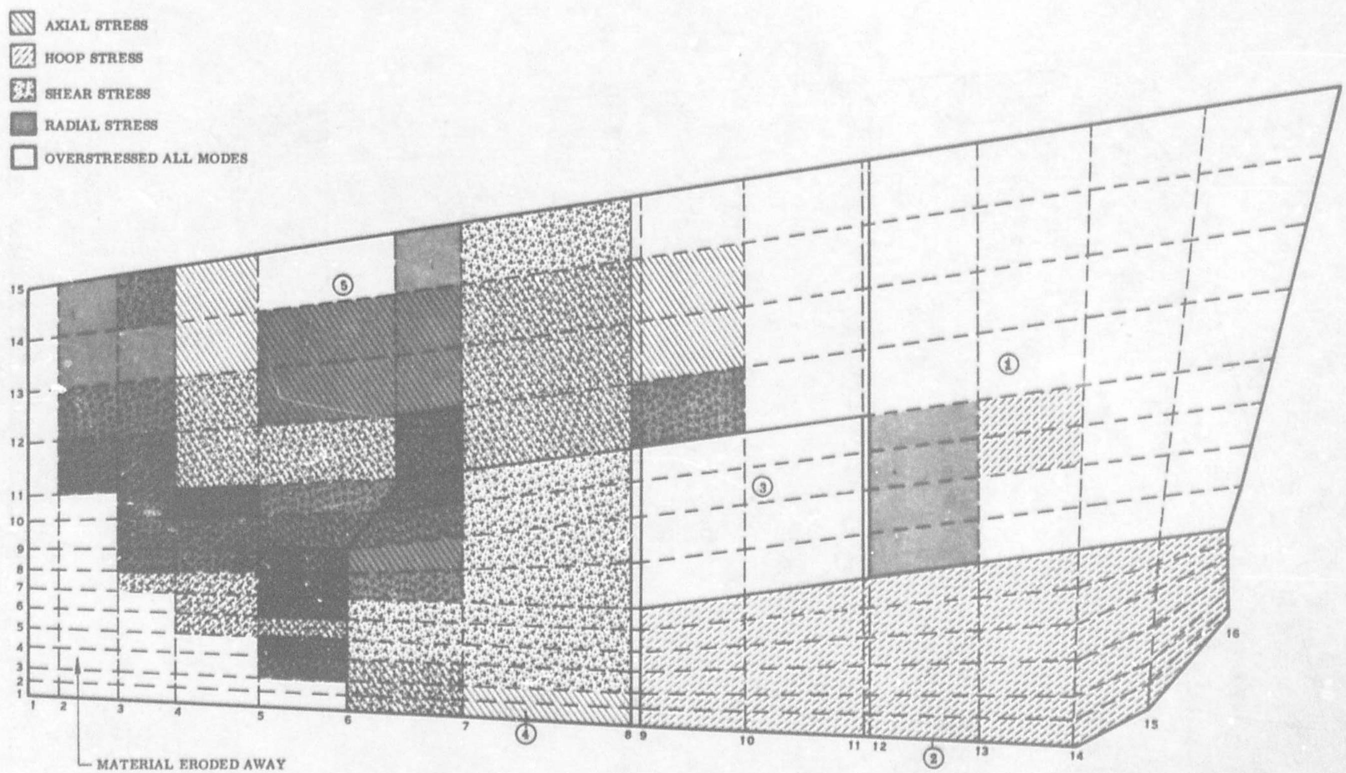

Figure 184. TU-520 HGSITVC, Overstressed Areas, Boundary Condition A at 25.1 Sec

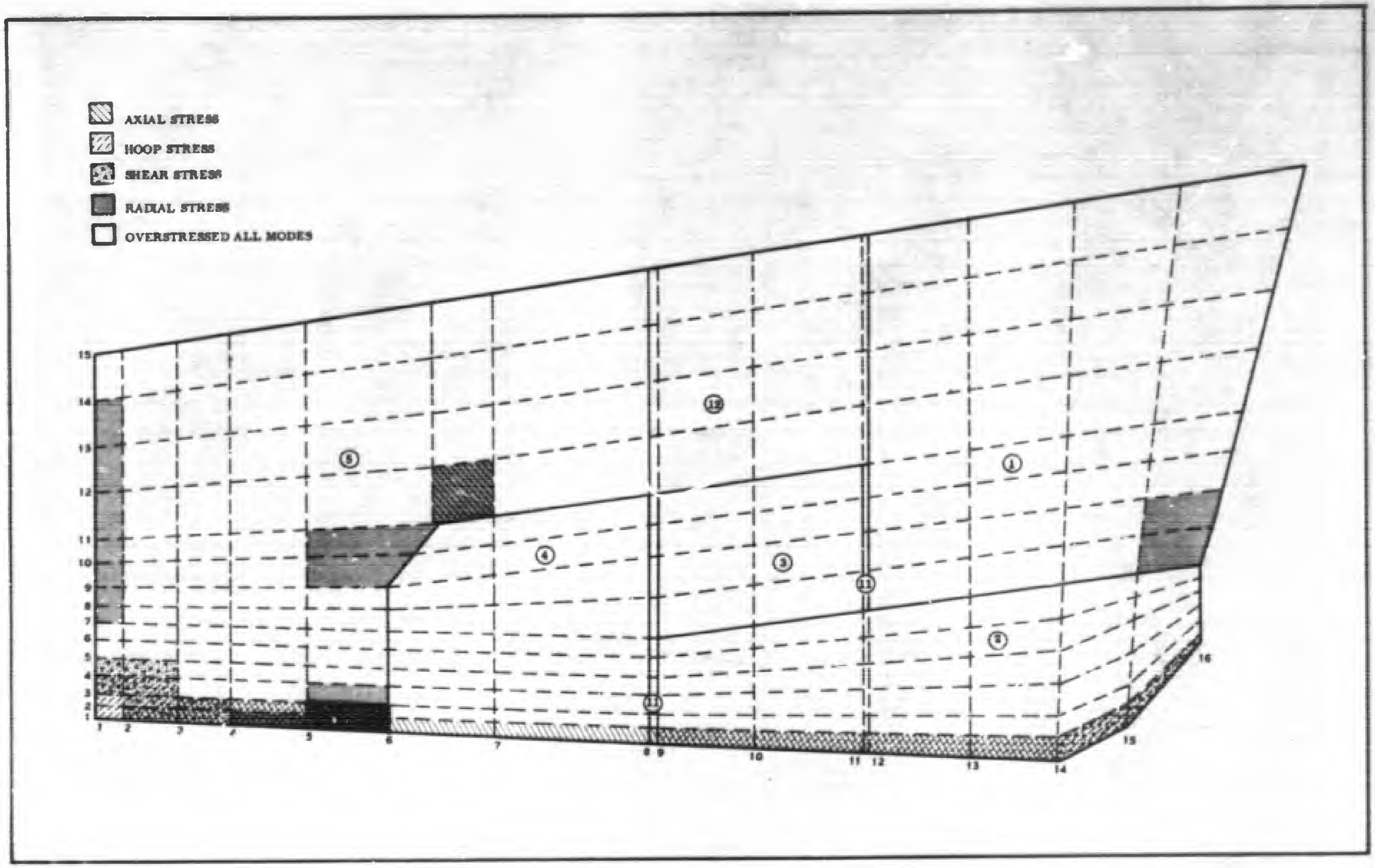

Figure 185. TU-520 HGSITVC, Overstressed Areas, Boundary Condition B at 5.0 Sec

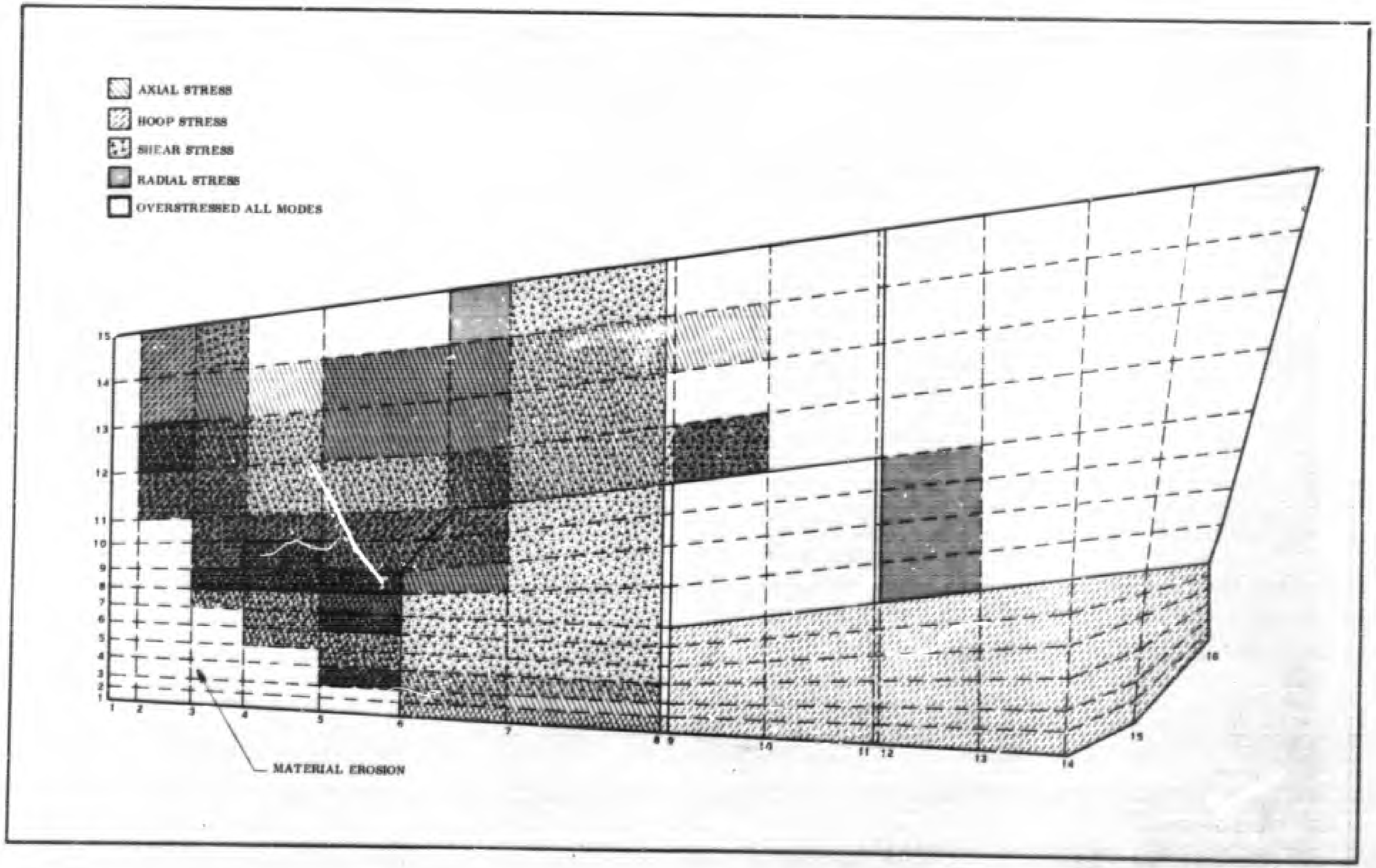

Figure 186. TU-520 HGSITVC, Overstressed Areas, Boundary Condition B at 25.1 Sec

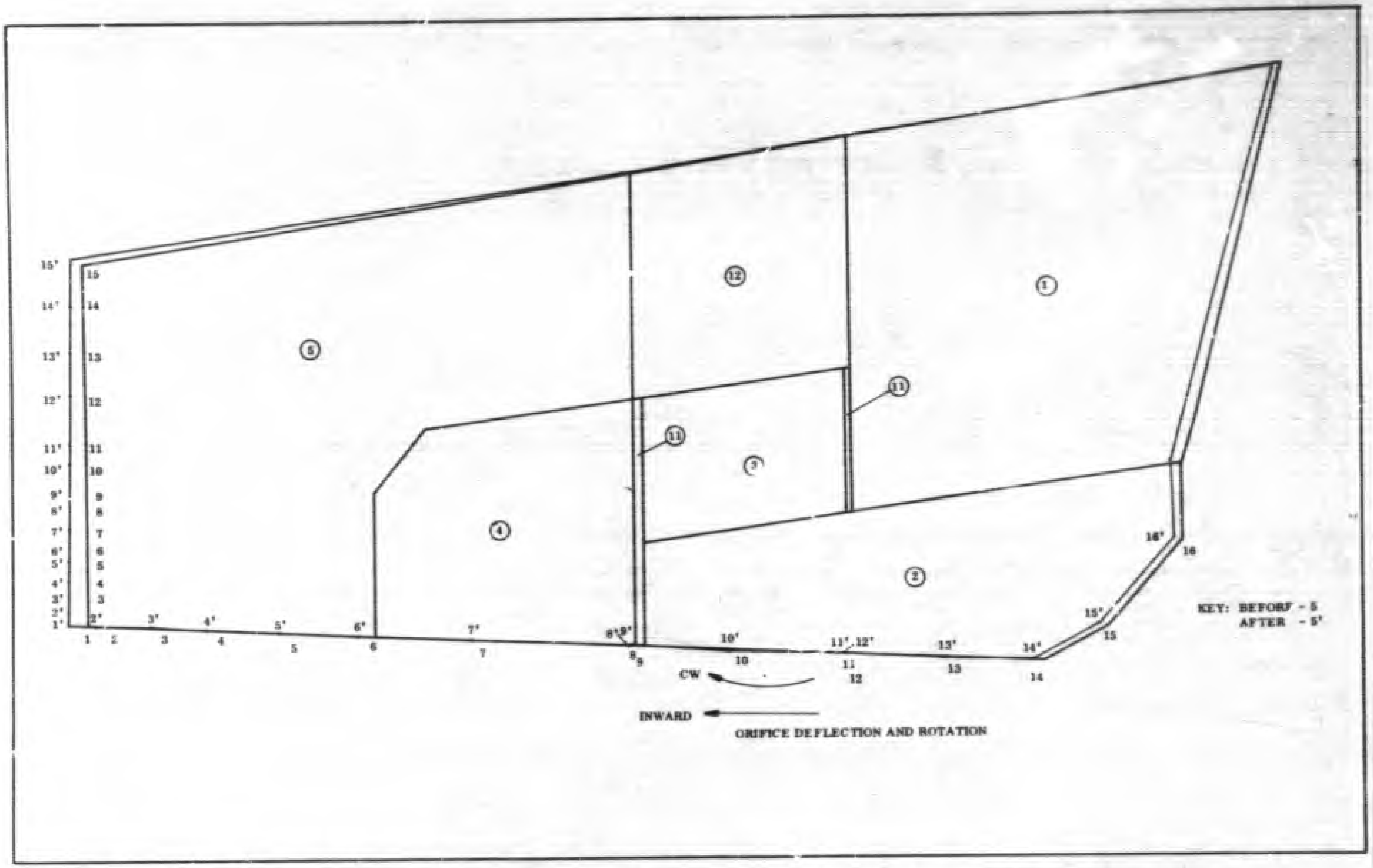

Figure 187. TU-520 HGSITVC Orifice Displacements, Boundary Condition A at 5.0 Sec

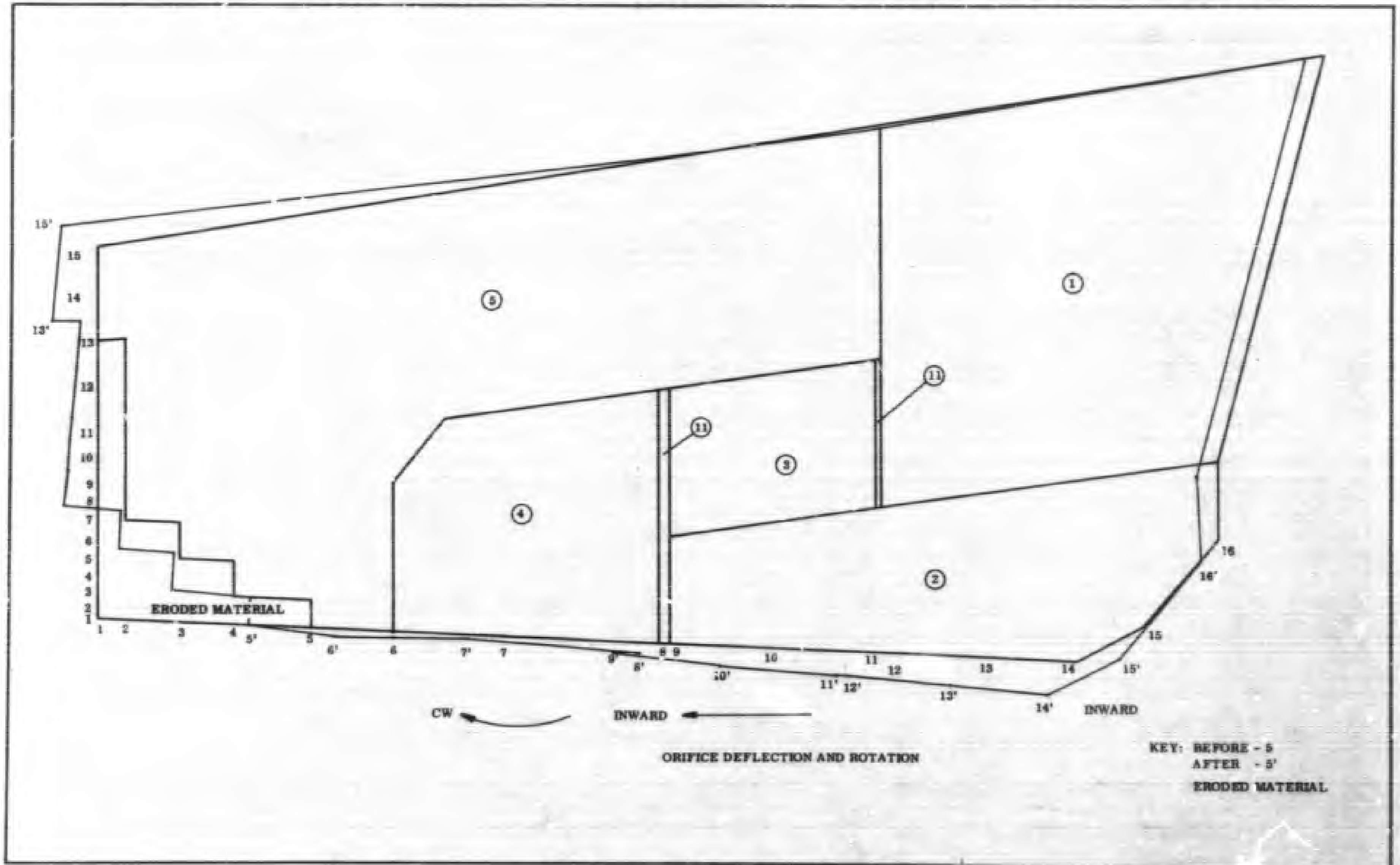

Figure 188. TU-520 HGSITVC Orifice Displacements, Boundary Condition A at 25.: Sec

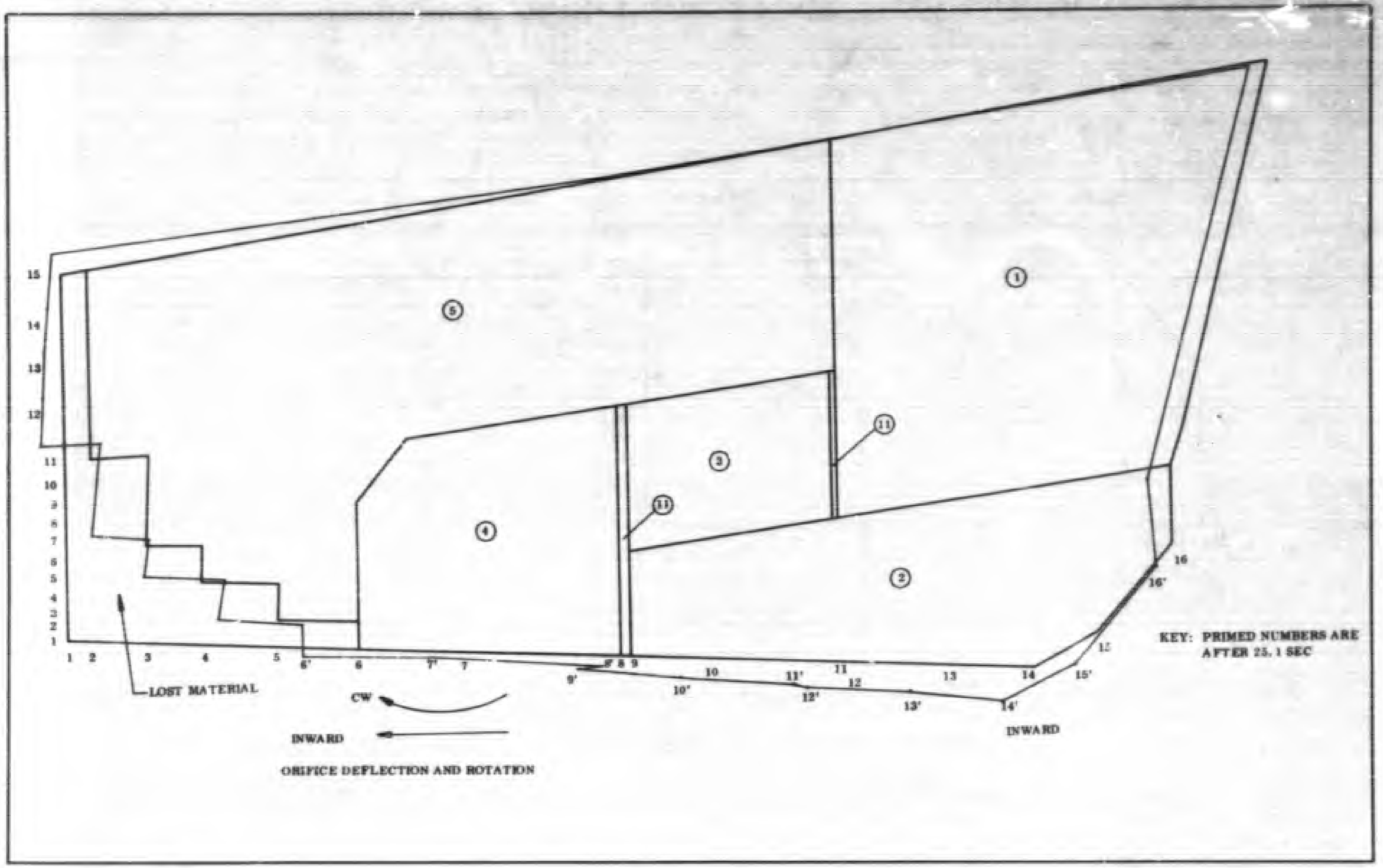

Figure 189. TU-520 HGSITVC Orifice Displacements, Boundary Condition A at 25.1 Sec

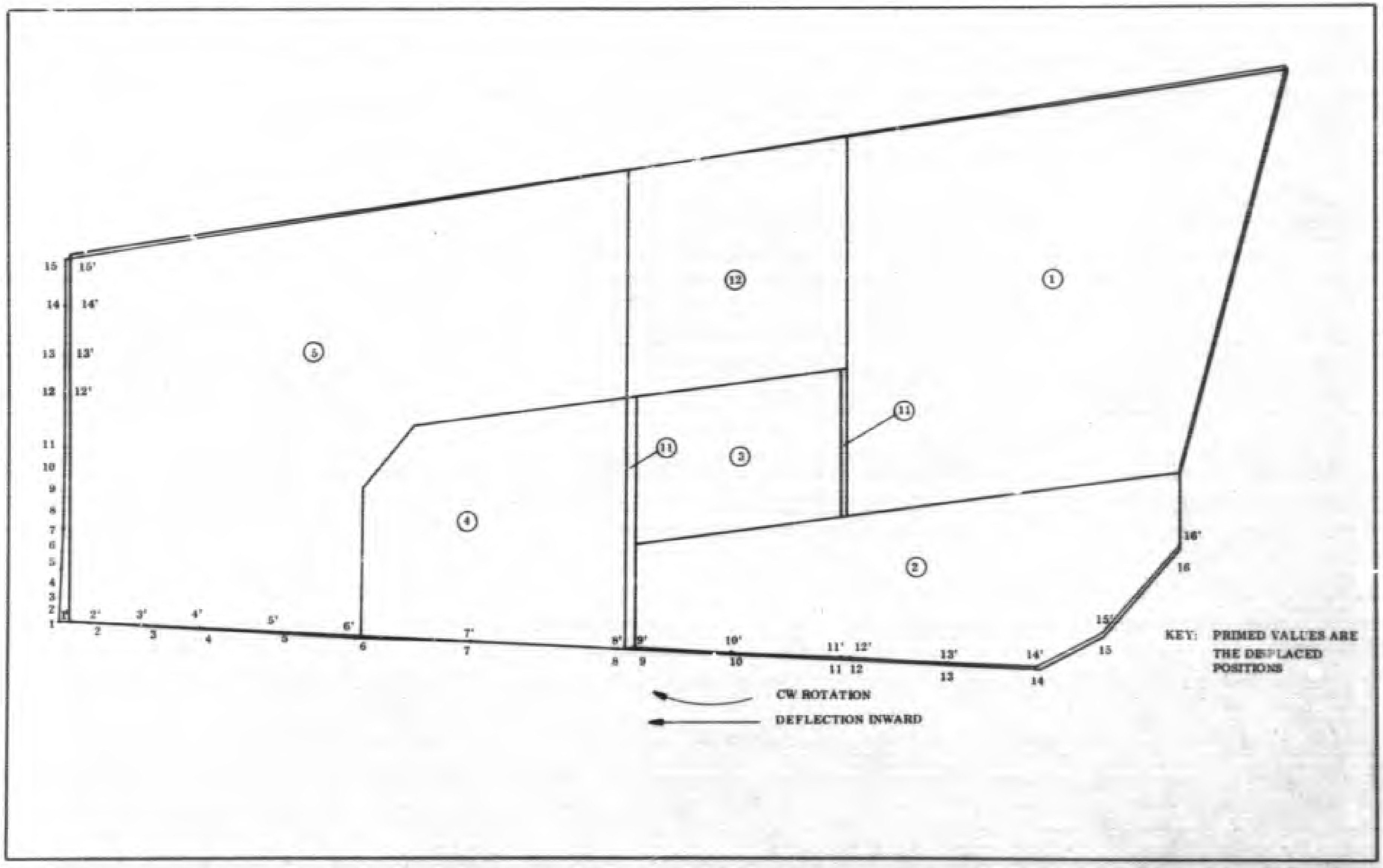

Figure 190. TU-520 HGSITVC Orifice Displacements, Boundary Condition B at 5.0 Sec

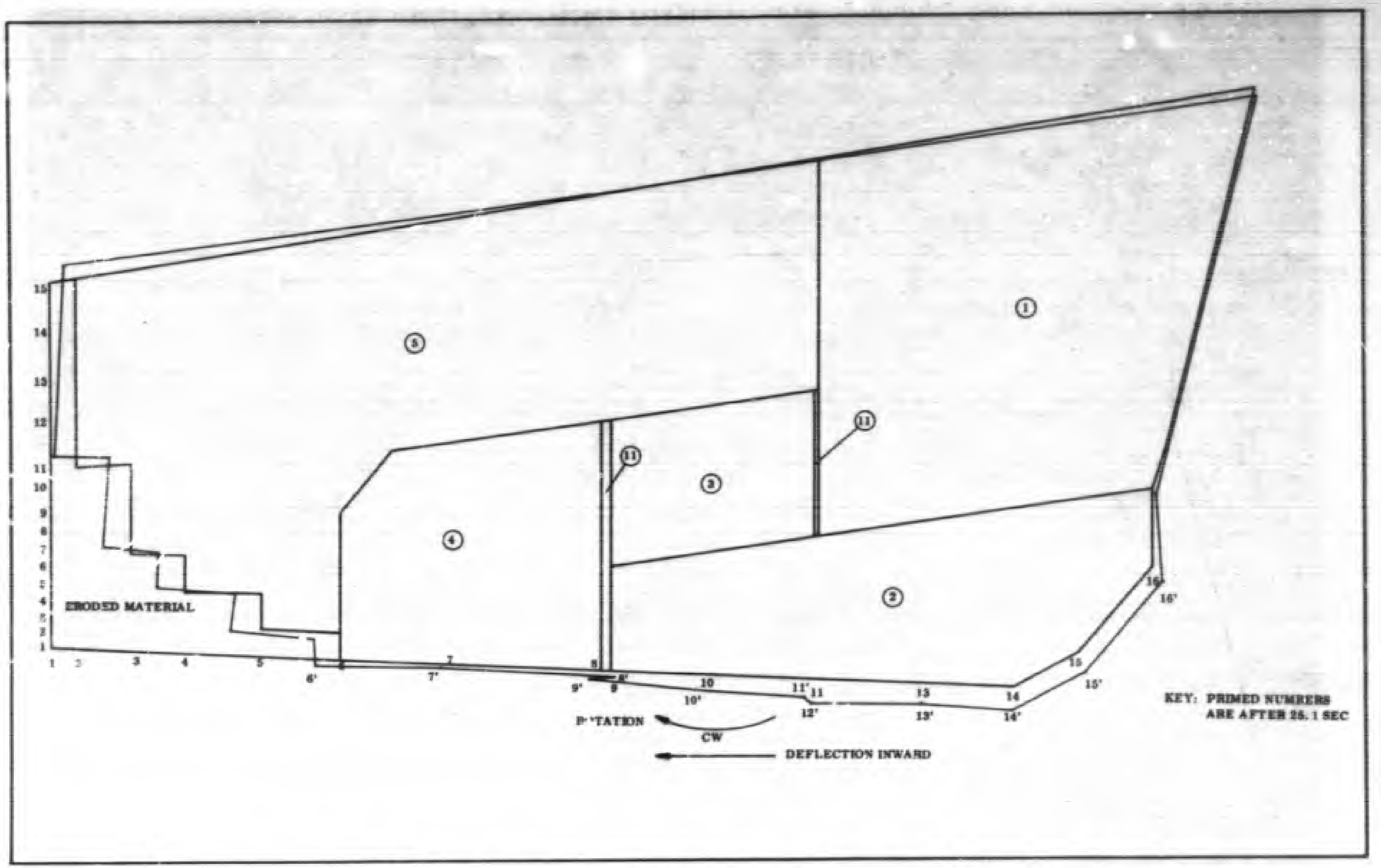

Figure 191. TU-520 HGSITVC Orifice Displacements, Boundary Condition B at 25.1 Sec

SECTION IV

CONCLUSIONS AND RECOMMENDATIONS

A review of the pretest orifice design-fabrication, the post-test evaluation, and the failure analysis provides information upon which conclusions and design recommendations may be drawn.

A review of the design-fabrication indicates that the orifice design includes too many parts and materials in a complex design.

The post-test evaluation, including hardware examination, orifice test performance, test movie analysis instrumentation data, and fabrication reports shows the following salient points.

1. The initial failure starts at 5 sec with orifice closed, and the failure continues throughout the TU-520-04 motor test. The three complete orifice failures occur at 35.7, 65.7, 77.5 sec in a 140 sec action time test. The fourth orifice was a partial failure and would have been a complete failure with a larger motor action time. Considerable redesign is required for all four ports to survive for 120 seconds.
2. The majority of ejected orifice material segments and the major orifice throat outward movement occurs during open orifice-open duty cycle. The size of ejected orifice material ports and the total outward movement of the orifice throat increases with the motor firing time. After 35

to 65 sec, the orifice throat outward movement and the size of ejected material parts tends to stabilize, probably due to the loss of valve control and orifice ports during this time span.

3. The first orifice port to fail (including a cracked ring of PTB) was the only orifice to include a full length PTB billet. The other three orifices contained a short PTB billet with a carbon cloth phenolic filler support ring. While the cracked billet did not start the failure, it contributed to the loss of the entire PTB ring during the firing.

4. No pyrolytic graphite ring segments were recovered from any of the orifices. Only a short circular segment of the three ejected copper-tungsten nuts was recovered.

5. The one remaining orifice contained only the throat subassembly and the insulation sleeve, while the valve pintle closed the orifice. The Graphite 90 inlet was radially cracked in three locations at the valve support leg cutouts, and it exhibited surface cracks at two other locations. The carbon cloth insulation sleeve was eroded at the inlet face, around the valve leg cutout holes, and the exit face. Chamber gas leakage through the closed orifice port is obvious when daylight shows through the eroded and cracked portions of the orifice after static test. The tungsten throat and nut twisted the inlet graphite and nearly pushed through it into the nozzle exit cone before the end of the static test.

The failure analyses including the aerodynamic, thermodynamic and structural analyses indicated the following.

1. During orifice-closed condition, the downstream orifice walls receive the largest increase of pressure (26 to 330 psia) concentrated in the downstream 180 deg orifice arc. The convective heat transfer coefficient increases from a value of 0.20 upstream to 1.84 downstream. The erosion changes from 0 upstream to 1.20 in. downstream.
2. During orifice-open condition, the upstream orifice walls receive a large increase of pressure from 26 psi to 388 psi, while the downstream orifice wall experiences a pressure increase from 330 to 388 psi. The upstream heat transfer coefficient increases from 0.20 to 1.62 while the downstream decreases from 1.84 to 0.06. The upstream erosion increases from 0 to 0.20 inch.
3. As early as 5 sec the downstream plane shows a number of material element failures (28 percent of PTB elements, 10 percent of pyrolytic graphite elements, 13 percent of Graphite 90 elements). At 25.1 sec massive material element failures indicate an early orifice failure (93 percent of PTB elements, 90 percent of pyrolytic graphite elements, 19 percent of Graphite 90 elements).
4. During orifice open duty cycle the throat orifice-pintle valve inter e moves outward as much as 0.150 in. beyond the expected movement due to thermal expansion of the tungsten and deflection of the valve supports holding the position transducer, indicating orifice throat, nut and inlet (throat subassembly)

outward movement due to breaking down of the adhesive bond holding the subassembly to the carbon cloth insulation sleeve after 16.0 seconds.

5. The initial failure starts with segments of the downstream PTB orifice aft exit cone ejecting while the orifice is closed. The early failure is due to downstream gas stagnation on the PTB material with the resulting large erosion, charring and chunking. The failure mechanism is the unsymmetrical heating and pressure loads around the PTB ring causing a hoop-shear stress failure on the downstream lip.
6. During orifice-open the upstream orifice plane PTB material is probably lost, although no structural analysis was run on this plane since the downstream orifice edge was deemed the most critical.
7. The orifice exit cone materials (PTB and pyrolytic graphite) have the grain oriented in the wrong direction for the downstream stagnation conditions. The grain is perpendicular to orifice centerline at present. The grain must be changed to parallel to orifice centerline to survive the orifice downstream environment.

A. CONCLUSIONS

The major problem areas are:

1. The differential heating, forces and erosion around the orifice-nozzle exit cone caused by

downstream closed port gas reattachment stagnation and the upstream open port hot gas injection shock fronts.

2. The unpredictable orifice throat subassembly outward movements during open orifice duty cycles and after 16 sec of motor firing time, when the adhesive bond breaks down.
3. Insufficient throat subassembly outer diameter support due to valve leg cutouts in the carbon cloth insulation sleeve and graphite inlet ring.

These problem areas caused the following orifice material problems.

1. PTB delamination and cracking along molding grain lines in hoop and shear failure;
2. Pyrolytic graphite delamination and cracking across grain in axial and shear failure;
3. Copper-tungsten nut cracking against grain in hoop failure;
4. Graphite cracking against grain in hoop-torsional shear failure.

B. RECOMMENDATIONS

The design recommendations to insure orifice 120 sec reliability provides the answers to the major orifice problem areas. The major changes recommended are as follows.

1. Change materials, processes and grain orientation and simplify the orifice design, the new materials to be more erosion resistant and not subject to spalling or chunking while subjected to differential heating and pressure forces around a 360 deg circumference.
2. Widen base for the valve leg support cutout holes and increase the insulation sleeve thickness to insure better support at the throat subassembly outer edge.
3. Provide a more heat resistant adhesive bond along the orifice material interfaces and provide a positive connection between the throat subassembly and the insulation sleeve.

The major orifice problem areas and related material problems along with orifice problem solutions are listed in Table XXV.

1. ORIFICE REDESIGN

A redesign of the orifice to insure a reliable assembly for a 120 sec HGSITVC duty cycle requires that the following steps be taken.

1. Consider the conclusions reached on major problem areas.
2. Consider the design recommendations on major problem solutions.

TABLE XXV

ORIFICE PROBLEMS AND SOLUTIONS

Material Problems	Major Problem Areas	Solutions
1. PTB delaminations and cracking with general fiber molding orientation in shear.	Primary a. High local stresses due to unsymmetrical heating and pressure in and around the orifice cavity during open and shut cycles. Secondary b. Defect in original billet as shown by quality control action.	a. Change raw material processing. b. Increase quality control non-destructive test effort before material acceptance.
2. Graphite cracking against grain hoop shear.	Primary a. Insufficient support around the outside diameter due to pintle leg cutouts and erosion of joints during static firing. Secondary b. Unsymmetrical shape between upstream 0 to 180 deg plane and lateral 90 to 270 deg plane. c. Outward movement of the throat subassembly after 10 to 15 sec on, when port opens and then banged back to initial position where port closed due to bond failure and nozzle load wedge action.	a. Increase thickness of insulation sleeve and move out leg hole cutouts. b. Decrease the thickness of the graphite ring and provide symmetrical ring shape. c. Provide shell retention ramp by the outer insulation sleeve to prevent movement in open pintle position. d. Change material.
3. Pyrolytic graphite delamination with grain and cracking against grain in shear.	Primary a. High local stresses contributed by differential heating around the orifice cavity. b. Fabrication process of bonding two rings together to form one inch ring.	a. Decrease differential heating stresses and weak bonding of pyrolytic graphite rings by shortening ring thickness to one half inch. b. Change material.

TABLE XXV (Cont)

ORIFICE PROBLEMS AND SOLUTIONS

Material Problems	Major Problem Areas	Solutions
4. Tungsten nut cracking against grain in hoop tension.	Primary a. Insufficient support at high temperature around outside diameter.	a. Press fit of insulation sleeve around the tungsten nut. b. Change material.

3. Evaluate current material and fabrication technology.
4. Define alternative orifice designs.
5. Preliminary analysis.
6. Preliminary orifice design selection.

By necessity, this orifice redesign effort cannot be extensive, but it does represent an interpretation of the existing design, the post-test evaluation, and the failure analysis to ascertain a preliminary redesign for a reliable 120 sec orifice.

a. Major Problem Areas--The major problems are: (1) the differential 360 deg orifice-nozzle exit wall heating, forces, and erosion, (2) the throat subassembly movement, and (3) the lack of subassembly support due to valve leg cutouts and fabrication bond lines. The problem areas center on the PTB, pyrolytic graphite, copper-tungsten nut and Graphite 90 materials failing by cracking and/or delamination.

b. Major Problem Solutions--The major solutions are (1) to change materials, processes and grain orientation while simplifying the design; (2) move out valve leg support location; and (3) provide a positive adhesive and connection between the throat subassembly and the orifice insulation sleeve.

2. CURRENT MATERIAL TECHNOLOGY

Current technology provides some new material, fabrication, and processes not available when the orifice design was originated in early 1966, plus improved standard fabrication processes. These materials and fabrication processes are listed below.

Material	Fabrication Process	Cure Process	Post Cure Processing	Comments
Graphite Cloth Phenolic	Tape wrap parallel to centerline	320° F 1,000 psi	Graphitization at 5,600° F	Graphitization of large tape wrapped billets is a new process.
Graphite Thornel Yarn Phenolic (Union Carbide)	3D woven - Avco process	320° F 1,000 psi	--	Thornel yarn and 3D weaving is a new process.

Material	Fabrication Process	Cure Process	Post Cure Processing	Comments
Graphite Cloth Phenolic	Edge grain pattern-layup (rosette)	320° F 1,000 psi	--	Improved standard fabrication process.
Pyroid - Large Pyrolytic Graphite Rings (Pyrogenics)	Vapor deposition parallel to surface high temperature furnace	--	--	Ring forming pyrolytic graphite is a new process.
PTC-Graphite Fiber Phenolic (Union Carbide)	Molded - 150 - statically with specif[illegible] fiber orientation	320° F 1,000 psi	Baked, impregnated graphitized, impregnated graphitized	Improved PTB grade.
Tungsten Wire (UTC)	Filament wound bonded with plasma arc sprayed tungsten	--	--	New tungsten fabrication process.
Tungsten Rings up to 8-10 in. Diameter	Forged and roll ring shaped Pressed and sintered Rough forged Plated	--	--	Improved standard fabrication process.
Graphite Cloth Phenolic	Tape wrap parallel to surface	320° F 1,000 psi	--	Improved standard fabrication process.
Graphite Cloth Graphite Bond Carborundum Carbitex	Flat laminate and cross-stitched	Binder and high temperature furnace	Graphitization at 5,600° F	New process.

A large number of alternative designs are possible with the above materials, fabrication techniques, and process changes. However, to insure compatibility with the existing design concept that has required nine upper stage and three first stage motors to develop, some of the materials application to the redesign will be on a limited basis.

3. ALTERNATIVE DESIGNS

Nine alternative orifice designs are proposed (Figures 192 thru 200).

A summary of the nine alternative designs is shown below with the design changes noted, as well as the reasons for the design change.

The orifice design criteria for a 156 inch diameter motor, submerged nozzle, with HGSITVC requires 16 orifice ports. Relative design criteria are listed below.

Web Time	120 sec
Average Chamber Pressure	700 psia
Propellant	Minuteman type
Grain Design	Segmented CP
Nozzle Throat Diameter	46.90 in.
Orifice Port Location Diameter	90.71 in.
Area Ratio Location (ϵ)	3.75
Orifice Throat Diameter	6.37 in.

Within the following envelope the alternative designs were developed.

Orifice Support Structure	Present Design	TU-52[illegible].04
Inner Carbon Cloth Liner (in.)	2.25	1.35
Steel Shell (in.)	1.25	1.50
Outer Carbon Cloth Liner (in.)	1.50	2.00
Orifice Wall		
Exit Cone Angle (deg)	3.00	3.00
Exit Cone Diameter (in.)	6.70	6.90
Orifice Length to Valve Pintle Interface (in.)	4.30	4.30
Orifice Length/Exit Diameter (in.)	1.56	1.61
Orifice Assembly		
Orifice Centerline to Start of Valve Support Leg Cutout (in.)	6.30	5.60
Orifice Largest Diameter (in.)	13.60	13.60

Alternate Designs

Design	Changes	Reason
Alternate 1 Modified Design	A. Replace PTB with graphitized graphite cloth phenolic parallel to centerline.	A. Provide an excellent uniform erosion liner with the plies oriented to resist downstream gas stagnation environment.
	B. Cut axial length of pyrolytic graphite and tungsten throat and nut.	B. Pull laminated washer back from downstream gas stagnation region.
	C. Reverse OD graphite ramp, and thread liners together.	C. Hold throat subassembly in place during open-port duty cycle.
	D. Eliminate bond lines in orifice and use Epon 934 for orifice-nozzle assembly.	D. More OD support for liner materials at elevated temperature.
Alternate 2 Modified Design	A. Replace PTB and carbon cloth insulation with one piece of carbon or graphite cloth phenolic edge grain layup.	A. Provide a good, uniform erosion liner with the plies oriented to resist downstream gas stagnation environment condition. Provide higher strength component that will not spall but is more susceptible to erosion.
	B. Decrease pyrolytic graphite axial length.	B. Pull laminated washer back from downstream gas stagnation region.
	C. Cut radial graphite thickness and thread to graphite cloth insulation.	C. Hold throat assembly in place during orifice open duty cycle.
	D. Eliminate bond lines in orifice and use Epon 934 for orifice-nozzle assembly.	D. More OD support for liner materials at elevated temperatures.

Alternate Designs (Cont)

Design	Changes	Reason
Alternate 3 Advanced Design	A. Shorten tungsten throat and replace tungsten nut with threaded tungsten-graphite connection.	A. Simplify design - allow maximum exit cone insert - eliminate tungsten nut cracking problem.
	B. Replace PTB and pyrolytic graphite with erosion resistant exit cone insert. Insert could be pyroid, carbitex, FTC or 3D thornel graphitized with grain or ply oriented parallel to orifice centerline.	B. Simplify design and provide maximum protection for downstream stagnation and upstream shock front.
	C. Reverse graphite OD ramp and provide a two-piece insulation and assembly connector sleeve of graphite cloth.	C. Hold throat assembly in place during orifice open condition with a stable, uniform eroding material.
	D. Eliminate bond lines in orifice and use Epon 934 for orifice nozzle assembly. Use 13.60 OD orifice assembly diameter to keep bond lines strong during 120 sec test.	D. More OD support for liner materials at elevated temperatures.
Alternate 4 New Design Concept	A. Provide two-piece tungsten orifice wall liner locked in on graphitized graphite cloth phenolic support block.	A. Eliminate erosion and maintain orifice wall shape.
	B. Bond throat subassembly to graphite cloth phenolic sleeve and the assembly to the nozzle. Adhesive is Epon 934. 13.60 in. orifice assembly OD used to keep bond lines strong during 120 sec test.	B. Simplify design; four components, three materials. Eliminate component material cracking and/or delaminating.
Alternate 5 Advanced Design	A. Shorten tungsten throat and replace tungsten nut with threaded tungsten-graphitized graphite cloth erosion liner, the graphitized graphite cloth replacing the PTB and pyrolytic graphite.	A. Simplify design; three components, three materials; minimize upstream and downstream erosion; eliminate previous poor performing materials.

Alternate Designs (Cont)

Design	Changes	Reason
Alternate 5 (Cont) Advanced Design	B. Use 13.60 OD orifice assembly to keep bond lines cool and strong during 120 sec test.	B. More OD support for liner materials at elevated temperature.
Alternate 6 New Design Concept	A. Provide one-piece forged or filament wound tungsten-tungsten bond throat and exit cone, over-wound with graphite yarn (thornel) phenolic.	A. Eliminate erosion at upstream and down-stream orifice wall. Simplify design: 3 components, 3 materials.
	B. Bond throat subassembly to graphite cloth phenolic tape wrap and total orifice assembly to nozzle. Adhesive is Epon 934. 13.60 in. orifice assembly OD used to keep bond lines cool and strong.	B. More OD support for liner materials at elevated temperature.
Alternate 7 Improved Design	A. Replace PTB and pyrolytic graphite washer with graphite cloth phenolic-edge grain. The orifice exit cone is combined with insu-lations here.	A. Minimize erosion at up- and downstream orifice faces, simplify design.
	B. Decrease radial thickness of graphite, and thread throat sub-assembly to erosion liner of graphite cloth.	B. Hold throat subassembly in place when orifice is open or highly heated; more OD support for liner materials at ele-vated temperatures.
Alternate 8 Advanced Design	A. Provide a forged tungsten throat trapped between two erosion liners of regraphitized graphite cloth phenolic tape wrapped at 30 deg to centerline; eliminate PTB, pyrolytic graphite, rubber tungsten nut and graphite.	A. Minimize upstream and downstream erosion; simplify design; elimi-nate poor performance materials.
	B. Throat and exit cone subassembly bonded and threaded to the graphite cloth phenolic insulation sleeve.	B. Hold throat subassembly in place during orifice open phase, or when highly heated; provide throat support.

Alternate Designs (Cont)

Design		Changes		Reason
Alternate 9 Improved Design	A.	Provide a standard thoria tungsten throat and retention nut with regraphitized inlet and exit erosion liners; eliminate PTV, pyrographite rubber, and graphite.	A.	Minimize orifice wall erosion. Simplify design. Eliminate poor performance materials.
	B.	Throat and exit cone subassembly bonded and threaded to the carbon cloth phenolic tape wrapped insulation sleeve and the total assembly is bonded to the nozzle.	B.	Hold throat subassembly in place during test; provide a solid throat support.

4. PRELIMINARY ANALYSIS

The nine alternate orifice designs were classified by the amount of change involved with respect to the TU-520.04 orifice, "modified" meaning the least change and "new concept" the most change. Modified design 2 was selected as closest to the original design and two-dimensional thermal gradients were run for the downstream orifice plane, assuming the same erosion as predicted for the PTB and the same wall heat transfer coefficients as used for the final thermal gradients in the failure analysis. Five time period thermal gradients are shown at $t = 5.0$ sec closed, $t = 16.0$ sec closed, $t = 16.1$ sec open, $t = 25.0$ sec open and $t = 25.1$ sec closed (Figures 201 thru 206).

The purpose of this preliminary analysis was to determine the temperature and stress effect on the carbon cloth exit core replacing the PTB and the temperature-stress effect on the tungsten throat-graphite support when carbon cloth replaced a part of the graphite ring. To show the temperature differences between alternate design 2 and the present orifice design, comparisons were made at three times 5.0, 16,0 and 25.0 sec (Table XXVI). The difference in temperature along the wall surfaces were slight.

However, a comparison of the present to modified design 2 thermal gradient at Section A-A (Figure 207) at $t = 25.1$ sec shows that the PTB has a higher temperature for a given radial length than the carbon cloth. This is due to the higher thermal conductivity of the PTB material. Figures 113 and 206 present the thermal gradients of the present and modified design at $t = 25.1$ seconds.

The present and modified orifice hoop stresses at Section A-A at $t = 25.1$ sec are compared in Figure 208. The two-dimensional present design hoop stress through Section A-A at $t = 25.1$ sec with Boundary Condition A is obtained from Figure 166. A one-dimensional present design hoop stress through Section A-A at $t = 25.1$ sec with the radial restraint of Boundary Condition A and using the two-dimensional thermal gradient (Figure 113) is also shown. While the one-dimensional hoop stresses are higher than the two-dimensional hoop stresses, the

TABLE XXVI

ORIGINAL ORIFICE AND ALTERNATE DESIGN 2 TEMPERATURE COMPARISONS
AT 5, 16, AND 25 SEC

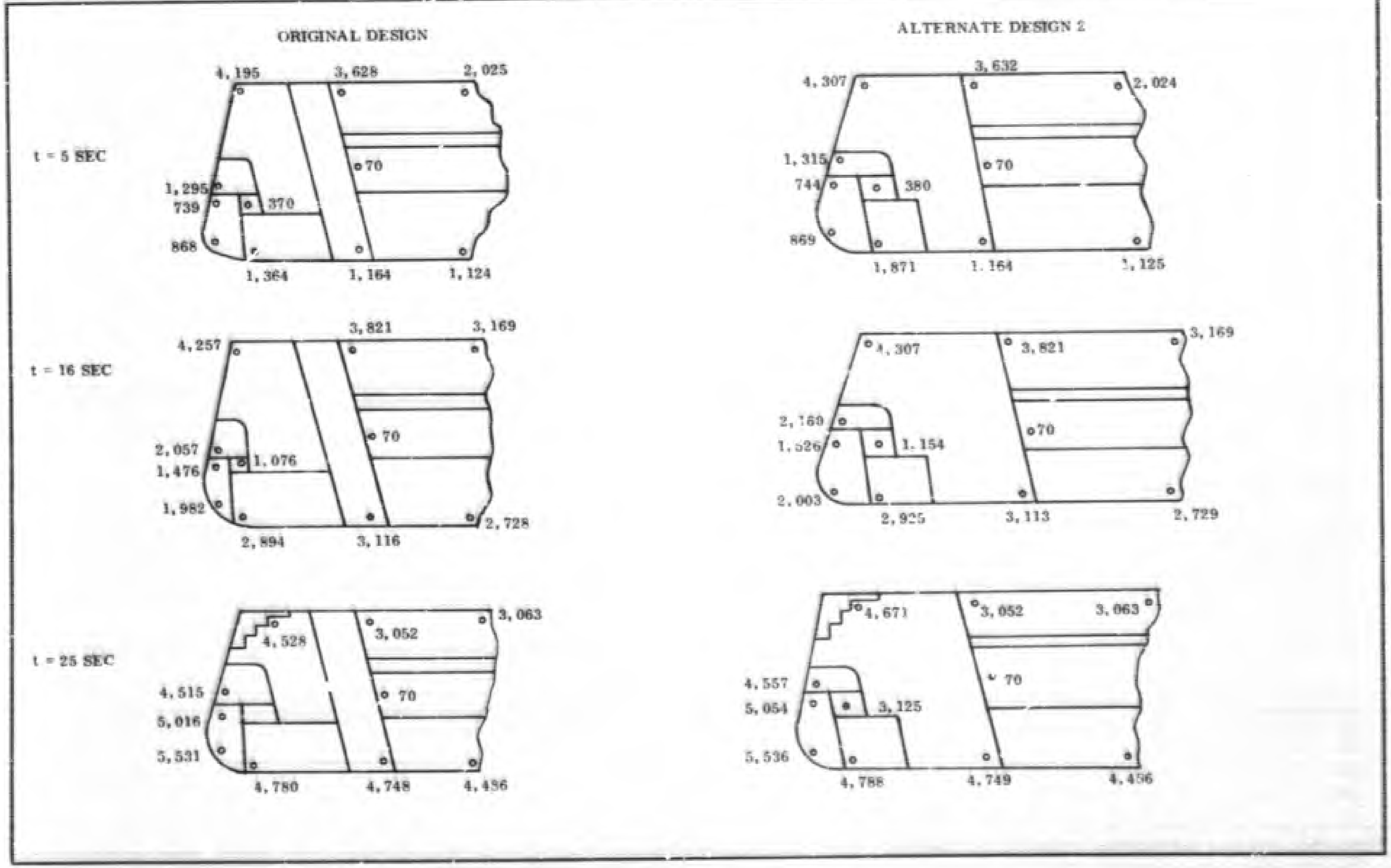

shape and slope of the two hoop stress curves are consistent. Thus, a one-dimensional modified hoop stress through Section A-A at t = 25.1 sec (Figure 208) while not completely accurate is a preliminary design indicator of the actual two-dimensional hoop stress.

The present design, one-and two-dimensional, material element hoop stress-actual and allowable is plotted vs element temperature (Figure 209). Where the allowable is lower than actual stress, the material elements are overstressed. Thus the present design, by the two-dimensional analysis with the PTB material, is overstressed from 5,500 to 3,100°F, or a distance of 0.50 in. from the eroded surface. The one-dimensional analysis of the present design shows an overstressed PTB material from 5,500 to 2,450°F, or a distance of 0.80 in. from the eroded surface.

The modified design (Section A-A at t = 25.1 sec) overstressed material curve is shown in Figure 210. The overstressed carbon cloth material extends back from the eroded surface a short distance of 0.10 inch. The material allowable curves for the carbon cloth and PTB material are obtained from Figures 145 and 141. Thus the carbon cloth in the modified design, while showing the same erosion depth as the PTB in the present design, has a smaller overstressed char layer thickness of 0.10 in. as compared to the PTB thickness of 0.50 to 0.80 inch. It is postulated that the smaller overstressed char layer thickness in the carbon cloth phenolic indicates a lower probability of a spalling, gouging, or chunking effect on the eroded surface.

A comparison of the present to modified orifice design temperature profile at Section B-B, t = 25.1 sec, through the throat plane is made in Figure 211. The modified design graphite ring shows a slightly higher temperature at radial length 1.75 in. due to proximity of carbon cloth insulation. The carbon cloth temperatures at radial length 3.25 in. of the present and modified design again merge together. (Figures 113 and 206 show the thermal gradients at Section B-B).

A comparison of the present and modified hoop stress at Section B-B and t = 25.1 sec is provided by Figure 212. Again the present design, one- and two-dimensional structural analysis hoop stresses do not agree exactly in numerical value but do show good agreement on the shape and slope of the hoop stress profile except through the hoop carbon cloth insulation liner. The modified design one-dimensional structural analysis hoop stress curve follows the present design hoop stress except where carbon cloth replaces graphite.

The present design structural analysis indicates that the tungsten actual one-dimensional hoop stress is higher than the allowable hoop stress (Figure 213). All the tungsten elements for a radial thickness of 0.65 in. are overstressed. An iterative analysis is necessary with the tungsten to use Young's modulus values that agree with the strain in./in. level. Only one iteration was made with present design. Usually several are needed before satisfactory agreement is made between Young's modulus and the strain.

The modified orifice stress condition (Figure 214) at the throat plane B-B, t = 25.1 sec, also indicates an overstressed tungsten condition. The tungsten requires an iteration of actual to predicted Young's modulus and strain to show a realistic stress condition.

A comparison of the designs in the throat plane indicates that although a different thickness combination of the three materials--tungsten, graphite and carbon cloth--was used, the net effect as measured by the +or - areas between the allowable and actual stresses of the materials is about the same.

5. FINAL SELECTION

The nine alternate designs (Figures 192 thru 200) may be classified as modified, improved, advanced and new concepts. The modified designs involve the least development change and the new concepts the most development change. The breakdown of the nine designs is as listed.

Designs	Modified	Improved	Advanced	New Concept
1	X			
2	X			
3			X	
4				X
5			X	
6				X
7		X		
8			X	
9		X		

To prove an orifice design that will survive a 120 sec motor test firing consistently a significant improvement is needed to the existing design without going to a new concept which would require a development program.

Thus the two improved designs would find immediate application with the three advanced designs held in reserve for future application.

Designs 7 and 9 are similar to design 2, which was subjected to a preliminary analysis at Section A-A orifice exit cone and Section B-B orifice throat plane, except that the pyrolytic graphite washer and rubber spacer have been removed. Design 7 substitutes graphite cloth phenolic for the carbon cloth billet, while design 9 retains carbon cloth as insulation sleeve for the graphitized graphite cloth erosion liners and support rings.

Current material technology programs have evaluated seven erosion liner materials: carbon and graphite cloth, pyrolytic graphite, graphitized graphite cloth phenolic, graphite, PTB and tungsten materials that have been used or could be used in orifice inlet and exit cone. The materials are evaluated in Table XXVII .

Material G, thoriated tungsten, is the orifice throat material; Material E, Graphite 90, has been used as the orifice inlet; while Materials A, PTB, and F, Pyrolytic Graphite, have been used in the orifice exit cone. Notice that the present

TABLE XXVII

MATERIAL PROPERTIES OF CANDIDATE ORIFICE EROSION LINERS

Material Properties	PTB (A) Graphitized Graphite Fiber Phenolic Molding	FM5063 (B) or Equivalent Carbon Cloth Phenolic Tape Wrapped	FM5014 (C) or Equivalent Graphite Cloth Phenolic Tape Wrapped	FM5228 (D) Graphitized Graphite Cloth Phenolic Tape Wrapped	Graphite 90 (E) Graphite Extruded	Pyrolytic (F) Graphite Edge Grain Washer Plate	2% Thoriated (G) Tungsten Forged
At Room Temperature							
Density (gr/cc)	1.40	1.51	1.44	1.40	1.90	1.80	19.45
Ultimate Compression (psi)	6,500-15,000	18,000-25,000	12,000-18,000	9,500-13,000	7,000- 7,800	10,000-45,000	148,000
Ultimate Tension (psi)	2,000- 3,150	10,000-18,000	6,600-10,500	10,000-11,400	1,370- 1,400	3,500-15,000	148,000
Thermal Conductivity $\left(\frac{Btu\text{-}ft}{hr\text{-}ft^2\text{-}^\circ F}\right)$	6.26	0.40-0.60	0.75-1.85	1.67*	68.00-92.00	106.00-225.00	97
Coefficient of Thermal Expansion (in./in.-°F) $\times 10^{-6}$	1.80-1.92	1.00-3.80	5.3 -5.8	2.2	0.85-1.20	1.53-12.00	2.40
At 750 - 1,000°F							
Ultimate Compression (psi)	6,250-10,000	10,600-17,000	4,000-10,000	8,660	7,400- 8,000	10,000-47,000	102,000-114,000
Ultimate Tension (psi)	1,200- 3,400	4,600- 7,200	4,600- 7,200	10,300	1,450- 2,040	3,500-15,000	102,000-114,000
Thermal Conductivity $\left(\frac{Btu\text{-}ft}{hr\text{-}ft^2\text{-}^\circ F}\right)$	6.26	0.50-1.10	0.75-2.95	NA	35.00- 72.00	68.00-183.00	76-79
Coefficient of Thermal Expansion (in./in.-°F) $\times 10^{-6}$	1.80-1.90 Estimate	0.25-2.50 Estimate	0.25-2.50 Estimate	NA	1.30-1.50	1.55-11.70	2.45
At 3,000 - 3,500°F							
Ultimate Compression (psi)	3,700	6,303	4,030	NA	8,800- 9,500	10,700-56,000	10,000- 18,50[illegible]
Ultimate Tension (psi)	1,200	3,250 Estimate	1,000 Estimate	NA	1,750- 2,650	3,500-18,500	10,000- 18,500
Thermal Conductivity $\left(\frac{Btu\text{-}ft}{hr\text{-}ft^2\text{-}^\circ F}\right)$	11.90-25.00	1.50-2.0	2.35-3.35	NA	11.00- 23.00	34.00-66.00	57.5-60
Coefficient of Thermal Expansion (in./in.-°F) $\times 10^{-6}$	2.0-2.6 Estimate	0.20-0.50 Estimate	0.20-0.50 Estimate	NA	1.80-2.30	2.55-13.90	3.0-3.10

NOTES: 1. No consideration was given to with and against grain properties.
2. Material properties given in Section 10B of report
 a. Graphite cloth - see carbon cloth references.
 b. FM5228 - see U S Polymeric vendor data.

orifice materials exhibit higher thermal conductivities than the proposed alternate materials B, C, and D. Also, the ratio of compression to tension allowable stresses for the present orifice materials is higher than the proposed alternate materials. When the liner material resembles a homogeneous material, with properties in each of three planes approximating each other and the compression and tension properties in each plane in low multiples (1 to 2) of each other, the design application and use of material increases. The PTB and Pyrolytic Graphite exhibited grains perpendicular to orifice centerline and parallel to the gas impingement and stagnation on the downstream plane. The replacement materials would be oriented 9 to 30 deg off parallel to orifice centerline.

As shown in the thermal-mechanical stresses in Sections A-A and B-B, the replacement of PTB with carbon cloth and Graphite 90 with carbon cloth decreases the temperature inside the orifice wall while showing the same or fewer elements in an overstressed condition.

Thus, the graphitized graphite cloth phenolic, D, in Design 7 and the graphite cloth phenolic, C, in Design 9 would be satisfactory from a thermostructural standpoint to be included in the final selection.

A further evaluation of the orifice liner materials is presented (Tables XXVIII and XXIX) by a comparison of preliminary erosion rates in the inlet and exit cone. The erosion rates are determined by the preliminary erosion rate formula with an erosion correction factor.

In the inlet, the Graphite 90 material shows the best erosion resistance but with a small increase in erosion. The graphitized graphite cloth phenolic can be used, providing a more stable, reliable, crack resistant material.

The comparison of the orifice exit cone materials shows that tungsten, pyrolytic graphite, graphite and graphitized graphite cloth represent the best materials, in that order. With the orifice closed, the erosion rate varies from 0 to 21.20 mils/sec and orifice open erosion rates vary from 0 to 10.40 mil/second. These erosion rates on the downstream plane will decrease with static test time,

TABLE XXVIII

ORIFICE INLET MATERIALS - COMPARISON BY PREDICTED EROSION

Inlet Conditions

- Fixed Submerged Orifice
- Propellant Formulation (MM)
  (β) Blowing Coefficient = 0.108
- Propellant Grain Configuration
  CP or Star
- Average Web Pressure = 700 psia
- Initial Throat Diameter = 6.37
- Average Convective Heat Transfer Coefficient (lbm/sq ft-sec) (h/cp) All Around Inlet Material = 0.57 Orifice Fully Open

$$\text{Preliminary Erosion Rate} = \frac{h/cp^{(\beta)}\ 12,000}{\rho}\ (F)\ (2)$$

Orifice Inlet Materials			Maximum Preliminary Orifice Erosion Rate Downstream Fully Open mil/sec	Comment
1.	Graphite 90	F = 0.78	4.8	3
2.	Carbon Cloth Phenolic Tape Wrapped FM5063 or Equivalent	F = 1.0	7.8	--
3.	Graphite Cloth Phenolic Tape Wrapped FM5014 or Equivalent	F = 1.0	8.2	1
4.	Graphitized Graphite Cloth Phenolic FM5228	F = 1.0	6.5	1

TABLE XXVIII (Cont)

ORIFICE INLET MATERIALS - COMPARISON BY PREDICTED EROSION

Notes:

1. Actual tests of graphitized graphite cloth phenolic (FM5228), graphite cloth phenolic tape wrapped (FM5014) and Graphite 90 were made in the Thiokol test motors TU-379, TU-391, TU-599. At pressures of 100 to 900 psia, throat diameters of 0.28 to 4.45 in. and web times of 15 sec indicated the FM5228 eroded halfway between the Graphite 90 and FM5014 materials erosion rate. Thus, the preliminary predicted erosion rate orifice fully open would actually be between 4.8 and 8.2 mil/seconds.
2. h/cp = convective heat transfer coefficient

   β = propellant formulation blowing coefficient

   ρ = density (lb/cu ft)

   12,000 = conversion term factor

   (F) = erosion correction factor
3. While the Graphite 90 has the lowest erosion rate, it exhibits the greatest amount of cracking when loaded unsymmetrically as in the orifice port.
4. INLET - MAXIMUM CONVECTIVE HEAT TRANSFER COEFFICIENTS

   h/cp - (lbm/ft^2-sec)

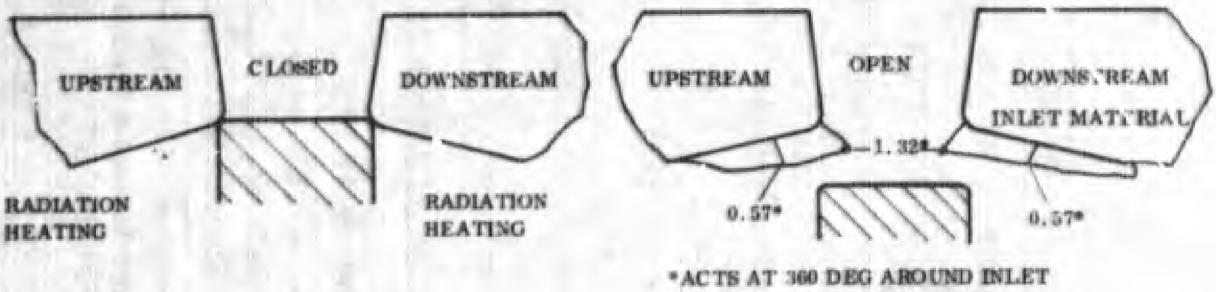

TABLE XXIX

ORIFICE EXIT MATERIALS - COMPARISON BY PREDICTED EROSION

Exit Conditions

- Fixed Submerged Orifice
- Propellant Formulation (MM)
  Blowing Coefficient = 0.108
- Propellant Grain Configuration
  CP or Star
- Average Web Pressure = 700 psia
- Initial Throat Diameter - 6.37
- Maximum Convective Heat
  Transfer Coefficient (lbm/ft^2-sec) = 1.84 Orifice Closed
  h/cp

$$\text{Preliminary Erosion Rate} = \frac{h/cp \ \beta \ 12{,}000}{\rho} (F) \ (1)$$

Orifice Exit Materials		Maximum Preliminary Erosion Orifice Downstream Closed mil/sec	Maximum Preliminary Erosion Orifice Downstream Open mil/sec	Comment
1. Pyrolytic Graphite	F = 0.25	5.30	2.59	(3) (4)
2. PTB - Graphitized Graphite Fiber Phenolic Molding	F = 1.0	27.20	13.33	(3)
3. Carbon Cloth Phenolic Tape Wrapped FM5063 or Equivalent	F = 1.0	25.20	12.32	(3)
4. Graphite Cloth Phenolic Tape Wrapped FM5014	F = 1.0	26.50	13.00	(2) (3)
5. Graphitized Graphite Cloth Phenolic FM5228	F = 0.89	21.20	10.40	(2) (3)

TABLE XXIX (Cont)

ORIFICE EXIT MATERIALS - COMPARISON BY PREDICTED EROSION

6.	Graphite 90	F = .78	15.70	7.70	3 4
7.	Tungsten		0	0	6

Notes:

1. h/cp = convective heat transfer coefficient
   - β = propellant formulation blowing coefficient
   - ρ = Density (lb/sq ft)
   - F = Erosion correction factor
2. Actual tests at Thiokol-Wasatch Division indicates material 5 FM5228 actual erosion is 21.20 M/S halfway between the erosion of material 6 Graphite 90 -15.70 M/S and material 4 FM5014 - 26.50 M/S.
3. Erosion rates will decrease with the eroded configuration on the downstream plane. The gas stagnation point will also shift further down the orifice downstream wall with static test time and erosion.
4. Graphite 90 or pyrolytic graphite was not considered in the orifice exit cone redesign because of its susceptibility to cracking or delamination.
5. Exit cone maximum convective heat transfer coefficients - h/cp (lbm/sq ft-sec).

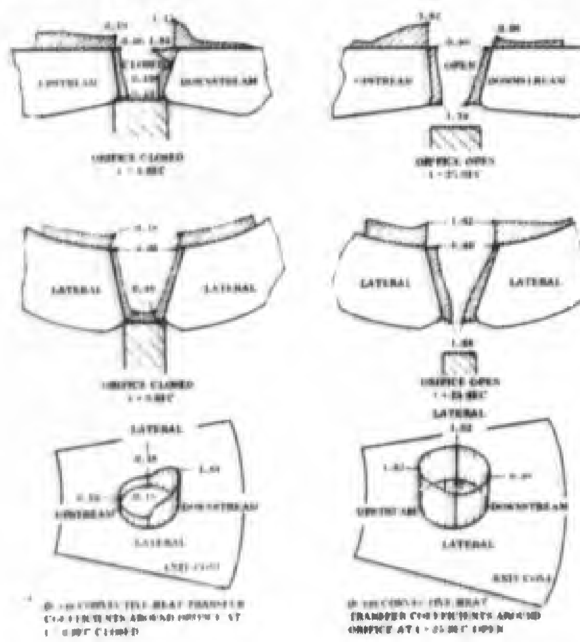

6. The effect of tungsten in the nozzle exit on the surrounding materials and injection performance is unknown.

as the erosion will decrease the heat transfer coefficient along the orifice wall. Assuming a 35.0 sec full open time and a 85.0 sec closed time for each orifice, the approximate erosion depth is given below for the four materials.

	Orifice Wall	Exit Cone Wall
Tungsten	= 0 in.	= 0 in.
Pyrolytic Graphite = 35(0.0026) + 85(0.0053)	= 0.54 in.	85(0.0043) = 0.37 in.
Graphite 90 = 35 (0.0077) + 85 (0.0157)	= 1.61 in.	85(0.0129) = 1.10 in.
Graphitized Graphite = 35(0.0104) + 85(0.0212)	= 2.16 in.	85(0.0147) = 1.25 in.

The tungsten and graphite would be eliminated on a preliminary basis. The tungsten, because of its design application development time and cost, and because of its effect on orifice injection when surrounding exit cone materials, is excessively eroded. The graphite cracking problems with unsymmetrical heating, pressure loading and erosion eliminate this material as an exit cone liner. The other materials, pyrolytic graphite oriented parallel to orifice centerline and the graphitized graphite cloth, would be acceptable if used as shown below.

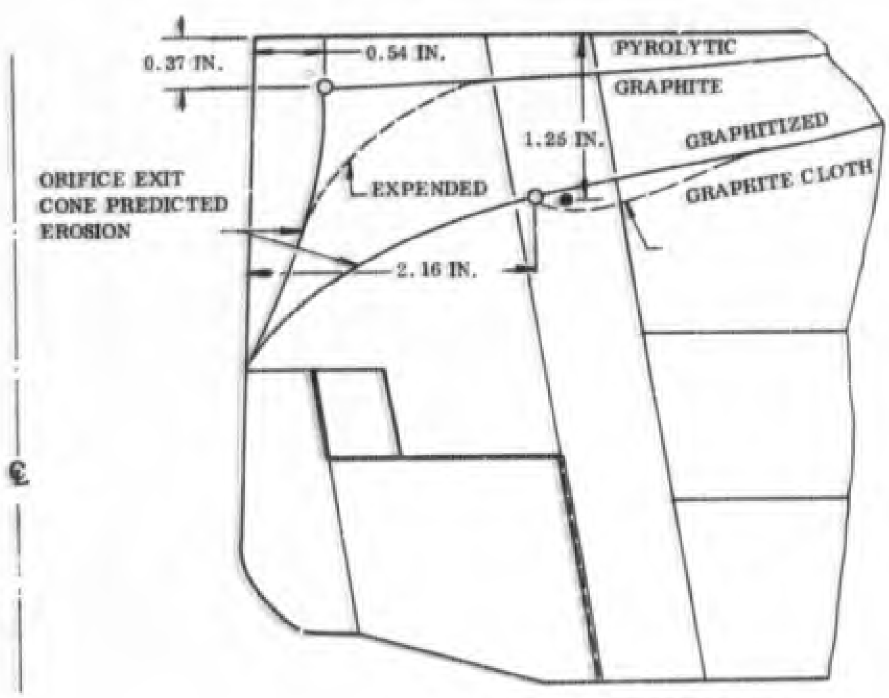

ORIFICE DOWNSTREAM PLANE
t = 120 SEC

The graphitized graphite cloth phenolic is acceptable for orifice injection performance in its eroded condition and is a more developed material for design application in the orifice exit cone. The pyrolytic graphite as an orifice exit cone in pyroid form (Figure 197 - Advanced Design) while not as fully developed and tested as the graphitized graphite would serve as a backup material in the final orifice design evaluation.

Thus, improved design 9 with three materials--2 percent thoriated tungsten, graphitized graphite cloth, and carbon cloth phenolic--and five rings, is the preliminary selected design from the nine alternative designs. Certain features of the advanced design concept 3, the pyroid pyrolytic graphite exit, would be held in reserve for future application.

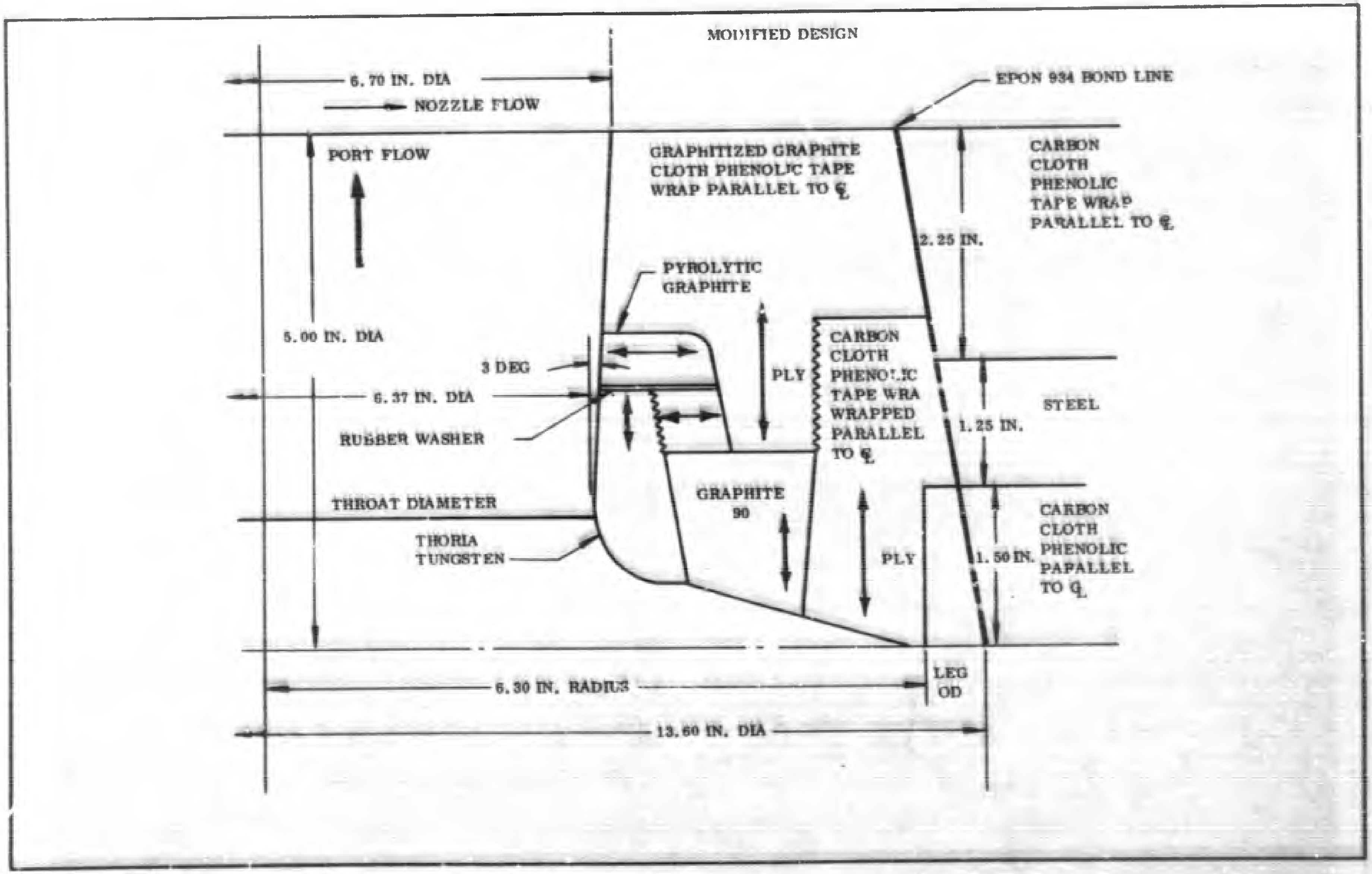

Figure 192. Alternative Orifice Design 1

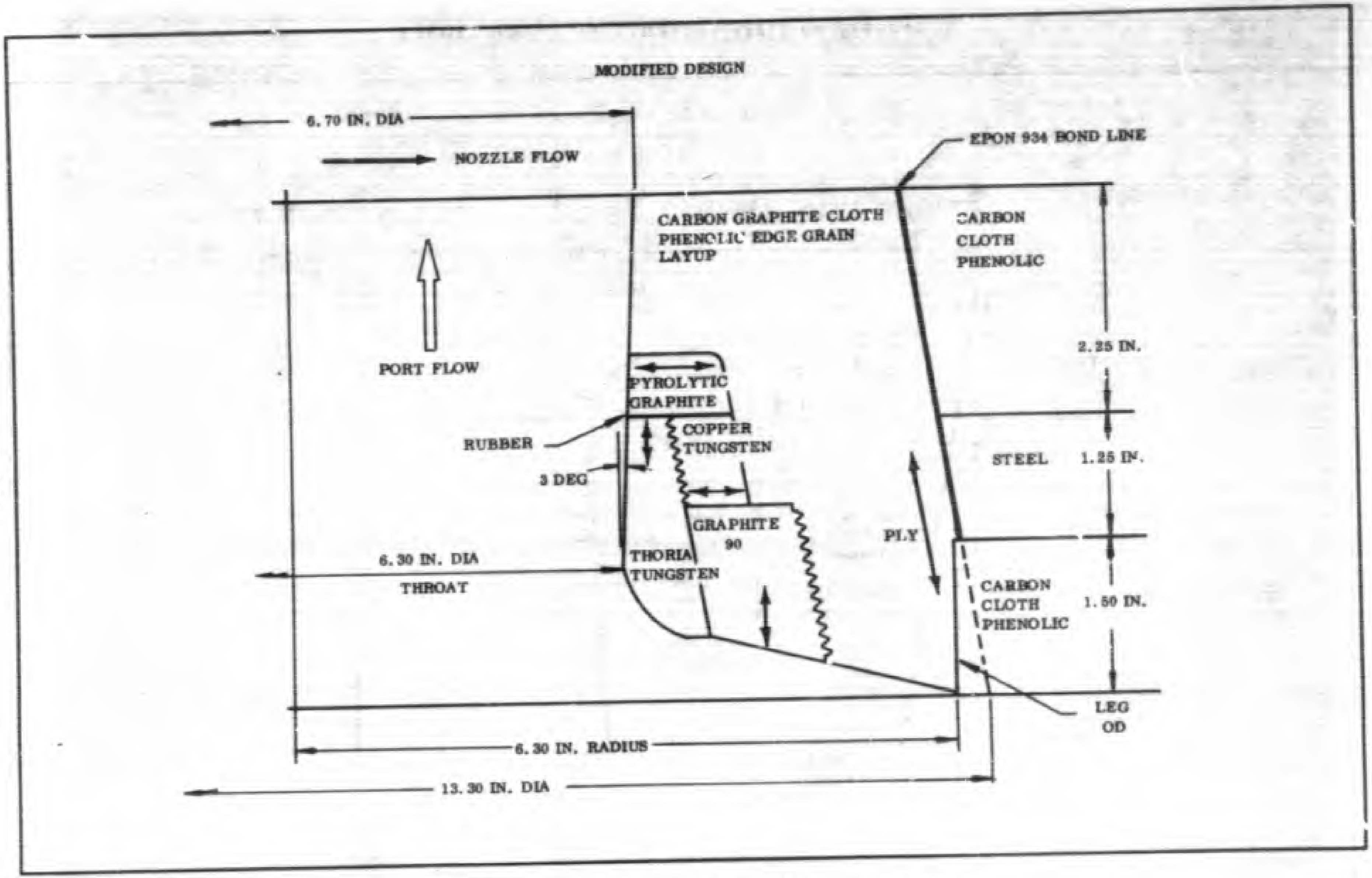

Figure 193. Alternative Orifice Design 2

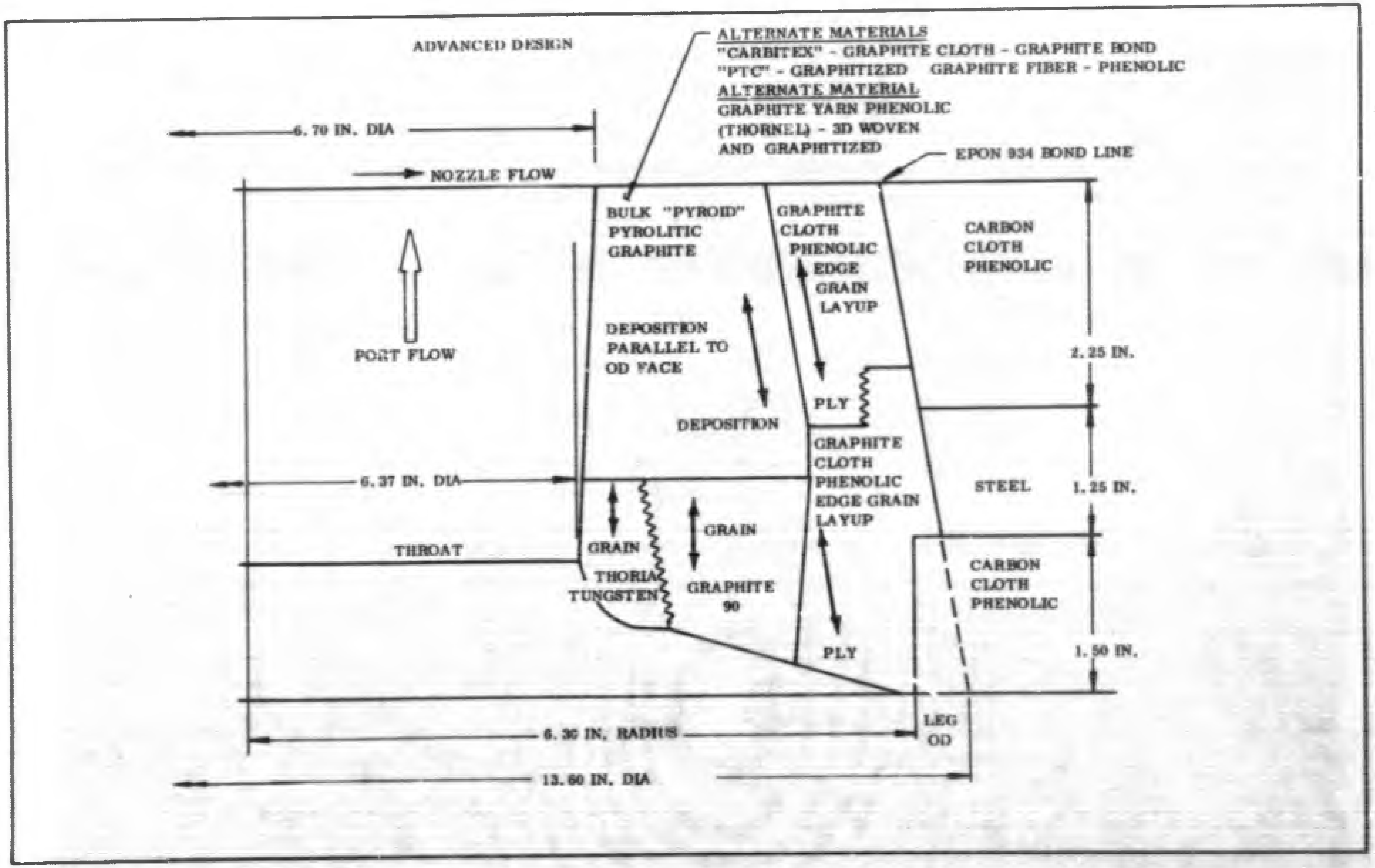

Figure 194. Alternative Orifice Design 3

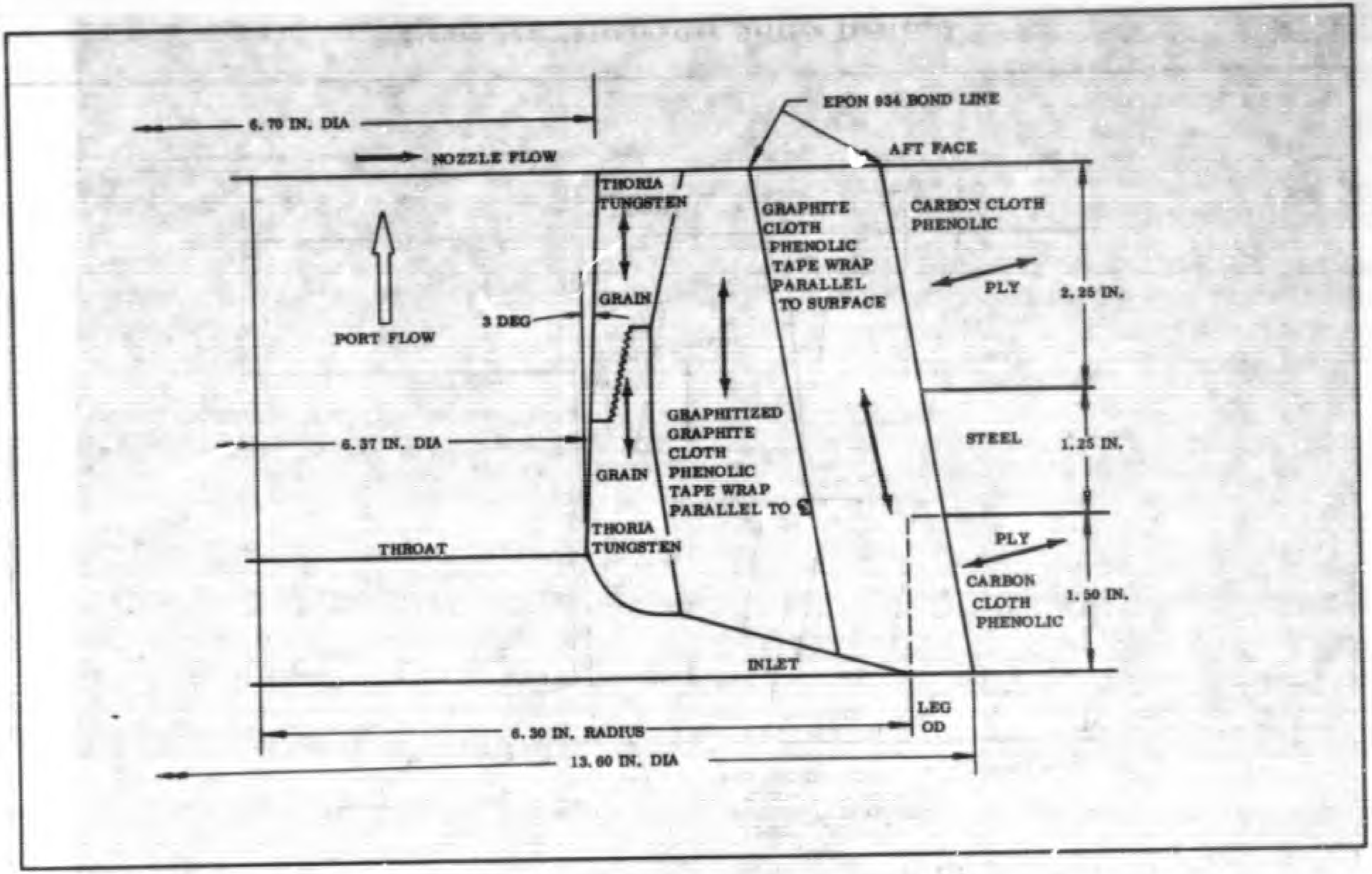

Figure 195. Alternative Orifice Design 4

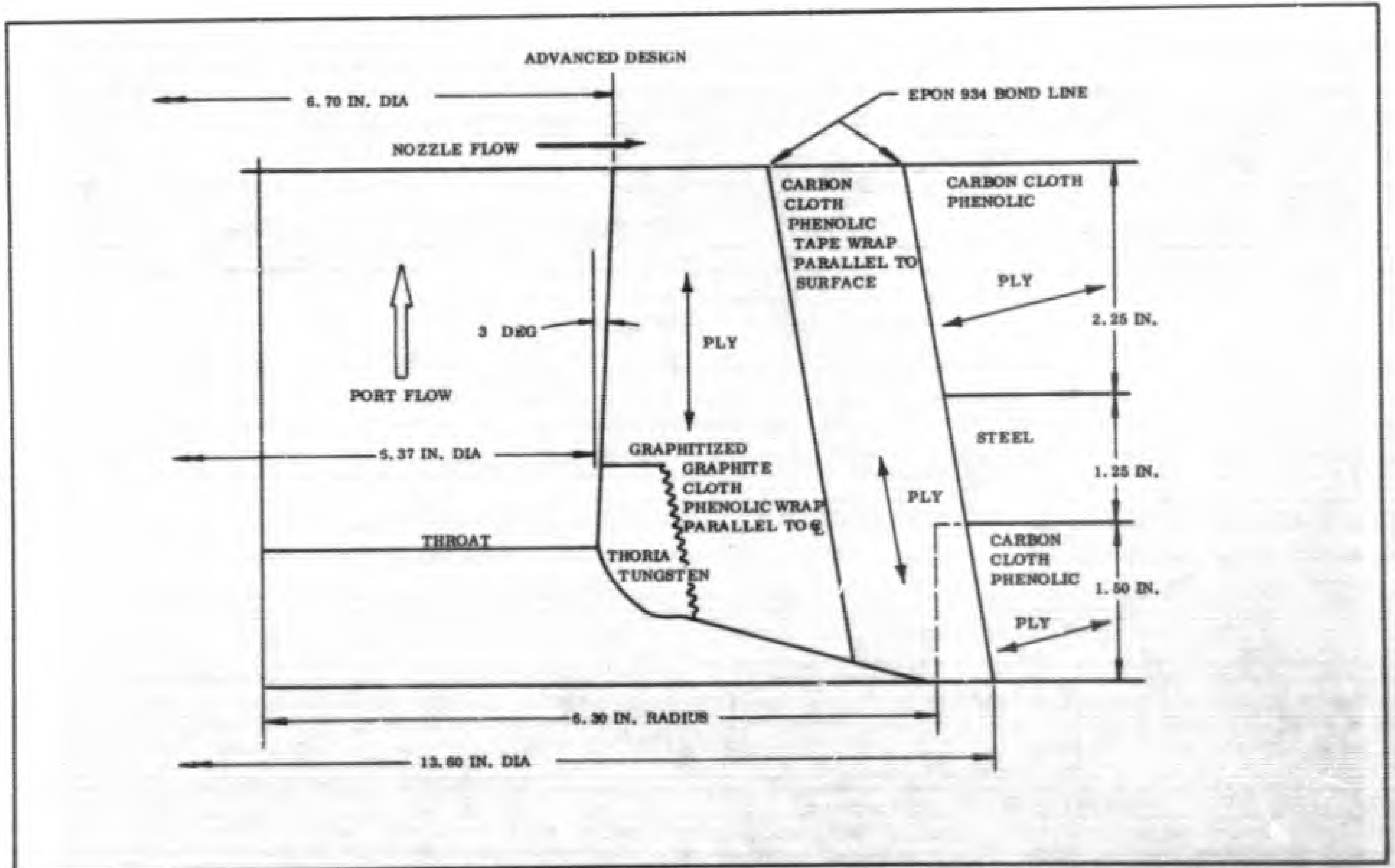

Figure 196. Alternative Orifice Design 5

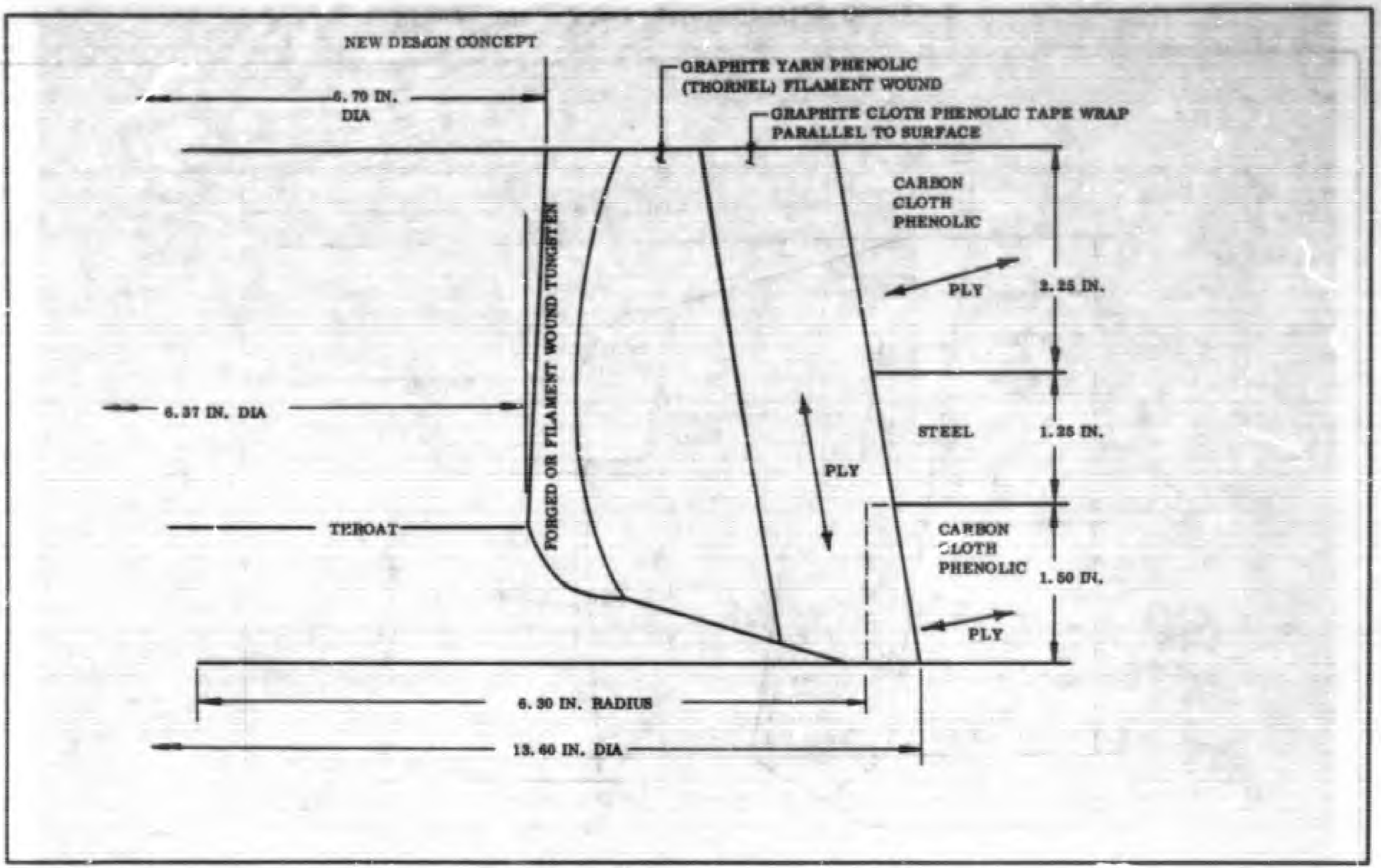

Figure 197. Alternative Orifice Design 6

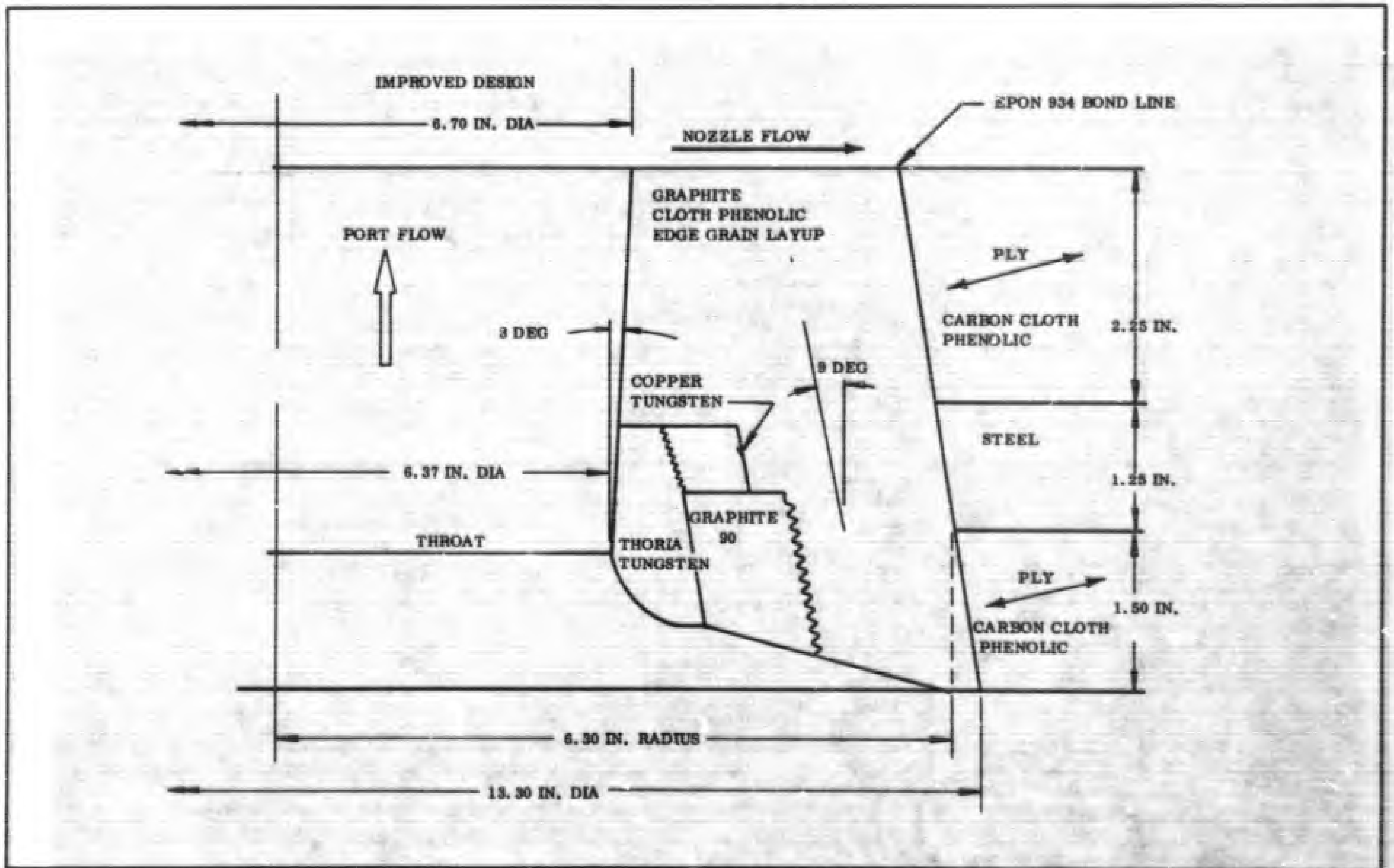

Figure 198. Alternative Orifice Design 7

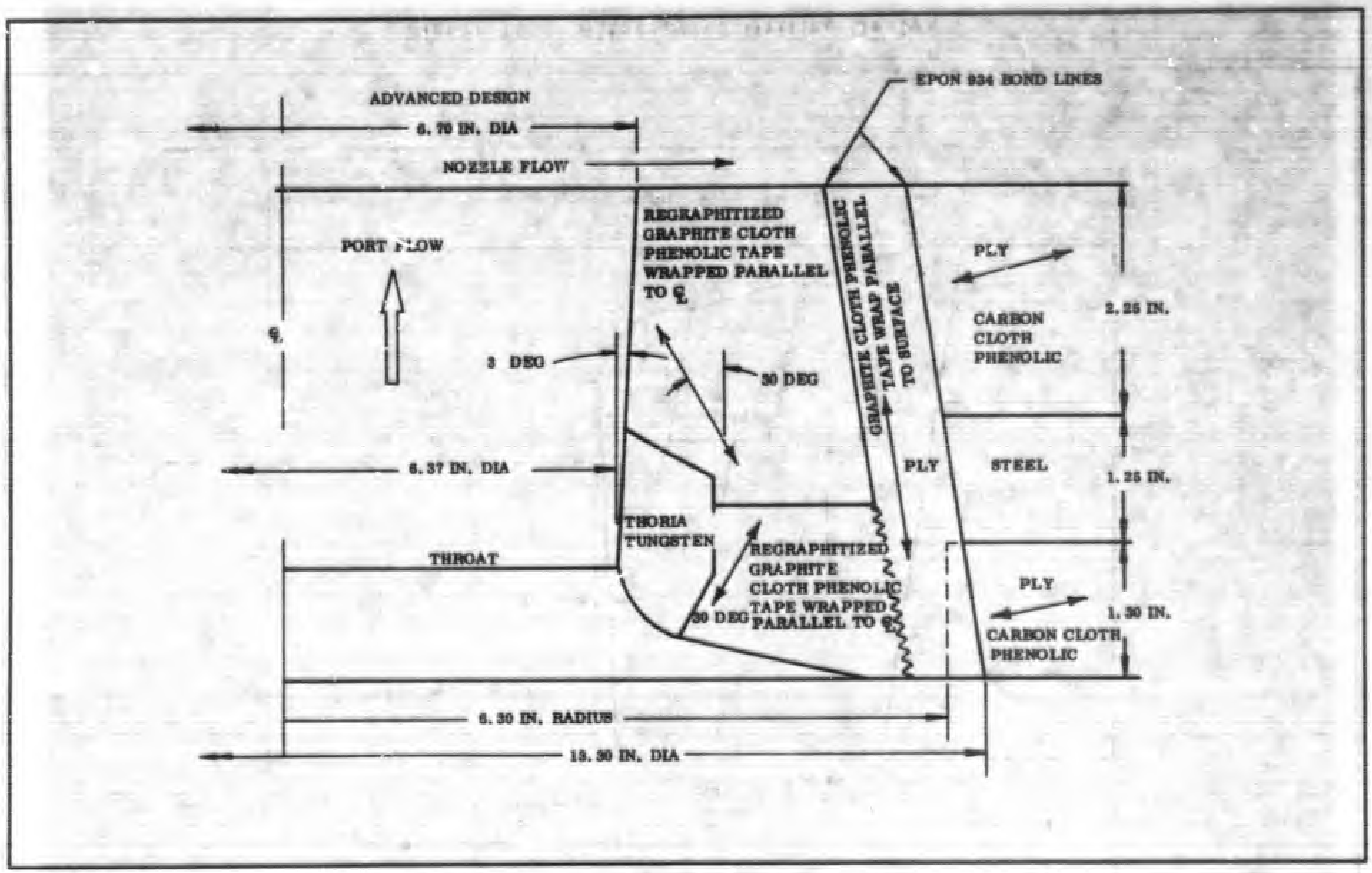

Figure 199. Alternative Orifice Design 8

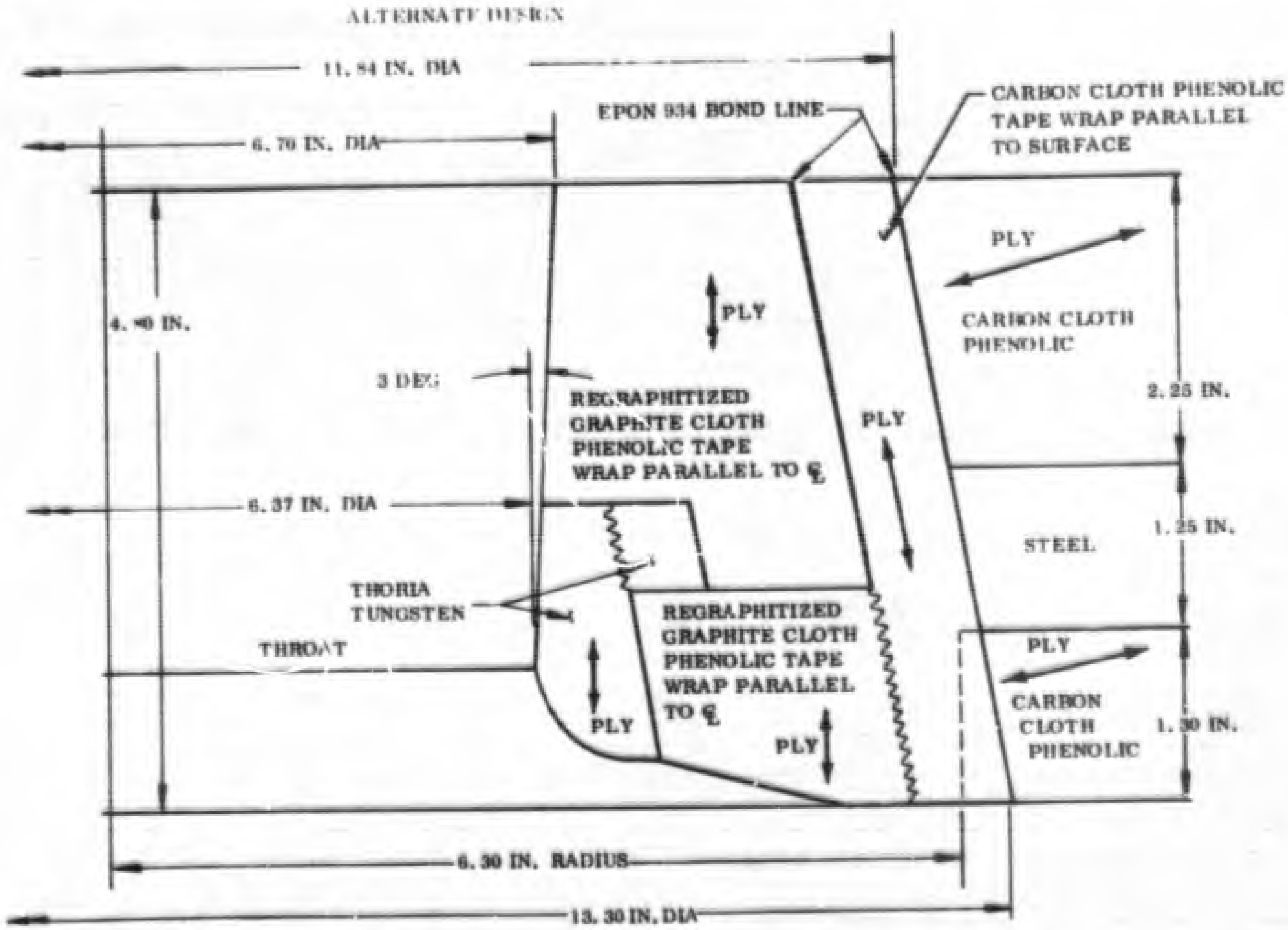

Figure 200. Alternative Orifice Design 9

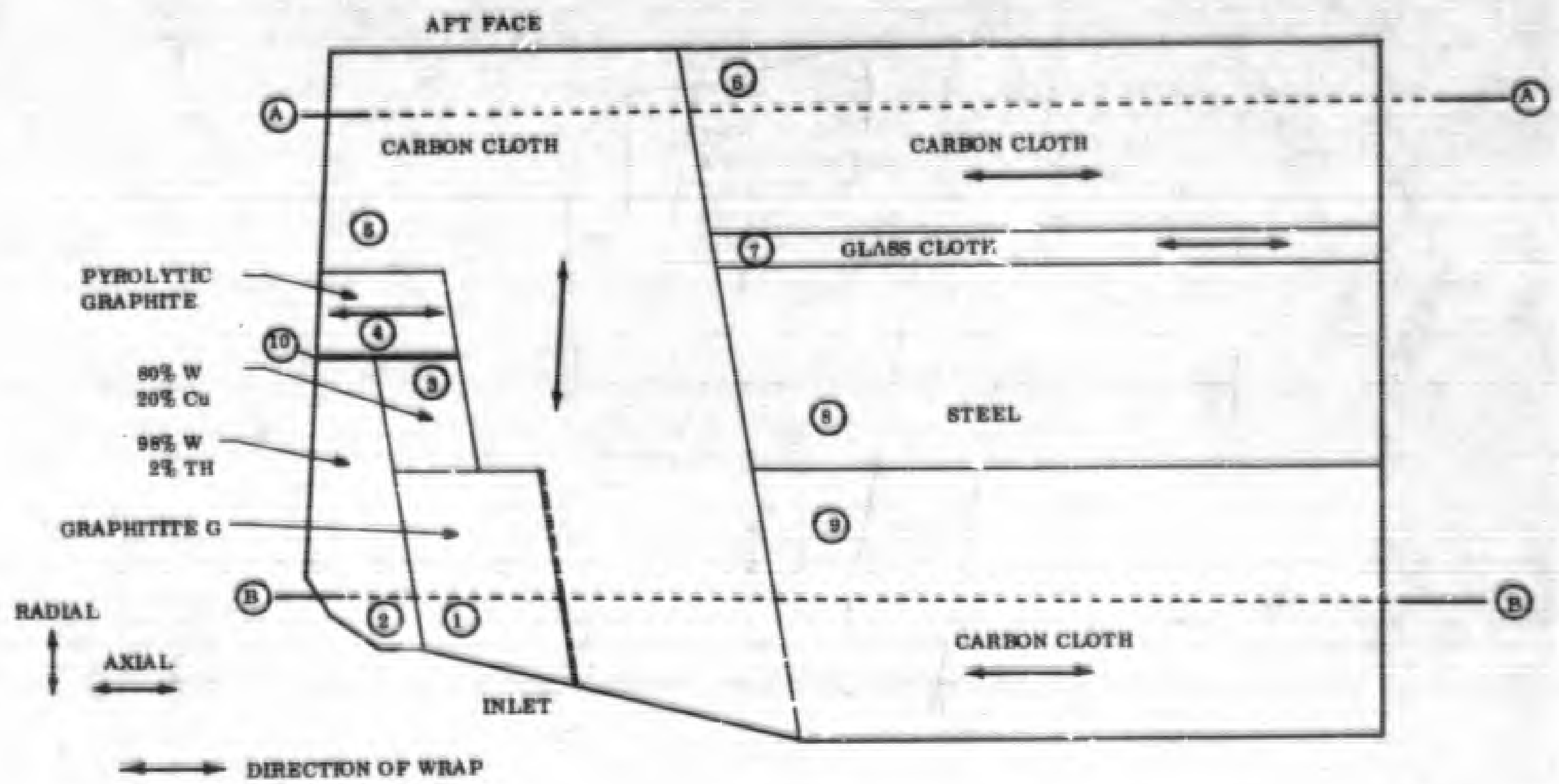

Figure 201. Alternate Orifice Design 2, Material Callouts

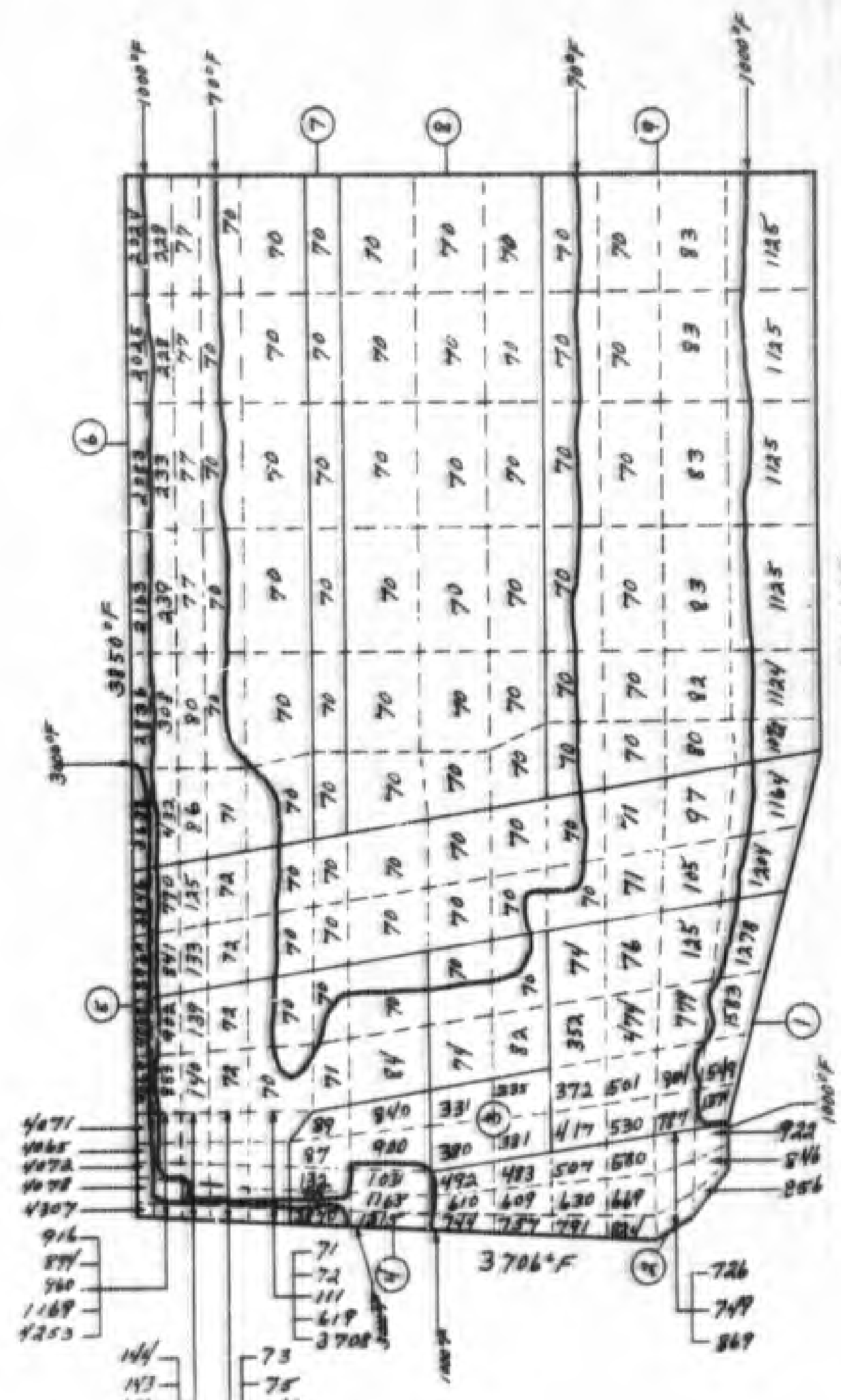

Figure 202. Alternate Orifice Design 2, Thermal Gradients at 5.0 Sec

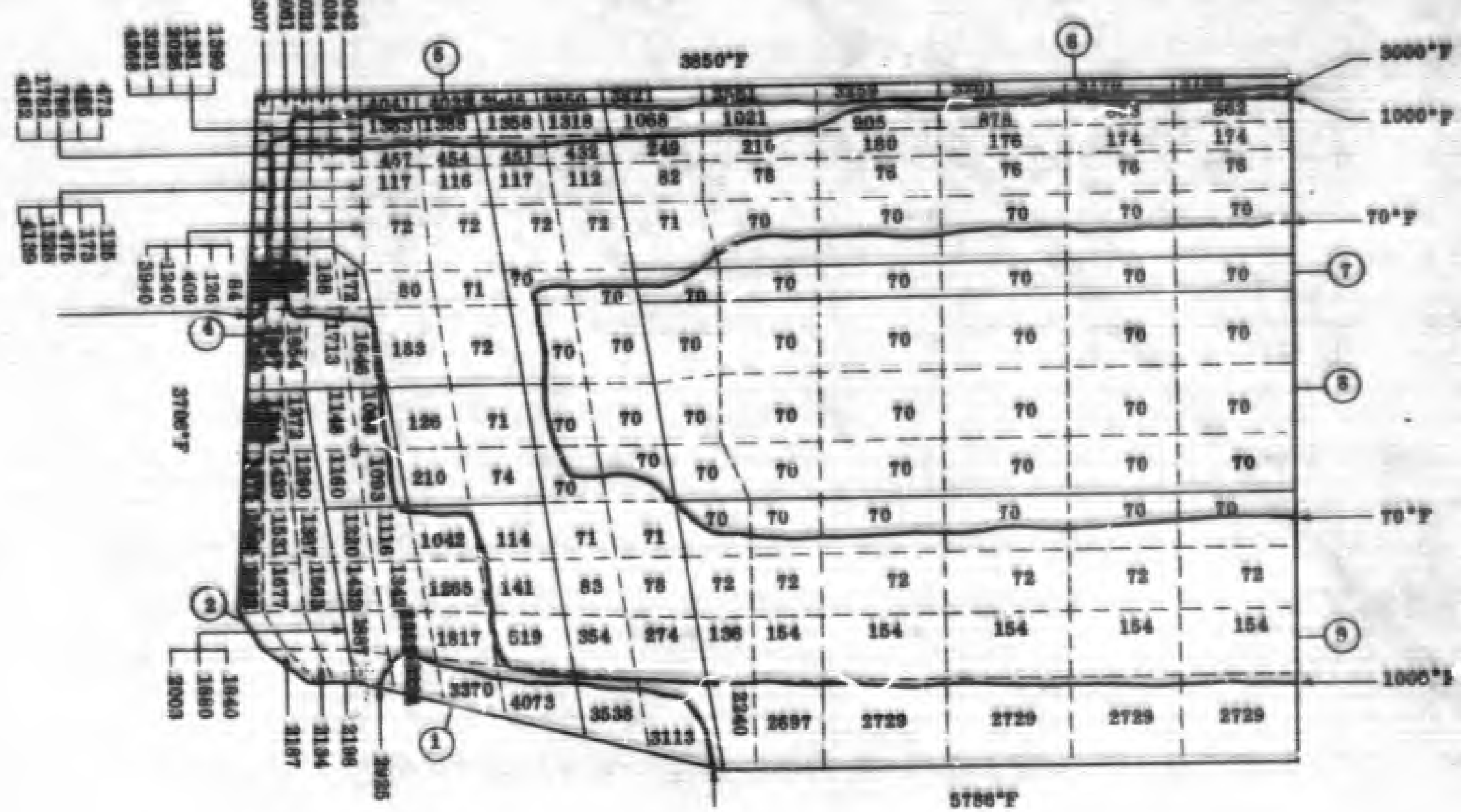

Figure 203. Alternate Orifice Design 2. Thermal Gradients at 16.0 Sec

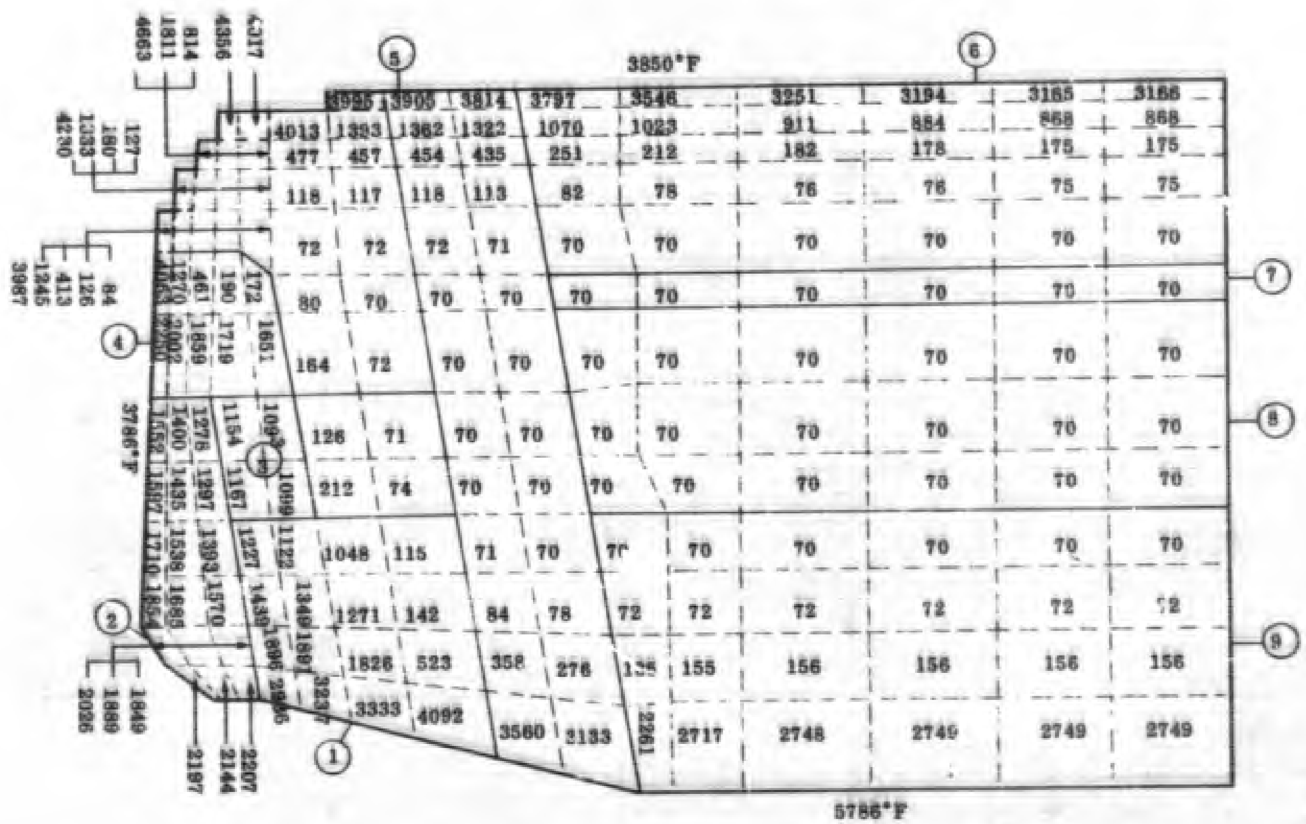

Figure 204. Alternate Orifice Design 2, Thermal Gradients at 16.1 Sec

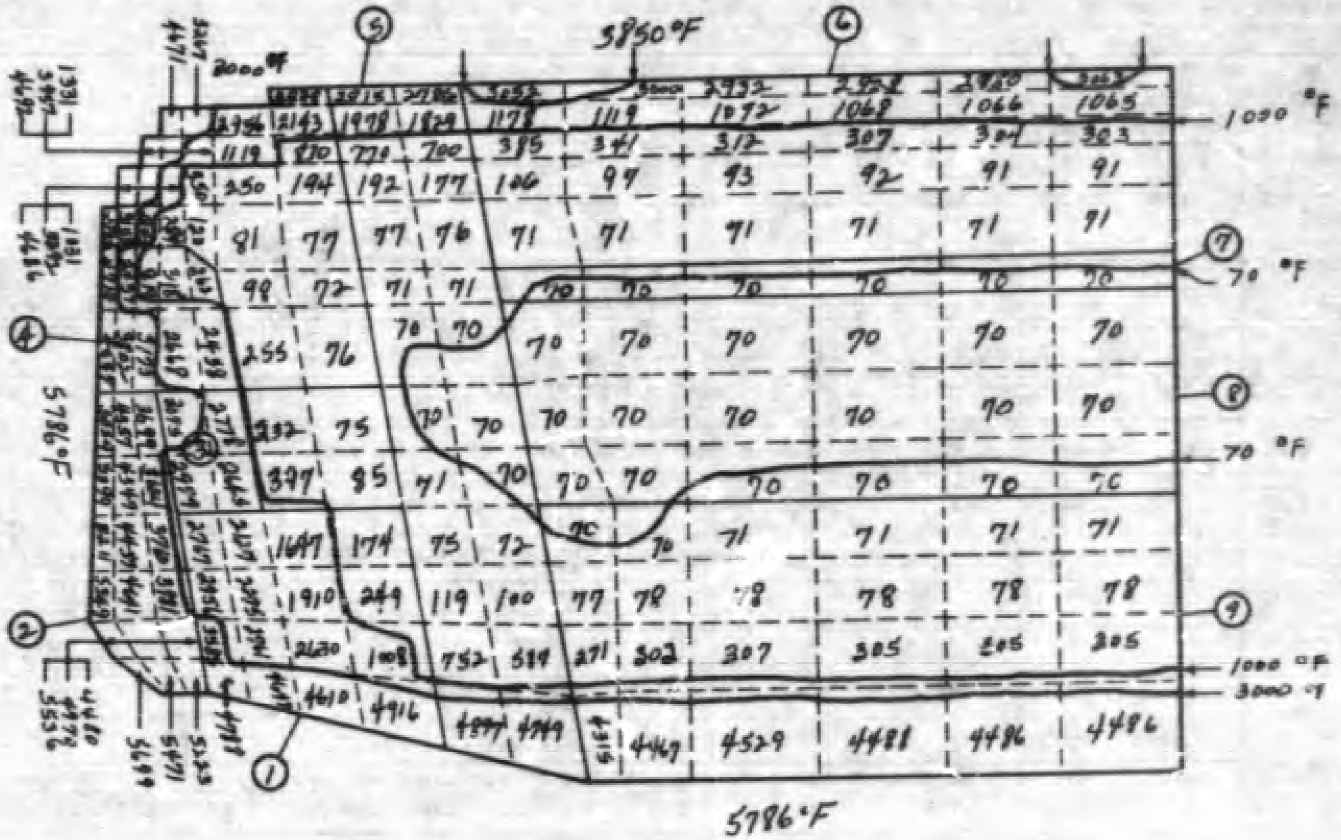

Figure 205. Alternate Orifice Design 2, Thermal Gradients at 25.0 Sec

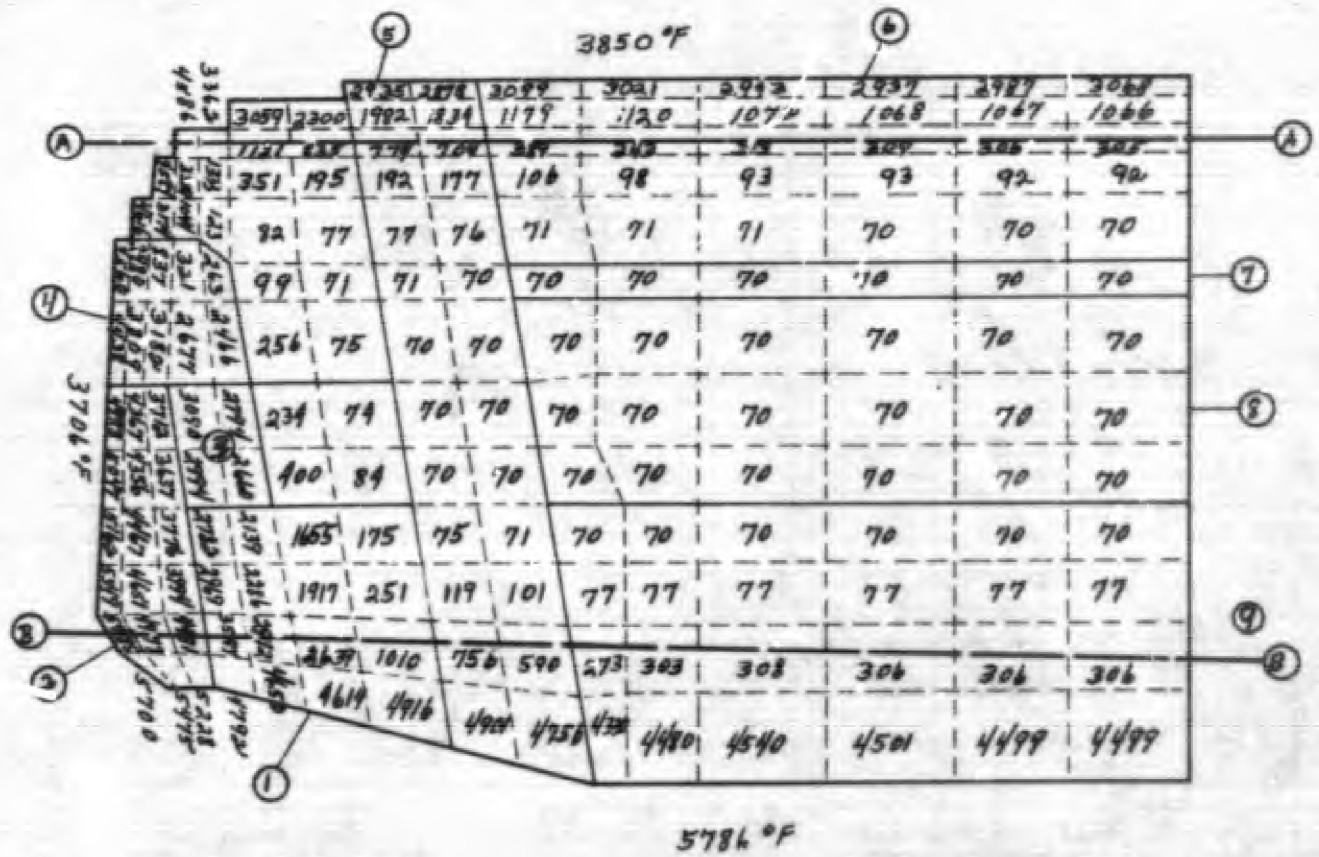

Figure 206. Alternate Orifice Design 2, Thermal Gradients at 25.1 Sec

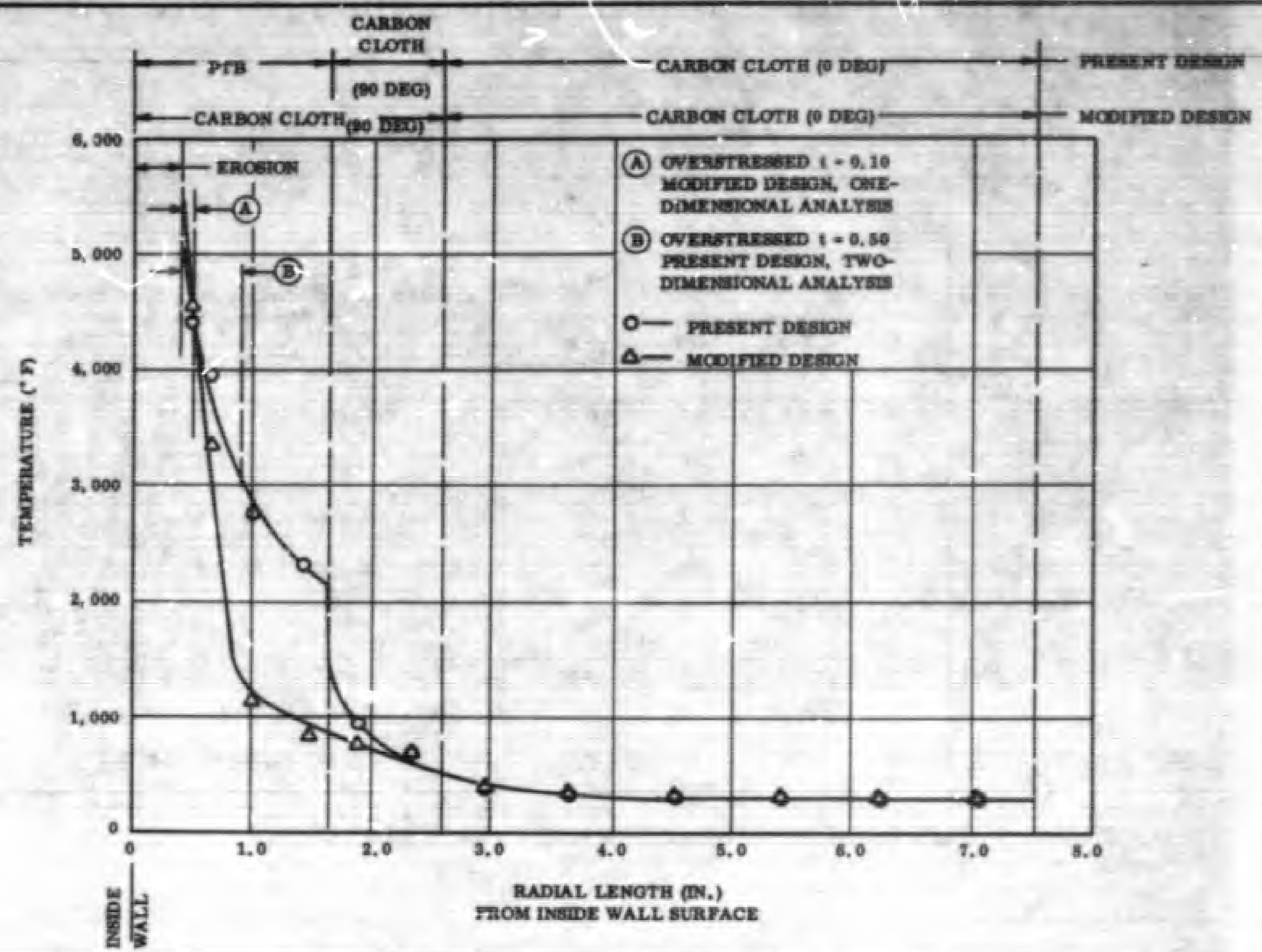

Figure 207. Present and Modified Orifice Design, Temperature Profile, Section A-A at 25.1 Sec

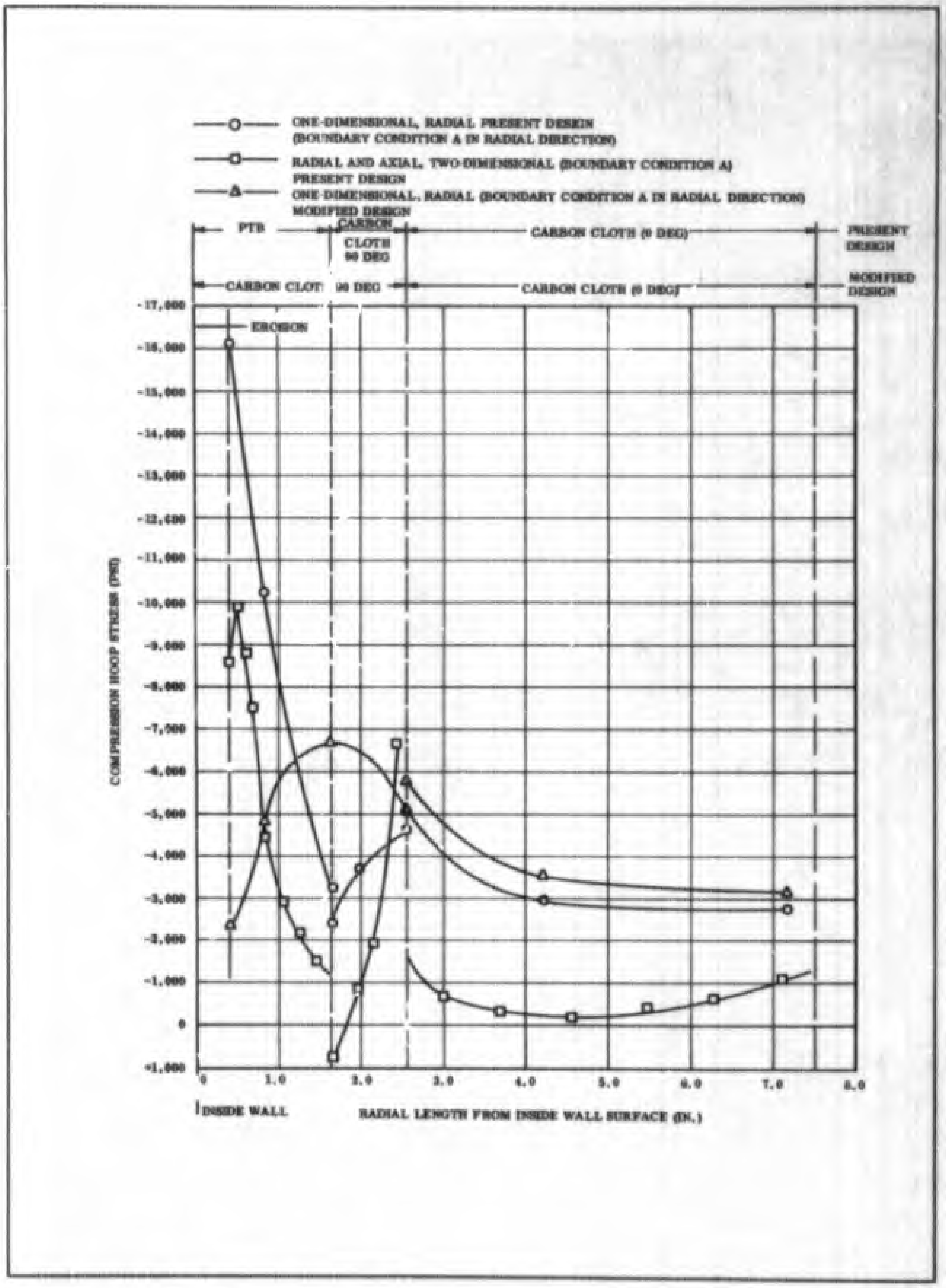

Figure 208. Present and Modified Orifice Design, Hoop Stress Profile, Section A-A at 25.1 Sec

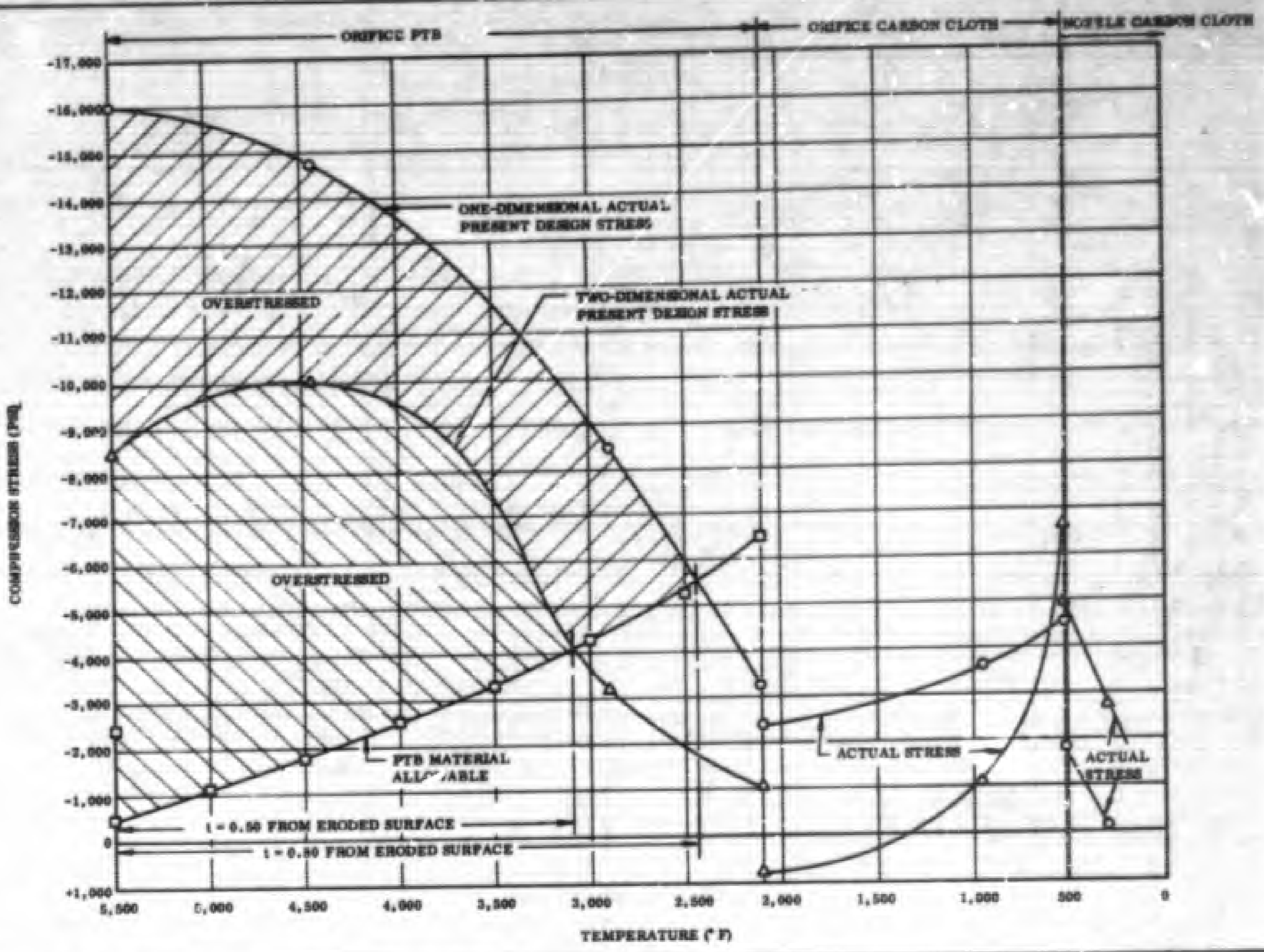

Figure 209. Present Design, Overstressed Material, Section A-A at 25.1 Sec

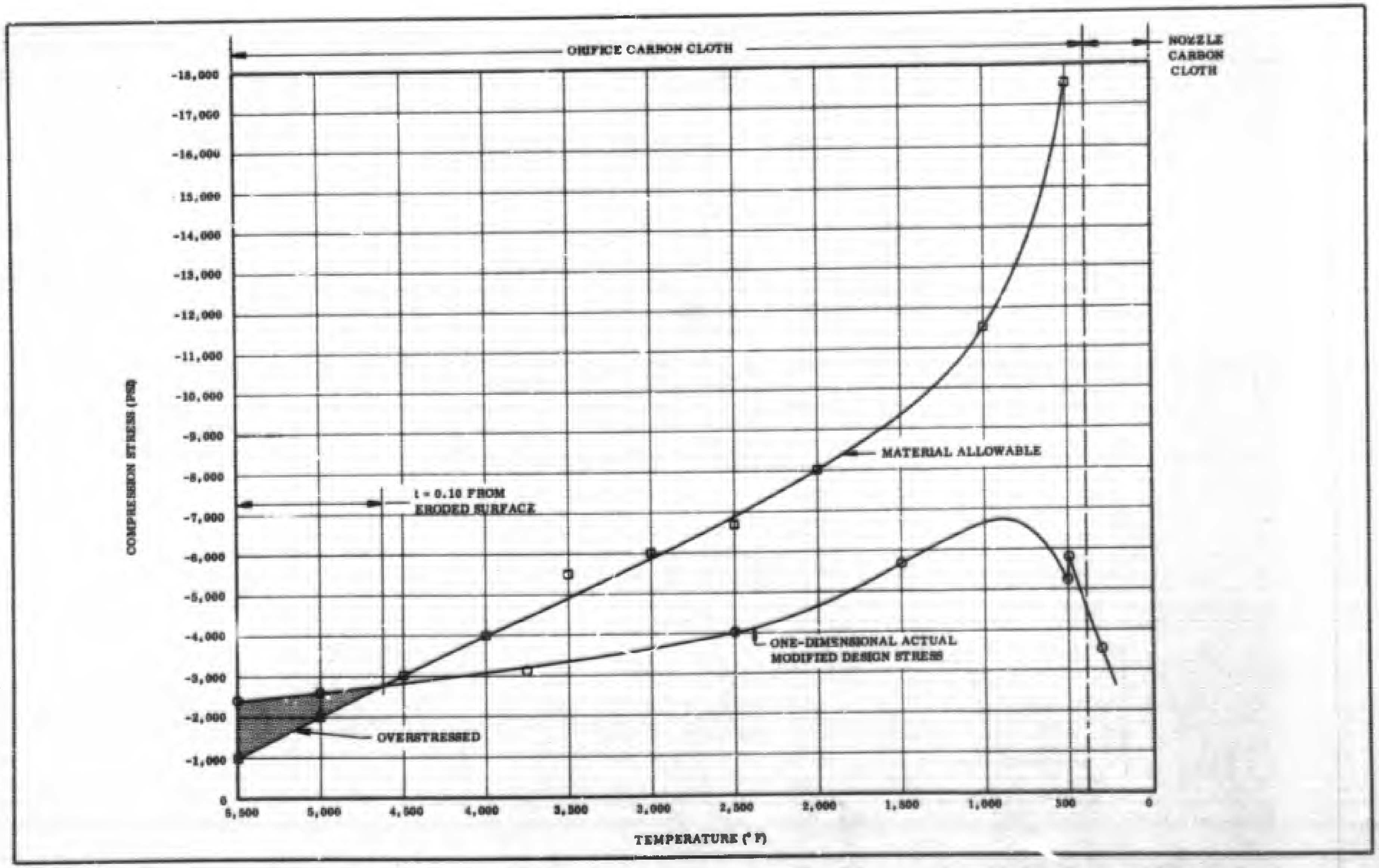

Figure 210. Modified Design, Overstressed Material, Section A-A at 25.1 Sec

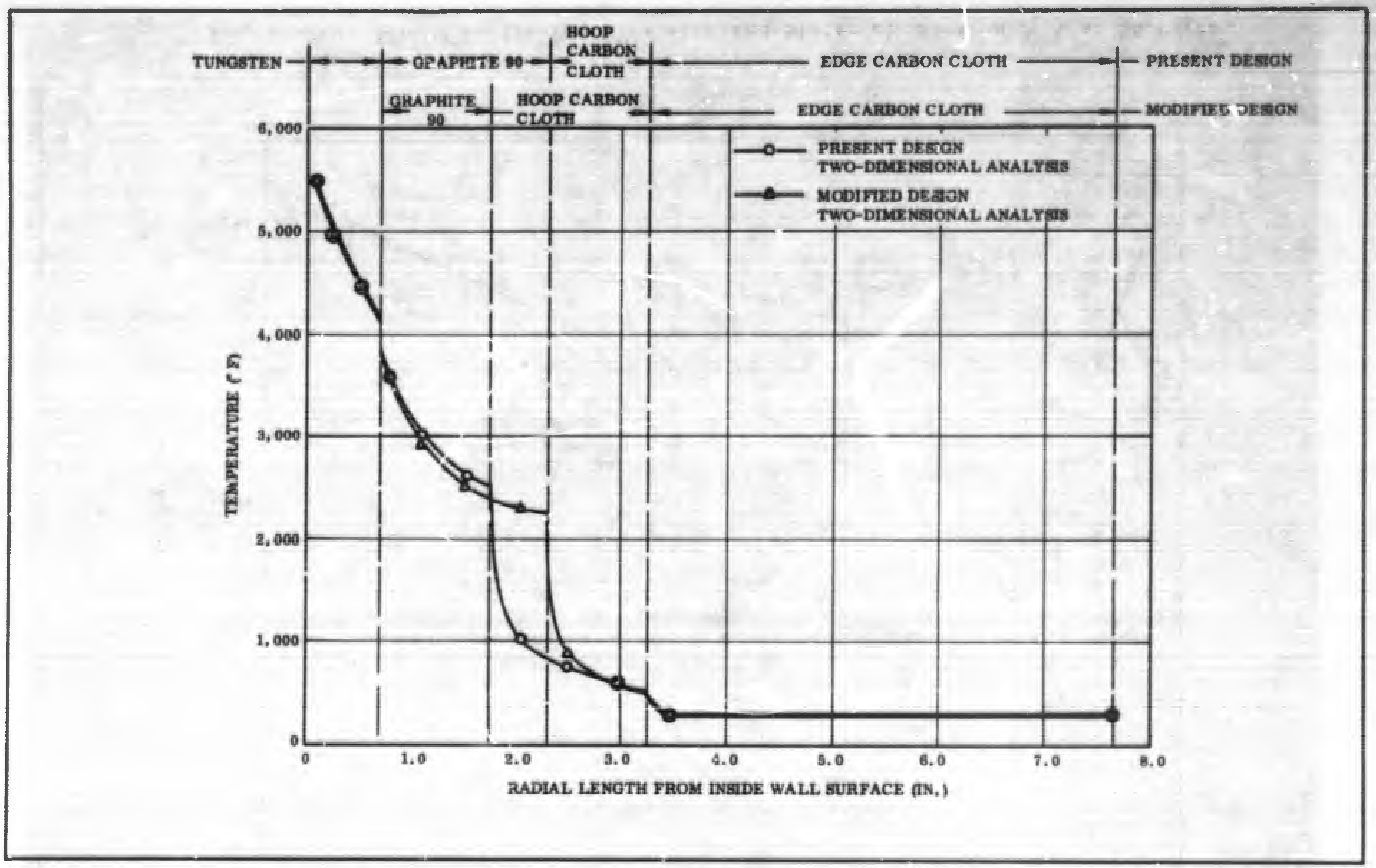

Figure 211. Present and Modified Orifice Design, Temperature Profile, Section B-B at 25.1 Sec

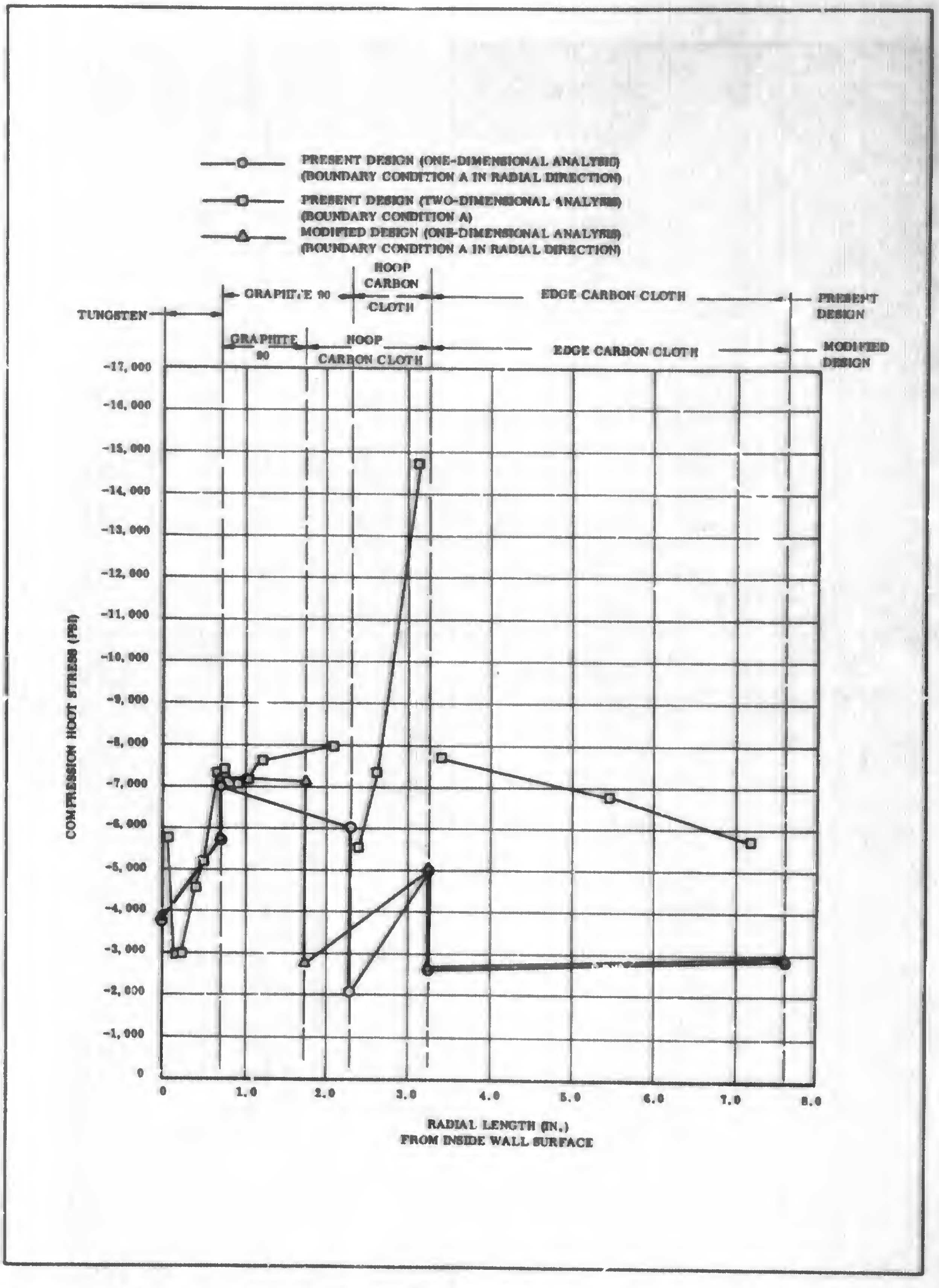

Figure 212. Present and Modified Orifice Design, Hoop Stress Profile, Section B-B at 25.1 Sec

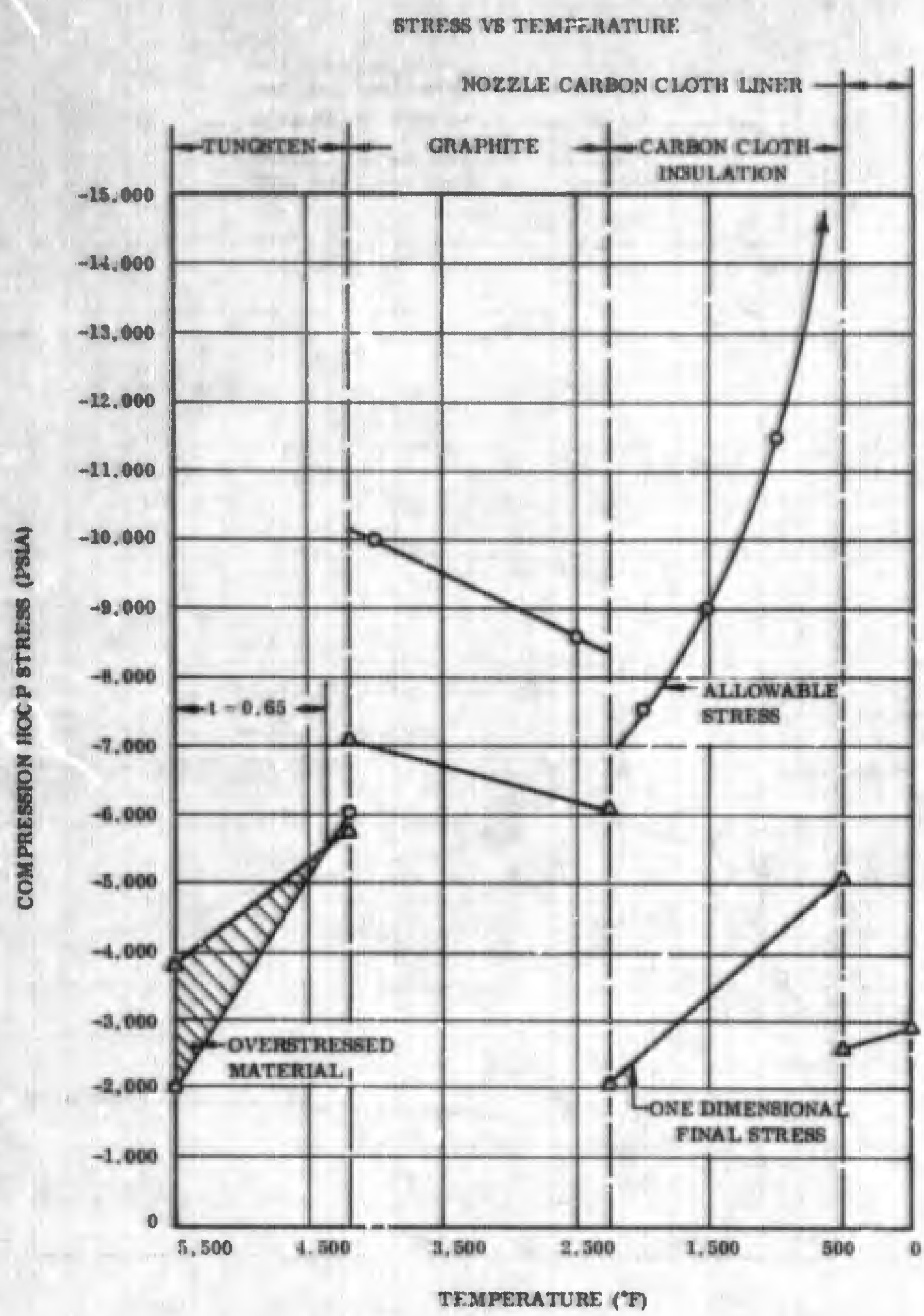

Figure 213. Present Design, Overstressed Material, Section B-B at 25.1 Sec

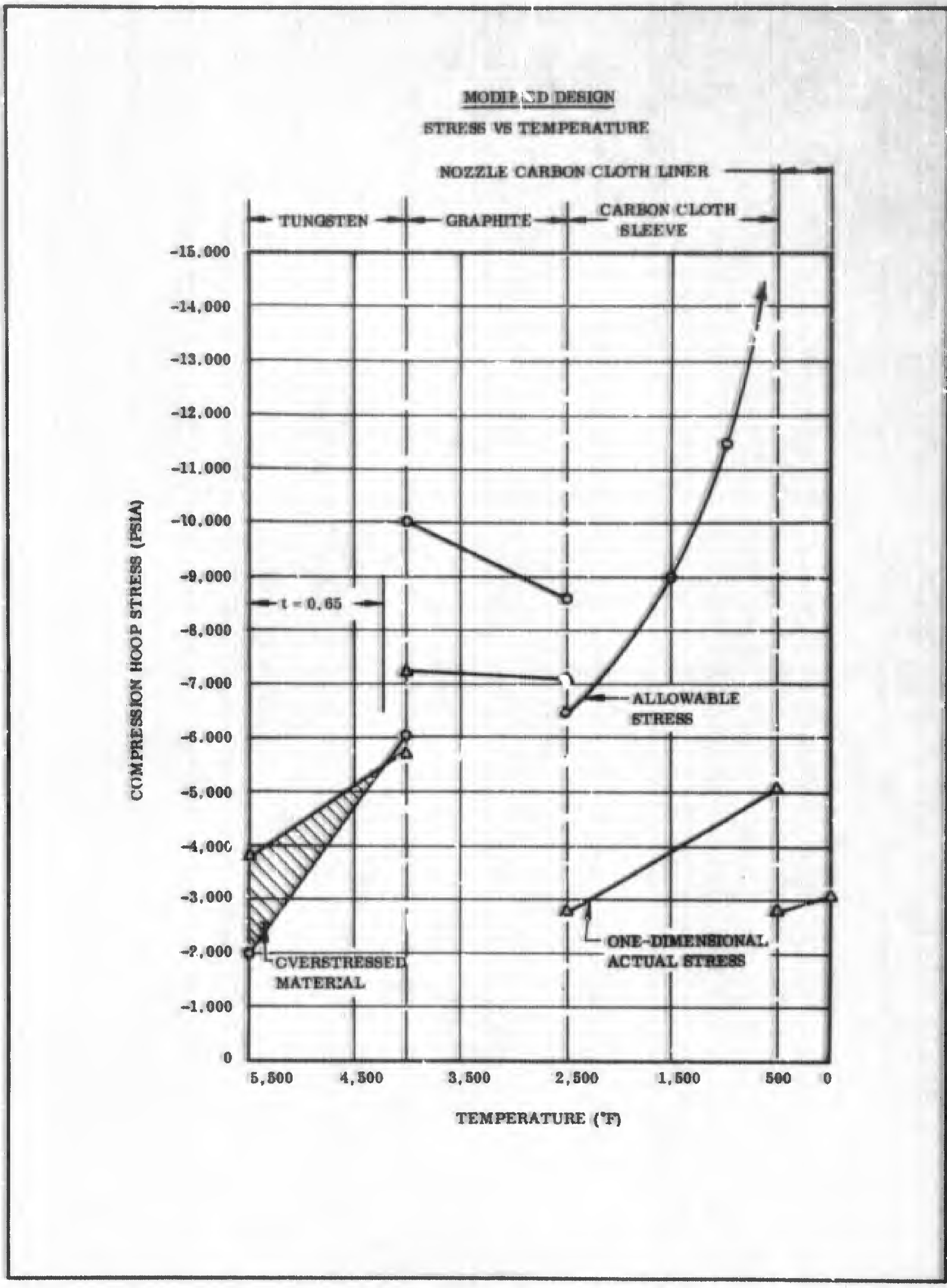

Figure 214. Modified Design, Overstressed Material, Section B-B at 25.1 Sec

Unclassified

Security Classification

DOCUMENT CONTROL DATA - R & D

(Security classification of title, body of abstract and indexing annotation must be entered when the overall report is classified)

1. ORIGINATING ACTIVITY (Corporate author) Thiokol Chemical Corporation Wasatch Division P.O. Box 524 Brigham City, Utah 84302	2a. REPORT SECURITY CLASSIFICATION Confidential 2b. GROUP IV

3. REPORT TITLE

PROGRAM FINAL REPORT, HOT GAS SECONDARY INJECTION THRUST VECTOR CONTROL DEMONSTRATION PROGRAM VOLUME II

4. DESCRIPTIVE NOTES (Type of report and inclusive dates)

Final Report February 1966 thru September 1968

5. AUTHOR(S) (First name, middle initial, last name)

Carver G. Kennedy, Manager, Large Motor Programs
Roy T. Minert, Project Engineer
D. Morley Cox, Valve Engineer

6. REPORT DATE	7a. TOTAL NO. OF PAGES	7b. NO. OF REFS
January 1969	1,084	None

8a. CONTRACT OR GRANT NO. AF 04(611)-11408 b. PROJECT NO. 623A	9a. ORIGINATOR'S REPORT NUMBER(S) 1268-20216
c. d.	9b. OTHER REPORT NO(S) (Any other numbers that may be assigned this report) TC5-163-12-8

10. DISTRIBUTION STATEMENT

This document is subject to special export controls and each transmittal to foreign governments or foreign nationals may be made only with prior approval of [redacted].

11. SUPPLEMENTARY NOTES None	12. SPONSORING MILITARY ACTIVITY Headquarters Air Force Flight Test Center Air Force Systems Command Edwards Air Force Base, California

13. ABSTRACT

This program was established by the Air Force and Thiokol Chemical Corporation to design, develop, and demonstrate a hot gas secondary injection thrust vector control system (HGSITVC) for large solid propellant rocket motors. The program was initiated in February 1966. Phase I of the program was the design, analysis, and optimization of a 156 in. diameter motor HGSITVC system. The data from this baseline design was used to design four test pintle valves for demonstration on 65 in. diameter test motors. Phase II consisted of designing a four valve, 120 in. diameter motor HGSITVC system using the basic designs and design data developed under Phase I. The 120 in. diameter test motor demonstrated four full scale 156 in. diameter motor pintle valves. The 156 in. diameter motor uses 16 pintle valves of the design tested. OK